Mineralogy, geochemistry and microfacies of late Quaternary periplatform sediments: Carbonate export cycles and secondary processes - Sanganeb Atoll and Abington Reef, Sudan, Central Red Sea

Mineralogie, Geochemie und Mikrofazies spätquartärer Periplattformsedimente: Karbonatexportzyklen und sekundäre Prozesse - Sanganeb Atoll und Abington Riff, Sudan, Mittleres Rotes Meer

Dissertation
zur Erlangung des Doktorgrades
der Mathematisch-Naturwissenschaftlichen Fakultät
der Christian-Albrechts-Universität
zu Kiel

vorgelegt von
Peter Emmermann

Kiel 2000

Referent/in: .....

Koreferent/in: .....

Tag der mündlichen Prüfung .....

Zum Druck genehmigt: Kiel, den .....

Der Dekan .....

ABSTRACT

Variations in carbonate production and sediment export of Sudanese off-shore reefs were studied in response to late Quaternary eustatic sealevel changes in the Red Sea.

A set of sediment cores obtained from the Sudanese shelf in the vicinity of Sanganeb Atoll and Abington Reef was analysed for glacial-interglacial variations of shallow-water input in the periplatform sediments that enclose the off-shore reefs in a present-day waterdepth of about 500 to 800 meters. The periplatform record reaches back to marine isotope stages 4 to 6 and all cores show the last glacial-interglacial cycle. Aragonite/calcite-ratios and strontium content of the periplatform sediments were analysed being excellent proxies for shallow-water export variations. In addition, the grainsize and component distribution patterns of the periplatform sediments were analysed and compared to the mineralogical data in order to separate sediment input variations from secondary processes like dissolution and precipitation of metastable carbonates at the seafloor.

The periplatform sediments are rather uniform and consist of a greenish-grey, quartz- and bio-detritic, foraminifer- and pteropod-bearing, nanno-ooze, which in proximal cores contains shallow-water calciturbidites.

During the last glacial marine isotope stage 2 (IS 2) and the following deglaciation this standard type of periplatform sedimentation was interrupted by submarine lithification (23,000-13,000 ^{14}C-years) and sapropel formation (13,000-8,500 ^{14}C-years). The last glacial eustatic sealevel lowstand caused a restriction of water-mass exchange between the Indian Ocean and the Red Sea. Accompanied by high evaporation rates during a predominantly arid climate (NE-monsoon) the salinities of Red Sea surface- and bottom-waters rose to values over 50‰. These high salinities restricted marine biota and led to scarcity or absence of planktic foraminifers and coral reefs vanished from the Red Sea. Diminished biogenic carbonate production was replaced by inorganic carbonate precipitation which was favoured by high salinities and reduced pelagic and shallow-water input. Stable oxygen isotopes and inorganic aragonite precipitation reached a maximum that coincides with highest bottom-water salinities of 57.5‰ at 14,480±110 ^{14}C-AMS years. This maximum coincided with the eustatic sealevel lowstand in the Red Sea and the Western Indian Ocean at about 15,000 ^{14}C-years, which corresponds to approximately 18,000 calendar years.

During the pase of submarine lithification the precipitation mode switched from an early phase of Mg-calcite and aragonite precipitation to a predominance of aragonite since 19,540±130 ^{14}C-AMS years, which points to progressive basin restriction in phase with sealevel lowering. The frequent alteration of lithified and unlithified layers within the lithified sequence was caused by terrigenous input variations. In the non-lithified layers a higher detritic input prevented carbonate precipitation and cementation.

Sapropel formation took place between 13,000 and 8,500 ^{14}C-years on the Sudanese shelf and terminated the lithification process and the hypersaline conditions of bottom- and surface-waters as shown by a significant decrease in oxygen isotope values of the lithified sediments and the sudden occurrence of planktic foraminifers. The deglaciation period in the Red Sea is marked

by a pluvial phase which led to stagnation of bottom-waters and a higher input of organic matter of terrestrial sources from the Sudanese hinterland, which is clearly recorded by an increased quartz content. The development of a pycnocline and the high input of organic matter caused oxygen depletion which led to the formation of a sapropel and increased aragonite preservation as shown by the unusual preservation spike in the periplatform record between 13,000 and 8,500 ^{14}C-years.

Except for the previously breaks in periplatform sedimentation it was shown to some extend that the overall late Quaternary shallow-water sediment export pattern varies in tune with glacio-eustatic sealevel variations as proposed by the highstand shedding theory (Schlager & James, 1978; Schlager *et al.*, 1994). Variations of aragonite/calcite-ratios and strontium-content in the periplatform sediments record the shallow-water export variations of the reefs but the signal is obscured by post- and syndepositional processes in concert with climatic and hydrologic anomalies of the nearly isolated Red Sea basin.

However, for the Holocene sealevel rise it was shown that highest shallow-water export is in phase with the flooding of the old Pleistocene reef structures at about 8,000 years BP. The significant increase in the accumulation rates of aragonite and strontium mark the onset of prolific reef growth and sediment export close to the end of the Holocene sealevel rise. This is also confirmed by a significant increase of the total reef growth area calculated for Sanganeb Atoll after the flooding of the Pleistocene reef surfaces which lie in 20 to 25 meter below present sealevel (mbps). The simulation of flooded reef areas at Sanganeb Atoll also showed that flooding and exposure of the inner lagoon, which reaches down to a present-day waterdepth up to 50 mbps has an important influence on carbonate production, whereas reef growth on submarine terraces has no significant impact on the total carbonate export because the areas are too small to produce significant amounts of sediment when compared to the total reef area.

A generally increased shallow-water sediment export during the Holocene is also shown by bulk sedimentation rates which are 1.5 to 2 times higher than glacial values, which is in the range of glacial-interglacial sediment export variations in the Bahamas.

Glacial-interglacial sediment-export variations in the Sudanese periplatform sediments are also shown by grainsize and component distribution patterns. During the Holocene the input of fine-grained aragonite dominates while during the glacial isotope stage 3 (IS 3) more coarse grained shallow-water components are found in the periplatform sediments. This points to (1) prolific reef growth and sediment export during IS 3 at Sanganeb Atoll and (2) to a glacial-interglacial shift in shallow-water carbonate production. During the Holocene sealevel highstand more fine grained aragonite was produced in the lagoon, while during glacial lowstands (IS 3) benthic carbonate production was limited to the outer slopes when the inner platform became exposed resulting in the export of relative coarse grained sediment.

Although coral reefs vanished from the Red Sea during marine isotope stage 2 (IS 2) the frequency of shallow-water derived calciturbidites was high during this phase as well as during IS 3. Radiocarbon dated scleractinian fragments of the turbidites are about 5,000 to 6,000 years older when compared to the stratigraphic position of the turbidite within the periplatform sequence. The stratigraphic position of the calciturbidites shows that older shallow-water sediments were re-

sedimented during the sealevel fall between isotopic event 3.3 (53,000 SPECMAP-years) and the sealevel lowstand at 14,840±110 ^{14}C-AMS years. Thus, the ages of the scleractinian fragments give evidence for shallow-water carbonate production and reef growth during IS 3 and possible early IS 2 up to 21,480±180 ^{14}C-AMS years at Sanganeb Atoll. Furthermore it shows, that a high frequency of calciturbidites is also found during sealevel fall and lowstands and that „highstand bundling“ as found in the Bahamas is not the case at Sanganeb Atoll.

As mentioned above the glacial-interglacial sediment export pattern in the Red Sea is obscured by post- and syn-depositional processes. Better preservation of aragonite as observed during the pluvial phase of the last deglaciation, which led to sapropel formation on the Sudanese shelf is also found during IS 3. Peaks in the aragonite and TOC curve coincide with decreased δ^{18}O-values and indicate short-termed preservation events in concert with monsoonal climate variations. In analogy to the Arabian Sea it was shown for the Red Sea that those variations are connected to high-latitude temperature oscillations. More humid phases (SW-monsoon) led to better aragonite preservation in analogy to the situation during the deglaciation.

The aragonite/calcite-ratios of the periplatform sediments are clearly altered by inorganic precipitation of aragonite during IS 2 and Mg-calcite during IS 4. Inorganic precipitation of Mg-calcite during IS 4 was favoured by increased salinities of up to 49‰ and reduced input of shallow-water components due to the limited occurrence or even absence of reefs. The frequent occurrence of micro-peloidal fabrics in the glacial periplatform sediments point to an early stage of Mg-calcite cementation. Mg-calcite and aragonite curves run anti-cyclic in the Sudanese periplatform record which shows that precipitation and input of Mg-calcite has an important influence on the aragonite/calcite-ratios.

Aragonite percentages during the last interglacial highstand(s) and the Holocene do not exceed values found during IS 3, which shows a much better preservation of aragonite during glacials and higher aragonite dissolution during interglacials in the Red Sea out of phase to the sealevel controlled export cycles. This is opposite to the patterns found around the Bahamas and in the Caribbean where aragonite dissolution works in phase with sediment export. The different patterns reflect the global aragonite dissolution cycles of the Indo-Pacific region, where dissolution is increased during interglacials, and of the Atlantic Ocean with its higher dissolution during glacials.

Calcite (LMC) variations in the Sudanese periplatform sediments mainly record variations in plankton productivity and reach their maxima during or at the end of each sealevel highstand. Lowest LMC percentages are found during sealevel lowstands when basin restriction led to increased salinities in the Red Sea and diminished the plankton assemblages. The general increase of LMC with depth in core points to increased replacement of meta-stable carbonate minerals by calcite, which also leads - in concert with higher dissolution - to reduced aragonite and Mg-calcite percentages during last interglacial highstands when compared to the Holocene.

KURZFASSUNG

In der vorliegenden Arbeit wurden die Auswirkungen spätquartärer Meerespiegelschwankungen im Roten Meer auf die benthische Karbonatproduktion und den Sedimentexport der Riffe vor der sudanesischen Küste untersucht.

Vom tiefen Schelf des Sudan wurden in der näheren Umgebung des Sanganeb Atolls und des Abington Riffs Sedimentkerne aus einer Wassertiefe von 500-800 m entnommen um in den sogenannten Periplatformsedimenten glazial-interglaziale Variationen im Flachwassereintrag zu untersuchen. Das Alter der Sedimente reicht bis in die Isotopenstadien 4 bis 6 zurück, womit jeder Kern mindestens einen vollen glazial-interglazialen Zyklus beinhaltet. Aragonit/Kalzit-Verhältnisse und Strontiumgehalte der Periplattformsedimente sind ideale Anzeiger für den Flachwassereintrag und wurden im Gesamtsediment und in der Feinfraktion gemessen. Zusätzlich wurden Korngrößen und Komponentenspektrum der Periplattformsedimente mit den mineralogisch-geochemischen Daten verglichen um das sedimentäre Eintragsignal von sekundären Prozessen wie z.B. Lösung und Ausfällung von metastabilen Karbonatmineralen am Meeresboden zu trennen.

Die Periplattformsedimente sind relativ einheitlich und bestehen aus einem grau-grünen, quarz- und bio-detritischen Nannofossilschlamm mit planktischen Foraminiferen und Pteropoden. In den Periplattformsedimenten der proximalen Kerne sind aus dem Flachwasserbereich stammende Kalziturbidite eingelagert. Die „normale“ Periplattformsedimentation auf dem sudanesischen Schelf wurde durch außergewöhnliche palaeozeanographische Ereignisse während des letzten Glazials und während des anschließenden Meerespiegelanstieges unterbrochen, die zur submarinen Lithifizierung (ca. 23.000 - 13.000 ^{14}C Jahre) und zur Sapropelbildung (ca. 13.000 - 8.500 ^{14}C Jahre) führten. Der letzte glazio-eustatische Meeresspiegeltiefstand führte zu einer verstärkten Einschränkung des Wassermassenaustausches zwischen dem Roten Meer und dem Indischen Ozean durch die geringe Wassertiefe über der Hanish-Schwelle, der einzigen Verbindung mit dem offenen Ozean. Der eingeschränkte Wassermassenaustausch bei gleichzeitig sehr hohen Verdunstungsraten in einer vollariden Phase (NE-Monsun) führte zu Salzgehalten des Oberflächen- und Bodenwassers von über 50‰. Die Folge dieser hohen Salzgehalte war eine stark eingeschränkte marine Faunengemeinschaft, in der planktische Foraminiferen fast vollständig fehlten und kein Riffwachstum mehr möglich war. Dadurch kam es zu einer verminderten biogenen Karbonatproduktion, die durch verstärkte anorganische Karbonatbildung kompensiert wurde. Die submarine Karbonatausfällung und Lithifizierung wurde durch geringe Sedimentationsraten und die hohen Salzgehalte des Bodenwassers begünstigt. Schwerste stabile Sauerstoffisotope und das Maximum an anorganischer Aragonitausfällung fallen mit den höchsten Salzgehalten des Bodenwassers von bis zu 57,5‰ zusammen. Dieses Salinitätsmaximum wurde bei 14.840±110 ^{14}C-AMS Jahren erreicht und entspricht der maximalen Isolation des Beckens während des glazialen Meeresspiegeltiefstandes vor ungefähr 15.000 ^{14}C-Jahren (etwa 18.000 Kalenderjahre BP) im Roten Meer und im westlichen Indischen Ozean.

Die mineralogische Zusammensetzung der lithifizierten Karbonate zeigt einen deutlichen

Wechsel zwischen einer frühen Phase in der Mg-Kalzit gemeinsam mit Aragonit ausgefällt wurde und einer späteren Phase, seit 19.540±130 ^{14}C-AMS Jahren, in der die Sedimente überwiegend aus Aragonit bestehen. Dieser Übergang deutet auf eine fortschreitende Einschränkung des Wassermassenaustausches im Zusammenhang mit dem stetig fallenden Meeresspiegel hin. Variationen im siliziklastischen Eintrag führten zum Wechsel zwischen lithifizierten und nicht lithifizierten Intervallen. In Phasen mit erhöhtem siliziklastischen Eintrag wurde die anorganische Karbonatausfällung und die Zementation verhindert, was durch die signifikant erhöhten Quarzgehalte der unlithifizierten Lagen verdeutlicht wird.

Zwischen 13.000 und 8.500 ^{14}C Jahren kam es zur Sapropelbildung auf dem sudanesischen Schelf, womit gleichzeitig die Phase der submarinen Lithifizierung abgeschlossen wurde. Die extrem hohen Salzgehalte des Boden- und Oberflächenwassers gingen drastisch zurück, was durch einen signifikanten Rückgang der Sauerstoffisotopenwerte in den lithifizierten Sedimenten und das Auftreten planktischer Foraminiferen belegt wird. Im Roten Meer ist die Deglaziation durch eine humide Phase gekennzeichnet, die zu stagnierenden Bodenwasserbedingungen und einem erhöhten Eintrag von organischem Material vom sudanesischen Hinterland führte, der zusätzlich durch erhöhte Quarzgehalte bestätigt wird. Die Ausbildung einer Pycnokline und der gleichzeitig hohe Gehalt an organischem Material führte zur Entwicklung einer Sauerstoff-Minimum-Zone im Bodenwasser, die zur Bildung des Sapropels und gleichzeitig zu außergewöhnlich guten Erhaltungsbedingungen für Aragonit führten. Die besonders gute Aragoniterhaltung ist in den Sedimenten des sudanesischen Schelfs in Form eines deutlichen Aragonitmaximums zwischen 13.000 und 8.500 ^{14}C-Jahren erkennbar.

Abgesehen von den oben dargestellten hydrologischen Besonderheiten, die zur Unterbrechung der normalen Periplattformsedimentation führten, konnte in dieser Untersuchung belegt werden, daß die generellen Muster im meerespiegelabhängigen Sedimentexport aus dem Flachwasser nach dem Prinzip des „highstand shedding“ (Schlager & James, 1978; Schlager *et al.*, 1994) in den Periplatformsedimenten des sudanesischen Schelfs überliefert wurden. Allerdings wurden die Variationen in den Aragonit/Kalzit-Verhältnissen und den Strontiumgehalten in den Periplatformsedimenten deutlich von post- und synsedimentären Prozessen überlagert, die im Zusammenhang mit klimatischen und hydrologischen Besonderheiten des nahezu isolierten Roten Meeres stehen.

Außergewöhnlich gut ist die Geschichte des Flachwasserexports der Riffe für das Holozän überliefert. Der höchste Sedimentexport am Sanganeb Atoll tritt gleichzeitig mit der Überflutung der alten pleistozänen Riffstructuren im Zuge des holozänen Meeresspiegelanstieges vor ungefähr 8.000 Jahren auf. Der signifikante Anstieg der Aragonit- und Strontiumakkumulationsraten markiert den Beginn von ausgedehntem Riffwachstum und Sedimentexport gegen Ende des holozänen Meeresspiegelanstiegs im Roten Meer. Dieses Produktions- und Exportmaximum wird ebenfalls in der Berechnung der überfluteten Riffoberflächen, während verschieder Meeresspiegelstände, am Sanganeb Atoll sichtbar. Ein deutlicher Anstieg in der produktiven Riffoberfläche tritt nach der Überflutung der pleistozänen Riffstrukturen auf, die heute etwa 20 m unter dem Meeresspiegel liegen. Die Berechnung der produktiven Oberflächen hat gleichzeitig gezeigt, daß die Überflutung

und das Trockenfallen der inneren Lagune des Sanganeb Atolls eine entscheidende Rolle im Karbonatbudget und im Sedimentexport spielen. Dem gegenüber spielt das Riffwachstum auf submarinen Terrassenan den steilen Hängen nur eine untergeordnete Rolle, da die Flächen im Verhältnis zur gesamten Riffoberfläche unbedeutend klein sind.

Ein generell erhöhter Flachwassersedimentexport während des Holozän ist außerdem durch die deutlich erhöhten Sedimentationsraten erkennbar, die etwa 1.5 bis 2 mal höher sind als die glazialen Werte. Ähnliche glazial-interglazial Schwankungen der Sedimentationsraten wurden in den Periplattformsedimenten der Bahamas gefunden.

Glazial-interglaziale Schwankungen im Sedimentexport aus dem Flachwasser konnten auch durch Korngrößen- und Komponenten-Verteilungsmuster in den Periplattformsedimenten des sudanesischen Schelfs gezeigt werden. Während des Holozäns überwog der Eintrag von feinkörnigem Aragonit, wohingegen in den glazialen Periplattformsedimenten, die während Isotopenstadium (IS) 3 abgelagert wurden, mehr grobkörnige Komponenten aus dem Flachwasser auftreten. Damit konnte gezeigt werden, daß (1) Riffwachstum und benthische Karbonatproduktion während IS 3 am Sanganeb Atoll stattfand und (2) daß ein signifikanter Unterschied in der Karbonatproduktion der Riffe zwischen glazialen Tiefständen und interglazialen Hochständen bestand. Während des holozänen Meeresspiegelhochstands wurde deutlich mehr feinkörniges, aragonitisches Material in der Lagune produziert, während bei niedrigerem Meeresspiegel im Glazial (IS 3) die benthische Karbonatproduktion überwiegend an den äußeren Hängen des Sanganeb Atolls stattfand, besonders in Phasen in denen die Basis der Lagune über dem Meeresspiegel lag.

Trotz der stark eingeschränkten bis gänzlich fehlenden benthischen Karbonatproduktion durch die Flachwasserriffe währen der hypersalinen Phase des Vollglazials (IS 2) ist die Häufigkeit von Kalziturbiditen hier, wie auch während IS 3, sehr hoch. Altersdatierungen (^{14}C-AMS) an Scleractiniern aus den Turbiditen zeigten, daß sie etwa 5.000-6.000 Jahre älter sind als es ihre stratigraphische Position innerhalb der Periplattformsequenz zeigt. Damit konnte belegt werden, daß es sich bei dem geschütteten Material um ältere, umgelagerte Flachwasssersedimente handelt, die während des Meeresspiegelrückgangs zwischen Isotopen-Event 3.3 (53.000 SPECMAP-Jahre) und dem glazialen Tiefstand vor 14.840±110 ^{14}C-AMS Jahren geschüttet wurden. Das Alter der Scleractinier ist ein weiterer Beweis für benthische Karbonatproduktion am Sanganeb Atoll während IS 3 und möglicherweise bis ins frühe Stadium 2 (21.480±180 ^{14}C-AMS Jahre). Weiterhin zeigt das gehäufte Auftreten von Kalziturbiditen während des Meeresspiegelrückgangs, daß am Sanganeb Atoll kein deutliches „highstand-bundling“ wie in den Bahamas auftritt.

Das glazial-integlaziale Muster im Sedimentexport des Roten Meeres wird von verschiedenen post- und synsedimentären Prozessen überlagert. Phasen besserer Aragoniterhaltung wie sie beispielsweise während der Sapropelbildung auf dem Schelf beobachtet wurden, traten ebenfalls während IS 3 auf. Maxima in den Aragonit- und TOC-Kurven korrelieren deutlich mit leichteren Sauerstoffisotopenwerten, die kurzfristige Erhaltungsereignisse im Zusammenhang mit monsungesteurten Klimaschwankungen anzeigen. In Analogie zur Arabischen See wurde auch für das Rote Meer gezeigt, daß diese Schwankungen mit Temperaturänderungen der höheren Breiten in Verbindung stehen. Humidere Phasen führten zu einer besseren Aragoniterhaltung in Analogie

zur Situation während der Deglaziation.

Zusätzlich sind die Aragonit/Kalzit-Verhältnisse durch die anorganische Ausfällung von Aragonit während IS 2 und Mg-Kalzit währen IS 4 überlagert. Die anorganische Ausfällung von Mg-Kalzit während IS 4 wurde begünstigt durch hohe Salzgehalte bis zu 49‰ und reduzierten Flachwassereintrag in einer Phase eingeschränkter benthischer Karbonatproduktion. Möglicherweise fand in dieser Phase kein echtes Riffwachstum statt. Das gehäufte Auftreten von mikropelloidalen Strukturen in den glazialen Periplattformsedimenten belegt eine frühe Phase der Mg-Kalzit Zementation. Mg-Kalzit- und Aragonitkurven der Periplattformsedimente zeigen einen signifikant antiparallelen Verlauf und es ist klar erkennbar, daß Eintrag sowie Ausfällung von Mg-Kalzit einen entscheidenden Einfluß auf die Aragonit/Kalzit-Verhältnisse hat.

Die Aragonitgehalte der Periplattformsedimente des letzten Interglazials und des Holozäns sind nicht erhöht gegenüber IS 3, was einer deutlich besseren Aragoniterhaltung in Glazialen und einer verstärkte Aragonitlösung in Interglazialen entspricht. Dies wiederum stellt ein gegenläufiges Muster zum meeresspiegelgesteuerten Sedimentexport dar. Das Lösungs/Erhaltungs Muster des Roten Meeres ist gegenläufig zu dem der Karibik und den Bahamas, wo Lösung und Erhaltung von Aragonit in Phase zum Sedimentexport auftreten. Die Unterschiede zwischen den Meeresgebieten spiegeln Unterschiede in den globalen Aragonitlösungszyklen wider. Im Indo-Pazifischen Raum ist die Aragonitlösung in Interglazialen deutlich erhöht, während im Atlantik eine verstärkte Lösung in Glazialen auftritt.

Die Variationen im Kalzitgehalt spiegeln das Signal der Planktonproduktivität wider und erreichen Maxima während oder gegen Ende der Meeresspiegelhochstände. Während glazialer Tiefstände war die Planktonproduktivität aufgrund der hohen Salzgehalte am geringsten. Die generelle Zunahme im Kalzitgehalt mit der Kerntiefe zeigt eine zunehmende Umwandlung metastabiler Karbonatminerale in Kalzit. Dies führte letztendlich, neben der erhöhten Lösung, auch zur Abnahme von Aragonit und Mg-Kalzit im letzten Interglazial im Vergleich zum Holozän.

ACKNOWLEDGEMENTS

At this place I would like to thank all the people who supported me and my work and helped to complete this thesis in so many different ways.

First of all I would like to thank Prof. Dr. Wolf-Christian Dullo for the supervision of my thesis and for all the support he gave me. I am very grateful to Mr. Dullo for the interim financial help he gave me with the position in the ECOMAR project and for the opportunity to work at the University of Sydney. I am very thankful to Dr. John Reijmer for all his advice, support and help during the time I was working at GEOMAR and the continuous collaboration during the second phase of my thesis in Pfinztal. John´s door was always open and he found as much time as needed to discuss results and various aspects of the study.

Thanks to Dr. Thomas Brachert who supported us during the cruise in the Red Sea and who helped with many of the lithologic descriptions on board and other scientific and practical work. Furthermore, he prepared the samples of the Marion Dufresne core and put those to our disposal. Besides, I thank Thomas for his steady interest in the project and for the intensive discussions we had about the „hard layers“ during my visit in Mainz. Finally, I would like to thank him for the intensive review on this thesis.

At this point I would also like to thank the crew of RV Meteor, who did the coring and supported us with technical help whenever needed. Furthermore, I would like to thank Prof. Dr. Peter Stoffers, who was the scientific chief of this cruise (M31/2) for the good co-operation and the technical and scientific support by all the members of his working group. I also want to thank all other scientists and students on board for their help.

Next I like to thank Dr. Alexandra Isern for the excellent collaboration at the Sydney University and for all the support she gave me during my stay and even later on. Under Alexandra’s supervision we did all the isotope- and XRD-measurements of the sediments from lithified interval. The discussion of the data together with Alexandra had a great influence on the interpretation of the submarine lithification in the Red Sea as suggested in this thesis. At this point I would also like to say thank you for the hospitality and help I received by all the other people I met at Sydney University, especially my college and friend Alexander Kritzky and my flat-mates at Boyce Street, were I lived.

I am grateful for the help of many people at GEOMAR but it is impossible to list them all at this place. First of all, I thank all the members of the „carbonate and reef“ group at GEOMAR, especially Florian Böhm, Rebecca Rendle, Andrea Perl, Dagmar Fraude, Jens Zinke and „Dr. Diierk“ Blomeier for a lot of intensive and fruitful discussions which often inspired me and had a strong input on my thesis. I want to express special thanks to Nils Andresen, who was doing a similar

study in the Caribbean. By the comparison of our results Nils and I had an extensive exchange of ideas and a permanent mutual feedback. Furthermore, I thank Nils for preparing and measuring the XRD- standards.

Besides the people of our working group, I would like to thank Claudia Willamowski, Sven-Oliver Franz, and Holger Cremer who also did their PhD in the Palaeoceanographic department at GEOMAR for their fellowship and help.

Very special acknowledgements I have to give to all the HIWIS and technical staff members at GEOMAR. I am very grateful to my long-lasting HIWI Simon Sorge who did most of the sample preparation, grainsize analysis, and foraminifer picking for the isotope measurements with greatest care and precision. But I also have to thank all the other HIWIS that worked for the project from time to time. At this point, I would also like to thank Sven Roth for doing the final spell- and layout-check of the manuscript.

I am thankful to Jutta Heinze and Dr. Heinz Lange, who were in charge of the XRD-machine at GEOMAR. They helped a lot and gave a good introduction into sample preparation, measuring procedure and interpretation of the diffractograms. I also want to thank Kerstin Wolf who did the XRF-measurement at the department of vulcanology at GEOMAR.

Next to the GEOMAR staff members I would specially like to thank two employees of „GTG“, Dagmar Rau, who prepared the thin-sections and Albert von Doentimchen, who was in charge for the SEM-device. He gave me a very good introduction and continuos technical assistance during my work with the SEM.

Additionally, I would like to thank Dr. Michael Joachimski from the University of Erlangen, who did most of the $\delta^{18}O$-analysis.

I want to express my very special thanks to Prof. Dr. Peter Grootes, the head of the Leibniz laboratory at Kiel, where the radiocarbon datings of the „hard layers“ and the turbidites were made. I thank Mr. Grootes for the time he spent with me helping to establish a reliable age model of the lithified interval and for the intensive discussions we had about the problem of submarine lithification in the Red Sea.

Finally I am very grateful to my parents, my wife Katrin and my son Paul for their interest in my work and their loving support, especially over the last two years which have not always been easy.

Financially, this study was supported by the German Science Foundation (DFG Du 129/10).

TABLE OF CONTENT

CHAPTER A: INTRODUCTION AND STUDY AREA

A.1 Introduction

The Sudanese deep shelf in the central part of the Red Sea is a unique site to study sedimentation in the vicinity of coral reefs and shallow-water carbonate platforms during the late Quaternary under extreme paleoceanographic and climatic conditions. The Red Sea is a young, narrow, land-locked marine rift-basin. Seafloor spreading is active in the axial zone and extentional tectonics and salt diapirism control the overall hydrography and the morphology of the reef-structures (Dullo & Montaggioni, 1998). The Red Sea basin is almost isolated and water mass exchange with the Indian Ocean is restricted by the shallow sill at Bab el Mandeb (Fig. A-2). Therefore, the signal of late Quaternary eustatic sealevel changes is amplified by glacial-interglacial salinity variations in the Red Sea which are clearly enhanced compared to open marine environments (Locke & Thunell, 1988; Almogi-Labin *et al*., 1991, 1998; Hemleben *et al*., 1996; Geiselhardt, 1998).

A set of sediment cores was obtained from the deep shelf in the vicinity of two isolated atoll-like reef-structures, Sanganeb Atoll and Abington Reef. The recovered sediments reach back to marine isotope stages 4 to 6 and predominantly consist of rather uniform greenish-grey periplatform ooze, with only a few intercalations of reef derived calciturbidites in the cores proximal to the reefs. The mineralogical, geochemical and microfacies composition of the periplatform sediments and reef derived calciturbidites were analysed in order to reconstruct temporal and spatial variations in the sediment production and export of the reefs in the Red Sea with respect to late Quaternary sealevel changes. It is assumed, that periplatform sediments generally record glacial-interglacial sealevel variations as a result of changes in the sediment production and export (highstand shedding, Fig. A-1) (Schlager & James, 1978; Boardman *et al.*, 1986; Reijmer *et al.*, 1988; Schlager *et al*., 1994). It is also possible that variations in the periplatform records are altered by secondary processes, like dissolution or precipitation of metastable carbonates on the seafloor in tune with glacial-interglacial hydrologic cycles (Droxler *et al*., 1990; Haddad & Droxler, 1996).

The „normal“ late Quaternary periplatform sedimentation on the Sudanese shelf was interrupted by hydrological anomalies during the last glacial sealevel lowstand (Taviani, 1998c). Restricted water mass exchange with the Indian Ocean and a constant arid climate led to increased salinities (>50 ‰) of surface and bottom waters (Winter *et al.*, 1983; Hemleben *et al.*, 1996). Under such hypersaline conditions marine life was significantly restricted (aplanktonic zone) and organic carbonate production was predominantly replaced by inorganic precipitation of aragonite and Mg-calcite on the seafloor (Brachert, 1996; 1999). In all studied sediment cores from the Sudanese shelf a characteristic about 50 to 100 cm thick interval occurs, in which lithified carbonate layers alternate with unlithified mud. The circumstances that led to submarine lithification and the formation of lithified layers are another focus of this study.

A.1.1 Carbonate sediment export and periplatform sedimentation

At present carbonate production in the shallow-water realm of the Bahamas is higher than the accommodation, which leads to a permanent sediment export by tide-waves, periodic storms, etc. from the shallow-water realm into the adjacent basins (Neumann & Land, 1975). Skeletal grains and non-biogenic components, like peloids and ooids are important constituents of the shallow-water sediments, but the by far largest quantity of sediment exported is cryptocrystalline carbonate mud. It is still not clear how the huge quantity of fine-grained, mostly aragonitic muds are formed in the shallow-water realm. Different modes of formation are discussed: (1) the skeletal disintegration of loosely bound particles like e.g. *Halimeda* plates (Neumann & Land, 1975), (2) physico-chemical precipitation in the water column (Macintyre & Reid, 1992; Milliman *et al*., 1993), (3) mechanical abrasion in high energy environments (Flügel, 1982), (4) bioerosion by boring endoliths and sediment feeders (Emmermann, 1994; Hassan, 1997) and (5) cryptocrystalline precipitation in beachrock and reef cavities (Friedman *et al*., 1974).

In the basins and on the slopes the exported shallow-water components mix with pelagic material to form the so-called periplatform sediments (Schlager & James, 1978). The skeletons of shallow-water organisms and the non-biogenic components predominantly consist of aragonite and Mg-calcite (high-Mg-calcite; HMC), while the shells of most planktic components, like foraminifers and coccolithophorids are composed of calcite (low-Mg-calcite; LMC) (Milliman, 1974; Scholle *et al*., 1983). Periplatform sediments are therefore enriched in aragonite and HMC when compared to a typical pelagic carbonate sediment that is dominated by LMC. It was also shown, that periplatform sediments are enriched in strontium (Boardman *et al*., 1986; Alexander, 1996), which is due to the significantly higher strontium values in most of the aragonitic shallow-water components compared to those in shells of pelagic organisms (Milliman, 1974). In addition, the abundance of shallow-water derived calciturbidites is often higher in the periplatform realm. So, in summary, periplatform sediments are enriched in aragonite, HMC and strontium, exhibit higher sedimentation rates and contain more shallow-water components in comparison to pelagic carbonate sediments.

Periplatform sediments record characteristic glacial-interglacial variations in mineralogy, microfacies, grainsize-distribution, sedimentation rates as well as frequency and composition of turbidites (Schlager *et al*., 1994). It was an important finding that the curves of aragonite/calcite ratios analysed in late Quaternary periplatform sediments from the Bahamas, the Caribbean, the Maldives and the Great Barrier Reef run parallel to the planktic stable oxygen isotope curves, with only small offsets (Droxler & Schlager, 1985; Reijmer *et al*., 1988; Droxler *et al*., 1990; Glaser & Droxler, 1993; Alexander, 1996; Dullo *et al*., 1997; Emmermann *et al*., 1999). In many cases, the aragonite curves even show the same saw-tooth pattern like the $\delta^{18}O$-curves, which clearly demonstrates the link between glacial-interglacial sealevel variations and the composition of periplatform sediments.

Interglacial highstand deposits are enriched in platform derived, fine-grained aragonite (Glaser & Droxler, 1991; Westphal, 1997; Rendle *et al*., in press 2000) with a high strontium content and show increased Mg-calcite values (Droxler *et al*., 1983; Droxler & Schlager, 1985; Boardman *et*

al., 1986; Droxler *et al*., 1990; Glaser & Droxler, 1991; Schlager *et al*., 1994). When compared to glacial lowstands in sealevel the sedimentation rates in these highstand deposits are high. The same holds for the frequency of calciturbidites (highstand bundling: Droxler & Schlager, 1985; Haak & Schlager, 1989). Studies of calciturbidite composition showed that highstand turbidites contain more non-skeletal grains derived from the platform interior, whereas lowstand deposits are enriched in skeletal grains from the reef-rim (Haak & Schlager, 1989; Reijmer *et al*., 1992).

The maximum of benthic carbonate production in reefs and carbonate platforms occurs close to the sealevel, because most organisms are phototrophic (algae) or live in symbiosis with phototrophic organisms like, e.g. scleractinian corals (e.g. Bosscher, 1992). So, in general it can be stated that the amount of carbonate that is produced on a platform is a function of the platform area that lies in the photic zone. The size of the platform area available for shallow-water carbonate production varies with sealevel. During a relative sealevel highstand the whole platform top is flooded, which causes an increased export of shallow-water sediment into the periplatform realm. During sealevel lowstands only parts of the platform or the slopes are flooded, depending on the size and shape of the platform. The smaller surface available to shallow-water carbonate production leads to reduced sediment export and lower aragonite, strontium and HMC content in the lowstand deposits when compared to periplatform sediments that formed during sealevel highstands. This model was named ”highstand shedding” (Fig. A-1) and might explain many of the overall

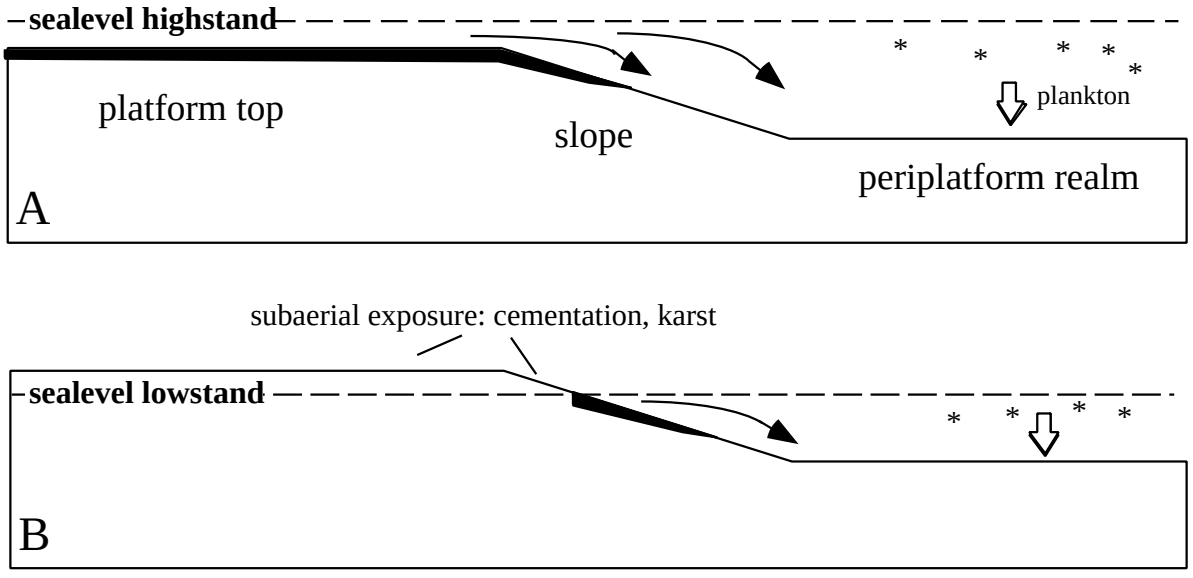

Figure: A-1: Schematic sketch of the highstand shedding model of carbonate systems (Schlager & James, 1978). A: The highstand situation. The platform top is flooded and a large area is available for maximum carbonate production in the photic zone, which causes a high export of shallow-water sediments into the periplatform realm where platform derived components mix with pelagic material. The highstand deposits are enriched in shallow-water derived strontium-rich aragonite and Mg-calcite when compared to lowstand deposits. B: During lowstands in sealevel the platform top and the upper slope are exposed and the area of shallow-water carbonate production is reduced to a small rim along the slope. The exposed carbonates are cemented by freshwater diagenesis within a very short period of time (Dravis, 1996).

glacial-interglacial patterns observed in periplatform sediments in the vicinity of productive carbonate platforms (Droxler & Schlager, 1985; Schlager *et al*., 1994).

But it is still debated if the glacial-interglacial variations are a pure signal of changes in sediment export caused by variations in flooded platform area corresponding to sealevel (Boardman *et al*., 1986; Schlager *et al*., 1994) or if syn- and post-depositional dissolution/preservation and submarine precipitation of metastable carbonates on the seafloor shape or modify the cycles (Droxler *et al*., 1983, 1988, 1990; Droxler & Schlager, 1985). Despite huge differences in size, morphology of the slope and the platform top as well as different modes of carbonate production and mechanisms of sediment export of the individual platforms, all aragonite records show the same characteristic saw-tooth pattern (Droxler *et al*., 1990; Alexander, 1996). In ideal settings like the large, flat-topped Bahamas this pattern might be explained by the highstand shedding theory (Schlager *et al*., 1994). When aragonite is a proxy for shallow-water export, different platform settings should be recorded in the aragonite signal and every individual platform should create its own characteristic aragonite curve. Droxler *et al*., (1990) and Haddad & Droxler (1996) therefore assumed that the saw-tooth pattern of aragonite curves could be explained by higher submarine dissolution of metastable carbonates in intermediate water depth. The origin of aragonite/calcite ratios is not fully understood yet, mainly because the contribution of sediment and dissolution to the record are difficult to separate.

A.1.2 Submarine lithification during the last glacial sealevel lowstand

During the last glacial sealevel lowstand salinities of Red Sea bottom- and surface-waters increased to values exceeding 50‰ (see e.g. Winter *et al*., 1983; Locke & Thunell, 1988; Hemleben *et al*., 1996; Geiselhardt, 1998). This was due to restricted water mass exchange with the Indian Ocean via the shallow sill at Bab el Mandeb and simultaneous constant arid conditions over the Red Sea. The high salinities led to restriction of marine life and to the development of the so called aplanktonic zone (e.g., Berggren & Boersma, 1969; Reiss *et al*., 1980). It is also assumed that mass extinction of reef organisms caused reef growth to cease during this period (Gvirtzman *et al*., 1977; Taviani, 1998a; b).

Reduced organic carbonate production during the last glacial salinity crisis was replaced by inorganic carbonate precipitation which led to the formation of lithified layers on the shelf and in the axial trough, between about 500 m and 2,700 m waterdepth over the entire Red Sea (Gevirtz & Friedmann, 1966; Milliman *et al*., 1969; Stoffers & Botz, 1990; Brachert, 1995; 1996; 1999; Hofmann *et al*., 1998). The lithified layers from the Sudanese shelf and the deeper parts of the central Red Sea predominantly consist of aragonite and Mg-calcite, with a dominance of aragonite that correlates with maxima in salinity. Similar crusts were observed in the Mediterranean deep sea, which predominantly consist of HMC. It is assumed that these crusts formed under the influence of cold hypersaline bottom-waters during the last glacial (Bernoulli & McKenzie, 1981; McKenzie & Bernoulli, 1982; Aghib *et al*., 1991; Allouc, 1990).

Since the lithified layers were discovered in the Red Sea (Natterer, 1898) different modes for their formation were suggested. It is generally assumed that high salinities of bottom-waters ac-

companied by low sedimentation rates favoured the inorganic precipitation of aragonite and Mg-calcite at the seafloor of the Red Sea. Brachert (1995, 1996 and 1999) observed stromatolitic and thrombolitic features in the lithified layers of the Sudanese shelf, which support the idea that precipitation of cryptocrystalline carbonates occurred under microbial activity below the photic zone similar to the formation of deep-water stromatolites (Playford *et al*., 1976; Böhm & Brachert, 1993) and micritic crusts on deep-shelf settings (Dromart, 1989) or fore-reef environments (Brachert & Dullo, 1991, 1994).

In this thesis the mineralogical and isotopic composition of the last glacial lithified interval was studied based on a high resolution radiocarbon stratigraphy. Lithified layers are present in all cores obtained in the vicinity of Sanganeb Atoll and Abington reef. They are often broken into chip-like fragments which float in a matrix of unlithified carbonate mud. The mineralogy of the interbedded muds showed a higher siliciclastic content when compared to the lithified sediments, which might have prevented lithification. The whole interval varies in thickness from about 50 cm to more than 100 cm and forms a characteristic marker bed in wide parts of the Red Sea. On the Sudanese shelf the interval of lithification reached from about 23,000 to 13,000 ^{14}C-yr (Almogi-Labin *et al*., 1991; Brachert, 1999, this study). A significant correlation between stable oxygen isotopes and the aragonite content in the lithified layers indicates a maximum in bottom-water salinities that occurred simultaneously to the main phase of aragonite precipitation at 14,840±110 ^{14}C-AMS yr. In the older parts, the grade of lithification is less intensive and Mg-calcite is more abundant or even the dominant carbonate mineral phase, which shows that carbonate precipitation on the Sudanese shelf switched from „normal"-glacial Mg-calcite precipitation (Ellis & Milliman, 1985) to the rare type of aragonite precipitation caused by a further increase in salinity. The majority of the Red Sea lithified layers formed by in-situ precipitation under warm, hypersaline bottom-water conditions and not by secondary lithification of older sediments at the seafloor. Therefore, the formation of the lithified layers can be seen as an active contribution to the carbonate production in the Red Sea which compensated for the lack of organic carbonate production that nearly ceased during the last glacial salinity crisis .

A.2 Study area

A.2.1 Red Sea

The Red Sea is a narrow, intra-continental rift basin positioned between the Arabian peninsula and East Africa (Fig. A-2). At present the Red Sea extends from 30°N to 12°N on a length of about 1,900 km and an average width of 280 km. The Red Sea rift is limited along most of its lengths by peripheral continental escarpments.

The extensive but relatively deep submarine shelfs (Fig. A-3) are terminated towards the axis by the marginal zone of the main trough which is characterised by a series of steep faults that dip basin-ward. Marine escarpments separate the marginal zone from the deep oceanic axial trough, where a maximum waterdepth of 2,920 m is reached. In the trench-like axial zone small isolated basins occur which are called deeps. These are partially filled with hypersaline hot brines (e.g. Ross

& Schlee, 1973). In the north the V-shaped Sinai peninsula separates the shallow Gulf of Suez (max. depth 70 m) from the deep Gulf of Aqaba (max. depth 1850 m, Mergner & Schuhmacher, 1974). In the south the Red Sea is connected with the Indian Ocean via the narrow strait at Bab el Mandeb, the real separation occurs about 140 km northwards at the Hanish Sill (13°40'), which lies in a present-day waterdepth of only 137 m (Morcos, 1970).

A.2.1.1 Geologic evolution of the Red Sea

In the Early Eocene the history of the Red Sea started with a phase of continental break-up which led to the separation of the Arabian and the Nubian crust shields. The continental rifting continued during the Middle Eocene and ended in the Oligocene (Kennett, 1982; Bonatti, 1985; Girdler & Southren, 1987). In the Late Oligocene (about 30 m.y.) the opening of the Red Sea started. Crustal thinning by a pre-Miocene uplift led to a lateral extension and the formation of the main basin. The rifting processes were interrupted during the Middle- and Late Miocene between about 15 and 5 m.y. ago (Styles & Hall, 1980). During the Pliocene, rifting continued and the axial trough was formed by intensive sea-floor spreading. The modern Red Sea can be seen as an embryonic ocean with spreading rates around 0.8-1.0 cm/ky and basaltic ocean crust forming in the axial trough (Kennett, 1982; Frisch & Loeschke, 1993).

A.2.1.2 Zonation and structure of the Sudanese Red Sea

Based on a climatic zonation the central Red Sea lies between 18 and 21°N (Geiselhardt, 1998). According to Ross & Schlee (1973) three physiographic regions can be distinguished in this part of the Red Sea basin (Fig. A-3).

1. The coastal shelf regions extend from the Sudanese and Saudi Arabian shorelines seawards for distances of 30-120 km. The shelf relief is fairly regular and only modified by morphologic heights relating to salt diapirism. Average depths of the shelfs fall in the range of 300-600 m, their sediments are predominantly calcareous. Sanganeb Atoll and Abington reef rest on major fault blocks which are related to extensional tectonics and diapirism of the underlying Middle-Miocene evaporites (Aboul-Basher, 1980; Braithwaite, 1982; Dullo & Montaggioni, 1998).

2. The shelfs are bordered by a „marginal zone" of irregular relief relating to a closely spaced system of faults towards the main trough. This zone is limited by a steep break towards the axis of the central Red Sea in a depth of 500-1,000m, from where it descends into the deep trough.

3. The axial trough, which is developed south of 23°N has an average depth of about 1,800 m. and reaches a maximum depth of 2,920 m. Miocene evaporites that underlie the Pliocene and Quaternary sediments on the shelf and the marginal zone are truncated in the main trough, where only Pliocene and Quaternary sediments overlie the basalts. The absence of the evaporites in the narrow axial zone indicates that the separation of the two margins is a post-Miocene event and probably of Pliocene or Quaternary age (Hofmann *et al*., 1998).

A.2.1.3 Present and past climate and hydrography

Present day climate of the Red Sea and its neighbouring East African and Arabian landmasses is arid, with very low annual precipitation and high rates of evaporation in the order of

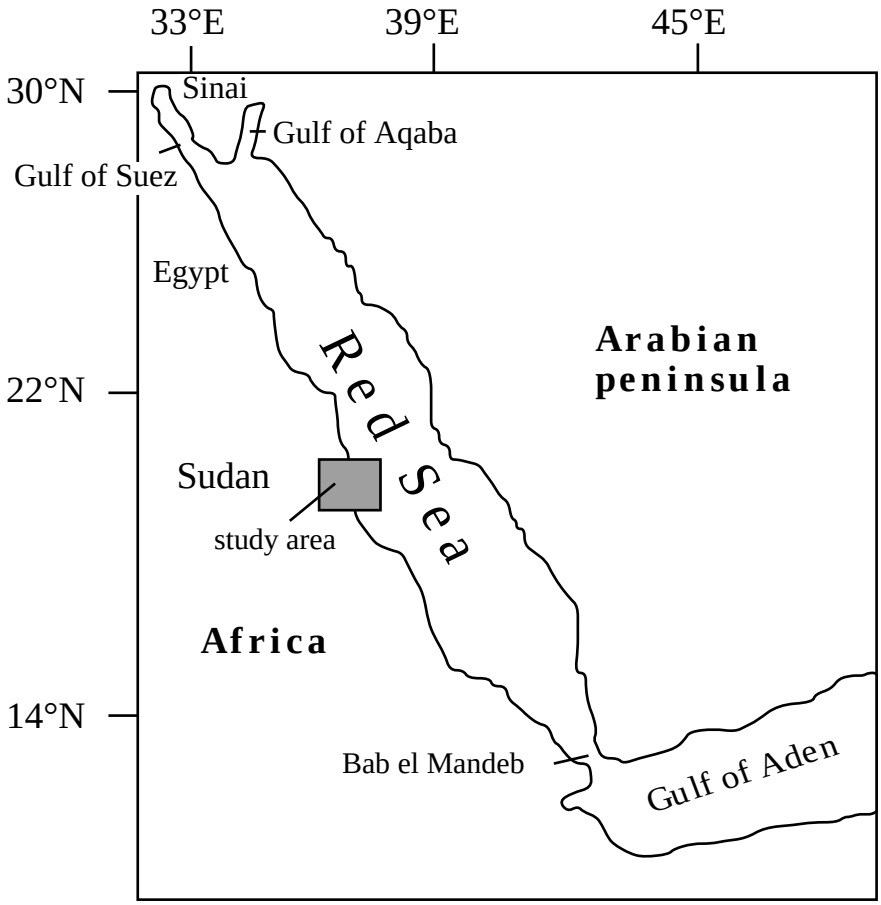

Figure A-2: Map of the Red Sea and the Gulf of Aden region, showing the intra-continental position of the Red Sea rift between the Arabian peninsula and East Africa. The Red Sea is connected to the Indian Ocean only via the shallow sill at Bab el Mandeb.

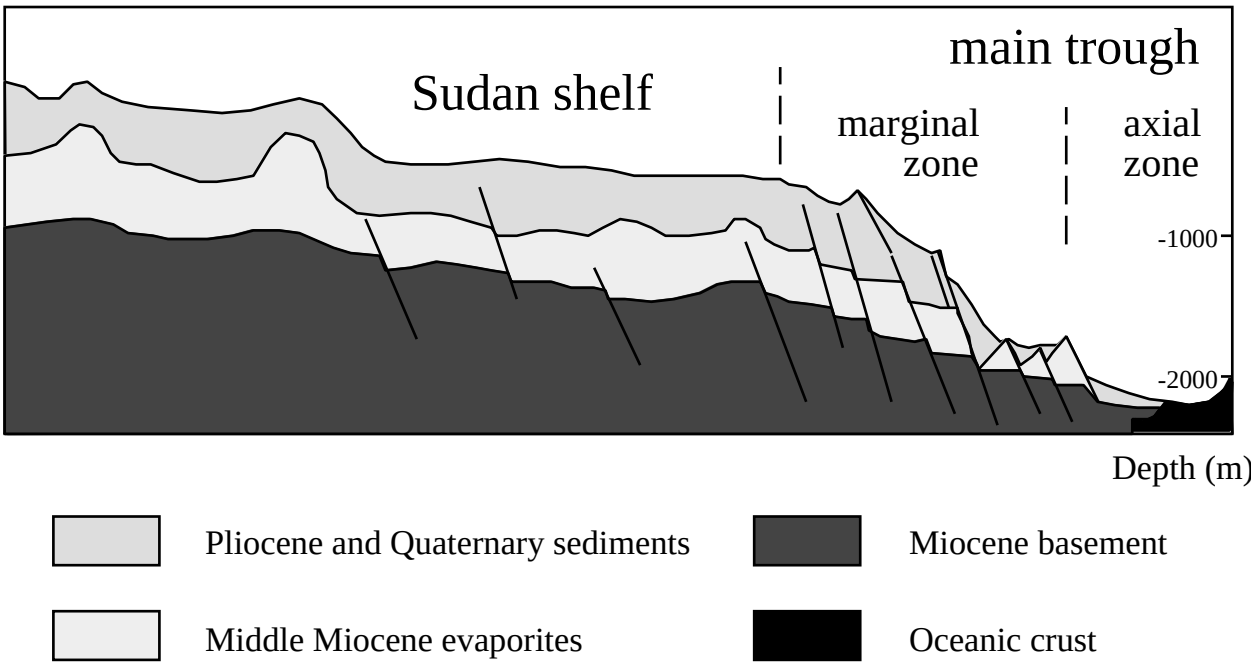

Figure A-3: Cross section through the Sudanese shelf and the adjacent main trough modified after Hofmann *et al*. (1998). The extensive and deep Sudanese shelf shows a step-like zonation due to extensional tectonics and salt diapirism. Many of the Sudanese offshore reefs are located on elevations caused by diapirism. The Sudanese shelf is terminated by the marginal zone of the main trough, which is characterised by a series of half-graben with faults dipping towards the axial zone. In the deep axial trough basaltic ocean crust forms and some of the deeps are filled with hypersaline hot brines.

2,000 mm/yr (Morcos, 1970). Freshwater influx is limited to episodic wadi activity (Grasshoff, 1975).

Nowadays Red Sea hydrography and circulation patterns are determined by the monsoon with its reversed seasonality. In summer a strong monsoonal wind blows over the Arabian Sea from SW, in winter the NE monsoon prevails (Fig. A-5). These monsoonal winds are responsible for a seasonal reversal of main wind directions in the southern Red Sea. South of 19°N NW-winds prevail in summer, while in winter winds blow from SE over the southern Red Sea. North of 19°N a more or less constant NW wind blows throughout the entire year (Neumann & McGill, 1962; Currie *et al*., 1973; Patzert, 1974).

The circulation pattern (Fig. A-5) in the Red Sea is anti-estuarine and is determined by the monsoonal wind system and a density circulation which is enforced by high evaporation in the isolated basin. In winter the Gulf of Aden surface waters flow northward into the Red Sea, driven by the prevailing SE-winds. Saline deep-water flows southward over the sill into the Gulf of Aden. Deep water masses are renewed in winter by oxygen-rich dense surface waters formed in the Gulf of Suez. The cool, high saline water sinks down and flows southward (Neumann & McGill, 1962). Additional sources contributing to the renewal of intermediate waters are cooler dense surface waters from the northern Red Sea and the outflow from the gulf of Aqaba (Cember, 1988). In summer a three-layer circulation pattern establishes. Red Sea surface waters flow south into the Gulf of Aden (prevailing NE-winds) which causes upwelling in the northern Red Sea, while cooler and normal saline Gulf of Aden waters flow into the Red Sea at an intermediate depth of 75-100 m (Maillard & Soliman, 1986). At the same time, cooler saline surface waters from the north flow southwards along density gradients over the sill into the Gulf of Aden (Grasshoff, 1969).

High evaporation rates and restricted water mass exchange with the Indian Ocean caused increased temperatures and salinities of Red Sea waters when compared to other oceans in a tropical environment. At present the surface salinities reach 40‰ or more in the north and decrease to about 37.5‰ in the south, due to the influx of less saline ocean waters. Overall subsurface salinities in the Red Sea are in the range of 40-41‰ (Siedler, 1968).

In summer sea-surface temperatures show a north-south gradient between 25°C in the north and up to 30°C in the south, which is linked to air temperatures. In winter highest temperatures of the surface waters are found in the central parts of the Red Sea. Generally, surface values do not fall below 24°C in the entire basin. Below 250 m waterdepth the temperatures are relatively constant and lie between 21.5-22°C throughout the entire year (Siedler, 1968; Morcos, 1970).

Due to the inflow of normal saline ocean water from the Gulf of Aden into the Red Sea a warm and shallow-water mass lies above a cooler (21-22°C) and saltier (40.5‰) water body that ranges from a waterdepth of 100 m to the sea bottom (Morcos, 1970). Below 100 m the oxygen content decreases and reaches a minimum between 200 and 650 m. Oxygen values reach from 0,5 ml/l in the south to 1,5-1,75 ml/l in the north, where vertical density circulation prevails. Below 700 m the bottom-water is generally well oxygenated (Neumann & McGill, 1962; Woelk & Quadfasel, 1996).

Red Sea surface waters are generally depleted of nutrients, a characteristic typical for silled

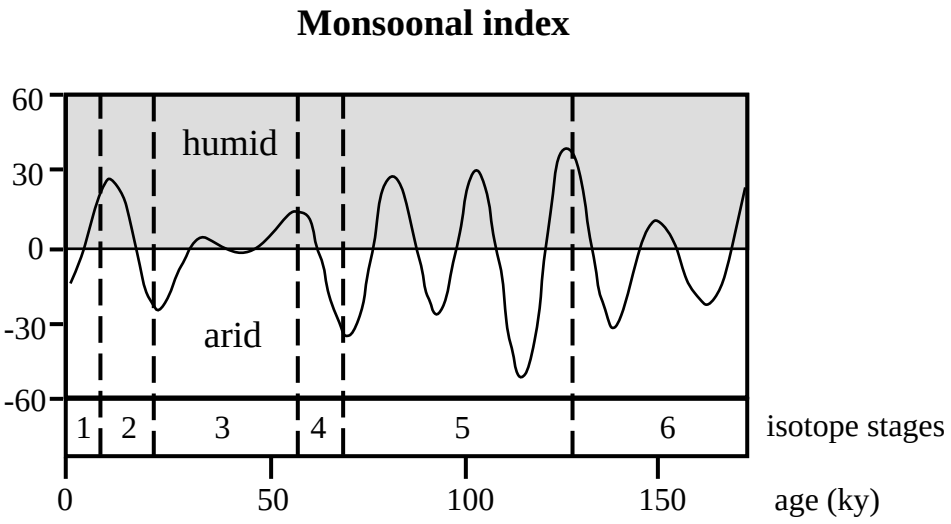

Figure A-4: Monsoonal index based on the precession index of Berger & Loutre (1991), modified after Almogi-Labin *et al*. (1998). It indicates the frequent changes between humid and arid phases in the Red Sea region during the late Quaternary.

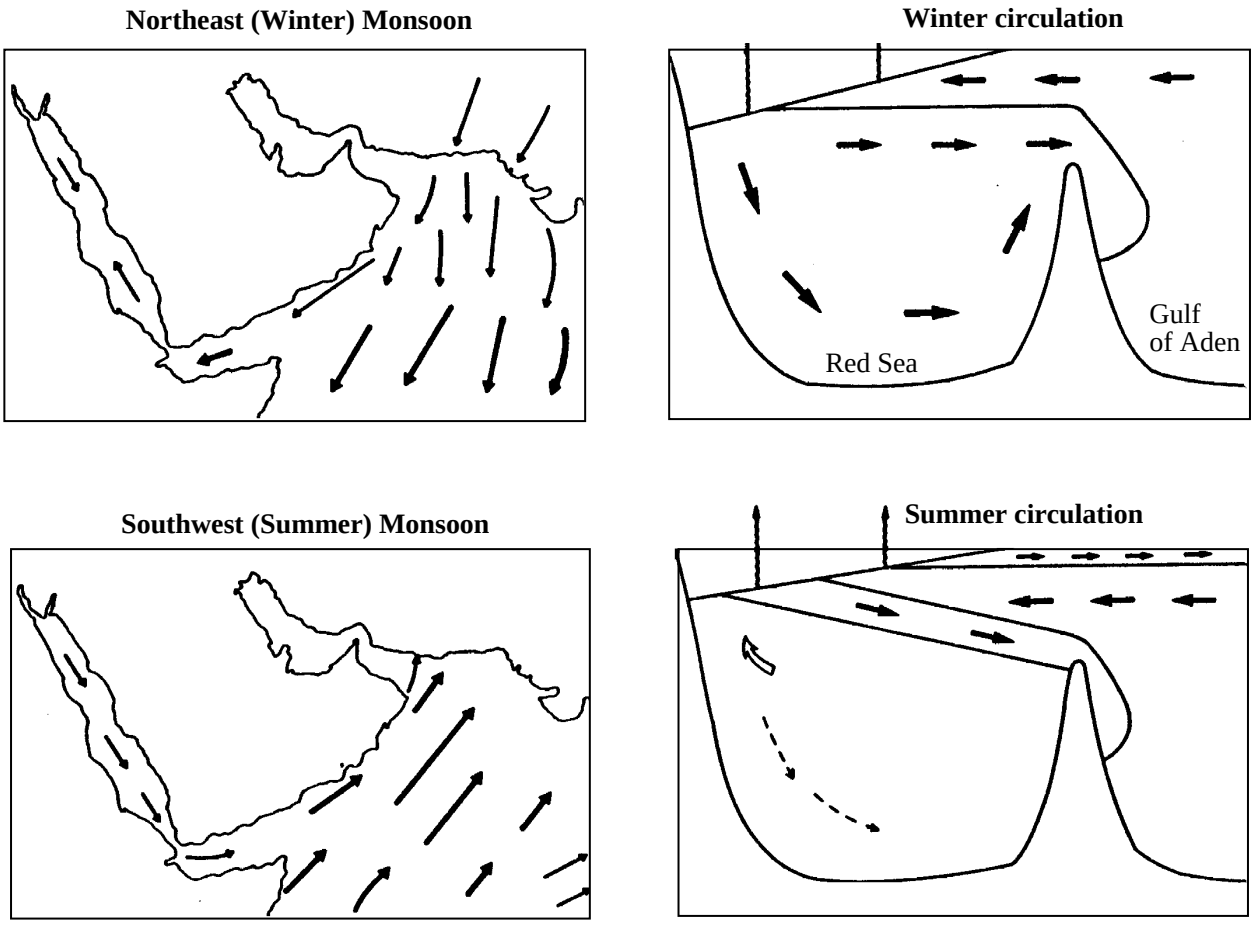

Figure A-5: Wind patterns and circulation in the Red Sea (from Currie *et al.*, 1973; Neumann & McGill, 1962; Patzert, 1974) modified after Locke (1986).

basins with a negative water balance (Demaison & Moore, 1980). The low nutrient content of Red Sea waters favours growth of coral reefs.

During the late Quaternary hydrography of the Red Sea basin was mainly controlled by glacial-interglacial variations in the Bab el Mandeb sea-strait dynamics and regional climate variations. During this interval the climate in the Red Sea and Gulf of Aden region was characterised by abrupt changes of humid and arid phases which were controlled by regular oscillation in orbital parameters (Rossignol-Strick, 1983; Sirocko, 1994; Geiselhardt, 1998). The 19 and 23 ky precession cycles might be the driving forces of the monsoon, which is indicated by the coherence between the monsoonal precession index (Fig. A-4; Berger & Loutre, 1991) and salinity anomalies as recorded by planktic foraminifers in the Red Sea (Hemleben *et al*., 1996). Times of high summer insolation led to increased monsoonal strength during interglacial phases and higher humidity over the Red Sea. During glacial phases the situation was vice versa and cold arid climate conditions prevailed (see e.g. Almogi-Labin *et al*., 1991, 1998; Hemleben *et al*., 1996; Geiselhardt, 1998).

At approximately 4,500 yr BP the present-day climate established as indicated by salinities of surface-waters and the depth of the mixed layer as estimated from pteropod preservation and abundance pattern (Almogi-Labin *et al*., 1991). According to CLIMAP Project Members (1981) and Thunell *et al*. (1988) glacial-interglacial variations in sea-surface temperatures varied only slightly in the Red Sea, e.g. temperatures increased for only 1-2°C between the last glacial maximum and the present.

A.2.1.4 Late Quaternary sedimentation in the Red Sea and on the Sudanese shelf

During the late Quaternary sedimentation on the shelf and in the main trough was dominated by the deposition of pelagic carbonate ooze. In the axial zone this type of sedimentation is obscured by the overwhelming precipitation of metal-enriched sediments and gravity transport processes (Taviani, 1998c). The metal-enriched sediments are formed in the deeps of the axial zone under the influence of hydrothermal activity within the hot brines (Blanc *et al*., 1998).

The rather uniform standard-type of pelagic carbonate sedimentation was interrupted during the late Quaternary by climatically driven hydrologic (paleoceanographic) anomalies, which led to formation of lithified layers during sea-level lowstands and the deposition of sapropels during pluvial phases (e.g. Milliman *et al*., 1969; Locke & Thunell, 1988; Almogi-Labin *et al*., 1991; Hofmann *et al*., 1998; Taviani, 1998c and Brachert, 1999).

During the late Quaternary siliciclastic input in the pelagic realm was generally low, but in wet phases increased run-off from the mainland reinforced terrigenous input, as demonstrated for the now inactive Khor Baraha or Sudan Delta (Ross & Schlee, 1973; Stoffers & Ross, 1977). On the Sudanese shelf, siliciclastic input by wind and gravity mass transport was relatively high. The studied periplatform sediments generally are rich in quartz and feldspar within the sand and fine fraction (30-70%), with clearly increased siliciclastic input during glacial phases (this study).

Periplatform ooze present on the Sudanese shelf in the vicinity of the offshore reefs has a similar composition as the standard-type of pelagic carbonate ooze, described as Normal Red Sea

Sediment (NRSS) by Taviani (1998c). The NRSS is a pteropod-globigerina nanno-ooze, which shows a very low diversity of planktic foraminifers, pteropods and coccolithophorids compared to other tropical-subtropical oceans (e.g. Herman, 1968; Berggren & Boersma, 1969; Winter *et al*., 1983; Ivanova, 1985). Sedimentation rates of the NRSS lie around 3-10 cm/ky and are slightly increased compared to pelagic carbonates in other oceans (Degens & Ross, 1969; Ivanova, 1985). This type of sediment is deposited in the Red Sea at least since isotope stage 5 to 6 (Schoell & Risch, 1976, this study) and probably since the Pliocene (Stoffers & Ross, 1977). In contrast to the pelagic ooze, reef derived and siliciclastic grains form a significant component of the periplatform sediments from the Sudanese shelf.

Black shales and sapropels occur in Plio/Pleistocene sediments marking periods of bottom-water stagnation (Stoffers & Ross, 1977). The latest sapropel event occurred between 13,000 and 8,500 ^{14}C-yr ago, when a 2-3 cm thick greenish-grey layer was deposited on the shelf and in the main trough during the last deglaciation. During this period the Red Sea climate was more humid (Rossignol-Strick, 1983) and enhanced precipitation and run-off from the mainland caused stratification of the water column. Therefore, an extensive oxygen minimum zone established at the end of the last glacial sealevel lowstand. Oxygen depletion accompanied by increased input of organic matter from terrestrial sources led to the formation of the organic rich sapropel and an unusually good aragonite preservation at the seafloor (Locke, 1986; Locke & Thunell, 1988; Almogi-Labin *et al*., 1991; Hofmann *et al*., 1998). This dark layer is found in all studied cores from the deep shelf close to Sanganeb Atoll and Abington Reef. The sapropel in general contains less biogenic components and more siliciclastics compared to the pelagic carbonate ooze. The absence of mesopelagic pteropods and foraminifers is accompanied by a carbonate content smaller than 15% (Herman, 1971; Besse & Taviani, 1982; Almogi-Labin *et al.*, 1991; Taviani, 1998c; this thesis).

A.2.1.5 Coral reefs of the Red Sea

In the Red Sea reef growth established during the Miocene when the basin reached a fully marine stage (James *et al*., 1988; Perrin *et al*., 1998). Two main phases of reef growth can be distinguished. In the first phase during the Miocene only small, short-lived fringing reefs of modest size and low biodiversity occurred. During this phase the Red Sea was connected with the Tethys Ocean via the Mediterranean seaway (Purser *et al*., 1990; Coleman, 1993; Sun & Esteban, 1994). This phase ended about 12 m.y. ago with a hypersaline phase and the deposition of evaporites (Stoffers & Kuhn, 1974; Stoffers & Ross, 1977; Braithwaite, 1987). The second phase was initiated when the Red Sea opened to the south and established a connection with the Indian Ocean about 5 m.y. ago (Pliocene) which led to the recolonisation of the basin (Coleman, 1974; Braithwaite, 1987).

Quaternary reef growth in the Red Sea is strongly controlled by eustatic sealevel variations and glacial-interglacial changes in climate and hydrography. Furthermore, rift related salt diapirism and siliciclastic input influenced the morphology and shape of the reefs. The majority of recent and Pleistocene Red Sea reefs are of the fringing reef type. They grow close to the mainland and are absent in front of wadi-mouths. Atolls and barrier reefs occur in central and southern part of the

Red Sea. Outlines and orientation of the reefs are mainly controlled by the tectonic framework of the rift basin (Dullo & Montaggioni, 1998).

Late Quaternary sea-level changes are well documented in onshore and offshore reef terraces in different parts of the Red Sea. Raised Pleistocene reef terraces can be correlated with interglacial sealevel highstands (e.g. Dullo, 1990; Gvirtzman, 1994; Dullo & Montaggioni, 1998; Plaziat *et al.*, 1998). Emerged Holocene reef terraces, which are commonly associated with erosional surfaces typically occur about 0.5 m above present sealevel. Those terraces might represent the higher-than-present Holocene sea-level in the Red Sea dated as 5,500-6,500 yr BP (Gvirtzman, 1994). Brachert & Dullo (1990, 1991) and Dullo *et al.* (1990) observed submerged terraces by submersible investigations that show features of drowned reefs. It is assumed that those reefs once grew on the terraces during lowered sealevel and drowned during fast pulses in the Holocene sealevel rise.

Late Quaternary reef growth might have been strongly affected by the increased salinities during glacial sealevel lowstands. Reefs vanished from the entire Red Sea during the last glacial, which was explained by salinities exceeding 50 ‰ (Taviani, 1998a; b). Other reasons, like a drop in sea-surface temperatures and the disruption of the internal organisation of reef communities caused by sea-level changes also must have played an important role. In the semi-enclosed Red Sea, with its high salinity conditions, the global phenomena of stress on ecosystems was amplified which led to faunal turnover and local extinction. The present Red Sea fauna (and flora) is a result of Holocene recolonisation (Gvirtzman *et al.*, 1977; Taviani, 1998a; b). Modern benthic shallow-water carbonate production in the Red Sea predominantly takes place in coastal fringing reefs (e.g. Loya & Slobodkin, 1971; Mergner & Schuhmacher, 1974; Gvirtzman & Buchbinder, 1978; Dullo & Montaggioni, 1998). At present skeletal carbonate production prevails in Red Sea reefs (Piller, 1994; Brachert, 1999).

The deeper fore-reefs and the slopes of some Sudanese reefs down to a waterdepth of 215 m were investigated with a submersible by Brachert & Dullo (1990, 1991) and Dullo *et al*., (1990). They found that phototrophic life is virtually absent below the euphotic zone and that biogenic carbonate production is taken over by heterotrophic encrusters like serpulids, ahermatypic corals, foraminifers, cryptic microbial crusts (Brachert & Dullo, 1991) and problematic microfossils (Brachert & Dullo, 1994; Brachert, 1996). The steep morphology of the upper slope of the atoll and barrier reefs extends to the sea-floor where the slopes merge with the flat-floored shelf (Brachert & Dullo, 1990; Brachert, 1993).

A.2.1.6 Sanganeb Atoll and Abington Reef

Modern Sanganeb Atoll and Abington Reef belong to a chain of fringing, barrier and atoll reefs following the Sudanese coast in the central Red Sea (Fig. A-6, Dullo *et al.*, 1990; Brachert & Dullo, 1994).

Sanganeb Atoll is located approximately 18 km offshore Port Sudan. The study area around Abington Reef lies about 120 km north of Sanganeb Atoll. The recent coral reefs are plastered onto the surface of older Pleistocene “reef” structures which, in turn, rest on the eroded surface of Miocene carbonates and evaporites (Aboul-Basher, 1980; Braithwaite, 1982). Sanganeb Atoll and Abington

Reef are no proper atolls according to Darwin (1876), but are located on top of steep walled structures, which rise about 500 to 600 m above the deep Red Sea shelf platform. These elevations are the remains of a horst structure related to extensional tectonics and salt diapirism (Aboul-Basher, 1980; Braithwaite, 1982; Dullo & Montaggioni, 1998).

In the following paragraph a description of the present-day Sanganeb Atoll is given. Abington Reef has not been studied in detail yet, except for the deeper fore-reef slopes (see Brachert & Dullo, 1990; Dullo *et al.*, 1990) whereas Sanganeb Atoll has been studied in great detail during the last two decades (e.g. Aboul-Basher, 1980; Mergner & Schuhmacher, 1985; Schuhmacher & Mergner 1985; Brachert & Dullo, 1990, 1994; Dullo *et al.*, 1990, 1994; Dullo & Montaggioni, 1998).

A.2.1.6.1 Morphology and zonation of Sanganeb Atoll

Sanganeb Atoll is a nearly enclosed, atoll-like reef-structure, which extends for about 6 km in N-S direction and only 2 km in E-W direction (Fig. A-7; Mergner & Schuhmacher, 1985; Schuhmacher & Mergner, 1985). The N-S elongated shape of Sanganeb Atoll reflects the tectonic structure of the shelf area which is determined by a N-S (10°) oriented horst and graben structure. To the north, east and south the central lagoon is separated from the open sea by a closed reef-structure, while on the western side the platform edge is characterised by inlets and patchy reef structures. Modern Sanganeb Atoll consists of two parts, a southern part enclosing a square like, shallow lagoon (5 to 10 m deep) and a northern part which is more elongated (Fig. A-7, 7). Maximum depth of the main lagoon is about 50 m. At the southern edge a nearly 250 m wide shallow reef platform is developed. Along the windward (east) side a steep dipping fore-reef follows seaward to a 15 m wide shallow reef platform. Sand ridges at the western (leeward) side of the lagoon prevent recent sediment export off the lagoon.

The lagoon and the shallow-water reef were investigated by Boomer seismics (500-2000 Hz). The results of the seismic survey are summarised in Dullo *et al.* (1994) and Dullo & Montaggioni (1998). The Holocene lagoonal sediments are well bedded and lie over an erosional discordance (Fig. A-10). They predominantly consist of carbonate mud with higher portions of skeletal sand and reach a thickness of about 3-5 m, which translates into a Holocene net sedimentation rate in the lagoon of 30-50 cm/ky. In the seismic record massive pillars are visible that might represent older patch reefs (Fig. A-10). An erosional discordance is also visible in the seismic profiles of the inner reef slopes that border the lagoon in about 25 m waterdepth. Those erosional surface was interpreted as emersion surface of the old Pleistocene reefs and it is assumed that they were re-colonised after flooding of the substratum during the Holocene sealevel rise. Based on this interpretation a vertical Holocene reef growth rate at Sanganeb Atoll between 1.6 m/ky on the leeward side and 2.4 m/ky on the windward side was estimated (Dullo *et al.*, 1994).

A sedimentary zonation of present-day Sanganeb Atoll was made by Aboul-Basher (1980). The sediments of the fore-reef and the reef platform are generally coarse grained (e.g. coral boulders on the fore-slope) and have a carbonate content of 95%. The most important sediment constituents are scleractinians, corallinaceans, encrusting foraminifers and reef dwellers like gastropods and pelecypods. The lagoonal sediments are generally fine grained and contain up to 80%

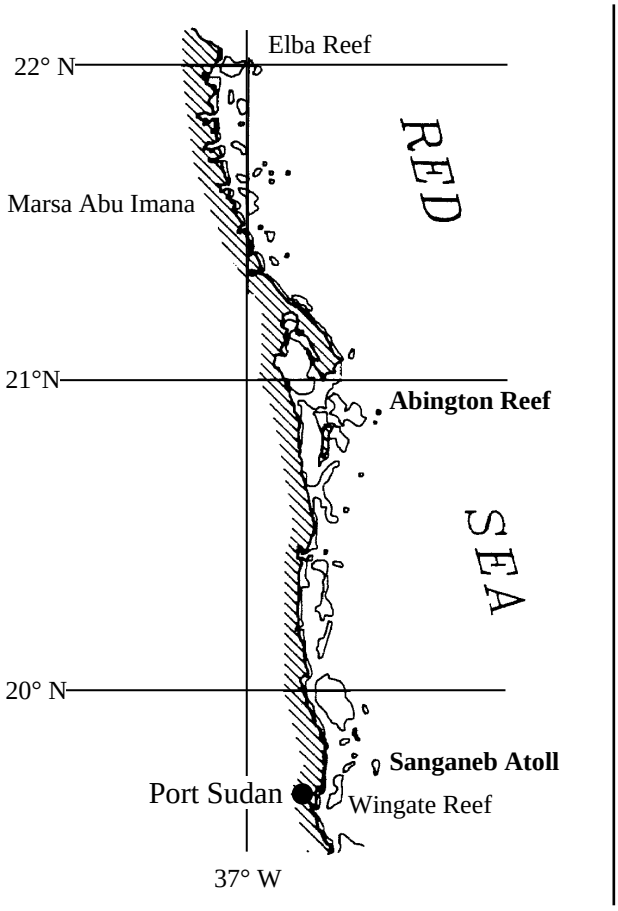

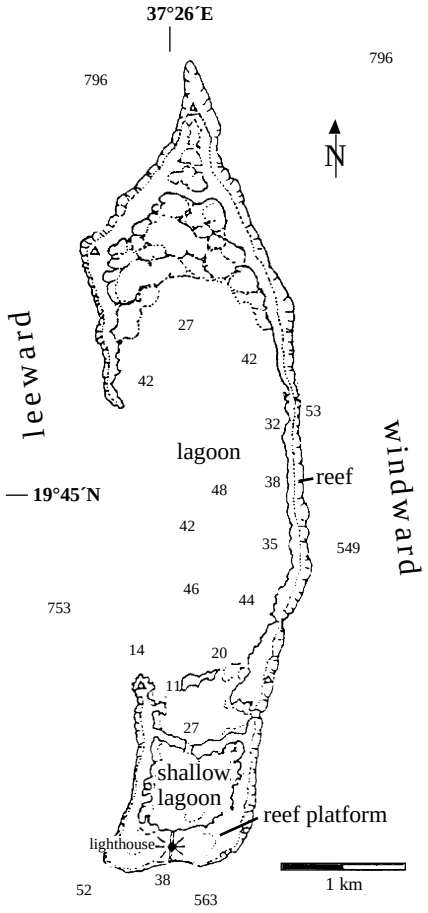

Figure A-6 (left): Map of the Sudanese offshore reefs, showing the study areas at Sanganeb Atoll and Abington reef, modified after Dullo *et al.* (1990).

Figure A-7(right): Morphologic zonation of Sanganeb Atoll, modified after Mergner & Schuhmacher (1985). Depth in meter.

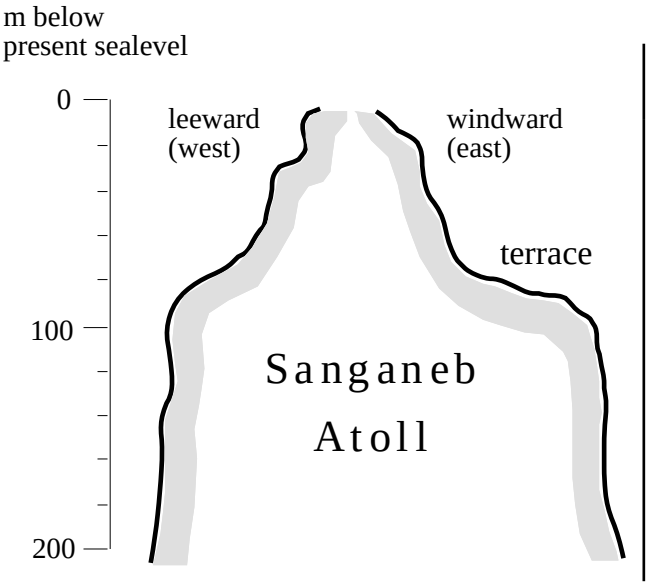

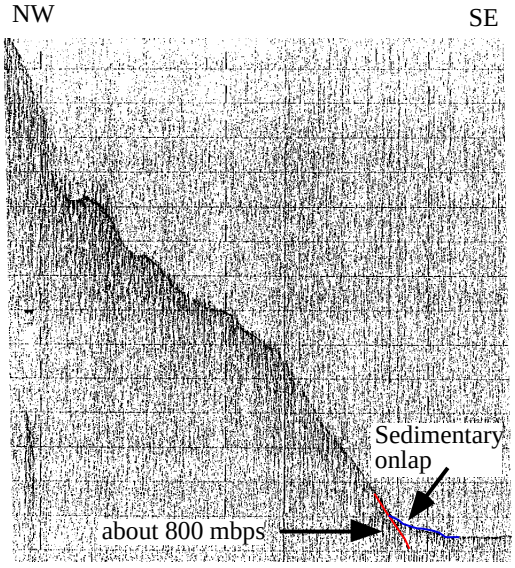

Figure A-8 (left): Drawing of the leeward and windward slopes of Sanganeb Atoll after submersible observations of Brachert & Dullo (1990,1991) and Dullo *et al*., (1990). Note the extensive submarine terrace on the windward margin, on which shallow-water reefs possibly grew during lowered sealevel.

Figure A-9 (right): SE-NW running 3.5 kHz seismic profile of the windward slope at Sanganeb Atoll, showing the onlap of periplatform sediments on the toe-of-slope (modified after Dullo *et al.* 1994). In analogy to the Bahamas it is assumed that this structure represents a Holocene sediment wedge (Dullo & Montaggioni, 1998). The Horst block elevates from a waterdepth of about 800 m.

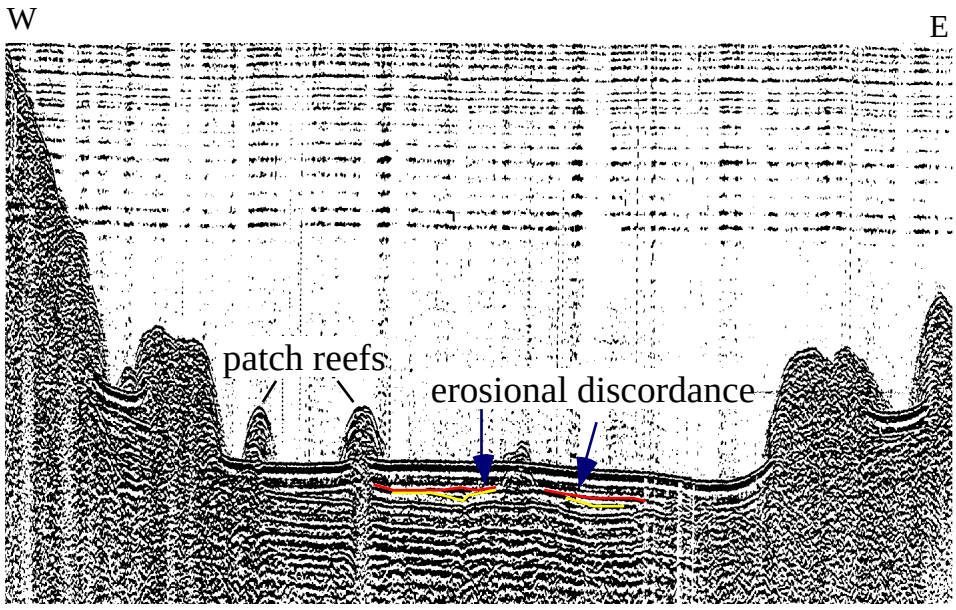

Figure A-10: W-E oriented seismic profile through the lagoon at Sanganeb Atoll. The erosional discordance is clearly visible between the old glacial emersion surface and the Holocene sediments. Patch reefs rest on those old surfaces. Maximum waterdepth of the lagoon is approximately 45 m. Lenght of the profile is about 800 m. Modified after Dullo *et al.* (1994).

carbonate silt. At present salinities up to 60‰ and temperatures higher than 35°C restrict biogenic carbonate production in the enclosed lagoon . Following Aboul-Basher (1980) about 20% of the lagoonal sediments are inorganic carbonate precipitates. Non skeletal components like pellets, ooids and compound grains are important in this environment. Green algae and sea-grass, molluscs, bryozoan and large benthic foraminifers (*Peneroplis*) are the main dwellers of this zone. The mineralogical composition of the modern shallow-water sediments at Sanganeb Atoll is dominated by Mg-calcite and aragonite, calcite plays no important role.

The deeper slopes and walls at Sanganeb Atoll down to about 215 m waterdepth were studied with a submersible (Brachert & Dullo, 1900,1991; Dullo *et al*., 1990). The walls are steeply inclined and exhibit a prominent terrace between 70 and 90 m below present sea-level on the windward (east) margin, while the leeward slopes exhibit a number of smaller terraces, which are covered by sand (Fig. A-8). Internal steps in the steep walls might be caused by normal faulting (Dullo & Montaggioni, 1998).

The shallow fore-reef slopes down to a waterdepth of about 60 m were studied in detail by Mergner & Schuhmacher (1985). On the windward side the fore-reef is characterised by very steep and overhanging slopes, while fore-reef slopes are gently inclined on the leeward side. The living fore-reef is terminated by a sedimentary slope in a waterdepth of about 53 m.

Below 120 m the steep slopes are characterised by flat surfaces and a spur and groove system. In addition, the walls are covered by ledges, which are a few cm thick and protrude about 25 cm horizontally from the walls. These ledges are covered by loose sediments that originate from

the shallow-water reefs. A detailed description of those structures is given by Brachert & Dullo (1990, 1991).

Below 215 m the slopes drop down nearly vertical to the toe-of-slope were a sedimentary onlap is visible in the seismic profiles (Fig. A-9). The toe-of-slope at Sanganeb Atoll is enclosed by deep channels or trenches that reach 700 to 900 m below present sealevel (Aboul-Basher, 1980). On the eastern side the deep shelf is bordered towards the main trough by a submarine threshold that elevates to a water-depth of 400-500 m. This barrier limited the sediment transport towards the main trough and trapped large amounts of the periplatform sediments on the deep shelf.

A.3 Objectives

The major part of this thesis focuses on sedimentological and paleoceanographical aspects of periplatform sedimentation on the Sudanese shelf during the late Quaternary. Variations in mineralogy, geochemistry and component distribution of the periplatform sediments as well as age and frequency of calciturbidites in the vicinity of Sanganeb Atoll and Abington Reef were analysed with respect to late Quaternary glacial-interglacial variations in the Red Sea.

Generally the idea of „highstand shedding“ will be put to a test. The question is raised if geochemical and mineralogical distribution patterns in periplatform sediments of the Sudanese shelf were created by shallow-water sediment export variations like proposed by the highstand-shedding model (Schlager & James, 1978) or by other syn- and postdepositional processes. Most important for the latter are climatically driven changes in the dissolution/preservation of metastable carbonates or the enhanced precipitation of Mg-calcite at the seafloor of the Red Sea (Ellis & Milliman, 1985).

As a new approach the mineralogical and geochemical dataset were compared with a quantitative microfacies analysis. The question is if variations in the distribution of characteristic shallow-water derived components correlate with the mineralogical and geochemical signal and if the frequency and composition of calciturbidites is controlled by the overall sediment export pattern.

Based on climate-stratigraphy and radiocarbon dating late Quaternary sealevel variations are adapted to the regional setting on the Sudanese shelf. The regional sealevel curve is used to model variations in the carbonate production potential at Sanganeb Atoll. It is tested in this thesis if shal low-water input as recorded in the periplatform sediments is in phase with the modelled shallow-water production of the reef or if offsets occur, due to storage effects within the platform, stepwise shedding or filtering processes.

The unique paleoceanographic and climatic setting of the relatively isolated Red Sea basin could have had an important influence on the composition of periplatform sediments and the calciturbidites. It is questionable if secondary processes, like for example the inorganic precipitation of metastable carbonates or the restriction of marine biota during the glacial salinity crisis obscured the sediment export signals in the Red Sea when compared to the overall patterns which are found at other periplatform sites in open sea environments, like for example the Bahamas.

Changes in salinities of surface- and bottom-waters which determined the distribution of carbonate secreting organisms are of special interest. A drastic increase in salinities could have

been the reason for the switch from organic to inorganic carbonate precipitation during the last glacial sealevel lowstand which also led to submarine lithification on the Sudanese shelf.

In this context, the switch from the submarine precipitation of Mg-calcite to that of aragonite as well as the alternation between lithified and unlithified layers as observed in the lithified interval are of special interest. Age and distribution as well as mineralogical and isotopic composition of the lithified interval of the Sudanese shelf are compared to those of other sites in order to reconstruct the paleoceanographic evolution of the Red Sea during the last glacial.

Glacial-interglacial variations in the Red Sea are reinforced by abrupt changes between humid and arid phases (monsoonal-climate). Those variations caused changes in the stratification and circulation of Red Sea waters which could have influenced the preservation potential of metastable carbonates on the seafloor. The question is if and how much the periplatform signal was changed by those climatic variations.

The Red Sea is the ideal laboratory to study glacial-interglacial variations because the paleoceanographic signals are significantly enhanced in the isolated basin. On the other hand, the extreme paleoceanographic situation caused unique scenarios, like for example the restriction of marine life during the last glacial. It is therefore expected that processes of periplatform sedimentation in the Red Sea can be more easily connected to paleoceanographic and sedimentological signals than elsewhere. The study of periplatform sedimentation in the Red Sea therefore is an important contribution to the understanding of the overall glacial-interglacial patterns found in late Quaternary periplatform sediments and generally to the sequence stratigraphy of modern and ancient carbonate platforms.

CHAPTER B: MATERIAL AND METHODS

B.1 Material

During *R.V. METEOR* cruise M31/2 (February 7th - March 2nd, 1995) six sediment cores were obtained from the periplatform area at Sanganeb Atoll and Abington Reef. Positions of the sediment cores are shown in Fig. B-1, waterdepth, sediment recovery and distance from the reefs are summarised in Tab. 1. In the following text only abbreviations for the individual cores will be used, e.g. S1 instead of M31/2-99-S1. Coring positions were selected based on Parasound survey and 3.5 kHz seismic profiles measured during a previous survey at Sanganeb Atoll (Dullo *et al*., 1994). Lithologic description of the sediments and sampling procedure were performed on board, only piston core S6 was opened after the cruise at GEOMAR in Kiel, Germany. In addition, selected sediment samples from piston core MD 921022 were studied (Tab. B-1), which were sampled and prepared by Thomas Brachert (University of Mainz) and Georg Heiss (GEOMAR, Kiel). This core was taken during Leg 73 by *R.V. Marion Dufresne* from the channel east of Sanganeb Atoll.

B.2 Methods

B.2.1 Sampling and sediment preparation

Sediment cores were opened on board for lithologic description and sampling. Sediment samples were taken with syringes every 10 cm (3 x 100 cm^3) for further analysis in the laboratory and for preparation of thin sections. Sand layers and sapropels were sampled in addition. Cores S6 and S1 at Sanganeb Atoll were selected as reference cores. Core S6 records a complete glacial-interglacial cycle, the periplatform sediments are rich in shallow-water grains and calciturbidites occur frequently. Core S1 was taken in a greater distance from the reef and therefore might record the paleoceanographic signals better than the proximal cores. It reaches back to marine isotope stage (IS) 5 but unfortunately this core contains not enough shallow-water components for quantitative analysis. Thus, no pointcount analysis was made in core S1 like in the cores at Abington Reef, which contain even less reef derived components. The complete set of analysis was only performed on the two reference cores, except for pointcounting and radiocarbon dating of turbidites in core S1. All other cores were analysed selectively to complete the data set and for spatial and temporal comparison of the cores (Tab. B-2). The lithified interval was sampled with higher resolution in the cores S1, S6 and AL. To preserve the sediment fabric of the lithified layers they were deep frozen with fluid nitrogen. The frozen sediments were cut in 2 cm slices using a rock saw and these slices were cut in two parts. One half was impregnated with resin for preparation of thin sections, the other half was used for geochemical and mineralogical analyses.

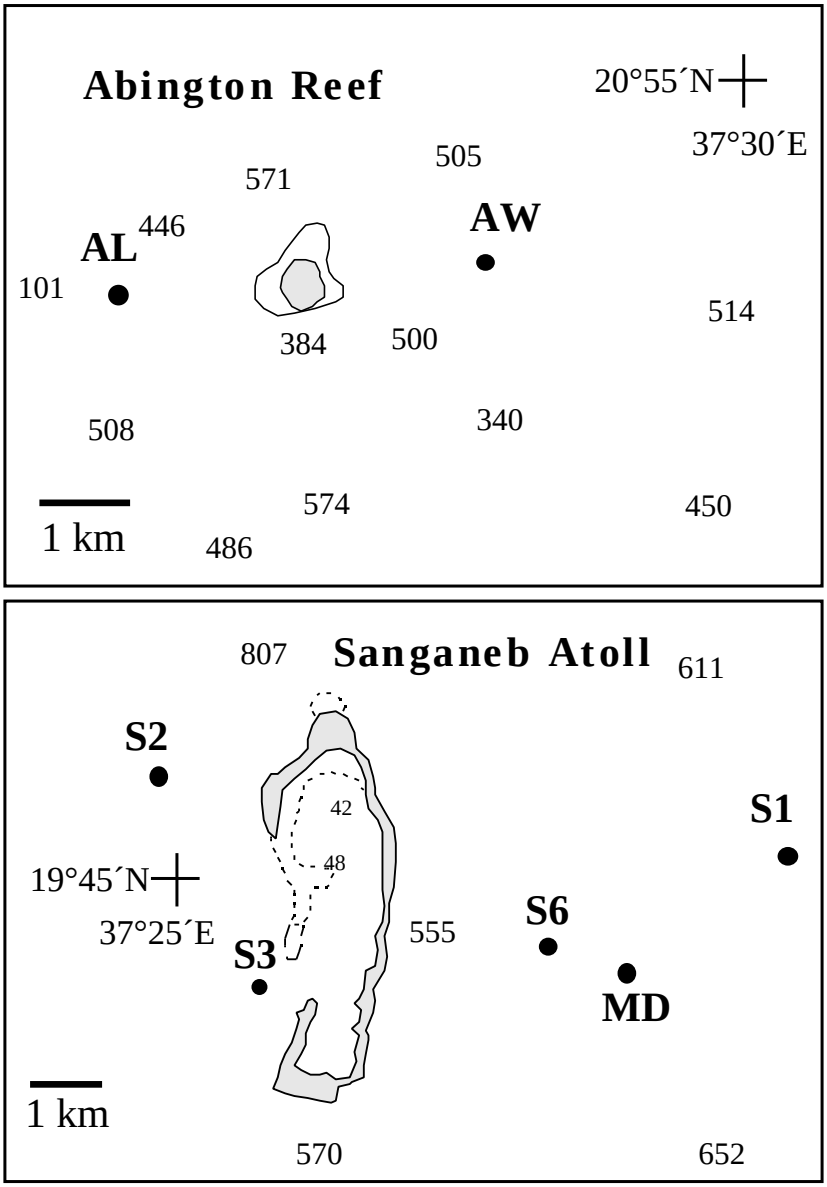

Figure B-1: Map of Abington Reef and Sanganeb Atoll showing the positions of the sediment cores. Depth in meter.

Table B-1: Position, waterdepth and recovery of the analysed sediment cores

For position of the cores also see Fig. B-1, Distance in km from the reef edge, Depth in m below present sealevel

Core/Type	**Recovery**	**Position**	**Distance** (km)	**Depth**
M31/2-96-AW (BC 6m)	575 cm	20°53.825 N/037°28.341 E	1.5 km. E	513m
M31/2-94-AL (BC 6m)	530 cm	20°53.670 N/037°25.740 E	1.5 km. W	498m
M31/2-99-S1 (BC 6m)	493 cm	19°45.150 N/037°29.754 E	5 km. E	771m
M31/2-99-S2 (BC 6m)	460 cm	19°45.894 N/037°24.797 E	1.5 km. W	810m
M31/2-99-S3 (BC 6m)	447 cm	19°44.321 N/037°25.641 E	toe-of-slope; W	757m
M31/2-99-S6 (GC 6m)	477 cm	19°44.566 N/037°27.968 E	2 km. E	744m
MD 921022 (PC 24m)	1540 cm	19°44,310 N/037°28,240 E	3 km. E	723 m

BC = Box core, GC = Gravity core, PC = Piston Core

Table B-2: Summary of the analytical procedures used in this study

Core S1 and S6 were selected as reference cores

	Cores						
Method	**S1**	**S6**	**S2**	**S3**	**MD**	**AL**	**AW**
Stable isotope analysis of planktic foraminifers	x	x	x	x	x	x	x
Stable isotope analysis of the hard layers	x	x				x	
Radiocarbon dating of the hard layers (^{14}C-AMS)	x	x					
Radiocarbon dating of the calciturbidites		x					
Grainsize analysis	x	x	x	x	x	x	x
Mineralogy of the bulk sediment (XRD)	x	x	x	x		x	x
Mineralogy of the hard layers	x	x				x	
Mineralogy of the fine fraction(s)	x	x	x	x			
Carbonate content and TOC (LECO)	x	x	x	x		x	
Geochemical analysis (XRF)	x	x	x	x			
Component analysis of periplatform sediments and calciturbidites (thin sections, coarse fraction)	x	x	x	x			
Pointcounting (thin sections)		x	x	x			

B.2.2 Grainsize analysis

Coarse and fine fraction were separated by wet sieving through a 63 µm sieve. In a second procedure, the coarse fraction (> 63 µm) was subdivided into 5 grainsize classes by dry sieving with an ATM Sonic Sifter (Type 23P) for 10 minutes. The dry weight of each fraction was measured and percentages of coarse and fine fractions were calculated. The resulting grainsize classes are summarised in the Tab. B-3.

Table B-3: Grainsize classes (from Tucker, 1985)

Grainsize class	**µm**	**phi-scale**	
silt and clay	< 63	> 4	fine fraction
very fine sand	63-125	4-3	coarse fraction
fine sand	125-250	3-2	
medium sand	250-500	2-1	
coarse sand	500-1000	1-0	
very coarse sand - rubble	>1000	< 0	

B.2.3 Stable Carbon and Oxygen isotopes

B.2.3.1 Sampling and analysing techniques

Approximately 20-30 tests of the planktic foraminifer *Globigerinoides ruber* (white) were selected from the 250-500µm size fraction in each sample (every 10 cm). The species *G. ruber* (white) is common in the Red Sea sediments and was used by most other authors for stable isotope analyses in different parts of the Red Sea (e.g. Deuser & Degens, 1969; Reiss *et al.*, 1980; Duplessy,

1982; Locke & Thunell, 1988; Hemleben *et al*., 1996).

C and O isotope ratios were measured with a Finigan mass spectrometer by Michael Joachimski at the University of Erlangen. After dissolution of the foraminifer shells and the carbonate sediments in 100% phosphoric acid the amounts of delta 45 (^{13}C, ^{16}O) and delta 46 (^{12}C, ^{18}O, ^{16}O) were detected several times. From the average delta 45 and 46 the $\delta^{18}O$ and $\delta^{13}C$ values were calculated after correction to standard NBS19, which was used for calibration of the mass spectrometer. Standard deviations (reproducibility of 10 replicates) of calculated stable isotope values range from 0.01 and 0.06 ‰ for $\delta^{18}O$ and 0.01 to 0.07‰ for $\delta^{13}C$ (reproducibility of 10 replicates). $^{18}O/^{16}O$- and $^{13}C/^{12}C$-ratios were calculated with respect to the Vienna PDB standard (V-PDB). Standard deviation for NBS19 in all analysis was 0.02‰ for $\delta^{18}O$ and 0.03‰ for $\delta^{13}C$.

Tests of planktic foraminifers are rare or absent in the lithified interval of the „aplanktonic zone“ (Berggren & Boersma, 1969; Reiss *et al*., 1980). Therefore, high resolution stable C and O isotope-measurements were performed every 2 cm on lithified particles (chips) and unlithified fine fraction (< 63 µm) of each sample. From the lithified chips small amounts of the sediments were removed for isotope analysis with a dental drill. The samples of the lithified interval were analysed with a Finigan mass spectrometer by Alexandra Isern at the University of Sydney, following the same procedure as described above.

B.2.3.2 Oxygen isotope stratigraphy - Age models

Definition of isotope stages, substages and events

Names of marine isotope stages and substages (IS) were used following the definition of Shackleton & Opdyke (1973) based on the pioneer work of Emiliani (1955). Generally, interglacial IS are labelled with odd numbers and glacial IS with uneven numbers. IS 1 represents the Holocene and IS 5 the last interglacial, which is separated into substages 5a, 5b, 5c, 5d and 5e based on internal $\delta^{18}O$-fluctuations. Substages 5a, 5c and 5e correspond to lighter $\delta^{18}O$-values when compared to 5b and 5d. The last glacial comprises IS 2, IS 3 and IS 4. IS 3 exhibits clearly lighter isotope values than IS 2 and IS 4 but does not reach fully interglacial values. IS 6 corresponds to the penultimate glacial (Fig. B-2).

Maxima and minima within individual IS are labelled after Imbrie *et al.* (1984) and are called SPECMAP-events or isotopic events in the following text. Those are the essential fix-points for the climate-stratigraphic correlation. Stage boundaries of individual IS were defined after Imbrie *et al.* (1984) and correspond to the SPECMAP events 1.0, 2.0, 3.0, 4.0, 5.0 and 6.0 (Tab. B-4).

Climate-stratigraphic correlation

A climate-stratigraphic age model was established by comparison of the analysed stable oxygen isotope curves (*G. ruber*) with the global SPECMAP-curve. The global SPECMAP curve published by Imbrie *et al*. (1984) is a stacked curve of planktic oxygen isotope records which represents global changes in ice volume during glacial-interglacial changes. The SPECMAP time scale is adjusted to these ice volume variations calculated from variations in earth orbital parameters. The

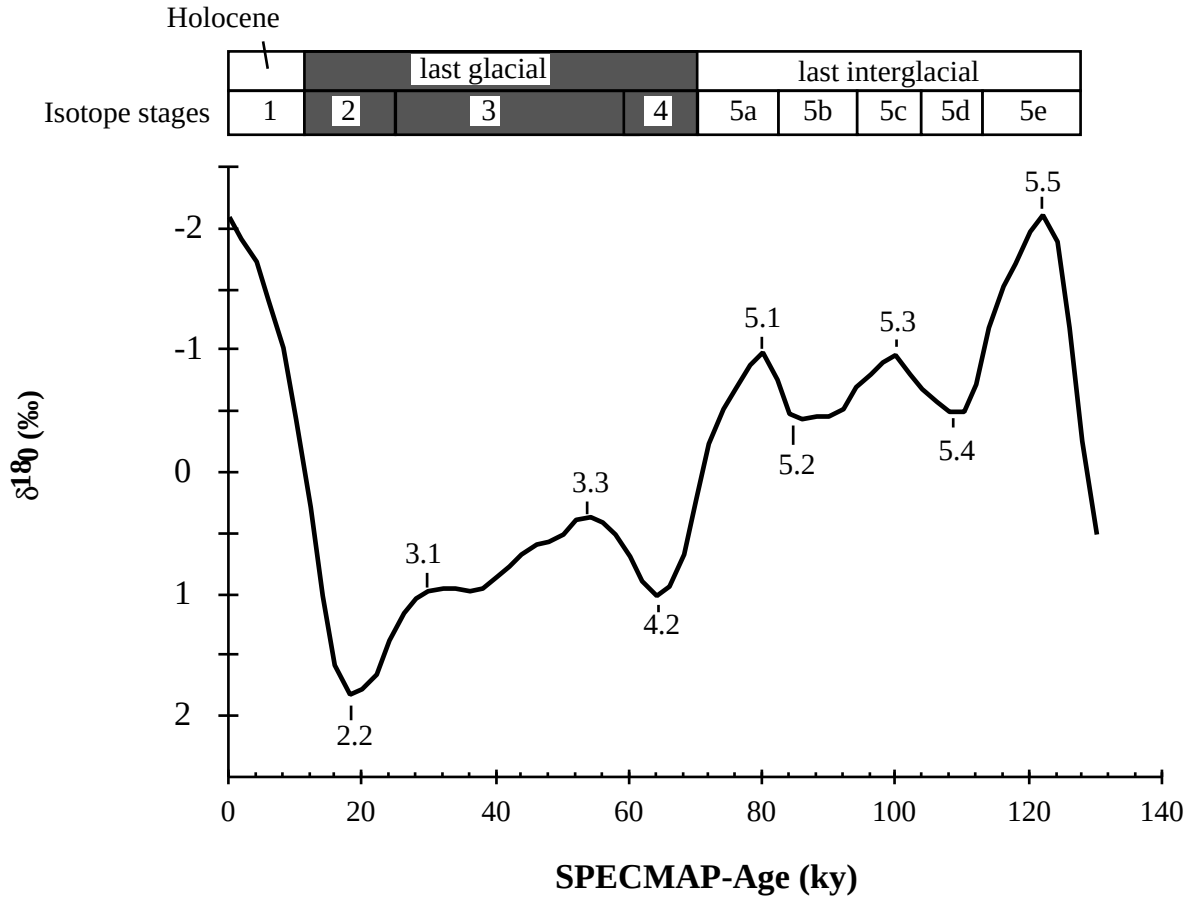

Figure B-2: Youngest parts of the SPECMAP-curve showing glacial-interglacial $\delta^{18}O$-variations since the last interglacial (IS 5). The numbers on the curve are SPECMAP events, the column above illustrates the individual isotope stages and substages as well as the glacial-interglacial cycles. Ages of events and stage boundaries are shown in Tab. B.4.

age model of the stacked SPECMAP curve incorporates uncertainties in the precise age of the individual events. For isotopic event 6.0, for example, Imbrie *et al*. (1984) propose an error of ±3,000 yr. In comparison to the new stacked isotope curve for low latitudes of Bassinot *et al*. (1994) differences in the absolute age of individual isotopic events occur in the range from 1,000 to 3,000 yr. By pattern matching, the turning-points present along the analysed $\delta^{18}O$ curves could be correlated with the individual events of the SPECMAP curve. Ages of those events are shown in Tab. B-4.

The planktic isotope record is not complete in the sediments of the aplanktonic zone. Therefore, top and base of the lithified interval were ^{14}C-AMS dated. The radiocarbon ages were used as additional stratigraphic fix-points for the age-modelling.

B.2.3.3 Computerised age modelling and stacked curves

In a second procedure ages for each depth-point along the $\delta^{18}O$-curves were calculated by linear interpolation („linage“ command) using the computer software AnalySeries (Paillard *et al.*, 1996). To do this, the program adjusts the isotope curves as good as possible to the SPECMAP curve using

Table B-4: Ages of isotopic events for the SPECMAP- and the low latitude stack

** no ages

Event	**SPECMAP stack (ky BP)** Imbrie et al. 1984, Tab. 6	**Low latitude stack (ky BP)** Bassinot et al. 1994, Tab. 4
1.1	6	**
2.0	12	11
2.2	19	17
3.0	24	24
3.1	28	30
3.3	53	52
4.0	59	57
4.2	65	62
5.0	71	71
5.1	80	79
	83	**
5.2	87	86
	95	**
5.3	99	97
	104	**
5.4	107	106
	114	**
5.5	122	122
6.0	128	127
6.2	135	133
6.3	146	**
6.4	151	**
6.5	171	**
6.6	183	**
7.0	186	186

the previously determined stratigraphic fix points (events) and calculates depth-age pointers between the well defined events.

The individual isotope curves were combined to one curve calculating average isotope values for each age-point. The errors of the stack are standard deviations of the average isotope values.

B.2.3.4 Sedimentation- and accumulation rates

To calculate sedimentation rates for the individual isotope stages, the lithified interval and the sapropel and for certain sea-level sequences the sediment thickness of the intervals were simply divided by their duration. To estimate average carbonate and siliciclastic sedimentation rates the

bulk sedimentation rates were multiplied with the average carbonate or terrigenous content, respectively. Sediment accumulation rates were estimated with the equation of Sturm (1998), (Equ. B-1). Dry densities of the carbonate and the siliciclastic fraction were taken from Franz (1999) as a good approximation for mixed type sediments above 20 m depth in core with
$Dd_{carbonate} = 0.78 g/cm^3 \pm 0.02$ and $Dd_{siliciclastic} = 1.06 g/cm^3 \pm 0.04$.

Equation B-1: Calculation of sediment accumulation rates after Sturm (1998)

$$AR_{carbonate} = \frac{S \times \%carbonate \times Dd\ (carbonate)}{10}$$

$$AR_{siliciclastic} = \frac{S \times \%siliciclastic \times Dd\ (siliciclastic)}{10}$$

AR = Accumulation rate
S = Sedimentation rate
Dd = Dry density

B.2.3.5 Calculation of salinities

Two different methods - both based on stable oxygen isotopes - were used for the calculation of paleo-salinities of Red Sea waters. (1) Paleo-salinities during IS 2 were calculated from stable oxygen isotopes analysed on bulk sediments and fine fraction of the lithified interval. (2) The stacked planktic oxygen isotopes were used to calculate the salinity variations of surface waters of the whole record.

Salinities during IS 2

High resolution stable oxygen isotopes and carbonate mineralogies (X-ray diffraction) were analysed on lithified and unlithified (<63 µm) samples in core S1. Stable isotopic data were corrected for fractionation during precipitation of aragonite, HMC, and LMC using mineral abundance derived from XRD-data. The following equations were used to calculate paleo-salinities of bottom- and surface-waters (Equ. B-2):

Equation B-2: Calculation of paleo-salinities based on stable $\delta^{18}O$-analysis and mineralogical composition of the lithified interval

1. Correction for the enrichment of $\delta^{18}O$ in aragonite and Mg-calcite (Gonzáles & Lohmann, 1985): Aragonite is enriched 1.5 to 2.0‰ and HMC is enriched 1.8 to 1.9‰ in $\delta^{18}O$ relative to calcite equilibrium:
$\delta^{18}O$(calcite) = [($\delta^{18}O$ * % Aragonite)-2‰]+ [($\delta^{18}O$ * % HMC)-2‰] +[($\delta^{18}O$ * % LMC)]
2. Conversion from PDB into SMOW (Standard Mean Ocean Water, Craig, 1966) after Coplen *et al*. (1983):
$\delta^{18}O$ SMOW = [$\delta^{18}O$ (PDB) +30.86] * 1.03091
3. Calculation of the $\delta^{18}O$ of palaeo bottom-water at 21° C, after O´Neil (1969):
a) 1000 ln α calcite-water = 2.78 ($10^6 T^{-2}$) -3.39, b) $\delta^{18}O$ calcite - α = $\delta^{18}O$ water
(ln α = temperature depending fractionation factor of $\delta^{18}O$ between calcite and water; T = temperature in kelvins)
4. Paleo-salinity after Craig (1966): **Salinity (‰) = [$\delta^{18}O$ water (SMOW) + 9.725]/0.287**

Salinities of surface waters based on planktic stable oxygen isotopes

The sea-surface salinities were calculated after the methods used by Hemleben *et al*. (1996) Geiselhardt (1998), see Equ. B-3, without further correction for temperature variations and the vital-effect of the foraminifers, which is small for *G. ruber* (pers. com. Rainer Zahn, GEOMAR Kiel, Germany).

Equation B-3: Calculation of paleo-surface salinities after (Hemleben *et al*., 1996; Geiselhardt, 1998;)

1. Calculation of the difference between the analysed $\delta^{18}O$-value of the foraminifer tests and that of mean ocean water (Vogelsang, 1990): $\Delta\delta^{18}\mathbf{O} = \delta\mathbf{c} - \delta\mathbf{w}$ ($\delta c = \delta^{18}O$ of the planktic foraminifer test; $\delta w = \delta^{18}O$ of mean ocean record)
2. Salinity difference to the present condition which is set at zero by definition: $\Delta\mathbf{S} = \Delta\delta^{18}\mathbf{O}/\mathbf{0.29}$ (ΔS = difference in salinity compared to today, 1‰ salinity change = 0.29‰ $\delta^{18}O$ (Craig, 1966))
3. Correction of the individual ΔS-values by the ΔS calculated on the core top: $\Delta\mathbf{S\ zero} = \Delta\mathbf{S} - \Delta\mathbf{S\ core\ top}$ (ΔS zero = offset of ΔS to recent salinity)
4. Addition of the ΔS zero to the present day surface salinity of the central Red Sea which is about 39‰ (Wyrtki, 1971): $\mathbf{S} = \mathbf{S\ recent} + \Delta\mathbf{S\ zero}$ (S = paleo-salinity in ‰, S recent = present salinity)

B.2.4 Radiocarbon ages

Calciturbidites and lithified layers in core S6 and S1 were radiocarbon dated in order to obtain the age of shallow-water input events and to determine the age of submarine lithification. Approximately 10 mg (= 1.2 mg C) of unaltered coral fragments were selected from the >1000 µm fraction from the sand layers for ^{14}C-AMS (Accelerator Mass Spectrometry) analysis. Samples of the lithified interval were selected after previous stable isotope and mineralogical analysis. From each sample a lithified chip and interspersed unlithified fine fraction (< 63 µm) were analysed.
The ^{14}C-AMS analysis were performed at the Leibniz Laboratory of the Christian-Albrechts-University in Kiel (Prof. Dr. P. Grootes). Samples were washed in 0,5 ml 30% H_2O_2 to remove organic mater, uppermost carbonate layers and adsorbed CO_2. For analysis, the samples were converted into CO_2 gas by dissolution with 100% phosphoric acid at 50 °C. ^{14}C-data were corrected for isotope fractionation using $^{13}C/^{12}C$-ratio that were analysed simultaneously with the AMS. The analytical errors of the AMS-measurement are smaller than ±1% for radiocarbon ages younger than 30,000 ^{14}C-AMS yr. The oldest sample in the dataset has a radiocarbon age of 45,650 ^{14}C-AMS yr with an error of +2,890/-2,120 years, which corresponds to +6.3/-4.6 %.
Resulting ages are conventional radiocarbon ages (Stuiver & Polach, 1977). No correction for reservoir age effects were made. Reservoir age corrections for Red Sea waters are difficult to determine due to the restricted circulation of deeper water masses, especially during the last glacial sealevel lowstand. Thus, calendar ages were calculated using the U/Th-calibration of Bard *et al*. (1993) derived from dated corals of Barbados and Mururoa without reservoir correction. This calibration curve (Equ. B-4) is only valid for radiocarbon ages between 8,500-20,000 yr. The calculated calendar ages should only be seen as an approximation.

Equation B-4: Calculation of calendar ages based on the U/Th-calibration obtained from corals of Barbados and Mururoa (Bard *et al*., 1993).

Calendar age (yr BP) = 1.24 * radiocarbon age (yr BP) - 840

B.2.5 Carbonate and total organic carbon (TOC)

Carbonate and organic carbon (TOC) content of the bulk sediments of cores AL, S1, S2, S3 and S6 were analysed with a LECO-analyser at GEOMAR. The sediments were hand ground to sizes smaller then 63 µm. Two specimens of each sample were analysed for organic carbon and total carbon (TC). In a first step, the TOC-content of a sample was measured after multiple dissolution of the biogenic carbonate with diluted HCL. In a second step the TC-content was analysed. Using the difference between TC % and TOC % the calcium carbonate content of the sample was calculated after Equ. B-5. Between replicates a maximum deviation of 0.5% for TC and 0.05% for TOC was tolerated. If differences exaggerated these values the sample was analysed again.

Equation B-5: Calculation of the carbonate-content from the analysed total carbon and organic carbon

$CaCO_3$ (%) = (TC (%) - TOC (%)) x 8.3

B.2.6 Mineralogy

B.2.6.1 X-ray diffraction

X-ray diffraction analysis (XRD) was performed with a Philips X-ray machine (PW 1710) at GEOMAR in Kiel to calculate the abundances of carbonate minerals and quartz in the bulk sediments and the fine fraction (X-ray beams are created by a Co-anode with a wave length of 1,7903Å at 40 kV and 40 mA).
Each sample was hand ground to sizes finer than 63 µm, homogenised and subsequently pressed into the specimen holder. The powder specimens were scanned from 28 to 40 2Θ. In this range the main peaks of the analysed minerals are present in the diffractogramme (Fig. B-3).

B.2.6.2 Aragonite/calcite ratios

The relative amounts of aragonite, LMC and HMC were calculated with the peak area method after Milliman (1974). Peak areas of main intensities were measured after peak correction with respect to quartz using the computer program MacDiff 3.0 (Petschik, 1993). To recalculate peak area ratios into aragonite/calcite ratios for each sample a calibration curve was used. The calibration curve was established experimentally by measuring known mixtures of skeletal aragonite (scleractinians)

and synthetic calcite by Nils Andresen for the XRD-machine at GEOMAR (Fig. B-4A). Standard deviations of three replicates for each standard sample were calculated. A linear increase in the errors ranging from 0.08% to 5.16% 2σ for aragonite/calcite-ratio between 0 and 35 % was observed. A linear correlation between standard deviation and aragonite/calcite ratios was used to calculate individual errors for each sample (Fig. B-4B). These errors include inhomogenity of the sample and errors in peak area measurement. It is important to mention that aragonite/calcite calibration curves found in the literature lead to completely different values when applied to the analysed peak area ratios. Only the shape of the aragonite curves vs. depth remains the same but not the percentages. The GEOMAR in-house calibration curve for example leads to aragonite/calcite ratios that are 20 to 40 percent higher than the published standard curve of Milliman (1974).

B.2.6.3 Aragonite Stratigraphy

Curves of aragonite/calcite ratios in periplatform sediments from the Bahamas, the Caribbean, the Maldives and the Great Barrier Reef run parallel to the planktic $\delta^{18}O$ curves. Therefore, they were used as a proxy for glacial-interglacial cycles in the worlds ocean (Droxler & Schlager, 1985; Reijmer *et al.*, 1988; Droxler *et al.*, 1990; Glaser & Droxler 1993; Alexander, 1996). During interglacial sea-level highstands, the aragonite/calcite-ratios in periplatform sediments are higher compared to glacial lowstands. When comparing the $\delta^{18}O$- and the curves of aragonite/calcite peak area ratios in the studied Red Sea cores one can see that both proxies show the glacial-interglacial cycles and turning-points (= events). Thus, additionally to isotope stratigraphy an aragonite-age model of core AW was created by pattern matching of the aragonite curve (bulk sediments) with the SPECMAP-curve (see chapter isotopes).

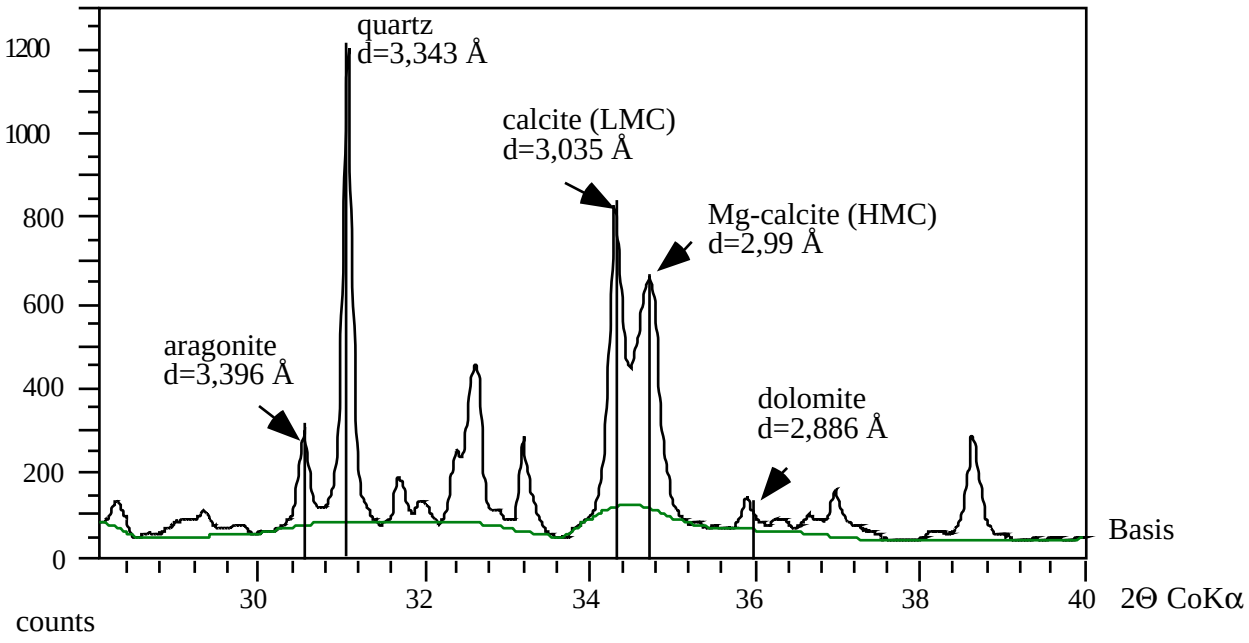

Figure B-3: Diffractogram showing the main peaks of the carbonate minerals and quartz with the d-values given in Milliman (1974).

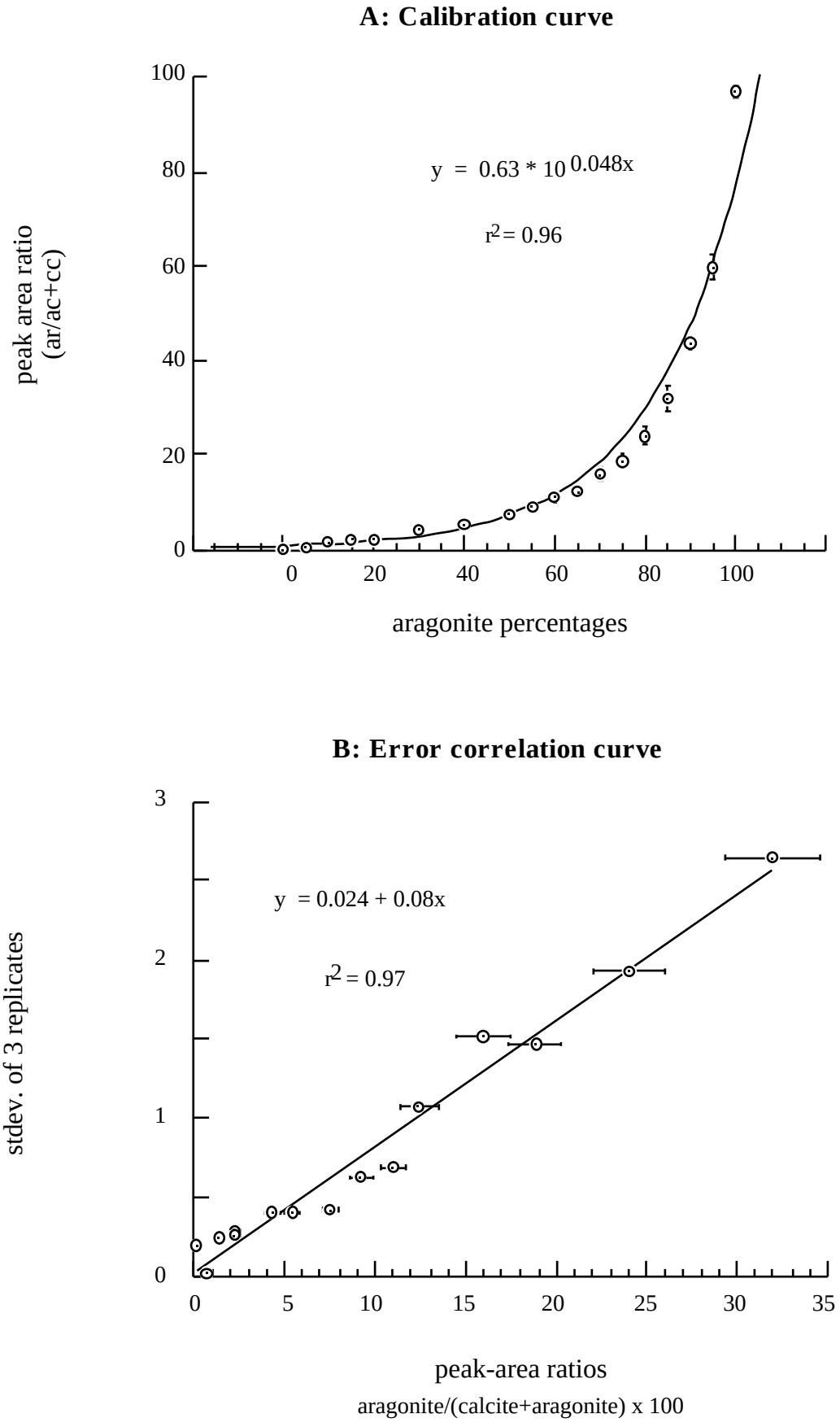

Figure B-4: (A) Calibration curve for the calculation of aragonite and calcite percentages in the sample based on peak-area ratios established by Nils Andresen at GEOMAR and (B) the error correlation curve derived from the standard deviations calculated for three replicates of each standard sample. Note that the errors show a linear increase with increasing aragonite/calcite ratios. With the equation of the correlation curve individual errors were calculated. Ar/(ar+cc) = peak areas of aragonite/(aragonite+calcite).

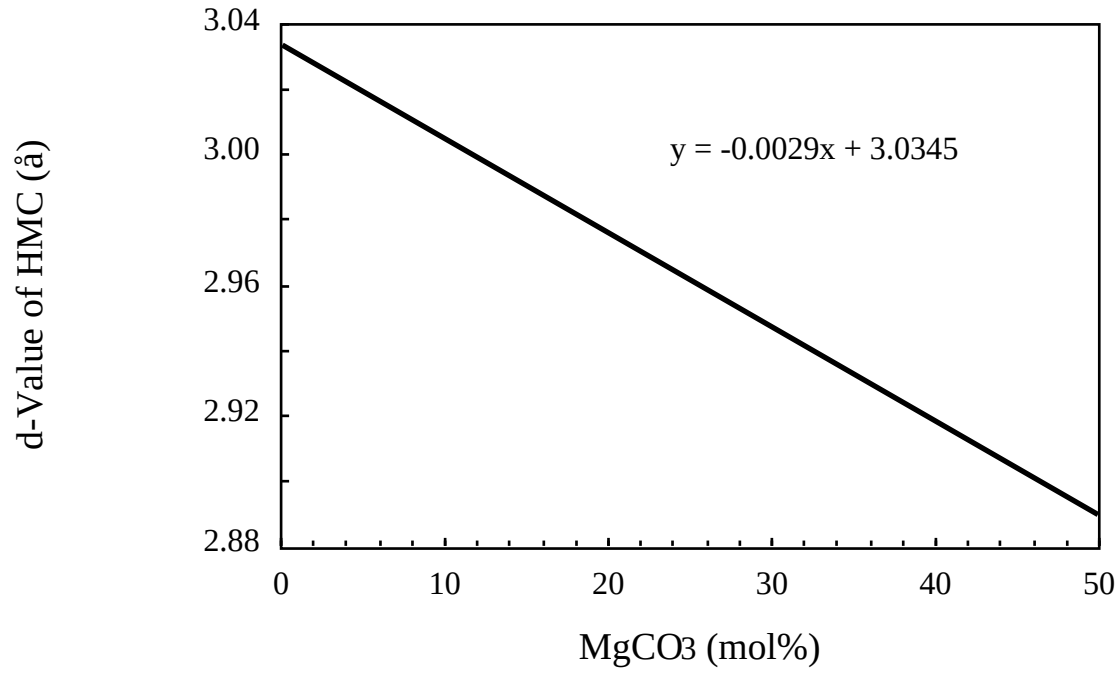

Figure B-5: Linear correlation curve between d-values of HMC peaks and the mol % of $MgCO_3$, modified after Hardy & Tucker (1988).

B.2.6.4 Mol % $MgCO_3$

From the d-values of individual HMC peaks analysed on periplatform and lithified sediments the $MgCO_3$ content of the samples was calculated using the linear correlation curve given in Hardy & Tucker (1988) (Fig. B-5).

B.2.6.5 Dolomite and Quartz intensities

As a relative scale for quartz concentration the height (intensity) of the main peak (d = 3.343 Å) was measured automatically with the MacDiff software. Dolomite quantities in analysed samples are too small for measurement of peak areas. Therefore, only intensities of the main peak were analysed to display the relative changes in dolomite concentration with depth in core. The position of the main peak (d ≈ 2.9 Å) varies with the Mg/Ca-ratios of the dolomite fraction for each sample.

B.2.7 Geochemistry

B.2.7.1 X-ray fluorescence

Major and trace elements (besides CO_2 and H_2O) of the bulk sediment were analysed with X-ray fluorescence (XRF) using a X´Unique sequential X-ray spectrometer at GEOMAR. The x-ray beams are created by a rhodium-tube. Samples were hand-ground to obtain a sample finer than 63 µm before preparing melting tablets. Those were automatically scanned in the XRF-machine. In each run the standards AN and NBS-97a were analysed to determine the analytical errors. In one series the standard KH-2 was used. The analytical error of the XRF-measurement lies below 10% for all elements, only MgO and TiO_2 show deviations of up to 35% from the rated values.

B.2.7.2 High- and low-Sr-aragonite

The high- and low-strontium aragonite concentration of the bulk sediment was calculated on a siliciclastic free-base using the method after Kenter (1985) and Boardman *et al.* (1986). Shallow-water aragonite is generally enriched in strontium (>7,500 ppm) while calcitic components of planktic sources contain less strontium (< 2,000 ppm) (Milliman, 1974; Morse & Mackenzie, 1990). Thus, the strontium content in periplatform sediments lies on a mixing line between low-Sr calcite and high-Sr aragonite (Boardman *et al.*, 1986) (Fig. B-6 and Equ. B-6). In this study the end members of 2,000 ppm for calcite and 8,500 ppm Sr for aragonite were chosen based on the composition of Red Sea reefal sediments (Gabrié & Montaggioni, 1982; Dullo, 1990; Piller & Mansour, 1990). Using the equation of the mixing line (Fig. B-6) together with the analysed aragonite- and strontium values of a sample the high- and low-strontium aragonite content could be calculated (Equ. B-6).

Equation B-6: Calculation of high- and low strontium aragonite (modified after Kenter, 1985 and Boardman *et al.*, 1986)

1. Calculation of the theoretic strontium content (Sr_{max}) of a sediment wherein all aragonite is of high-strontium-aragonite sources ($arag_{bulk}$ = analysed aragonite percentage): $\mathbf{Sr_{max} = 65 \times arag_{bulk} + 2000}$
2. Calculation of the high-Sr aragonite percentage of the sample using the analysed Sr content (Sr_{bulk}): $\mathbf{High\text{-}Sr\text{-}aragonite = (Sr_{bulk}/Sr_{max}) \times arag_{bulk}}$
3. Calculation of the low-Sr-aragonite content: $\mathbf{Low\text{-}Sr\text{-}aragonite = arag_{bulk} - High\text{-}Sr\text{-}aragonite}$

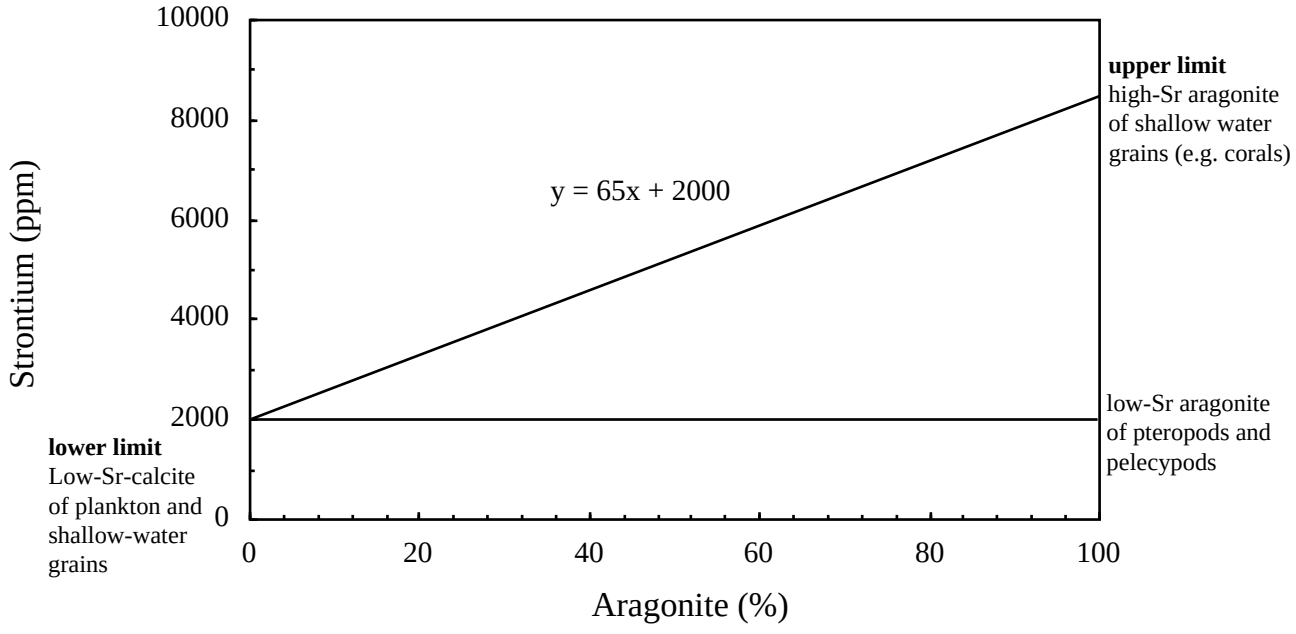

Figure B-6: Diagram showing the mixing line between low-Sr calcite (2,000 ppm) and high-Sr aragonite (8,500 ppm) for Red Sea periplatform sediments.

B.2.8 Microfacies

B.2.8.1 Thin section preparation

Unlithified periplatform sediments were impregnated with resin under high-vacuum before preparation of thin sections (size 28x48 mm, about 30µm thick). Additionally, large sized (5x5 cm) thin sections were made from calciturbidites following the same procedure. For the microscopic analysis of the lithified interval a continuous series of large thin sections (7x5 cm) was made of the whole sequence of core S1. The deep frozen sediment sections were vacuum dried before impregnation with resin.

The microfacies was documented with black&white photography under the light microscope. The pictures were also stored digital on Photo-CD´s for further use (photo plates, on-line facies catalogue). All photographs were made with ILFORD FP 4 Plus (125 ASA) black and white prints.

B.2.8.2 Classification and Taxonomy

Samples of the sieve fractions were studied under the binocular for taxonomic determination of planktic foraminifers and pteropods. Planktic foraminifers were identified in the coarse fraction using the determination characteristics described by Bé (1977) and Hemleben *et al*. (1989), the classification of pteropods was based on studies of Almogi-Labin (1982) and Ivanova (1985). For the identification of skeletal and non-skeletal shallow-water components in thin sections works of Dullo (1987, 1990) and Piller (1994) were used.

B.2.8.3 Pointcounting

A quantitative component analysis of the thin sections (periplatform sediments and calciturbidites) was performed under the light microscope with an automatic point-counting device (Model F, Prior Scientific Instruments). To obtain the modal composition of each sample 200 points per thin section were counted in a grid after the grain-solid method (Dunham, 1962). After pointcounting the individual components were summarised into 9 facies-indicative groups (pointcount groups), like e.g. „plankton“ or „reef builders“ (see Chapter C. 9). The statistical error of pointcounting is described by the standard deviation after Chayes (1956) (Equ. B-7).

Equation B-7: Statistical error of pointcounting

$$\text{error} = \pm 100 \times \sqrt{\frac{p\,(1-p)}{n}}$$

n = total number of counts (200)

p = percentage of the component

The application of Equ. B-7 leads to a symmetrical (Gauss) distribution of the absolute error, with a maximum at p = 50% (error = ±3.5, with n = 200). That means that rare components have higher relative errors. If the percentage of a component in the sample for example is 2% the absolute error is ± 0.9% but the relative error gets extremely high and is ±45%. The higher the component abundance the smaller the relative error.

CHAPTER C: RESULTS

C.1 Lithology: Sediment sequence and lithofacies

The lithologic profiles of the studied sediment cores are shown in Fig. C.1-1. All cores exhibit the same characteristic sediment sequence (Fig. C.1-2) which is dominated by a rather uniform greenish-grey periplatform ooze with interbedded skeletal shallow-water sands (calciturbidites) in the proximal cores. This standard type of sedimentation is interrupted by a lithified interval which was built during marine isotope stage (IS) 2. On top of this interval a sapropel occurs that marks the transition between IS 2 and the Holocene (IS 1).

C.1.1 Holocene sediments (IS 1)

The uppermost parts of the sequence consist of the Holocene sediments in all cores, except for core S3 and AW, where lithified sediments of IS 2 occur directly at the top of core. The Holocene sequence is 45-125 cm thick and predominantly consists of characteristic periplatform sediments (Schlager & James 1978), which can be described as a mixture of a pelagic carbonate ooze and shallow-water derived components (Fig. C.1-3, Plate 3-1/2). The matrix content of these greenish-grey, silty-sandy, nanno-ooze varies between 10-75% (point-counting). It decreases in the proximal cores, where the sediments become generally coarser. The micritic matrix is rich in silty quartz- and biodetrital clasts. The main components are pteropods and planktic foraminifers, terrigenous grains (quartz, feldspar), bioclasts and shallow-water reef components (scleractinians, coralline red algae, encrusting foraminifers, large benthic foraminifers, molluscs and pellets). Bioturbation destroyed the primary sediment structures and led to a mottled texture with distinct burrows. Coarse sediments are enriched in these burrows.

In the proximal core S6 two medium-coarse grained sand layers are intercalated in the nanno-ooze (11-17 cm and 83-96 cm). These skeletal sands (pack/grainstones) are rich in shallow-water platform-derived components. The deeper layer shows inverse gradation and an erosional base contact (compare to Plate 3-6).

C.1.2 Sapropel (Termination I)

Downcore the greenish-grey nanno ooze becomes gradually darker. After a distinct sedimentary boundary a 3-5 cm thick sapropel follows (Plate 3-4). Only in core S6 a 2 cm thick, white, medium-size sand layer separates the dark greenish-grey periplatform ooze from the sapropel. The sapropel is always fine laminated, contains 0.5-1.5% organic carbon, has a relatively low carbonate content (30-40%) with a high aragonite/calcite ratio (70-90%). The main components are siliciclastic grains and bioclasts. The plankton content is smaller than 10% and the assemblage is dominated by epipelagic pteropods (*Creseis chierchiae*, *Limacina trochiformis*). The sapropel marks the last deglaciation phase (Termination I) in the Red Sea and is about 13,000 to 8,500 ^{14}C-yr old (Almogi-Labin *et al*., 1991; Hofmann *et al*., 1998; this study).

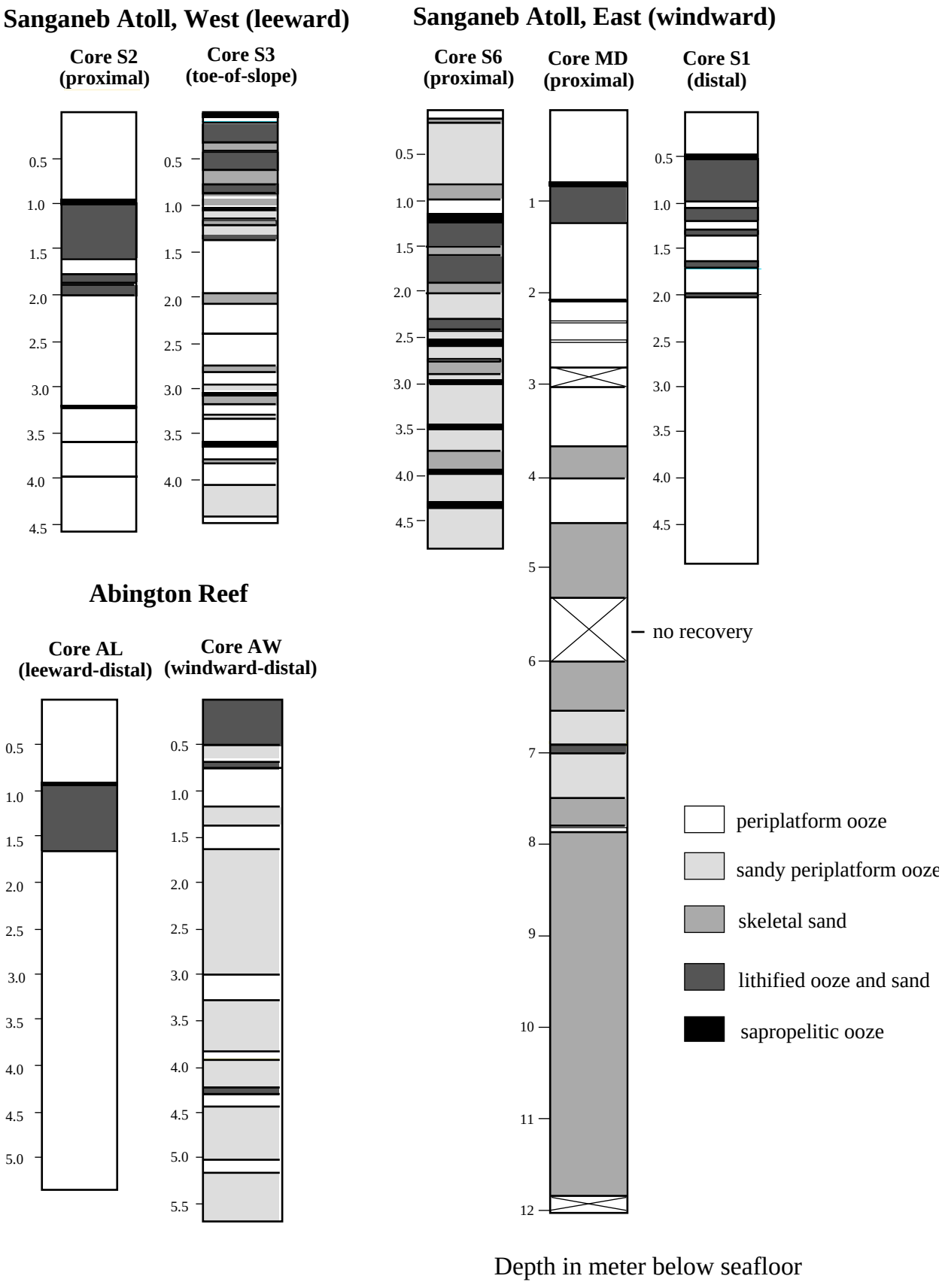

Figure C.1-1: Lithologic profiles of the studied sediment cores. The lithologies are explained within the description of the litho-stratigraphic units in the text.

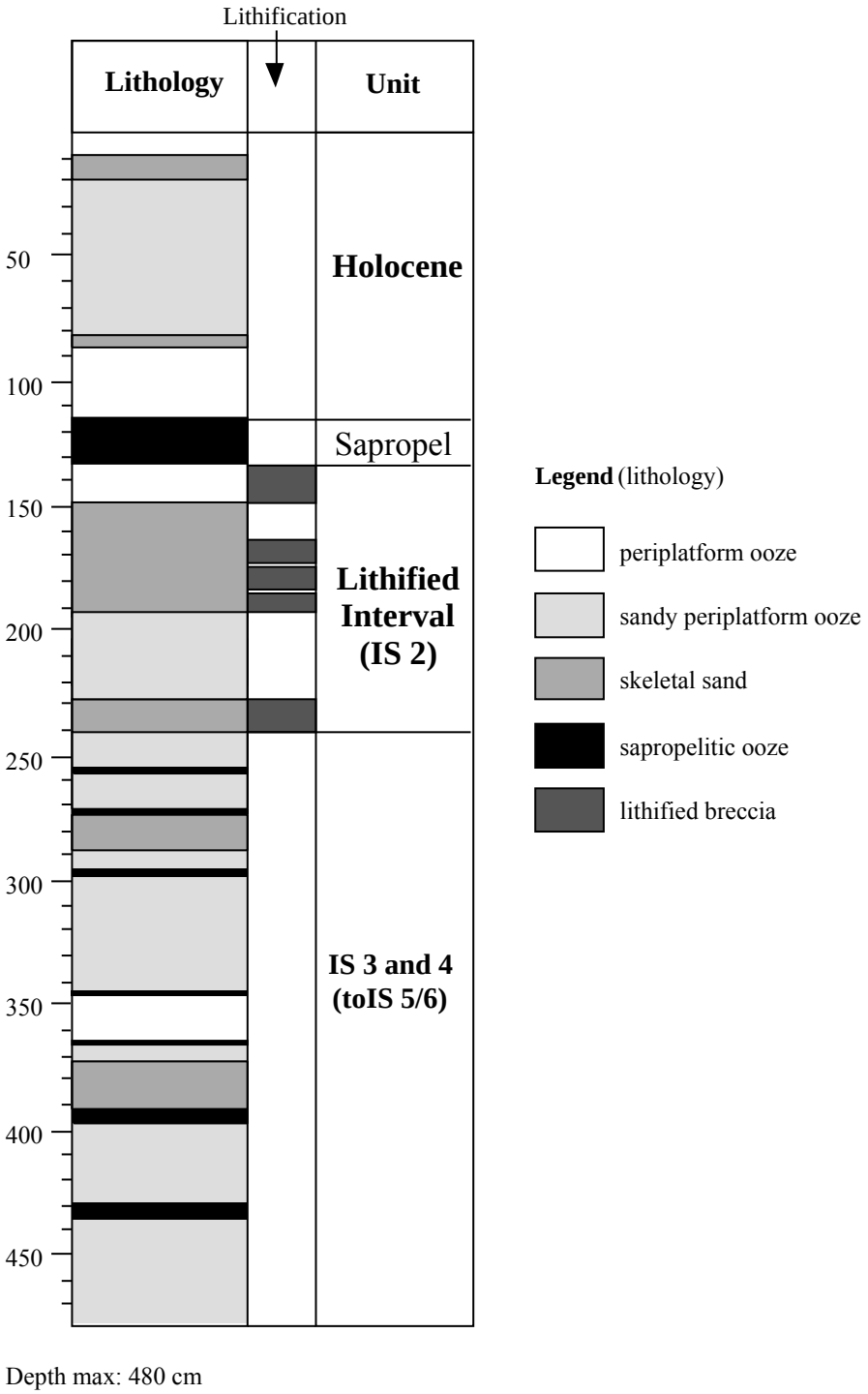

Figure C.1-2: Characteristic sediment sequence like observed in all cores which were obtained in the vicinity of Sanganeb Atoll and Abington Reef (core S6).

C.1.3 Lithified interval (IS 2)

The thickness of the lithified interval varies between 45 and 110 cm. The sediments consists of lithified carbonate layers interbedded with unlithified nanno-ooze, mud layers and skeletal sands. In the sediment cores most of the lithified layers are brecciated and occur as an irregular meshwork of platy, chip-like components (Plate 3-5) and unlithified sediment. Only in the cores S1 and MD the first 5 cm of the lithified interval are laminated and not brecciated. It is discussed in the literature if brecciation occurred during the coring process (Taviani, 1998c) or earlier at the seafloor possibly by seismic activity (pers. com. Brachert, 1998). In the upper part of the interval the lithified components are dominated by pebble-sized, laminated mudstones and structureless microspar-chips. Downcore the grade of lithification decreases and the chips become less abundant. They are replaced by sand-sized nodular components and lithified peloids. In the proximal cores the lithified components often consist of skeletal pack-, grain- and rudstones.

The lithified layers are separated by unlithified skeletal sand and mud in the proximal cores S3 and S6. The other cores show a more or less continuous 50 to 70 cm thick, breccia interval. In the cores S1 and S2 other lithified beds occur below the main interval, which are separated by 10 to 20 cm thick mud layers. Further isolated, cm-thick lithified beds occur in deeper parts of core S1 (in 130, 165 and 200 cm), core MD (in 345 and 700 cm) and core AW (in 425 cm). In core S1 the two chip-layers in 165 and 200 cm form the base of thin sapropelitic beds.

The plankton assemblage in the lithified interval is dominated by the pteropod *Creseis acicula*, planktic foraminfera are rare or absent. Therefore, this sequence is also called „aplanktonic zone“ (Berggren & Boersma, 1969; Reiss *et al*., 1980). In thin sections it can be observed that the inner and outer surfaces of many pteropod shells are covered by epitaxial aragonite. A detailed description of the micro- and ultrastructure of the lithified layers is found in Brachert (1996, 1999) and Hofmann *et al*. (1998).

In the proximal cores skeletal sands are abundant in the lithified interval, which can be totally or partially lithified. Most of those sands were interpreted as shallow-water calciturbidites and in some cases graded bedding and an erosional base contact is present (Plate 3-6/7/8). These skeletal sands are dominated by reef-derived shallow-water components (a detailed description of the composition is given in Chapter C.9).

On the Sudanese shelf the lithified interval comprises an age of about 23,000 to 13,000 ^{14}C-yr (Almogi-Labin *et al*., 1991; Brachert, 1996, 1999; Hofmann *et al*., 1998; Emmermann *et al*., 1999), which covers most of marine isotope stage 2 (IS 2).

C.1.4 Pleistocene sediments (IS 3 to IS 6)

Below the lithified interval again the same standard type of sedimentation as described for the Holocene sequence is found. Greenish-grey (silty-sandy) periplatform ooze (Plate 3-1/2) is the major sediment type in the entire interval that reaches from the base of the lithified interval to the bottom of the cores. Compared to the Holocene periplatform sediments it is coarser grained and becomes a sandy ooze in core S3 and S6. Also in core AW from the windward side at Abington Reef sandy ooze layers are present within the periplatform ooze. The sediment composition is

similar to that of the nanno-ooze from the top of the core but shows slightly increased amounts of shallow- water components.

Several 1-5 cm thick, dark sapropelitic layers occur interbedded with the greenish-grey nanno-ooze. Some of the sapropelitic layers are laminated, the top boundary is always bioturbated and shows a mottled texture. The sapropels are extremely water-rich and the faunal assemblage is often dominated by pteropods.

In the proximal cores calciturbidites (Plate 3-6/7/8; pack-/grainstones and rudstones) occur frequently within the periplatform sediments. The lower part of core MD (3.5-12 m) is dominated by very coarse skeletal sand/gravel layers. The calciturbidites are 5-20 cm thick in the cores S3 and S6 and can reach 30 to > 100 cm in core MD. Graded bedding was observed in two of the sand layers in core S3 (195-205 cm) and S6 (270-285 cm). The matrix of the skeletal sands and gravels reaches < 30% and consists of bio-detrital nanno-ooze. Both, the percentage of planktic foraminifers and pteropods as well as the percentage of terrigenous components are < 10%. The major components of the calciturbidites are shallow-water derived grains. The skeletal rudstones at 370-400 cm in core MD contain scleractinian fragments and other reef derived rubble > 2 cm in diameter!

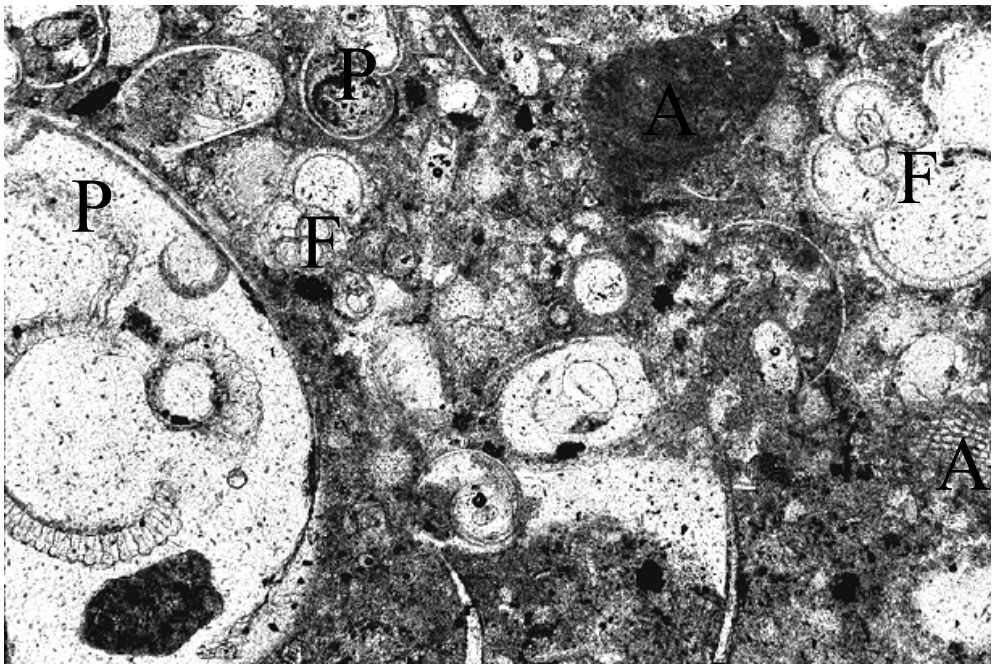

Figure C.1-3: Characteristic pteropod- (P) and foraminfer (F) -rich periplatform ooze, which contains shallow-water derived components (coralline red algae, A). Note the micropeloidal structures scattered within the bio-detritic matrix, which suggests an early stage of Mg-calcite precipitation at the seafloor.- Core S6, 90 cm, 100x.

C.2 Stratigraphy and age models

The age model of the studied cores is based on climate-stratigraphic correlation of planktic oxygen isotope curves and aragonite/calcite-ratios (core AW) with the global SPECMAP-curve (Imbrie *et al*., 1984). Climate-stratigraphic age modelling was not possible in the lithified interval due to the lack of planktic foraminifers. In this interval radiocarbon dating was used to create a high resolution time record for the last glacial sea-level lowstand in the Red Sea. Scleractinian fragments from calciturbidites were radiocarbon dated and used as an independent time control of the shallow-water sediment export.

C.2.1 Climate-stratigraphy

In Fig. C.2-1 the climate stratigraphic correlation of the cores AL, AW and S1 is shown. Next to the oxygen isotope curves the climate-stratigraphic correlation with the aragonite curve was shown for core AW. The oxygen isotope curves of the other cores can be found in Fig. C.5-2 to C.5-4 in Chapter C.5. The depth-age plots that resulted from the climate-stratigraphic correlation of the isotope and aragonite curves are shown in Fig. C.2-2. The depth-position of age-fix points are summarised in Tab. C.2-1. The analysed isotope values with the analytical errors of the isotope measurement can be found in Appendix 1.

C.2.1.1 Isotope stratigraphy

The correlation of the Red Sea $\delta^{18}O$-curves with the global SPECMAP-curve is fairly straightforward in all cores, except for core MD. In the cores AL, S6 and S2 SPECMAP-event 1.1 (Holocene highstand, about 6,000 yr BP) is clearly visible, while major parts of the Holocene sequence are not recorded in core S3. In cores S1 and MD only the latest Holocene sediments are missing. Isotopic event 2.2 (19,000 SPECMAP-yr) was not recorded in the planktic oxygen isotope curves of any core. In all cores, except for core MD, glacial isotope stages IS 3 and IS 4 can be clearly distinguished and show a high resolution record. The events 3.3 (53,000 SPECMAP-yr) and 4.2 (65,000 SPECMAP-yr) are clearly visible.

The cores S2, S3 and S6 end at the transition from IS 4 to IS 5, while the cores S1 and AL reach further back in time and clearly show the glacial-interglacial boundary (isotopic event 5.0, 71,000 SPECMAP-yr). The events 5.1 (80,000 SPECMAP-yr) and 5.2 (87,000 SPECMAP-yr) of the last interglacial are also visible in the isotope record of both cores. The sedimentary history of these cores ends at the transition between isotopic events 5.2 and 5.3. In core AW the isotope record is not complete and reaches from the base of the lithified interval to isotopic event 5.5. Older parts were not measured and the Holocene sequence is missing. Substages 5a to 5e are clearly developed in the isotope record of this core. Additionally, aragonite stratigraphy of core AW was performed (C.2.1.2).

In Core MD (piston core) the entire isotope record seems to be stretched in stage 5 due to the extreme thickness of shallow-water sands. Nevertheless substages 5a, 5b and 5c are visible and show isotope values of 0.6, -1.0 and -0.6‰ respectively, which are comparable to those in other cores. Isotopic event 4.2 is not detected, it might be situated in the missing core interval between

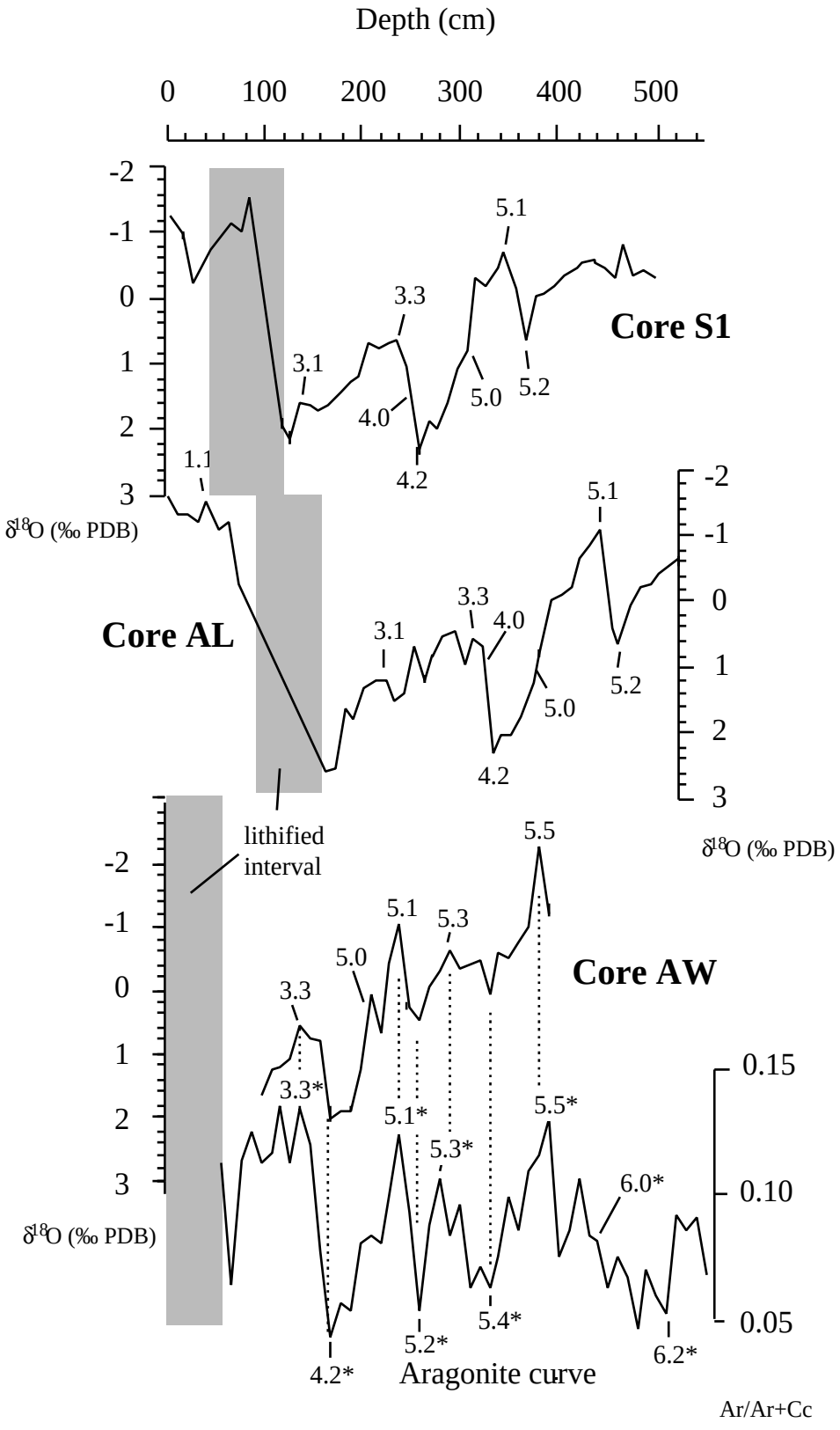

Figure C.2-1: Stable oxygen isotope curves analysed on planktic foraminifers showing the individual age-fix points (SPECMAP-events) which where determined by climate-stratigraphic correlation with the SPECMAP curve. Isotope curves of the other cores are shown in Fig C.5-2 to C.5-4, Chapter C.5. For core AW the isotope record is not complete and reaches down only to event 5.5 (older parts were not measured). Additionally, the aragonite-curve of core AW is shown which was used for climate-stratigraphic correlation (see aragonite stratigraphy). * mark the turning points along the aragonite curve which correspond to SPECMAP events. The lithified interval comprises an age of about 13,000 to 23,000 ^{14}C-AMS yr. In this period planktic foraminifers are rare or absent (aplanktonic zone).

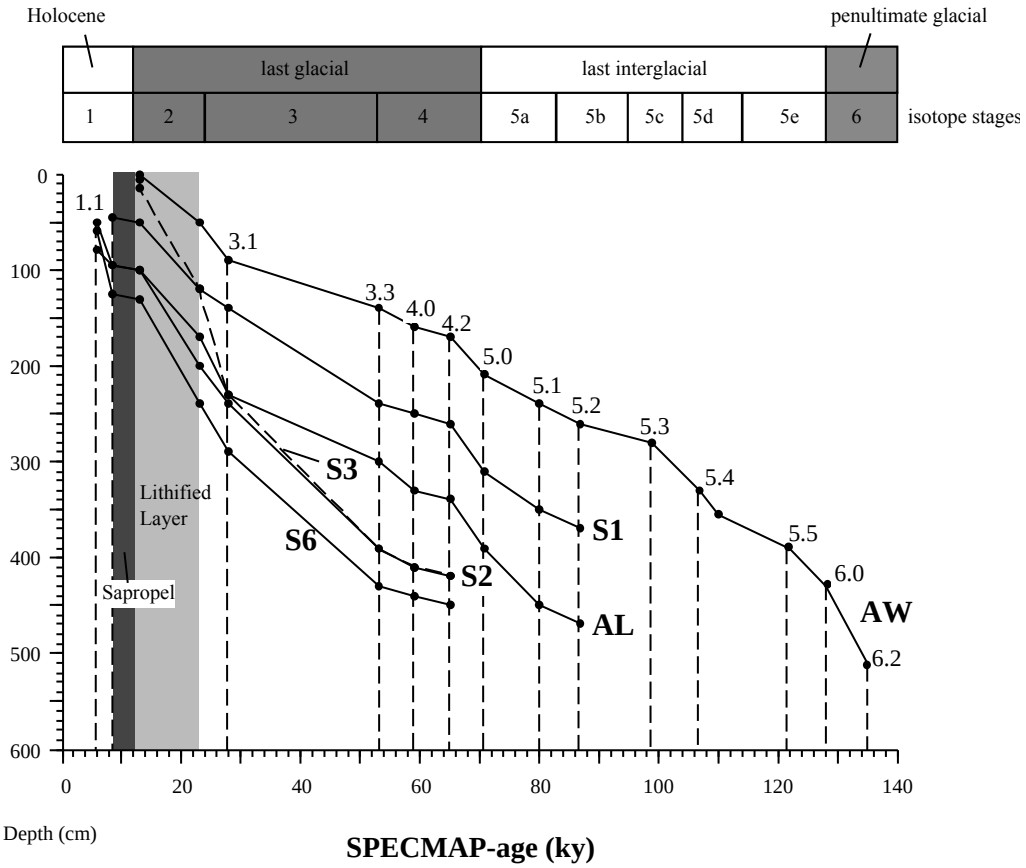

Figure C.2-2: Depth-age plots of the studied cores as a result of climate-stratigraphic correlation of oxygen isotope and aragonite curves (AW), completed with radiocarbon ages of the lithified interval and the sapropel. Depth and ages of the stratigraphic fix-points are summarised in Tab. C.2-1.

Table C.2-1: Position of age-fix-points

Fix-point	Age (ky)	Depth (cm)						
	SPECMAP	AL	AW	S1	S2	S3	S6	MD
1.1	6	50			80		60	2
Top Sapropel	8.5	95		45	95		125	85
Base Sapropel	13	100		50	100	7	130	90
Top LAL	13	100	0	50	100	15	130	90
Base LAL	23	170	50	120	200	120	240	135
3.1	28	230	90	140	240	230	290	
3.3	53	300	140	240	390	390	430	230
4.0	59	330	160	250	410	410	440	250
4.2	65	340	170	260	420	420	450	
5.0	71	390	210	310				300
5.1	80	450	240	350				320
	84	460	250	360				365
5.2	87	470	260	370				395
	95		270					
5.3	99		280					855
	103		300					
5.4	107		330					
	110		355					
5.5	122		390					
6.0	128		430					
6.2	135		510					

230-240 cm. Because of the unclear record core MD was not used for age modelling.

C.2.1.2 Aragonite stratigraphy

For core AW an aragonite-age model was established after pattern matching of the aragonite- with the global SPECMAP curve (Fig. C.2-1). The aragonite record in core AW reaches back to IS 6 (135,000 SPECMAP-yr), the Holocene sequence is completely missing. The last interglacial (IS 5) is fully developed in core AW and substages 5a-5e can be found in the aragonite record. Thus, AW is the only core which records the last interglacial sea-level highstand (5e, Emian = 110,000-128,000 SPECMAP-yr). The depth-age plot of core AW based on aragonite stratigraphy is shown in Fig. C.2-2.

C.2.2 Radiocarbon Ages

^{14}C-AMS dating was performed on lithified chips and the unlithified fine fraction of the lithified interval in cores S1 and S6. Radiocarbon ages of calciturbidites from the Holocene, the lithified interval and IS 3 where measured on scleractinian fragments in core S6 in order to obtain the age of shallow-water input events. Conventional ages (Stuiver & Polach, 1977) with individual errors and the calculated calendar ages (after Bard *et al.*, 1993) are shown in Tab C.2-3.

C.2.2.1 Radiocarbon ages of the lithified interval

In core S1 the radiocarbon ages of lithified chips and non-lithified fine fraction show a similar increase with depth in core (Fig. C.2-3). The ^{14}C-AMS ages range from 22,200 +200/-190 (lithified) and 20,730 ±230 ^{14}C-AMS yr (non-lithified) at the base of the lithified interval (121 cm) to 13,310±80 and 14,070±130 ^{14}C-AMS yr at the base of the sapropel (49 cm). The uppermost part of the sapropel in core S1 (47 cm) has an radiocarbon age of 12,930±90 and 12,840±90 ^{14}C-AMS yr in both series. Generally radiocarbon ages of the non-lithified series are about 500 to 1,500 yr older than those of the lithified series. This is not the case in the older and less lithified parts (100-120 cm). Here lithified samples are about 1,000 yr (117 cm) and 1,500 yr (121 cm) older than the unlithified mud. In both series one significant (87-89 cm) and three smaller (in 53, 73 and 105 cm) age inversions are visible in the record (Fig. C.2-3), which might be due to mixing and reworking of the sediments or disturbance during coring processes.

Sedimentation rates of lithified and unlithified series are similar in the upper part of the lithified interval in core S1 (50-100 cm), in which average rates of about 10 cm/ky (lithified) and 11 cm/ky (fine fraction) could be calculated. In the deeper and less lithified part the sedimentation rates of the unlithified series are much higher (15 cm/ky) than those obtained from the lithifed samples (5 cm/ky).

In core S6 the radiocarbon ages analysed on lithified samples show a more or less linear decrease from the base of the lithified interval to the youngest parts close to the base of the sapropel (Fig. C.2-4). The radiocarbon ages reach from 24,670 +220/-210 ^{14}C-AMS yr (230 cm) to 12,960±60 ^{14}C-AMS yr (132 cm), and show no inversions. Like in the lithified series of core S1 average „sedimentation rates“ are lower in the deeper part (5.3 cm/ky between 200-230 cm) and higher in the upper part (11.7 cm/ky between 230-130 cm).

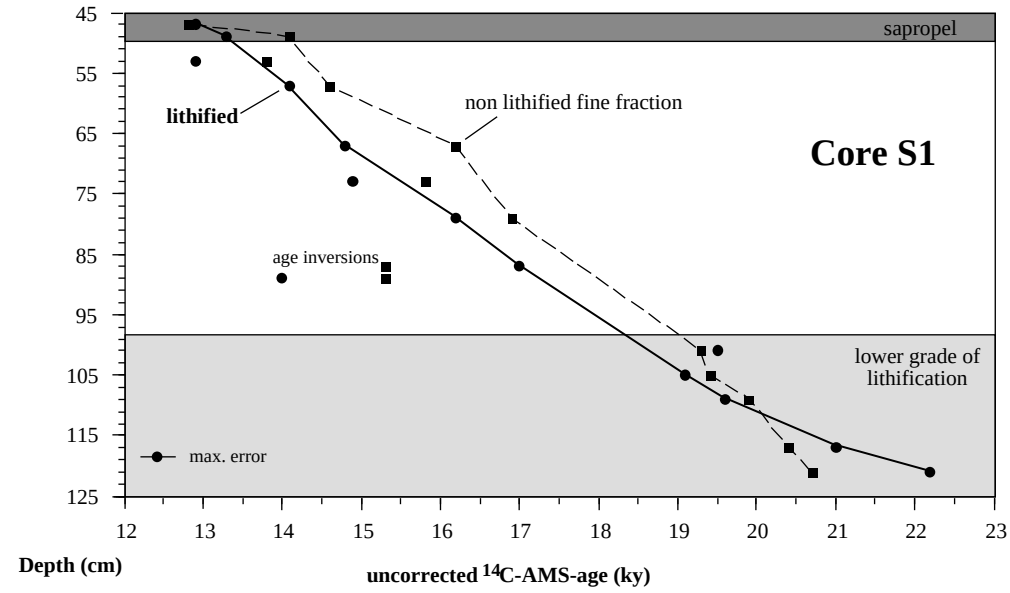

Figure C.2-3: Depth vs. ^{14}C-AMS ages of the lithified interval in core S1 based on uncorrected radiocarbon ages obtained on lithified bulk sediment and unlithified fine-fraction. Both time series show a downcore increasing trend with a significant age inversion between 87 and 98 cm depth in core. ^{14}C-AMS ages of the unlithified samples are generally 500-1,500 yr older, except for the lower and less lithified parts (lower grade of lithification).

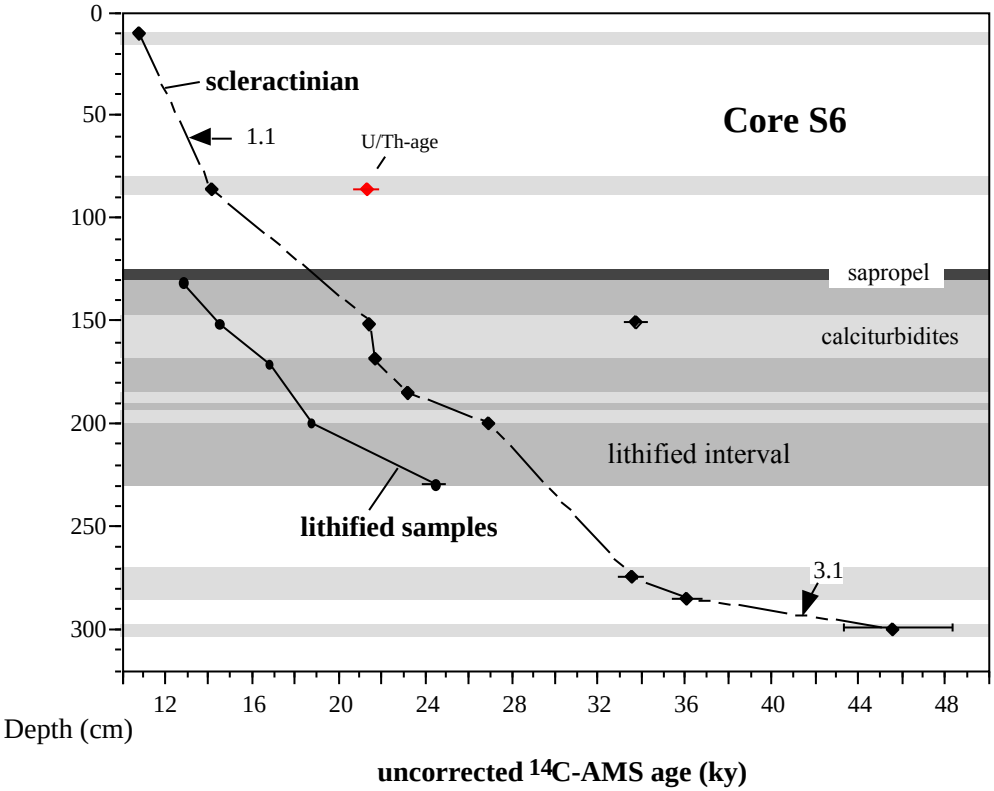

Figure C.2-4: Depth vs. ^{14}C-AMS ages of the lithified interval and of scleractinians selected from calciturbidites in core S6. ^{14}C-AMS ages of the lithified samples show a more or less linear age increase with depth. Scleractinian fragments (diamonds) from the calciturbidites are generally older than the surrounding sediments. This is shown by the discrepancies between ages of scleractinians within calciturbidites and lithified samples as well as the stratigraphic position of isotopic events. SPECMAP-event 3.1 for example (28,000 yr after Imbrie *et al*. (1984) is situated between two calciturbidites with scleractinian ages of about 36,000 and 46,000 ^{14}C-AMS yr. Scleractinian fragments of the calciturbidite in 86 cm were additionally U/Th-dated and show an age of 20,902±553 yr BP which is about 6,500 yr older than the corresponding ^{14}C-AMS age of 14,270±90 yr.

C.2.2.2 Ages of calciturbidites

Radiocarbon ages were analysed on scleractinian fragments that were collected from individual calciturbidites in core S6 (Fig. C.2-4). ^{14}C-AMS ages decrease from 45,650 +2890/-2120 yr in a depth of 300 cm to 10,870±60 yr in the youngest sand layer in a depth of 10 cm. Compared to radiocarbon ages of lithified sediments the particles of calciturbidites are about 5,000-8,500 yr older in comparable depth intervals (Fig. C.2-4). Further evidence for age offsets between scleractinian fragments from calciturbidites and periplatform sediments is found in the Holocene sequence. The youngest sand-layer has a ^{14}C-AMS age of 10,870±60 yr and occurs in a depth of 10 cm, while isotopic event 1.1 (6,000 SPECMAP-yr) occurs at a depth of 60 cm in the stable oxygen isotope record (Fig. C.2-4). Similar offsets were observed in a calciturbidite at 300 cm which is close to the depth-position of isotopic event 3.1 (28,000 SPECMAP-yr) in 290 cm. The sand has a ^{14}C-AMS age of 45,650 +2,890/-2120 yr.

The sand layer in 86 cm was U/Th-dated in addition to the ^{14}C-AMS analysis. An U/Th-age of 20,902±553 yr BP was measured while the ^{14}C-AMS age of the same sample is only 14,270±90 yr. It is assumed, that the U/Th-age is not reliable due to the very small amount of scleractinian material that was available for the measurement (200mg instead of 2000mg) and because of contamination as indicated by the high concentration of ^{232}Th in the sample (pers. com P. Grootes, 1999; see Tab. C.2-2).

Table C.2-2: U/Th-age, with concentrations and activities of the isotopes

			errors
^{238}U corr. concentration	(ppm)	4.0215	0.0327
^{238}U activity	(ppm/g)	3.0002	0.0244
^{234}U/^{238}U activity-ratio		152.5465	6.7744
^{230}Th concentration	(ppb)	0.0133	0.0003
^{230}Th activity	(ppm/g)	0.6070	0.0138
^{232}Th concentration	(ppb)	82.7285	0.3932
^{230}Th/^{238}U activity-ratio		0.2023	0.0049
Age	(years BP)	20,902	553.37

Table C.2-3: ^{14}C-AMS ages of the lithified interval and caliturbidites

* Radiocarbon after Stuiver & Pollach 1977. ** corrected for calendar ages using the U/Th-calibration of Bard *et al*. (1993) dated on corals from Barbados and Mururoa (valid for 8,500-20,000 ^{14}C-years BP). No reservoir age correction was performed. † U/Th dated.

Depth	Conventional age*	pos. error	neg. error	Calendar age**	% error	
(cm)	(^{14}C-years BP)			(years BP)	pos.	neg.
S1-lithified bulk sediment						
47	12930	90	-90	15193	0.7	-0.7
49	13310	80	-80	15664	0.6	-0.6
53	12900	90	-90	15156	0.7	-0.7
57	14080	100	-100	16619	0.7	-0.7
67	14840	110	-110	17562	0.7	-0.7
73	14890	80	-80	17624	0.5	-0.5
79	16160	120	-120	19198	0.7	-0.7
87	17010	130	-130	20252	0.8	-0.8
89	13940	100	-100	16446	0.7	-0.7
89	14010	80	-70	16532	0.6	-0.5
100	19540	130	-130	23390	0.7	-0.7
105	19060	160	-160	22794	0.8	-0.8
109	19640	150	-140	23514	0.8	-0.7
117	21040	200	-200		1.0	-1.0
121	22200	200	-190		0.9	-0.9
S1-unlithified fine fraction (< 63 µm)						
47	12840	90	-90	15082	0.7	-0.7
49	14070	130	-130	16607	0.9	-0.9
53	13810	70	-70	16284	0.5	-0.5
57	14630	110	-100	17301	0.8	-0.7
67	16270	150	-150	19335	0.9	-0.9
67	16150	90	-90	19186	0.6	-0.6
73	15810	120	-120	18764	0.8	-0.8
73	15980	100	-100	18975	0.6	-0.6
79	16930	150	-140	20153	0.9	-0.8
87	15330	90	-90	18169	0.6	-0.6
87	15360	80	-80	18206	0.5	-0.5
89	15080	90	-90	17859	0.6	-0.6
89	15290	80	-80	18120	0.5	-0.5
100	19280	150	150	23067	0.8	0.8
105	19380	150	-150	23191	0.8	-0.8
109	19880	120	-120	23811	0.6	-0.6
117	20420	130	-120			
121	20730	230	-230			
S6-sand layers (scleractinians)						
10	10870	60	-60	12639	0.6	-0.6
86	14270	90	-90	16855	0.6	-0.6
86	14270			20902±553†		
150	33740	580	-540		1.7	-1.6
150	21480	180	-180		0.8	-0.8
170	21920	160	-160		0.7	-0.7
185	23250	170	-160		0.7	-0.7
200	27020	270	-260		1.0	-1.0
274	33620	610	-560		1.8	-1.7

C.2.3 Stratigraphic zonation

As a result of climate-stratigraphic correlation, radiocarbon dating and lithologic zonation of the sediment cores from the Sudanese shelf, a generalised stratigraphic zonation of the periplatform sequence was compiled. In addition, the bio-zonation of Reiss *et al.* (1980) based on main plankton distribution is shown (Fig. C.2-5). A stacked isotope curve for the study area is shown in Fig. D-1, Chapter D. 1.

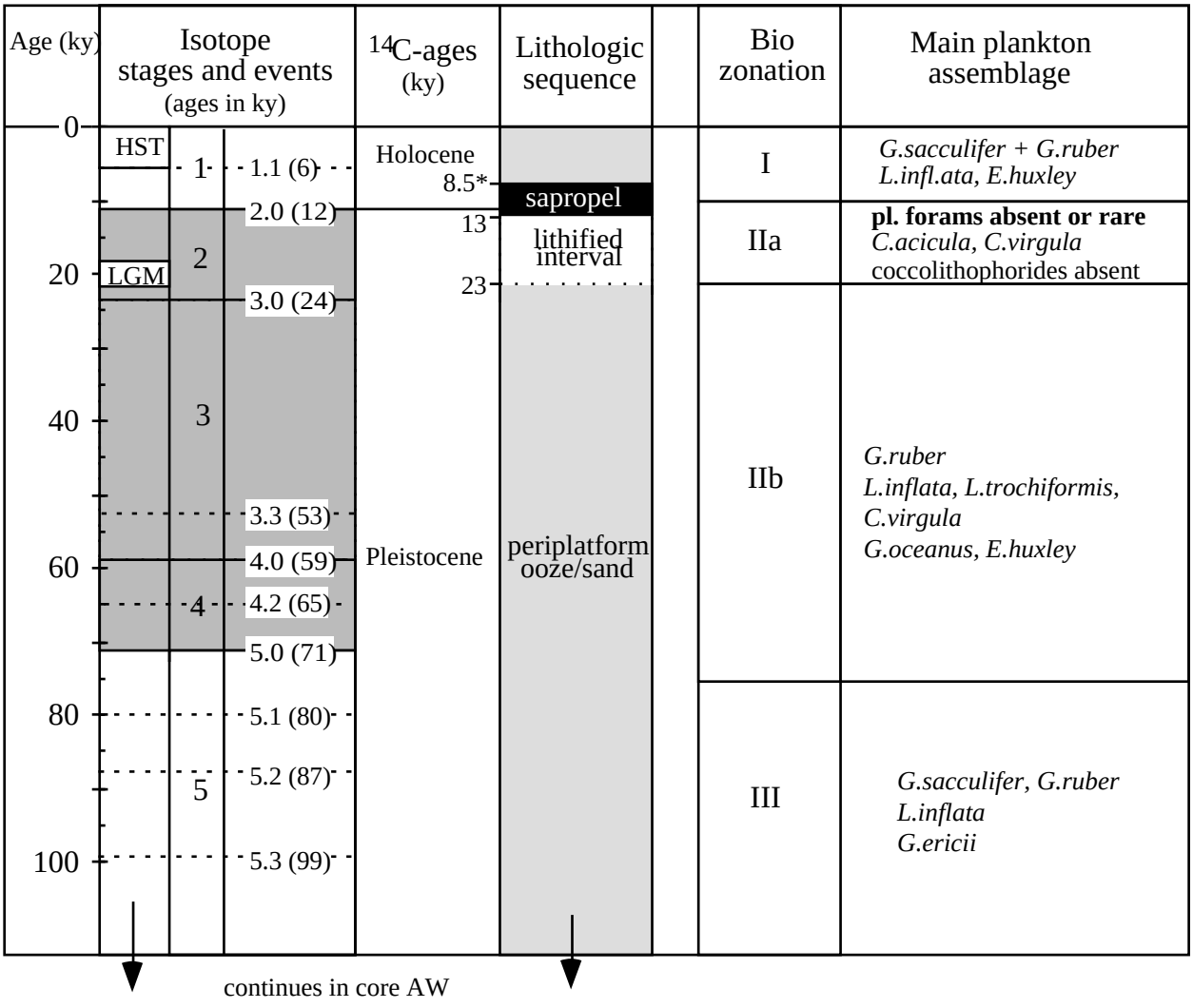

Figure C.2-5: Stratigraphic zonation of the late Quaternary sediment record from the Sudanese shelf, based on isotope and aragonite stratigraphy, radiocarbon dating and lithology. Bio-zonation after Reiss *et al*. (1980). Core AW reaches down to IS 6 the penultimate glacial, which is not shown in the figure. The radiocarbon age of the top of the sapropel (*) is taken from Almogi-Labin *et al.* (1991). Ages of the isotopic events were taken from Imbrie *et al.* (1984). LGM is the last glacial maximum and HST the Holocene sealevel highstand.

C.3 Sedimentation- and accumulation rates

Sedimentation rates (SR) and carbonate/siliciclastic accumulation rates (AR) were calculated for individual isotope stages, the lithified interval and the sapropel (thickness of calciturbidites was subtracted). In addition SR and AR were determined for certain time intervals, like for example sealevel falls and rises. Uncertainties in the age models propagate and are the major source of errors in the calculation of sedimentation rates. In Tab. C.3-1 bulk sedimentation rates are summarised of individual isotope stages and sealevel cycles. The carbonate mineral and siliciclastic accumulation rates are shown in Tab. C.3-2.

C.3.1 Bulk sedimentation rates

Temporal variations in bulk sedimentation rates (SR) are illustrated in Fig. C.3-1 and C.3-2. At Sanganeb Atoll average SR are higher in proximal cores S2, S3 and S6 (5.5-9 cm/ky) compared to rates in the distal core S1 (3.9 cm/ky). Higher rates in the proximal cores might be explained by increased shallow-water input close to the reef. Average SR in core AL at the leeward side at Abington Reef (6.5 cm/ky) are about 15-40% higher than in core AW (4 cm/ky) from the windward side, even though both cores are taken at the same distance from the reef.

Bulk sedimentation is highest in the late Holocene (since 8,500 ^{14}C-yr = top sapropel). Cores with a fully developed Holocene sediment sequence (AL, S2, S6) reach sedimentation rates of 11-13 cm/ky (Fig. C.3-2). Lowest rates of 1-1.6 cm/ky were calculated for the sapropel in all studied cores.

The SR of the lithified interval can not be compared with those of normal periplatform sediments, because it was formed by inorganic carbonate precipitation at the seafloor (e.g. Milliman *et al.*, 1969; Brachert, 1999). The sedimentation rates are in the range of 4.5-10 cm/ky with highest rates in proximal cores. These values confirm SR of the lithified interval based on radiocarbon ages (see Chapter C. 2.3).

Average SR of periplatform sediments during glacial stages IS 3 and IS 4 stay below the Holocene values and range for 3.1-7.4 cm/ky. The last interglacial (IS 5) is only fully developed in core AW. Here an average SR of 3.9 cm/ky was calculated, which is not a significant increase compared to glacial values. Even during the last interglacial sealevel highstand of IS 5e the SR of the periplatform sediments (4.2 cm/ky, see Tab. C.3-1) do not exceed glacial values, which is in contradiction to the highstand shedding theory. It is also remarkable that highest SR of IS 5 occur during lowered sealevel of IS 5d (7.9 cm/ky).

SR rates of sealevel cycles (highstands, rises and falls) were calculated in addition to those of individual isotope stages. A characteristic sealevel related pattern in bulk sedimentation rates can be observed in all cores (Fig. C.3-2, Tab. C.3-1). SR during sealevel rises (5.2-5.1, 4.2-3.3, sapropel) are lower than during sealevel falls (5.1-4.2, 3.3 - base of lithified interval). This is only different in the older parts of core AW, where higher bulk SR were calculated for the sealevel rises between isotopic events 6.2-5.5 (9.2 cm/ky) and 5.4-5.3 (6.3 cm/ky). It is also remarkable that extremely high SR rates are calculated for the interval between the top of the sapropel and isotopic event 1.1,

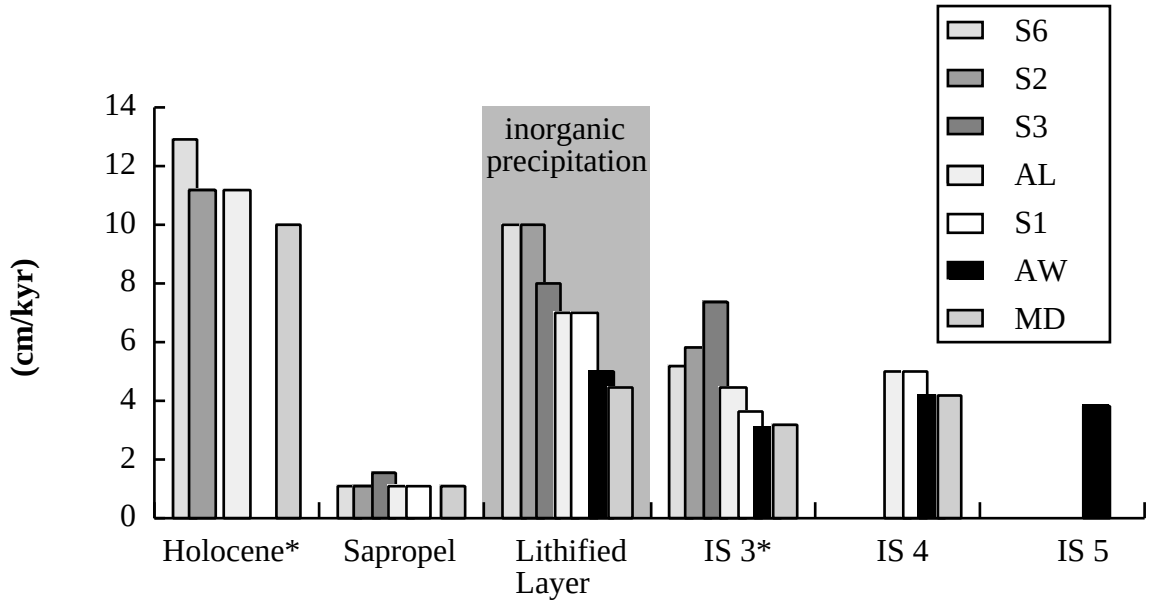

Figure C.3-1: Bulk sedimentation rates of individual isotope stages, the sapropel and the lithified interval (without calciturbidites). Holocene* means the upper part of the Holocene sequence above the sapropel, IS3* begins at the base of the lithified interval. The high sedimentation rates of the lithified interval are due to inorganic precipitation of aragonite and Mg-calcite at the seafloor.

Table C.3-1: Sedimentation rates (without calciturbidites)

Holocene* = core top - top sapropel; IS3* = base of lithified interval - 4.0; Late Holocene* = since 6 ky BP; AW* = based on aragonite stratigraphy; Ages after SPECMAP and radiocarbon dating of the sapropel and the lithified interval

	Age (kyBP)	AL	AW*	S1	S2	S3	S6	MD
Holocene*	0-8.5	11.2	0.0		11.2	0.0	12.9	10.0
Sapropel	8.5-13	1.1	0.0	1.1	1.1	1.6	1.1	1.1
Lithified interval	13-23	7.0	5.0	7.0	10.0	8.0	10.0	4.5
IS 3*	23-59	4.4	3.1	3.6	5.8	7.4	5.1	3.2
IS 4	59-71	5.0	4.2	5.0				4.2
IS 5	71-128		3.9					
IS 5a	71-84	5.4	3.1	3.8				5.0
IS 5b	84-95		1.8					
IS 5c	95-103		3.8					
IS 5d	103-110		7.9					
IS 5e	110-128		4.2					
Late Holocene*	0-6	8.3			13.3		10.0	
1.1 - top sapropel	6-8.5	18.0			6.0		26.0	33.2
base lithified interval - 3.3	23-28	5.0	3.0	4.0	6.3	8.2	5.8	3.2
3.3-4.2	53-65	3.3	2.5	1.7	2.5	2.5	0.8	
4.2-5.1	65-80	7.3	4.7	6.0				
5.1-5.2	80-87	2.9	2.9	2.9				5.7
5.2-5.3	87-99		1.7					21.7
5.3-5.4	99-107		6.3					
5.4-5.5	107-122		4.0					
5.5-6.2	122-135		9.2					

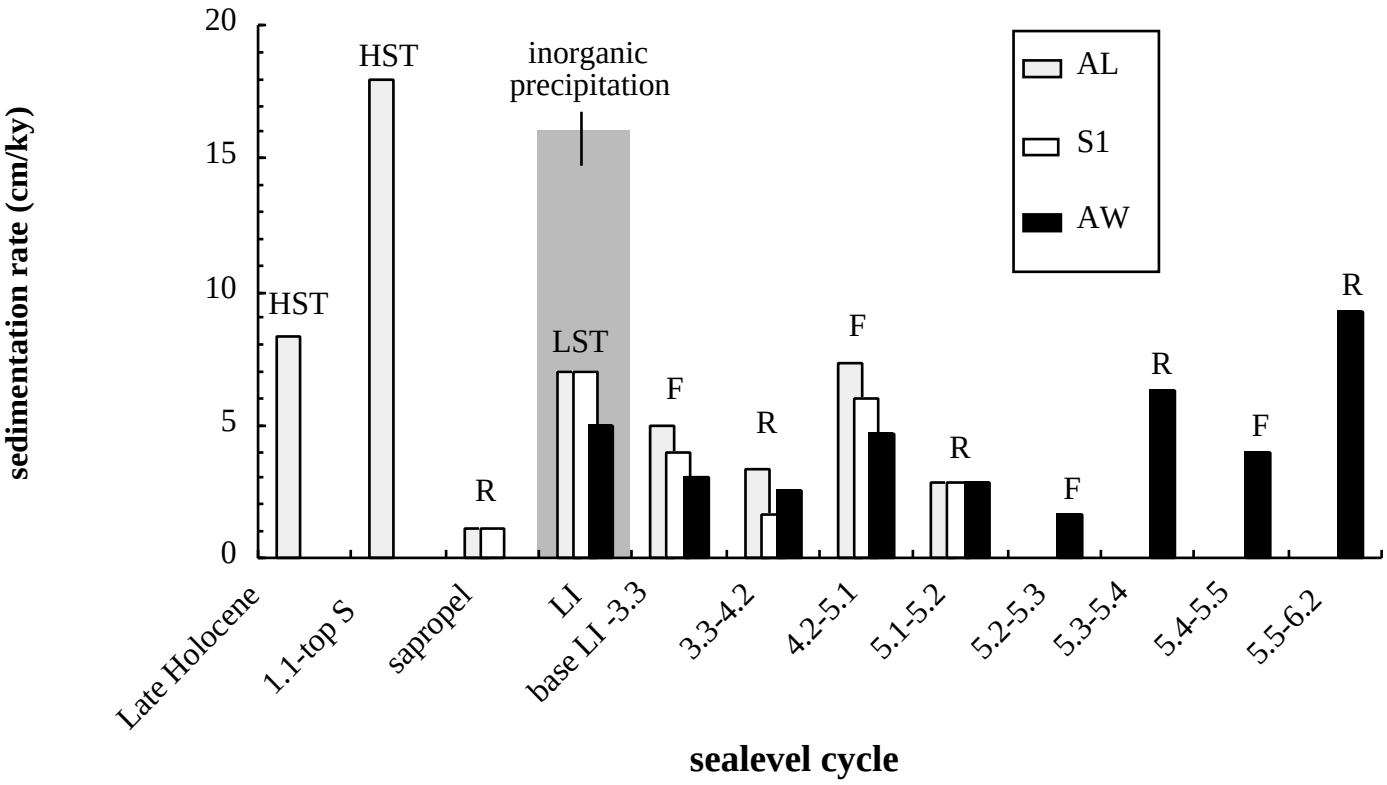

Figure C.3-2: Bulk sedimentation rates calculated for sealevel cycles, examples for core S1, AL and AW. Note the pattern in SR that emerged for fall (F) and rise (R) in sealevel. SR are higher during sealevel falls when compared to phases of rising sealevel. This pattern is different in older parts of core AW where highest SR are reached during the sealevel rise between isotopic event 6.2 and 5.5. SR are significantly higher during the latest phase of the Holocene transgression. HST = sealevel highstand, LST = lowstand, sap = sapropel, LI = lithified interval.

when sealevel was even higher than present in the Red Sea (e.g. Gvirtzman, 1994). In this period bulk sedimentation rates reach values of 20-26 cm/ky. For the late Holocene (since isotopic event 1.1) bulk SR are in the range of 8-13 cm/ky.

C.3.2 Carbonate and siliciclastic accumulation rates

In addition to the bulk sedimentation rates the accumulation rates (AR) were calculated for individual carbonate mineral phases and for the siliciclastic fraction. In Tab. C.3-2 the average AR of carbonate minerals and the siliciclastic component are shown.

In general carbonate and siliciclastic accumulation rates show the same trends and patterns like the SR of the bulk sediment (see Fig. C.3-1 and C.3-2). The average bulk AR lie between 35-75 g/m²*yr with lowest values found in core S1 at Sanganeb Atoll.

The average carbonate AR are in the range of 15-40 g/m²*yr and are highest in the Holocene, where they reach average values between 50-70 g/m²*yr and a maximum of nearly 180 g/m²*yr between the top of the sapropel and isotopic event 1.1 in core S6 at Sanganeb Atoll. Glacial carbonate AR are low compared to Holocene values and reach only about 10-30 g/m²*yr. Values calculated for substage 5a do not exceed the glacial AR.

The AR of aragonite are significantly higher than those calculated for calcite and Mg-calcite, except for core S1, where all three carbonate phases reach similar values. The aragonite accumulationrates range for 7-24 g/m^2*yr and are highest in cores at Abington Reef and in core S6 at Sanganeb Atoll. Temporal variations of the aragonite AR show the same patterns as observed for the bulk SR.

The average siliciclastic AR lie between 20 to 40 g/m^2*yr and significantly exceed the carbonate accumulation at Sanganeb Atoll. At the more carbonate dominated Abington Reef the carbonate accumulation is more than twice as much as the siliciclastic rate. In the lithified interval of the proximal cores at Sanganeb Atoll the maximum in siliciclastic AR of 65-70 g/m^2*yr is reached.

Table C.3-2: Sediment accumulation rates

Arag = aragonite, Silic = siliciclastic

	Percentage of total sediment					Accumulation rate (g/m^{2}xyr)					
	$CaCO_3$	**Arag.**	**LMC**	**HMC**	**Silic.**	**Bulk**	**$CaCO_3$**	**Silic.**	**Arag.**	**LMC**	**HMC**
Core AL											
Holocene*	80.2	52.2	10.5	17.5	11.2	93.4	69.9	23.5	45.5	9.2	15.2
Sapropel	63.5	43.8	7.6	12.2	1.1	9.8	5.5	4.3	3.8	0.7	1.1
LI	65.3	37.1	6.7	21.5	7.0	61.4	35.6	25.8	20.3	3.7	11.7
IS 3*	68.6	43.1	10.2	15.3	4.4	38.6	23.8	14.8	14.9	3.5	5.3
IS 4	70.4	39.0	11.4	20.0	5.0	43.1	27.4	15.7	15.2	4.4	7.8
IS 5a	75.0	45.1	13.2	16.7	5.4	45.8	31.5	14.3	19.0	5.5	7.0
Late Holocene	81.4	52.0	10.7	18.7	8.3	69.3	52.9	16.5	33.8	7.0	12.1
1.1 - top sapropel	80.7	53.5	10.7	16.5	18.0	150.1	113.2	36.9	75.1	15.0	23.2
base LI - 3.3	69.1	43.5	10.1	15.4	4.3	37.6	23.3	14.2	14.7	3.4	5.2
3.3-4.2	64.5	38.2	10.2	16.2	3.3	29.3	16.8	12.5	9.9	2.6	4.2
4.2-5.1	74.2	42.9	12.4	18.9	7.3	62.5	42.5	20.0	24.5	7.1	10.8
5.1-5.2	77.3	44.9	12.9	19.6	2.9	24.1	17.2	6.9	10.0	2.9	4.4
Core S1											
Holocene*	58.5	34.2	13.8	10.2							
Sapropel	38.4	27.6	6.3	4.5	1.1	10.6	3.3	7.3	2.4	0.5	0.4
LI	42.6	23.1	6.5	12.3	7.0	65.8	23.3	42.6	12.6	3.6	6.7
IS 3*	42.6	19.9	10.3	12.4	3.6	34.0	12.0	22.0	5.6	2.9	3.5
IS 4	57.1	19.1	12.8	25.3	5.0	45.0	22.3	22.7	7.4	5.0	9.9
IS 5a	59.6	23.6	15.3	19.3	3.8	34.4	17.9	16.5	7.1	4.6	5.8
base LI - 3.3	42.7	20.3	10.2	12.2	4.0	37.6	13.3	24.3	6.3	3.2	3.8
3.3-4.2	46.6	17.8	10.9	17.5	1.7	15.5	6.1	9.4	2.3	1.4	2.3
4.2-5.1	60.3	20.7	14.6	23.0	6.0	53.5	28.2	25.3	9.7	6.8	10.8
5.1-5.2	57.8	26.0	13.8	18.9	2.9	25.7	12.9	12.8	5.8	3.1	4.2

Table C.3-2 (continued): Sediment accumulation rates

Arag = aragonite, Silic = siliciclastic

	Percentage of total sediment					Accumulation rate ($g/m^2 x yr$)					
	$CaCO_3$	**Arag.**	**LMC**	**HMC**	**Silic.**	**Bulk**	**$CaCO_3$**	**Silic.**	**Arag.**	**LMC**	**HMC**
Core S2											
Holocene*	58.9	36.0	10.9	12.0	11.2	100.0	51.4	48.6	31.4	9.5	10.4
Sapropel	36.4	30.5	2.7	3.2	1.1	10.6	3.2	7.5	2.6	0.2	0.3
LI	32.6	26.5	3.2	2.9	10.0	96.9	25.4	71.5	20.7	2.5	2.2
IS 3*	41.2	22.1	8.2	10.8	5.8	55.1	18.7	36.4	10.1	3.7	4.9
Late Holocene	61.8	36.7	11.8	13.3	13.3	118.3	64.3	54.0	38.2	12.2	13.8
1.1 - top sapropel	44.3	30.4	7.3	6.6	6.0	56.2	20.7	35.4	14.2	3.4	3.1
base LI - 3.3	41.3	22.5	8.2	10.6	6.3	59.8	20.4	39.4	11.1	4.1	5.2
3.3-4.2	42.3	19.9	8.7	13.7	2.5	23.5	8.3	15.3	3.9	1.7	2.7
Core S3											
Sapropel	39.9	28.2	6.2	5.6	1.6	14.7	4.8	9.9	3.4	0.8	0.7
LI	34.0	21.5	5.0	6.3	10.0	96.5	26.5	70.0	16.7	3.9	4.9
IS 3*	47.3	26.3	8.8	11.5	7.8	72.1	28.7	43.4	15.9	5.3	7.0
base LI - 3.3	47.4	27.3	8.7	11.5	7.8	72.6	28.9	43.7	16.7	5.3	7.0
3.3-4.2	46.5	17.1	7.6	21.9	2.5	23.2	9.1	14.2	3.3	1.5	4.3
Core S6											
Holocene*	63.0	35.0	13.8	12.6	12.9	114.4	63.6	50.8	35.4	13.9	12.7
Sapropel	37.6	27.0	6.7	4.0	1.1	10.6	3.3	7.3	2.3	0.6	0.3
LI	38.6	24.9	8.2	8.0	10.0	95.2	30.1	65.1	19.4	6.4	6.2
IS 3*	46.7	27.0	10.3	9.5	5.1	47.8	18.7	29.1	10.8	4.1	3.8
Late Holocene	63.2	36.5	13.5	13.3	10.0	88.3	49.3	39.0	28.5	10.5	10.3
1.1 - top sapropel	64.1	34.3	14.6	12.1	20.0	176.1	99.9	76.2	53.5	22.8	18.9
base LI - 3.3	46.9	27.3	10.3	9.4	5.8	54.2	21.3	32.9	12.4	4.7	4.3
3.3-4.2	45.8	21.7	10.2	13.8	1.7	15.5	6.0	9.6	2.8	1.3	1.8

C.4 Grainsize distribution

Grainsize analysis was performed in order to reconstruct glacial-interglacial variations caused by changes in the mode of shallow-water sediment export as it was shown for the Bahamas (e.g. Rendle *et al*. in press, 2000). In this study only minor glacial-interglacial variations in grainsize distribution were found. Average percentages of individual isotope stages, the sapropel, the lithified interval and calciturbidites are summarised in Tab. C.4-1 and C.4-2, the entire dataset is given in Appendix 2. Grainsize classes and corresponding values on the phi-scale are summarised in Tab. B-3 in Chapter B. 2.2.

C.4.1 Periplatform sediments

The periplatform sediments are generally moderate to poorly sorted, show a negative skewness and are dominated by the fine fraction (< 63µm) (Fig. C.4-2, Tab C.4-1). The fine fraction percentages fall in the range of 65-95% and reach highest values in core AL (90-95%) at Abington Reef. Generally the periplatform sediments are coarser grained at the windward side of the reefs and reach highest percentages of coarse fraction in the cores MD and S6 at Sanganeb Atoll. The percentages of very-fine to fine sand dominate within the sand size classes and are more frequent than middle-, coarse, and very coarse sand fractions.

Only modest trends in glacial-interglacial grainsize distribution patterns were found (Tab. C.4-1, Fig. C.4-1). Average percentages of the fine-fraction are highest in the Holocene periplatform sediments (76-94%), with a maximum in core AL at Abington Reef.

The periplatform sediments of IS 3 contain about 3-7% less fine fraction compared to the Holocene sediments, and are enriched in very-fine to medium sand (Tab. C.4-1). This might show an increased input of coarser grained sediments during IS 3 when compared to the Holocene.

During IS 4 average percentages of fine fraction are increased for about 2-8% when compared to IS 3, except for distal core S1 at Sanganeb Atoll and core AL at Abington Reef, where no clear differences were found. In proximal core S6 at Sanganeb Atoll average percentages of fine fraction calculated for IS 4 (74.2%) nearly reach Holocene values (75.5%). This pattern was not found in core MD were percentages of the sand fractions are even higher during IS 4 (34.2%) when compared to IS 3 (31.5%).

Average percentages of fine fraction calculated for IS 5 (78.0-93.7%) are similar or slightly increased when compared to IS 4 and reach Holocene values in core AL at Abington Reef. This is different in core MD where the percentages of fine fraction reach only 39.4% during IS 5 and clearly stay below glacial values. This is explained by an increased input of coarse grained shallow-water components into the periplatform sediments close to Sanganeb Atoll during the last interglacial sealevel highstand. Unfortunately, the other proximal cores at Sanganeb Atoll (S3 and S6) do not extend to IS 5. In core AW at Abington Reef individual substages of IS 5 (5a-5e) do not show any significant differences in grainsize distribution (Tab. C.4-1).

C.4.2 Sapropel

The grainsize distribution pattern of the sapropel (Fig. C.4-3) differs from that of the

periplatform sediments in the proximal cores (S2, S3, S6, MD) but shows no significant differences in core AL and S1. The average percentage of fine fraction in the sapropels of the proximal cores (67-75%) is clearly less when compared to „normal“ periplatform sediments. Core MD and S2 at Sanganeb Atoll contain 19% and 27% very-fine sand, respectively. A relatively high percentage of very-coarse sand (9%) was found in the sapropel of core S3. The higher percentages of the very-fine sand fractions correspond to an increased amount of terrigenous components and points to the incorporation of lithified components in the sapropel.

C.4.3 Lithified interval

The grainsize distribution of the unlithified layers within the lithified interval (Fig. C.4-4) is clearly dominated by reworking and brecciation of the lithified beds. Except for core AL all other cores show clearly increased average percentages of the very-coarse sand and the granule fraction (15.7-31.7%) when compared to the „normal“ periplatform sediments (up to 8.6%). A second, but much smaller increase in the sand fraction is found in medium- to fine sand in core S6 (11%) and S3 (7%). The fine fraction reaches only 54-60% in all cores except for core AL (88%).

C.4.4 Calciturbidites

In core S6 two calciturbidites are interbedded in the Holocene sequence at 10 cm and at 86-90 cm. Both have a clearly bimodal grainsize distribution and show maxima in the medium-sand fraction (15-18%). In those layers the fine fraction reaches only 50-57% of the total sediment.

The grainsize distribution of the calciturbidites interbedded within the lithified interval in core S3 and S6 clearly differs between leeward (S3) and windward (S6) position at Sanganeb Atoll (Fig. C.4-5). The sand layers from windward core S6 contain more sand (65-80%) with a maximum in the coarse to medium sand fraction, while those from the leeward core S3 are finer grained (45-55% sand) and show a maximum in the fine sand fraction (Fig. C.4-5).

The calciturbidites that occur within peripatform sediments of IS 3 show no clear differences between lee- and windward side but are generally finer grained than those of the lithified interval (28-50% sand). The calciturbidites in IS 3 have a bimodal grainsize distribution with a crest in the medium-sand fraction (11-21%). Only the calciturbidite at 370-390 cm in core S6 shows a linear increasing trend from very coarse to very fine sand.

Table C.4-1: Grainsize distribution (average %) for isotope stages, the lithified interval, and the sapropel

Grainsize class	**< 63**	**63-125**	**125-250**	**250-500**	**500-1000**	**>1000**
Phi-scale	**> 4**	**4-3**	**3-2**	**2-1**	**1-0**	**< 0**
Core AL						
Holocene	93.64	2.60	1.68	1.30	0.71	0.07
Sapropel	91.41	3.75	2.20	1.52	0.63	0.49
Lithified interval	88.00	3.80	3.53	2.31	1.18	1.18
IS 3	90.81	4.12	2.98	1.61	0.25	0.23
IS 4	91.36	3.89	2.76	1.37	0.38	0.24
IS 5a	93.41	3.10	2.20	1.00	0.15	0.12
IS 5b	93.74	2.96	2.11	0.91	0.18	0.10

Table C.4-1 (continued): Grainsize distribution (average %) for isotope stages, the lithified interval and the sapropel

Grainsize class	**< 63**	**63-125**	**125-250**	**250-500**	**500-1000**	**>1000**
Phi-scale	**> 4**	**4-3**	**3-2**	**2-1**	**1-0**	**< 0**
Core AW						
Lithified interval	53.36	4.57	4.17	3.83	3.58	30.49
IS 3	75.51	7.61	5.82	3.42	0.94	6.69
IS 4	83.97	6.04	4.79	2.61	1.06	1.53
IS 5	83.26	6.42	5.28	3.20	1.14	0.70
IS 5a	84.25	6.30	5.42	3.22	0.56	0.25
IS 5b	81.28	6.74	6.36	3.21	2.20	0.21
IS 5c	78.04	8.01	7.51	4.04	1.99	0.41
IS 5d	81.64	6.39	5.94	3.86	1.22	0.95
IS 5e	82.83	6.44	5.78	3.33	1.39	0.23
IS 6	85.50	7.07	3.48	2.58	0.82	0.54
Core S1						
Sapropel	85.69	8.56	2.77	1.27	1.07	0.65
Lithified interval	56.68	4.09	2.41	2.34	2.77	31.70
IS 3	84.42	6.96	4.13	1.84	0.80	1.84
IS 4	84.41	5.24	5.22	2.75	1.29	1.10
IS 5a	86.46	5.34	4.30	2.69	0.83	0.39
IS 5b	87.07	5.14	3.91	2.57	0.84	0.48
Core S2						
Holocene	89.53	4.62	2.49	2.01	1.20	0.17
Sapropel	67.27	26.71	4.69	0.94	0.38	0.02
Lithified interval	59.69	8.44	2.36	1.46	1.65	26.40
IS 3	83.55	10.87	3.18	1.05	0.34	1.01
IS 4	85.66	9.41	2.73	1.07	0.56	0.56
Core S3						
Sapropel	71.20	7.55	9.54	2.12	0.98	8.61
Lithified interval	59.57	5.54	6.94	6.21	2.64	19.10
IS 3	75.16	8.10	9.60	4.84	0.67	1.63
IS 4	82.36	7.96	6.22	2.29	0.67	0.50
Core S6						
Holocene	75.53	7.50	8.79	5.37	2.61	0.19
Sapropel	59.72	10.16	16.01	12.68	1.16	0.29
Lithified interval	53.89	6.81	9.75	11.19	2.66	15.71
IS 3	69.18	13.49	10.52	5.71	0.79	0.31
IS 4	74.16	12.52	8.45	3.66	0.84	0.37
Core MD						
Sapropel	69.64	18.66	9.45	1.64	0.55	0.07
IS 3	68.55	13.46	10.80	3.34	1.26	2.59
IS 4	65.82	11.32	14.07	5.20	1.72	1.86
IS 5a	39.40	16.78	28.69	12.68	1.29	1.16

Table C.4-2: Average grainsize distribution in calciturbidites (in %)

Grainsize class	< 63	63-125	125-250	250-500	500-1000	>1000
Core S3 (depth in cm)						
Lithified interval(30-40)	47.91	5.48	7.77	7.24	3.70	27.92
Lithified interval(60-80)	55.24	6.71	10.61	9.09	4.62	13.74
Lithified interval(93-96)	44.59	22.26	25.62	7.36	0.10	0.06
IS 3(195-204)	64.88	7.11	7.17	11.00	7.88	1.96
IS 3(274-277)	50.03	8.00	14.77	20.93	5.78	0.49
IS 3(300-314)	65.03	6.77	11.16	15.28	1.64	0.13
IS 3(377)	72.01	6.68	8.64	12.18	0.45	0.04
Core S6 (depth in cm)						
IS 1(10)	56.64	4.37	8.03	15.00	13.30	2.65
IS 1(86-90)	50.33	6.95	14.00	18.31	8.78	1.65
Lithified interval(150-170)	34.25	3.93	8.07	13.18	8.28	32.29
Lithified interval(185)	17.80	2.35	8.75	34.05	25.32	11.72
Lithified interval(200)	35.38	1.61	4.64	22.38	23.22	12.77
IS 3(270-285)	58.49	11.66	13.65	12.36	3.14	0.70
IS 3(370-390)	61.60	16.56	13.55	7.24	0.90	0.15

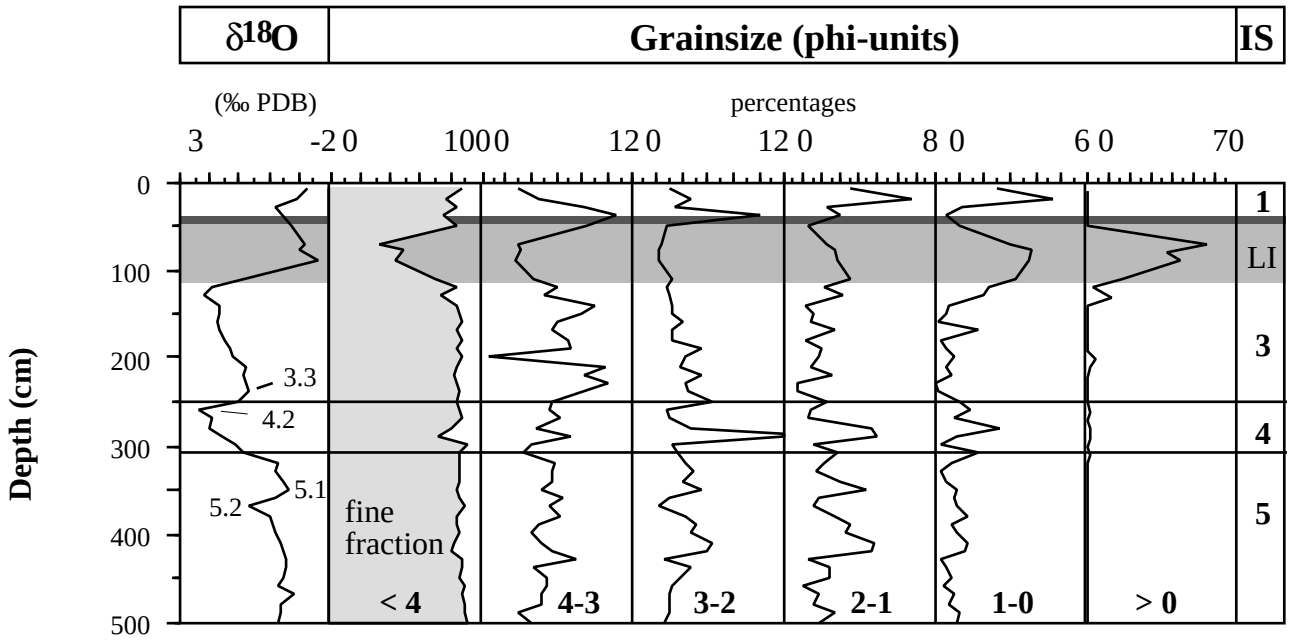

Core S1

Figure C.4-1: Percentages of grainsize classes in core S1 as an example for the downcore variations in the grainsize distribution pattern. Glacial-interglacial variations are only very weakly reflected in the grainsize logs. Very-fine to medium sand (4-1 phi) curves to some extend resemble variations of the planktic oxygen isotope record between IS 5 and the base of the lithified interval. Note the increased very fine to fine sand (4- phi) percentages in the sapropel and the increase of medium to coarse sand (2-0 phi) within the Holocene sequence. The amount of very coarse sand and rubble becomes significantly highest in the lithified interval due to the brecciation of the lithified layers. IS = isotope stages, LI = lithified interval, s = sapropel

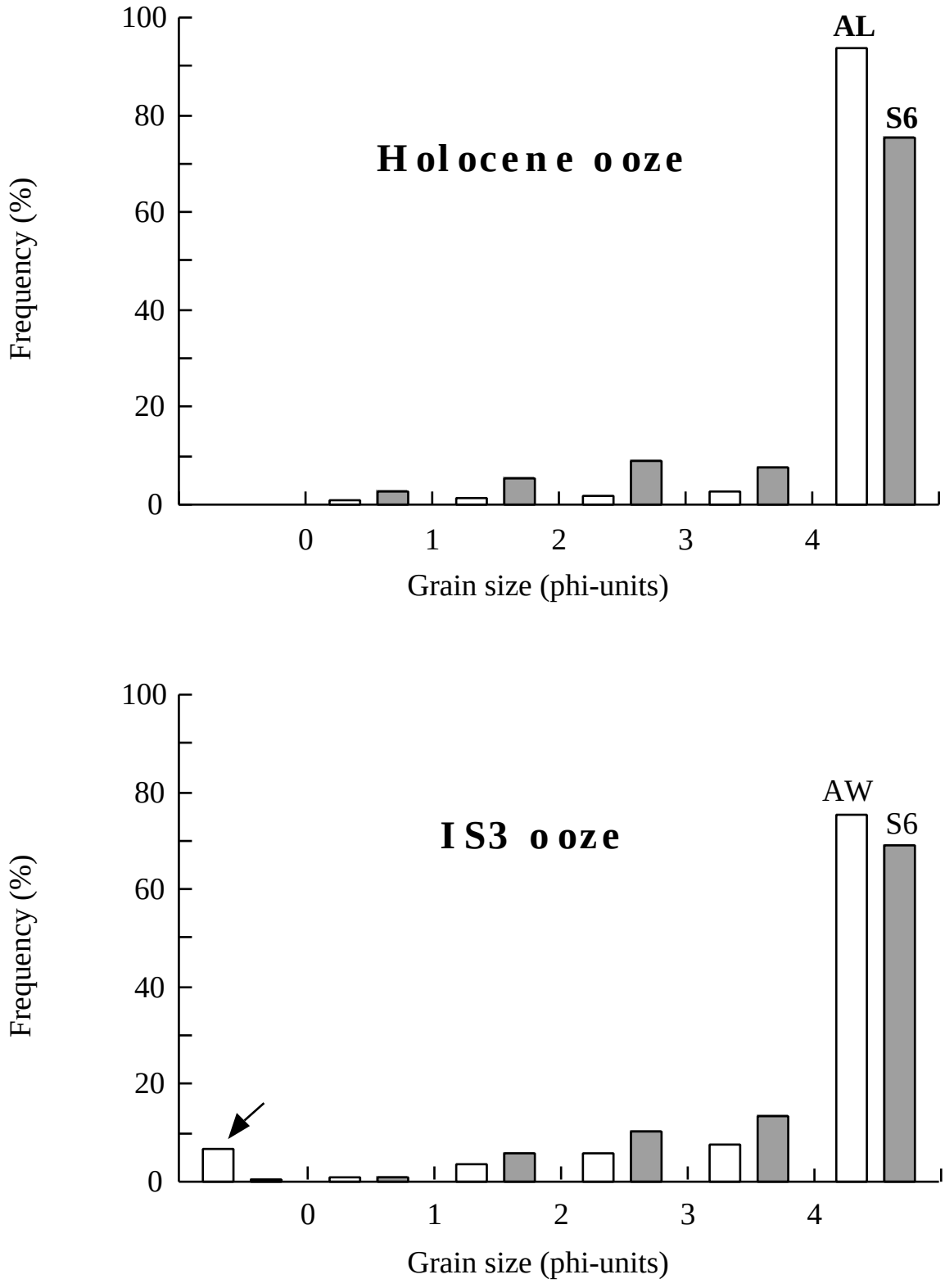

Figure C.4-2: Grainsize frequency in interglacial (Holocene) and glacial (IS 3) periplatform sediments from the Sudanese shelf. The examples from core AL, AW and S6 clearly demonstrate the dominance of the fine-fraction. Note the slight increase in coarser sand during IS 3 in core S6 (arrow).

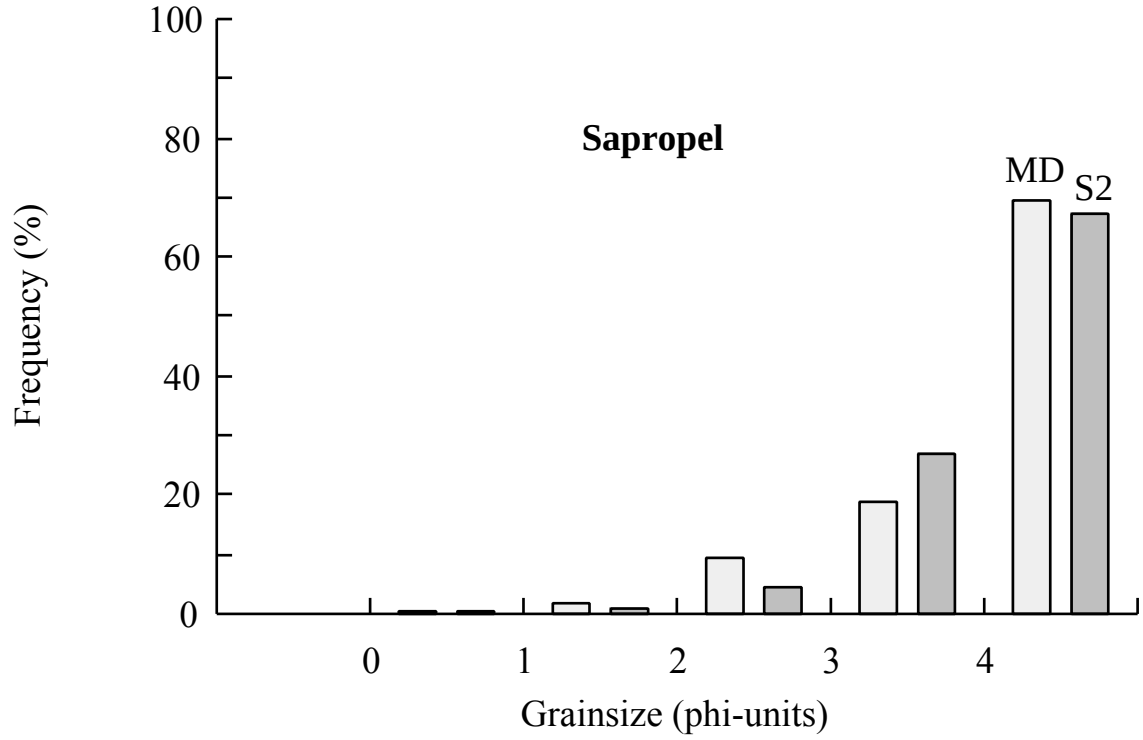

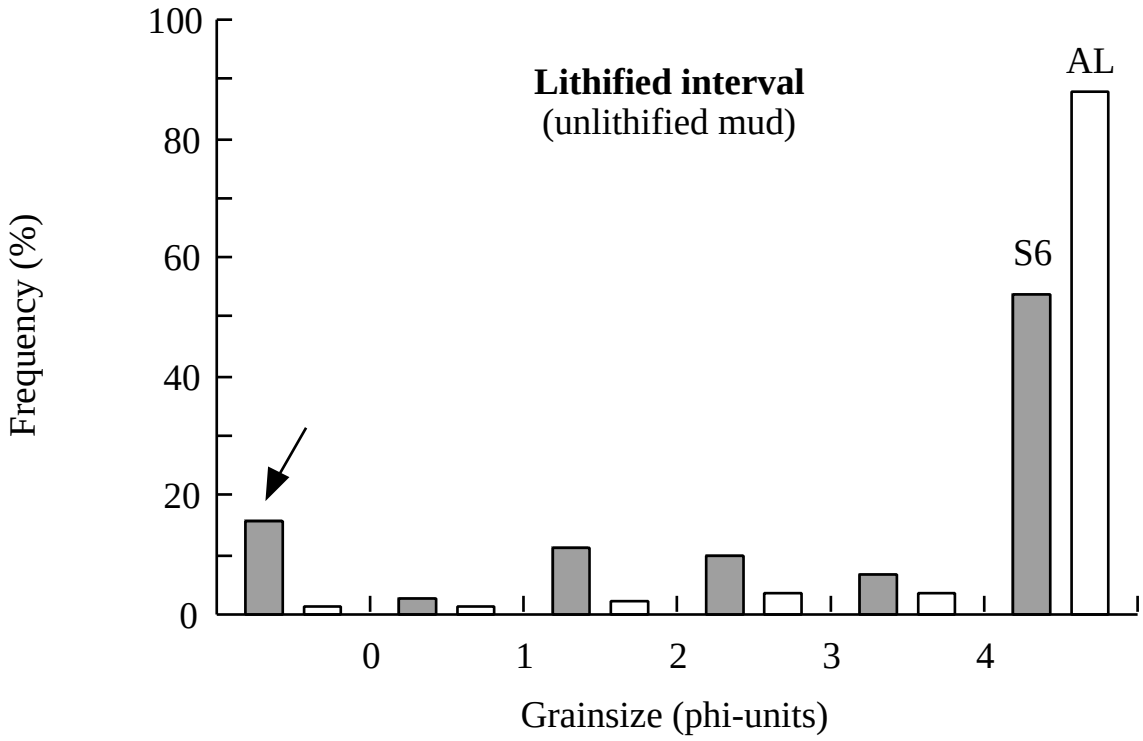

Figure C.4-3 (top): Grainsize frequency distribution of the sapropel shown for core MD and S2. Note the increased very-fine sand fraction (3 to 4 phi-units) when compared to the periplatform sediments.

Figure C.4-4 (bottom): The grainsize distribution in the lithified interval is determined by the brecciation of the lithified beds into chip-like components. Those cause a significant increase in very-coarse sand and granule in all cores except for core AL. The arrow points to clearly increased percentages in the size classes below 0 phi (> 1000 µm) of core S6.

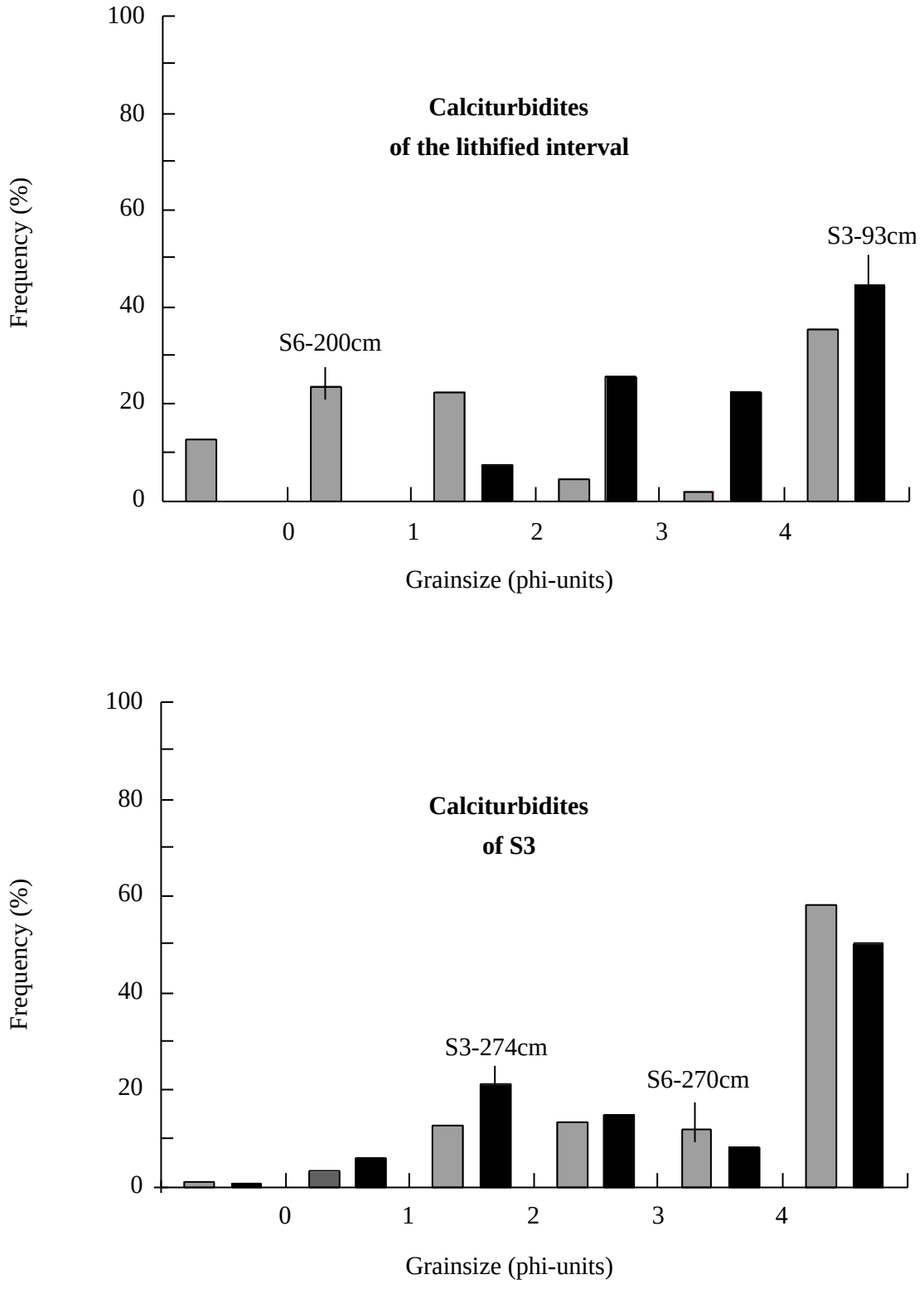

Figure C.4-5: Grainsize frequency distribution of glacial calciturbidites. The upper figure shows two examples from the lithified interval, the lower figure from IS 3. Calciturbidites from the lithified interval show characteristic differences between lee- and windward side. The windward sediments from core S6 (here in 200 cm) are much coarser grained and exhibit a maximum in the coarse- to medium-sand fractions (0-2 phi). The leeward calciturbidites are finer grained and show a maximum in the fine-sand fraction (2-3 phi). The calciturbidites of IS 3 show no significant differences between lee- and windward position and are generally finer grained than those from the lithified layer.

C.5 Stable carbon and oxygen isotopes

Stables carbon isotopes were conducted in parallel to the stable oxygen isotopic measurements of planktic foraminifers, which were used for climate-stratigraphic correlation. In addition to planktic foraminifer tests the stable C and O isotopes of lithified components and the unlithified fine fraction of the lithified interval (aplanktonic zone) were analysed. A C/O-plot of all measurements is shown in Fig. C.5-1. Two distinct isotopic groups can be distinguished (1) the relatively light isotopes analysed on planktic foraminifers which show a somehow negative trend between C- and O-isotopes and (2) the heavier isotope values analysed on sediments from the lithified interval which exhibit more or less positive trends. The isotope values of the unlithified fine fraction are generally lighter than those analysed on lithified sediments. The results of all isotope measurements, including analytical errors are given in Appendix 1-A.

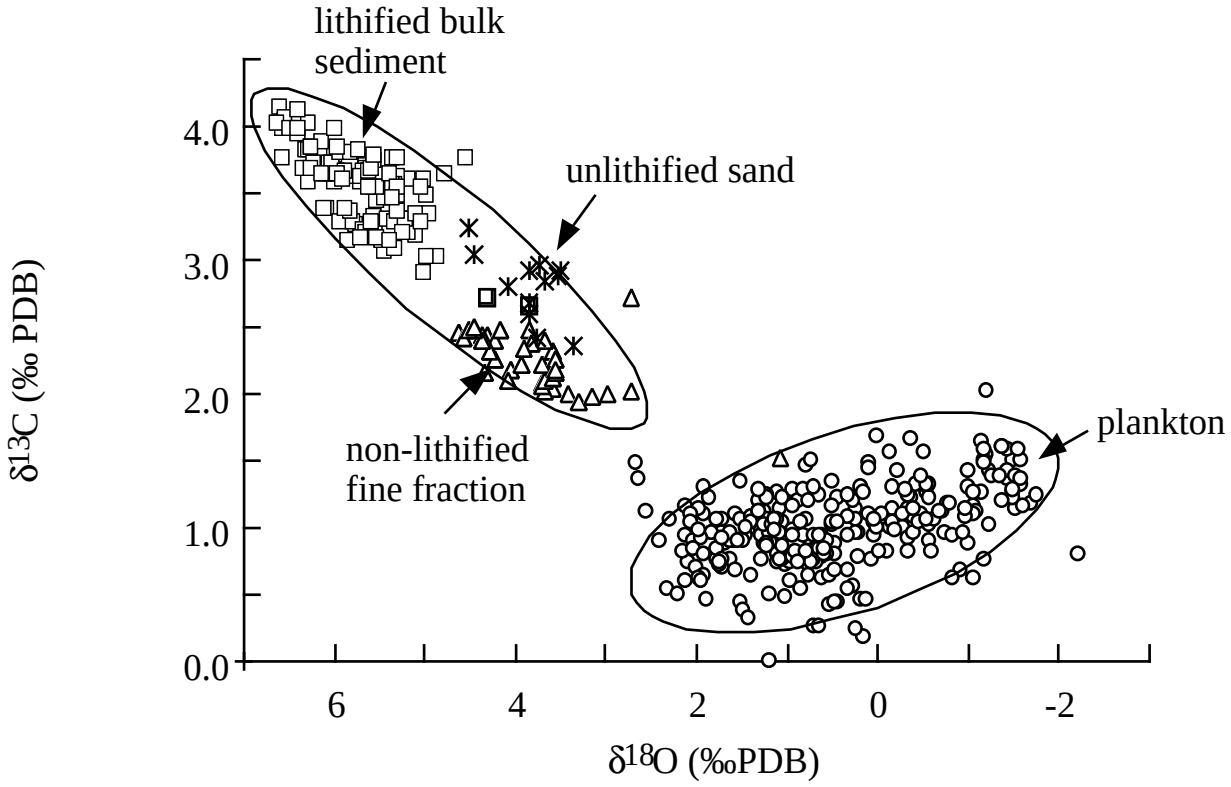

Figure C.5-1: C/O-plot showing the correlation between stable carbon- and oxygen isotopes in the analysed sediment cores. See text for description.

C.5.1 Stable isotopes of planktic foraminifers

C.5.1.1 Oxygen isotopes

Downcore variations of the carbon- and oxygen-isotope values are shown in Fig. C.5-2, C.5-3 and C.5-4. In all studied cores (except for MD) the $\delta^{18}O$-curves show the characteristic saw-tooth pattern caused by late Quaternary climate variations which are recorded in the tests of planktic

foraminifers (e.g. Emiliani, 1955). Changes in the isotopic composition of paleo-seawater are mainly caused by ice volume variations and changes in salinity and temperature of Red Sea waters (e.g. Hemleben *et al.,* 1996). Generally lighter oxygen isotope values occur during interglacials and heavier values in glacial stages.

The $\delta^{18}O$ values in the analysed cores are in the range of -2.2‰ (IS 5e) and 2.4‰ (IS 4), which leads to a glacial-interglacial amplitude of 4.6‰. Such a high glacial-interglacial amplitude in planktic oxygen isotopes in the Red Sea cores can be explained with extremely high salinities of Red Sea waters during glacial sea-level lowstands (e.g. Hemleben *et al.,* 1996). No reliable planktic isotope-record was found in the lithified interval (IS 2) due to scarcity or absence of planktic foraminifers (aplanktonic zone). Extremely depleted glacial $\delta^{18}O$ values of about -1.0‰ were analysed on foraminifer tests found in the unlithified layers of the lithified interval of the cores S1 and S2 (Fig. C.5-3, C.5-4). In the proximal cores at Sanganeb Atoll (Fig. C.5-4) IS 3 is recorded with very high resolution. In all three cores small scale variations in the isotope curves were found. The $\delta^{18}O$-minima are labelled A to E, wherein event E coincides with isotopic-event 3.3 (Fig. C.5-4) and coincide with maxima in the aragonite and TOC curves.

The calculation of sea-surface salinities based on $\delta^{18}O$-values of planktic foraminifers is shown in Chapter D.2-1.

C.5.1.2 Carbon isotopes

The carbon isotopes analysed on planktic foraminifers record variations in the productivity of Red Sea surface waters. Enriched $\delta^{13}C$-values in shells of planktic foraminifers indicate higher phyto-plankton productivity (photosynthesis) in the surface water, while depleted $\delta^{13}C$-values occurred when respiration was enhanced (Broecker, 1992).

The glacial-interglacial patterns of the $\delta^{13}C$-curves show a negative correlation to the $\delta^{18}O$-signal. Generally average interglacial $\delta^{13}C$-values are heavier than glacial ones, which is vice versa to the glacial-interglacial variations of the $\delta^{18}O$-records. Nevertheless, maxima and minima in the $\delta^{13}C$-curves show significant phase offsets compared to the isotopic events on the oxygen isotope curves. Maxima of the $\delta^{13}C$-curves occur above the corresponding peaks of the $\delta^{18}O$-curves in many cases (Fig. C.5-3). The $\delta^{13}C$-values vary between 0 and 2‰. Lightest values < 1‰ are found at the transition from IS 4 to IS 3, while heaviest values occur in the Holocene (1.5‰) and in IS 5 (1.7‰). A further maximum in the $\delta^{13}C$-record occurs during IS 3 in all cores (Fig. C.5-3 and C.5-4). In the aplanktonic interval enriched values of 1.5-2‰ were analysed which coincide with extremely depleted $\delta^{18}O$-values in cores S1 and S2 (see oxygen isotopes).

C.5.2 Stable isotopes of the lithified interval

In Fig. C.5-5 the downcore variations in $\delta^{13}C$ and $\delta^{18}O$ of the lithified interval are shown, the complete data with analytical errors can be found in Appendix 1. The stable isotopic composition of the lithified components documents the composition of paleo-bottom water during the last glacial (IS 2) on the Sudanese shelf, if inorganic precipitation took place in equilibrium with bottom-water.

C.5.2.1 Oxygen isotopes of lithified particles

Stable oxygen isotope values analysed on lithified particles range between 4.9 and 6.6‰ (see Fig. C.5-5). Only in core S6 lighter values were measured on the coarse fraction of calciturbidites (3.4-4.5‰) and of dark periplatform ooze above the sapropel (2.3-5.9‰).

Generally the $\delta^{18}O$-values of the lithified series in the three cores show an increasing trend from the base of the lithified interval to their absolute maxima that occur in depth of 75-65 cm (S1), 150-130 cm (S6) and 120 cm (AL), respectively. Those maxima occur at about 14,840±110 ^{14}C-AMS yr in core S1 (67 cm) and 14,630±70 ^{14}C-AMS yr in core S6 (150 cm). In this core the maximum is present directly below the base of the sapropel. Thus, heaviest $\delta^{18}O$-values of the bottom-waters occur long after isotopic event 2.2 at about 19,000 SPECMAP-yr (Tab. B-4). After their maxima $\delta^{18}O$-values decrease again in core S1 and S6 and reach minima of 5.5-‰ in the sapropel of core S1 and 2.3‰ in the dark periplatform ooze in core S6 (Fig. C.5-5). In core AL $\delta^{18}O$-values above the maximum oscillate between 5.3 and 6.3‰ without a clear trend.

In the deeper parts of the lithified interval, below a core depth of 100 cm (S1), 200 cm (S6) and 150 cm (AL), the grade of lithification is lower and the number of less- or non-lithified layers is increased compared to the sections above. The boundary between the lower, less lithified interval

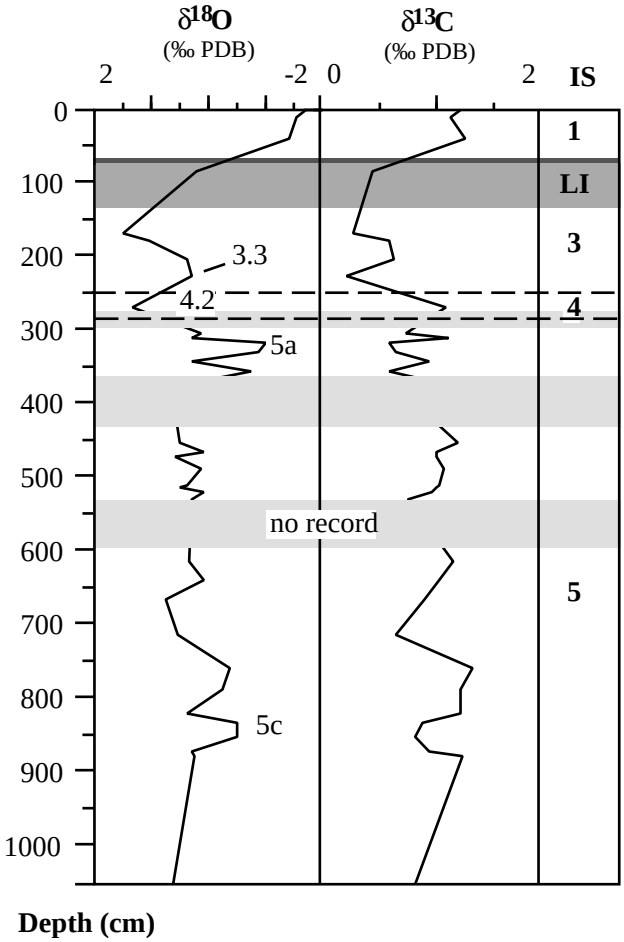

Figure C.5-2: Stable isotope records of piston core MD. No clear glacial-interglacial pattern is developed like in the other cores, due to missing core sections (no record) and the high frequency of coarse-grained calciturbidites in IS 5 (see Chapter C.1.4). Therefore, this core was not used for further age-modelling. Isotope values of substages 5a and 5c are in the range of those in other cores.

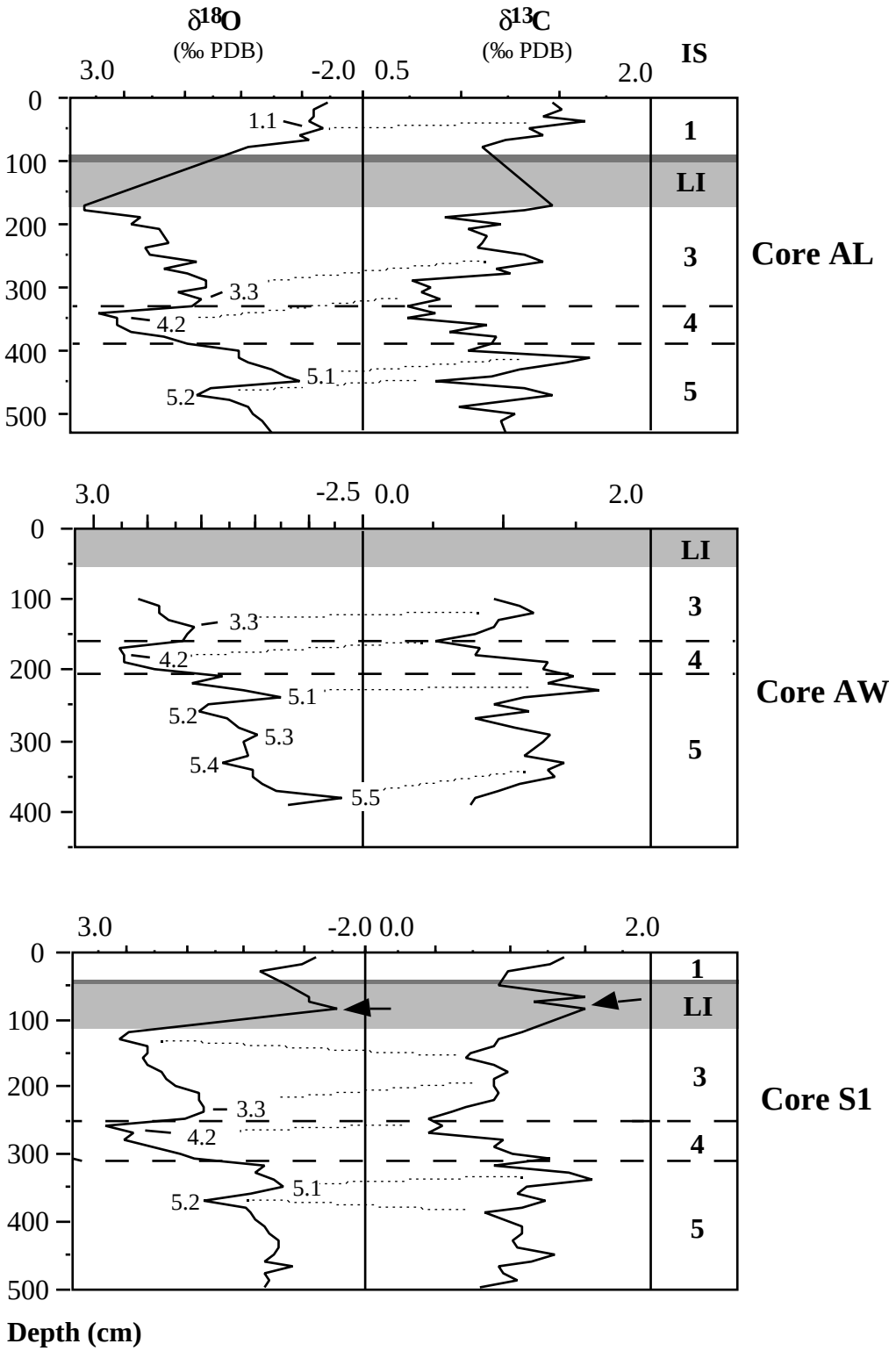

Figure C.5-3: Planktic stable C- and O isotopes of the cores AL, AW and S1. The $\delta^{18}O$-curves show the characteristic glacial-interglacial variations, with lighter values in interglacials and heavier values in glacials. Isotopic event 2.2 is not recorded in the lithified interval (LI). Note the extremely light isotope and heavy carbon values analysed on *G. ruber* tests from the LI (arrows). Numbers on the $\delta^{18}O$-curves are SPECMAP events. The trends in the $\delta^{13}C$-curves show a somehow negative correlation to those in the oxygen isotope records (oxygen isotopes are plotted on a reversed axis) with distinct phase offsets (dotted lines). In most cases maxima in the $\delta^{13}C$ curve occur above the peaks in the $\delta^{18}O$-curves.

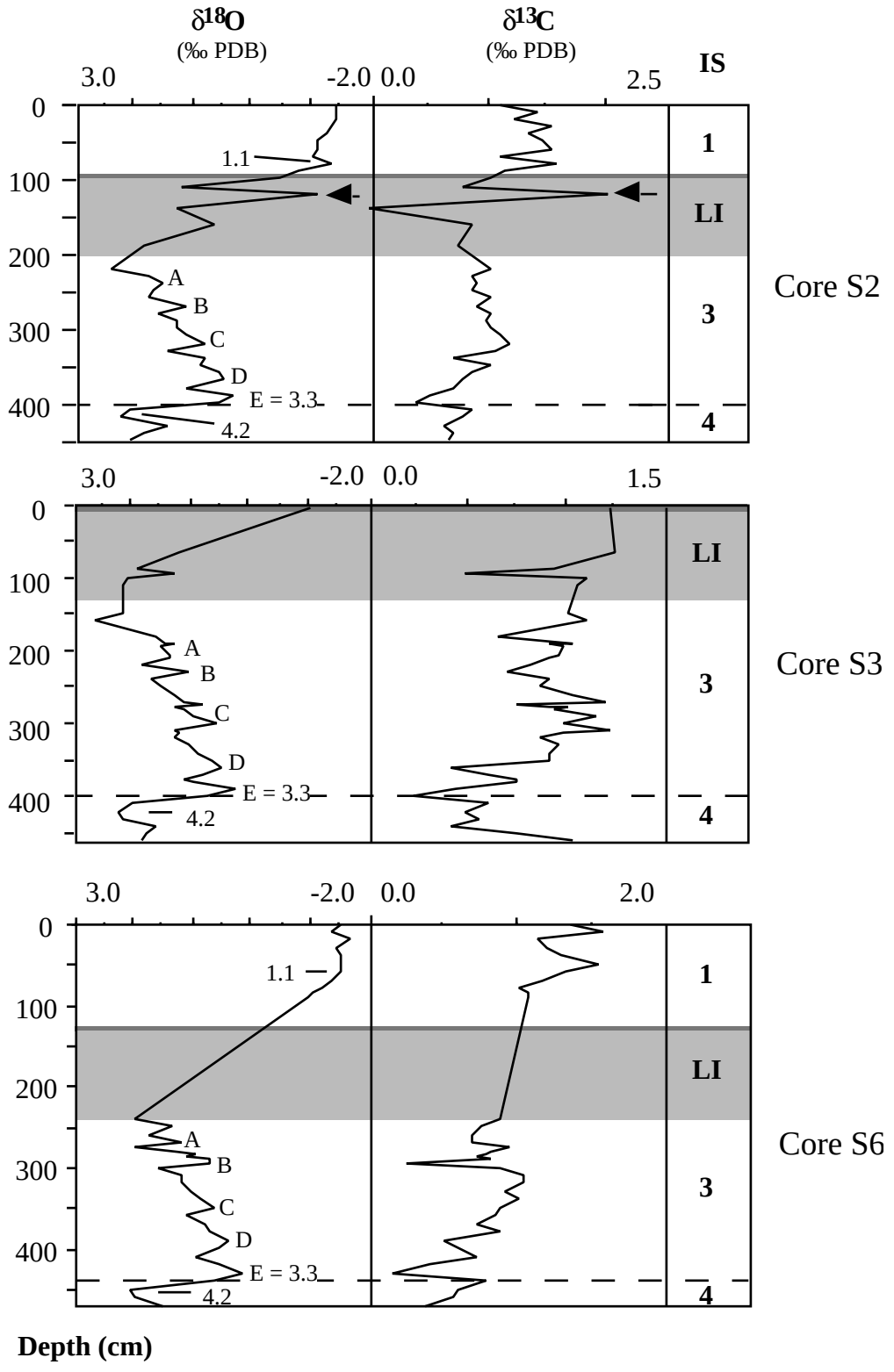

Figure C.5-4: Logs of the planktic $\delta^{18}O$- and $\delta^{13}C$ variations in the proximal cores at Sanganeb Atoll. Note the high resolution of IS 3 with the same small scale cycles (A-E) in the oxygen isotope curves of all three cores. Those cycles might represent short-term hydrologic or climatic variations. A negative correlation is visible between C- and O curves with the earlier mentioned offsets (Fig. C.5-4) in core S2. Cores S3 and S6 show a parallel increase of both proxies towards the base of the lithified interval (LI). As in core S1, extremely light oxygen and heavy carbon isotope values occur within the lithified interval of IS 2 (arrows).

and the upper strongly lithified part was dated at 19,540±130 and 18,920±110 ^{14}C-AMS yr in the cores S1 and S6, respectively. In the lower interval of core S1 δ^{18}O-values show a strong oscillation with amplitudes of 0.5 to 1.0‰ between lighter values in less lithified layers and heavier values in layers with a higher grade of lithification (all analysed on lithified particles!).

In contrast to core S1, high amplitude oscillations within the lithified interval of core S6 were caused by the frequent occurrence of lithified and non-lithifed skeletal sands (calciturbidites) with generally lower δ^{18}O-values compared to „normal“ lithified chips (mudstones).

C.5.2.2 Oxygen isotopes of the unlithified fine fraction

Compared to the lithified particles the stable oxygen isotopes of the unlithified fine fraction in core S1 are generally lighter and show a completely different trend (Fig. C.5-5). δ^{18}O-values of the unlithified fine fraction vary between 3 and 4.6‰. From the base of the lithified interval (125 cm) isotope values increase from 3‰ to a maximum of 4.5‰ between 117 and 100 cm in the less lithified part of core S1. This interval was ^{14}C-AMS dated at 20,420±130 to 19,280±150 yr. Thus, the δ^{18}O-maximum of the unlithified fine fraction occurs much earlier than the one found for the lithified particles. Above this maximum the δ^{18}O-values decrease again towards the base of the sapropel, where values decline once more from 3.7 to 1‰ between 50 and 45 cm.

C.5.2.3 Carbon isotopes of the lithified particles

The δ^{13}C-curves of lithified samples show parallel trends to the δ^{18}O-record in core S1 and S6, while no clear trend is visible in core AL (Fig. C.5-5). In core S1 and S6 the same maxima and minima as in the oxygen isotope curves can be found, even most of the small scale oscillations are recorded in both proxies. The analysed δ^{13}C-values are generally 2-2.5‰ lighter when compared to δ^{18}O-values and vary between 2.7-4.3‰.

C.5.2.4 Carbon isotopes of the unlithified fine fraction

The δ^{13}C-curve of unlithified fine fraction in core S1 shows a totally different trend compared to that of lithified samples (Fig. C.5-5). ^{13}C/^{12}C-ratios of unlithified samples are generally 1-1.5‰ lighter than those of lithified sediments and vary between 1.5-2.5‰.

The δ^{13}C-curve generally shows a parallel trend to the δ^{18}O-curve of the unlithified fine fraction but small scale oscillations are different. After a δ^{13}C-maximum (2.5‰) in about 115-120 cm values decrease towards the base of the sapropel (2‰) with two positive excursions in about 90 and 70 cm. It needs to be mentioned that the absolute δ^{13}C-maximum is reached in the deeper parts of the sapropel layer (2.7‰ at 47 cm) before values drop to their minimum of 1.5‰ (Fig. C.5-5).

C.5.3 Salinities of Red Sea waters during IS 2

In various previous studies salinities of Red Sea waters during the last glacial sealevel lowstand were estimated to be greater than 50‰. Those values were based on salinity tolerances of plankton species, planktic and benthic stable oxygen isotopes and by water balance models (e.g. Assaf & Hecht, 1974; Winter *et al.*, 1983; Hemleben *et al.*, 1996; Geiselhardt, 1998). As a further proxy the stable oxygen isotopes of the lithified particles and unlithified fine fraction were used to calculate

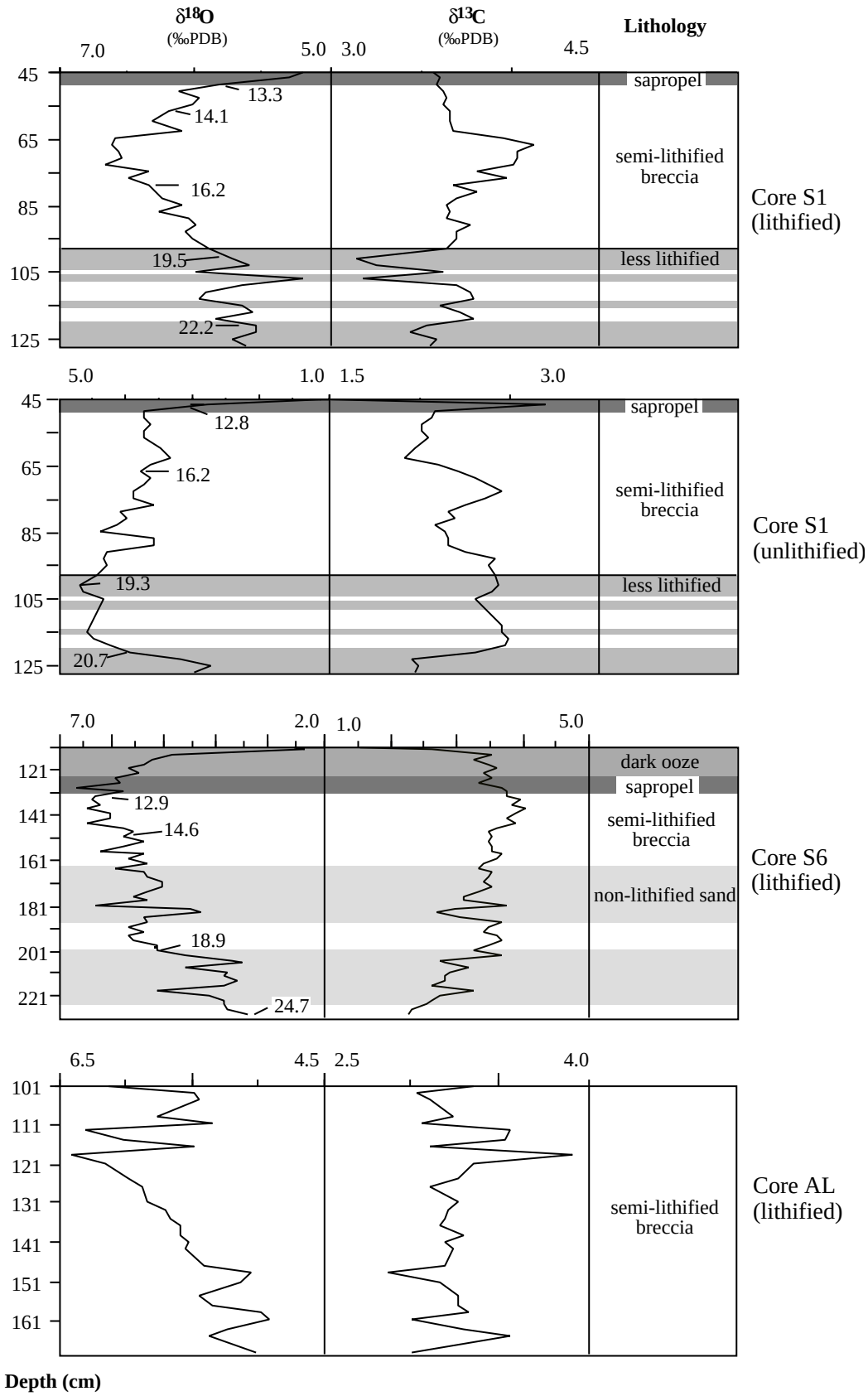

Figure C.5-5: Stable C and O isotopes analysed on lithified components and unlithified fine fraction of the lithified interval. Numbers on the $\delta^{18}O$- curves of core S1 and S6 are uncorrected ^{14}C-AMS ages in ky, the exact ages with errors are given in Tab. C.2-3. Coloured in medium grey are the layers with a lower grade of lithification within the older, less lithified parts of the lithified interval in core S1. The light grey colour shows non lithified sands in core S6. See text for description.

paleo-salinities of surface- and bottom-waters for an estimated water temperature of 21°C (see Chapter B-2.3.5). Parts of the results are shown in Tab. C.5-1, the complete dataset can be found in Appendix 4-B.

Salinities in lithified samples of core S1, which might represent bottom-water conditions, are in the range of 52-57.5‰. Highest salinities that exceed 57‰ are found at a depth of 60-80 cm which corresponds to 14,840±110 ^{14}C-AMS yr (67 cm).

Based on δ^{18}O-values measured on the unlithified fine-fraction of core S1 (surface water?) salinities between 39-51‰ were calculated. Highest salinities occur in the deepest parts of the lithified interval in 100-121 cm, which corresponds to the time period from 19,280±150 to 20,730±230 ^{14}C-AMS yr. It is obvious that δ^{18}O-values and salinities between 87 and 89 cm (*italic* in Tab. C.5-1) are clearly lower when compared to that of surrounding sediments and that the reduced values correspond to the major age inversion of the unlithified samples in core S1 (see Fig. C.2-3, Chapter C. 2.2.1).

Table C.5-1: Salinities based on stable oxygen isotopes of the lithified interval
Cc = calcite

Depth (cm)	**δ^{18}O** (‰ PDB)	**Aragonite** %	**LMC** %	**HMC** %	**δ^{18}O** (calcite)	**δ^{18}O Cc** (SMOW)	**δ^{18}O** water	**Salinity** (21°)	**^{14}C-AMS age** (yr)
Lithified bulk sediment									
47	5.29	88.2	4.1	7.7	3.61	34.63	5.40	52.70	12930
49	5.80	79.5	3.6	16.9	4.10	35.13	5.90	54.45	13310
53	5.95	80.1	4.3	15.5	4.26	35.30	6.07	55.03	12900
57	6.17	82.1	6.1	11.7	4.52	35.57	6.34	55.98	14080
67	6.60	83.8	6.3	9.9	4.95	36.01	6.78	57.52	14840
73	6.63	83.7	4.7	11.6	4.96	36.02	6.79	57.54	14890
79	6.33	80.8	6.3	12.9	4.67	35.73	6.50	56.53	16160
87	6.25	77.9	5.4	16.7	4.58	35.63	6.40	56.18	17010
101	5.70	57.3	4.5	38.2	3.99	35.02	5.79	54.07	19540
105	5.97	73.2	4.5	22.3	4.28	35.32	6.09	55.11	19060
109	5.63	74.1	4.1	21.8	3.93	34.96	5.73	53.86	19640
117	5.56	72.4	4.9	22.6	3.87	34.90	5.67	53.65	21040
121	5.54	65.6	4.4	30.0	3.84	34.87	5.64	53.53	22200
Unlithified fine fraction									
47	2.73	72.8	13.0	14.1	1.19	32.14	2.91	44.02	12840
49	3.68	8.9	29.3	61.8	2.38	33.36	4.14	48.30	14070
53	3.60	56.3	13.8	29.8	2.06	33.04	3.81	47.15	13810
57	3.71	58.4	15.6	26.0	2.20	33.18	3.95	47.65	14630
67	3.72	66.9	15.9	17.2	2.23	33.21	3.98	47.74	16150
73	3.84	68.9	13.1	18.0	2.30	33.29	4.06	48.02	15810
79	4.05	52.1	19.0	28.9	2.61	33.60	4.37	49.10	16930
87	*3.55*	*49.5*	*19.2*	*31.3*	*2.11*	*33.09*	*3.86*	*47.32*	*15330*
89	*3.55*	*53.1*	*18.5*	*28.5*	*2.10*	*33.07*	*3.84*	*47.28*	*15290*
101	4.63	45.2	14.6	40.3	3.09	34.10	4.87	50.85	19280
105	4.29	47.8	14.8	37.4	2.76	33.76	4.53	49.66	19380
109	4.38	44.4	16.4	39.2	2.88	33.88	4.65	50.09	19880
117	4.44	44.4	15.2	40.4	2.92	33.92	4.69	50.23	20420
121	3.91	49.1	16.7	34.2	2.42	33.40	4.17	48.43	20730

C.6 Total organic carbon (TOC) and calcium carbonate

Glacial-interglacial variations in the carbonate content indicate changes in carbonate production by plankton, shallow-water organisms and inorganic precipitation as well as the preservation of those carbonates at the seafloor. A further important point is the „dilution“ of the carbonates by the siliciclastic input from the mainland. An increase in TOC indicates a better submarine preservation and/or times of very high planktic carbon production or increased input of carbon from terrestrial sources. The carbonate and TOC variations with depth in core are shown in Fig C.6-1, the complete data-set with the analytical errors is given in Appendix 3.

C.6.1 Total organic carbon (TOC)

Average total organic carbon content ranges from 0.23-0.35%, without clear differences between the investigated cores. Maxima and minima in TOC vary between 0.9-2% and 0.1-0.15%, respectively. Maxima in TOC are found in or a few cm above the sapropel and coincide with light peaks in the oxygen isotope record, i.e. during IS 3 in proximal cores (A-E, see Fig. C.6-1). Many of those TOC-maxima are associated with the occurrence of dark, sapropelitic layers (Fig. C.6-1). The TOC peaks that occur directly above the main sapropel on top of the lithified interval lie between 0.6 and 1.6%. Only in core AL a peak is found within the sapropel itself that reaches about 1%. The increased TOC values that coincide with sapropel formation are accompanied by lowered carbonate values. Some of the before mentioned TOC peaks (0.5-2%) found in IS 3 (e.g. S6 - 360 cm; S3 - 390 cm) also coincide with a decrease in carbonate content (Fig. C.6-1). In core AL the general trends of the TOC-curve clearly resembles the saw-tooth pattern of the $\delta^{18}O$ curve during the interval from IS 5 to IS 3.

C.6.2 Carbonate content

Average carbonate content of the bulk sediments varies between 46% in cores S2 and S3 at the leeward side of Sanganeb Atoll and 73% in core AL at Abington Reef. Carbonate values are 15-30% higher at Abington Reef. At Sanganeb Atoll the carbonate content in cores from the leeward side is about 5-10% lower than in cores from the windward side, except for the Holocene. This points to an increased siliciclastic input at the leeward side of Sanganeb Atoll, which dilutes the carbonate input.

A clear glacial-interglacial pattern is found with generally higher carbonate-content in interglacials. In Holocene sediments values reach 60% at Sanganeb Atoll and 80% at Abington Reef. After an extended minimum during the sapropel formation (33-40%; 60% in AL) a sharp increase can be observed during the early Holocene that peaks close to isotopic event 1.1. In periplatform sediments of core S1 and AL that were deposited during the last interglacial (IS 5) carbonate content also exceeds glacial values and varies between about 65% and 85%. Lower carbonate values were analysed in the glacial sediments. At Sanganeb Atoll lowest values of 30-40% were measured on unlithified bulk sediments of the lithified interval (IS 2). During IS 3 and IS 4 average carbonate values are increased compared to the lithified interval and reach 41-46% and

45-57%, respectively. In core S1 carbonate content is clearly increased during IS 4 and reaches > 60%, which is in the range of interglacial values. Glacial-interglacial variations on a higher resolution are present in cores S1 and AL, where isotopic events 5.1 and 5.2 are clearly marked in the carbonate record (Fig. C.6-1).

In general, the trends of the calcium carbonate curves are opposite to that of the quartz intensities and the SiO_2-content (Chapter C. 7.4 and C. 8.1), which can be interpreted as proxies for siliciclastic input.

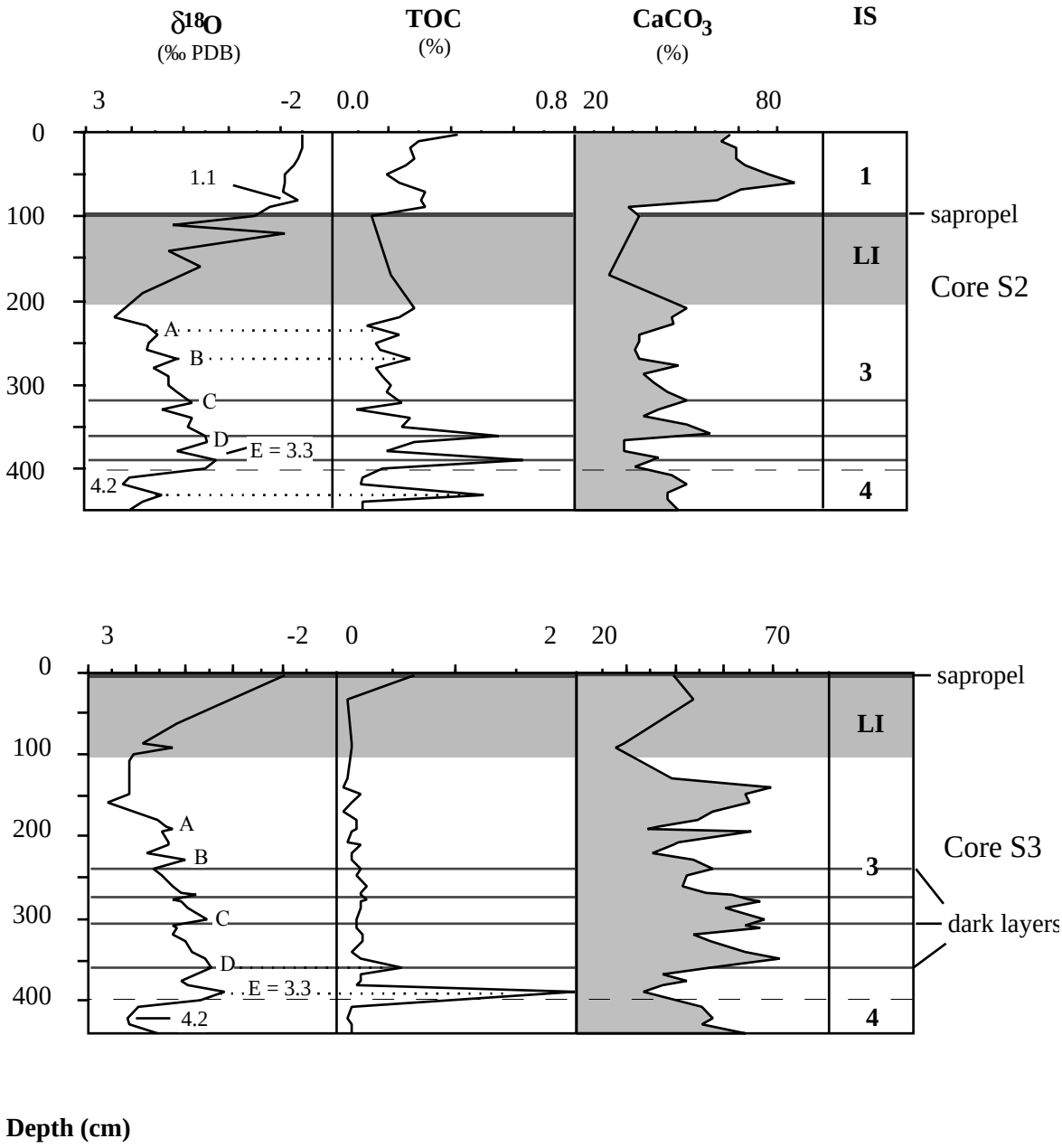

Figure C.6-1: TOC- and $CaCO_3$ logs of cores from Sanganeb Atoll and Abington Reef. Most of the peaks (A-E) found during IS 3 correlate with maxima in the TOC-curves in proximal cores (S2, S3, S6). Peak E coincides with SPECMAP event 3.3. TOC-maxima correspond with the occurrence of the sapropel on top of the lithified layer and with some sapropelitic beds (dark layers) deeper in core. IS = isotope stage, LI = lithified interval.

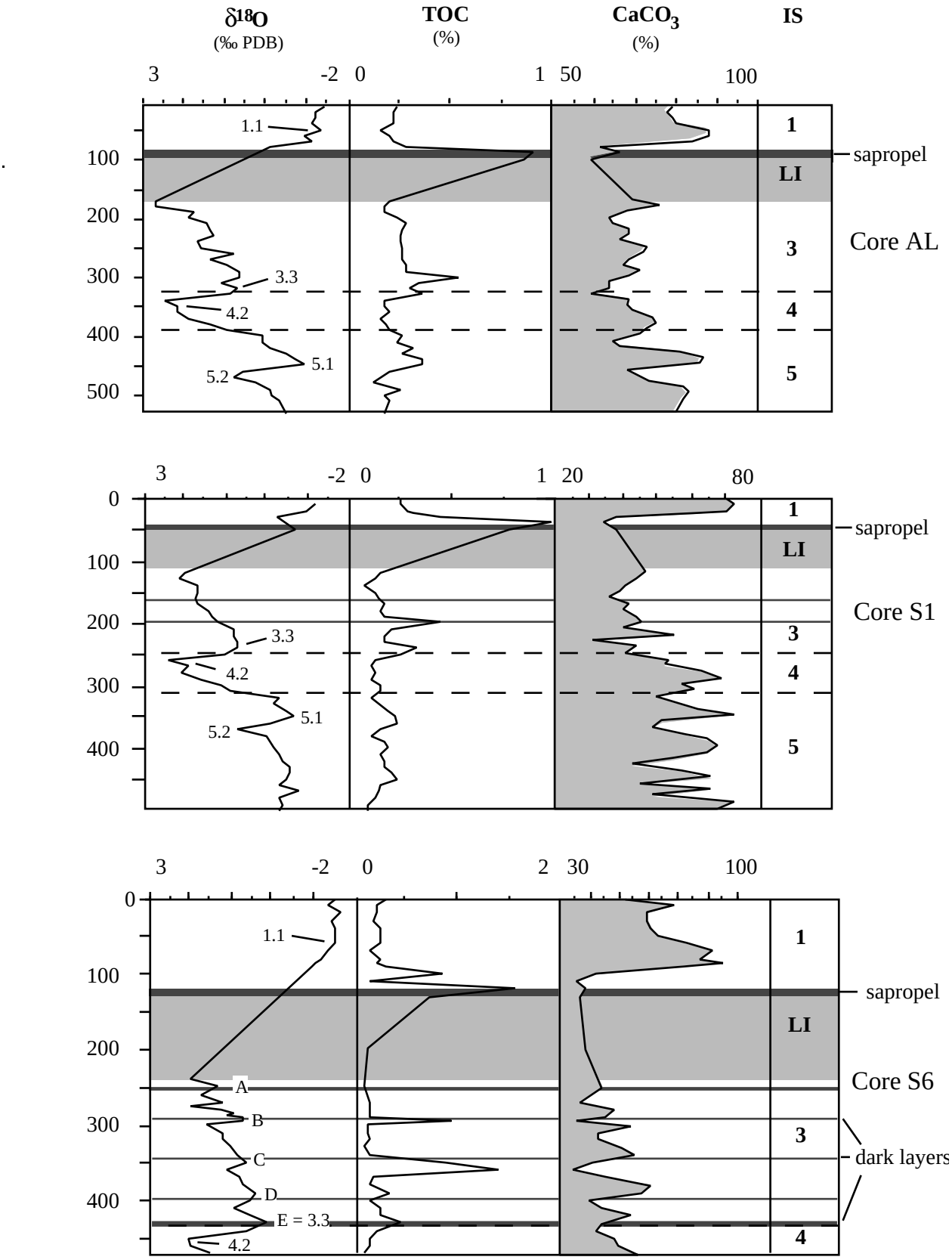

Figure C.6-1 (continued): Caption see left page

C.7 Mineralogy

Modern and late Quaternary sediments from the Sudanese shelf are a mixture of siliciclastic and carbonatic components. This is due to a high biogenic carbonate production accompanied by an increased siliciclastic input from the hinterland. A quantitative mineralogical analysis of the periplatform sediments, the lithified interval and the calciturbidites allows to determine variations in the deposition of individual mineral phases in time and space. The mineralogical composition of the sediments was analysed using X-ray diffraction. Aragonite/calcite-ratios were calculated based on peak-area ratios of aragonite, low magnesium calcite (LMC) and high magnesium calcite (HMC). Dolomite percentages could not be calculated due to very small peak areas. The peak-height was measured instead as a scale for dolomite concentration and variation with depth in core. Dolomite was neglected for further calculation of carbonate mineral abundances. Besides the carbonate minerals, quartz forms the second major constituent of the periplatform sediments and can be seen as a proxy for terrigenous input. Peak height was also used as a measure for quartz concentrations. The complete mineralogical dataset is given in Appendix 4-A to 4-E.

C.7.1 Carbonate mineralogy of periplatform sediments

C.7.1.1 Aragonite

Aragonite is the prevalent carbonate mineral phase in the studied sediments. In the carbonate fraction of periplatform sediments (bulk and fine fraction) the aragonite percentages range between 45-60% which corresponds to a total rock percentage of 23-45%, depending on the carbonate content. Differences in average aragonite percentages between bulk sediment and fine fraction of periplatform sediments are not significant (Δ = 1-3%). The logs of the aragonite/calcite-ratios are shown in Fig. C.7-1 to C.7-3. The complete dataset with the average aragonite and calcite abundances for individual isotope stages, the lithified interval and the sapropel are summarised in Appendix 4.

For spatial comparison between cores average aragonite percentages for IS 3 where calculated because this time interval is fully developed in all studied cores. Average aragonite percentages in IS 3 represent the general spatial trends, which are also visible in all other stages and substages if developed. Highest aragonite percentages of IS 3 bulk sediments were analysed in cores AL and AW at Abington Reef (63% and 59%). At Sanganeb Atoll average aragonite percentages are slightly lower and lie at 54-57% in proximal cores S2, S3, S6. This means, that aragonite percentages in cores taken at a distance of about 1.5 km from Abington Reef are higher than those in cores taken very close to the large Sanganeb Atoll. Calculated for total rock the aragonite percentage is about twice as high in core AL at Abington Reef (43%) than in cores at Sanganeb Atoll (20-26%). Smallest aragonite portions where measured in periplatform sediments of core S1 (47%), which was taken at a distance of about 5 km from the reef. The aragonite percentage in proximal periplatform sediments at Sanganeb Atoll is about 10% higher compared to those in distal core S1.

The aragonite curves of bulk sediment and fine fraction principally show the same glacial-interglacial pattern as the planktic $\delta^{18}O$-curve, with generally higher average aragonite percentages of 45-65% during interglacial sealevel highstands (IS 1, IS 5a, 5c, 5e) and interstadials (IS 3) and

lower aragonite values (30-55%) during glacial and interglacial lowstands (IS 2, IS 4, IS 5b, IS 5d and IS 6) (Fig. C.7-1 to C.7-3). It is an important finding, that aragonite percentages of the interglacial sealevel highstands do not exceed or even stay below values found for IS 3. Highest average interglacial aragonite values were found in the Holocene (58-65%) and lowest glacial values occur in sediments of IS 4 (33-55%).

Maximum aragonite glacial-interglacial amplitudes reach about 15% in core AL and 23% in core AW at Abington Reef. In the cores at Sanganeb Atoll these amplitudes are generally higher and vary between 30-35% (bulk sediment). Aragonite glacial-interglacial amplitudes analysed within the fine fraction of core S1 are even larger and reach up to 70%. This is because aragonite values of the fine fraction drop down to 0% during isotopic event 4.2, 5.2 and in a depth of 410 cm. Generally maxima and minima of the aragonite curves coincide with the SPECMAP events of the isotope curves with only small depth offsets of a few cm. Emmermann *et al*. (1999) showed that those depth offsets correspond to time-offsets between both proxies, caused by small time differences between flooding/exposure of the reef platforms (sealevel) and sediment export variations. It is remarkable that even the small-scale cycles (events A-E) that occur in the isotope curves of the proximal cores at Sanganeb Atoll (Fig. C.7-1/C.7-2) during IS 3 are found within the aragonite curves of the fine-fraction (only partially in bulk sediment). The aragonite maxima that coincide with events A-E also correlate with maxima in the TOC record.

Independent from glacial-interglacial variations the absolute maxima in the aragonite curves were found in the sapropel (69-84%) on top of the lithified interval, which possibly points to an unusually good aragonite preservation caused by stagnating bottom-water conditions during a pluvial phase of the last deglaciation (e.g. Almogi-Labin *et al*., 1991; Hofmann *et al.*, 1998).

C.7.1.2 Low Magnesium Calcite (LMC)

Planktic foraminifers and coccoliths build their tests of LMC (Milliman, 1974; Morse & Mackenzie, 1990). Therefore, the LMC-curves to some extend reflect changes in plankton productivity. However, it has to be kept in mind that input and submarine dissolution/precipitation of the less-stable carbonate phases aragonite and HMC might have overprinted the original LMC signal.

Average LMC percentages of periplatform sediments reach only 15-25% of the carbonate mineral fraction (8-13% of total rock). No clear differences in the average percentages between bulk and fine fraction were found. Highest average LMC values in IS 3 sediments (like for aragonite a comparison between sites is based on average mineral abundances of IS 3) were analysed in cores S1 and S6 at the windward side of Sanganeb Atoll (23-24%). Cores at the leeward side at Sanganeb Atoll and at Abington Reef have lower LMC percentages (19-20% and 15-17% respectively). This means that periplatform sediments in distal core S1 at Sanganeb Atoll contain about 10% more LMC within the carbonate fraction than in core AL at Abington Reef. If LMC percentages are calculated for total rock no clear differences between cores can be found. During IS 3 the LMC percentages of total rock vary between 8-10% in all cores (Fig. C.7-1 to C.7-3).

Downcore variations of the LMC content reflect a weak glacial-interglacial pattern which is

overlain by a generally increasing trend with depth in core. This trend points to a progressive replacement of the metastable carbonates aragonite and HMC with depth in core. In general, the LMC-curves in cores at Sanganeb Atoll are more irregular and show more small scale variations of higher amplitude than those at Abington Reef. In core AL the glacial-interglacial pattern is best developed but individual maxima and minima on the LMC curve show distinct offsets to the corresponding isotopic events during IS 5. Most peaks occur above the corresponding events on the $\delta^{18}O$ curve (see Fig. C.7-3). Furthermore, the peaks that occur during IS 5 and IS 4 show a significant correlation to those of the planktic $\delta^{13}C$ record (see Fig. C.5-3. Chapter C. 5.1).

Lowest LMC values were found for unlithified sediments of IS 2 in all cores, except for the bulk sediments of core S6. A reduced LMC content also coincides with isotopic event 4.2 in all cores (Fig. C.7-1 to C.7-3). Lower glacial LMC values point to reduced pelagic carbonate production during phases of increased sea-surface salinities as a result of restricted water mass exchange with the Indian Ocean in tune with glacial sealevel lowstands (e.g. Berggren & Boersma, 1969; Reiss *et al.*, 1980; Winter *et al.*, 1983; Locke & Thunell, 1988; Hemleben *et al.*, 1996). Highest LMC percentages (35%) in core AW occur close to the base of the core and point to a high plankton productivity during an interstadial phase of IS 6 or at the end of interglacial IS 7 (Fig. C.7-3). Unfortunately the stratigraphic resolution of the aragonite curve is to low in this part of core AW. However, Holocene LMC values are clearly increased compared to the last glacial IS 2 but stay below values found for IS 3 and IS 5 in all cores.

C.7.1.3 High Magnesium Calcite (HMC)

In the Sudanese periplatform sediments HMC plays an important role, because it is the main constituent of the shallow-water reef sediments in the Red Sea which even dominates over aragonite in many sites (Aboul-Basher, 1980; Piller & Mansour, 1990). Therefore, it is expected that variations in the HMC-content of Sudanese periplatform sediments record changes in shallow-water sediment export.

Despite the prevalence of HMC in reef sediments at Sanganeb Atoll (Aboul-Basher, 1980) and other Sudanese reefs (Braithwaite, 1982) the HMC percentages in the studied periplatform sediments reach only 20-30% of the carbonate fraction (11-17% of total rock). Highest average HMC percentages were analysed in core S1 (29% in IS 3). In all samples the Mg-content of the Mg-calcite lies between 10 and 16 mol %, with only a few exceptions. No significant correlation between the $MgCO_3$-content and the amount of HMC in the samples can be observed (Fig. C.7-4).

All HMC-curves show an anticyclic pattern to the aragonite and the isotope curves. The minima and maxima are much more distinct compared to the aragonite curve (higher amplitude) and the saw-tooth pattern is present in all curves (Fig. C.7-1 to C.7-3). High HMC percentages occur in glacials and stadials, lower values were found in interglacials and interstadials. Highest HMC values correspond to isotopic event 4.2 (45-55%, bulk). In the periplatform sediments of core AW the HMC percentages are even about 10% less during IS 6 when compared to event 4.2. Apart from interglacial and interstadial minima lowest HMC values were found in the sapropel (10-20%). From the sapropel to the top of the cores the HMC percentages rise again by about 10%.

C.7.1.4 Dolomite intensities

It was not possible to measure the peak areas of dolomite in the diffractograms due to very small abundances of this carbonate mineral in the samples. Therefore, only the peakheights were measured, which can be used as a scale for dolomite concentration in the samples and variations with depth in individual cores. Logs of dolomite concentrations in the sediment cores can be found in Fig. C.7-1 to C.7-3. Dolomite intensities range between 0-250 counts in periplatform sediments of all cores.

The curves of the dolomite intensities show a characteristic glacial-interglacial pattern similar to that found in the quartz curves. Lower dolomite intensities below 50 counts are present in Holocene and IS 5 bulk periplatform sediments. Higher dolomite concentrations were found in glacial sediments (IS 2-4; IS 6) and the sapropel. The parallel trends to the quartz curves point to a predominantly input of dolomite from the mainland, where older Pleistocene coastal fringing reefs had been exposed to meteoric diagenesis and erosion during lowered sea-level (e.g. Aboul-Basher, 1980).

C.7.2 Carbonate mineralogy of calciturbidites

The calciturbidites are deposits of periodic, short term events, which to some extend record the original mineralogical composition of the reefal sediments. The average mineralogical composition of individual calciturbidites is shown in Tab. C.7-1.

The carbonate content of the calciturbidites (bulk sediments) in core S3 and S6 at Sanganeb Atoll does not differ significantly from that in glacial periplatform sediments (30-60% carbonate), but is increased for about 10-20% in the Holocene calciturbidites (70-80% carbonate) when compared to periplatform sediments.

The average aragonite percentages in individual calciturbidites in core S3 and S6 (bulk and fine fraction) vary between 40-80%; aragonite percentages of 55-60% (25-30% of total rock) prevail in most of the sand layers. These average aragonite values are in the range of those for periplatform sediments of core S3 and S6 (55%).

The calcite percentages in the calciturbidites vary between 10-24% LMC (3-11% total rock) and 11-38% HMC (3-17%) and coincide quite well with average values of the periplatform sediments in core S3 and S6 (18-22% LMC and 22-26% HMC). In contrast to periplatform sediments carbonate mineral percentages of bulk and fine fraction can differ significantly in the calciturbidites (Δmax. = 16%) without any distinct trend.

Dolomite intensities in the calciturbidites reach 8-72 counts (aver. = 45 counts) in bulk sediments and 32-102 counts (aver. = 68 counts) in the fine fraction, which is no big difference to dolomite concentrations in periplatform sediments in core S3 and S6 (aver. = 42-75 counts).

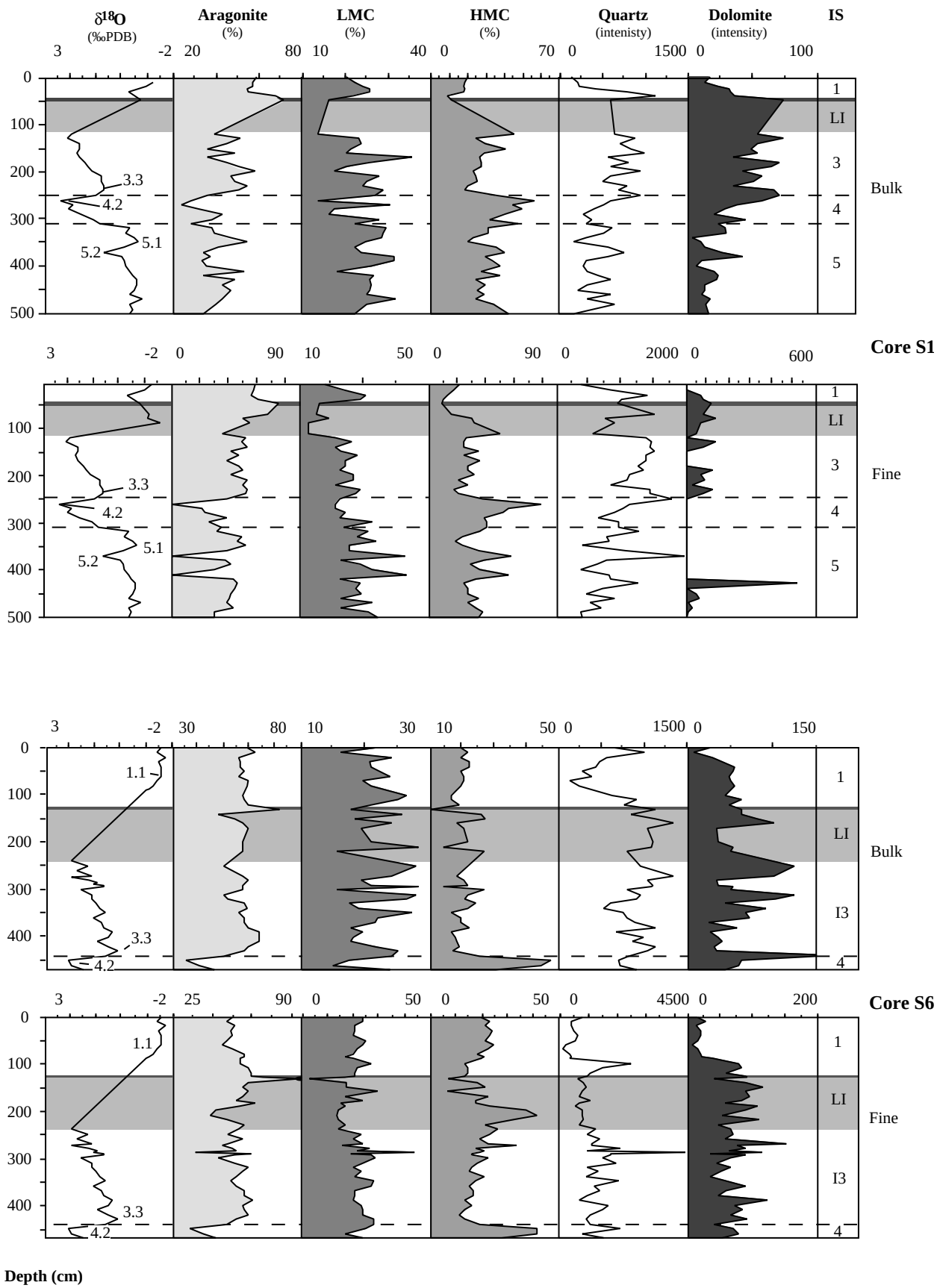

Figure C.7-1: Carbonate mineralogy and quartz-intensities of the bulk sediments and the fine fractions in the cores S1 and S6. Numbers on the isotope curve are isotopic events, IS = isotope stages, LI = lithified interval.

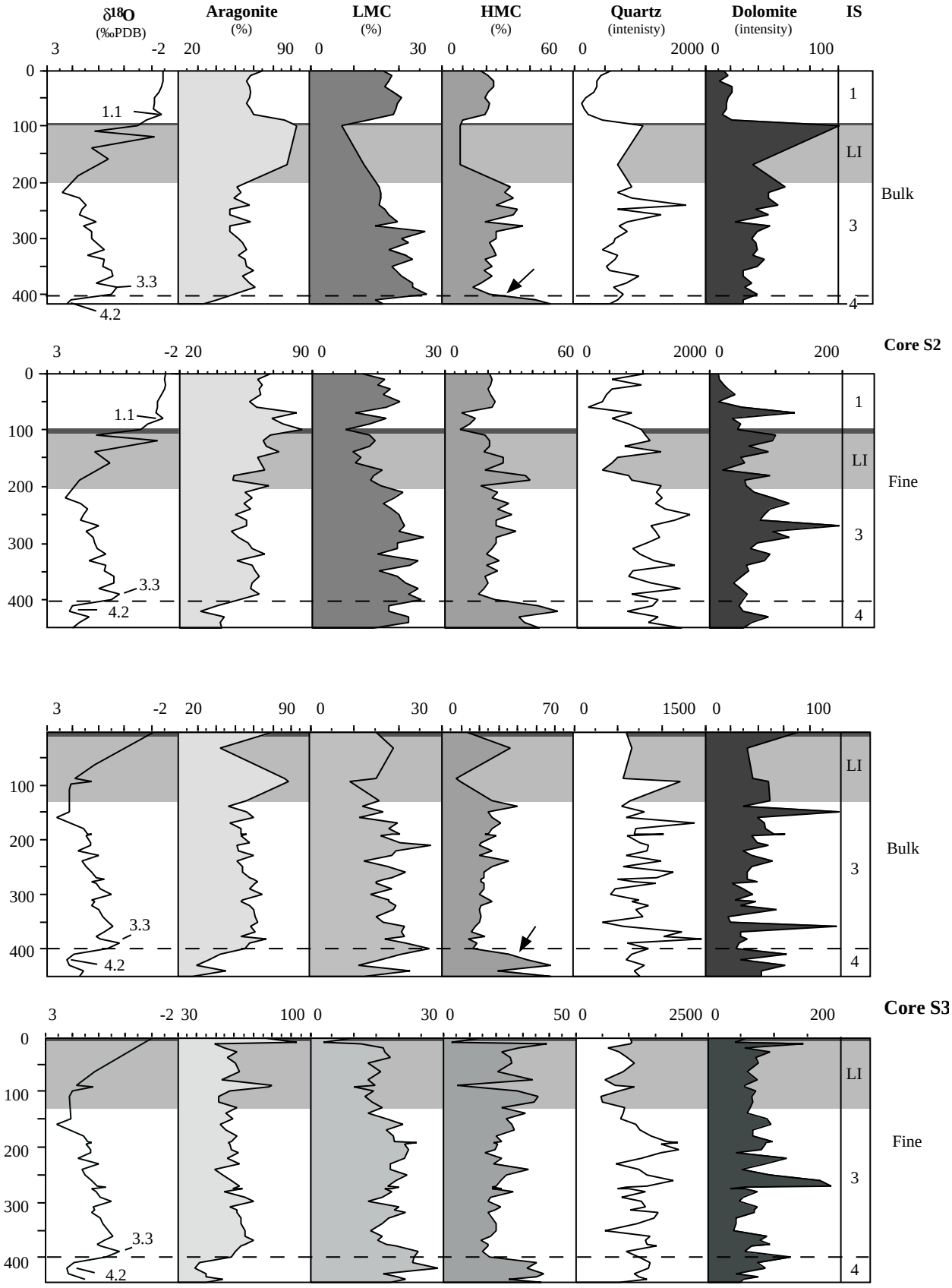

Figure C.7-2: Mineralogical logs of bulk sediment and fine fraction as analysed by X-ray diffraction in the cores S2 and S3. Arrows point to the sharp decrease in the HMC content during the sealevel rise from event 4.2 to 3.3. Numbers on the isotope curve are isotopic events, IS = isotope stages, LI = lithified interval.

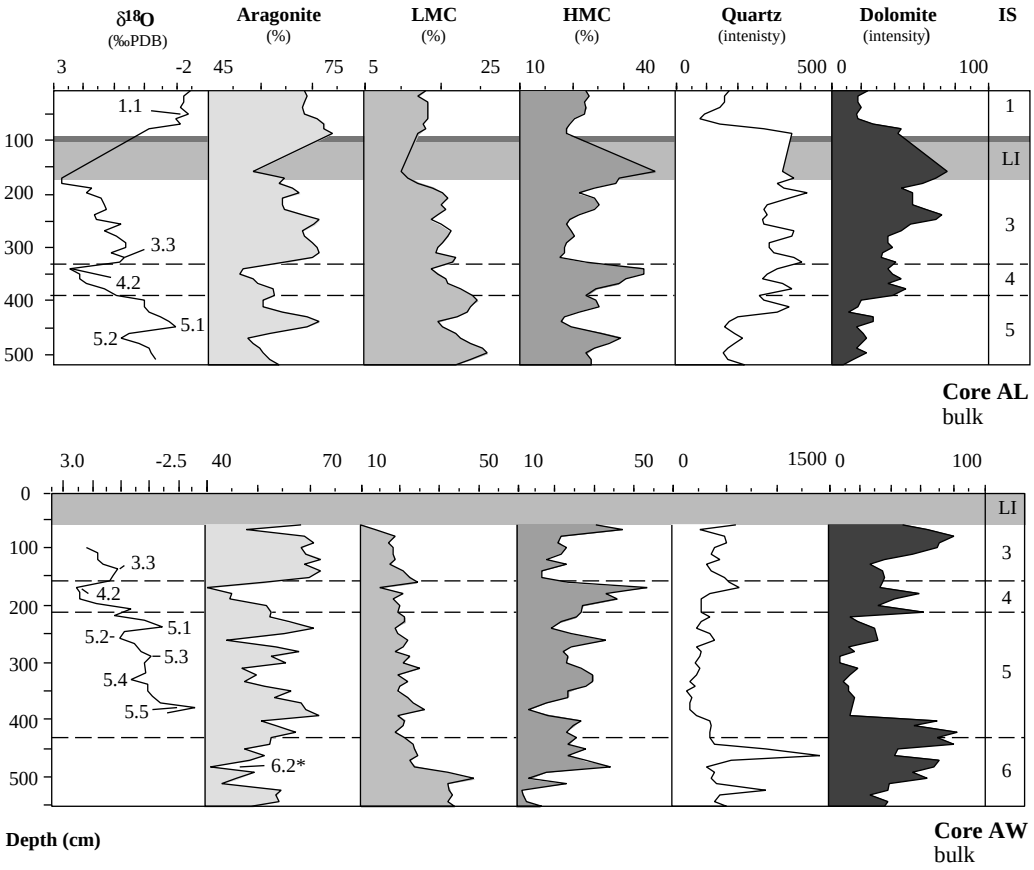

Figure C.7-3: Mineralogical logs of the sediment cores at Abington Reef. In this cores only the mineralogy of the bulk sediments was determined by X-ray diffraction analysis. Core AW reaches down to IS 6, the penultimate glacial, where LMC-percentages are significantly increased. Numbers on the isotope curve are SPECMAP events, 6.2* on the aragonite curve corresponds to the same isotopic event (aragonite stratigraphy). IS = isotope stages, LI = lithified interval.

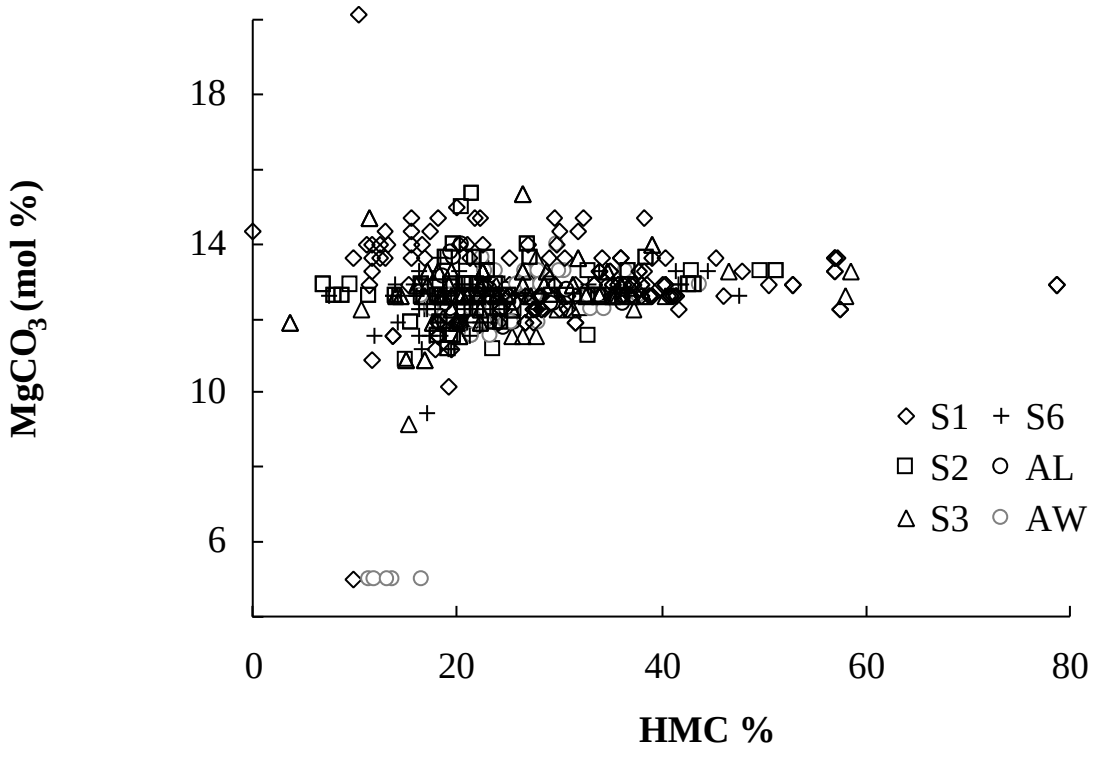

Figure C.7-4: Mol% $MgCO_3$ vs. Mg-calcite percentages of the bulk sediments, fine fraction and lithified sediments.

Table C.7-1: Mineralogical composition of calciturbidites

Ar = aragonite (%), LMC = calcite (%), HMC = Mg-calcite (%), Dolo = dolomite intensity, Quartz in intensity, Depth position of turbidites in cm, LI = lithified interval, IS = isotope stage

	Bulk sediment					**Fine fraction**				
	Ar	LMC	HMC	Quartz	Dolo	Ar	LMC	HMC-	Quartz	Dolo
Core S3 (cm)										
LI(30-40)	43	19	37	672	33	59	18	24	899	83
LI(60-80)						58	15	27	733	68
LI(93-96)	80	10	11	1227	49	79	10	11	1131	56
IS3(195-204)	54	16	30	640	35	58	21	21	1624	87
IS3(274-277)	61	17	22	601	37	62	19	20	927	49
IS3(300-314)	58	17	25	621	33	63	17	20	1208	64
IS3(377)	54	22	24	1036	27	66	17	17	1354	93
Core S6 (cm)										
IS1(10)	62	16	22	1004	8	53	24	23	488	30
IS1(86-90)						61	19	21	435	32
LI(150-170)	57	21	22	1171	72	62	22	17	843	102
LI(185)						67	15	18	755	58
LI(200)	58	21	22	1099	36	47	15	38	804	91
IS3(270-285)	59	22	20	1191	68	54	22	24	1411	97
IS3(370-390)	61	20	20	902	37	63	21	16	1096	79

C.7.3 Carbonate mineralogy of the lithified interval

Aragonite/Calcite-ratios of the lithified interval were analysed on lithified chips and unlithified fine fraction separately in order to reconstruct (1) submarine lithification at the sea-floor and (2) biogenic carbonate production and sediment export during the last glacial sea-level lowstand. If inorganic carbonate precipitation occurred in equilibrium with paleo-bottom-waters the mineralogy of the lithified samples might reflect the composition (salinity, alkalinity) of bottom waters. The unlithified fine fraction might represent conditions of surface waters as recorded in the tests of plankton and shallow-water organisms. The mineralogical composition of lithified and unlithified samples of core S1 are shown in Fig. C.7-5.

C.7.3.1 Aragonite content of the lithified interval

Lithified samples

The average aragonite percentage analysed on lithified chips is 77%, which is clearly increased compared to values in periplatform sediments and calciturbidites. The aragonite curve runs anticyclic to the $\delta^{18}O$ curve and shows parallel trends to the $\delta^{13}C$ curve except for the uppermost parts of the sequence (from 65 cm upwards) (Fig. C.7-5, and Fig. C.5-5, Chapter C. 5.2). In the lower, less lithified parts, aragonite minima (57-63%) are found in non-lithified beds and aragonite percentages

are generally lower than in the upper section (above 100 cm) of the lithified interval. In this upper and stronger lithified part highest aragonite percentages (83-84%) are found between 65-75 cm, which coincides with a $\delta^{18}O$ maximum at 14,840±110 ^{14}C-AMS yr ago (uncorrected radiocarbon age). The absolute aragonite maximum is not analysed in the lithified interval itself but in the sapropel on top. Here aragonite values analysed on lithified particles reach nearly 90%.

Unlithified fine fraction

Average aragonite percentages in the unlithified fine fraction are about 15% less than in lithified samples and reach about 53% on average. The aragonite curve shows a more or less parallel trend to the $\delta^{18}O$ curve analysed of the fine fraction, but the isotope maximum can not be found on the aragonite curve (Fig. C.7-5). Instead the aragonite maximum occurs at 65-75 cm (> 60%) and coincides with a significant peak on the $\delta^{13}C$ curve (Fig. C.5-5, Chapter C. 5.2). In addition, it becomes clear that the aragonite maximum in the fine fraction occurs in the same depth as in the lithified samples. The aragonite curve of the fine fraction shows a steady increase between 120 and 80 cm, without large scale oscillations, which is followed by a sharp increase between 80 and 70 cm (16,930±150 ^{14}C-AMS yr ago) where aragonite values rise from 45 to 60%. Just like in the lithified series the highest aragonite values were found in the sapropel (70%).

C.7.3.2 LMC

Lithified samples

Average LMC values in the carbonate fraction of lithified samples are very low and reach only about 5%. LMC percentages are higher in the upper part of the lithified interval above 87 cm (17,010±130 ^{14}C-AMS yr) and reach a maximum of 7% between 79-73 cm (about 16,160±120 to 14,890±80 ^{14}C-AMS yr ago). As for the aragonite distribution curve LMC values reach their maximum in the sapropel (10%).

Unlithified fine fraction

Average LMC percentages of about 17% were analysed on the unlithified fine fraction which are more than 10% higher compared to lithified bulk sediments. They lie below values observed in periplatform sediments of IS 3 in core S1 (23%). Lower LMC values during IS 2 point to restricted plankton (aplanktonic zone) production during the last glacial sealevel lowstand in the Red Sea (e.g. Reiss *et al*., 1980). No significant trends are visible in the LMC curve (Fig. C.7-5). Again highest values were found in the sapropel (30%).

7.3.3 HMC

Lithified samples

The HMC curve of the lithified samples runs anticyclic to the aragonite curve but parallel to the $\delta^{18}O$ record (reversed axis!) except for the sapropel (Fig. C.7-5). This is opposite to the trend that was observed in the periplatform sediments of all cores. The average HMC percentage (18%) is about 10% less than those for periplatform sediments (29% in IS 3, core S1). The HMC values

are clearly higher in the lower, less lithified parts, where maxima coincide with the less lithified layers (Fig. C.7-5). The highest HMC values of about 40% were analysed on lithified particles from a layer in 100 cm depth in core (19,540±130 ^{14}C-AMS yr). In the sapropel HMC values of lithified samples decrease to 0%.

Unlithified fine fraction

Average HMC percentages of the unlithified fine fraction reach about 30%. The HMC curves run anticyclic to the aragonite and $\delta^{18}O$ records of the fine fraction. HMC values are higher in the section between 120-80 cm (35-40%) and reach a minimum at 65-75 cm (10-20 cm). At the base of the sapropel HMC values increase to 60% and drop down to 10-20% at the top.

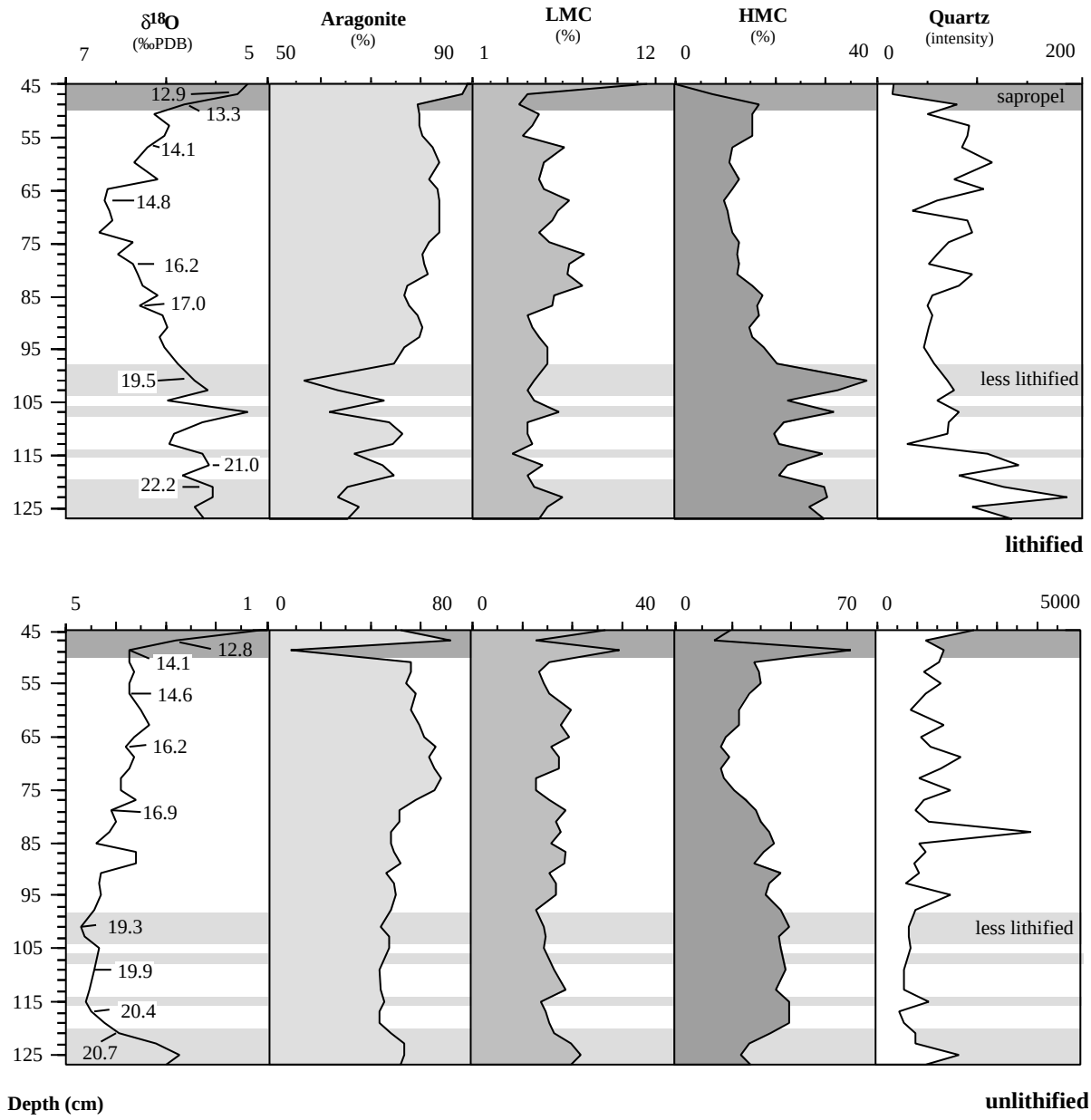

Figure C.7-5: Variations of carbonate mineral abundances and quartz-intensities of lithified bulk sediment (top) and fine fraction samples (bottom) of the lithified interval in core S1. In light grey the predominantly unlithified muds, which contain significantly less lithified chips and pebbles than other layers. Numbers on the isotope curve are uncorrected ^{14}C-AMS ages in ky, the exact ages with errors are given in Tab. C.2-3.

C.7.4 Quartz intensities

C.7.4.1 Periplatform sediments

Relative variations of quartz intensities analysed with X-ray diffraction can be seen as a scale for changes in siliciclastic input. Percentages of SiO_2 and the relative amounts of terrigenous grains in thin sections confirm the temporal variations in quartz intensities. Variations in the quartz-content of the periplatform sediments is shown in Fig. C.7-1 to C.7-3.

Generally quartz intensities analysed of bulk sediments reach 300-800 counts and are clearly less than in samples of the fine fraction, where average quartz intensities range for 1000-1200 counts. The differences in quartz intensities between bulk sediment and fine fraction can be explained by a lower siliciclastic input by coarser grains. Highest amounts of the quartz grains in the thin-sections are found in the silt fraction and are therefore interpreted as windblown input from the mainland. Quartz content in periplatform sediments at Abington Reef is about 50% less than in sediments at Sanganeb Atoll.

The curves of quartz intensities of bulk sediment and fine fraction show characteristic glacial-interglacial variations and run anti-parallel to the curves of carbonate content (Fig. C.6-1). Lower quartz intensities were found in interglacial sediments of the Holocene and IS 5 (150-500 counts in bulk sediment and 800-900 counts in fine fraction), while values in glacial periplatform sediments are clearly increased (300-900 counts in bulk sediment and 1100-1600 counts in fine fraction).

C.7.4.2 Calciturbidites

Average quartz intensities of the calciturbidites are summarised in Tab. C.7-1. Quartz intensities in the calciturbidites of the cores S3 and S6 vary between 600-1,000 counts in bulk sediment and 400-1,600 counts in fine fraction. Average bulk quartz intensities of the calciturbidites (800 counts) are equivalent to those of bulk periplatform sediments. In the fine fraction of the calciturbidites the average quartz intensities (1,000 counts) are slightly less than in periplatform sediments (1,200 counts). No significant temporal or spatial variations of the quartz content in the calciturbidites were found.

C.7.4.3 Lithified interval

Downcore variations of quartz intensities within the lithified interval are shown in Fig. C.7-5. Intensities of quartz found in lithified samples and unlithified fine fraction of are largely different. In the lithified samples average quartz intensities are extremely low and reach only 80 counts, with maxima of 110-190 counts in the lower, less lithified parts. In the unlithified fine fraction an average of 1,300 counts was calculated which is in good accordance with average values of the fine fraction from periplatform sediments (1,350 counts in IS 3, core S1).

The curve of the quartz intensities of the unlithified fine fraction displays a moderate increase between a depth of 115 cm and the top of the sapropel from about 1,000 to 2,000 counts. An outstanding maximum of 3,900 counts in 83 cm can not be correlated to any other proxy.

It seems that the quartz content and the grade of lithification exhibit some correlation. It is possible that a higher quartz content prevents lithification or that lithification events coincide with low siliciclastic input rates.

C.8 Geochemistry

X-ray fluorescence analysis of the bulk periplatform sediments in the cores at Sanganeb Atoll was performed. The geochemical composition of the periplatform sediments is an independent tool to distinguish siliciclastic- from carbonate input of the periplatform sediments.

The major goal of the geochemical analysis was the determination of the strontium content in the periplatform sediments as a proxy for shallow-water input. Higher strontium-content (>7,500 ppm) is characteristic for shallow-water components, like for example scleractinian corals, green algae and ooids. The shells of coccoliths, planktic foraminifers and pteropods have clearly lower strontium-contents (1,500-1,800 ppm) (Milliman, 1974; Morse & Mackenzie, 1990).

Furthermore the amount of high- and low-Sr aragonite in the periplatform sediments was calculated. It was suggested that the distribution patterns of high-Sr aragonite in Bahamian periplatform sediments record glacial-interglacial variations in shallow-water sediment export, while low-Sr-aragonite displays the input patterns of pteropod shells (Boardman *et al.*, 1986). If variations in the strontium-content of periplatform sediments record variations in shallow-water sediment export it can be used as an independent method to test the aragonite/calcite-ratios.

C.8.1 Distribution of main constituents

The raw data of the XRF-analysis are summarised in Appendix 5-A. Downcore variations of main constituents are shown in Fig. C.8-1. Average percentages of the element distribution for individual isotope stages, the lithified interval and the sapropel are given in Tab. C.8-1, those for the calciturbidites are shown in Tab. C.8-2.

C.8.1.1 Siliciclastic components

It was not possible to calculate a modal mineral composition of the siliciclastic fraction, but it is likely that the source for the terrigenous material was a magmatic rock of granitoid composition, even if weathering and sedimentary processes changed the original mineral distribution. The main siliciclastic components of the bulk periplatform sediments are SiO_2 (27-32%) and Al_2O_3 (8-9%). If we calculate the SiO_2 and Al_2O_3 content on a carbonate-free base the percentages reach about 60% SiO_2 and 17% Al_2O_3 which is common for mafic granites and granodiorites (Wimmenauer, 1985). The H_2O phase (about 5%) might belong to mica or clay minerals which incorporate water in their crystal lattice. Other main phases of predominantly siliciclastic origin are Na_2O (2-3%), Fe_2O_3 (4-5%), MgO (4%) and K_2O (about 1%). These elements are abundant in feldspars and other rock forming magmatic minerals. Parts of the MgO could be incorporated in HMC-crystals and dolomite.

The oxides that are predominantly contributed to the formation of siliciclastic minerals (SiO_2, Al_2O3, K_2O, TiO_2, Fe_2O_3) show parallel trends and match the curve of quartz intensities (Fig. C.7-1 and C.7-2). The glacial-interglacial variations of the SiO_2 content can be seen as a proxy for all siliciclastic minerals and for changes in siliciclastic input. Highest average SiO_2 values are found in IS 3 (33-34%) and lower SiO_2 concentrations are visible in the Holocene (22-23%), IS 4 (26-31%) and IS 5 (24-25% in S1). In the Holocene sequence percentages of siliciclastic phases decrease after a peak on top of the sapropel and reach a minimum that coincides with isotopic event 1.1,

from where concentrations rise again up-core.

C.8.1.2 Manganese

The MnO-curves are clearly different from that of the siliciclastic phases, but show similar trends during the Holocene. Manganese (MnO) shows only minor average variations with depth in core. Values vary between 0.07-0.075% between IS 1 and IS 4. An increase in MnO is only visible in periplatform sediments of IS 5 in core S1, where average values rise to 0.09%. Further dominant peaks that reach 0.1-0.15% are observed on top of the sapropel layer and in younger Holocene sediments. At this point the manganese curve shows the same pattern as the SiO_2-curve, with a significant minimum at event 1.1.

C.8.1.3 Magnesium

The magnesium (MgO) curves can be seen as combined signal of Mg-calcite and siliciclastic input. Average MgO values are increased in glacials (3.9-4.3% in IS 3-4) and are lowered in Holocene periplatform sediments (3.5%). The main trends of the MgO-curves are also found on the HMC-curves (Fig. C.7-1 and C.7-2). Maxima coincide with events 4.2 and 5.2, minima correspond to events 3.3 and 5.1. In the Holocene the siliciclastic input pattern clearly dominates the magnesium signal.

C.8.1.4 Calcium and carbonate content

About 25-30% of the bulk sediment consists of CaO the main constituents of carbonate minerals. An average CO_2 content of 20-24% was analysed independently with the LECO analyser. To form $CaCO_3$ (MgO is neglected, also CaO in apatite or gypsum) the same quantity of CaO (20-24%) is needed. If the amount of CaO that belongs to the carbonate fraction is subtracted from the total amount of CaO it becomes clear that only approximately 5-6% of the CaO belongs to the siliciclastic mineral fraction. The calcium variations correlate very well with those of the carbonate curves (see Fig. C.6-1), even though about 5% of the CaO belong to the siliciclastic fraction. CaO values are clearly increased during the Holocene (above the sapropel) and IS 5 (31-34%) and are lower in glacials (25% in IS 3, 25-30% in IS 4). The higher CaO values found in IS 4 (core S1) correlate with lower siliciclastic input. The question is raised if higher carbonate production or less dilution by siliciclastic components are the reason for this pattern.

C.8.1.5 Phosphate

The phosphate distribution curves are different from the siliciclastic and the carbonate ones. In the distal core S1 the phosphate curve correlates well with the $\delta^{18}O$ curve and shows the same glacial-interglacial pattern with some small offsets (Fig. C.8-1). In the proximal cores no such correlation between the phosphate and the oxygen isotope signal was found. In the Holocene sequence of core S6 the phosphate curve resembles that of siliciclastic input curves. It is likely that parts of the phosphate are derived from weathering of magmatic rocks, in which apatite is a common accessory mineral.

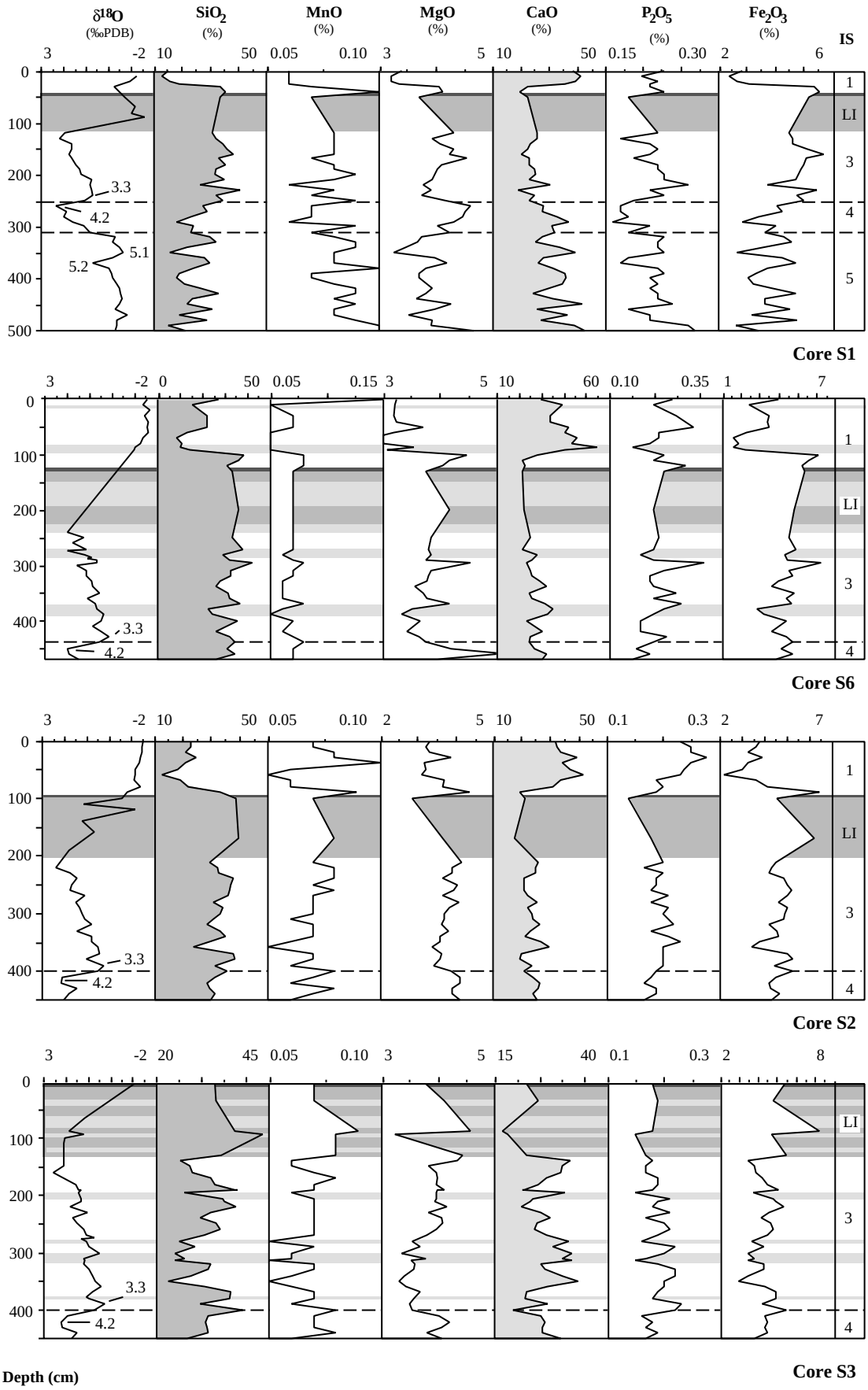

Figure C.8-1: Distribution of major elements in the cores at Sanganeb Atoll. IS = isotope stages, LI = lithified interval. Calciturbidites in light grey. Variations in SiO_2 are a signal for siliciclastic input and show a significant correlation to Al_2O_3, TiO_2 and K_2O which are not shown in this plot.

Table C.8-1: Average chemical composition calculated for individual isotope stages, the lithified interval and the sapropel

All values in percent, except for Sr (ppm), CO_2 (LECO) is the CO_2 content analysed with the LECO analyser, CaO (silicate) is the CaO percentage of the siliciclastic fraction, Sr (carbonate) is calculated on a siliciclastic-free base, Sr-arag = strontium aragonite.

	SiO_2	**MnO**	**MgO**	**CaO**	**CO_2** (LECO)	**CaO** (silicate)	**P_2O_5**	**Fe_2O_3**	**Sr** ($CaCO_3$)	**High-Sr-arag**	**Low-Sr-arag**
Core S1											
Holocene	22.25	0.07	3.56	32.92	25.72	7.20	0.22	3.68	3104	31.4	27.6
Sapropel	33.71	0.07	3.73	22.60	16.90	5.70	0.18	5.22	5115	55.1	16.8
LI	32.46	0.08	4.02	24.41	18.75	5.66	0.20	4.86	3850	38.2	17.6
IS 3	33.85	0.08	4.08	24.04	18.76	5.28	0.21	4.89	2547	23.6	23.0
IS 4	25.72	0.07	4.34	30.40	25.12	5.28	0.18	3.93	1889	15.1	18.1
IS 5a	25.21	0.08	3.74	31.18	26.21	4.97	0.21	3.87	2139	18.9	22.8
IS 5b	24.28	0.09	3.94	32.91	25.84	7.07	0.22	3.79	2160	19.0	22.0
Average	27.19	0.08	3.95	29.71	23.56	6.15	0.21	4.14	2444	22.5	22.7
Core S2											
Holocene	21.89	0.07	3.50	33.62	25.93	7.68	0.23	3.76	3572	36.6	24.6
Sapropel	39.12	0.07	2.86	21.80	16.00	5.80	0.14	4.55	6467	72.8	11.0
LI	39.53	0.08	3.28	19.66	14.33	5.32	0.16	5.39	6416	71.6	9.7
IS 3	33.26	0.07	3.78	23.57	18.12	5.45	0.20	4.66	3296	32.2	21.5
IS 4	30.44	0.07	4.04	25.50	19.80	5.70	0.18	4.43	2381	20.2	17.6
Average	30.18	0.07	3.70	26.31	20.22	6.09	0.20	4.43	3442	35.5	21.5
Core S3											
Sapropel	33.30	0.07	3.78	22.24	17.57	4.67	0.18	5.39	4811	51.5	19.0
LI	37.29	0.09	4.60	17.07	13.08	3.99	0.18	7.29	5791	63.6	13.2
IS 3	32.10	0.07	3.84	25.65	20.07	5.58	0.19	4.46	3481	34.7	22.0
IS 4	30.64	0.07	4.03	26.45	21.38	5.07	0.17	4.33	2308	19.4	17.7
Average	32.08	0.07	3.88	25.43	20.38	5.04	0.19	4.55	3479	35.5	21.6
Core S6											
Holocene	23.29	0.08	3.52	34.32	26.14	8.17	0.23	3.73	3422	34.4	23.4
Sapropel	33.80	0.07	3.75	21.60	16.55	5.05	0.22	5.44	5122	55.1	16.6
LI	33.80	0.07	3.75	21.60	16.55	5.05	0.22	5.44	5122	51.7	7.0
IS 3	32.17	0.07	3.78	26.27	20.00	6.26	0.21	4.53	3471	34.6	22.2
IS 4	31.22	0.07	4.25	28.75	22.11	6.64	0.18	4.39	2612	23.4	19.5
Average	28.74	0.07	3.75	29.51	23.13	6.38	0.22	4.24	3406	34.4	22.2

Table C.8-2: Average chemical composition of calciturbidites

All values in percent, except for Sr (ppm), CO_2 (LECO) is the CO_2 content analysed with the LECO analyser, CaO (silicate) is the CaO percentage of the siliciclastic fraction, Sr (carbonate) is calculated on a siliciclastic-free base, Sr-arag = strontium aragonite.

	SiO_2	**MnO**	**MgO**	**CaO**	**CO_2** (LECO)	**CaO** (silicate)	**P_2O_5**	**Fe_2O_3**	**Sr** ($CaCO_3$)	**High-Sr-arag**	**Low-Sr-arag**
Core S3											
Turb-LI(30-40)	33.47	0.07	4.10	24.66	19.34	5.32	0.19	4.83	2545	22.9	20.3
Turb-LI(93-96)	43.65	0.08	3.23	17.87	12.43	5.44	0.15	4.75	6162	68.4	11.4
Turb-IS3(195-204)	26.59	0.06	3.96	30.55	24.55	6.00	0.15	3.72	3674	36.0	18.0
Turb-IS3(300-314)	25.16	0.06	3.54	31.31	25.09	6.22	0.17	3.61	3673	37.0	21.4
Core S6											
Turb-IS1(10)	15.79	0.05	3.20	39.18	30.32	8.86	0.20	2.46	3409	35.1	27.2
Turb-IS1(86-90)	12.27	0.05	3.32	47.81	34.98	12.83	0.16	1.93	4332	0.0	0.0
Turb-LI(200)	36.26	0.07	4.18	22.59	17.40	5.19	0.20	4.87	3040	30.5	27.0
Turb-IS3(270-285)	33.55	0.07	3.83	24.83	18.92	5.91	0.18	4.63	3572	36.0	22.5
Turb-IS3(370-390)	28.06	0.06	3.67	32.99	24.28	8.72	0.23	3.63	3832	39.2	21.7

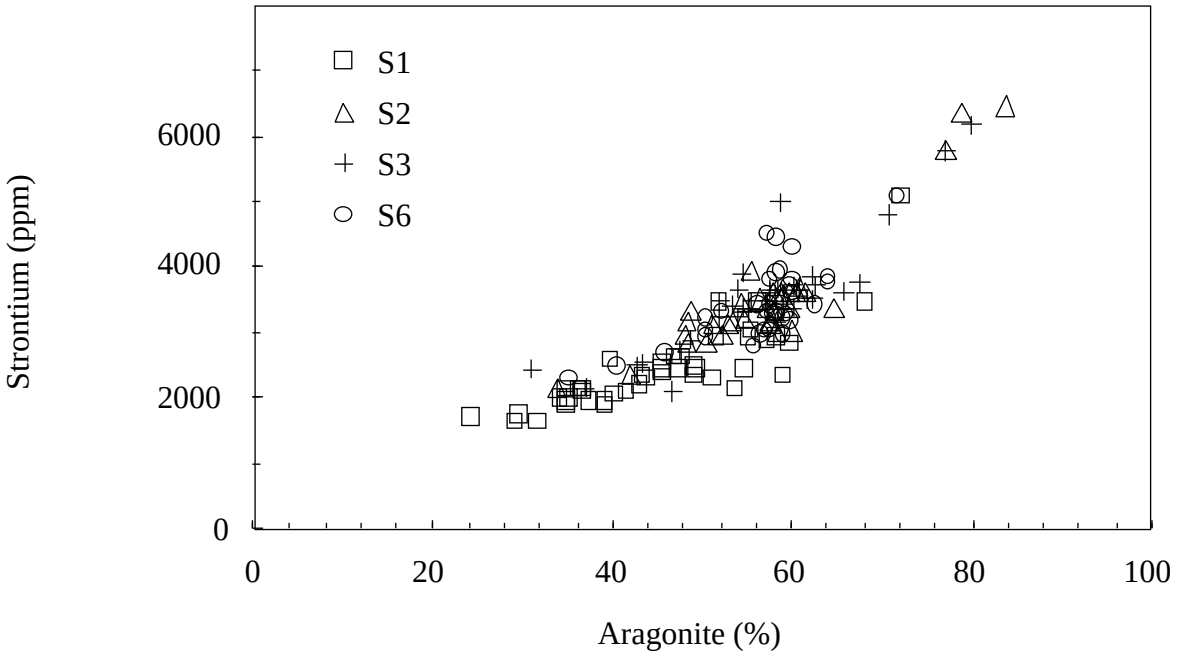

Figure C.8-2: Plot of the aragonite vs. strontium content of the bulk sediments at Sanganeb Atoll showing a positive, nearly linear correlation.

C.8.2 Strontium content

C.8.2.1 Periplatform sediments

Average strontium content of the carbonate fraction in the periplatform sediments varies between 2,500 and 3,500 ppm (1,300-1,700 ppm in total rock). In core S1 which was taken about 5 km east of Sanganeb Atoll strontium values are about 1.5 times lower than in the proximal cores S2, S3 and S6 (closer than 2 km). Generally, strontium- and aragonite contents of the bulk carbonate fraction show a positive correlation (Fig. C.8-2).

Downcore variations of the strontium content show the same glacial-interglacial variations as the aragonite curves. Maxima and minima in the strontium curves coincide with SPECMAP events on the oxygen isotope curves but glacial-interglacial amplitudes are less prominent in the strontium record similar to the variations in the aragonite curves (Fig. C.8-3). Average Holocene strontium content varies between 3,100 and 3,600 ppm. In Holocene periplatform sediments of core S1 strontium values are increased by about 600 ppm when compared to glacial values (IS 3). However, in proximal cores Holocene values are not significantly increased. Strontium values of the sapropel show the same spike as the aragonite curves, with highest strontium values of 5,000-6,500 ppm (see Fig. C.8-3). The average glacial strontium values of the carbonate fraction of the periplatform sediment lie between 2,500-3,000 ppm in IS 3 and 2,000-2,500 ppm in IS 4. As in the aragonite curves, absolute minima in strontium content coincide with isotopic event 4.2. The strontium values found for IS 5 (core S1) are clearly less than in IS 3 and reach 2,100-2,200 ppm. Substages 5a, 5b and 5c are clearly recorded in the strontium curve. The relatively high strontium- and aragonite content found in the periplatform sediments of IS 3 coincide with increased concentrations of shallow-water biota during this isotope stage compared to interglacial stages (see Chapter C. 9).

C.8.2.2 Calciturbidites

The strontium contents of some of the calciturbidites in the proximal cores S3 and S6 at Sanganeb Atoll are increased when compared to average strontium values of periplatform sediments (see Fig. C.8-3 and Tab. C.8-1). For example, the calciturbidite that occurs at 86-100 cm in the Holocene sequence of core S6 has a strontium content of 4,500-5,300 ppm, while average values of the Holocene periplatform sediments reach only 3,000-3,500 ppm in this core. Further calciturbidites with increased strontium values occur in core S6 in a depth of 280-295 cm (3,800 ppm) and 360 cm (4,500 ppm) as well as in core S 3 in 93 cm (6,200 ppm). In all other calciturbidites the strontium values are in the range of those from normal periplatform sediments and vary from 3,000 to 3,500 ppm. The high strontium content (5,000 ppm) that corresponds to isotopic event 3.3 on the oxygen isotope curve in core S3 could not be correlated with the occurrence of a calciturbidite.

C.8.3 High- and low-strontium aragonite

Variations in the distribution of high- and low-strontium aragonite are shown in Fig. C.8-3. The calculated values are listed in Appendix 5-B. The high-Sr curves perfectly match the strontium curves with only very small deviations (Fig. C.8-3). Average high-Sr-aragonite values are

significantly lower in core S1 (22.5%) compared to the proximal cores at Sanganeb Atoll which reach exactly the same average value of 35 ± 0.5%.

In contrast, the low-Sr-aragonite values do not show any difference between proximal and distal sites and range from 21 to 23% on average. The downcore variations in the low-Sr-aragonite curves are clearly different from that of the high-Sr-aragonite curves and show partially opposite trends (Fig. C.8-3). Nevertheless, glacial-interglacial variations are fully developed in all cores, showing higher values during interglacials lowest values during glacials. In core S1 for example maxima in low-Sr-aragonite are found in the Holocene, IS 3, IS 5a and 5c (up to 30%), while lower values occur during IS 4 (12%), in the lithified interval and the sapropel (about 15%).

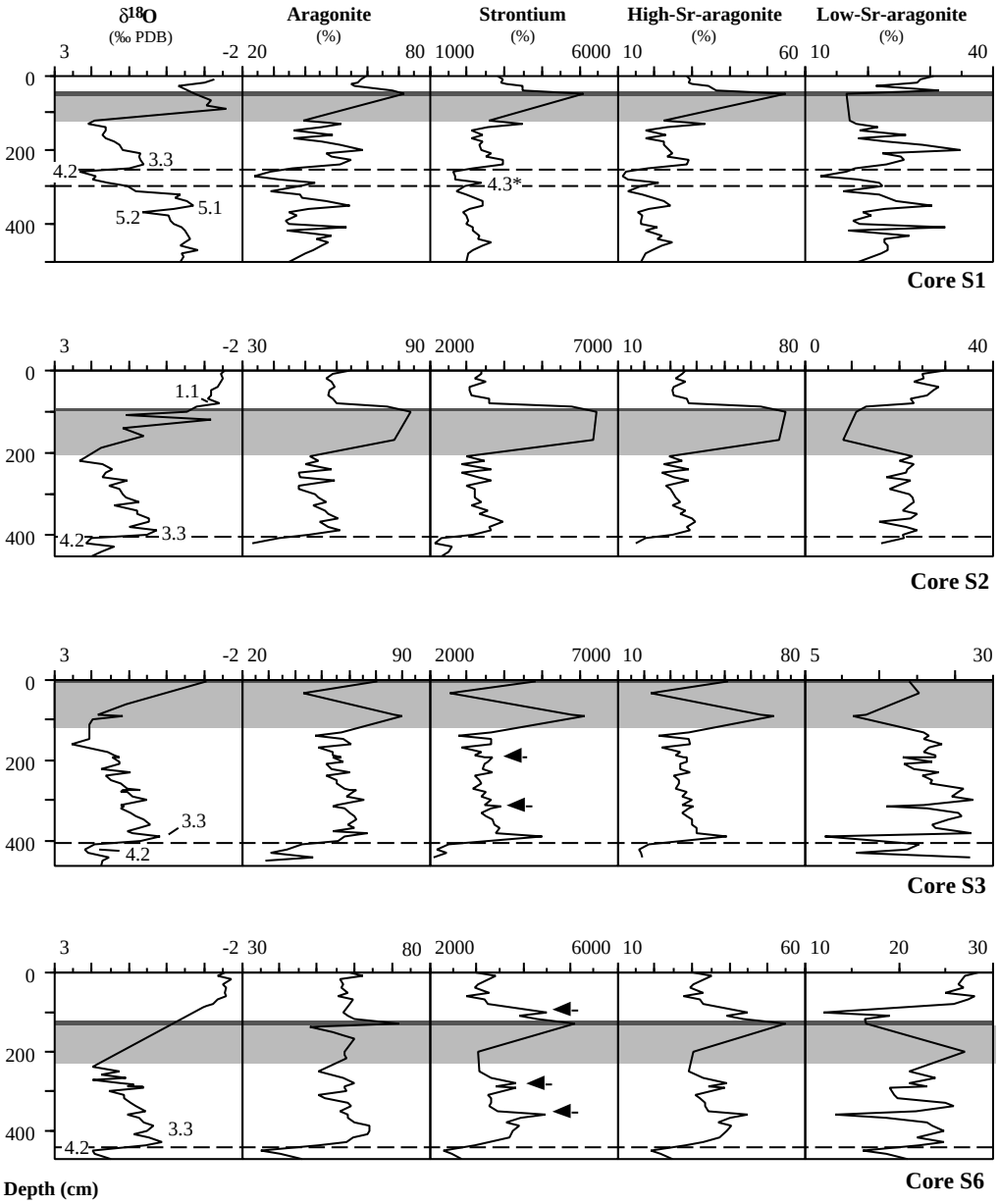

Figure C.8-3: Strontium and aragonite variations and the distribution of high- and low-Sr aragonite in the cores at Sanganeb Atoll. Arrows point to the position of calciturbidites that correspond to peaks in the strontium and high-Sr aragonite curves. Numbers on the isotope curve are SPECMAP events, the lithified layer is indicated with a light grey background, the sapropel on top is somewhat darker. Note the good correlation of strontium and high-Sr aragonite with the curves of aragonite percentages and the oxygen isotope signal. A peak (4.3*) in the aragonite and strontium curves of core S1 might correlate with SPECMAP event 4.3 which is not found in the isotope curves.

C.9 Microfacies analysis

Identification of components and quantitative microfacies analysis (pointcounting) were performed in thin-sections under the microscope. In addition, the wet-sieved coarse fraction was studied under the stereo-microscope to determine planktic foraminifers and pteropod species. All shallow-water biogenic components were determined on a lower taxonomic level. The goal of the pointcount analysis was to determine characteristic, facies-indicative component categories (e.g. „reef builders“ or „plankton“). It is assumed that temporal and spatial variations in the distribution of sediment components records changes in the sediment export at Sanganeb Atoll. Furthermore it was checked if variations in mineralogical and geochemical composition of the sediments correlate with the abundances of components, for example if the frequency of „reef builders“ coincides with higher aragonite and strontium values.

C.9.1 Determination and description of main sediment components

C.9.1.1 Calcareous algae

Calcareous algae are important constituents in reef and shallow-water sediments. In thin sections of the periplatform sediments at Sanganeb Atoll only coralline and articulate red algae are of significant abundance.

Coralline red algae (Rhodophyta) are the prevalent group of calcareous algae in the sediments studied (Plate 2, Fig. 2/3). In thin sections fragments of red algae show the characteristic, very fine cellular-structure, which often merges into dark micrite without internal structure. Isolated fragments of coralline red algae (rhodoliths) are rare compared to encrustations on other bioclasts, very often on coral fragments. Besides the encrusting and rhodolith forming taxa, segments of geniculate red algae could be identified. Geniculate red algae are widespread in various reef sediment facies. In thin-sections coralline red algae reach only 1-2% of total rock in periplatform sediments and up to 6% in calciturbidites.

Only a few isolated segments of the green alga (codiacean) *Halimeda* are found in thin-sections and in the coarse fraction, even though Aboul-Basher (1980) described the distinct appearance of *Halimeda*-fragments in the lagoonal sediment facies of Sanganeb Atoll with dense *Halimeda* meadows in the shallow-water zone (algae-zone) above 5 m waterdepth. It is likely that most of the skeletal fragments of this green alga disintegrated into aragonite needles before downslope transport. Partially lithified dasycladacean fragments (thallus and branches) were also found occasionally in the studied sediments.

Micritic envelopes are present on many skeletal grains in the periplatform sediments at Sanganeb Atoll (Plate 2, Fig. 1/8). This micritisation is caused by endolithic algae, which corrode shell fragments in the shallow-water zone (Tucker, 1985). Grains with micritic envelopes are attributed to the pointcount group „coated grains“ while structureless micritic grains are classified as „peloids“. Peloids occur frequently in the samples. The shape is angular to semi-rounded which makes it easy to distinguish them from faecal pellets.

C.9.1.2 Foraminifers

Planktic foraminifers

The average abundance of planktic foraminifers (Plate 1, Fig. 1) in the periplatform sediments analysed by pointcounting of thin sections reaches only 3%, nevertheless foraminifers are a dominant component in the coarse fraction (40-50%). The most abundant planktic foraminifer species in the periplatform sediments at Sanganeb Atoll are listed in alphabetic order: *Globigerina bulloides* d´Orbigny 1826, *Globigerinoides ruber* (d´Orbigny) 1839, *Globigerinoides sacculifer* (Brady) 1877, *Orbulina universa* (d´Orbigny) 1839. In the Holocene and last interglacial periplatform sediments at Sanganeb Atoll *Globigerinoides ruber* and *Globigerinoides sacculifer* are the dominant foraminifer species. In the lithified interval planktic foraminifers are rare or absent. Compared to interglacial sediments *G. sacculifer* is less abundant in the foraminifer assemblage of IS 3 and IS 4. *Globigerina bulloides* and *Orbulina universa* are also widespread in the periplatform sediments at Sanganeb Atoll. For further reading about species distribution of planktic foraminifers in Red Sea sediments the reader is referred to Berggren & Boersma (1969); Ivanova (1985); Reiss *et al*. (1980) and Geiselhardt (1998).

Large benthic foraminifers

The identification of benthic foraminifers in thin sections is based on the previous work by Dullo (1987) and Piller (1994). Small, large and encrusting benthic foraminifers were counted separately in thin sections. Most of the recent large benthic foraminifers (Plate 1, Fig. 3) live in the shallow-water environment and have symbiotic zooxanthellate algae. Abundant in thin sections are tests and shell fragments of miliolid foraminifers of the genera *Amphisorus* and *Sorites* which are characteristic for the seagras-zone in shallow marine lagoonal facies (Dullo, 1987; Piller, 1994). From the order Rotaliina, species of the genera *Amphistegina, Heterostegina* and *Operculina* prevail. *Planorbulinella larvata* (Parker&Jones, 1865) is also quite common in the periplatform sediments (Plate 1, Fig. 4). The average percentages of large foraminifers range between 0.1-0.7% in individual cores at Sanganeb Atoll.

Small benthic foraminifers

Small benthic foraminifers (Plate 1 Fig. 2) live in very different environments, ranging from the shallow marine to the deep sea-floor. A whole variety of agglutinating (Textulariina) and porcellaneous (Miliolina) shells and fragments of small benthic forminifers occur in the sediments at Sanganeb Atoll. The dominance of certain taxonomic groups was not observed. Average percentages of small benthic foraminifers are rare and vary between 0.6-1.5%.

Encrusting foraminifers

Next to coralline red algae sessile foraminifers are important binders of reef sediments. At Sanganeb Atoll sessile foraminifers only occur in the calciturbidites of core S3, in which average percentages vary between 1-2% of the bulk sediment. Most fragments of sessile foraminifers found in the thin-sections do not encrust other skeletal grains but occur as isolated grains. Chambers of the foraminfera are sometimes filled with the matrix of the periplatform sediments, or with a dark micrite, which can be structureless to micropeloidal. The most abundant taxa that were identified in

thin sections are *Acervulina inhaerens raineri, Planorbulina mediterranensis* d'Orbigny (1826), and *Planorbulina acervalis* (Brady, 1884). They are the main encrusters in the reef (binders) and in the rubble zone of modern coral reefs (Dullo, 1987).

C.9.1.3 Corals (Coelenterata)

Scleractinians

Scleractinian fragments (Plate 2, Fig. 1/2) are good facies indicators for reef environments. The active growth of constructive zooxanthellate (reef-building) corals in the Red Sea is restricted to the upper 30-40m of the water column, but their distribution reaches down to a waterdepth of about 110-120m (Bosscher, 1992). No taxonomic classification of the coral fragments in the cores at Sanganeb Atoll was possible. However, many of the angular coral fragments have micritic envelopes or are encrusted by coralline red algae. It is therefore assumed that most fragments were derived from the shallow-water reef zone. Characteristic skeletal structures, like intra-skeletal cavities and septa walls are rare. In the microstructure of the skeletons spherolitic fibres of aragonite can be found in some of the grains.

Octocorals

Only the spicules of soft corals of the taxa alcyonaceans were found in the periplatform sediments. Even though soft corals are widespread in recent reef environments, they only have a little preservation potential. In the coarse fraction alcyonacean spicules are enriched in some of the samples. In thin-sections octocoral spicules are extremely rare, smaller fragments might be confused with scleractinian fragments.

Hydrozoan

Even though two species of hydrozoans with calcified skeletons are abundant in reef environments (*Millepora dichotoma*, Forskal, 1775 and *Millepora platiphylla* Ehrenberg, 1834), no skeletal fragments were clearly identified in the periplatform sediments. Altered milleporid fragments, which show a mesh-like microstructure may have been confused with skeletal fragments of red algae.

C.9.1.4 Molluscs

Pteropods

Tests and shell fragments of planktic gastropods (pteropods) (Plate 1, Fig. 5) are widespread in the coarse fraction (30-40%) but reach only 2-4% of the total rock in quantitative thin-section analysis. The abundant pteropod species that where identified in the periplatform sediments at Sanganeb Atoll are listed in alphabetic order: *Creseis acicula* (Rang) 1828, *Creseis virgula* (Rang) *virgula* (Rang) 1828, *Creseis virgula* (Rang 1828) *conica* Escholtz 1829, *Limacina inflata* (d´Orbigny) 1836, *Limacina trochiformis* (d´Orbigny) 1836. The classification of pteropod species is based on Almogi-Labin (1982) and Ivanova (1985). The coiled tests of *L. inflata* dominate the interglacial pteropod assemblage. In the aplanktonic zone the plankton assemblage is dominated by cone-shaped tests of the epipelagic and eurythermal pteropod *C. acicula.* This species is indicative of high salinities and it is also able to withstand strongly metahaline conditions (Geiselhardt, 1998). In the periplatform sediments that were deposited during IS 3 and IS 4 (and beginning of IS 5) the

pteropod species *L. trochiformis* and *C. virgula* are quite common next to *L. inflata*..

Benthic molluscs

Scaphopods, gastropods and pelecypods are common dwellers of the shallow-water realm in modern coral reef environments. At Sanganeb Atoll pelecypod shells are a main constituent of the present-day reef sediments (Aboul-Basher, 1980). Nevertheless, the amount of shallow-water derived mollusc shells (all molluscs except for planktic pteropods) reaches only 1-3% of the total rock in the periplatform sediments. It is likely that large numbers of the mollusc shells disintegrated into small bioclasts which were not classified.

C.9.1.5 Bryozoan

Fragments of bryozoans (Plate 1, Fig. 8) are generally very rare in the studied periplatform sediments. In the modern Red Sea reef environment bryozoan are secondary settlers on corals and mollusc shells or live as ramose forms in the lagoon. In thin sections and in the coarse fraction branches of ramose forms prevail. Reiss & Hottinger (1984) found recent bryozoan build-ups in the Red Sea on deeper terraces (90 m), where they play an important role as pioneers in the formation of secondary hardgrounds.

C.9.1.6 Serpulids and Annelids

Tubes and calcified boreholes of serpulid- and annelid worms (Plate 2, Fig. 5) occur in low abundance in the periplatform sediments at Sanganeb Atoll. In the recent Red Sea reef environment worms of those taxa encrust coral and coral rock and bore holes into the substrate (e.g. Emmermann, 1994; Hassan, 1997). The burrows are often lined with calcite and therefore have a high preservation potential. Traces and burrows of worms do have a great depth range from the reef flat to the steep slope below the euphotic zone. In the latter serpulids play an important role as carbonate producers (Brachert, 1999).

C. 9.1.7 Echinoderms

Only plates and spines of echinoids (Plate 1, Fig. 7) are found in the periplatform sediments even though other groups of echinoderms occur frequently in the shallow-water reef environment. Holothurians, asteroids and ophiurids are quite abundant groups which live on sandy substrates predominantly in the lagoonal zone of recent Red Sea reefs, while crinoids are sessile organisms that settle on the reef slopes. With crossed nicols under the light microscope sections through echinoderm fragments show the characteristic uniform extinction.

C.9.1.8 Pellets

Faecal pellets (Plate 2, Fig. 6) are produced in protected environments, like the lagoonal zone by organisms like gastropods, crustacean and polychaets. They have a regular, oval shape and show no internal structure and a higher content in organic matter is usual. In some of the larger pellets, which reach 300-600 µm in length, silt-sized sediment grains are visible. True faecal pellets are rare in thin sections of the periplatform sediments.

C.9.1.9 Compound grains

Compound grains (Plate 2, Fig .7) are very rare in the periplatform sediments at Sanganeb

Atoll. These aggregates are formed by cementation or organic binding of individual carbonate particles. Such aggregates form in shallow-protected environments below the tidal zone.

C.9.1.10 Ooids/Spherolites

Ooids are extremely rare in the periplatform sediments. Aboul-Basher (1980) describes ooids and pellets as the major non-biogenic constituents in the sediments of the shallow (< 8m waterdepth) lagoonal zone of the recent Sanganeb Atoll. Instead of true ooids spherolitic components (Plate 2, Fig. 4) with a characteristic radial-fibrous structure occur in the periplatform sediments, but in very low abundances. Those are much smaller (about 100µm across) than normal ooids and bioclastic nuclei are missing.

C.9.1.11 Bioclasts

In this category all unidentifiable fragments of biogenic components are grouped. In the shallow-water realm abrasion and disintegration by wave action, bioerosional processes, diagenetic alteration and micritisation of sediment particles lead to a permanent production of non specific bioclasts. Nevertheless dissolution and bioturbation at the sea-floor play a further important role in the disintegration of biogenic components.

C.9.1.12 Lithoclasts

A very exotic group of components in the sediments around Sanganeb Atoll are rubble sized fragments of magmatic rock (granitoid), which were found in the coarse fraction of core S6 from the windward side. The origin of those fragments is not clear. They might be derived from the Palaeozoic basement of Sanganeb Atoll itself or they were transported from the coastal escarpments to the deep shelf.

Most intraclasts (Plate 3, Fig. 5) are found in the lithified interval and the adjacent sediments. It is assumed that those components were formed by the brecciation of the lithified or semi-lithified layers at the sea-floor. Most of the clasts are angular but also semi-rounded particles are abundant. The intraclasts range from pebble-sized, chip-like fragments (brecciation) to fine-sandy peloidal grains (bioturbation?). It is remarkable that the rounded, peloidal grains are most abundant in the lower and less lithified parts of the lithified interval.

C.9.1.13 Siliciclastic mineral grains

Mineral grains and silty detritus of quartz (Plate 3, Fig. 3) are highly abundant in the periplatform sediments. The frequency of quartz clearly dominates over other siliciclastic components, wherein feldspar, dark minerals and mica are the most abundant. The siliciclastic grains are predominantly angular and bordered by crystal facets. A large portion of the siliciclastic components consist of windblown silt-sized grains that form a detritic fraction of the matrix. The larger, sand-size quartz and feldspar grains might be transported by rivers and turbidite currents. The Sudan Delta which prograded onto the Red Sea shelf during the last glacial sealevel lowstand might have caused an increased siliciclastic input in this part of the Sudanese deep shelf (Stoffers & Ross, 1977).

C.9.1.14 Matrix

In thin-sections „matrix“ was defined as very-fine silty biodetritic and siliciclastic micrite.

Fine grained bioclasts and micritic components often merge with the matrix. In many sample a characteristic peloidal texture was observed. It originates from clusters of micro-pellets and gives the matrix a clotted appearance. In analogy to the Bahamas it is assumed that the peloidal structures were caused by interstitial precipitation of fine-grained Mg-calcite (e.g. Wilber & Neumann, 1993). The occurrence of micro-peloids in the thin-sections supports the idea of widespread submarine inorganic HMC precipitation in the Red Sea as proposed by Ellis & Milliman (1985). Components, with larger chambers or voids, like pteropods or foraminifers are often filled with matrix.

C.1.9.15 Porosity

The internal porosity consists of voids in biogene components, which are not filled with sediments or cement. Intra-particle porosity is often found in large coiled pteropods and planktic foraminifers. Inter-particle porosity was observed in coarser sediments, like skeletal pack- and grainstones which are characteristic for the reef-flat and upper slope facies at Sanganeb Atoll (Aboul-Basher, 1980).

C.9.2 Quantitative microfacies analysis - pointcounting

Pointcount analysis was performed on three sediment cores (S2, S3 and S6), which were taken in proximal positions at Sanganeb Atoll (Fig. B-1). It is expected, that the component distribution in periplatform sediments and calciturbidites reflects glacial-interglacial as well as leeward-windward variations in sediment export of the reef. After determination and quantification of components in thin sections they were grouped into diagnostic facies categories (pointcount groups). The eight pointcount groups are summarised in Tab. C.9-1. The results of the pointcount analysis are given in Appendix 6, average percentages of the individual groups for isotope stages and calciturbidites can be found in Tab. C.9-2. Downcore variations in the component distribution are shown in Fig. C.9-2. In Fig. C.9-1 two pie-diagrams are shown as an example for the distribution of components in the periplatform sediments and the calciturbidites.

C.9.2.1 Plankton

In the category „plankton“ planktic foraminifers and pteropods (planktic gastropods) are gathered, which are dwellers within an open marine, pelagic environment. Tests and shell fragments of planktic foraminifers and pteropods where counted separately in thin sections. The sum of foraminifers and pteropods is seen as a signal of the plankton productivity and the input into the periplatform sediments.

In core S6 (windward) and S2 (leeward) the variations in plankton abundance exhibit a clear glacial-interglacial pattern (Fig. C.9-2). Highest average plankton percentages of 11-12% are reached in Holocene sediments. In both cores the Holocene plankton content shows a significant increase after a minimum above the top of the lithified interval. Average glacial plankton percentages are clearly less than Holocene values and show minima in IS 4 and IS 2 (3-5%), whereas the plankton content in sediments of IS 3 reaches about 6% on average in both cores. The glacial plankton content in core S3 from the toe-of-slope at the leeward side is in the same range but does not increase during IS 3. No differences in plankton abundances in periplatform sediments from both

sides of the reef were found. Average plankton content in periplatform sediments in cores S2 and S6 is about 7-8%. In the shallow-water sands in core S3 and S6 the percentages of planktic shell fragments are significantly decreased compared to the surrounding periplatform sediments.

C.9.2.2 Reef builders

Following the studies of Aboul-Basher (1980) the most important sediment constituents in the recent reef flat (south), the windward reef margin and the upper slope at present-day Sanganeb Atoll are scleractinian corals, coralline red algae and encrusting foraminifers. These three components are summarised to the group „reef builders“. It is assumed that despite different filtering processes (disintegration/dissolution, diagenesis and transport) and the additional occurrence of non-constructive azooxanthellate corals on deeper fore-reef slopes, the facies group „reef builders“ is a significant proxy for the sediment export production of the reef.

The average percentages of reef biota vary between 1.7-3.7% in the periplatform ooze, with higher values in proximal cores S3 and S6 (Tab. C.9-2). Scleractinians and calcareous red algae are the prevalent constituents of reef biota in periplatform ooze and sand layers, encrusting foraminifers only play a minor role (< 0.3%). In the periplatform ooze on the leeward side at Sanganeb Atoll percentages of coralline algae are slightly increased compared to scleractinians. This might reflect the dominance of articulate red algae on the leeward, lagoonal side with sandy terraces on the upper slope.

Table C.9-1: Pointcounting categories

Pointcount group	Components	Signal/Proxy for
Plankton	planktic foraminifers pteropods	planktic input
Reef builder	scleractinians coralline red algae encrusting foraminifers	shallow-water input from the reef zone
Shallow-water grains	peloids compound grains coated grains large benthic foraminifers echinoderms molluscs green algae	shallow-water input in general
Bioclasts		origin in different environments
Lithoclasts		mostly reworked hard layers
Terrigenous grains		terrigenous input by wind and other transport mechanisms
Matrix		mixture of nanno-fossils, siliciclastic- and bio-detritus (fine carbonate mud of shallow-water sources), in-situ precipitates
Others	small benthic foraminifers bryozoan serpulids and annelids porosity spherolites undetermined components	unspecified components

Significant glacial-interglacial variations in the abundance of reef biota were found in the sediment cores (Fig. C.9-2). In the Holocene periplatform sediments percentages of reef biota stay below 1% on average (S2 and S6). In core S3 and S6 average percentages of reef biota are increased during IS 3 where values reach about 4-5%. In the sediments of IS 2 and IS 4 abundances of reef builders are decreased compared to IS 3 and reach Holocene values (1-2%). Most maxima in the distribution of „reef builder“ (Fig. C.9-2), that can reach up to 20-30%, occur in calciturbidites. Some of the peaks correlate with maxima in the abundance of „shallow-water grains“ or minima in the plankton curve.

The calciturbidites are notably enriched in reef biota compared to periplatform sediments (Fig. C.9-1 and C.9-2). In core S3 the percentage of reef biota in sand layers reaches 14% on average, which is a 3-fold increase compared to the periplatform ooze. In core S6 only 6.8% of the components are reef derived which is only twice the percentage analysed in periplatform sediments. In the sand layers scleractinians are the dominant constituent in reef biota. Again, red algae are more abundant in the sediments from the leeward side. The frequency of calciturbidites is high during IS 2 and IS 3 while only two turbidites occur in the Holocene sequence in core S6 (Fig. C.9-2). The glacial calciturbidites are clearly enriched in reef biota compared to those of the Holocene and percentages of „reef builder“ are generally highest in glacial turbidites in core S3 from the toe-of-slope.

C.9.2.3 Shallow-water grains

Many components of the category „shallow-water grains“ also occur in the reefal sediments at recent Sanganeb Atoll, but are more widespread in the lagoonal, seagrass- and micro-atoll zone (Aboul-Basher, 1980). In this group peloids, compound- and coated grains together with fragments of calcareous green algae, echinoderms, molluscs and large benthic foraminifers are summarised. Green algae are extremely rare in the periplatform sediments, even though *Halimeda* fragments occur widespread in the lagoonal sediments (Aboul-Basher, 1980). Some of the large benthic foraminifers may derived from the deeper water environment but the prevailing amount of taxa is known to live in the shallow-water zones of tropical seas.

Average percentages of shallow-water grains in periplatform ooze vary between 4-7%, without any significant differences between the sites. The most abundant components of shallow-water origin in periplatform sediments from both sides at Sanganeb Atoll are peloids (average = 2-3%). Molluscs get only important in core S6 were average percentages reach about 2.5%. In the calciturbidites the percentages of shallow-water grains are 2-3 times higher than in periplatform ooze and reach about 12% on average. Compound grains are increased in the sand layers of core S3 (1.7%) when compared to core S6 (0.3%). All other components do not show significant differences in spatial distribution.

The distribution of „shallow-water grains“ in the periplatform ooze shows a similar glacial-interglacial pattern as „reef builders“ with increased average values in IS 3 (5-10%) compared to the Holocene (2.5-3.7%) in the cores S2 and S6. In core S2 a maximum in shallow-water components of 13% coincides with event 3.3 (Fig. C.9-2) whereas percentages at event 4.2 converge to 0%. In core S3 from the toe-of-slope the percentages of shallow-water grains are also increased during IS

3 (5.6%) when compared to IS 2 and IS 4 (3.0 and 2.5%). Maxima in the abundance of „shallow-water grains“ reach 10-20% in core S3 and S6 and coincide with calciturbidites except for the maximum at 140 cm in core S3 (Fig. C.9-2).

C.9.2.4 Bioclasts

The average percentages of bioclasts in the periplatform ooze lies between 10.4-13.5% and are highest in core S6 from the windward side. In cores S3 and S6 the average percentage of bioclasts in calciturbidites (12.1-12.3%) are in the same range as in periplatform sediments (10.5-13.0%). The abundance of bioclasts does not show any significant correlation with the occurrence of calciturbidites and the frequency of „reef builders“ and „shallow-water grains“ in the periplatform sediments. Downcore variations are similar to those in plankton distribution and show increased values in the Holocene and in IS 3. This pattern is best developed in the periplatform ooze of core S2 where average values during the Holocene and IS 3 reach 12-13% and only 7-9% during IS 2 and IS 4. Remarkable are the distinct small scale oscillations with an amplitude of 5-10% during IS 3 and the Holocene in this core (Fig. C.9-2).

C.9.2.5 Lithoclasts

The average percentages of lithoclasts are small and reach 3-4% in the periplatform ooze and 3-5% in the calciturbidites. Generally values are higher in IS 2 and show maxima of 10-15% on top of the lithified interval and in the sapropel. The distribution pattern of lithoclasts is clearly tied to the occurrence of the lithified interval.

C.9.2.6 Terrigenous grains

The percentages of terrigenous components in the periplatform sediments at Sanganeb Atoll lie between 13% and 17%. Highest average percentages are found in core S2. In the interbedded calciturbidites in core S3 the average percentages of terrigenous grains (6%) are only half of the amount found in the periplatform ooze (Tab. C.9-2).

A clear glacial-interglacial pattern in the distribution of terrigenous components is present in cores S2 and S6. No clear downcore pattern emerges in core S3. The pointcount results confirm the mineralogical (quartz) and geochemical records (SiO_2). The trends are opposite to variations in matrix content (Fig. C.9-2). Terrigenous content is lower in the Holocene periplatform sediments when compared to glacial sediments and the sapropel. Holocene terrigenous values in periplatform sediments of core S2 and S6 drop after their maxima of 25-35% on top and above the lithified interval/sapropel to a minimum < 5%, which coincides with isotopic event 1.1. Holocene terrigenous percentages increase upwards again up to 10%. Compared to the Holocene the average terrigenous content of glacial periplatform sediments in core S2 is clearly increased and varies between 17-23%, showing two distinct maxima during IS 3 at 340-350 cm (26%) and 240 cm (36%). In core S6 the average percentages of terrigenous grains in periplatform sediments are increased during IS 3 (16%) but values during IS 4 (11%) stay below Holocene values (13%) and reach a minimum of 7% that coincides with event 4.2.

C.9.2.7 Matrix

The matrix is the most abundant component-category in the periplatform sediments at Sanganeb

Atoll. Average values lie between 37-43%. In the calciturbidites, matrix contents are generally lower and reach 12-29% on average. However, some of the calciturbidites reach matrix percentages as high as in periplatform sediments (Tab. C.9-2). Lowest matrix contents were analysed in the calciturbidites from core S3, where matrix percentages can fall to 5-10%.

The matrix percentages show a clear temporal variation with highest values in the Holocene and in IS 4. The Holocene maximum of about 60% is reached in core S6 at the end of a sharp increase that starts on the top of the lithified interval. Above this maximum values drop to about 50%. In core S2 the Holocene maximum reaches 70% at a depth of 80 cm which coincides with isotopic event 1.1 (Fig. C.9-2). In IS 4 the matrix content in core S6 and S2 is even higher than in the Holocene. In the periplatform sediments of this glacial stage maxima of over 60% were found and average values reach 50 and 54%, respectively. In core S3 the matrix content is also higher in periplatform sediments of IS 4 (53%) when compared to IS 2 and IS 3. In these isotope stages lowest average matrix percentages are found in all cores (32-47%). It is remarkable that the matrix content is reduced to < 5% on top of the lithified interval/sapropel in core S2, which coincides with a high amount of lithoclasts and terrigenous components.

C.9.2.8 Others

In this group all unspecified and non-characteristic components were summarised. Average percentages of this category vary from about 12 to 20% in the periplatform sediments and reach 20 to 32% in the calciturbidites (Tab. C.9-2). A significantly higher amount of „others“ in the calciturbidites might be simply caused by the higher frequency of grains in the sands when compared to the more matrix dominated periplatform sediments.

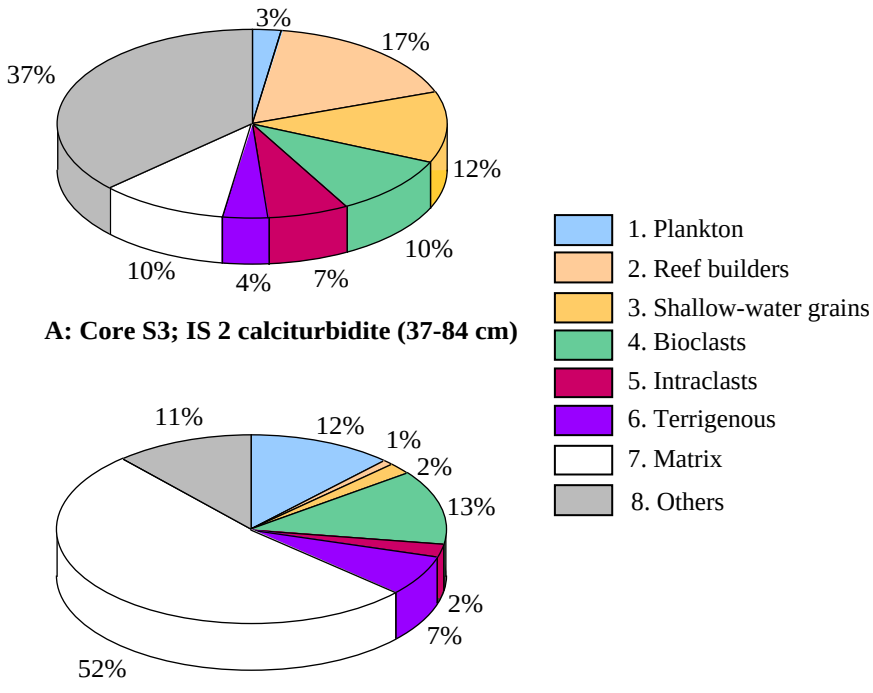

Figure C.9-1: Pie diagrams of the component distribution in a calciturbidite from the lithified interval (A) and a “normal” Holocene periplatform sediment (B). Note the significant increase of reef builders and shallow-water grains in the turbidite and simultaneous decrease in matrix and plankton abundances when compared to the periplatform sediment.

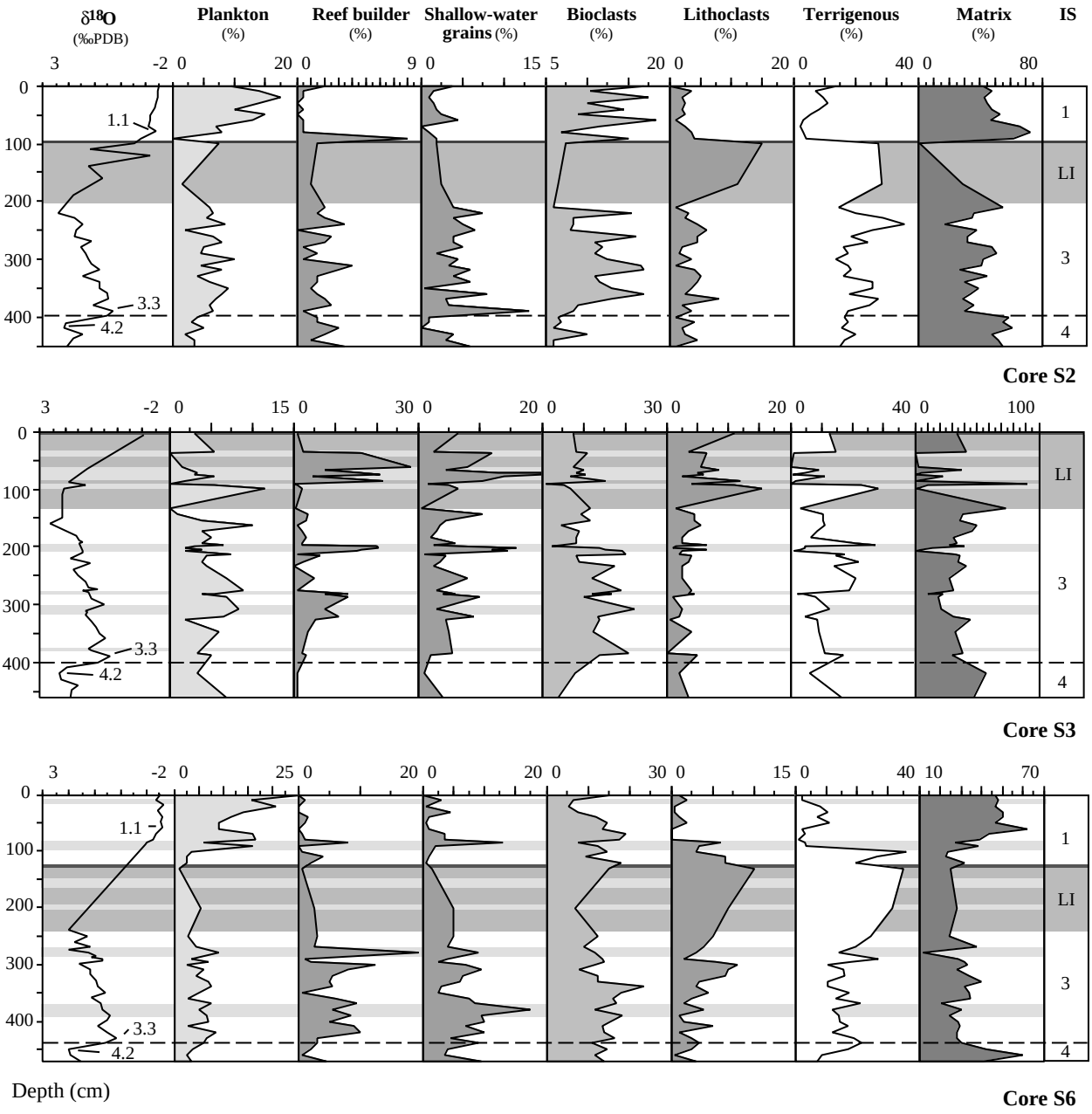

Figure C.9-2: Downcore variations in the percentages of diagnostic pointcounting categories in the cores S2, S3 and S6 at Sanganeb Atoll. Marked in grey is the lithified interval, in darker grey the sapropel on top. The light grey bars in core S3 and S6 indicate the position of calciturbidites and sand layers. No calciturbidites occur in core S2. Components that belong to individual pointcounting categories are summarised in Tab. C.9-1. Numbers on the oxygen isotope curve are SPECMAP events. The maximum absolute statisitcal error of pointcounting is ±3.5 % for 200 counts per sample.

Table C.9-2: Average percentages of component groups calculated for isotope stages and individual calciturbidites

All values in percent, maximum absolute errors of pointcounting lie between ±0.2 and ±3.5 %. In core S6 no unlithified periplatform sediments occurred during IS 2 (lithified interval)

	pteropods	plankt.foram	**1. Plankton**	corallinacean	scleractinian	encrusting forams	**2. Reef builders**	peloids	compound grains	coated grains	green algae	echinoderms	large benthics	molluscs	**3. Shallow water grains**	**4. Bioclasts**	**5. Intraclasts**	**6. Terrigenous grains**	**7. Matrix**	**8. Others**
Periplatform sediments																				
Core S2																				
IS1	5.3	6.7	**12.0**	0.5	0.1	0.0	**0.6**	1.2	0.1	0.0	0.1	0.6	0.1	0.4	**2.4**	**12.8**	**2.2**	**6.9**	**51.5**	**10.9**
IS2	3.8	1.1	**4.9**	1.5	0.1	0.0	**1.6**	3.8	0.0	0.3	0.1	0.4	0.0	0.4	**4.9**	**9.1**	**4.4**	**23.0**	**38.9**	**12.6**
IS3	2.8	3.4	**6.2**	1.4	0.2	0.0	**1.6**	3.6	0.0	0.1	0.2	0.6	0.2	0.2	**4.8**	**12.1**	**3.6**	**20.1**	**38.4**	**12.8**
IS4	1.8	1.6	**3.4**	2.2	0.0	0.0	**2.2**	2.6	0.0	0.0	0.0	0.2	0.0	0.0	**2.8**	**7.0**	**2.8**	**16.9**	**53.9**	**10.9**
Average	3.4	3.6	**7.0**	1.5	0.1	0.0	**1.7**	2.8	0.0	0.1	0.1	0.5	0.1	0.2	**3.7**	**11.1**	**3.6**	**17.0**	**42.8**	**12.4**
Core S3																				
Sapropel	3.0	0.0	**3.0**	1.0	0.0	0.0	**1.0**	6.5	0.0	0.0	0.0	0.0	0.0	0.0	**6.5**	**7.5**	**11.0**	**12.5**	**34.0**	**24.5**
IS2	2.0	1.7	**3.7**	0.7	0.2	0.3	**1.2**	2.0	0.0	0.3	0.3	0.3	0.0	0.5	**3.0**	**5.0**	**6.2**	**12.5**	**47.5**	**20.0**
IS3	2.9	2.2	**5.1**	1.8	2.2	0.4	**4.4**	2.3	0.0	0.2	0.9	0.7	0.2	1.3	**5.6**	**11.7**	**3.3**	**12.9**	**36.0**	**20.3**
IS4	2.3	3.0	**5.3**	0.8	0.0	0.3	**1.0**	1.5	0.0	0.3	0.5	0.3	0.0	0.0	**2.5**	**6.0**	**2.8**	**11.3**	**52.8**	**16.8**
Average	2.7	2.1	**4.9**	1.6	1.7	0.4	**3.7**	2.3	0.0	0.2	0.7	0.6	0.1	1.1	**5.1**	**10.4**	**3.8**	**12.7**	**38.4**	**20.1**
Core S6																				
IS1	4.0	7.3	**11.3**	0.0	0.7	0.1	**0.8**	0.6	0.0	0.1	0.3	0.4	0.2	2.0	**3.7**	**13.4**	**2.7**	**12.7**	**40.7**	**16.9**
IS3	3.2	2.4	**5.6**	1.3	3.6	0.4	**5.3**	2.5	0.3	0.6	1.0	0.9	0.9	3.3	**9.5**	**13.7**	**4.3**	**16.2**	**31.5**	**12.3**
IS4	1.0	2.3	**3.3**	0.7	1.7	0.0	**2.3**	2.0	0.0	0.2	1.8	0.3	1.3	1.5	**7.2**	**13.3**	**2.0**	**10.8**	**47.5**	**14.2**
Average	3.3	4.5	**7.8**	0.7	2.2	0.2	**3.1**	1.6	0.1	0.4	0.8	0.6	0.6	2.6	**6.7**	**13.5**	**3.4**	**14.1**	**37.1**	**14.5**
Calciturbidites (Depth in cm)																				
Core S3																				
37-85	2.2	0.4	**2.6**	7.0	8.1	1.4	**16.5**	2.6	4.6	1.4	1.9	0.6	0.7	1.7	**13.5**	**10.0**	**6.6**	**3.9**	**10.1**	**34.4**
198-204	1.8	0.8	**2.7**	5.5	9.2	2.8	**17.5**	1.8	1.5	1.3	4.3	2.2	3.0	2.3	**16.5**	**16.3**	**3.3**	**2.8**	**7.0**	**32.0**
96	11.5	0.0	**11.5**	1.0	1.0	0.0	**2.0**	1.5	0.0	0.0	3.5	1.5	0.0	0.0	**6.5**	**7.0**	**15.5**	**28.5**	**1.5**	**26.5**
276	2.5	3	5.5	4.5	7.5	1	13	1	1	0	1	3	0	3.5	**9.5**	12	3.5	2	10.5	45.5
313	2	4.5	6.5	4.5	5.5	1	11	2.5	1.5	0.5	3	0.5	1	1	**10.0**	13.5	2	4.5	31	22
377	1	2.5	3.5	1	0.5	0.5	2	2.5	0	0.5	1.5	1	0	0	**5.5**	21	0	11	39.5	18
Average	2.7	1.1	3.8	5.5	7.1	1.5	14.0	2.2	2.8	1.1	2.5	1.2	1.1	1.7	**12.5**	12.3	5.5	5.9	12.5	32.1
Core S6																				
10	2.5	13.0	**15.5**	1.0	0.0	0.0	**1.0**	0.5	0.0	0.0	2.5	0.0	0.0	1.5	**4.5**	**6.5**	**2.0**	**2.0**	**48.5**	**18.5**
86	2.5	3.5	**6.0**	3.0	4.5	0.5	**8.0**	3.5	0.5	3.0	3.5	0.0	2.5	4.0	**17.0**	**7.5**	**6.0**	**3.0**	**27.5**	**32.5**
200	0.5	5.0	**5.5**	0.5	2.0	0.0	**2.5**	1.0	0.0	0.0	1.5	0.5	2.0	0.5	**5.5**	**7.0**	**7.0**	**31.5**	**28.5**	**11.0**
280-290	2.3	4.0	**6.3**	1.5	8.8	0.0	**10.3**	1.5	0.3	1.5	0.3	2.3	0.8	4.5	**11.0**	**12.5**	**2.3**	**20.5**	**20.5**	**24.8**
360-390	2.8	2.8	**5.5**	1.0	5.8	0.6	**7.4**	3.6	0.3	0.6	3.1	2.5	0.6	3.0	**13.8**	**15.8**	**2.3**	**15.0**	**27.8**	**15.8**
Average	2.3	4.5	**6.8**	1.3	5.2	0.3	**6.8**	2.5	0.2	0.9	2.3	1.7	0.9	3.0	**11.6**	**12.1**	**3.2**	**15.3**	**28.5**	**19.4**

CHAPTER D: DISCUSSION

The discussion chapter of this thesis is subdivided into three sections. In the first part the stacked oxygen isotope record and the age model developed for the Sudanese shelf are adapted to late Quaternary eustatic sealevel variations. Shallow-water carbonate production and reef growth is modelled and discussed for certain sealevel stands at Sanganeb Atoll.

In the second chapter the palaeoceanographic and climatic aspects of periplatform sedimentation of the Sudanese shelf are discussed. This chapter focuses on hydrographic and climatic variations that might have influenced the composition of the periplatform sediments, like the submarine aragonite preservation during pluvial phases. Another topic that is discussed in this section is the inorganic carbonate precipitation and the formation of lithified layers on the Sudanese shelf during the last glacial, which can be seen as a break in „normal“ periplatform sedimentation.

The last part of the discussion focuses on the periplatform sedimentation itself. The mineralogical and geochemical dataset together with the results of the microfacies analysis are discussed with respect to glacial-interglacial shallow-water sediment export variations (glacio-eustatic sealevel) and secondary signals which might have affected the periplatform record.

No significant leeward - windward differences occur at Sanganeb Atoll and Abington Reef. Spatial variations in the composition of periplatform sediments were mainly caused by proximal - distal effects resulting in reduced shallow-water input with increasing distance from the reef edge.

D.1 Eustatic sealevel variations and productive reef growth area

Variation in sediment export are dominated by the interplay between sediment supply and the creation of accommodation space on the platform (e.g. Everts & Reijmer, 1995). Both factors are primarily controlled by eustatic sealevel variations during the late Quaternary. The highstand shedding model proposes that changes in shallow-water sediment export and distribution patterns are controlled by relative sealevel variations (Schlager & James, 1978; Schlager *et al*., 1994). During relative highstands in sealevel, when the platform top is flooded sediment production is at its maximum and overproduction can be exported into the periplatform realm. Sediment production is reduced when the platform drowns or when the main production area becomes subaerialy exposed. In the Sudanese Red Sea no „real“ drowning events were observed. But it is likely that reefs which grew on deeper submarine terraces during lowered sealevel drowned after rapid sealevel rises (pulses).

Exposure of the platform, might have occurred quite common during the late Quaternary. During such „lowstand situations“ benthic carbonate production might have shifted to the platform slopes, deeper terraces and deeper parts of the platform, which were in the shallow-water zone during some of the lowstands. The sediment production was lower compared to highstands because of the smaller area available for reef-growth and carbonate production. So, the individual morphology of the platform and the timing and position of the relative sealevel are crucial factors determining sediment export variations.

In the first part of this section late Quaternary eustatic sealevel variations found in Barbados

(Fairbanks, 1989; Bard *et al*., 1990), New Guinea (Chappell & Shackleton, 1986), the Western Indian Ocean (Colonna *et al*., 1996; Dullo *et al*., 1996a, 1998) and Sinai Peninsula (Gvirtzman, 1994) are discussed and compared with the stacked isotope age model of the Sudanese Red Sea (Fig, D.1-1 and 1-2).

In the second part of the section variations in the size of reef-growth area at Sanganeb Atoll are calculated for different sealevel curves and varying depth limits of prolific reef growth. The variations in the reef growth area are compared with the glacial-interglacial variations in the composition of the periplatform sediments.

Fig. D.1-1 shows the stacked oxygen isotope curve derived from the studied cores and the compiled sealevel curves. The new stack for the Sudanese Red Sea reaches back to isotopic event 5.5, which corresponds to an age of 122,000 SPECMAP-yr. All ages that were established by climate-stratigraphic correlation with the SPECMAP time scale are called SPECMAP-yr in the text. The SPECMAP time scale is based on orbital tuning, adjusted and controlled by radiocarbon dating (Imbrie *et al*., 1984). The analysed radiocarbon ages of the lithified interval and of the calciturbidites are not corrected for reservoir effects and are specified as ^{14}C-AMS-yr in the following text. The calendar ages that might correspond to the ^{14}C-AMS -ages can be found in Tab. C.2-3. Other than ^{14}C-AMS- and SPECMAP-ages are specified in the text.

For the reconstruction of relative sealevel variations at Sanganeb Atoll and Abington Reef it is assumed that during the last 125,000 yr none or only minor tectonic activity influenced the central part of the Red Sea. Accordance of ages and elevations of Pleistocene Red Sea reefs with those from the Western Indian Ocean suggest crustal stability of the Sudanese shelf for the last 240,000 yr and rules out recent subsidence or uplift (Braithwaite, 1982). Tectonic stability of the central part of the Red Sea during this period is also proposed by Gvirtzman (1994) and Taviani (1998a).

D.1.1 Eustatic sealevel during the last 125,000 years

D.1.1.1 Last interglacial

Based on U/Th-dated corals from uplifted reef terraces of Saudi Arabia Dullo (1990) suggested three sealevel maxima during the last interglacial (IS 5) at 85,000, 104,000 and 118,000 yr. BP (U/Th) that reached or exceeded the present sealevel position. Investigations of Gvirtzman (1994) confirmed the occurrence of three highstands during the last interglacial at Sinai Peninsula in the northern part of the Red Sea which coincide with isotopic events 5.1, 5.3 and 5.5. The Eemian highstand (isotopic substage 5e) correlates with the lightest isotope values of the stacked curve from the Sudanese Red Sea. Eustatic sealevel was 2 to 8 m higher than present at that time as shown by various studies (e.g. Chappell & Shackleton, 1986; Bard *et al.*, 1990; Neumann & Hearty, 1996; Hearty, 1998; Vézina *et al*., 1999).

Sealevel might have also reached present level at isotopic event 5.1 and 5.3. The sealevel pinning points in the Red sea were reconstructed from raised terraces and do not agree with observations from New Guinea (Chappell & Shackleton, 1986) and Barbados (Bard *et al*., 1990)

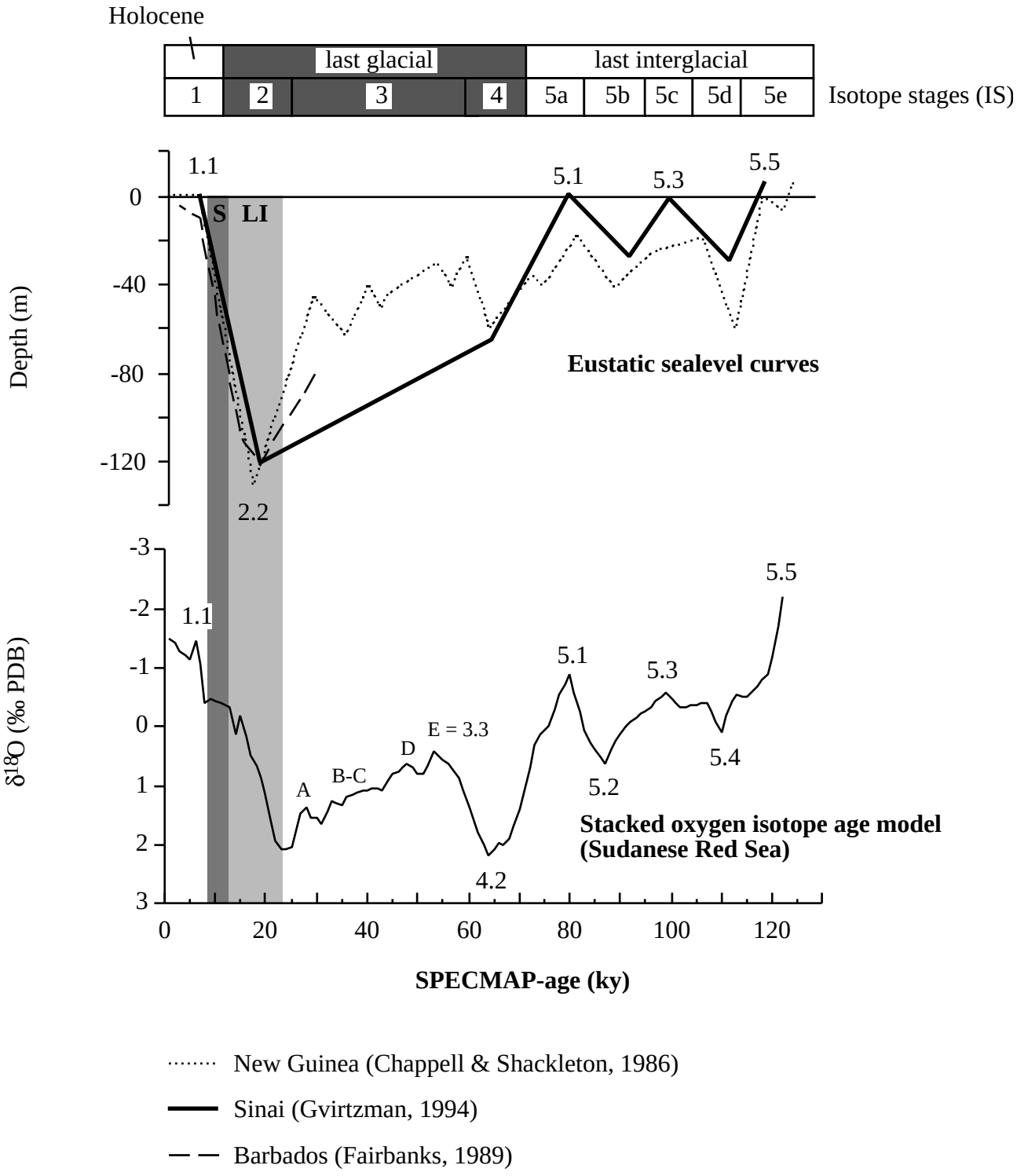

Figure D.1-1: Eustatic sealevel curves from New Guinea (Chappell & Shackleton, 1986), Barbados (Fairbanks, 1989) and Sinai Peninsula (Gvirtzman, 1994) compared to the stacked oxygen isotope curve of the Sudanese Red Sea. The $\delta^{18}O$-curves of the individual cores were correlated with the global SPECMAP curve (Imbrie, *et al.*, 1984) and stacked to produce a general curve for the Sudanese Red Sea. Calculated average isotope values in 1,000 year steps with standard deviations are given in Appendix 1-B. The lithified interval (LI) comprises an age of 13,000 to 23,000 ^{14}C-yr; the top of the sapropel (S) is 8,500 ^{14}C-yr (Almogi-Labin *et al*., 1991). Numbers along the isotope curve indicate SPECMAP events. During IS 3 the isotope curve shows short-termed oscillations labelled A-E, which are clearly visible in the proximal cores (Fig. D.2-3).

where sealevel reached 19 and 20 m below present sealevel (mbps), respectively. The three highstands in the Red Sea during the last interglacial also coincide with peaks in the stacked aragonite record (Fig. D.3-2).

During the last interglacial substages 5b and 5d sealevel fell clearly below present-day level. At Sinai Peninsula sealevel stands of 28 ± 5 mbps and 29 ±5 mbps were suggested for isotopic events 5.2 and 5.4, respectively (Gvirtzman, 1994). A lowered sealevel during substages 5b and 5d is also indicated by heavier oxygen isotope values and reduced aragonite/calcite-ratios found in the Sudanese periplatform sediments when compared to interglacial highstands 5a, 5c and 5e (Fig. D.1-1, Fig. D.3-2).

D.1.1.2 The lowstand during IS 4

Gvirtzman (1994) found an about 5-10 m wide submarine terrace at a waterdepth of 60-65 mbps, which is present for a few tens of kilometres along the Sinai Peninsula. He suggested, that this terrace formed as a wave cut notch during a lowstand in sealevel close to isotopic event 4.2. Further submarine terraces at a depth of 60 and 90 mbps are widespread in many parts of the Red Sea (Dullo & Montaggioni, 1998). At Sanganeb Atoll the prominent terrace on the windward side reaches from about 70 to 95 mbps (Brachert & Dullo, 1990). The stacked isotope record and the aragonite/calcite ratios from the Sudanese shelf clearly record event 4.2, about 64,000 SPECMAP yr ago (Fig. D.1-1, D.3-2). When sealevel reached 60 to 65 mbps at this time the deep terraces at Sanganeb Atoll and other Sudanese reef margins must have reached the ideal waterdepth for prolific shallow-water reef growth. It is therefore surprising that the aragonite percentages - which are seen as a proxy for shallow-water sediment export - are at minimum in the periplatform sediments that were deposited during IS 4. This discrepancy between the periplatform record and reef growth on the terrace could indicate that (1) an increased submarine precipitation of HMC on the seafloor suppressed the aragonite signal, (2) the terraces were too small for sufficient carbonate sediment production and subsequent export when compared to benthic carbonate production on the steeper walls of the horst block and (3) no large-scale, shallow-water reef growth occurred during IS 4 due to high salinities of up to 49‰ (Fig. D.2-2).

D.1.1.3 Sealevel variations during IS 3

The sealevel curve from New Guinea (Chappell & Shackleton, 1986) shows that sealevel reached approximately 30 mbps during early stage 3 (about 60,000 SPECMAP-yr) and about 70 mbps at the IS 2/3 boundary (24,000 SPECMAP-yr). A more detailed sealevel record for this time interval is not available and small scale variations along the New Guinea curve can not be transferred to other regions because of global differences in high-frequency fluctuations of eustatic sealevel during IS 3 (Labeyrie *et al.*, 1987). Nevertheless, the oxygen isotope and aragonite curves from the Sudanese shelf show a similar decreasing trend as the New Guinea sealevel curve, but do not correspond with respect to small scale oscillations

D.1.1.4 The last glacial lowstand at 14,840±110 ^{14}C-AMS yr

The last glacial sealevel lowstand in the Red Sea was proved by submerged karst features in a depth of -120 m at Sanganeb Atoll and other Sudanese reefs (Brachert & Dullo, 1990) and by a submarine notch at Sinai Peninsula at the same depth (Gvirtzman, 1994). Unfortunately isotopic event 2.2 is neither recorded in the planktic δ^{18}O curves nor in the aragonite/calcite ratios of the periplatform sediments on the Sudanese shelf. The isotope record is incomplete because planktic foraminifers were absent or rare in the central part of the Red Sea during the hypersaline interval and the aragonite record had been obscured by inorganic carbonate precipitation at the seafloor.

To complete the stratigraphic and palaeoceanographic record during the last glacial, δ^{18}O analyses were also performed on lithified sediments. Heaviest δ^{18}O values of the lithified samples reach their maximum at 14,840±110 ^{14}C-AMS yr ago. If inorganic carbonate precipitation took place in equilibrium with bottom-water the radiocarbon ages of the lithified samples indicate that highest bottom-water salinities occurred at this time. This points to a last glacial sealevel lowstand and the maximum of basin isolation in the Red Sea at 14,840±110 ^{14}C-AMS yr ago, about 2,000 to 4,000 yr after isotopic event 2.2 at 19,000 or 17,000 SPECMAP-yr (Imbrie *et al.*, 1984 and Bassinot *et al*., 1994, respectively).

Studies from the Western Indian Ocean (Mayotte, Comoro archipelago) indicate a last glacial sealevel lowstand at 18,200 U/Th-yr (Colonna *et al*., 1996; Dullo *et al*., 1998), which corresponds to a radiocarbon age of about 15,400 ^{14}C-yr. This is in good correspondence with our data and gives evidence for a sealevel lowstand in the Red Sea simultaneous to that found in the Western Indian Ocean (Fig. D.1-2).

D.1.1.5 The postglacial sealevel rise

Postglacial and Holocene sealevel reconstruction from the Western Indian Ocean (Colonna *et al*., 1996; Dullo *et al*., 1996a, 1998) are compared to the oxygen isotope record of planktic foraminifers and of radiocarbon dated lithified samples from the Sudanese shelf (Fig. D.1-2). In Fig. D.1-3 the postglacial sealevel history is illustrated for Sanganeb Atoll.

The postglacial sealevel rise in the northern part of the Western Indian Ocean was marked by two sharp pulses, between 11,000 to 11,200 ^{14}C-yr and 8,800 to 8,500 ^{14}C-yr (original U/Th-ages obtained on corals are converted in ^{14}C-ages for better comparison with the Red Sea age model). These pulses correspond to the Bølling meltwater point (= MWP 1A, about 11,200 ^{14}C-yr) and the Post Younger Dryas event (= MWP 1B, about 9,000 ^{14}C-yr) in the North Atlantic (Fairbanks, 1989). A steep increase in the oxygen isotope record from the Sudanese Red Sea indicates a fast sealevel rise that might correspond to MWP 1B in the Western Indian Ocean (Fig. D.1-2). In the Red Sea the pulse begins after an extensive plateau in the oxygen isotope curve from 13,000 to 8,500 ^{14}C-yr. It might be speculated if the plateau somehow reflects the Oldest and the Younger Dryas cooling events which are also indicated in the δ^{18}O-record from the Island of Mayotte (Colonna *et al*, 1996).

D.1.1.6 Holocene sealevel and initiation of reef growth

The late Holocene sealevel highstand at about 6,000 SPECMAP-yr ago is clearly indicated

by a peak (-1.5‰) in the stacked Red Sea isotope record (Fig. D.1-2). At the Sinai Peninsula the highstand that corresponds to the mid Holocene climate optimum (Imbrie *et al.*, 1984), is dated at 5,200 U/Th-yr BP and sealevel was estimated to be 0.5 ±0.2m higher than present (Gvirtzman, 1994).

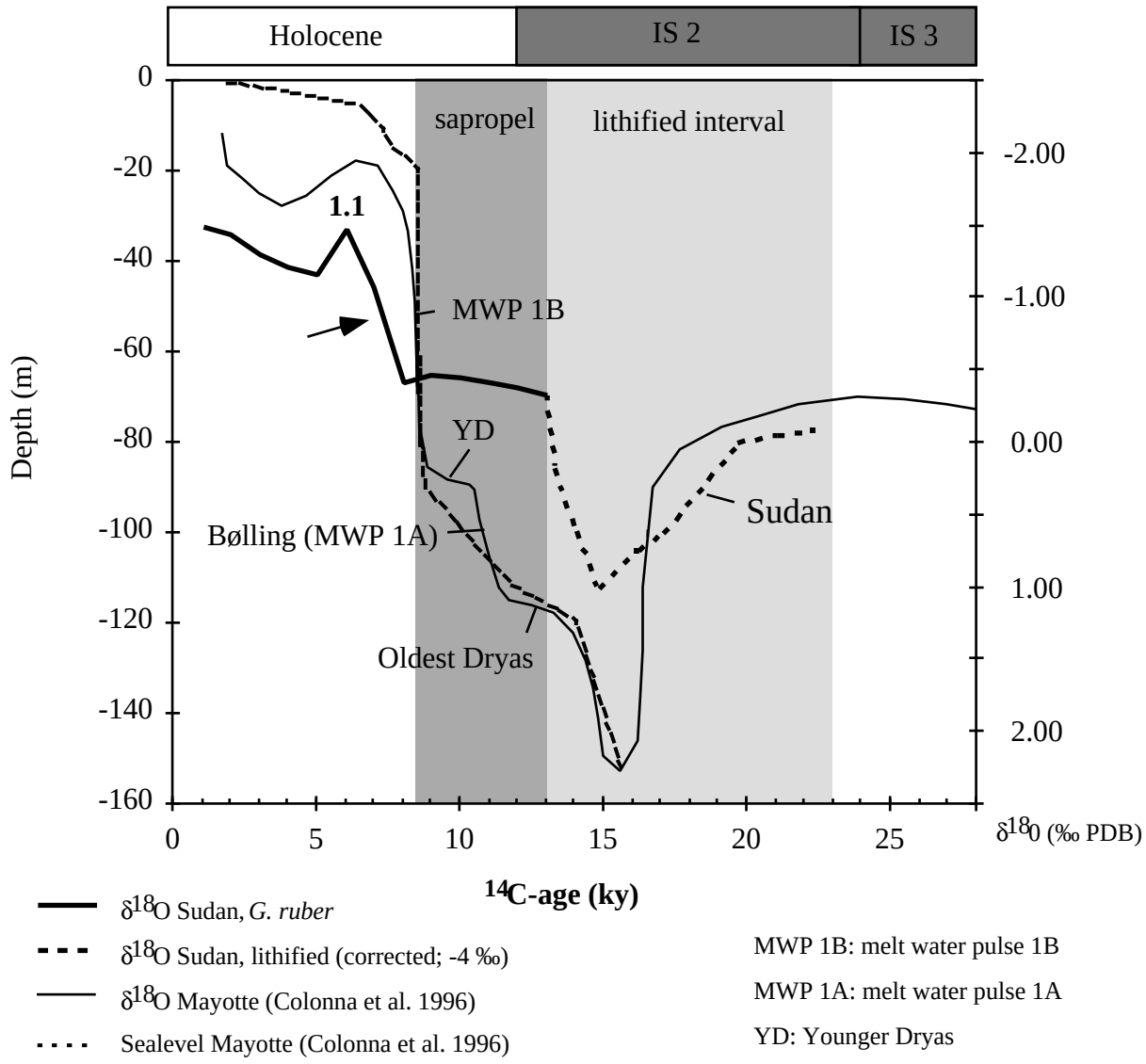

Figure D.1-2: Curve of the eustatic sealevel during the last glacial and the Holocene sealevel rise from the Island of Mayotte, Western Indian Ocean compared to the combined oxygen isotope record analysed on planktic foraminifera and lithified samples. The sealevel curve and the $\delta^{18}O$-curve from Mayotte (Colonna *et al*, 1996) indicate a sealevel lowstand at about 15,000 ^{14}C-yr (about 18,000 yr BP) which coincides with the heaviest $\delta^{18}O$-values of the lithified samples of the Sudanese shelf. The good correlation suggests a sealevel lowstand in the Red Sea at 14,840±110 ^{14}C-AMS yr (uncorrected age). The steep increase in the Sudanese isotope record between 8,000 and 7,000 SPECMAP-yr (arrow) might indicate melt-water pulse 1B (Post Younger Dryas) found in the Western Indian Ocean data. The extensive plateau between 13,000 and 8,500 ^{14}C-yr on the Sudanese curve coincides with a pluvial phase in the Red Sea during deglaciation, which led to the deposition of the sapropel (Almogi-Labin *et al,* 1991) and might reflect the Younger and Oldest Dryas high latitude cooling events. δ18O-values of the lithified samples were corrected for fractionation effects and adapted to the planktic oxygen isotope curve by substraction of -4‰ for each data point.

In seismic profiles of the inner reef slopes that border the lagoon at Sanganeb Atoll erosional surfaces are visible in 20 to 25 m waterdepth. On those erosional surfaces Holocene reef growth might have initiated about 8,000 to 9,000 ^{14}C-yr ago (see Fig. D.1-3) in analogy to the sealevel curve from Mayotte (Colonna *et al*., 1996). The initiation of reef growth and prolific sediment export is indicated by a simultaneous peak in high-strontium- and bulk-aragonite accumulation rates in the periplatform sediments (Fig. D.3-11 and D.3-12). Thus, no significant time offset occurred between flooding of the old Pleistocene substratum and the enormous rise in sediment export production as recorded on the Sudanese shelf.

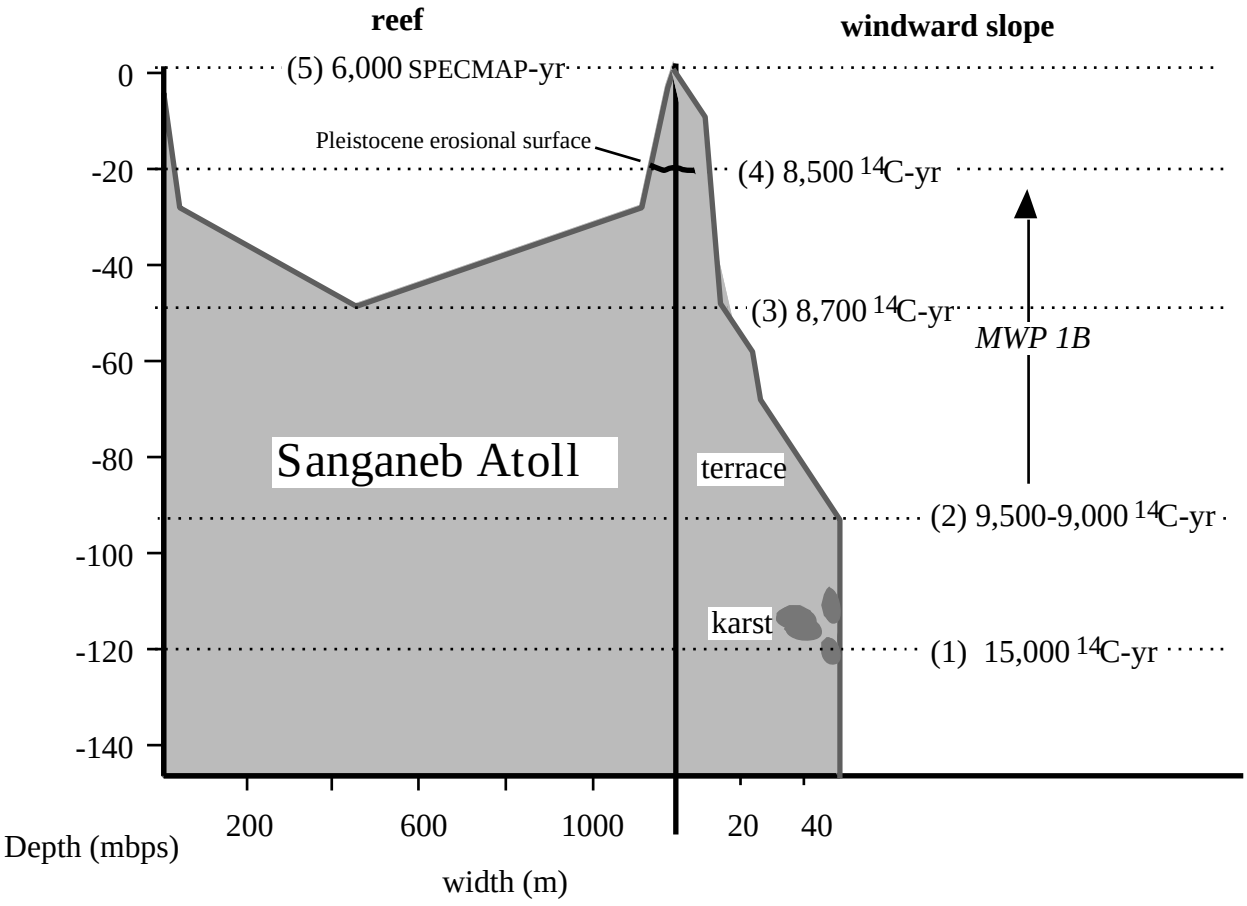

Figure D.1-3: Reconstruction of eustatic sealevel positions at Sanganeb Atoll for the deglatiation and the Holocene sealevel rise. The firure shows, that eustatic sealevel in analogy to the Western Indian Ocean (Colonna *et al*, 1996) might have reached the lagoon in 60 to 50 mbps at Sanganeb Atoll at about 8,700 ^{14}C-yr (3) and flooded the Pleistocene emersion surface in 20 mbps at about 8,500 ^{14}C-yr (4). This coincides with a drastic increase in aragonite accumulation rates (AR) on the Sudanese shelf. The sealevel lowstand in about 120 mbps is documented by karst features present in this waterdepth (1). Postglacial sealevel reached the base of the deep submarine terrace in 90 mbps at about 9,000 to 9,500 ^{14}C-yr (2).

D.1.2 Changes in the productive shallow-water reef area at Sanganeb Atoll in phase with sealevel variations

The maximum in benthic carbonate production of reefs and carbonate platforms occurs close to sealevel, because most organisms are phototrophic (algae) or live in symbiosis with phototrophic organisms (e.g. scleractinian corals). The transparency of Red Sea water is generally very high (Reiss & Hottinger, 1984) and hermatypic corals occur down to a waterdepth of 130 m (Fricke & Schuhmacher, 1983). However, at present, highest benthic carbonate production and prolific reef growth in the Red Sea occurs within the upper 30-40 m of the water column and linear coral growth rates decrease significantly with waterdepth (Heiss, 1995). Nevertheless, it is known from other sites, for example the deeply submerged but highly productive Pedro Bank in the Caribbean, that extensive benthic carbonate production might occur also in greater waterdepth of up to 60 m (Glaser & Droxler, 1991; Dullo, 1997).

D.1.2.1 Calculation of reef areas

Variations in the size of productive reef area at Sanganeb Atoll in tune with relative sealevel changes were calculated for the last 120,000 SPECMAP-yr based on combined sealevel data from the Western Indian Ocean (Colonna *et al.*, 1996), Sinai Peninsula (Gvirtzman, 1994) and New Guinea (Chappell & Shackleton, 1986).

Evaluation of the flooded surface areas (Fig. D.1-4) are based on the present-day hydrography of Sanganeb Atoll (Mergner & Schuhmacher, 1985; Schuhmacher & Mergner, 1985), seismic profiles (Dullo & Montaggioni, 1998) and submersible observations (Brachert & Dullo, 1990; 1991). For each sealevel pinning point the reef area was determined which was covered by a water column of 30 m or 60 m. Those depth were chosen as two lower limits for prolific reef growth. In Fig. D.1-4 the calculation of the reef areas is demonstrated, the results are given in Tab. D.1-1 to D.1-3. It has to be mentioned that the determination of the areas is a simplified estimation based on limited data available.

Method

Total reef areas at Sanganeb Atoll were measured in 25, 10 and 0 m below present sealevel on the map shown in Fig. D. 1-4A with the computer software NIH Image 1.62 and later interpolated for 5 m sealevel steps. The areas covered by a water column of 30 and 60 m, respectively (30 m and 60 m limit in Tab. D-1) were calculated as follows:

(1) area for the 30 m limit = total area in depth x - total area in depth (x+30) and

(2) area for the 60 m limit = total area in depth x - total area in depth (x+60)

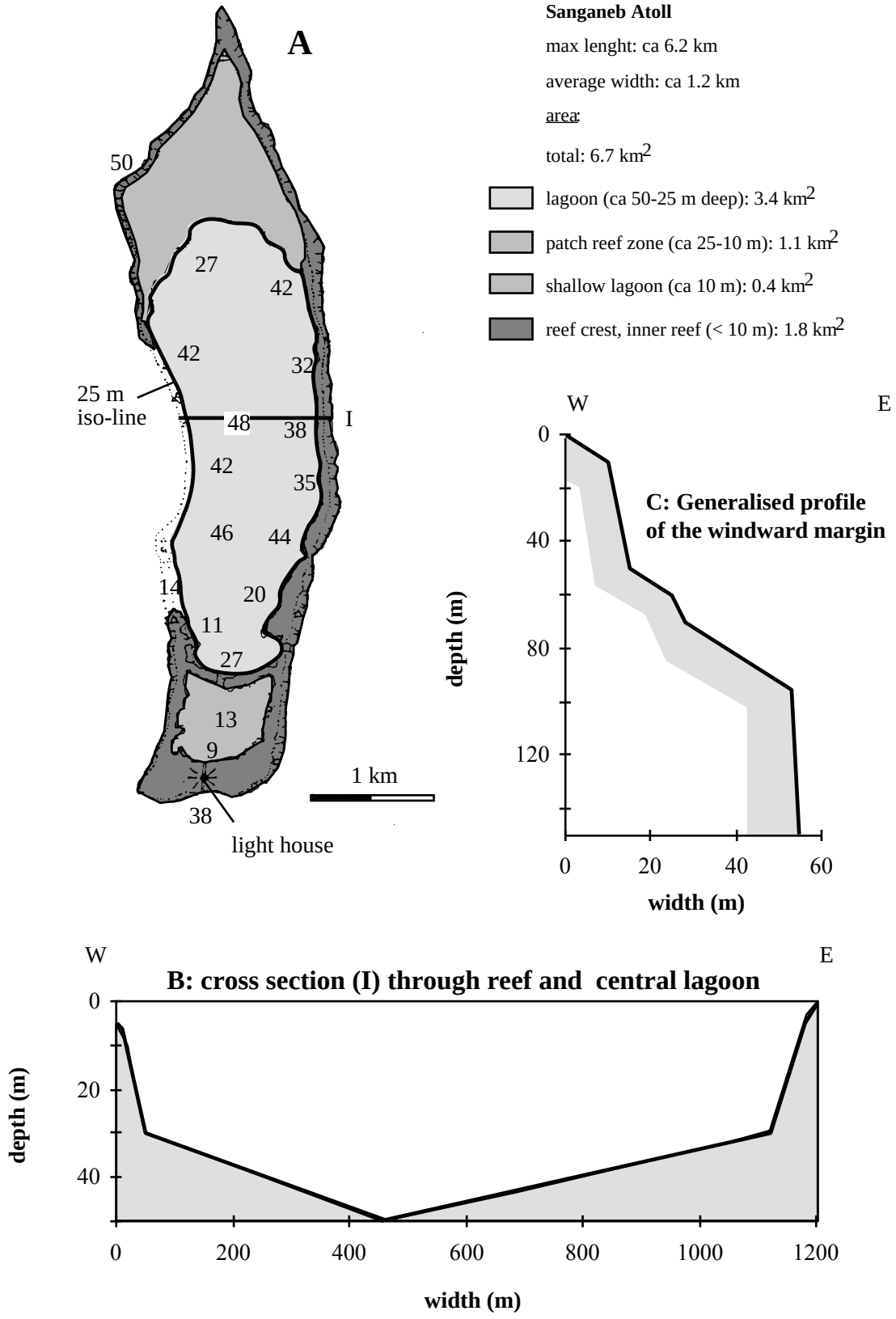

Figure D.1-4: (A) Bio- and geomorphologic zonation of Sanganeb Atoll (numbers indicating waterdepth in meter). (B) Cross section (I) trough the central lagoon and (C) generalised profile of the eastern (windward) margin. The productive areas during different sealevel positions were calculated based on these maps and profiles, which were compiled and modified after scuba-diving profiles of Mergner & Schuhmacher (1985), seismic profiles (Dullo & Montaggioni, 1998) and sea maps published in Mergner & Schuhmacher (1985) and Schuhmacher & Mergner (1985). The morphology of the slopes was taken from profiles of Mergner & Schuhmacher (1985) and submersible observations of Brachert & Dullo (1990, 1991). Calculation methods are described in detail in the text.

For the Holocene sealevel rise shallow-water reef areas were calculated taking in account the flooding of the Pleistocene emersion surface in 20 mbps (30 and 60 m limits (emersion) in Tab.D-1). In this scenario the maximum reef area (6.7 km^2) is already reached in 20 mbps. For a water depth above 20 mbps the reef areas are calculated as follows:

(1) 30 m emersion (<20 mbps) = total area in depth 0 - total area in depth (x+30) and

(2) 60 m emersion (<20 mbps) = total area in depth 0 - total area in depth (x+60).

Based on the profile of the windward slope at Sanganeb Atoll (Fig. D. 1-4C) the slope areas were calculated under the assumption that the slope morphology as shown in the profile continuous on a length of 6 km in N-S direction on both sides of the reef.
The length of slope segments were calculated for 5 m depth intervals using the following equation:

$$\text{slope lenght} = \sqrt{\text{slope hight}^2 + \text{slope width}^2}$$

Slope areas in km^2 were simply calculated by the multiplication of the slope length by 0.006 (6 km N-S extension). The slope areas covered by 30 and 60 m of water were calculated as follows:

(1) slope area (30m limit) in depth x = (Σ slope area in depth (x+5) to depth (x+30)) x 2 and

(2) slope area (60m limit) in depth x = (Σ slope area in depth (x+5) to depth (x+60)) x 2.

The total productive areas flooded by a water column of 30 and 60 m were simply calculated as the sum of slope and shallow-water reef areas for certain sealevel positions under the assumption that the Pleistocene emersion surface was flooded when sealevel reached 20 mbps during the Holocene sealevel rise.
Based on the calculations of reef and slope areas (Tab. D. 1-1 and 1-2) the productive reef areas were calculated for pinning points of the sealevel curve based on data from Sinai Peninsula (Gvirtzman, 1994), the Western Indian Ocean (Colonna *et al.*, 1996) and New Guinea (Chappell & Shackleton, 1986). The glacial lowstand in 120 mbps at about 15,000 ^{14}C-yr was deduced from stable oxygen isotope data of the lithified samples (Chapter D. 1.1.4).

D.1.2.2 Productive reef areas and shallow-water input

The total shallow-water platform area of present-day Sanganeb Atoll is about 6.7 km^2 and is composed of the central lagoon (3.4 km^2), a patch reef zone (1.1 km^2), a shallow lagoon (0.4 km^2) and the reef crest/platform (1.8 km^2). The complete slope area down to a waterdepth of 60 mbps is smaller than 1 km^2 (Fig. D.1-4).

Fig D. 1-5 shows temporal variations of the calculated reef areas for both depth limits (30 m and 60 m) together with the combined sealevel curve. Both curves of productive reef areas show a good correspondences to the sealevel curve throughout the entire interval. It has to be mentioned that the calculation of reef areas is uncertain during IS 5 because the old reef morphology was not

known. Nevertheless, sealevel and productive area are in good correspondence during the last interglacial, even though the calculation was based on the present-day morphology of Sanganeb Atoll. In the following discussion, productive reef area is used as a proxy for shallow-water carbonate production.

The largest productive area is reached at 8,500 SPECMAP-yr (> 7 km^2), in concert with the flooding of the Pleistocene emersion surface. This peak coincides with highest accumulation rates of high-Sr aragonite in the periplatform sediments (Fig. D.3-12, Chapter D. 3) and points to increased shallow-water sediment production and export. In the curve for the 30 m depth limit the size of productive areas drops again to 4.4 km^2 after this maximum. Such a drop is also found in the high-Sr aragonite accumulation rates. The productive reef area becomes reduced because the deeper parts of the lagoon fall below the depth limit for prolific reef growth. This is not the case in the simulation with the 60 m depth limit. Here the size of productive reef area does not drop after the maximum.

Furthermore, both curves show a peak in productive area of about 3 km^2 during early IS 3 at about 53,000 SPECMAP-yr, which was caused by flooding of the inner reef and lagoon (50 mbps) at Sanganeb Atoll in tune with the sealevel rise between isotopic event 4.2 (60 mbps) and 3.3 (30 mbps).

During the last interglacial highstands 5a, 5c and 5e the reef growth area in the calculation with the 30 m depth limit reached about 4 km^2, which is significantly lower than during the Holocene and only a small increase when compared to early IS 3. The model might suggest that carbonate production during the last interglacial highstands stood below that of the Holocene, which is in good agreement with the relatively low sedimentation rates and aragonite accumulation rates found in the periplatform sediments of IS 5. However, no differences between Holocene and last interglacial highstand areas were found in the simulation using the 60 m depth limit (Fig. D.1-5). As mentioned above the model exhibits uncertainties for the last interglacial period.

The minimum in the aragonite percentages found in the periplatform record during IS 4 corresponds to a reduced productive area (< 1 km^2) and shows that the influence of the deep terraces is insignificant, due to their relative small surface area when compared to the shallow reef and the lagoon (Fig. D.1-4).

Between 36,000 and 8,500 SPECMAP-yr both curves show a total productive area < 1 km^2, which was caused by the complete exposure of the shallow-water platform when sealevel dropped below 50 mbps.

It has to be kept in mind that the simulation of the productive area at Sanganeb Atoll is only an estimation, but it still shows that parts of the sediment input pattern found in the periplatform sediments at Sanganeb Atoll could be explained by variations in the productive area which are caused by late Quaternary sealevel fluctuations.

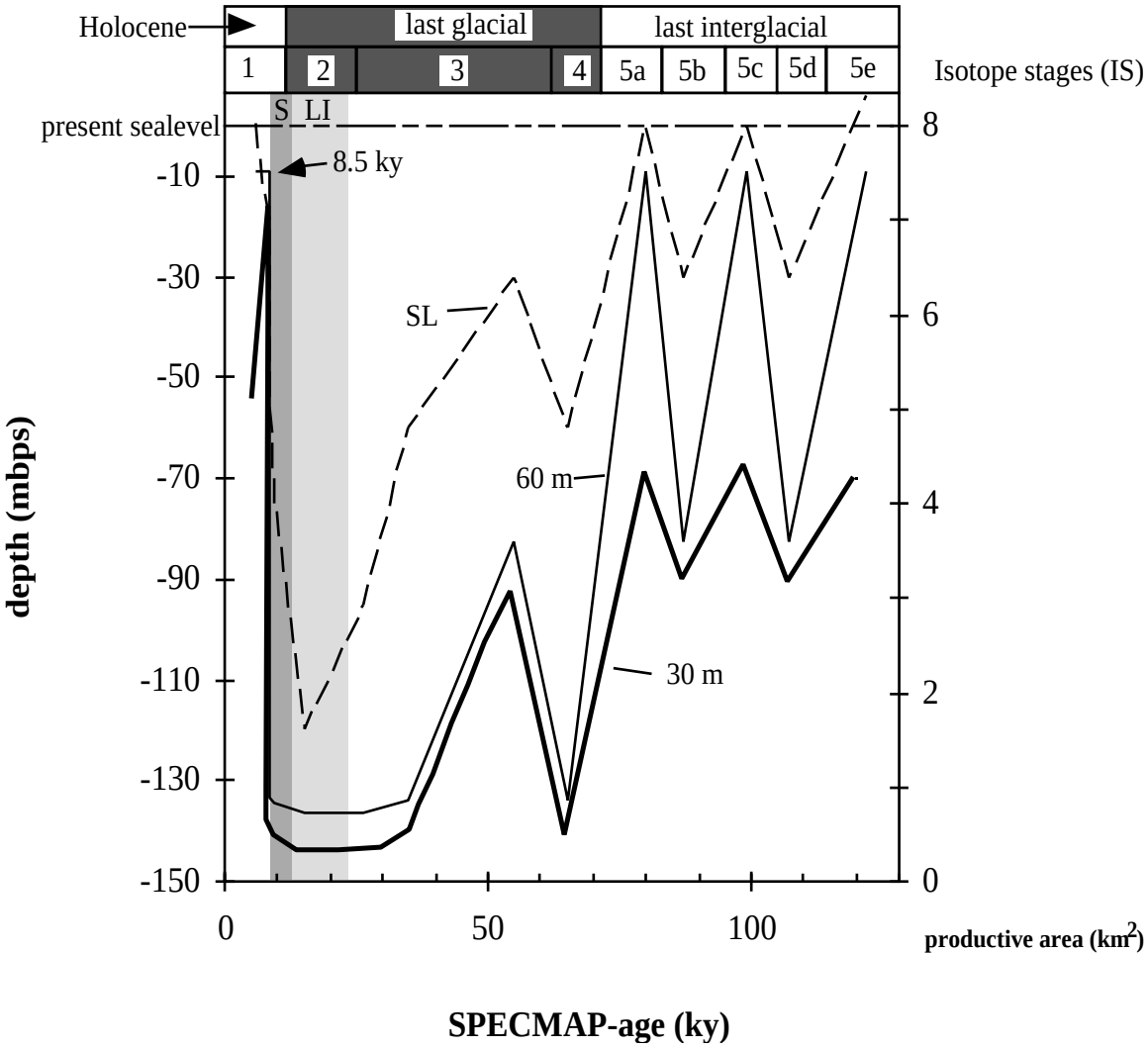

Figure D.1-5: Productive areas at Sanganeb Atoll calculated for eustatic sealevel variations based on the Sinai sealevel curve of Gvirtzman (1994) combined with data from the Western Indian Ocean (Colonna *et al*., 1996; Dullo *et al*., 1996a) and the New Guinea curve (Chappell & Shackleton, 1986). Variations in the size of productive reef areas for both depth limits of prolific reef growth (30 and 60 m) generally show a good correspondence with the sealevel curve (SL). The maximum in productive reef areas that is reached at about 8,500 SPECMAP-yr coincides with a peak in the aragonite accumulation rates of the periplatform sediments and indicates increased shallow-water sediment export in phase with flooding of the old Pleistocene reef structures. Reef areas are smallest between about 35,000 and 8,500 SPECMAP-yr when sealevel dropped below 50 m, the depth of the shallow-water lagoon at Sanganeb Atoll. The good correspondence of productive reef area and sealevel suggests that variations in shallow-water carbonate production and sediment export might occur in phase with sealevel variations. The parallel trends between reef area and aragonite accumulation rates support this idea (Fig. D.3-11 and D.3-12). S = sapropel, LI = lithified interval, SL = sealevel.

Tab. D. 1-1: Calculation of reef areas at Sanganeb Atoll

	reef area (km²)				
sealevel (mbps)	total reef area	30m limit	60m limit	30m limit (emersion)	60m limit (emersion)
0	**6.7**	**4.0**	**6.7**	**4.0**	**6.7**
5	5.8	3.8	5.8	4.7	6.7
10	**4.9**	**3.5**	**4.9**	**5.3**	**6.7**
15	4.4	3.7	4.4	6.0	6.7
20	3.9	3.9	3.9	6.7	6.7
25	**3.4**	**3.4**	**3.4**	**3.4**	**3.4**
30	2.7	2.7	2.7	2.7	2.7
35	2.0	2.0	2.0	2.0	2.0
40	1.4	1.4	1.4	1.4	1.4
45	0.7	0.7	0.7	0.7	0.7
50	**0.0**	**0.0**	**0.0**	**0.0**	**0.0**

Tab. D. 1-2: Calculation of slope areas and total productive areas

sealevel (mbps)	slope width (m)	slope length (m)	slope area (km²)	slope 30m limit	slope 60m limit	reef+slope, 30m limit (emersion)	reef+slope, 60m limit (emersion)
0	0		0.000	0.21	0.41	4.41	7.52
5	5	7.07	0.042	0.19	0.40	5.09	7.50
10	10	7.07	0.042	0.18	0.39	5.66	7.48
15	10.625	5.04	0.030	0.18	0.40	6.36	7.50
20	11.25	5.04	0.030	0.18	0.41	7.06	7.53
25	11.875	5.04	0.030	0.19	0.43	3.79	4.25
30	12.5	5.04	0.030	0.21	0.44	3.13	3.60
35	13.125	5.04	0.030	0.21	0.45	2.45	2.94
40	13.75	5.04	0.030	0.21	0.45	1.78	2.26
45	14.375	5.04	0.030	0.22	0.45	1.12	1.58
50	15	5.04	0.030	0.23	0.45	0.46	0.90
55	20	7.07	0.042	0.23	0.44	0.46	0.87
60	25	7.07	0.042	0.23	0.42	0.46	0.85
65	26.5	5.22	0.031	0.24	0.42	0.49	0.85
70	28	5.22	0.031	0.24	0.42	0.48	0.84
75	33	7.07	0.042	0.23	0.41	0.46	0.82
80	38	7.07	0.042	0.22	0.40	0.43	0.79
85	43	7.07	0.042	0.20	0.38	0.41	0.77
90	48	7.07	0.042	0.19	0.37	0.38	0.74
95	53	7.07	0.042	0.18	0.36	0.36	0.72
100	53	5.00	0.030	0.18	0.36	0.36	0.72
105	53	5.00	0.030	0.18	0.36	0.36	0.72
110	53	5.00	0.030	0.18	0.36	0.36	0.72
115	53	5.00	0.030	0.18	0.36	0.36	0.72
120	53	5.00	0.030	0.18	0.36	0.36	0.72
125			0.030				

Tab. D. 1-3: Variations of productive reef areas in tune with sealevel variations during the last 120,000 years

areas in km^2

^{14}C-Age (ky)	sealevel (m)	area 30m limit (emersion)	area 60m limit (emersion)
0	0.0	4.41	7.52
6	0.5	5.07	7.52
8.5	-20.0	7.06	7.53
8.7	-50.0	0.46	0.90
9.5	-75.0	0.46	0.82
15	-120.0	0.30	0.72
26.5	-95.0	0.30	0.72
35	-60.0	0.46	0.85
55	-30.0	3.13	3.60
65	-60.0	0.46	0.85
80	0.0	4.39	7.52
87	-30.0	3.13	3.60
99	0.0	4.39	7.52
107	-30.0	3.13	3.60
122	6.0	4.39	7.52

D.2 Palaeoceanography and climate during the last glacial

Besides information about reef growth and sealevel history, the periplatform sediments from the Sudanese shelf record palaeoceanographic and climatic signals. In the first two paragraphs of this chapter (D. 2.1 to 2.3) the $\delta^{18}O$-signal as recorded by planktic foraminifers is interpreted with respect to variations in sea-surface salinities and the climatically driven (monsoonal) changes in hydrographic conditions, like sealevel variations, temperatures, water circulation patterns and oxygenation of the water masses. Those palaeoceanographic parameters are important because they controlled distribution of marine life and influenced the shallow-water input signal of the periplatform sediments. In the paragraphs D. 2.4 to 2.5 the palaeoceanographic conditions are discussed which led to submarine lithification during the last glacial and subsequent sapropel formation on the Sudanese shelf.

D.2.1 Restrictions in reef growth due to high sea-surface salinities during IS 2 and IS 4 as recorded by planktic foraminifers

The planktic $\delta^{18}O$-curves of the studied cores show the characteristic saw-tooth pattern with high amplitude oscillations of late Quaternary climate variations which are recorded in the tests of planktic foraminifers. This is also clearly visible in the stacked isotope curve which is calculated as an average of the individual cores (Fig. D.2-1). Compared to the SPECMAP curve the $\delta^{18}O$ values of the Sudanese isotope stack show only small deviations during interglacials and prominent deviations towards heavier values in glacials (Fig. D.2-1). Variations of the $\delta^{18}O$ values in the analysed cores reach a glacial-interglacial amplitude of about 4.5‰. Considering even heavier $\delta^{18}O$-values during the LGM - up to 3.3‰ were obtained from pteropods in the central Red Sea by Hemleben *et al.* (1996) - a maximum amplitude of 5 to 6 ‰ can be assumed for the central Red Sea. The global glacial-interglacial amplitude of the world ocean water due to the ice-effect (waxing and waning of ice shields) is estimated to be only 0.8 to 1.2 ‰ (Chappell & Shackleton, 1986; Labeyrie *et al*., 1987; Fairbanks, 1989; Schrag *et al*., 1997). Therefore it is suggested that the increased glacial-interglacial amplitudes in the Red Sea were caused by increased salinities during

---

Figure D.2-1 (upper fig. to the right): Stacked oxygen isotope curve for the Sudanese Red Sea (stdev. see Appendix 1-B), in comparison with the SPECMAP curve of Imbrie *et al* (1984) and the global $\delta^{18}O$ variations of seawater (δw) due to changes in ice volume as calculated by Vogelsang (1990). The increased glacial-interglacial amplitude of the Red Sea isotope record, when compared to the SPECMAP stack, is caused by deviations during major and minor sealevel lowstands. It is suggested that the Red Sea basin became restricted during lowered sealevel which led to increased salinities during arid climate conditions (e.g. Locke & Thunell, 1988; Hemleben *et al*, 1996). The increased glacial-interglacial $\delta^{18}O$-amplitude was caused by increased glacial salinities. Unfortunately, isotopic event 2.2 is not recorded in the central part of the Red Sea, due to the absence of planktic foraminifers caused by salinities > 50‰ (see Fig. D.2-2). S = sapropel, LI = lithified interval.

Figure D.2-2 (lower fig. to the right): Sea-surface salinities for the Sudanese Red Sea as calculated from planktic oxygen isotopes after the method described by Hemleben *et al* (1996) and Geiselhardt (1998). Calculated salinities can be found in Tab. D.2-1. The salinities of the aplanktonic zone (open circles) were calculated from $\delta^{18}O$-values analysed on unlithified fine fraction (Tab. C.5-1). The calculation shows that during the aplanktonic interval (23,000 to 13,000 ^{14}C-yr) salinities exceeded 50‰, which caused major restriction of marine life and reef growth (e.g. Reiss *et al*, 1980; Taviani, 1998a, b). During IS 4 salinities of surface-waters reached up to 49‰ which also might have caused restrictions of benthic shallow-water biota as indicated by reduced aragonite input on the Sudanese shelf. S = sapropel, LI = lithified interval.

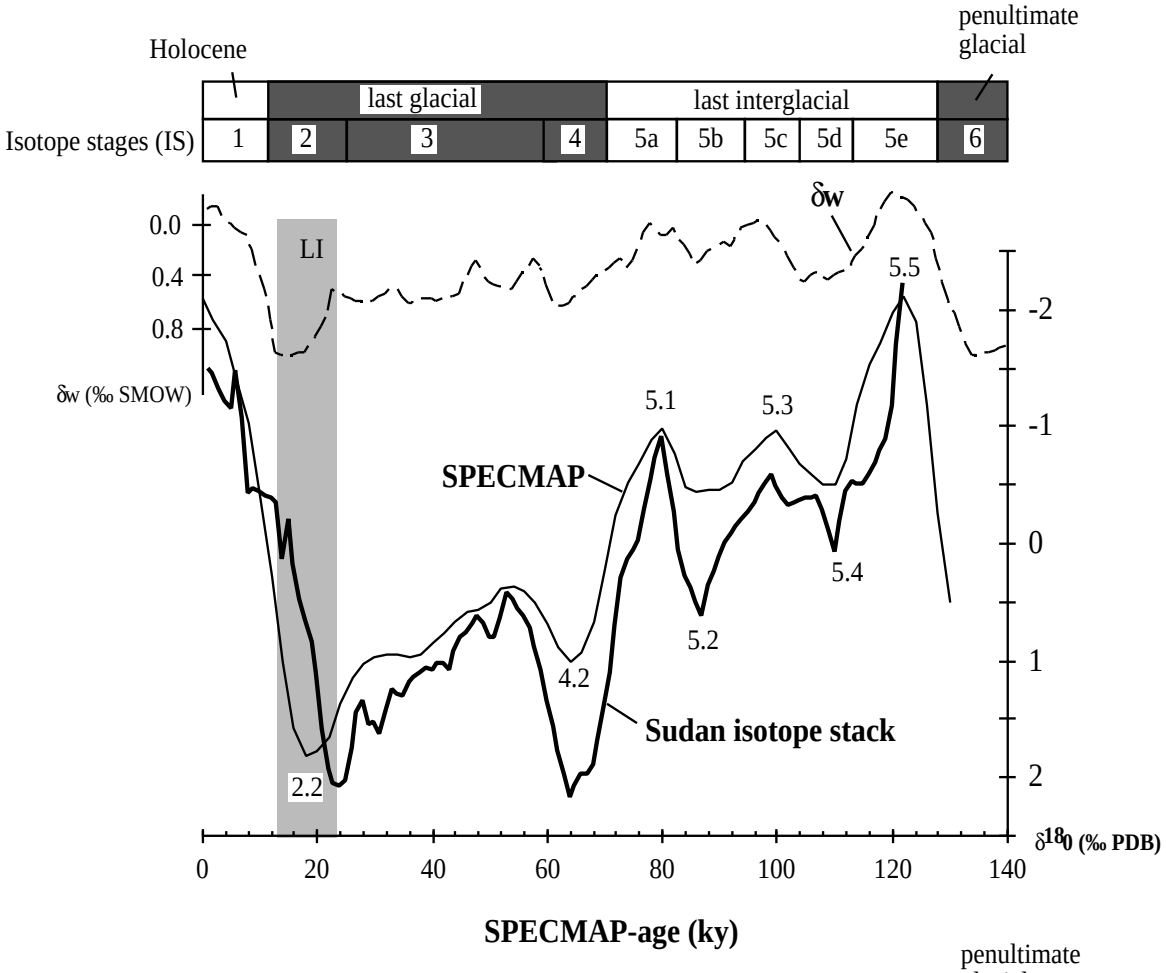
Holocene
penultimate glacial
last glacial
last interglacial
Isotope stages (IS)
1
2
3
4
5a
5b
5c
5d
5e
6
δw
LI
δw (‰ SMOW)
SPECMAP
Sudan isotope stack
5.1
5.3
5.5
5.4
5.2
4.2
2.2
δ18O (‰ PDB)
SPECMAP-age (ky)

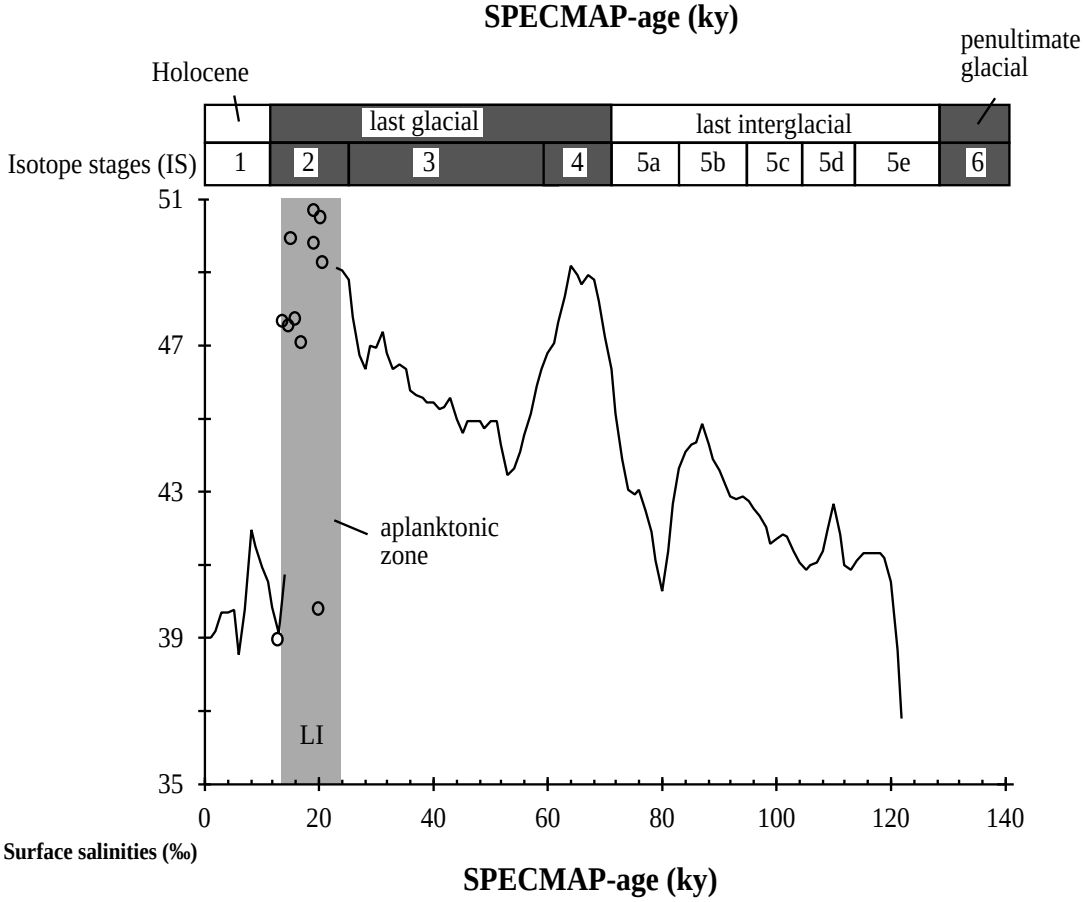
Holocene
penultimate glacial
last glacial
last interglacial
Isotope stages (IS)
1
2
3
4
5a
5b
5c
5d
5e
6
aplanktonic zone
LI
Surface salinities (‰)
SPECMAP-age (ky)

glacial sea-level lowstands (e.g. Berggren, 1969; Reiss *et al*., 1980; Winter *et al*., 1983; Almogi-Labin *et al*., 1991; Hemleben *et al*., 1996; Geiselhardt, 1998; Taviani, 1998c).

For the stacked planktic oxygen isotope curve (Fig. D.2-1) palaeo-salinities of surface-waters were calculated (Equ. B-3, Chapter B.3.5). The results are shown in Tab. D.2.1 and Fig. D.2-2. At present surface salinities in the central Red Sea lie at about 39‰ (Wyrtki, 1971). The calculated palaeo-salinities close to 49‰ during glacial stage 4 are in good agreement with the calculations of Geiselhardt (1998). At present, corals in most regions can only tolerate salinities up to 37‰ (Bosscher, 1992), whereas in the Red Sea growth at salinities well over 40‰ can be observed (e.g. Reiss & Hottinger, 1984).

Restriction of reef organisms is likely during IS 2, when surface salinities reached up to 51‰. This is supported by the absence of *G. ruber* in the sediments of the Sudanese shelf most of the time, which indicates that salinities must have exceeded 49‰, the upper salinity tolerance of this species (Hemleben *et al*., 1996). If there was no reef growth during IS 2, the origin of the frequently occurring, reef-derived skeletal sands can be explained only by reworking of older reef sediments. Furthermore, the question is raised if reef-building corals tolerated salinities close to 49‰ during IS 4 or if such high salinities restricted reef growth. Restriction or absence of reef growth is also supported by the fact that no reefs of this age have been found in the Red Sea region so far.

Table D. 2-1: Sea-surface salinities calculated from planktic oxygen isotopes

For methods and abbreviations see Equ. B-3, Chapter B. 2.3.5. Ages are based on the SPECMAP time scale

Age (ky)	δw (‰ SMOW)	δc (‰ PDB)	error st.dev.	Δ $\delta^{18}O$ (‰ PDB)	Δ S (‰)	Δ S zero (‰)	S (‰)
1	-0.11	-1.49	0.01	-1.38	-4.74	0.0	39.0
5	0.00	-1.16	0.02	-1.15	-3.98	0.8	39.8
10	0.37	-0.45	0.48	-0.82	-2.83	1.9	40.9
15	1.01	-0.20	0.82	-1.21	-4.19	0.6	39.6
20	0.87	1.11	0.84	0.24	0.84	5.6	44.6
25	0.56	2.03	0.22	1.47	5.06	9.8	48.8
30	0.60	1.53	0.16	0.93	3.22	8.0	47.0
35	0.55	1.31	0.21	0.75	2.60	7.3	46.3
40	0.59	1.09	0.14	0.50	1.72	6.5	45.5
45	0.54	0.80	0.18	0.26	0.89	5.6	44.6
50	0.45	0.80	0.14	0.35	1.20	5.9	44.9
55	0.45	0.56	0.18	0.11	0.38	5.1	44.1
60	0.47	1.35	0.39	0.88	3.04	7.8	46.8
65	0.57	2.08	0.08	1.51	5.19	9.9	48.9
70	0.37	1.39	0.12	1.03	3.54	8.3	47.3
75	0.29	0.06	0.38	-0.23	-0.79	4.0	43.0
80	0.09	-0.90	0.13	-0.99	-3.43	1.3	40.3
85	0.23	0.39	0.17	0.16	0.54	5.3	44.3
90	0.17	0.12	0.00	-0.05	-0.19	4.6	43.6
95	0.02	-0.27	0.00	-0.29	-1.00	3.7	42.7
100	0.11	-0.49	0.00	-0.60	-2.06	2.7	41.7
105	0.45	-0.38	0.00	-0.83	-2.86	1.9	40.9
110	0.41	0.09	0.00	-0.32	-1.09	3.6	42.6
115	0.20	-0.50	0.00	-0.70	-2.41	2.3	41.3
120	-0.24	-1.17	0.00	-0.93	-3.21	1.5	40.5

D.2.2 Depleted glacial isotope values - humid events at the end of the peak glacial?

During the last glacial the salinities in Red Sea surface-waters increased to values exceeding 50‰. Therefore planktic foraminifers almost completely vanished from the central and northern Red Sea (e.g. Berggren & Boersma, 1969; Reiss *et al*., 1980; Geiselhardt, 1998). In the studied periplatform sediments planktic foraminifers are rare or absent and the plankton assemblage is dominated by the epipelagic, euryhaline pteropod *Creseis acicula.*

Only the planktic foraminifer *G. ruber* was found occasionally in the lithified interval (IS 2), which suggests that the salinities exceeded 49‰ most of the time in this part of the Red Sea. This was also observed in other cores from the central part of the Red Sea (Hemleben *et al*., 1996; Geiselhardt, 1998).

Extremely light $\delta^{18}O$-values of about -1.0 to -1.5‰ were analysed on the tests of *G. ruber* individuals of the lithified interval within cores S1 and S2. These $\delta^{18}O$-values fall in the range of normal interglacial values found in the Red Sea but occur in a fully glacial stage. Brachert (1996) found relatively light oxygen isotope values (0.9-1.0‰) in the denser lithified layers (bulk sediment) of the last glacial that correlate with the occurrence of planktic foraminifers („planktonic foraminifer events“) at the toe-of-slope at Sanganeb Atoll. Depleted glacial isotope value of about -1.2 ‰ were also analysed on tests of *G. ruber* selected from glacial sediments in core KL11 (Hemleben *et al*., 1996) positioned about 150 km NE of Sanganeb Atoll. In core KL 32 from the southern Red Sea planktic oxygen isotope values during IS 2 show high amplitude oscillations between about 4‰ and -2‰ (Geiselhardt, 1998; fig. 15, 16).

The widespread occurrence of *G. ruber* tests showing extremely light „interglacial“ $\delta^{18}O$-values within the last glacial interval (IS 2) might indicate (1) that resedimentation processes occurred during the last glacial when „starving“ was a basin-wide phenomenon and erosional bottom-currents were strong enough or (2) that local populations of *G. ruber* survived in less saline surface-waters close to estuarines or re-colonised parts of the basin during short phases of reduced sea-surface salinities. The activity of Sudanese rivers during the last glacial is well documented for the Sudan Delta close to Port Sudan (Stoffers & Ross, 1977; Aboul-Basher, 1980). This is indicated by increased siliciclastic input during IS 2 in the periplatform sediments close to Sanganeb Atoll. Sirocko (1994) showed by analysing eolian input variations into Arabian Sea sediments, that the intensity of the dry NE-monsoon ceased abruptly at the end of the last glacial maximum, which caused increased rainfall over the Red Sea. Pluvial conditions close to the end of the peak glacial coincide with the occurrence of „*G. ruber events*“ at Sanganeb Atoll between 16,150±90 and 19,280±150 ^{14}C-AMS yr (67-105 cm in core S1, unlithified).

D.2.3 Small scale monsoonal cycles during IS 3

In proximal cores at Sanganeb Atoll marine isotope stage (IS) 3 is very expanded. This is due to increased sedimentation rates close to the reef (5-7.5 cm/ky during IS 3) when compared to more distal cores (3-4.5 cm/ky). IS 3 is not so well developed in periplatform sites outside the Red Sea, like the Bahamas (Droxler *et al.*, 1983; Droxler, 1986; Reijmer *et al.*, 1988) or Walton Basin (Glaser, 1991; Glaser & Droxler, 1991).

D.2.3.1 Monsoonal climate variations during IS 3

All proximal cores at Sanganeb Atoll show the same small-scale cycles in the planktic $\delta^{18}O$ record (Fig. D.2-3). The minima in the $\delta^{18}O$ and maxima in the aragonite curves are labelled A to E and occur at 27,000 (A = event 3.1), 33,000 (B), 42,000 (C), 48,000 (D) and 53,000 SPECMAP-yr (E = event 3.3).

Schulz *et al*. (1998) found a general relationship between monsoonal climate variations in sediments of the Arabian Sea and the rapid temperature fluctuations in high northern latitudes as recorded in the GISP2 ice-core. Laminated, organic-rich sediments of the Arabian Sea reflect high monsoon-induced biological productivity and correlate with mild interstadial climate events in the North Atlantic. Bioturbated sediments that indicate lowered SW-monsoon correlate with high latitude atmospheric cooling.

In analogy to the neighbouring Arabian Sea it is assumed that the cycles found in the Red Sea isotope curves during IS 3 are also caused by variations in monsoonal climate which might be linked to high latitude temperature variations. Phases of enhanced NE-monsoon activity caused relatively high aridity and low air-temperatures, whereas increased SW-monsoon led to warmer and pluvial conditions over the Red Sea (e.g. Duplessy, 1982). During more arid phases evaporation-rates were higher and led to increased salinities of Red Sea waters. Such high salinities accompanied by lower sea-surface temperatures resulted in heavier oxygen isotope values of the foraminifer tests during phases of enhanced NE-monsoon. During the warmer and pluvial phases of prevailing SW-monsoon activity, the evaporation/precipitation-ratio was lower than during the arid phases which led to lower salinities of Red Sea surface-waters. The more humid, low salinity phases during IS 3 are indicated by lighter oxygen isotope values that coincide with the events A to E.

D.2.3.2 Enhanced aragonite preservation during humid phases of IS 3

Changes in circulation pattern and hydrographic conditions caused variations in dissolution or precipitation of aragonite and HMC on the seafloor of the Red Sea. The circulation and composition of Red Sea deep and surface-waters depends on (1) prevailing wind directions (monsoon), (2) ratio of precipitation and evaporation (monsoon) and (3) variations of in- and outflow via the Strait of Bab el Mandeb (sealevel).

The events A to E (IS 3) on the aragonite curve are paralleled in the TOC curve by increased organic carbon values (see Fig. D.2-3), which gives evidence for a climatically enhanced preservation model.

It is suggested that aragonite- and TOC preservation were favoured during humid phases of IS 3 when the SW-monsoon prevailed. Enhanced rainfall caused the development of a pycnocline and the formation of oxygen depleted bottom-waters (Fig. D.2-4A) similar to the situation at the end of the last glacial (Almogi-Labin *et al.*, 1991; Hofmann *et al.*, 1998). The development of less oxygenated bottom-water during more humid phases of isotope stage 3 led to a better aragonite preservation (events A-E). At the end of each pluvial phase, the NE-monsoon re-established over the Red Sea. This caused a more arid climate and a higher evaporation similar to the present-day situation (Fig. D.2-4B). Nowadays, dense and highly saline surface-waters form at the northern

end of the Red Sea and cause an anti-estuarine circulation, with good admixture and oxygenation of the bottom-water (Neumann & McGill, 1962; Locke & Thunell 1988). Lower aragonite/calcite ratios indicate good ventilated, oxygen-rich bottom-waters resulting in higher dissolution of aragonite at the seafloor.

It seems that the world wide glacial-interglacial variations in aragonite dissolution (Milliman, 1975; Volat *et al.*, 1980; Droxler *et al.*, 1983, 1988, 1990; Keir & Berger, 1985; Opdeyke & Walker, 1992) were overlain by short-term aragonite preservation cycles during IS 3 in the Red Sea.

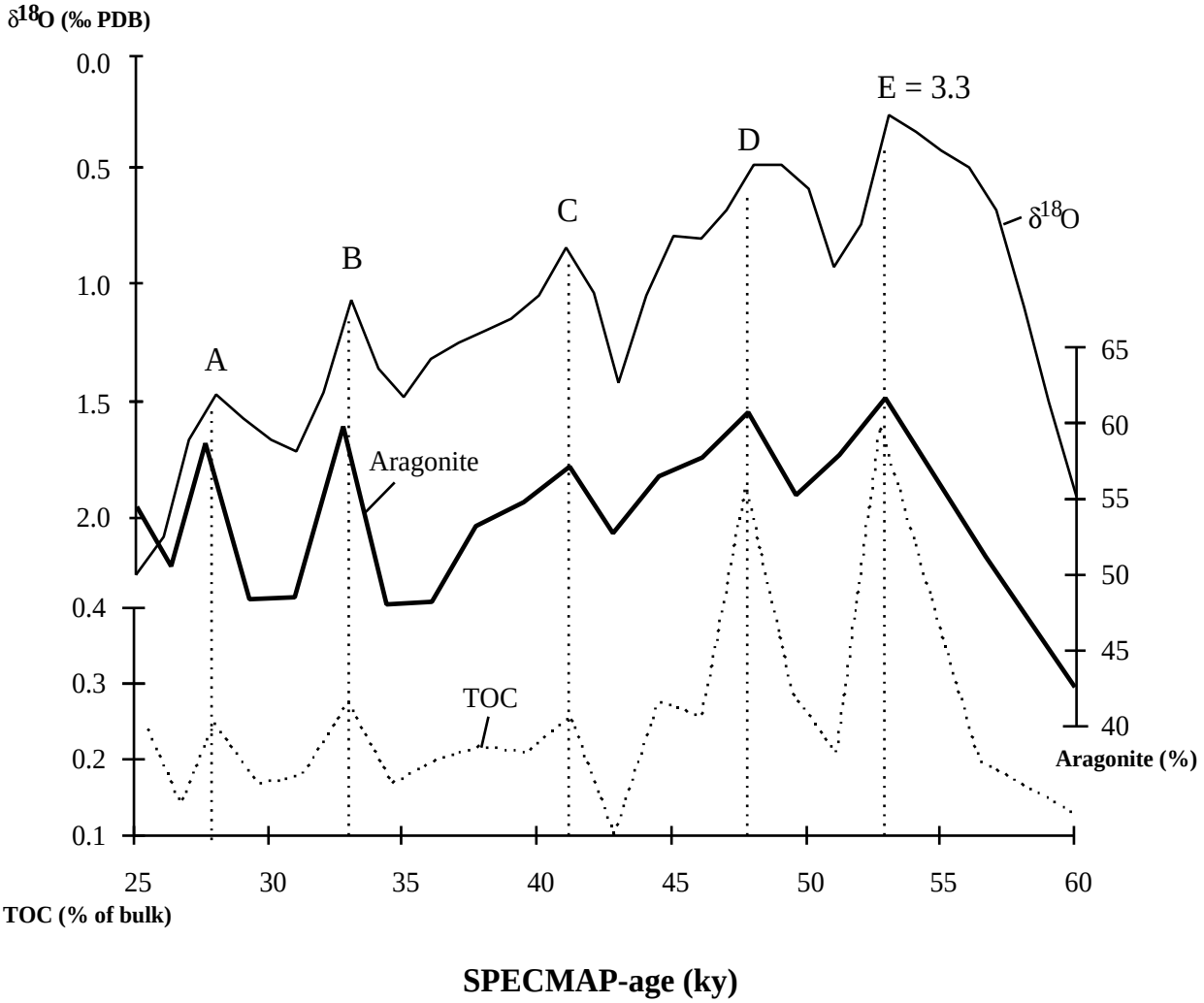

Figure D.2-3: Planktic $\delta^{18}O$-, aragonite- and TOC record of core S2 during IS 3 at Sanganeb Atoll; A to E mark peaks in the $\delta^{18}O$-record which coincide with preservation events of aragonite and organic matter. It is assumed in analogy to sediments of the Arabian Sea (Schulz *et al,* 1998) that the cycles were caused by variations in monsoonal climate which coincide with the high-latitude temperature oscillations found in the GISP2 ice-core. Phases of enhanced SW-monsoon led to pluvial conditions over the Red Sea, which might have caused short-termed stagnation of the deeper water masses in analogy to the last deglaciation phase (Almogi-Labin *et al.*, 1991). Oxygen depletion of bottom-waters caused better preservation of aragonite and TOC in the periplatform sediments of the Sudanese shelf.

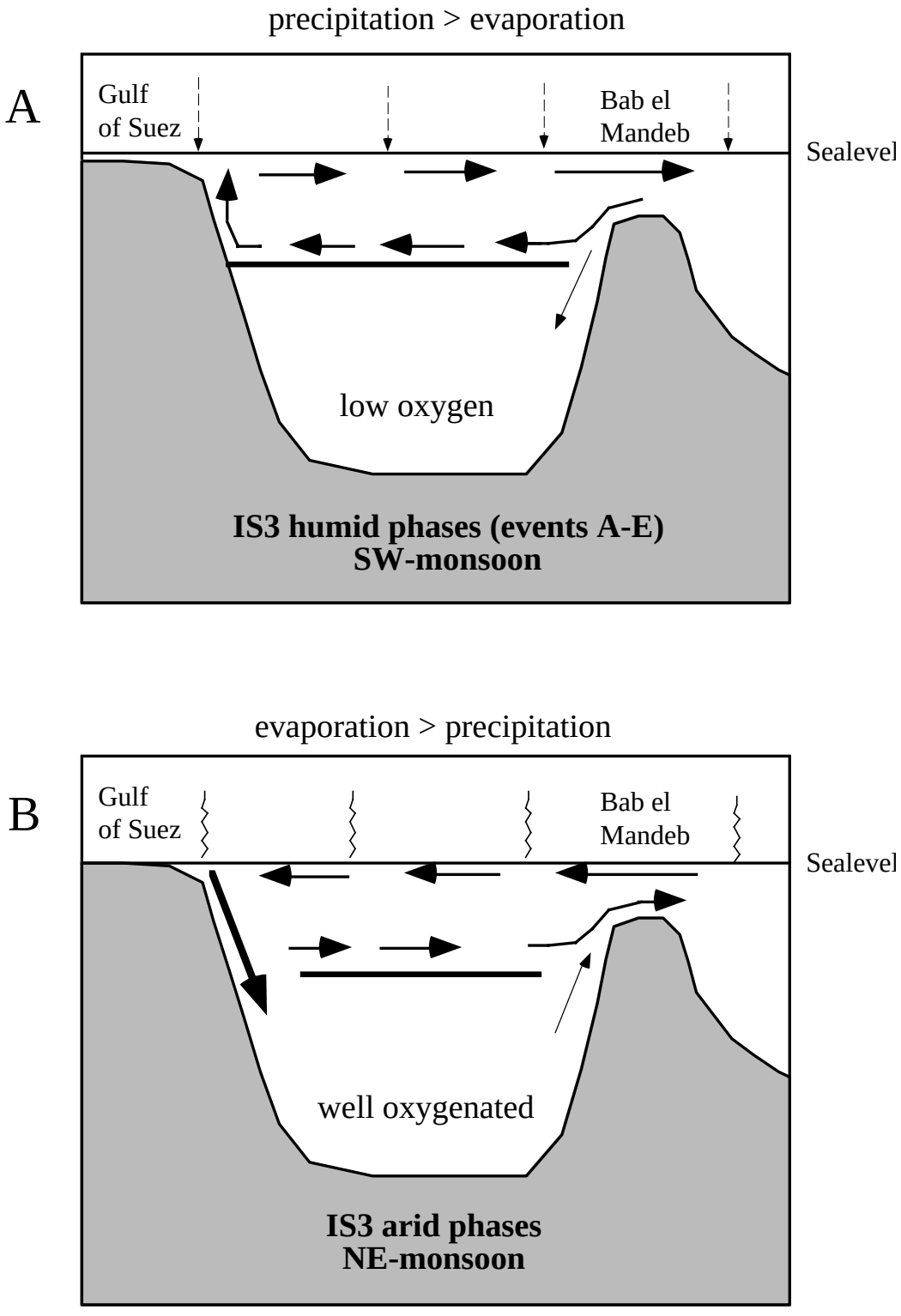

Figure D.2-4: Hydrographic conditions on the Sudanese shelf during (A) humid phases (SW-monsoon) of IS 3 which led to enhanced aragonite and TOC preservation and (B) during arid phases (NE-monsoon) with better oxygenation of bottom-waters and increased dissolution of organic matter and aragonite. Increased rainfall during the humid phases led to the development of a pycnocline and of an extensive oxygen minimum zone (OMZ) in the deeper parts of the Sudanese shelf (A). Under more arid conditions an anti-estuarine circulation pattern established similar to the present-day situation, with the formation of deep-water by the down-welling of high saline surface-waters at the northern end of the Red Sea (Cember, 1988; Locke & Thunell, 1988; Geiselhardt, 1998).

D.2.4 Submarine lithification and sapropel formation on the Sudanese deep shelf

During the late Quaternary normal periplatform sedimentation on the Sudanese deep shelf in the vicinity of Sanganeb Atoll and Abington reef was interrupted by climatically driven hydrological anomalies. A break in deposition of normal periplatform sediments occurred (1) from about 23,000 to 13,000 ^{14}C-yr in which lithified carbonate layers formed in hypersaline bottom-water during the glacial sealevel lowstand, and (2) during the following deglaciation between 13,000 and 8,500 ^{14}C-yr when an organic-rich sapropel formed in stagnating bottom-water (Fig. D.2-5). The palaeoceanographic evolution linked to lithification and sapropel formation on the Sudanese shelf is summarised in Tab. D.2-5 at the end of this section.

D.2.4.1 Age and distribution of the lithified layers (IS 2)

Submarine lithification during the last glacial sealevel lowstand is not limited to the Sudanese deep shelf but was reported from various sites of the Red Sea, ranging from the deep axial zone at 2,704 m waterdepth to the shelf regions at 512 m (e.g. Gevirtz & Friedmann, 1966; Milliman *et al.*, 1969; Brachert & Dullo, 1990; Stoffers & Botz, 1990; Brachert, 1995; 1996, 1999; Taviani, 1998c). Formation of lithified layers in the Red Sea occurred during the last glacial sealevel lowstand but is also documented from previous glacials (Milliman *et al*., 1969). In the cores from the Sudanese shelf a lithified layer occurs in periplatform sediments of the penultimate glacial (IS 6) of core AW at Abington Reef. Further isolated lithified layers are present in cores close to Sanganeb Atoll, most of them formed during IS 3.

The formation of late Quaternary carbonate crusts is not unique to the Red Sea but was also reported from the Mediterranean (Bernoulli & McKenzie, 1981; McKenzie & Bernoulli, 1982; Allouc, 1990; Aghib *et al*., 1991) and the Bahamas (Mullins, 1985; Wilber & Neumann, 1993).

Timing of the last submarine lithification phase on the Sudanese shelf

In Tab. D.2-2 ages of lithified sediments that formed during the last phase of submarine lithification in the Red Sea are compiled. Those ages fall in the range between 4,670 to 26,000 ^{14}C-yr. In the studied cores the youngest lithified particles were dated as 12,930 ±90 (S1) and 12,960±60 (S6) ^{14}C-AMS yr. This age was analysed on small lithified particles which occur dispersed in the sapropel layer on top of the lithified interval. It is likely that such particles stem from the uppermost part of the youngest crust layer and in a later stage were incorporated into the sapropel. An age of about 13,000 ^{14}C-yr is in good accordance with ages for the top of the lithified interval given by Almogi-Labin *et al.* (1991). They assigned an age of 13,000 ^{14}C-yr for the base of the postglacial in the Red Sea. This date was compiled from various ^{14}C-ages obtained from the base of the sapropel and the top of the crust from various sites within the Red Sea (Ku *et al.*, 1969; Risch, 1976; Ivanova, 1985) and coincides with the onset of deglaciation in the North Atlantic as proposed by Fairbanks (1989).

Submarine lithification in the Red Sea might have continued until about 11,000 ^{14}C-yr. This is indicated by radiocarbon datings by Milliman *et al.* (1969) and Stoffers & Botz, (1990). This was also suggested by micropalaeontological studies of Berggren & Boersma (1969) and Reiss *et al*. (1980). They showed that the lithified interval coincides with low abundances or even absence of

A: sapropel formation (13-8,500 ^{14}C-years)

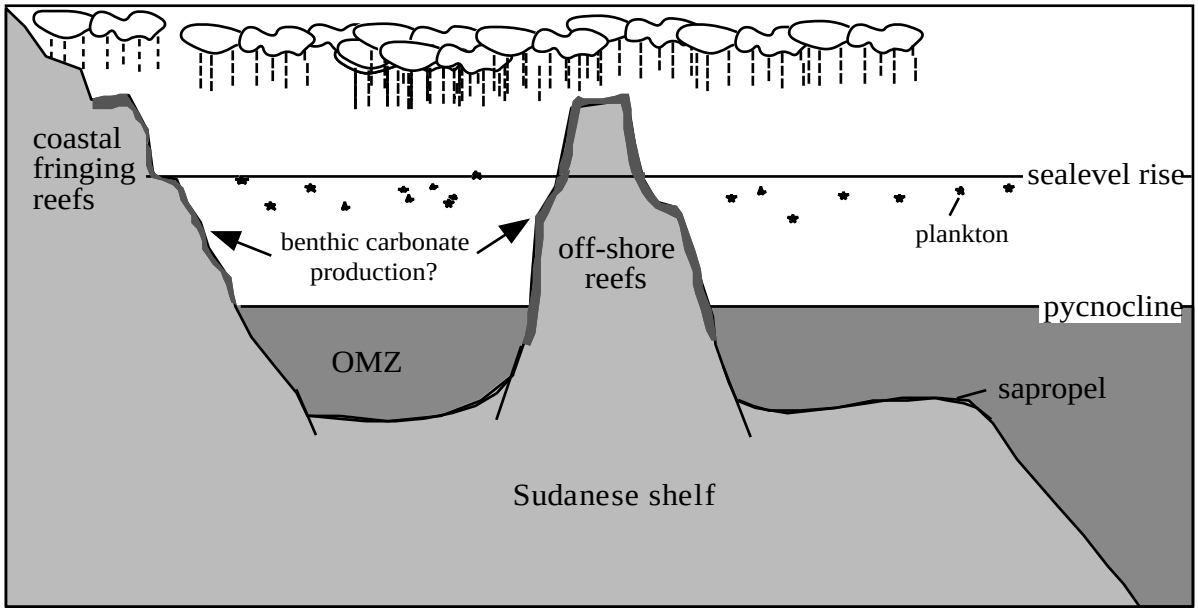

B: inorganic carbonate precipitation (23-13,000 ^{14}C-years)

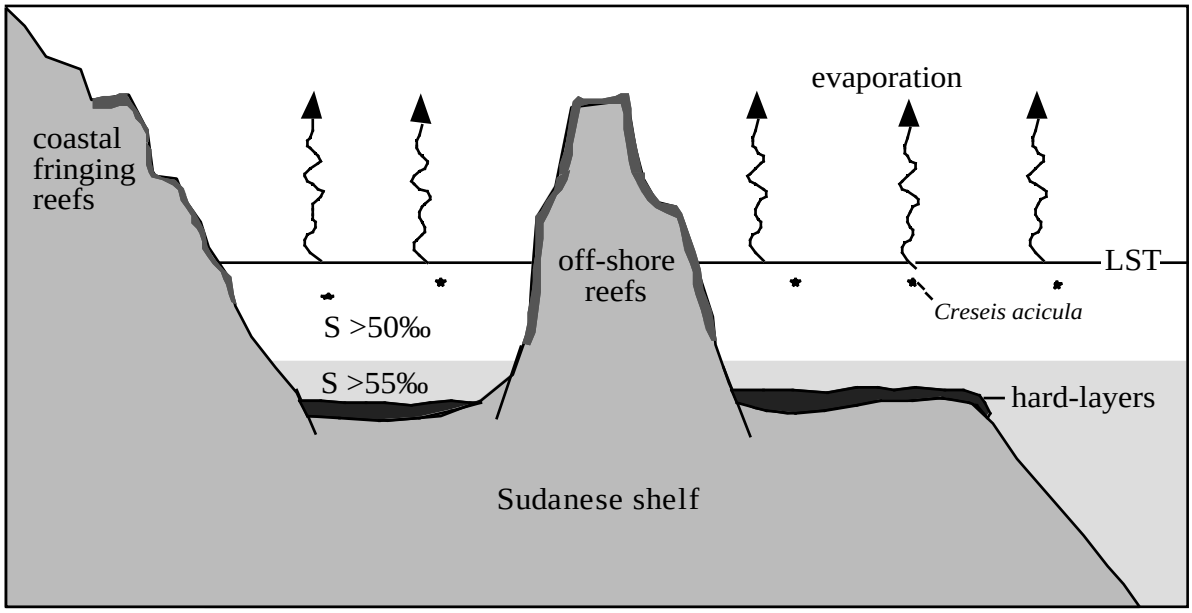

OMZ: oxygen minimum zone

LST: sealevel lowstand

S: salinity

Figure D.2-5 Sketch of the palaeoceanographic conditions on the Sudanese shelf during sapropel formation (A) and submarine lithification (B). The sealevel lowstand during IS 2 was accompanied by increased evaporation rates which led to increased salinities of bottom- and surface waters > 50‰ between 23,000 and 13,000 ^{14}C-yr in the Sudanese Red Sea (B). Under such conditions biogenic carbonate production became restricted and an aplanktonic interval established, which was characterised by a monospecific occurrence of the epipelagic pteropod *Creseis acicula*. Reduced pelagic and shallow-water input favoured inorganic carbonate precipitation on the shelf which led to submarine lithification and the formation of lithified layers (e.g. Brachert 1999). The hypersaline phase was followed by a more humid phase between 13,000 and 8,500 ^{14}C-yr (A). The formation of a pycnocline caused stagnation and oxygen depletion of deeper-water masses of the Sudanese shelf, which led to the deposition of a sapropel and a better preservation of aragonite (e.g. Almogi-Labin *et al,* 1991), which is indicated by increased TOC-values and a significant aragonite peak in the periplatform record.

planktic foraminifers. The top of this „aplanktonic interval“ falls at the boundary between IS 2 and the Holocene at about 11-12,000 SPECMAP-yr. Nevertheless, in sediments on the Sudanese shelf planktic foraminifers occur in great abundances directly above the top of the lithified interval.

The top of the lithified interval in the studied cores from the Sudanese shelf is clearly bordered by the sapropel layer. The onset of the last lithification phase, however is difficult to determine and to date, because of the isolated occurrence of thin lithified layers below the main interval. In literature ages for the onset of the last lithification phase in the Red Sea range from about 26,000 to 17,300 ^{14}C-yr (Tab. D.2-2).

On the Sudanese shelf the base of the lithified interval was dated on lithified chips at 22,200±200 ^{14}C-AMS yr in core S1. However, in core S6 the first occurrence of lithified sediments at the base of the lithified interval was dated at 24,670±220 ^{14}C-AMS. Older ages found in core S6 might be explained by the admixture of older shallow-water components, which occur frequently in the dated sample. Despite this time difference the onset of the phase of primarily aragonite precipitation was dated at 19,540±130 and 18,920±110 in core S1 and S6, respectively.

Thus, it was show in correspondence with the ages given by Almogi-Labin *et al.* (1991) that the last phase of submarine lithification on the Sudanese shelf occurred between about 13,000 and 22-23,000 ^{14}C yr which covers most of IS 2.

Table D.2-2: ^{14}C-ages of the lithified interval compiled from the literature

Author	**Top**	**Base**
Milliman *et al*. (1969)	11,000	20,000
Locke (1986); Locke & Thunell (1988)	11,000	18,000
Stoffers & Botz (1990)	4,670	26,000
Almogi-Labin *et al*. (1991)	13,000	23,000
Hofmann *et al*. (1998)	15,200 12,900	20,640 (axial zone) 17,323 (Sudanese shelf)
This study	13,000	22-23,000 (HMC and aragonite) 19,000 (aragonite crust)

Time offsets and age-inversions

Between 19,280±150 and 13,310±80 ^{14}C-AMS yr - the interval of maximum aragonite precipitation in core S1 - the ^{14}C-AMS ages analysed on unlithified fine fraction are on average 500-1,500 yr older compared to those for lithified samples (see Fig. C.2-3). The time offsets can be explained by (1) an increased admixture of older detrital sediment in the unlithified fine fraction and (2) a postdepositional diagenetic overprint caused by a later cementation of the lithified sediments. The admixture of older detritic sediment is supported by a much higher quartz content of the unlithified fine fraction in comparison to the lithified sediment (Fig. C.7-4, Chapter C.7.4.3). It is assumed that older carbon of terrestrial sources was transported simultaneously with the siliciclastic detritus from the Sudanese hinterland onto the shelf.

Other remarkable features are four age inversions, which occur in both time series of core S1, but not in core S6, possibly because of the lower sampling resolution in this core (Fig. C.2-3). The major age inversion occurs within a depth interval of only 30 cm (105 to 75 cm), in which ages of the lithified samples and unlithified fine fraction drop from 19,540±130/19,380±150 to 13,940±100/ 15,330 ^{14}C-AMS yr and increase up-core again to 17,010±130/16,930±150 ^{14}C-AMS yr. The simultaneous occurrence of the age inversions in both time series excludes an analytical error and indicates that the same process must have influenced the lithified sediments and the unlithified fine fraction. This also indicates that submarine cementation of the lithified sediments could not have caused these age inversions. It is most likely that bioturbation, reworking processes or partially destruction of the sediment sequence by the coring process caused the inversions.

D.2.4.2 Oxygen isotopes and salinities of the lithified interval (IS 2)

It is widely accepted that the heavy isotopic composition of the lithified sediments indicates high salinities of Red Sea waters during the last glacial sealevel lowstand of IS 2 (e.g. Deuser & Degens, 1969; Milliman, 1977; Brachert, 1996, 1999) (Tab. D.2-3 and D.2-4). Those increased salinities caused inorganic carbonate precipitation and cementation at the seafloor and led to restriction of the Red Sea fauna (e.g. Berggren & Boersma, 1969; Gvirtzman *et al.*, 1977; Reiss *et al.*, 1980; Taviani, 1998a; b). In addition, low sedimentation rates caused by reduced biogenic carbonate input favoured inorganic carbonate precipitation (Brachert, 1996, 1999).

Heaviest δ^{18}O values of 5-7‰ found in lithified samples of the cores studied are in good accordance with highest values given in the literature (Tab. D.2-3). The clear correspondence of the highest aragonite percentages with the heaviest oxygen isotope values in the lithified samples (Fig. C.7-4, Chapter C.7.3) give evidence for enhanced aragonite precipitation during times of increased bottom-water salinities. Salinities of bottom-waters reached a maximum of 57.5‰ at 14,840±110 ^{14}C-AMS yr when restriction of the basin reached its maximum during the sealevel lowstand.

Table D.2-3: Stable isotopic composition of lithified samples from the Red Sea

Author	**Location**	**min.** δ^{18}O	**max.** δ^{18}O	**min.** δ^{13}C	**max.** δ^{13}C
Stoffers & Botz (1990)	entire Red Sea	-1.3	+7.1	-6.0	+4.0
Brachert (1996, 1999)	Sudanese shelf	+4.6	+5.6	+3.0	+3.9
Taviani (1998c)			+6.6		+3.7
Hofmann *et al.* (1998)	Sudanese axial zone and shelf	+4.6	+7.0	+2.5	+4.2
This study: lithified	Sudanese shelf	+3.4	+7.0	+2.7	+4.3
This study: mud	Sudanese shelf	+3.0	+4.6	+1.5	+2.5

Much lighter values were analysed on the unlithified fine fraction. Here the δ^{18}O values vary between 3.0 and 4.6‰. When these values are corrected for the fractionation-effect of aragonite and HMC during precipitation (see Equ. B-2, Chapter B.2.3.5) they range between -0.2 and +3.1‰

(core S1). Higher values between +2.0 and +3.0‰ are found for the majority of the samples and are in good accordance with theoretic $\delta^{18}O$ values of *G. ruber* tests (LMC) that formed in equilibrium with glacial Red Sea surface-waters (Hemleben *et al.*, 1996). This indicates that the unlithified fine fraction formed in equilibrium with Red Sea surface-waters.

Besides differences in absolute oxygen isotope values between lithified and unlithified sediments the $\delta^{18}O$-maximum of the unlithified samples occurs at 19,280±150 ^{14}C-AMS, about 5,000 yr earlier than the maximum in the lithified samples. This time difference might be caused by a post-depositional cementation of the lithified sediments in equilibrium with hypersaline bottom-waters. It is likely that large portions of the unlithified and lithified sediment already formed in a first stage through in-situ precipitation from the water column in a similar process as the present-day whitings in the Bahamas and the Trucical Coast of the Persian Gulf (e.g. Milliman *et al.*, 1993). Such an early precipitation phase is indicated by highest $\delta^{18}O$-values of the unlithified samples between 19,280±150 and 20,420±130 ^{14}C-AMS yr which corresponds to highest salinities of surface waters of 50-51‰. The constant decrease in oxygen isotope values of the unlithified series after this maximum points to increasing humidity and temperatures of surface waters since about 18,000-19,000 SPECMAP-yr in the Red Sea (CLIMAP Project Members, 1981; Thunell *et al.*, 1988; Almogi-Labin, *et al.*, 1998; Geiselhardt, 1998).

Table D. 2-4: Salinities and temperatures of Red Sea waters during IS 2

Author	**Method**	**Location**	**Salinity (‰)**	**Temp. (°C)**
Assaf & Hecht (1974)	sea-strait model		50	
Reiss *et al.* (1980)	plankt. distribution	Gulf of Aqaba	>50 (surface)	min. 4°C drop (winter)
CLIMAP (1981)				2°C drop
Halicz & Reiss (1981)	foram distribution $\delta^{18}O$ (foram)	Gulf of Aqaba	>50 (surface)	15-17
Winter *et al.* (1983)	$\delta^{18}O$ microfoss. distrib.		>50 (surface)	
Ivanova (1985)	plankt. distribution	Entire Red Sea	high	5°C drop
Locke & Thunell (1988); Thunell *et al.* (1988)	plankt. and benth. faunal distribution.	Central Red Sea	8.5‰ higher than present	2°C drop
Almogi-Labin *et al.* (1991)	$\delta^{18}O$ (plankton)	Central Red Sea	48 (surface)	
Hemleben *et al.* (1996)	$\delta^{18}O$ benth. foram $\delta^{18}O$ pteropods	Central Red Sea	53-55 (surface and bottom)	
Emmermann *et al.* (1997; 1998); this paper,	$\delta^{18}O$ (crust, mud)	Sudanese shelf	57.5 (bottom) 51 (surface)	21 21
Geiselhardt (1998)	$\delta^{18}O$ (foram)	Northern Red Sea Southern Red Sea	57 (surface) <49 (surface)	20
Brachert (1999)	$\delta^{18}O$ (crust)	Sudanese shelf	44-53 (bottom) 43-52 (bottom)	21 19

D. 2.4.3 Mechanisms of submarine lithification

The data obtained from three sediment cores from the Sudanese shelf confirm a two-phase (inorganic) precipitation model for the formation of the lithified layers as suggested by Brachert (1996; 1999) and Hofmann *et al.*, (1998). Aragonitic spherolites are widespread in the lithified and unlithified sediments from the Sudanese shelf and suggest a first nucleation phase in the water column. Hofmann *et al*. (1998) described the origin of the spherolites as microbial aggregates which had formed the original precipitation nuclei. At present stellate aragonite precipitates from hypersaline Dead Sea waters (Neev & Emery, 1967) which show comparable fabrics to the spherolites of the Red Sea. Fringes of aragonite occur on the outer walls of pteropod shells and interlock with the spherolites or the cryptocrystalline matrix. These fabrics give clear evidence for a second phase of submarine cementation.

The mineralogical data suggest sedimentation/precipitation cycles which were terminated each by a phase of significantly increased detritic input as shown by the higher quartz and LMC content in the unlithified layers. These input variations might have caused the ultimate alternation of lithified layers and unlithified mud.

In the sediment cores obtained from the Sudanese shelf as well as cores described in the literature most of the lithified layers are broken into chip-like fragments. This brecciation was simply explained as destruction during the coring process (e.g. Taviani, 1998c), but Brachert (1996) showed that some of the chips are surrounded by tube-like encrusters, suggesting that the lithified layers were already brecciated at the seafloor. It is likely that earthquakes, which are common in the Red Sea region (the most recent earthquake occurred in November 1995, Dullo & Montaggioni, 1998) caused the brecciation of the brittle crusts on the seafloor.

Switch from magnesium calcite to aragonite precipitation

Stoffers & Botz (1990) studied the mineralogical and geochemical composition of lithified layers from 27 cores covering most of the Red Sea between about 16.5°N and 26°N. They found that HMC is the dominating mineral phase in most of the crusts, which cover an age interval from about 5,000-26,000 ^{14}C-yr. Aragonite is the prevailing carbonate mineral in the crusts from the Sudanese shelf with an average of 77%, which is clearly increased when compared to analysed values in normal periplatform sediments (52%). HMC is more abundant in the lower and less lithified parts that formed between 22,200±200 and 19,540±130 ^{14}C-AMS yr, where it reaches an average of 35% of the carbonate-fraction instead of 12% in the stronger lithified interval above. These data confirm the observation that the older lithified layers within the lithified interval generally contain more HMC, which was thought to be an inversion product of primarily precipitated aragonite (Milliman *et al*., 1969). However, the parallel trends of the δ^{18}O- and the aragonite curve of the lithified samples in core S1 suggest that the rise in bottom-water salinities led to a constant increase of the aragonite/Mg-calcite precipitation ratio (Fig. C.7-4, Chapter C.7.3).

In contrast, HMC-rich and not aragonitic crusts formed in the Mediterranean during the last glacial sealevel lowstand in cold, hypersaline bottom-waters (Bernoulli & McKenzie, 1981; McKenzie & Bernoulli, 1982; Aghib *et al*., 1991; Allouc, 1990). The examples from the

Mediterranean show that not only salinity but also water temperature controls if aragonite or HMC precipitates. The temperature of Red Sea bottom-waters were extremely warm and ranged between 19-21°C throughout the peak glacial (CLIMAP Project Members, 1981; Thunell *et al*., 1988). A constant increase in water-temperature since about 19,000 SPECMAP-yr might have favoured the increased precipitation of aragonite, under hypersaline bottom-water conditions. This temperature increase and the continuous rise of bottom-water salinity could have caused a switch in the precipitation mode from HMC-rich to aragonite dominated lithified layers as shown by the sudden increase in aragonite percentages since 19,540±130 ^{14}C-AMS yr.

Aragonite precipitation in the Red Sea was restricted to the peak glacials when salinities exceeded a certain limit (50 to 51‰). During glacial isotope stage 4 only Mg-calcite precipitated from bottom-waters (Milliman *et al.*, 1969; Milliman, 1977; Ellis & Milliman, 1985). In this period Red Sea salinities did not exceed 49‰ as obtained from δ^{18}O-analysis of planktic foraminifers (Tab. D.2-1).

Siliciclastic input prevents submarine lithification

Low sedimentation rates are a prerequisite for hard-ground formation and submarine lithification and preferentially occur during lowstands and transgressive phases (e.g. Sarg, 1988). In the Red Sea inorganic precipitation of carbonate and submarine cementation occurred when pelagic sedimentation rates dropped as a consequence of the restricted plankton productivity during the high salinity phase of IS 2 (Brachert, 1999).

Quartz intensities are more than 10-times lower in lithified sediments compared to the unlithified fine fraction (Fig. C.7-4, Chapter C.7.4.3). Therefore, it is likely that short phases of increased siliciclastic input during an interval of generally low pelagic sedimentation rates prevented submarine lithification of individual layers and caused the ultimate alternation between lithified and unlithified sediments.

Sedimentation rates of the lithified interval

In spite of the low biogenic carbonate production during IS 2, the average deposition rates of the lithified interval on the Sudanese shelf are close to or exceed interglacial sedimentation rates. The deposition rates calculated for the lithified interval vary between 4.5 and 10 cm/ky, which is in good accordance with rates calculated by Hofmann *et al*. (1998) and Brachert (1999) and with average rates of pelagic sedimentation in the Red Sea during the late Quaternary, which lie between 3 and 10 cm/ky (Taviani, 1998c).

The high deposition rates of the lithified interval show that inorganic precipitation and cementation of carbonates compensated the generally low pelagic and shallow-water input, which was caused by the restriction of biogenic carbonate production during the aplanktonic interval of IS 2 (e.g. Reiss *et al.*, 1980; Winter *et al.*, 1983; Hemleben *et al.*, 1996). This shows that the formation of the lithified layers had a positive contribution to the bulk carbonate budget during times of low biogenic carbonate production.

D.2.4.4 Deglaciation and sapropel formation

The phenomenon of sapropel formation in the Red Sea, especially during the last deglaciation was already studied in great detail by e.g. Gevirtz & Friedmann (1966); Locke & Thunell (1988); Almogi-Labin *et al.* (1991) and Hofmann *et al.* (1998). The dark, about 3 to 5 cm thick, organic rich layer occurs on top of the lithified interval within the entire Red Sea in a water-depths < 800m (Herman, 1971; Besse & Taviani, 1982; Locke & Thunell, 1988; Hofmann *et al*., 1998; Taviani, 1998c).

In the Red Sea sapropel formation was not restricted to the last glacial and deglaciation and seems to be associated with times of bottom-water stagnation (Almogi-Labin *et al.*, 1991; Hofmann *et al.*, 1998; Locke & Thunell, 1988; Taviani, 1998c). In the cores at the Sudanese shelf, dark shales and organic rich sapropels are also interbedded in older sediments. Hofmann *et al.* (1998) documented that sapropel formation already occurred in the axial trough of the central Red Sea at about 15,200 ^{14}C-yr, whereas sapropel formation on the Sudanese shelf began at 12,900 ^{14}C-yr about 2,300 yr later after lithification had ceased. This is in good agreement with our data, which indicate that sapropel formation on the shelf started at 12,840±90 ^{14}C-AMS yr (unlithified fine fraction of core S1). The early sapropel formation in the trough might indicate that stagnation of bottom-water started somewhat earlier in the deeper parts and migrated to shallower water-depths with time.

Higher aragonite (70%) and TOC percentages (up to 2%) accompanied by a characteristic pteropod assemblage as well as the unusually good preservation of pteropod shells indicate low oxygen conditions of bottom-waters at times of sapropel formation (Almogi-Labin, *et al.*, 1991., Hofmann *et al.*, 1998; this study). A world-wide aragonite (pteropod) preservation spike was observed during the deglaciation which was caused by the drastic drop of the Aragonite Compensation Depth (ACD). During the deglaciation the ACD in the Western Indian Ocean is found in 2,500 m waterdepth, compared to a depth of 1,200 m during full glacial conditions (Berger, 1977).

However, for the Red Sea it was suggested that the deglaciation was marked by enhanced rainfall during a humid phase which led to the development of a pycnocline and to stagnation of bottom-waters. Bottom-water stagnation caused oxygen depletion which led to better preservation of aragonite and organic matter (Locke & Thunell, 1988; Almogi-Labin *et al*., 1991; Hofmann *et al*., 1998). Hofmann *et al.* (1998) showed that the high TOC content of the sapropel results from an increased input of organic matter of terrestrial sources caused by enhanced run-off from the mainland. This can be confirmed by the high siliciclastic content analysed in the sapropels of the studied cores.

Sapropel formation ended at 8,500 ^{14}C-yr when the humid phase over the Red Sea ceased and oxygenation of bottom and intermediate waters improved (Locke, 1986; Locke & Thunell, 1988; Almogi-Labin *et al*., 1991; Hofmann *et al*., 1998).

In contrast to the preservation model the data of this study point to another model to explain the high aragonite percentages found in the sapropel. It is obvious that the high aragonite values coincide with highest strontium concentrations within and on top of the sapropel (Fig. D.3-2 and D.3-4). Preservation of aragonitic, low-Sr pteropod shells could not explain this phenomenon. Therefore, it is suggested that reworking of inorganically precipitated aragonite from the lithified

interval and possibly diffusion of Sr into the sapropel is responsible for increased high-Sr aragonite content of the sapropel and not solely preservation. This is supported by the frequent occurrence of lithified particles within and above the sapropel.

Average bulk sedimentation rates of the sapropel on the Sudanese shelf are extremely low (1-1.6 cm/ky) when compared to normal periplatform sedimentation (4-9 cm/ky). The average values on the Sudanese shelf lie slightly below the sedimentation rates that were calculated by Almogi-Labin *et al*. (1991) for the central Red Sea (2.5-3 cm/ky). The low bulk sedimentation rates of the sapropel are in good accordance with the sequence stratigraphic model for siliciclastic shelf systems, which propose lowest sedimentation rates during sealevel rises (Sarg, 1988). Additionally, the high siliciclastic content indicates that pelagic- and shallow-water carbonate production and input were still low during the deglaciation following to the high salinity phase of IS 2.

Table D.2-5: Summary of submarine lithification (IS 2) and sapropel formation (deglaciation) on the Sudanese shelf

Age (^{14}C-yr)	**Lithology**	**Process**	**Sealevel**	**Oceanography/ Climate**	**Biota**
since 8,500	periplatform ooze	sedimentation of shallow-water grains and plankton	close to present level	similar to present	fully developed
13-8,500	sapropel	preservation peak of aragonite and organic matter	rise (deglaciation)	stagnating bottom-water during a pluvial phase	re-establishing after last glacial
19-13,000	(1) lithified aragonite layers	max. inorganic aragonite precipitation in supersaturated bottom- and pore-waters, secondary cementation	lowstand - initial rise	limited water exchange and high evaporation; increasing humidity and temperatures	aplanktonic zone, planktic forams rare or absent, limited benthic carbonate production
	(1b) aragonite chips	brecciation during early stages of lithification by earthquake shocks			
	(2) unlithified mud-layers	increased detritic sediment input prevents lithification of mud-layers			no clear evidence for shallow-water reef growth
	(3) frequent calciturbidites	shedding of older reef sediments			
23-19,000	HMC-rich lithified particles	early stage of lithification, submarine precipitation of aragonite and HMC in „cooler“ bottom-waters	fall-lowstand	high salinity due to basin restriction; maximum cooling and arid	
IS 3	aragonite- and organic-rich layers	preservation events	fall	abrupt monsoonal variations; stagnation vs. deep-water circulation	prolific benthic and pelagic carbonate production

D.3 Shallow-water sediment export and secondary signals

In this chapter the temporal and spatial variations in the aragonite/calcite-ratios of the periplatform sediments are discussed with respect to late Quaternary sealevel variations. At present it is still debated if the variations in carbonate mineralogy record (1) more or less primary shallow-water sediment export which can be altered by filtering processes during transport and/or (2) post- and syndepositional processes like dissolution or precipitation of metastable carbonates at the sea-floor or in the water-column (Fig. D.3-1).

The periplatform sediments on the Sudanese shelf record sediment input from three main sources (1) the shallow-water reefs (2) planktic organisms and (3) the Sudanese mainland and exposed shelf slopes (debris of older Pleistocene reefs and siliciclastic sediments; Fig. D.3-1). Changes in plankton productivity and terrigenous input caused variations in the mineralogy of the periplatform sediments which modified the shallow-water input signal.

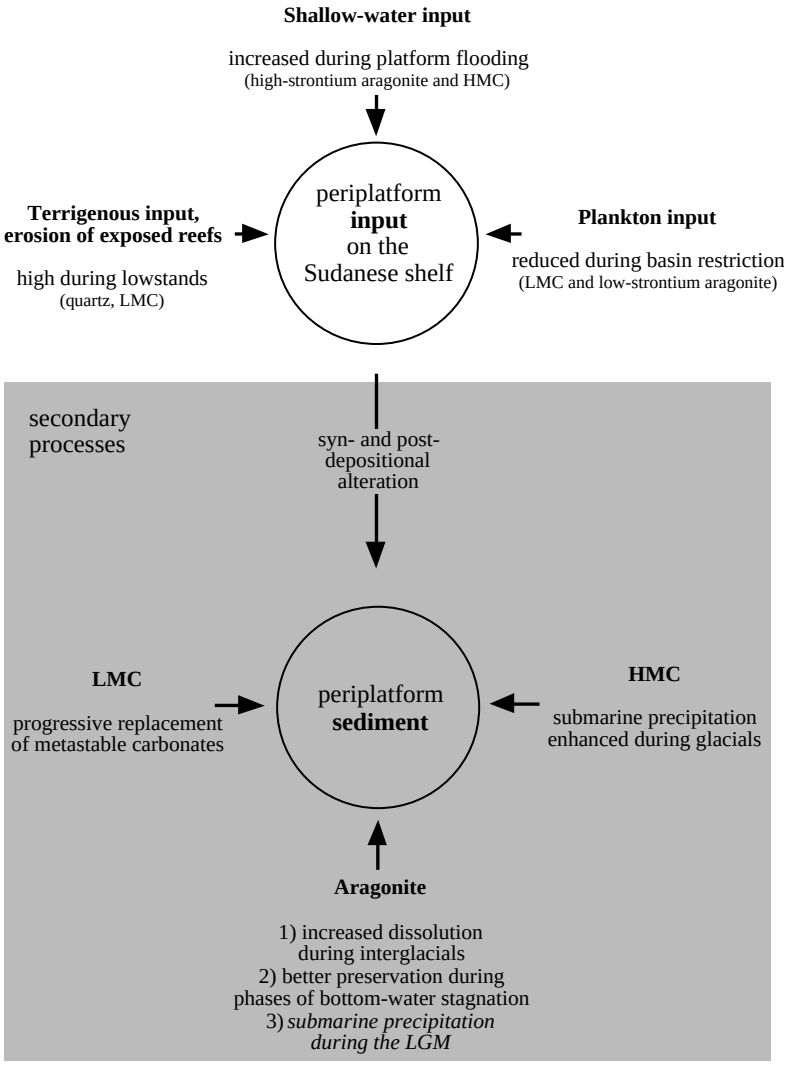

Figure D.3-1: Periplatform sedimentation model. The periplatform sedimentation on the Sudanese deep shelf is controlled by the interaction of three major input sources (1) the siliciclastic input, (2) the shallow-water carbonate production and (3) plankton input. The primary input signal is altered by various syn- and postdepositional processes like (1) inorganic precipitation of aragonite and HMC at the seafloor, (2) variations of the dissolution and preservation of aragonite and (3) progressive replacement of metastable carbonates by LMC with time. The graph illustrates the most important controlling factors of periplatform sediment composition.

D.3.1 Aragonite/Calcite ratios

In Fig. D.3-2 the stacked curves (average of individual cores) of the carbonate mineral distribution in the periplatform sediments from the Sudanese shelf are shown.

The curves of aragonite percentages of bulk sediment and fine fraction run parallel to the $\delta^{18}O$-curves of planktic foraminifers (Fig. D.3-2). This was also shown for other late Quaternary periplatform sediments from e.g. the Bahamas, the Maldives, the Caribbean and the Queensland Trough (Droxler, 1986; Boardman *et al*., 1986; Droxler *et al*., 1988, 1990; Reijmer *et al*., 1988; Glaser, 1991; Glaser & Droxler, 1991; Alexander, 1996; Emmermann *et al.*, 1999; Rendle *et al.*, in press, 2000). Increased aragonite percentages coincide with lighter values in the isotope records. This is not only valid for glacial-interglacial changes but also for smaller scale variations within the isotope stages as shown for IS 3 (Chapter D. 2.3). It is remarkable that the percentages of aragonite are not significantly higher in interglacial highstand deposits (IS 5 and Holocene) when compared to glacial isotope stage 3, which would be expected following the highstand shedding theory. Such deviations can be explained by a generally increased aragonite dissolution during interglacials in the Red Sea (Almogi-Labin *et al*., 1991) and the Indo-Pacific realm (Volat *et al*., 1980; Broeker 1995). Minima in the aragonite curves generally correlate with heavier oxygen isotope values, except for in the lithified interval. Here higher aragonite values are mainly due to inorganic precipitation at the seafloor. Higher aragonite values are also found during phases of increased aragonite preservation, as demonstrated for the sapropel that formed during the last deglaciation on the Sudanese shelf (Chapter D. 2.4).

Another striking feature within the aragonite/calcite curves from the Sudanese shelf is that HMC runs anti-parallel to the aragonite- and $\delta^{18}O$-records (Fig. D.3-2). HMC peaks when aragonite shows a minimum and vice versa. The absolute maximum in the HMC record is found during glacial IS 4 and not during the LGM, when aragonite precipitation dominated (Chapter D. 2.4). The anti-cyclicity between aragonite and HMC was also observed at other periplatform sites like the Bahamas (Droxler, 1986) and Pedro Bank, Nicaragua Rise (pers. com. Nils Andresen, GEOMAR) and was interpreted as enhanced precipitation of HMC during glacial phases in water depth below 1000 m (Droxler, 1986). Furthermore, it is surprising that aragonite is the dominant mineral phase in the periplatform sediments even though HMC dominates over aragonite in the Red Sea shallow-water reef sediments (Aboul-Basher, 1980; Piller & Mansour, 1990).

The stacked LMC-curve records main glacial-interglacial variations in eustatic sealevel and shows a constant increasing trend with depth in core. LMC maxima during IS 3 are found 2-3,000 yr after highstands in the sealevel curve of New Guinea (Chappell & Shackleton, 1986). The same kind of offsets is observed for the last interglacial substage 5a, where the LMC maximum occurs at 77,000 SPECMAP-yr, 3,000 yr after isotopic event 5.1 at 80,000 SPECMAP-yr (Fig. D.3-2). Substages 5c and 5e coincide with further maxima on the LMC curve without significant offsets. The lowest LMC percentages clearly coincide with the last glacial sealevel lowstand (IS 2) and prevail during the entire aplanktonic interval (Reiss *et al.*, 1980). Thus, variations in LMC percentages record changes in plankton productivity which is strongly connected to Red Sea surface-salinities and to eustatic sealevel variations.

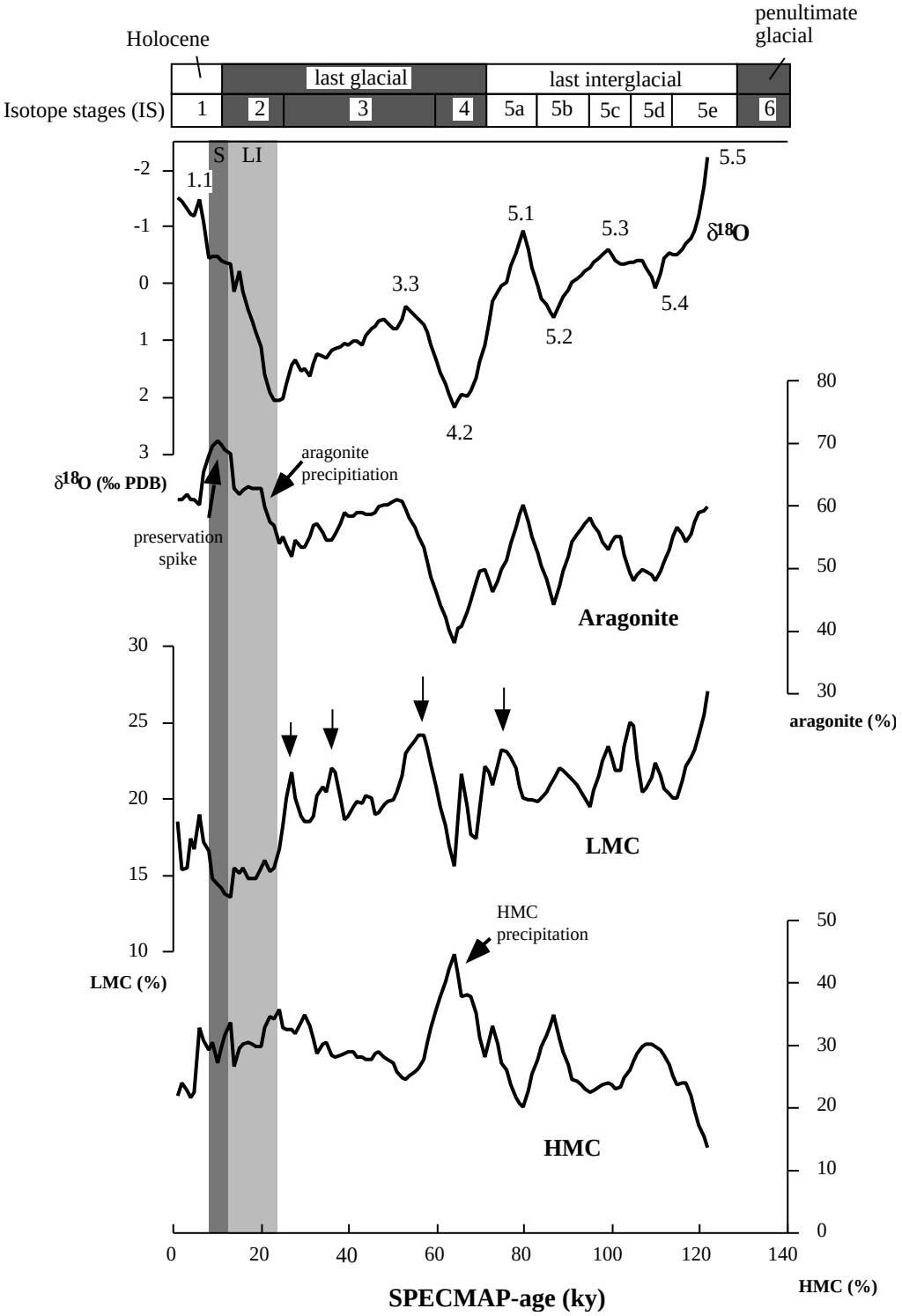

Figure D.3-2: Stacked curves of carbonate mineral distribution in periplatform sediments from the Sudanese shelf (Sanganeb Atoll and Abington Reef). Standard deviations are shown in Appendix 4.-D The aragonite curve clearly resembles the stacked oxygen isotope curve but shows a significant preservation spike between 13,000 and 8,500 ^{14}C-yr (sapropel, arrow). Aragonite percentages during interglacial sealevel highstands do not exceed values found in IS 3, which suggests increased aragonite dissolution during interglacials out of phase with highstand shedding. The HMC stack shows an anticyclic pattern to the aragonite curve and reaches a maximum during IS 4, probably due to enhanced precipitation of Mg-calcite during this sealevel lowstand. This is not the case during IS 2 when inorganic precipitation was dominated by aragonite. The LMC-stack which can be seen as a signal of plankton productivity also shows glacial-interglacial variations. The arrows point to maxima in the LMC-record that occur 2,000-3,000 yr after the highstands indicated in the New Guinea sealevel curve during IS 3 (Chappell & Shackleton, 1986) and during IS 5a, while maxima during IS 5c and 5e shown no significant offsets to the corresponding highstands. The LMC minimum coincides with the aplanktonic interval (LI). Generally LMC increases with depth in core, which suggests a progressive replacement of the metastable carbonate minerals with depth in core and explains the low Holocene values. S = sapropel, LI = lithified interval.

The average aragonite/calcite ratios of a large number of late Quaternary periplatform sediments are shown in Tab. D.3-1, together with the data of the periplatform sediments from the Sudanese shelf and those of pelagic carbonate ooze from the main trough of the deeper Red Sea. Most of the literature data are given in percent of the carbonate fraction but also as the percentage of the fine carbonate fraction and even as the percentage of the clay-sized fraction of the total sediment (Boardman *et al*., 1986). In the periplatform sediments from the Sudanese shelf no significant differences between the carbonate-mineral percentages of fine fraction (< 63 µm) and bulk sediment were found. The average aragonite/calcite ratios of the literature data were calculated for a time-interval that can be compared with the record from the Sudanese Red Sea, which reaches back to IS 6 at maximum. This is essential if general trends between different sites are compared.

Table D.3-1: Mineralogy of periplatform sediments compiled from literature

Mineral abundances in percent

Location	Core	Author	Water-depth	Interval	Arag.	HMC	Arag. +HMC	LMC
Bahamas, TOTO	GS 7705-34	Droxler *et al.* (1983)	1935m	126 ky	50.7			
Bahamas, TOTO	5 cores	Droxler & Schlager (1985)	720-740m	IS 6/7	57.6	9.5	67.1	32.9
Bahamas, LBB		Mullins (1984)	850m	IS 5/6	46.5	17.7	64.2	35.8
Bahamas, NW-Prov.Ch.		Kenter, (1985)	675m	IS 5/6	43.7	15.8	59.5	40.4
Bahamas, NW-Prov.Ch.	CH-8201-07	Boardman*et al.* (1986)	675m	IS 6.2	42.6	17.9	60.5	
Bahamas, Nicholas Ch.		Droxler (1986)	610m	IS 5/6	54.3	16.9	71.2	28.8
Bahamas, Exuma Sound		Droxler (1986)	655m	IS 5/6	62.5	24.1	86.6	13.4
Bahamas, Exuma Sound	Hole 632A	Reijmer *et al.* (1988)	1996m	IS 6.2	41.3	24.0	65.3	38.6
Maldives	Hole 716B	Droxler *et al.* (1990)	540m	IS 6.2	65.4	9.1	74.5	25.5
Jamaica shelf	PC-21	Glaser & Droxler (1991)	570m	IS 6.2	68.8	16.8	85.6	14.4
Pedro Bank	PC-89	Glaser & Droxler, (1991)	450-570m	IS 6.2	66.4	15.1	81.5	18.5
Queensland Trough	Hole 823	Alexander (1996)	1638m	IS 6	40.6			
Red Sea, Abington Reef	AL	this study	498m	IS 5.2	60.8	23.8	84.6	15.4
Red Sea, Abington Reef	AW	this study	513m	IS 6.2	53.4	23.9	77.3	22.7
Red Sea, Sanganeb Atoll	S1	this study	771m	IS 5.2	45.1	30.4	75.5	24.5
Red Sea, Sanganeb Atoll	S2	this study	810m	IS 4.2	56.9	24.2	81.1	18.9
Red Sea, Sanganeb Atoll	S3	this study	757m	IS 4.2	59.0	26.0	85.0	15.0
Red Sea, Sanganeb Atoll	S6	this study	744m	IS 4.2	56.6	21.7	78.3	21.7
Red Sea, shelf-deep sea	V14-115/123	Gevirtz & Friedman (1966)	384-1737m		7.3	32.7	40.0	60.0
Red Sea, deep sea	CH61-153	Locke & Thunell (1988)	2704m	18 ky	24.2	30.2	54.4	46.6

D.3.1.1 Sources of aragonite in the periplatform sediments

Aragonite in periplatform sediments of the Sudanese shelf is derived from three different sources: (1) shallow-water skeletal grains, non-biogenic components and cements (2) submarine precipitation from the water-column and seafloor cementation and (3) shells of planktic pteropods. Primary input and precipitation are strongly influenced by post-depositional dissolution of the metastable aragonite at the seafloor. It is important to mention that in the Red Sea aragonite dissolution is not in phase with the shallow-water export signal. Generally aragonite-dissolution is higher during interglacials and reduced during glacials (e.g. Almogi-Labin *et al*., 1991, 1998). This is opposite to the dissolution pattern found in the Atlantic realm, where aragonite dissolution is in phase with the shallow-water export (e.g. Droxler & Schlager, 1985). Therefore, the shallow-water aragonite export signal is enhanced by submarine dissolution in the Bahamas and the Caribbean, whereas in the Red Sea and the Indo-Pacific glacial-interglacial differences in shallow-water export become equalised by later dissolution processes. This is clearly indicated by similar aragonite percentages found in glacial (IS 3) and interglacial periplatform sediments on the Sudanese shelf (Fig. D.3-2).

However, the overall average aragonite content of late Quaternary periplatform sediments (Present up to IS 7) ranges between 40 and 70% (Tab. D.3-1) and is in good correspondence to the Red Sea values (45 to 60%).

High- and low strontium aragonite

In order to separate aragonite of shallow-water sources from aragonite of other sources the high-Sr aragonite content was calculated. Aragonitic shallow-water components are generally enriched in strontium with concentrations exceeding 7,000 ppm (Milliman, 1974; Morse & Mackenzie, 1990). Therefore, the carbonate fraction of periplatform sediments is enriched in „high-strontium“ aragonite when compared to pelagic carbonate ooze (Boardman *et al.*, 1986; Alexander, 1996). The strontium content of important carbonate components is summarised in Tab. D.3-2.

Averages strontium concentrations within the carbonate fraction of the periplatform sediments from the Sudanese shelf lie at about 3,000 ppm, within a range from 1,500 ppm to 6,500 ppm. They fall in the same range as periplatform sediments from the Queensland Trough (Alexander, 1996) but are significantly lower than sediments from the Bahamas, which reach average values of about 4,700 ppm (Boardman *et al*., 1986) (Fig. D.3-3).

Lower strontium concentrations in Red Sea periplatform sediments might be caused by the predominately skeletal origin of the shallow-water, reef-derived grains (Piller & Mansour, 1990; Piller, 1994; Brachert, 1999;) and the limited abundance of green algae, like *Halimeda* or *Penicillus* (Gabrié & Montaggioni, 1982; Piller, 1994). Major contributors to high-strontium aragonite in the Bahamas, like for example ooids, *Halimeda* plates, and inorganic precipitated aragonite (whitings, e.g. Milliman, 1993) are less abundant or even absent in the Red Sea. This was confirmed by the quantitative microfacies analysis of the periplatform sediments at Sanganeb Atoll.

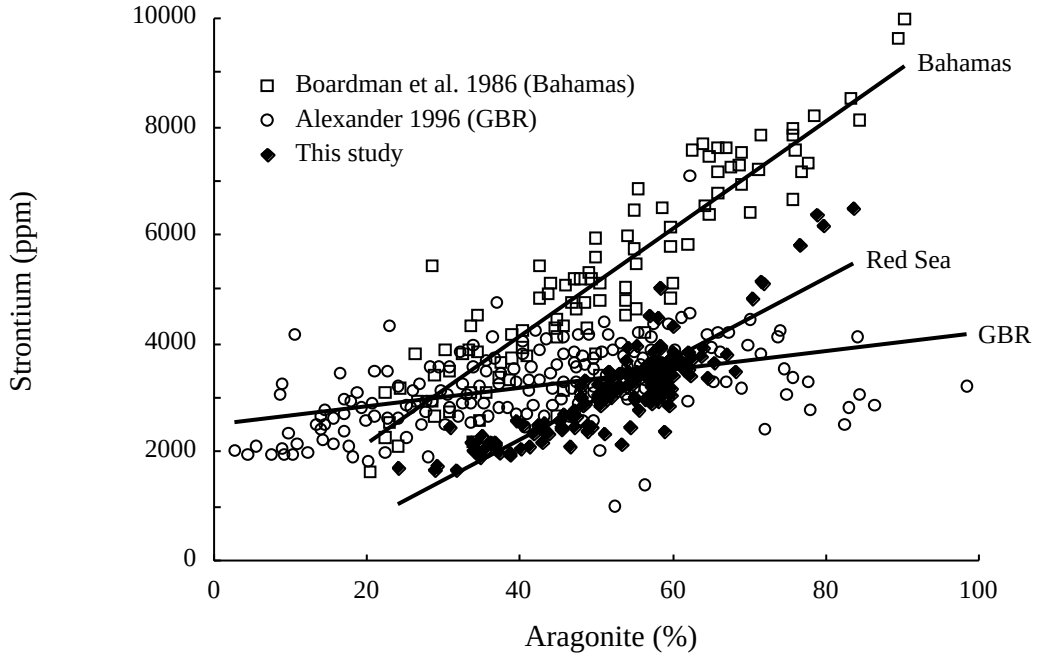

Figure D.3-3: Aragonite vs. strontium concentrations of periplatform sediments from the Sudanese shelf (this study) compared to the Bahamas (Boardman *et al*., 1986) and the Queensland Trough, Australia (Alexander, 1996). The Bahamian Sr- and aragonite values clearly exceed those from the Red Sea and the Queensland Trough, which is due to a higher abundance of high-Sr-aragonite components in the Bahamian bank-top sediments when compared to reef dominated systems like the Grear Barriere Reef and the Red Sea, with a dominant skeletal carbonate production. Red Sea reef sediments contain an average of 5,000-5,700 ppm Sr (El Sayed, 1984; Piller & Mansour, 1990), whereas the values found in periplatform sediments are clearly reduced and lie at 3,000 ppm on average. The difference is explained as dilution by input of low-Sr components like planktic foraminifers, coccolithophorids or pteropods.

Table D.3-2: Mineralogy, strontium- and $MgCO_3$ content of carbonate sediment components

[+] from Milliman (1974); † in (Morse & Mackenzie (1990); * Aissaoui *et al*. (1986)

Component	Mineralogy	Strontium (%)[+]	Strontium average	$MgCO_3$ (mol %) shoal water †	$MgCO_3$ (mol %) general †
High-Sr, shallow-water components					
peloids	arag	0.8-1.0	0.9		
ooids	arag	0.94-1.06	0.97		
aggregates	arag	0.92-0.97	0.95		
Halimeda	arag		0.88		
Penicillus	arag		0.87		
Scleractinian	arag	0.68-0.95	0.83		5.9-16.7
Bryozoan	arag	0.54-0.87	0.7		
Serpulids	arag	0.65-1.0	0.82		
aragonite cements		< 1.0	0.9-1.0*	0-0.5*	
Low-Sr, HMC-rich shallow-water components					
Corallinacean	HMC		0.23	10-25	8.3-35
-articulate	HMC	0.14-0.21	0.18		
-crustose	HMC	0.23-0.41	0.27		
Benthic foram	HMC	0.15-0.2	0.18	1-15	
Bryozoan	HMC	0.19-0.4	0.27	0-11	0.2-13.1
Serpulids	HMC	0.17-0.37	0.27		
Echinoderms	HMC		0.22	10-15	
-Echinoids	HMC	0.14-0.2	0.16		4.8-19
HMC-cements		0.04-0.08	0.06	6-17*	
Low-Sr, shallow-water components					
Molluscs			0.19		
-Scaphopods	arag		0.19		
-Pelecypods	arag /LMC	0.03-0.3	0.17		0-3.6
-Gastropods	arag (LMC)	0.01-0.37	0.2		0-2.4
Low-Sr, plankton shells					
Planktic foraminifers	LMC	0.1-0.16	0.13	<1-2	
Coccolithophorids	LMC			<1-2	
Pteropods	arag	0.026-0.1	0.08		

Fig. D.3-4 shows the stacked high- and low Sr aragonite curves of the cores at Sanganeb Atoll. The high-Sr-aragonite curve runs parallel to the bulk-aragonite signal and shows an even better positive correlation with the original strontium curve, whereas the low-Sr-signal is different and shows partially opposite trends to the other curves. Therefore, the high-strontium aragonite signal in the periplatform sediments at Sanganeb Atoll was interpreted to some extend as the original shallow-water input signal. The primary shallow-water export variations of strontium and high-Sr-aragonite in tune with eustatic sealevel variations are influenced in the same way as the aragonite curves by secondary processes like dissolution, inorganic precipitation and preservation.

The significantly increased aragonite-, high-Sr-aragonite- and Sr-values within the sapropel on top of the lithified interval (Fig. D.3-4) point to a period of better preservation of high-Sr-aragonite. It is suggested that high-Sr-aragonite was enriched in the sapropel by infiltration of lithified particles from the top of the lithified interval. A minimum was found in the low-Sr-aragonite record of the sapropel , which indicates a relatively low content of pteropod aragonite despite the high aragonite preservation potential. This points to a relatively low input of pteropod shells during the deglaciation phase following the aplanktonic interval, which is also shown by the pointcount results (Fig. D.3-5A).

The distribution patterns of scleractinians, which indicate shallow-water sediment export, show similar trends as the high-Sr-aragonite signal (Fig. D.3-5B). The percentages of scleractinians are highest during most of IS 3 and are clearly reduced since about 30,000 SPECMAP-yr, during the peak glacial (IS 2) as well as during IS 4. Only a small increase in both proxies can be observed at the beginning of the Holocene. The high plankton input (low-strontium) as shown by pteropod and foraminifer abundances during the Holocene most likely diluted the original shallow-water input signal.

In core S1 (Fig. C.8-3) variations in the low-Sr-aragonite curve coincide with glacial-interglacial variations in the bulk-aragonite signal. This shows that the bulk-aragonite signal in the distal core S1 is strongly influenced by the input of low-Sr aragonite. Main contributors to the low-Sr-aragonite fraction are aragonitic pteropod and pelecypod shells. Thus, the low Sr-aragonite curves analysed for periplatform sediments from the Sudanese shelf record two signals (1) plankton productivity and preservation of pteropod shells, and (2) input and preservation of pelecypod shells that derived from the shallow-water. In the proximal core S6 the pteropod distribution pattern and the variations in low-Sr-aragonite show similar trends (Fig. D.3-5A). This might indicate that the low-Sr-aragonite signal predominantly resembles variations in pteropod productivity. Both proxies show that aragonite input by pteropods was lowest during the last glacial IS 2 even though the plankton assemblage was dominated by pteropods during this period (Reiss *et al.*, 1980; Hemleben *et al*., 1996). Pteropod frequency and percentages of low-Sr aragonite increased simultaneously at 8,000 SPECMAP-yr and give evidence for a fully re-established plankton production since this time in the Red Sea as suggested by Hemleben *et al*. (1996).

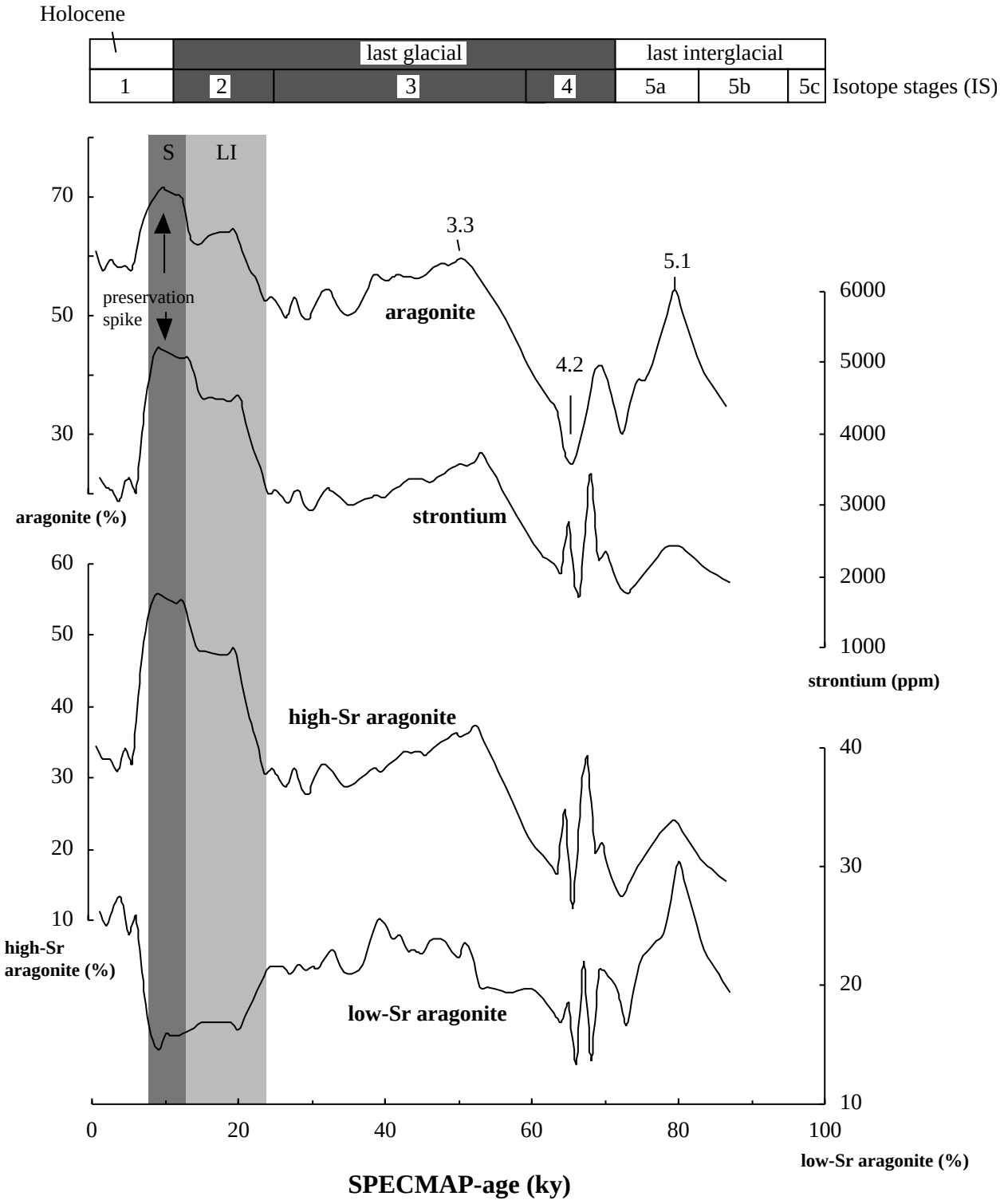

Figure D.3-4: Stacked low- and high-Sr aragonite curves of the periplatform sediments at Sanganeb Atoll in comparison with the stacked aragonite and strontium curve. Average values with stdev. are given in Appendix 5-C. The content of both aragonite-forms were calculated after the method of Kenter (1985) and Boardman *et al.* (1986). The high-Sr aragonite curve is nearly identical to the strontium curve and was interpreted as a signal of shallow-water sediment export variations, which was changed by later processes as shown for example by the preservation spike during the phase of sapropel deposition (arrow). The low-Sr-aragonite signal is predominantly shaped by the input of planktic pteropods but might also be influenced by shallow-water pelecypods. The increased values during IS 5a and the Holocene indicate increased plankton productivity during interglacials. S = sapropel, LI = lithified interval.

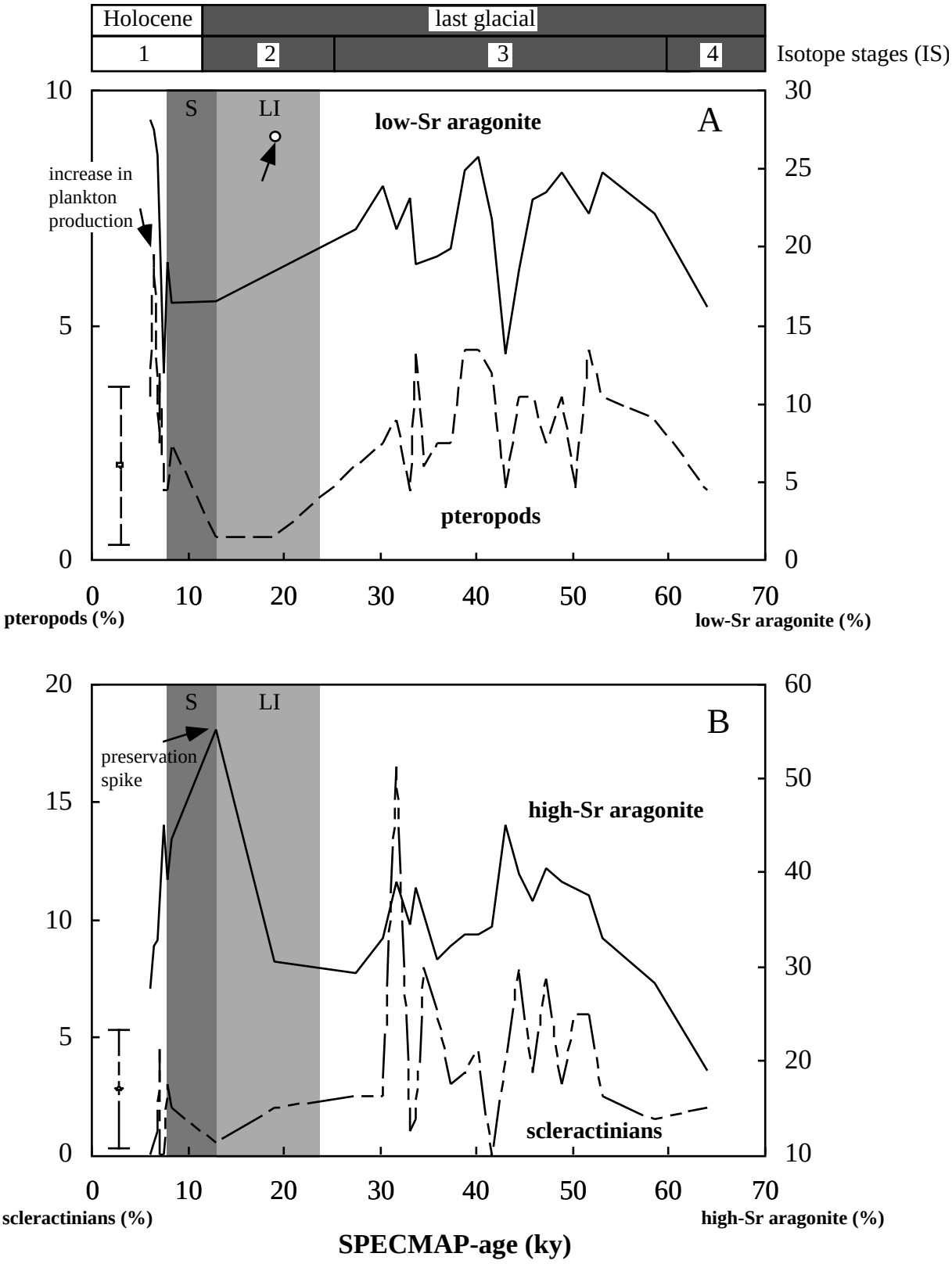

Figure D.3-5: (A) Comparison of low-Sr aragonite variations in core S6 with the pteropod shell abundances analysed by pointcounting. Both curves show similar trends, which confirms that the low-Sr-aragonite signal records pteropod input variations in the periplatform sediments. The arrow within the lithified interval points to an isolated datapoint. (B) Comparison of high-Sr aragonite in core S6 with the distribution of scleractinians in the periplatform sediments. Both proxies show a similar signal with increased values during IS 3, which suggests skeletal shallow-water sediment production and export during IS 3. Higher input of coarse grained shallow-water components during IS 3 when compared to the Holocene might have been caused by lower dilution with fine-grained aragonite during lowered sealevel. During the Holocene more fine-grained aragonite sediment was produced in the inner lagoon, while during lowered sealevel of IS 3 skeletal carbonate production prevailed along the outer slope of Sanganeb Atoll. Error bars show the maximum absolute error of pointcounting. S = sapropel, LI = lithified interval.

D.3.1.2 Sources of high-magnesium calcite and $MgCO_3$

The HMC content of periplatform sediments (Tab. D.3-1) varies between 9 and 24% with highest values in cores from Exuma Sound, Bahamas (Droxler & Schlager, 1985; Reijmer *et al*., 1988). The clearly higher HMC-content of periplatform sediments in the Red Sea (22-30%) is explained by (1) high HMC content of reefal sediments (> 50%) due to the high abundance of HMC-rich skeletal components, like for example coralline red algae (e.g. Aboul-Basher, 1980; Piller & Mansour, 1990) when compared to platforms like the Bahamas and (2) enhanced submarine HMC precipitation during glacial phases. Ellis & Milliman (1985) estimated that more than 50% of the deep Red Sea lutites are inorganically precipitated. In thin sections of the periplatform sediments of Sanganeb Atoll micropeloidal fabrics occur frequently in the micritic matrix (Fig. C.1-3). The same structures were described by Brachert (1999) in the sediments of the lithified interval. These are characteristic for an early stage of HMC cementation as observed on Bahamian slopes (Wilber & Neumann, 1993).

It still remains unclear what process caused the ultimate decrease in HMC when comparing the shallow-water values which can exceed an average of 50% of the carbonate fraction with the ones present in the periplatform sediments. It is remarkable that, even though HMC is more abundant in reefal sediments of the Red Sea, aragonite on average dominates in the periplatform sediments. This indicates a loss of HMC during downslope transport and before the ultimate deposition in the periplatform realm. Partially dissolution of the metastable Mg-calcite in the water column might have caused this phenomenon (Walter & Burton, 1990; Sabine & MacKenzie, 1995; Milliman *et al*., 1999). However, Mg-calcite is an important constituent of the periplatform sediments from the Sudanese shelf and has a significant influence on glacial-interglacial variations of the aragonite/ calcite ratios.

$MgCO_3$-content

The $MgCO_3$ content of the Mg-calcite in the periplatform sediments varies between 10 and 16 mol % (Fig. C.7-4, Chapter C.7.1.3), which falls in the range of modern shallow-water carbonate sediments (5 to 18%, average 14%; Morse & Mackenzie, 1990). Only a vague correlation between $MgCO_3$- and HMC content was found in the periplatform sediments as shown for core S1 (Fig. D.3-6). However, some of the major trends of the HMC signal are also visible in the $MgCO_3$ curve. The simultaneous increase in $MgCO_3$ and HMC during IS 4 is present in all cores and points to (1) increased input of $MgCO_3$-rich shallow-water components, like e.g. coralline red algae (10-25 mol % $MgCO_3$, see Tab. D.3-2) or (2) inorganic precipitation of $MgCO_3$-rich HMC at the seafloor. No evidence for increased shallow-water input during IS 4 was found in this study, whereas precipitation of $MgCO_3$-rich Mg-calcite during glacial periods was shown by many previous studies (Gevirtz & Friedmann, 1966; Milliman *et al*., 1969; Ellis & Milliman, 1985; Wilber & Neumann, 1993).

D.3.1.3 LMC- and plankton-variations

The average percentage of LMC is approximately 15 to 25% of the carbonate fraction. In contrast to the periplatform sediments on the shelf it clearly dominates in the pelagic carbonate ooze of the deeper Red Sea in which it reaches 47-60% of the carbonate fraction (Gevirtz &

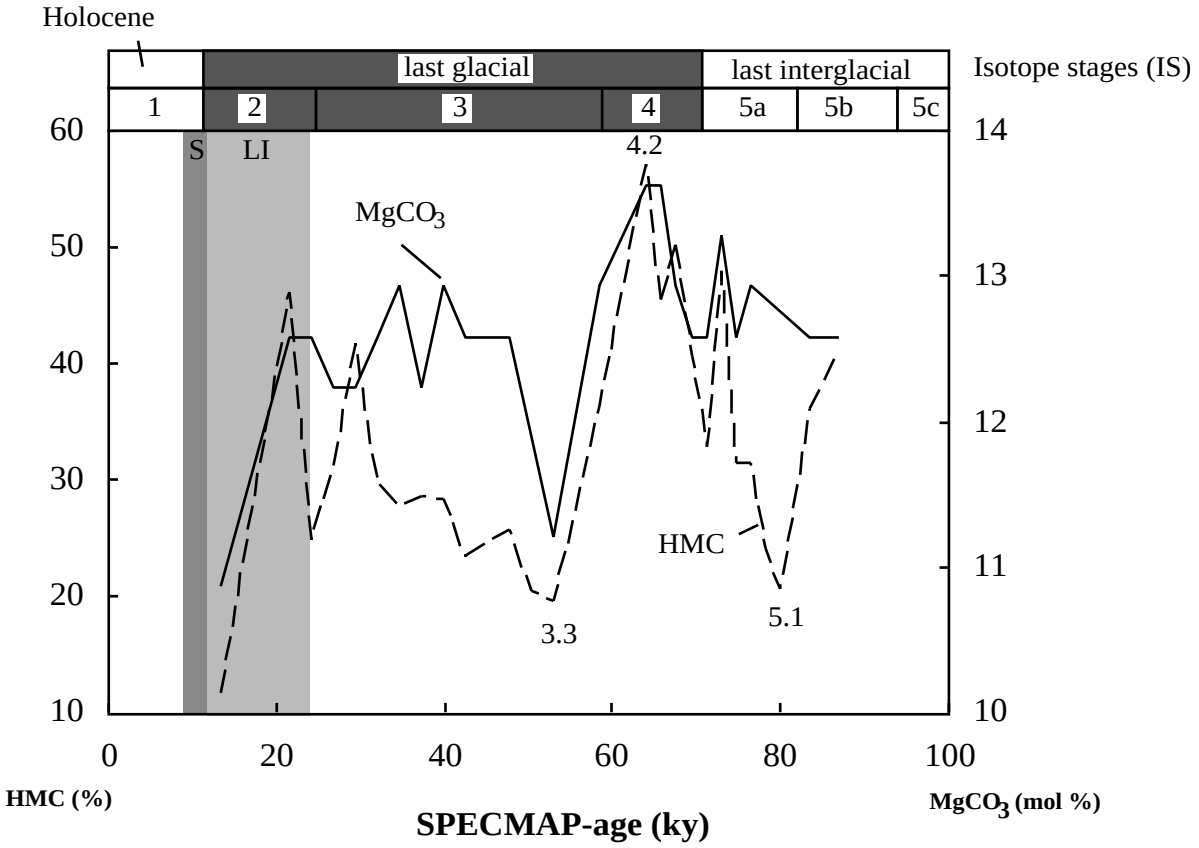

Figure D.3-6: $MgCO_3$ and HMC variations with time in core S1. Both curves show some similar trends and a clear increase during glacial isotope stage 4, which supports the idea of increased submarine precipitation of Mg-calcite during glacial sealevel lowstands. S = sapropel, LI = lithified interval.

Friedmann, 1966; Locke & Thunell, 1988). LMC contents in other periplatform sites are similar to those found on the Sudanese shelf, but are increased in Bahamian periplatform sediments where average values range between 30-40% (Tab. D.3-1).

Two important sources for LMC in the periplatform sediments are (1) shells of planktic foraminifers and coccolithophorids and (2) reworked carbonates from raised Pleistocene reefs along the Sudanese coast (Aboul-Basher, 1980). Such reworked carbonates were not found in thin sections, but it is possible that they exclusively contribute to the fine fraction. In the thin-sections meteoric calcite cements are also rare or absent and skeletal shallow-water components show more or less their primary shell structures.

Planktic foraminifer abundances show similar trends as the LMC-record and the $\delta^{18}O$-signal (Fig. D.3-7). This correlation indicates, that variations in the LMC curve mainly record changes in plankton productivity, which was clearly reduced during IS 2. In the Holocene periplatform sediments, however, the LMC values of the bulk carbonate fraction stay below values analysed in sediments of IS 3 and IS 5, even though the abundances of planktic foraminifers reached a maximum at 8,000 SPECMAP-yr (Fig. D.3-7). This might be explained by the simultaneously increased production and export of metastable carbonates as indicated by the high aragonite accumulation rates, which possibly diluted the LMC content (Fig. D.3-8). Furthermore, relatively low Holocene calcite values display the increasing trend with depth in core found in all LMC curves. Such a trend points to post-depositional displacement of the metastable carbonates aragonite and HMC by calcite.

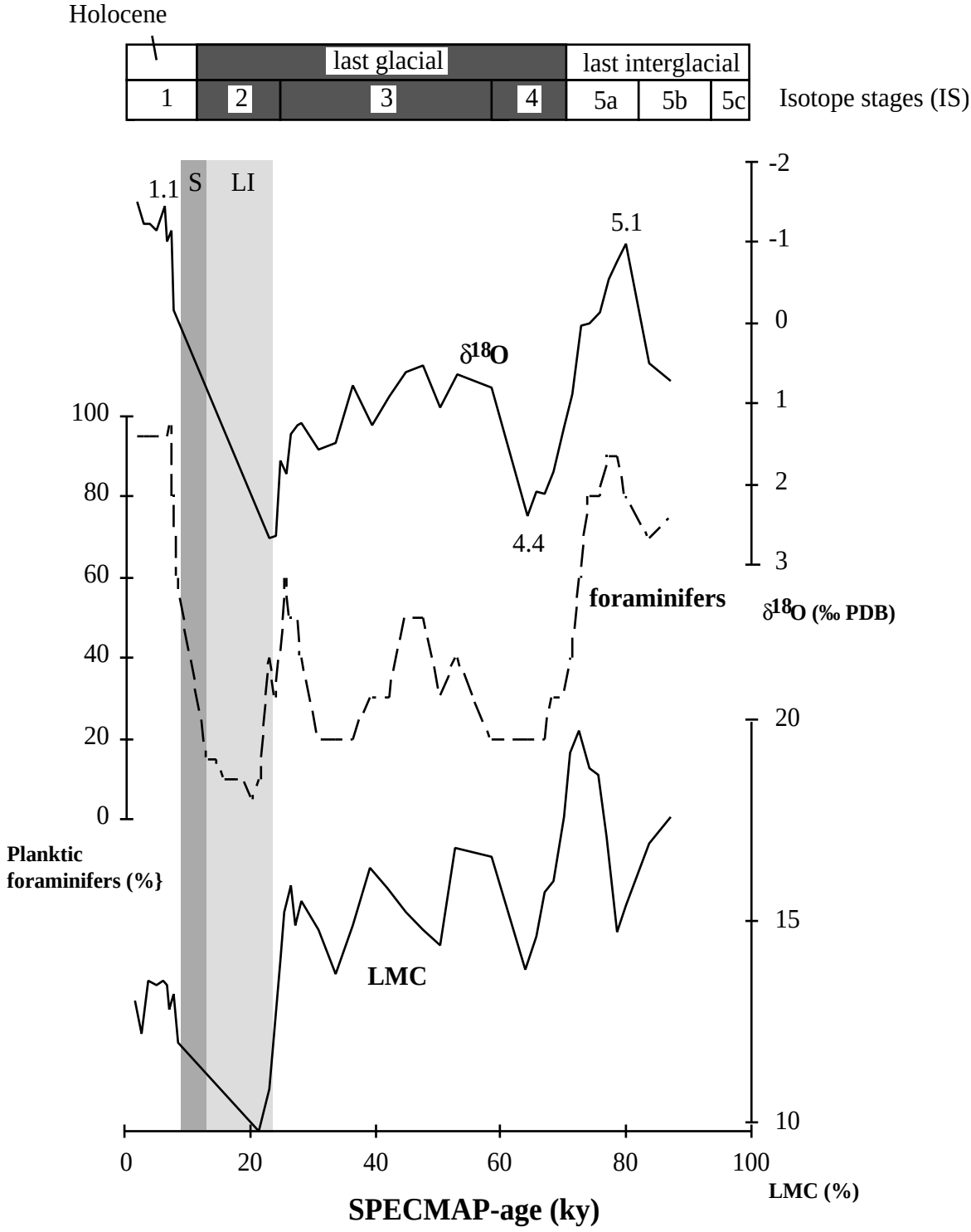

Figure D.3-7: LMC-record, estimated frequency of planktic foraminifera in the 250-500 µm grainsize class and planktic $\delta^{18}O$ signal of core AL, Abington Reef. The foraminifera distribution shows the same glacial-interglacial variations as the oxygen isotope curve, with higher abundances during the Holocene and IS 5a and a minimum during the aplanktonic interval (LI). The LMC-curve shows similar oscillations with an increasing trend with depth in core, possibly caused by progressive replacement of meta-stable carbonates. Numbers on the isotope curves are SPECMAP events. S = sapropel, LI = lithified interval.

D.3.2 Aragonite and carbonate accumulation- and sedimentation rates

Accumulation rates of aragonite and high-Sr-aragonite in the vicinity of Sanganeb Atoll yield information on the carbonate sediment export potential of the reef. Carbonate production of modern and ancient coral reefs and carbonate platforms exceeds by far the storage capacity in the shallow-water realm (Neumann & Land, 1975). Overproduction is therefore exported to the periplatform sites and adjacent basins. Some dissolution might occur in the reef environment and during transport (Milliman *et al*., 1999). Fig. D.3-10 shows that aragonite accumulation decreases with distance from the reef, which indicates reduced input of shallow-water derived aragonite with greater distance from the source. Higher aragonite dissolution in the distal core S1 is unlikely because waterdepth does not increase with distance from the reef.

D.3.2.1 Increased shallow-water input since 8,000 SPECMAP-yr

Temporal variations in aragonite/calcite-ratios record changes of mineral abundances in each individual sample. The ratios do not represent the absolute amount of a carbonate mineral that is deposited during a certain time interval. This is clearly visible for Holocene aragonite and high-Sr-aragonite AR which are significantly increased compared to older sediments, while aragonite percentages do not show such an increase and do not even exceed glacial values (Fig. D.3-8 and D.3-9). These differences indicate that a significantly higher carbonate sediment export occurred during the Holocene sealevel highstand when the total shallow-water reef area was flooded, even though this is not indicated by the aragonite/calcite-ratios.

Droxler *et al.* (1983) showed, that the increase in aragonite content in periplatform sediments preceded bank flooding in the Bahamas by about 8,000 yr, which suggests, that higher aragonite sediment export during highstands is not the reason for higher aragonite content in the periplatform sediments (Fig. D.3-11). However, the aragonite accumulation rates at Sanganeb Atoll show a sharp increase at about 8,000 SPECMAP-yr which equals or shortly follows the flooding of the platform (lagoon) and the onset of reef growth in the Red Sea at 9,000-10,000 yr BP (Taviani, 1998a; b).

D.3.2.2 Low accumulation rates during the last interglacial

Bulk and carbonate sedimentation rates (SR) of late Holocene periplatform sediments (recent to 8,500 ^{14}C-yr) from the Sudanese shelf are 1.5 to 2 times higher than those of glacial sediments. This pattern is similar to the Bahamas where interglacial sedimentation rates are also 1.5 times higher than glacial ones (Schlager *et al.*, 1994). The overall higher interglacial sedimentation rates in periplatform sediments were explained by highstand shedding. However, in the Red Sea only the Holocene sedimentation rates are significantly increased but values during last interglacial-highstands (5a, 5c, 5e) fall in the range of glacial sedimentation rates. It is surprising that no increased shallow-water export could be proved for substages 5a, 5c and 5e, when sealevel reached or exceeded present level in the Red Sea (Dullo, 1990; Gvirtzman, 1994). Flooding of the platform top at Sanganeb Atoll during all major highstands should have caused a similar sediment production and export as during the Holocene. But in none of the highstands during IS 5 the aragonite accumulation rates reached those of the Holocene as shown in Fig. D.3-8 and D.3-9. Therefore, it is most likely that

progressive post depositional replacement of aragonite by calcite led to reduced aragonite AR in the older highstand deposits.

D.3.2.3 Re- and transgressional patterns in sedimentation rates

The SR show a characteristic re- and transgressional pattern in the periplatform sediments on the Sudanese shelf (Fig. D.3-12). SR are lowest during phases of eustatic sealevel rise and highest during sealevel fall which is characteristic for siliciclastic shelf systems (e.g. Vail *et al*, 1977; Sarg, 1988; Schlager, 1992). A similar re- and transgressional pattern in sedimentation rates was observed during IS 3 to IS 5 in the periplatform sediments of core M35049 at Pedro Bank, Caribbean, a carbonate dominated system (Emmermann *et al*., 1999). The characteristic highstand-lowstand patterns as found in previous studies (see e.g. Droxler & Schlager, 1985; Reijmer, 1991; Schlager, *et al*, 1994) display average SR for individual isotope stages. The higher resolution SR-patterns of the Sudanese shelf reflect sediment export variations in concert with sea-level changes. This pattern is best developed during the last deglaciation and the Holocene (Fig. D.3-12). SR were extremely low during the early sealevel rise between about 13,000 and 8,500 ^{14}C-yr (sapropel). Between 8,000 and 6,000 SPECMAP-yr sedimentation rates show an enormous increase and reach an absolute maximum close to the Holocene sealevel highstand. After 6,000 SPECMAP-yr the SR drop again and reach „normal“ Holocene values, which still are higher than glacial ones. Such a pattern most likely was developed during earlier sealevel sequences but could not be confirmed due to the lower time resolution in the older parts of the periplatform sequence.

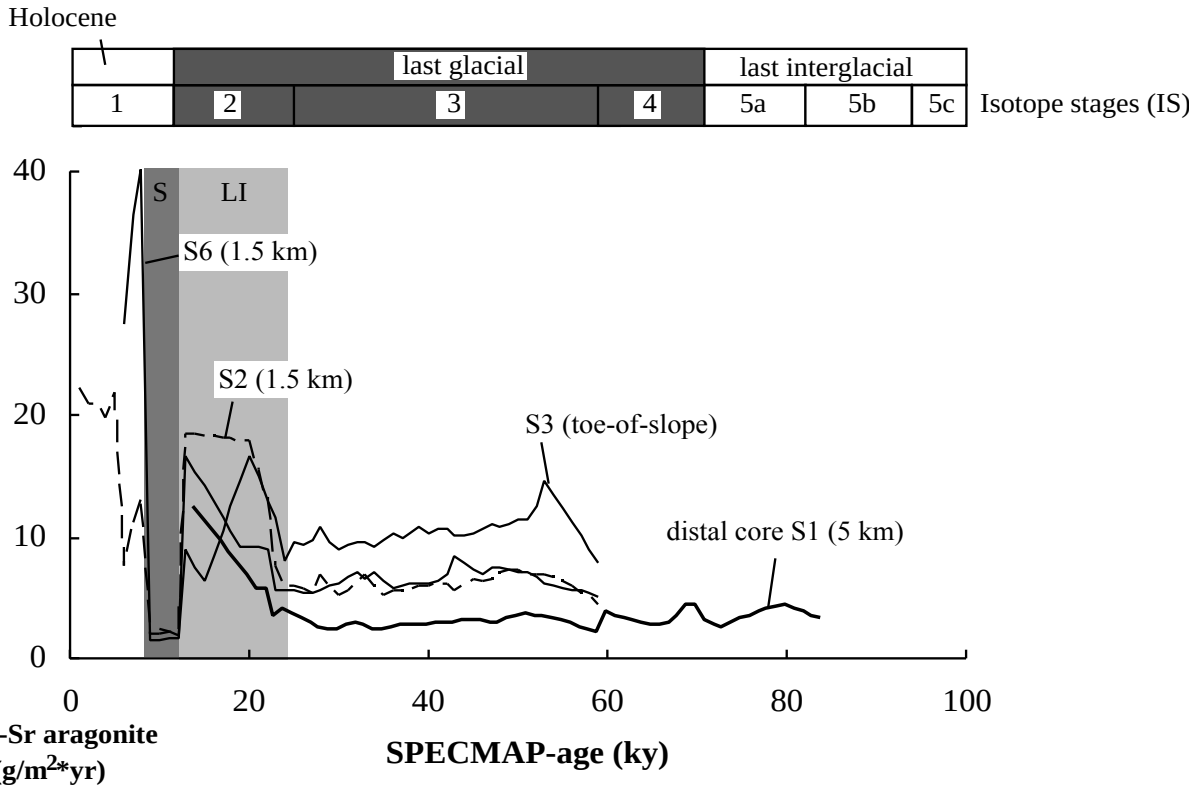

Figure D.3-10: Accumulation rates of high-Sr-aragonite in the periplatform sediments at Sanganeb Atoll. AR decrease with distance from the reef, which points to reduced shallow-water sediment input in the distal core S1. Increased dissolution of aragonite or carbonate in the distal core S1 is unlikely because all cores were taken in approximately same waterdepth. S = sapropel, LI = lithified interval.

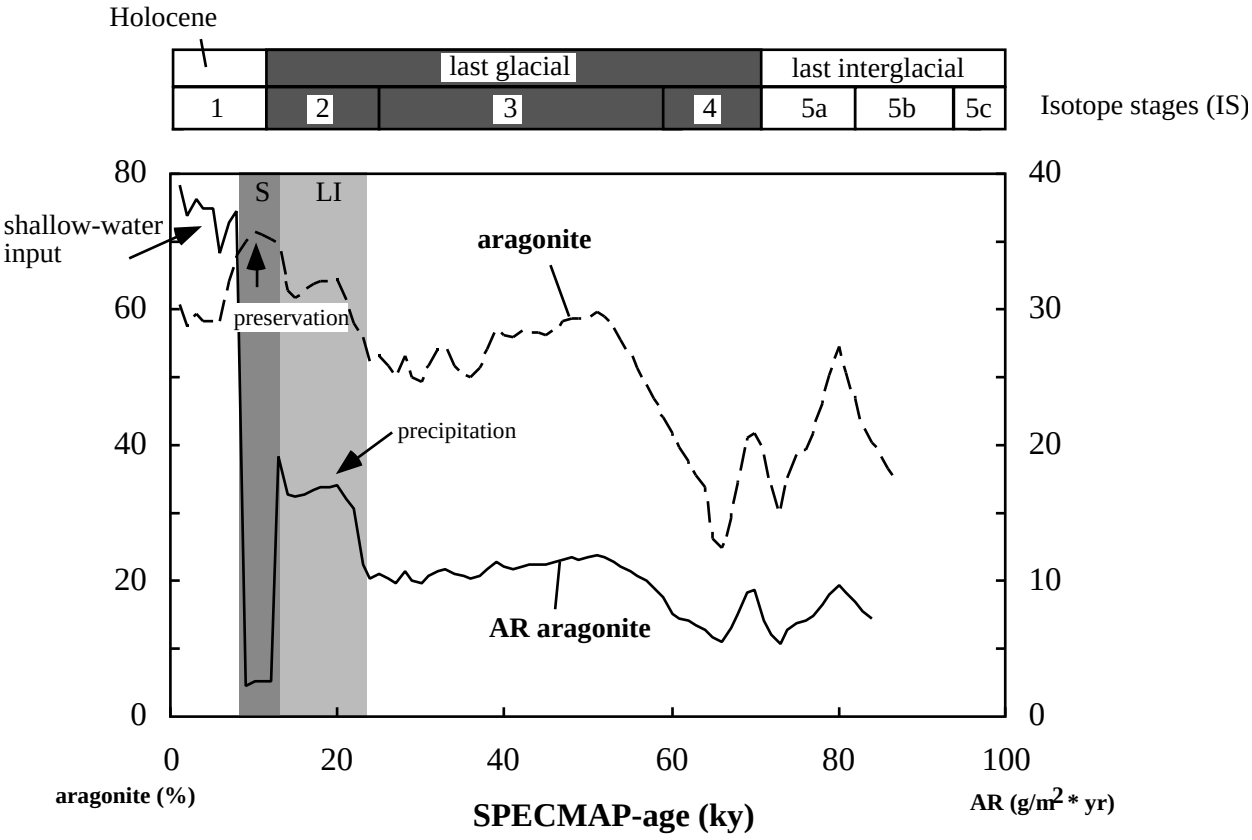
Holocene
last glacial
last interglacial
1
2
3
4
5a
5b
5c
Isotope stages (IS)
S
LI
shallow-water input
aragonite
preservation
precipitation
AR aragonite
aragonite (%)
AR (g/m2 * yr)
SPECMAP-age (ky)

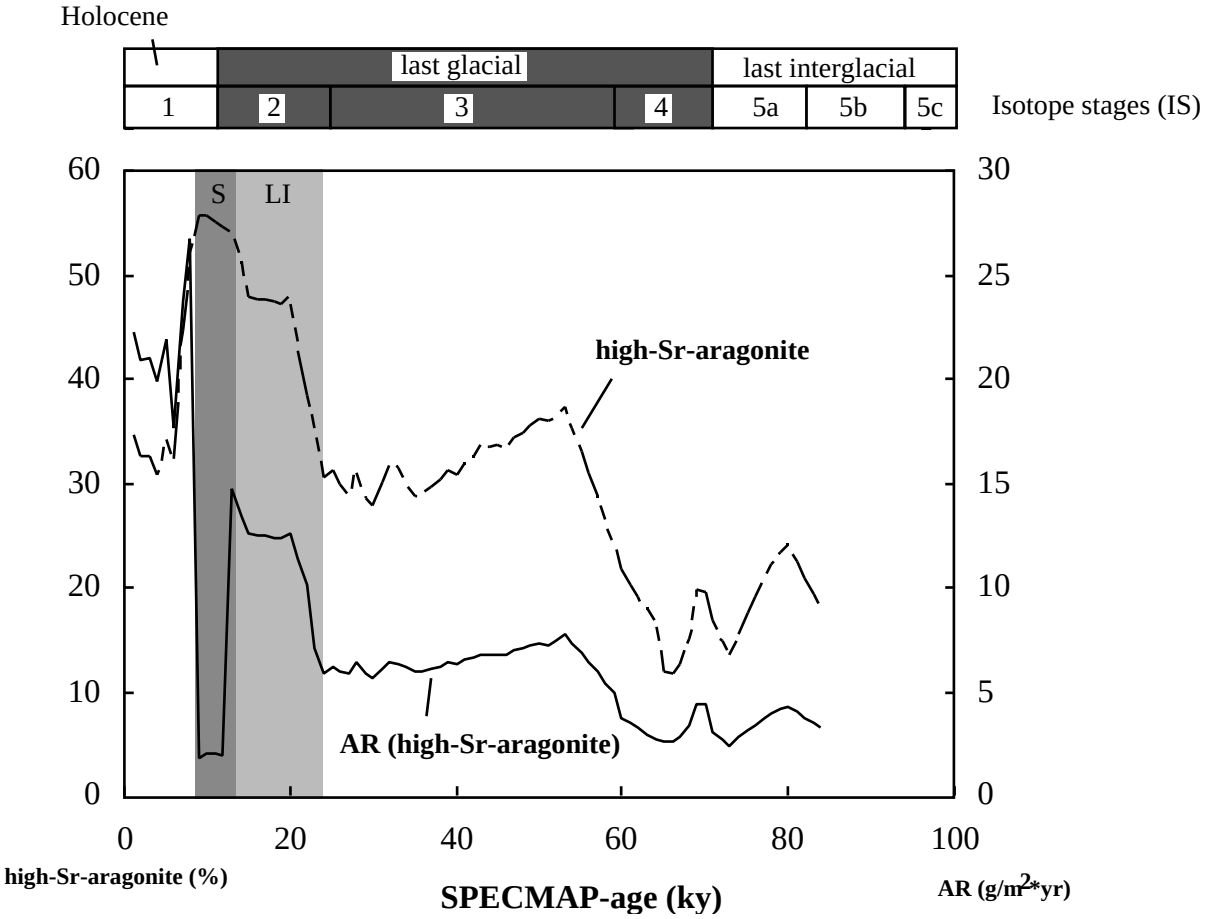
Holocene
last glacial
last interglacial
1
2
3
4
5a
5b
5c
Isotope stages (IS)
S
LI
high-Sr-aragonite
AR (high-Sr-aragonite)
high-Sr-aragonite (%)
AR (g/m2*yr)
SPECMAP-age (ky)

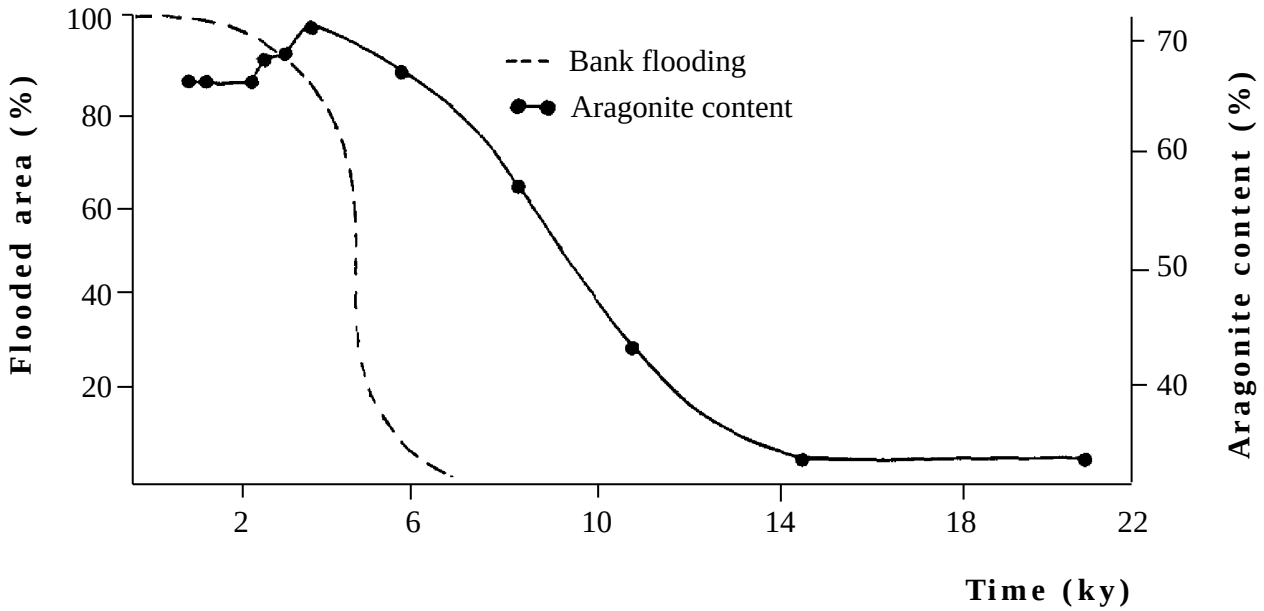

Figure D.3-11: Increase in aragonite content and platform flooding of the Bahamas, after Droxler *et al*, (1983). For the Bahamas it was shown that the aragonite percentages started to increase long before the platform top was flooded during the Holocene sealevel rise. Thus, it was assumed that not shallow-water sediment export caused the increase in aragonite but reduced dissolution of the metastable carbonate mineral. However, at Sanganeb Atoll the Holocene sealevel rise and the increase in (high-Sr) aragonite accumulation are in phase (Fig. D.1-5, D.3-8 and D.3-9).

Figure D.3-8 (upper fig. to the left): Aragonite accumulation rates (AR) and aragonite percentages of the bulk carbonate fraction in periplatform sediments at Sanganeb Atoll (stacked curves). Average values and stdev. can be found in Appendix 4-F. The AR curve clearly indicates an increased input of shallow-water derived sediments during the Holocene since 8,000 SPECMAP-yr, shortly after the flooding of the old Pleistocene reef structures at Sanganeb Atoll. The peak in the accumulation rates coincides with reinforced shallow-water benthic carbonate production and sediment export after Holocene reefs had re-colonised the old substratum. The maximum follows to a phase of lowest aragonite accumulation rates during the deglaciation between 13,000 and 8,500 ^{14}C-yr. This phase is characterised by an unusally good preservation of aragonite (preservation spike). In analogy to the aragonite percentages the AR show no increase of aragonitic shallow-water input during the last interglacial compared to IS 3. Only during the Holocene AR are significantly increased. S = sapropel, LI = lithified interval.

Figure D.3-9 (lower fig. to the left): Accumulation rates of high-Sr-aragonite on the Sudanese shelf in the vicinity of Sanganeb Atoll and the percentages of high-Sr-aragonite of the bulk carbonate fraction (stacked curves). Average values and stdev. are given in Appendix 5-D. AR of high-Sr-aragonite show the same variations as those of bulk-aragonite (Fig. D.3-11), with one significant difference: After the maximum in high-Sr-aragonite AR at 8,500 yr the values drop down again. This is an important finding which was also shown by the simulation of productive areas (Chapter D.1.2). In the model reduced values occur when the Holocene sealevel rise exceeds 20-15 mbps and the deeper parts of the lagoon fall below the zone of prolific carbonate production. S = sapropel, LI = lithified interval.

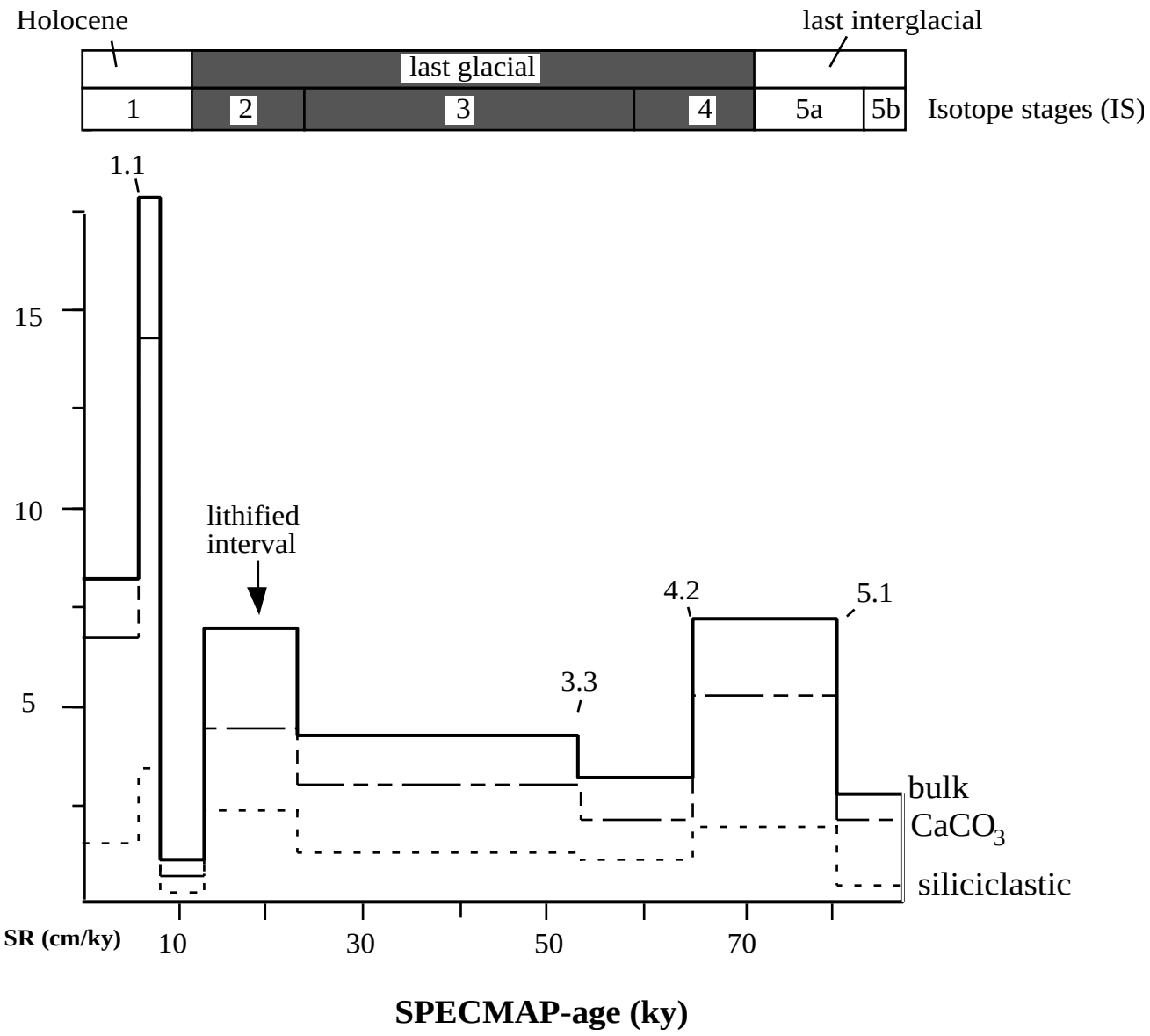

Figure D.3-12: Bulk-, siliciclastic- and carbonate sedimentation rates of periplatform sediments of core AL, Abington Reef. Siliciclastic- and carbonate sedimentation rates (SR) show the same re- and transgressional pattern. SR are lowest during phases of eustatic sealevel rise and highest during falling sealevel which is characteristic for siliciclastic shelf systems (e.g. Vail *et al*, 1977; Sarg, 1988; Schlager, 1992). Nevertheless, the parallel trends of siliciclastic- and carbonatic SR on the Sudanese shelf indicate that also the carbonate SR might develop such a pattern. It is suggested that the sealevel related SR-patterns as described above replace the glacial-interglacial SR-patterns on a higher resolution. The characterisitc highstand-lowstand patterns as found in previous studies (see e.g. Droxler & Schlager, 1985; Reijmer, 1991; Schlager, *et al*, 1994) display average SR for individual isotope stages. The higher resolution SR-patterns of the Sudanese shelf reflect sediment export variations in concert with sea-level changes. 1.1, 3.3, 4.2 and 5.1 are SPECMAP events.

D.3.3 Offsets between aragonite and oxygen isotope curves

Small systematic offsets between maxima and minima in the curves of aragonite/calcite-ratios of bulk periplatform sediments that coincide with individual SPECMAP events on the isotope curves were observed in all studied cores in the vicinity of Sanganeb Atoll and Abington Reef. During lowstands (4.2, 5.2) the aragonite curve precedes the isotope curve, during highstands (3.3, 5.1, 5.3) aragonite lags behind the $\delta^{18}O$-signal (Tab. D.3-3).

Droxler *et al*. (1988) found similar mismatches between aragonite and $\delta^{18}O$-curves in Pleistocene periplatform ooze of the Bahamas. They state that aragonite cycles are climatically driven and a result of sediment export and dissolution in intermediate water depth. Offsets between $\delta^{18}O$ and aragonite in the Bahamas occur mainly at glacial/interglacial transitions, where increases in the aragonite content usually lag behind $\delta^{18}O$ depletion. This agrees with findings in the periplatform sediments on the Sudanese shelf, in which aragonite lags behind the $\delta^{18}O$ signal even during minor sealevel rises e.g. from event 4.2 to 3.3. When the observed offsets between oxygen isotope and aragonite curves correspond to time offsets, these fall in the range of few hundred to about 6,000 years (Tab. D.3-3).

During rising sealevel aragonite-export most likely lagged behind sealevel. Examples from Florida (Shinn, 1980; Shinn *et al*., 1989), the Great Barrier Reef (Davies & Montaggioni, 1985) and St. Croix (Adey, 1987) show a time lag of 500 to 2,500 years between flooding of old substratum and reef initiation. Tipper (1997) showed by modelling of carbonate production on reef platforms that such a lag comes naturally and is induced by stress on the reef organisms in shallowest water depth during flooding. During sealevel falls aragonite export became reduced long before the sealevel lowstand was reached. This might have caused the primary decrease in aragonite input during periods of sealevel fall, before the oxygen isotopes showed their actual minimum.

Table D.3-3: Depth- and time-offsets between aragonite- and isotope curves in cores AL and S1

Fix-points	Age (ky)	Iso depth (cm)	Arag depth (cm)	Depth offsets (cm)	Average SR (cm/ky)	St. dev.	Time-offsets (ky)
Core S1							
top	4	0.0	0.0	0.0			
2.0	12	36.4	36.4	0.0	4.5	0.0	0.0
top LI	13	50.4	50.0	0.4	4.6	0.1	0.1
2.2	19	81.1	81.1	0.0	7.7	0.1	0.0
base LI	23	119.5	120.0	-0.5	7.7	0.1	-0.1
3.1	28	136.5	135.2	1.4	4.0	0.3	0.3
3.3	53	239.7	230.0	9.7	4.0	0.2	2.4
4.0	59	250.0	250.0	0.0	2.5	1.1	0.0
4.2	65	260.5	270.0	-9.5	2.5	1.1	-3.7
5.0	71	296.0	302.0	-6.0	5.6	0.4	-1.1
5.1	80	349.6	350.0	-0.4	5.6	0.4	-0.1
	83	358.6	362.9	-4.3	3.6	0.9	-1.2
5.2	87	370.7	380.0	-9.3	3.7	0.9	-2.5
	95	436.7	413.3	23.3	6.2	2.9	3.8
5.3	99	470.0	430.0	40.0	6.3	2.9	6.4
Core AL							
top	0	0.0	0.0	0.0	0.0	0.0	
1.1	6	73.0			12.2		0.0
2.0	12	91.0	80.0	11.0	4.8	2.6	2.3
top LI	13	100.0	100.0	0.0	4.8	2.6	0.0
2.2	19	131.1	131.1	0.0	7.8	0.0	0.0
base LI	23	170.0	170.0	0.0	7.8	0.0	0.0
3.1	28	190.7	188.6	2.1	4.9	0.4	0.4
3.3	53	320.0	305.0	15.0	4.9	0.4	3.1
4.0	59	330.0	325.0	5.0	2.5	1.2	2.0
4.2	65	340.0	345.0	-5.0	2.5	1.2	-2.0
5.0	71	384.0	385.0	-1.0	7.0	0.5	-0.1
5.1	80	450.0	445.0	5.0	7.0	0.5	0.7
	83	457.5	455.7	1.8	3.0	0.8	0.6
5.2	87	467.5	470.0	-2.5	3.0	0.8	-0.8
	95	508.2	510.0	-1.8	5.0	0.1	-0.4
5.3	99	530.0	530.0	0.0	5.2	0.3	0.0

D.3.4 Temporal and spatial variations in component distribution

In numerous studies the compositional variations in periplatform sediments and calciturbidites from platform slopes and adjacent basins were analysed to reconstruct the evolution of the platform/ basin-transition in space and time, i.e. with respect to sealevel variations (e.g. Droxler *et al.*, 1983; Droxler & Schlager, 1985; Haak & Schlager, 1989; Reijmer, 1991). Many of these studies have a sequence-stratigraphic background and try to link relative sealevel with stratal geometry generated by the interplay between sediment supply and accommodation space on the platform (Schlager, 1992, 1993; Everts, 1994; Everts & Reijmer, 1995; Blomeier, 1997; Westphal, 1997).

The major reason for studying slope- and periplatform sediments instead of those on banktops is that lowstands are times of subaerial exposure and erosion on the platform tops, whereas periplatform and slope sediments might record complete sequences without hiatuses. However, the original signal of the platform might be adjusted by various processes like: (1) sorting and filtering, (2) different susceptibility of individual components to erosion and dissolution, (3) time lags between sediment production and downslope transport and (4) syn- and postdepositional alteration.

Variations in the productive area of the reef caused changes in the total amount of sediment export and possibly in the composition of the exported sediments. The composition of shallow-water sediments that form during a sealevel lowstand along the reef rim will differ from those derived from a fully developed carbonate platform during a highstand as shown for the Bahamas (Haak & Schlager, 1989).

The compositional variations of periplatform sediments in the vicinity of Sanganeb Atoll may record reef evolution under the influence of eustatic sealevel fluctuations during the last 65,000 SPECMAP-yr. Even though the morphology of Sanganeb Atoll and the regional sealevel history is known very well, local oceanographic parameters might change the expected sediment export parameters. The last glacial salinity crisis probably caused extinction of reefs during IS 2 (Gvirtzman *et al*., 1977; Taviani, 1998a; b). This would have led to a hiatus in sediment supply. However, during IS 2 the frequency of calciturbidites rich in unaltered reef components is very high in the cores close to Sanganeb Atoll.

D.3.4.1 Component distribution in periplatform sediments compared to the composition of reef sediments

The composition of recent Red Sea reef sediments (Tab. D.3-4) is compared to those from periplatform core top samples at Sanganeb Atoll. The percentage of „reef builders“ (scleractinian, coralline red algae, encrusting foraminifers) in the uppermost layers of the periplatform sediments is about 1% or less of the total sediment. In the geological record such a low amount of reef components in the periplatform sediments could be interpreted as reduced reef growth as would be expected during a sealevel lowstand. During the entire Holocene the values do not exceed 2-3%, except for the interval between 8,000-6,000 SPECMAP-yr, which coincides with a peak in the aragonite accumulation rates.

Aboul-Basher (1980) estimated the percentages of corals and red algae in the recent reefal and lagoonal sediments of Sanganeb Atoll to vary between 20 to 50% and 10 to 40%, respectively.

Average percentages of corals and red algae in reef and shallow-water sediments from other parts of the Red Sea vary between 10 to 30% and 5 to 10%, respectively (Tab. D.3-4).

The discrepancy between the percentages of shallow-water grains in Holocene and Pleistocene periplatform sediments and those within the reef environment might be explained as follows:
(1) The shallow-water fraction is diluted by pelagic- and siliciclastic input in the periplatform realm.
(2) The high percentage of matrix/fine-fraction of the periplatform sediments indicates a predominant export of carbonate mud instead of coarse grained shallow-water components. Sorting and filtering processes within the shallow-water environment and during transport reduce the number of coarse grained shallow-water components. Perl (1997) demonstrated that filter processes and sediment disintegration by bioerosion along the fore-reef slopes of the fringing reefs at Aqaba led to a drastic reduction of scleractinian fragments in some of the samples when compared to the composition of the „original“ reef sediment.

Table D.3-4: Frequency distribution of skeletal and non-skeletal grains in Red Sea reefal sediments (in %)

Author	**Piller (1994)**	**Dullo (1990)**		**Gabrié (1982)**	**Aboul-Basher (1980)**				
Location	Safaga, Egypt	Saudi-Arabia (recent)	Saudi-Arabia (Pleistocene)	Aqaba, Jordan	Schaab Baraja, Sudan	Abu-Haschisch, Sudan	Wingate, Sudan	Towartit, Sudan	Sanganeb, Sudan
non-biogenic	10				15-40	0-10	0-20	0-25	0-30
-pellets	0±1								
-comp. grains	9±10								
-ooids	0±1								
foraminifers	14±12	11	7						
corals	10±12	15	8	33±18	30-70	40-65	40-60	40-60	20-50
bryozoan	0±0			0±0					
molluscs	12±8	17	8	14±7					
-aragonitic		12	3						
-calcitic		5	5						
echinoderms	1±1	10	8	2±1					
red algae	4±5	11	7	9±7	0-30	0-40	0-40	0-30	10-40
Halimeda	1±5			0±0	0-20	3-35	0-20	0-30	0-40

D.3.4.2 Glacial-interglacial variations in component distribution

The contents of periplatform sediments is dominated by matrix (40%), terrigenous grains (13-17%), bioclasts (10-14%) and non-specified components („others“ 12-20%) (Tab. C.9-2). The average percentages of the pointcount groups (see Tab. C.9-1) with environmental significance stay below 10%. „Plankton“ (pteropods, foraminifers) reaches 5-8%, „reef builders“ (e.g. scleractinian, coralline red algae) vary from 2-4% and other „shallow-water grains“ (e.g. non-

skeletal grains, large benthic foraminifers) range from 4-7%. This distribution pattern suggests a dilution of original shallow-water sediments by pelagic and siliciclastic input.

During the Holocene and IS 4 the matrix content is clearly increased compared to IS 3 and IS 2 (Fig. C.9-1). This points to prolific reef growth and increased export of fine-grained shallow-water sediments at Sanganeb Atoll during the Holocene sealevel highstand. It is likely that large portions of the fine-grained, mostly aragonitic sediments derived from the lagoon, where at present the dominant portion of fine grained sediments are produced (Aboul-Basher, 1980). However the high matrix content during IS 4 can not be explained by the highstand shedding pattern. During the sealevel lowstand of IS 4 (about 60 mbps) the platform at Sanganeb Atoll was completely exposed and sediment export production on deeper terraces was significantly lower than during the Holocene highstand, due to the smaller shallow-water area available for prolific reef growth. In addition, high surface salinities restricted reef growth during IS 4. Furthermore, it is expected that the exported sediments from the steep slopes and terraces are generally coarser grained than the ones that derived from the lagoon. Therefore, the high matrix content accompanied by highest Mg-calcite percentages in the periplatform sediments gives further evidence for the inorganic precipitation of this mineral during IS 4.

Terrigenous input is low during the Holocene but increases during glacial isotope stages 2-4, with a maximum during IS 2. This is also indicated by the distribution-pattern found in SiO_2 and quartz-contents and reflects the characteristic glacial-interglacial input pattern suggested by the sequence stratigraphic concept of siliciclastic shelf systems (Vail *et al.*, 1977, 1991; Schlager, 1992).

The plankton input in the periplatform sediments recorded by the distribution of foraminifers and pteropods reflects the palaeoceanographic variations of Red Sea surface waters (Berggren & Boersma, 1969; Reiss *et al*., 1980; Ivanova, 1985; Geiselhardt, 1998). Low plankton percentages during IS 2 and IS 4 indicate the restriction of marine biota during sealevel lowstands, when salinities of Red Sea surface waters reached up to 53‰. Increased plankton percentages during IS 3 compared with IS 2 and IS 4, indicate that during this stage planktic fauna recovered, resulting from reduced salinities due to a higher sealevel and increased humidity over the Red Sea (Hemleben *et al.*, 1996; Almogi-Labin *et al*., 1998). The amount of bioclasts is also reduced during IS 2 and IS 4 when compared to the Holocene and IS 3, which might indicate a generally restricted biogenic carbonate production during this high-saline phases.

Input of coarse grained shallow-water biota is significantly increase during IS 3 when compared to the Holocene. This points to (1) a prolific shallow-water benthic carbonate production during IS 3 and a high export of coarser grained shallow-water sediments during this glacial stage, and (2) less dilution by fine-grained shallow-water components from the platform interior (lagoon) during lowered sealevel. Benthic carbonate production and reef growth during IS 3 is also indicated by two drowned framework build-ups observed on the submerged terraces at a present-day waterdepth of 60 and 90 mbps at Sanganeb Atoll (Brachert & Dullo, 1990, 1991).

Variations in mineralogy, grainsize and component distribution clearly show a glacial-interglacial sediment export pattern at Sanganeb Atoll. During the Holocene sealevel highstand the export of fine-grained aragonite from the inner lagoon prevails, while during lowered sealevel of IS

3 the benthic carbonate production is restricted to the outer slopes of the atoll. This idea is confirmed by studies from the Bahamas which showed that during interglacial highstands the input of fine-grained bank-top derived aragonite is significantly higher than during glacials, whereas lowstand deposits are enriched in coarser-grained components from the reef rim (e.g. Grammer & Ginsburg, 1992; Westphal, 1997).

D.3.4.3 Spatial variations in sediment input

No significant differences were found in the composition of periplatform sediments when comparing the lee- and windward side of Sanganeb Atoll. Only slightly increased percentages of scleractinians, molluscs and peloids occurred during IS 3 in the windward core (Fig. D.3-13). The dominance of scleractinians in the windward core might reflect the general morphology of Sanganeb Atoll with the reef crest exposed to the windward side and the opening lagoon on the leeward side (Fig. A-7).

The spatial distribution of shallow-water components present in calciturbidites at Sanganeb Atoll show the following pattern: Turbidites from the windward core S6 contain more matrix, terrigenous grains and contain less shallow-water grains than those from windward core S3 (Fig. D.3-14). This difference reflects the proximal position of the leeward core S3, which was obtained directly at the toe-of-slope (Fig. B-1). It is remarkable that core S2 from the leeward side, which was taken in a similar distance as core S6 contains no calciturbidites.

D.3.4.4 Timing and frequency of glacial calciturbidites

In the proximal periplatform sediments at Sanganeb Atoll shallow-water calciturbidites are frequent during IS 2 and IS 3. The ages of scleractinian fragments in glacial calciturbidites are about 5,000 to 6,000 yr (up to 19,000 yr) older in comparison with the surrounding sediments (Fig. C.2-4). The youngest turbidite in IS 2 was deposited on the shelf at 14,630±70 ^{14}C-AMS yr but the radiocarbon age of the scleractinian grains within this turbidite is 21,480±180 ^{14}C-AMS yr. The difference between the radiocarbon age of the scleractinian fragments and the age of the embedding sediments might be explained by (1) admixture of older scleractinian fragments and (2) shedding of older shallow-water sediments.

The incorporation of older scleractinian fragments during the downslope transport might have led to radiocarbon ages of the sediments older than the timing of turbidite deposition. This might imply that export and in-situ production occurred simultaneously . But so far no direct evidence was found for shallow-water reef growth during IS 2 in the Red Sea. Gvirtzman *et al*. (1977) and Taviani (1998a; b) suggest that reef organisms among many other organisms vanished from the Red Sea during the last glacial salinity crisis. Thus, it seems unlikely that the shallow-water components that occur in the last glacial calciturbidites were formed during the peak glacial.

This supports the idea that the shallow-water sediments were produced long before their downslope transport. It is possible that the radiocarbon ages represent the time of in-situ sediment production in the shallow-water realm. These sediments might have been re-sedimented and incorporated into the turbidity currents during the sealevel fall between event 3.1 and the last glacial sealevel lowstand at 14,840±110 ^{14}C-AMS yr. A high frequency of turbidite input during falling

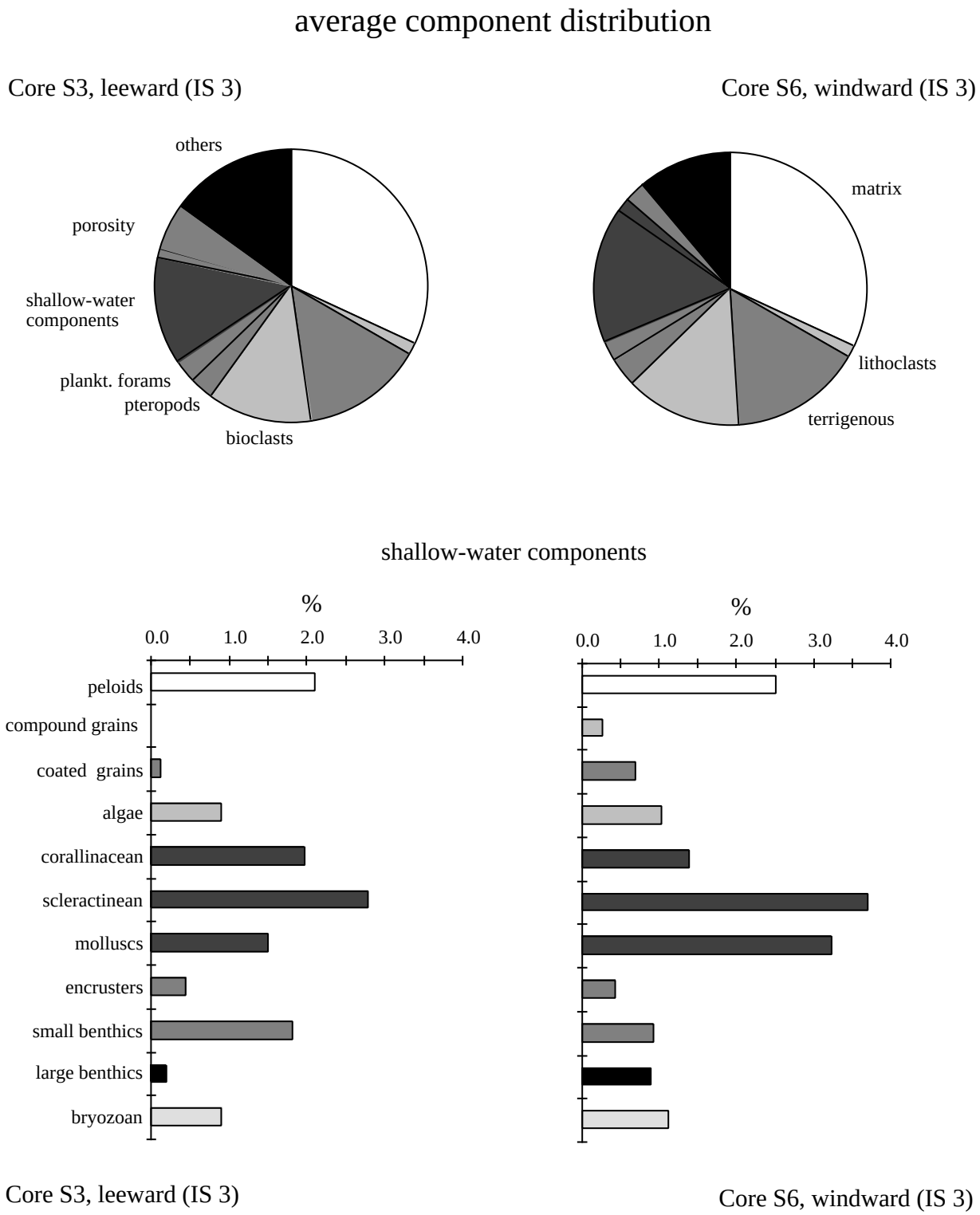

Figure D.3-13: Comparison of the component distribution of IS 3 periplatform sediments as analysed by pointcounting of core S3, from the western (leeward) side and core S6 from the eastern (windward) side at Sanganeb Atoll. No significant differences are visible, except for slightly increased scleractinian and mollusc abundances in the windward core, which might reflect the zonation of the atoll, with a reef crest on the windward side and a lagoon opening to the leeward side.

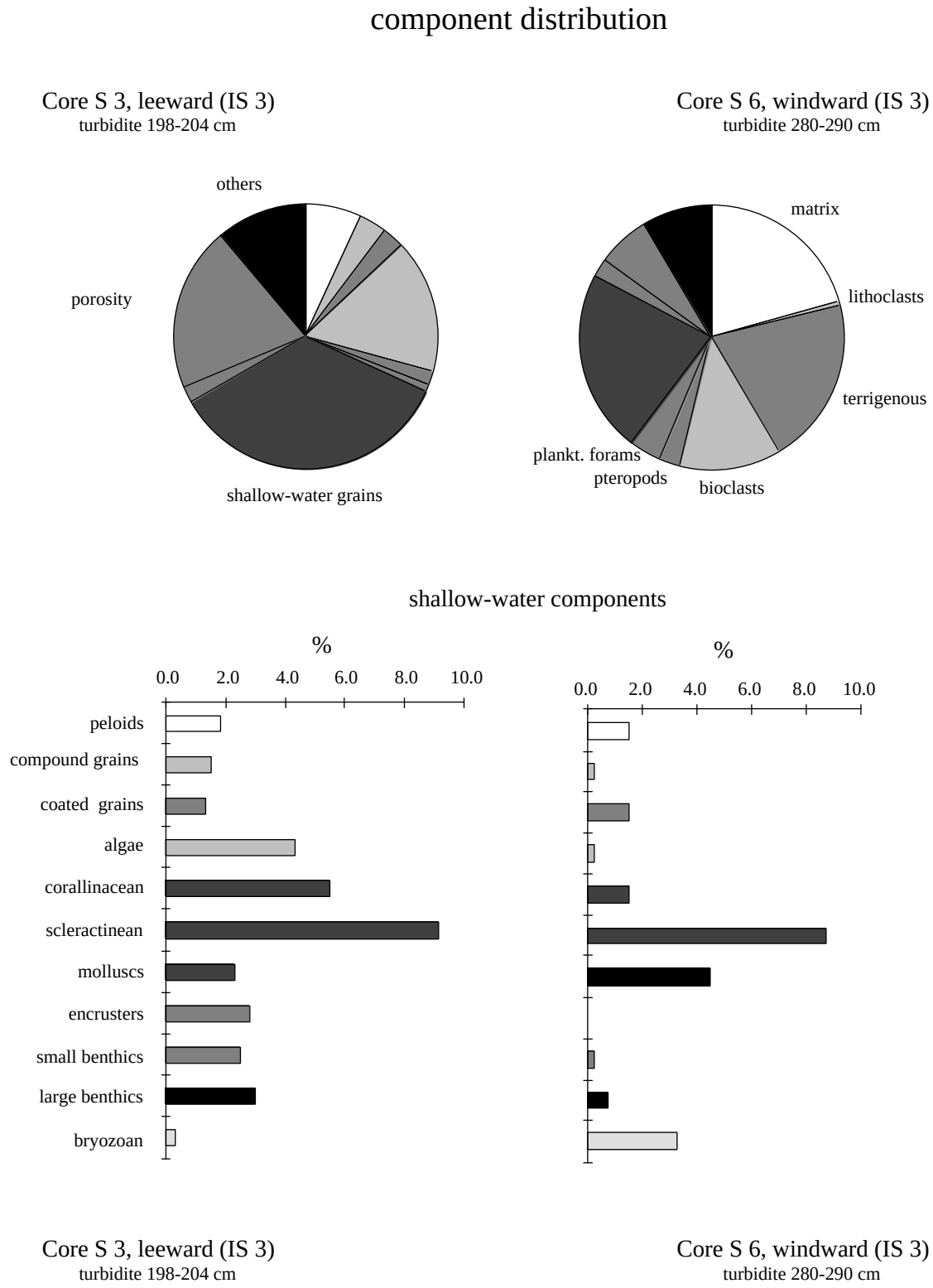

Figure D.3-14: Comparison of calciturbidite composition of core S3 (leeward) and core S6 (windward). Turbidites from the windward side generally contain more matrix and terrigenous grains but have a lower porosity and contain less shallow-water grains than those from windward side. This difference might reflect the proximal position of the leeward core S3, which was obtained directly at the toe-of-slope. The calciturbidites of the more distal core S6 from the windward side consist of skeletal packstones, while grainstones dominate in the proximal core from the leeward side. It is remarkable that core S2 from the leeward side, which was taken in a similar distance as core S6 contains no calciturbidites at all. Only slight differences in the distribution of shallow-water components between the lee- and the windward turbidites can be found. However, variability of the component distribution of individual calciturbidites is so high that no significant differences between leeward and windward position can be shown.

sealevel was also proposed by Shanmugam & Maiola (1982; 1984) but contradicts the highstand-bundling model of Droxler & Schlager (1985) which suggests a higher frequency of calciturbidites during sealevel highstands in phase with increased carbonate production on the flooded platform top. Following the radiocarbon ages obtained from the scleractinians, shallow-water reef growth might have occurred at Sanganeb Atoll during IS 3 and the beginning of IS 2 up to 21,040±200 ^{14}C-AMS yr. It is likely that reef-growth and carbonate production took place in the deep parts of the lagoon and on the deep terraces which are found in a present-day waterdepth of 60 to 90 mbps in the Red Sea (Brachert & Dullo, 1990; Gvirtzman, 1994; Dullo & Montaggioni, 1998). This supports the idea of reef growth on Red Sea deep terraces during late IS 3 in analogy to the drowned reefs on the fore-slope of the island of Mayotte in the Western Indian Ocean (Dullo *et al*.; 1998).

The age differences between the skeletal grains of the calciturbidites and their stratigraphic position in the periplatform sequence has major implications for the sequence-stratigraphic analysis of such sediments. It shows that the analysis of calciturbidites could lead to wrong interpretations of sediment export variations if only the stratigraphic position within the periplatform sequence is known.

CONCLUSIONS

Sediment export

The present study clearly showed that the overall sediment export pattern (highstand shedding) as recorded in periplatform sediments is also found in the vicinity of the Sudanese offshore reefs in the central Red Sea.

A clear highstand-lowstand pattern is developed in the Sudanese periplatform sediments. During the Holocene sealevel highstand sedimentation rates are 1.5 to 2 times higher than during lowstands in sealevel and the export of fine grained aragonite from the inner lagoon of Sanganeb Atoll dominates. During lowered sealevel of marine isotope stage 3 benthic shallow-water carbonate production and reef growth were restricted to the outer slopes, which led to prevailing export of coarser grained skeletal components. During the pleniglacial (IS 2) and during marine isotope stage 4 (IS 4) reef growth and benthic carbonate production were significantly restricted by high salinities of 49‰ (IS 4) up to 57‰ (IS 2), which is shown by the diminished input of shallow-water derived components in periplatform deposits of these lowstand periods.

It was also shown in this study, that eustatic sealevel controlled sediment export by variations of the reef growth areas. This was demonstrated for the Holocene sealevel rise at Sanganeb Atoll. Flooding of the old Pleistocene reef structures at about 8,000 SPECMAP-years caused a sudden increase in reef growth area, which led to an simultaneous rise in the shallow-water sediment export without major time-offsets. This export peak is clearly recorded in the aragonite and strontium accumulation rates in the periplatform sediments.

Scleractinian fragments within shallow-water calciturbidites are on average 5,000 to 6,000 years older than the stratigraphic position of the turbidites within the periplatform sequence. The scleractinian ages give evidence for prolific reef growth at Sanganeb Atoll during IS 3 and early IS 2 up to 21,040±200 ^{14}C-AMS years ago and show that older shallow-water sediments were re-sedimented and shedded preferentially during the sealevel fall between isotopic event 3.3 (30 mbps) and the last glacial sealevel lowstand in the Red Sea (120 mbps) at 14,840±110 ^{14}C-AMS years. A clear highstand-bundling pattern as suggested for the Bahamas (Droxler & Schlager, 1985; Schlager *et al*., 1994) was not found in the Sudanese Red Sea.

Secondary processes

This study also showed that the sediment export cycles in the Red Sea were strongly influenced by syn- and postdepositional processes in the nearly isolated Red Sea basin, with its specific hydrographic and climatic situation during the late Quaternary. Enhanced aragonite dissolution out of phase with the sediment export cycles occurred during interglacials. To some extend it equalised differences in shallow-water sediment export in the periplatform record between interglacial highstands and glacial lowstands.

Monsoonal climate variations caused a better aragonite preservation during pluvial phases often accompanied by a good preservation of organic matter and sapropel formation. Significant

aragonite preservation occurred during the last deglaciation, between 13,000 and 8,500 ^{14}C- years and also during short-termed events of IS 3. Enhanced SW-monsoon caused higher rainfall over the Red Sea, which led to the formation of a pycnocline and low oxygenation of the deeper water masses.

A further very important process that altered the original input-signal is the precipitation of metastable carbonates at the seafloor. During the pleniglacial (IS 2) the signal is overlain by the inorganic precipitation of aragonite and Mg-calcite caused by increased bottom-water salinities of up to 57‰. Aragonite/calcite ratios and micropeloidal fabrics clearly showed the increased precipitation of Mg-calcite during IS 4. The sedimentary record indicates that the submarine precipitation of Mg-calcite had a significant influence on the composition of the Red Sea periplatform sediments and that it to a great extend modified the aragonite/calcite cycles.

Submarine lithification

The standard type of periplatform sedimentation on the Sudanese shelf was interrupted during the last glacial, when the eustatic sealevel drop caused a maximum in basin isolation. At the same time arid climate conditions led to a drastic increase in surface- and bottom water salinities. Salinities of up to 57‰ significantly influenced marine life and reduced biogenic carbonate production. High salinities of Red Sea waters together with a low pelagic and shallow-water input favoured the inorganic carbonate precipitation at the seafloor and submarine lithification.

The main phase of inorganic carbonate precipitation and submarine lithification on the Sudanese shelf took place between 13,000 and 23,000 ^{14}C-yr. Highest salinities coincide with heaviest δ^{18}O-values and the maximum of aragonite precipitation, which occurred at 14,840±110 ^{14}C-AMS yr. This timing corresponds very well with the sealevel lowstand in the Red Sea and the Western Indian Ocean.

In addition, the precipitation mode of the lithified layers switched from an early phase of Mg-calcite and aragonite precipitation (less lithified interval) to the predominance of aragonite since 19,540±130 ^{14}C-AMS yr. Causes for this switch are increased salinities of Red Sea waters due to progressive basin restriction in tune with the glacial sealevel fall.

The frequent alternations between lithified and unlithified layers within in lithified interval were caused by variations in siliciclastic input. Phases of higher siliciclastic input prevented submarine lithification as shown by significantly increased quartz intensities of the unlithified layers compared to lithified samples.

REFERENCES

Aboul-Basher, H. M. (1980) Fazielle Untersuchungen der Karbonatsedimente im Roten Meer - Sudan. PhD-Thesis, Philips-Universität.

Adey, W. (1987) Coral reef morphogenesis: a multidimensional model. Science, 202, 831-837.

Aghib, F. S., Bernoulli, D. & Weissert, H. (1991) Hardground formation in the Bannock Basin, Eastern Mediterranean. Marine Geology, 100, 103-113.

Aissaoui, D. M., Buigues, D. & Purser, B. H. (1986) Model of reef diagenesis: Mururoa Atoll, French Polynesia. In: Reef Diagenesis (Ed. by J. H. Schroeder and B. H. Purser), pp. 25-52. Springer, Berlin - Heidelberg.

Alexander, I. (1996) Late Quaternary sedimentation off the Queensland continental margin (Northeast Australia) in response to sea level fluctuations. unpublished Ph.D., University of Edinburgh.

Allouc, J. (1990) Quaternary crusts on slopes of the Mediterranean Sea: a tentative explanation for their genesis. Marine Geology, 94, 205-238.

Almogi-Labin, A. (1982) Stratigraphic and palaeoceanographic significance of late Quaternary pteropods from deep-see cores in the Gulf of Aqaba (Elat) and northernmost Red Sea. Marine Micropalaeontology, 7, 53-72.

Almogi-Labin, A., Boaz, L. & Duplessy, J.-C. (1986) Quaternary palaeoceanography, pteropod preservation and stable-isotope record of the Red Sea. Palaeogeography, Palaeoclimatology, Palaeoecology, 57, 195-211.

Almogi-Labin, A., Hemleben, C., Meischner, D. & Erlenkeuser, H. (1991) Palaeoenvironmental events during the last 13,000 years in the central Red Sea as recorded by Pteropoda. Palaeoceanography, 6(1), 83-98.

Almogi-Labin, A., Hemleben, C. & Meischner, D. (1998) Carbonate preservation and climatic changes in the central Red Sea during the last 380 kyr as recorded by pteropods. Marine Micropalaeontology, 33, 87-107.

Assaf, G. & Hecht, A. (1974) Sea straits: A dynamic model. Deep Sea Research, 21, 947-958.

Bard, E., Hamelin, B. & Fairbanks, R. G. (1990) U/Th ages obtained by mass spectrometry in corals from Barbados. Sea level during the past 130,000 years. Nature, 346, 456-458.

Bard, E., Fairbanks, R. G., Arnold, M. & Hamelin, B. (1992) 230Th/243U and ^{14}C-ages obtained by mass spectrometry in corals from Barbados (West Indies), Isabela (Galapagos) and Mururoa (French Polynesia). In: The Last Deglaciation: Absolute and Radiocarbon Chronologies, Vol. 2 (Ed. by E. Bard and W. S. Broecker), pp. 103-110. Kluwer Academic, Dordrecht. NATO ASI Series I, Global Environmental Change.

Bard, E., Arnold, M., Fairbanks, R. & Hamelin, B. (1993) 230Th-234U and ^{14}C ages obtained by mass spectrometry on corals. Radiocarbon, 35(1), 191-199.

Bassinot, F. C., Labeyrie, L. D., Vincent, E., Quidelleur, X., Shackleton, N. J. & Lancelot, Y. (1994) The astronomical theory of climate and the age of the Brunhes-Matuyama magnetic reversal. Earth and Planetary Science Letters, 126, 91-108.

Bathurst, R. G. C. (1975) Carbonate sediments and their diagenesis. Elsevier, Amsterdam, Oxford, New York, 658 pp.

Bé, A. W. H. (1977) An ecological, zoogeographic and taxonomic review of recent planktonic foraminifera. In: Oceanographic micropalaeontology, Vol. 1 (Ed. by A. T. S. Ramsay), pp. 796. Academic Press.

Berger, W. H. (1977) Deep-sea carbonate and the deglaciation preservation spike in pteropods and foraminifera. Nature, 269, 301-304.

Berger, A. & Loutre, M. F. (1991) Insolation values for the climate of the last 10 million years. Quaternary Science Review, 10, 297-317.

Berggren, W. A. (1969) Micropalaeontologic investigations of Red Sea cores - summation and synthesis of results. In: Hot Brines and Recent Heavy Metal Deposits in the Red Sea (Ed. by E. T. Degens and D. A. Ross), pp. 329-335. Springer-Verlag.

Berggren, W. A. & Boersma, A. (1969) Late Pleistocene and Holocene planktonic foraminifera from the Red Sea. In: Hot Brines and Recent Heavy Metal Deposits in the Red Sea (Ed. by E. T. Degens and D. A. Ross), pp. 282-298. Springer-Verlag.

Bernoulli, D. & McKenzie, J. M. (1981) Hardground formation in the Hellenic trench: penesaline to hypersaline marine carbonate diagenesis. In: Programme HEAT, Campagne submersible, Les fossés helleniques, 19 aout - 15 septembre 1979, Vol. No. 23 (Ed. by J. Dercourt), pp. 197-213. Publications du centre natinal pour l'exploitation des Oceans (CNEXO): Resultats des campagnes a la mer. Geochimie isotopique et microscope electronique a balayage (MEB).

Besse, D. & Taviani, M. (1982) The last Quaternary sapropelitic level in the Red Sea: its micropalaeontological-mineralogical characteristics and palaeoceanographic significance. In: INQUA XI Congress, Vol. Abstract 1, pp. 36, Moscow.

Blanc, G., Anschutz, P. & Pierret, M.-C. -. (1998) Metalliferous sedimentation in the Atlantis II Deep: a geochemical insight. In: Sedimentation and Tectonics of Rift Basins: Red Sea-Gulf of Aden (Ed. by B. H. Purser and D. W. J. Bosence), pp. 505-520. Chapman & Hall, London.

Blomeier, D. (1997) Evolution einer unterjurassischen Karbonatplattform: Sequenzstratigraphie und Ablagerungsbedingungen am Hochplateau des Jebel Bou Dahar (Hoher Atlas, Marokko). PhD, Christian-Albrechts-Universität.

Boardman, M. R., Neumann, A. C., Baker, P. A., Dulin, L. A., Kenter, R. J., Hunter, G. E. & Kiefer, K. B. (1986) Banktop responses to Quaternary fluctuations in sea-level recorded in periplatform sediments. Geology, 14, 28-31.

Böhm, F. & Brachert, T. C. (1993) Deep-water stromatolites and Frutexites Maslov from the early and middle Jurassic of S-Germany and Austria. Facies, 28, 145-168.

Bonatti, E. (1985) Punctiform initiation of seafloor spreading in the Red Sea during transition from a continental to an oceanic rift. Nature, 316, 33-37.

Bosscher, H. (1992) Growth potential of coral reefs and carbonate platforms. Ph.D. Thesis, Vrije Universiteit, Amsterdam.

Brachert, T. C. (1993) Laminated microbial carbonates and tepee structures from the deep Red Sea. unpublished draft.

Brachert, T. C. (1994) Palaeoecology of enigmatic tube microfossils forming “cryptalgal” fabrics (Late Quaternary, Red Sea). Paläontologische Zeitschrift, 68(3/4), 299-312.

Brachert, T. C. (1995) Non-skeletal carbonate production within a deep ocean basin: The “hard layer” of the glacial Red Sea. unpubl. draft.

Brachert, T. C. (1996) Klimasteuerung von Karbonatsystemen: Fallbeispiele zur Biofazies und flachmariner Ökosysteme im Känozoikum. Habilitation, Johannes Gutenberg Universität.

Brachert, T. C. (1999) Non-skeletal carbonate production and stromatolithe growth within a Pleistocene deep ocean (Last Glacial Maximum, Red Sea). Facies, 40, 211-228.

Brachert, T. C. & Dullo, W. C. (1990) Correlation of deep sea sediments and fore-reef carbonates in the Red Sea: an important clue for basin analysis. Marine Geology, 92, 255-267.

Brachert, T. C. & Dullo, W.-C. (1991) Laminar micrite crusts and associated fore-slope processes, Red Sea. Journal of Sedimentary Petrology, 61(3), 354-363.

Brachert, T. C. & Dullo, W.-C. (1994) Micrite crusts on Ladinian fore-slopes of the Dolomites seen in the light of a modern scenario from the Red Sea. Abhandlungen der Geologischen Bundesanstalt, 50, 57-78.

Braithwaite, C. J. R. (1982) Patterns of accretion of reefs in the Sudanese Red Sea. Marine Geology, 46, 297-325.

Braithwaite, C. J. R. (1987) Geology and palaeontology of the Red Sea region. In: Red Sea (Ed. by A. J. Edwards and S. M. Head), pp. 22-44. Pergamon Press, Oxford.

Broecker, W. S. (1995) The glacial world according to Wally, Lamont-Doherty earth observatory of Columbia University, 318 pp.

Cember, R. P. (1988) On the source, formation, and circulation of Red Sea deep water. Journal of Geophysical Research, 93(C7), 8175-8191.

Chappell, J. & Shackleton, N. J. (1986) Oxygen isotopes and sea level. Nature, 324, 137-140.

Chayes, F. (1956) Petrographic Modal Analysis. Wiley, New York, 113 pp.

Chen, C. (1969) Pteropods in the hot brine sediments of the Red Sea. In: Hot Brines and Recent Heavy Metal Deposits in the Red Sea (Ed. by E. T. Degens and D. A. Ross), pp. 313-316. Springer-Verlag.

CLIMAP Project Members (1981) Seasonal reconstruction of the Earth’s surface at the last glacial maximum. Geological Society of America, Map Chart Ser., 241, 1043-1051.

Coleman, R. G. (1974) Geologic background of the Red Sea. In: The Geology of Continental Margins (Ed. by C. A. Burke and C. L. Drake), pp. 743-751. Springer, Berlin.

Coleman, R. G. (1993) Geologic evolution of the Red Sea. Oxford University Press, Oxford, 186 pp.

Colonna, M., Casanova, J. & Dullo, W.-C. (1996) Sea-level changes and $\delta^{18}O$ record for the past 34,000 yr from Mayotte Reef, Indian Ocean. Quaternary Research, 46, 335-339.

Coplen, T. B., Kendall, C. & Hopple, J. (1983) Comparison of stable isotope reference samples. Nature, 302, 236-238.

Craig, H. (1966) Isotopic composition and origin of the Red Sea and Salton Sea geothermal brines. Science, 154, 1544-1548.

Currie, R. I., Fisher, A. E. & Hargraves, P. M. (1973) Arabian Sea upwelling. In: Ecological studies 3: The Biology of the Indian Ocean (Ed. by J. Jacobs), pp. 37-52. Springer, New York.

Darwin, C. (1876) Über den Bau und die Verbreitung der Corallen-Riffe. Schweitzerbat´sche Verlagsbuchhandlung, Stuttgart.

Davies, P. & Montaggioni, L. (1985) Reef growth and sea-level change: The environmental signature. In: 5th international coral reef symposium, Vol. 3, pp. 477-515.

Degens, E. T. & Ross, D. A. (1969) Hot Brines and Recent Heavy Metal Deposits in the Red Sea. Woods Hole Oceanographic Institution Woods Hole, Massachusetts.

Demaison, G. J. & Moore, G. T. (1980) Anoxic environments and oil source bed genesis. AAPG Bulletin, 64, 1179-1209.

Deuser, W. G. & Degens, E. T. (1969) O18/O16 and C13/C12 ratios of fossils from the hot-brine deep area of the central Red Sea. In: Hot Brines and Recent Heavy Metal Deposits in the Red Sea (Ed. by E. T. Degens and D. A. Ross), pp. 336-347. Springer-Verlag.

Deuser, W. G., Ross, E. H. & Waterman, L. S. (1976) Glacial and pluvial periods: their relationship revealed by Pleistocene sediments of the Red Sea and Gulf of Aden. Science, 191, 1168-1170.

Dravis, J. J. (1996) Rapidity of freshwater calcite cementation- implications for carbonate diagenesis and sequence stratigraphy. Sedimentary Geology, 107, 1-10.

Dromart, G. (1989) Deposition of upper Jurassic fine-grained limestones in the western sub-alpine basins, France. Pal. Pal. Pal., 69, 23-43.

Droxler, A. W. (1984) Late Quaternary glacial cycles in the Bahamian deep basins and in the adjacent Atlantic Ocean. PhD, University of Miami.

Droxler, A. W. (1986) Comment on “Banktop responses to Quaternary fluctuations in sea level recorded in periplatform sediments. Geology, 1039-1040.

Droxler, A. W., Schlager, W. & Whallon, C. C. (1983) Quaternary aragonite cycles and oxygen-isotope record in Bahamian carbonate ooze. Geology, 11, 235-239.

Droxler, A. W. & Schlager, W. (1985) Glacial versus interglacial sedimentation rates and turbidite frequency in the Bahamas. Geology, 13, 799-802.

Droxler, A. W., Bruce, C. H., Sager, W. W. & Watkins, D. H. (1988) Pliocene-Pleistocene variations in aragonite content and planktonic oxygen-isotope record in Bahamian periplatform ooze, Hole 633A. In: Proceedings of the Ocean Drilling Program, Scientific results, Vol. 101 (Ed. by J. A. A. jr. and W. Schlager), pp. 221-236.

Droxler, A. W., Haddad, G. A., Mucciarone, D. A. & Cullen, J. L. (1990) Pliocene-Pleistocene aragonite cyclic variations in holes 741A and 716B (the Maldives) compared with hole 633A (the Bahamas): records of climate-induced CaCO3 preservation at intermediate water depths. In: Proceedings of the ODP, Scientific Results, Vol. 115 (Ed. by R. A. Duncan, J. Backman and L. C. Peterson), pp. 539-567.

Dullo, W.-C. (1987) Pleistozänen Riffe des nördlichen Roten Meeres. Habilitationschrift, Universität Erlangen-Nürnberg.

Dullo, W.-C. (1990) Facies, fossil record, and age of Pleistocene reefs from the Red Sea (Saudi Arabia). Facies, 22, 1-46.

Dullo, W. (1995) Factors controlling Holocene reef growth: An interdisciplinary approach. Facies, 32, 145-188.

Dullo, W.-C., Moussavian, E. & Brachert, T. C. (1990) The foralgal crust facies of the deeper fore reefs in the Red Sea: a deep diving survey by submersible. Geobios, 23(3), 261-281.

Dullo, W.-C., Hassan, M., Heiss, G. A., Reijmer, J. J. G., Schuhmacher, H. & d‘Vries, E. (1994) Holozäne Karbonatproduktion im Roten Meer.

Dullo, W.-C., Eisenhauer, A., Heiss, G. A., Wischow, D., Camoin, G. F., Colonna, M. & Montaggioni, L. (1996a) Coral and Reef Growth in the western Indian Ocean (La Réunion, Mayotte and Seychelles). In: Global and Regional Controls on Biogenic Sedimentation. I Reef Evolution., Vol. Sb2 (Ed. by J. Reitner, F. Neuweiler and F. Gunkel), pp. 23-27. Research Reports.-Göttinger Arb. Geol. Paläontol., Göttingen.

Dullo, W.-C., Reijmer, J. J. G., Schuhmacher, H., Eisenhauer, A., Hassan, M. & Heiss, G. A. (1996b) Holocene Reef Growth and Recent Carbonate Production in the Red Sea. In: Global and Regional Controls on Biogenic Sedimentation. I Reef Evolution., Vol. Sb2 (Ed. by J. Reitner, F. Neuweiler and F. Gunkel), pp. 13-17. Research Reports.-Göttinger Arb. Geol. Paläontol., Göttingen.

Dullo, W.-C. (1997) Die Plattformhangmorphologie der Pedro Bank in der Karibik. Geol. Bl. NO-Bayern, **47**(Heft 1-4), 303-320.

Dullo, W.-C, Reijmer, J., Andresen, N. & Emmermann, P. (1997) Meeresspiegelschwankungen und ihre geologische Überlieferung im Karbonatsystem. Geowissenschaften, 15(9), 296-300.

Dullo, W. C. & Montaggioni, L. (1998) Modern Red Sea coral reefs: a review of their morphologies and zonation. In: Sedimentation and Tectonics of Rift Basins (Ed. by B. H. Purser and D. W. J. Bosence), pp. 583-594. Chapman & Hall, London.

Dullo, W.-C., Camoin, G. F., Blomeier, D., Colonna, M., Eisenhauer, A., Faure, G., Casanova, J. & Thomassin, B. A. (1998) Morphology and sediments of the fore-slopes of Mayotte, Comoro Islands: direct observations from a submersible. Spec. Publs int. Ass. Sediment., 25, 219-236.

Dunham, R. J. (1962) Classification of carbonate rocks according to depositional texture. AAPG Mem., 1, 108-121.

Duplessy, J. C. (1982) Glacial to interglacial contrasts in the northern Indian Ocean. Nature, 295, 494-498.

El-Sayed, M. K. (1984) Reefal sediments of Al-Ghardaqa, Northern Red Sea, Egypt. Marine Geology, 56, 259-271.

Ellis, J. P. & Milliman, J. D. (1985) Calcium carbonate suspended in Arabian Gulf and Red Sea waters: biogenic and detrital, not “chemogenic”. Journal of Sedimentary Petrology, 55(6), 805-808.

Emiliani, C. (1955) Pleistocene temperatures. Journal of Geology, 63(3), 9538-9578.

Emmermann, P. (1994) Untersuchung rezenter Bohrspuren endolithischer Makrobohrer in Riffgesteinen mit Hilfe der Computertomographie. Diplom, Christian-Albrechts-Universität.

Emmermann, P., Isern, A. & Reijmer, J. (1997) A stable isotopic and mineralogic study of a lithified carbonate layer precipitated during the last glacial maximum in the Red Sea. In: AGU fall meeting, Vol. 78 (46), pp. F361. supplement to EOS, San Francisco, USA.

Emmermann, P., Isern, A. & Reijmer, J. (1998) Precipitation of a lithified carbonate layer in the Red Sea under extreme palaeoceanographic conditions of the last glacial maximum. In: 15th international sedimentological congress of the IAS, pp. 316-317. Publicaciones de la Universidad de Alicante, Alicante, Spain. Sedimentology at the dawn of the third millennium.

Emmermann, P., Reijmer, J. & Andresen, N. (1999) Sedimentation rates of Quaternary periplatform sediments based on aragonite/calcite ratios: Sudanese Red Sea vs. Pedro Bank, Caribbean. In: Geo Research Forum: On the determination of sediment accumulation rates, Vol. 5 (Ed. by P. Bruns and C. Haas), pp. 67-86. Trans Tech Publications.

Everts, A.-J. (1994) Carbonate sequence stratigraphy of the Vercors (French Alps) and its bearing on Cretaceous sea level. PhD, Vrije Universiteit.

Everts, A. J. W. & Reijmer, J. J. G. (1995) Clinoform composition and margin geometry of a Lower Cretaceous carbonate platform (Vercors, SE France). Palaeogeography, Palaeoclimatology, Palaeoecology, 119, 19-33.

Fairbanks, R. G. (1989) A 17,000-year glacio-eustatic sea level record: Influence of glacial melting rates on the Younger Dryas event and deep-ocean circulation. Nature, 342, 637-642.

Flügel, E. (1982) Microfacies Analysis of Limestones. Springer Verlag, Berlin, 375 pp.

Franz, S. O. (1999) Pliozäne Zeitreihen zur Rekonstruktion der Tiefenwasserzirkulation und der siliziklastischen Amazonasfracht im Äquatorialen Westatlantik (Ceara Schwelle, ODP Leg 154). PhD, Christian-Albrechts Universität.

Fricke, H. W. & Schuhmacher, H. (1983) The depth limits of Red Sea stony corals: an ecophysiological problem. Marine Ecology, **4**, 163-194.

Friedman, G. M., Amiel, A. J. & Schneidermann, N. (1974) Submarine cementation in reefs: Example from the Red Sea. Journal of Sedimentary Petrology, 44(3), 816-825.

Frisch, W. & Loeschke, J. (1993) Plattentektonik. Wissenschaftliche Buchgesellschaft, Darmstadt.

Gabrié, C. & Montaggioni, L. (1982) Sedimentary facies from the modern coral reefs, Jordan Gulf of Aqaba, Red Sea. Coral Reefs, 1, 115-124.

Geiselhardt, S. (1998) Late Quaternary palaeoceanographic and palaeoclimatologic history of the Red Sea during the last 380.000 years: Evidence from stable isotopes and faunal assemblages. Tuebinger Mikropalaeontologische Mitteilungen, 17, 87.

Gevirtz, J. L. & Friedmann, G. M. (1966) Deep- Sea carbonate sediments of the Red Sea and their implications on marine lithification. Journal of Sedimentary Petrology, 36(1), 143-151.

Girdler, R. W. & Southren, T. C. (1987) Structure and evolution of the northern Red Sea. Nature, 330, 716-721.

Glaser, K. S. (1991) Late Quaternary periplatform sediments and environments on the North-eastern Nicaragua Rise, Caribbean Sea. Ph.D. Thesis (unpublished), Rice University.

Glaser, K. S. & Droxler, A. W. (1991) High production and highstand shedding from deeply submerged carbonate banks, Northern Nicaragua Rise. Journal of Sedimentary Petrology, 61(1), 128-142.

Glaser, K. S. & Droxler, A. W. (1993) Controls and development of Late Quaternary periplatform carbonate stratigraphy in Walton Basin (North-eastern Nicaragua Rise, Caribbean Sea). Palaeoceanography, 8(2), 243-274.

Gonzáles, L. A. & Lohmann, K. C. (1985) Carbon and oxygen isotopic composition of Holocene reefal carbonates. Geology, 13, 811-814.

Grammer, G. M. & Ginsburg, R. N. (1992) Highstand versus lowstand deposition on carbonate platform margins: insight from Quaternary foreslopes in the Bahamas. *Marine Geology*, **103**, 125-136.

Grasshoff, K. (1969) Zur Chemie des Roten Meeres und des inneren Golfs von Aden nach Beobachtungen von F.S. Meteor während der Indischen Ozean Expedition 1964/65. Meteor-Forschungs-Ergebnisse, A6, 1-76.

Grasshoff, K. (1975) The hydrochemistry of landlocked basins and fjords. In: Chemical Oceanography, Vol. 2 (Ed. by J. P. Riley and J. Skirow), pp. 456-597. Academic Press, New York.

Gvirtzman, G. (1994) Fluctuations of sea-level during the past 400,000 years: the record of Sinai, Egypt (Northern Red Sea). Coral Reefs, 13, 203-314.

Gvirtzman, G., Buchbinder, B., Sneh, A., Nir, Y. & Friedman, G. M. (1977) Morphology of the Red Sea fringing reefs: A result of the erosional pattern of the last-glacial low-stand sea level and the following Holocene recolonisation. In: 2e Symposium international sur les coraux et récifes coralliens fossiles, Vol. 89, pp. 480-491. Memoires Bureau Recherche Geologique Minieres.

Gvirtzman, G. & Buchbinder, B. (1978) Recent and Pleistocene coral reefs and coastal sediments from the Gulf of Eilat. In: Tenth international Congress of Sedimentology, Vol. Post-Congress Excursion Y4, pp. 163-191, Jerusalem.

Haak, A. B. & Schlager, W. (1989) Compositional variations in calciturbidites due to sea-level fluctuations, late Quaternary, Bahamas. Geologische Rundschau, 78(2), 477-486.

Haddad, G. A. & Droxler, A. W. (1996) Metastable $CaCO_3$ dissolution at intermediate water depths of the Caribbean and western North Atlantic: Implications for intermediate water circulation during the past 200,000 years. Palaeoceanography, 11(6), 701-716.

Halicz, E. & Reiss, Z. (1981) Paleoecological relations of foraminifera in a desert-enclosed sea - the Gulf of Aqaba (Elat), Red Sea. *Marine Ecology*, **2**(1), 15-34.

Hardy, R. & Tucker, M. (1988) X-ray powder diffraction of sediments. In: Techniques in Sedimentology (Ed. by M. Tucker), pp. 191228. Blackwell Scientific Publications, Oxford.

Hassan, M. (1997) Modification of carbonate strata by bioerosion and bioaccretion on coral reefs of the Red Sea. PhD, Christian-Albrechts-Universität.

Hearty, P. J. (1998) The geology of Eleuthrea Island, Bahamas: a rosetta stone of Quaternary stratigraphy and sea-level history. Quaternary Science Reviews, 17, 333-355.

Heiss, G. A. (1995) Carbonate production by Scleractinian corals at Aqaba, Gulf of Aqaba, Red Sea. Facies, 33, 19-34.

Hemleben, C., Spindler, M. & Anderson, O. R. (1989) Modern planktonic foraminifera. Springer, 363 pp.

Hemleben, C., Meischner, D., Zahn, R., Almogi-Labin, A., Erlenkeuser, H. & Hiller, B. (1996) Three hundred eight thousands year long stable isotope and faunal records from the Red Sea: Influence of global sea level change on hydrography. Palaeoceanography, 11.

Herman, Y. (1968) Evidence of climatic changes in Red Sea cores: means of correlation of Quaternary successions. In: 8th Congress of the International Association of Quaternary Research, pp. 325-348.

Herman, Y. (1971) Vertical and horizontal distribution of pteropods in Quaternary sequences. In: The Micropalaeontology of Oceans (Ed. by B. M. Funnell), pp. 463-468. Cambridge University Press.

Hofmann, P., Schwark, L., Brachert, T., Badaut, D., Rivière, M. & Purser, B. H. (1998) Sedimentation, organic geochemistry and diagenesis of cores from the axial zone of the southern Red Sea: relationships to rift dynamics and climate. In: Sedimentation and Tectonics of Rift Basins (Ed. by B. H. Purser and D. W. J. Bosence), pp. 479-504. Chapman & Hall, London.

Hubbard, D. K., Miller, A. I. & Scaturo, D. (1990) Production and cycling of calcium carbonate in a shelf-edge reef system (St. Croix, US Virgin Islands): Applications to the nature of reef systems in the fossil record. Journal of Sedimentary Petrology, 60(3), 335-360.

Imbrie, J., Hays, J. D., Martinson, D. G., McIntyre, A., Mix, A. C., Morley, J. J., Pisias, N. G., Prell, W. L. & Shackleton, N. J. (1984) The orbital theory of Pleistocene climate: Support from a revised chronology of the marine $\delta^{18}O$ record. In: Milankovitch and Climate, Part 1 (Ed. by A. L. e. a. Berger), pp. 269-305. D. Reidel Publishing Company.

Ivanova, E. V. (1985) Late Quaternary biostratigraphy and palaeotemperatures of the Red Sea and the Gulf of Aden based on planktonic foraminifera and pteropods. Marine Micropalaeontology, 9, 335-364.

James, N. P., Coniglio, M., Aissaoui, D. M. & Purser, B. H. (1988) Facies and geological history of an exposed Miocene rift-margin carbonate platform: Gulf of Suez, Egypt. American Association of Petroleum Geologists Bulletin, 72, 55-572 ?

Keir, R. S. & Berger, W. H. (1985) Late Holocene carbonate dissolution in the equatorial Pacific: reef growth or neoglaciation? In: *The carbon cycle and atmospheric CO2: Natural variations Archean to present - American Geophysical Union Geophysical Monograph, Vol. 32* (Ed. by E. T. Sundquist and W. S. Broecker), pp. 208-220, Washington DC

Kennett, J. (1982) Marine Geology. Prentice-Hall, 813 pp.

Kenter, R. J. (1985) Sealevel fluctuations recorded as rhythmic deposition in the Northwest Providence Channel, Bahamas. MS-thesis, Miami University.

Ku, T.-L., Thurber, D. L. & Matthieu, G. G. (1969) Radiocarbon chronology of Red Sea sediments. In: Hot Brines and Recent Heavy Metal Deposits in the Red Sea (Ed. by E. T. Degens and D. A. Ross), pp. 348-359. Springer, New York.

Labeyrie, L. D., Duplessy, J.-C. & Blanc, P. L. (1987) Variations in mode of formation and temperature of oceanic deep waters over the past 125,000 years. Nature, 327, 477-482.

Locke, S. M. (1986) The palaeoceanographic record of the last glacial-interglacial cycle in the Red Sea and Gulf of Aden. Masters of Science, Pennsylvania State University.

Locke, S. & Thunell, R. C. (1988) Palaeoceanographic record of the last glacial/interglacial cycle in the Red Sea and Gulf of Aden. Palaeogeography, Palaeoclimatology, Palaeoecology, 64, 163-187.

Loya, Y. & Slobodkin, L. B. (1971) The coral reefs of Eilat (Gulf of Eilat, Red Sea). In: Regional variations in Indian Coral Reefs, Vol. 28 (Ed. by D. R. Stoddart and M. Yonge), pp. 117-139. Symposium of the Zoological Society of London.

Macintyre, I. G. & Reid, R. P. (1992) Comment on the origin of aragonite needle mud: a picture is worth a thousand words. Journal of Sedimentary Petrology, 62(6), 1095-1097.

Macintyre, I. G. & Reid, R. P. (1995) Crystal alteration in a living calcareous alga (Halimeda): Implications for studies in skeletal diagenesis. Journal of Sedimentary Petrology, 65(1), 143-153.

Maillard, C. & Soliman, G. (1986) Hydrography of the Red Sea and exchanges with the Indian Ocean in summer. Oceanologica Acta, 9(3), 249-269.

McKenzie, J. A. & Bernoulli, D. (1982) Geochemical variations in Quaternary hardgrounds from the Hellenic Trench region and possible relationship to their tectonic setting. Tectonophysics, 86, 149-157.

Mergner, H. & Schuhmacher, H. (1985) Quantitative Analyse von Korallengemeinschaften des Sanganeb-Atolls (mittlerse Rotes Meer). I. Die Besiedlungsstruktur hydrodynamisch unterschiedlich exponierter Außen- und Innenriffe. Helgoländer Meeresuntersuchungen, 39, 375-417.

Mergner, H. & Schuhmacher, H. (1974) Morphologie, Ökologie und Zonierung von Korallenriffen bei Aqaba, (Golf von Aqaba, Rotes Meer). Helgoländer wissenschaftliche Meeresuntersuchungen, 26, 238-258.

Milliman, J. D. (1974) Marine carbonates. Springer Verlag.

Milliman, J. D. (1975) Dissolution of aragonite, Mg-calcite and calcite in the North Atlantic Ocean. Geology, 461-462.

Milliman, J. D. (1977) Interstitial waters of late Quaternary Red Sea sediments and their bearing on submarine lithification. Kingdom of Saudi Arabia, Red Sea research 1970-75. Mineral Resources Bulletin, 22-M(i-iii + M1-M6).

Milliman, J. D., Ross, D. A. & Ku, T.-L. (1969) Precipitation and lithification of deep-sea carbonates in the Red Sea. Journal of Sedimentary Petrology, 39(2), 724-736.

Milliman, J., Freile, D., Steinen, R. & Wilber, R. (1993) Great Bahama Bank aragonitic muds: mostly inorganically precipitated, mostly exported. J Sediment Petrol, 63/4, 589-595.

Milliman, J. D., Troy, P. J., Balch, W. M., Adams, A. K., Li, Y.-H. & Mackenzie, F. T. (1999) Biologically mediated dissolution of calcium carbonate above the chemical lysocline? Deep-Sea Research I, 46, 1653-1669.

Morcos, S. A. (1970) Physical and chemical oceanography of the Red Sea. Marine Biology Annual Review, 18, 73-202.

Morse, J. W. & Mackenzie, F. T. (1990) Geochemistry of Sedimentary Carbonates. In: Developments in Sedimentology, Vol. 48, pp. 179-239. Elsevier.

Mullins, H. T. (1985) Modern deep-water carbonates along the Blake-Bahamas boundary. In: SEPM Core Workshop No. 6 (Ed. by P. D. Crevello and P. M. Harris), pp. 461-490, New Orleans. Deep-water Carbonates: Build-ups, Turbidites, Debris Flows and Chalks.

Natterer, K. (1898) Expedition S.M. Schiff “Pola” in das Rote Meer, Nördliche Hälfte (Oktober 1895 - May 1896). Denkschriften Akademie der Wissenschaften in Wien, Mathematisch-Naturwissenschaftliche Klasse, 65, 445-572.

Neev, D. & Emery, K. O. (1967) The Dead Sea. Depositional processes and environment of evaporites. Bull. Geol. Surv. Israel, 41, 147.

Neumann, A. C. & McGill, D. A. (1962) Circulation of the Red Sea in early summer. Deep-Sea Research, 8, 223-235.

Neumann, A. C. & Land, L. S. (1975) Lime mud deposition and calcareous algae in the Bight of Abaco, Bahamas: a budget. Journal of Sedimentary Petrology, 45(4), 763-786.

Neumann, A. C. & Hearty, P. J. (1996) Rapid sea-level changes at the close of the last interglacial (substage 5e) recorded in the Bahamian island geology. Geology, 24(9), 775-778.

Opdeyke, B. N. & Walker, J. C. G. (1992) Return to the coral reef hypothesis: basin to shelf partitioning of CaCO3 and its effect on atmospheric CO2. Geology, 20, 733-736.

O´Neil, J. R. (1969) Oxygen isotope fractionation in divalent metal carbonates. Jour. Chem. Phys., 51, 5547-5558.

Paillard, D., Labeyrie, L. & Yiou, P. (1996) AnalySeries 1.0 a7 PPC, Macintosh program performs time-series analysis. Eos Trans. AGU, 77, 379.

Patzert, W. C. (1974) Wind-induced reversal in the Red Sea circulation. Deep-Sea Research, 21, 109-121.

Perl, A. (1997) Quantitative und qualitative Sedimentanalyse an Saumriffhängen im Golf von Aqaba (Jordanien - Nördliches Rotes Meer). M.Sc., Christian-Albrechts-Universität.

Perrin, C., Plaziat, J.-C. & Rosen, B. R. (1998) Miocene coral reefs and reef corals of the south-western Gulf of Suez and north-western Red Sea: Distribution, diversity and regional environmental control. In: Sedimentation and Tectonics of Rift Basins: Red Sea-Gulf of Aden (Ed. by B. H. Purser and D. W. J. Bosence), pp. 296-319. Chapman & Hall, London.

Petschik. (1993) MacDiff: Analysis of X-ray diffraction data.

Piller, W. E. (1994) The Northern Bay of Safaga (Red Sea, Egypt): An actuopalaeontological approach. IV. Thin section analysis. Beitr. Paläontologie, 18, 1-73.

Piller, W. E. & Mansour, A. M. (1990) The Northern Bay of Safaga (Red Sea, Egypt): An actuopalaeontological approach. II. Sediment Analysis and Sedimentary Facies. Beitr. Paläont. Österr., 16, 1-102.

Playford, P. E., Cockbain, A. E., Druce, E. C. & Wray, J. L. (1976) Devonian stromatolites from the Canning Basin, Western Australia. Developments in Sedimentology, 20, 389-411.

Plaziat, J. C., Baltzer, F., Choukri, A., Conchon, O., Freytet, P., Orszag-Sperber, F., Raguideau, A. & Reyss, J. L. (1998) Quaternary marine and continental sedimentation in the Northern Red Sea and Gulf of Suez (Egyptian coast): Influences of rift tectonics, climatic changes and sea-level fluctuations. In: Sedimentation and Tectonics of Rift Basins: Red Sea-Gulf of Aden (Ed. by B. H. Purser and D. W. J. Bosence), pp. 537-573. Chapman & Hall, London.

Purser, B. H., Phillobos, E. R. & Soliman, M. (1990) Sedimentation and rifting in the NW part of the Red Sea: a review. Geological Society of France Bulletin, 8, 371-384.

Reches, Z., Erez, J. & Garfunkel, Z. (1987) Sedimentary and tectonic features in the north-western Gulf of Eilat, Israel. Tectonophysics, 141, 169-180.

Reijmer, J. J. G. (1991) Sea level and sedimentation on the flanks of carbonate platforms. PhD Thesis, Vrije Universiteit, Amsterdam.

Reijmer, J. J. G., Schlager, W. & Droxler, A. W. (1988) Site 632: Pliocene-Pleistocene sedimentation cycles in a Bahamian basin. In: Proceedings of the Ocean Drilling Program, Scientific Results, Vol. 101 (Ed. by J. A. J. Austin and W. Schlager), pp. 213-220.

Reijmer, J. J. G., Schlager, W., Bosscher, H., Beets, C. J. & McNeill, D. F. (1992) Pliocene/Pleistocene platform facies transition recorded in calciturbidites (Exuma Sound, Bahamas). Sedimentary Geology, 78, 171-179.

Reiss, Z., Luz, B., Almogi-Labin, A., Halicz, E., Winter, A., Wolf, M. & Ross, D. A. (1980) Late Quaternary palaeoceanography of the Gulf of Aqaba (Elat), Red Sea. Quaternary research, 14, 294-308.

Reiss, Z. & Hottinger, L. (1984) The Gulf of Aqaba. Springer, Berlin-Heidelberg-New York-Tokyo.

Rendle, R. H., Reijmer, J. J. G., Kroon, D. & Henderson, G. M. (in press 2000) Mineralogy and sedimentology of the Pleistocene to Recent on the leeward margin on Great Bahama Bank. ODP Scientific Results, 166.

Risch, H. (1976) Microbiostratigraphy of core-sections of the Red Sea. Geologisches Jahrbuch, D 17, 3-14.

Ross, D. A. & Schlee, J. (1973) Shallow structure and geological development of the southern Red Sea. Geological society of American Bulletin, 84, 3827-3848.

Rossignol-Strick, M. (1983) African monsoons, an immediate climate response to orbital insolation. Nature, 304, 46-49.

Sabine, C. L. & Mackenzie, F. T. (1995) Bank-derived carbonate sediment transport and dissolution in the Hawaiian Archipelago. Aquatic Geochemistry, 1, 189-230.

Sarg, J. F. (1988) Carbonate sequence stratigraphy. In: Sea-level changes: an integrated approach, Vol. 42 (Ed. by C. K. Wilgus, B. S. Hastings, C. G. S. C. Kendall, H. W. Posamentier, C. A. Ross and J. C. Van Wagoner), pp. 155-182. Society of Economic Palaeontologists and Mineralogists, Tulsa, Oklahoma, USA Special Publication.

Schlager, W. (1992) Sedimentology and sequence stratigraphy of reefs and carbonate platforms. Am. Assoc. Petrol. Geol. Contin. Educ. Course Note Series, 34, 71.

Schlager, W. (1993) Accommodation and supply - a dual control on stratigraphic sequences. Sediment. Geol., 86, 111-136.

Schlager, W. & James, N. (1978) Low-magnesian calcite limestones forming at the deep-sea floor, Tongue of the Ocean, Bahamas. Sedimentology, 25, 675-702.

Schlager, W., Reijmer, J. J. G. & Droxler, A. W. (1994) Highstand shedding of carbonate platforms. Journal of Sedimentary Research, B64(3), 270-281.

Schoell, M. & Risch, H. (1976) Oxygen- and carbon isotope analysis on planktic foraminifera Core VA 01-188 P (Southern Red Sea). Geologisches Jahrbuch, D 17, 15-932?

Scholle, P., Bebout D.G. & Moore, C. (1983) Carbonate depositional environments. The American Association of Petroleum Geologists, 708 pp.

Schrag, P., Hampt, G. & Murray, D. (1997) Oxygen isotopic composition of interstitial waters from Leg 154: Determination of the temperature and isotopic composition of the glacial ocean. In: Proceedings of the ocean drilling program, scientific results, Vol. 154 (Ed. by N. Shackleton, W. Curry, C. Richter and T. Bralower).

Schroeder, J. H. & Nasr, D. H. (1983) The fringing reefs of Port Sudan: I. Morphology - Sedimentation - Zonation. Essener Geogr. Arb., 6, 29-44.

Schuhmacher, H. & Mergner, H. (1985) Quantitative Analyse von Korallengemeinschaften des Sanganeb-Atolls (mittleres Rotes Meer). II Vergleich mit einem Riffareal bei Aqaba (nördliches Rotes Meer) am Nordrand des indopacifischen Riffgürtels. Helgoländer wiss. Meeresunters., 39, 419-440.

Schuhmacher, H., Kiene, W. & Dullo, W.-C. (1995) Factors controlling Holocene reef growth: An interdisciplinary approach. Facies, 32, 145-188.

Schulz, H., vonRad, U. & Erlenkeuser, H. (1998) Correlation between Arabian Sea and Greenland climate oscillations of the past 110,000 years. Nature, 393, 54-57.

Shackleton, N. J. & Opdyke, N. D. (1973) Oxygen isotope and palaeomagnetic stratigraphy of equatorial Pacific core V28-238: oxygen isotope temperatures and ice volumes on a 10^5 year and 10^6 year scale. *Quaternary Research*, **3**, 39-55.

Shanmugam, G. & Maiola, R. J. (1982) Eustatic control of turbidites and winnowed turbidites. Geology, 10, 231-235.

Shanmugan, G. & Maiola, R. J. (1984) Eustatic control of calciclastic turbidites. Marine Geology, 56, 273-278.

Shinn, E. (1980) Geologic history of Grecian Rocks, Key Largo Coral Reef Marine Sanctuary. Bulletin of Marine Science, 30, 646-656.

Shinn, E. A., Steinen, R. P., Lidz, B. H. & Swart, P. K. (1989) Perspectives: Whitings, a sedimentologic dilemma. Journal of Sedimentary Petrology, 59(1), 147-191.

Siedler, G. (1968) Schichtungs- und Bewegungsverhältnisse am Südausgang des Roten Meeres. Meteor Forschungsergebnisse, 4, 1-76.

Sirocko, F. (1994) Abrupt change in monsoonal climate: evidence from the geochemical composition of Arabian Sea sediments. Habilitation, Christian-Albrechts-Universität.

Stoffers, P. & Kuhn, R. (1974) Red Sea evaporites: a petrographic and geochemical study. In: Initial Reports of the Deep Sea Drilling Project (Ed. by R. N. Whitmarsh, O. E. Weser and D. A. Ross), pp. 821-847. US Government Printing Office, Washington.

Stoffers, P. & Ross, D. A. (1977) Sedimentary history of the Red Sea. Mineral Resources Bulletin, 22-H, i-iv + H1-H19, 849-865.

Stoffers, P. & Botz, R. (1990) Carbonate crusts in the Red Sea: Their composition and isotope geochemistry. In: Facets of Modern Biogeochemistry (Ed. by V. Ittekot, S. Kempe, W. Michaelis and A. Spitzy), pp. 242-252. Springer.

Stoffers, P., Botz, R. & Scholten, J. (1990) Isotope geochemistry of primary and secondary carbonate minerals in the Shaban Deep (Red Sea). In: Sediments and Environmental Geochemistry. Selected Aspects and Case Histories (Ed. by D. Heling, P. Rothe, U. Förstner and P. Stoffers), pp. 83-94. Springer, Berlin.

Stuiver, M. & Polach, H. (1977) Discussion: Reporting of ^{14}C Data. Radiocarbon, 19(3), 355-363.

Sturm, A. (1998) Das Problem der Trockendichten bei der Berechnung von Akkumulationsraten in marinen Sedimenten. Diplomarbeit, Christian-Albrechts-University.

Styles, P. & Hall, S. A. (1980) A comparison of the seafloor spreading histories of the western Gulf of Aden and the central Red Sea. Atti. Conv. Lincei., 47, 2981-3006.

Sun, Q. & Esteban, M. (1994) Palaeoclimatic controls on sedimentation and diagenesis and reservoir quality: lessons from Miocene carbonates. Bulletin of the American Association of Petroleum Geologists, 78, 519-543.

Taviani, M. (1998a) Post-Miocene reef faunas of the Red Sea: glacio-eustatic controls. In: Sedimentation and Tectonics of Rift Basins: Red Sea-Gulf of Aden (Ed. by B. H. Purser and D. W. J. Bosence), pp. 574-582. Chapman & Hall, London.

Taviani, M. (1998b) Stable tropics not so stable: climatically driven extinction of reef associated molluscan assemblages (Red Sea and western Indian Ocean; last interglacial to present). In: Reefs and Carbonate Platforms in the Pacific and Indian Oceans, Vol. 25 (Ed. by G. F. Camoin and P. J. Davies), pp. 69-76. Special Publications of the international Association of Sedimentologists.

Taviani, M. (1998c) Axial sedimentation of the Red Sea transitional region (22°-25° N): pelagic, gravity flow and sapropel deposition during the late Quaternary. In: Sedimentation and Tectonics of Rift Basins: Red Sea-Gulf of Aden (Ed. by B. H. Purser and D. W. J. Bosence), pp. 574-582. Chapman & Hall, London.

Thunell, R. C., Locke, S. M. & Williams, D. F. (1988) Glacio-eustatic sea-level control on Red Sea salinity. Nature, 334, 601-604.

Tipper, J. C. (1997) Modelling carbonate platform sedimentation-Lag comes naturally. Geology, 25, 495-498.

Tucker, M. E. (1985) Einführung in die Sedimentpetrologie. Enke, Stuttgart.

Vacher, H. L. & Hearty, P. J. (1989) History of stage-5 sea level in Bermuda: with new evidence of a rise to present sea level during substage 5a. Quaternary Science Reviews, 8, 159-168.

Vail, P. R., Mitchum, R. M. & Thompson III, S. (1977) Seismic stratigraphy and global changes of sea level, part 4: Global cycles of relative changes of sea level. In: Seismic Stratigraphy - Applications to Hydrocarbon Exploration, Vol. Memoir 26 (Ed. by C. E. Payton), pp. 83-97. The American Association of Petroleum Geologists.

Vail, P. R., Audemard, F., Bowman, S. A., Eisner, P. N. & Perez-Cruz, C. (1991) The stratigraphic signatures of tectonics, eustasy and sedimentology - an overview. In: Cycles and events in Stratigraphy (Ed. by Einsele), pp. 617-658. Springer, Berlin-Heidelberg.

Vézina, J., Jones, B. & Ford, D. (1999) Sea-level highstands over the last 500,000 years: evidence from the Ironshore Formation on Grand Cayman, British West Indies. Journal of Sedimentary Research, 69(2), 317-327.

Vogelsang, E. (1990) Paläo-Ozeanographie des Europäischen Nordmeeres an Hand stabiler Kohlenstoff- und Sauerstoffisotope, pp. 136. Christian-Albrechts-Universität, Kiel.

Volat, J.-L., Pastouret, L. & Vergnaud-Grazzini, C. (1980) Dissolution and carbonate fluctuations in Pleistocene deep-sea cores: a review. Marine Geology, 34, 1-28.

Walter, L. M. & Burton, E. A. (1990) Dissolution of Recent platform carbonate sediment in marine pore fluids. American Journal of Science, 220, 601-643.

Westphal, H. (1997) Sediment input and diagenesis of periplatform carbonates on a leeward slope of Great Bahama Bank. PhD, Christian-Albrechts-Universität.

Wilber, R. J. & Neumann, A. C. (1993) Effects of submarine cementation on microfabrics and physical properties of carbonate slope deposits, Northern Bahamas. In: Carbonate Microfabrics (Ed. by R. Rezak and D. L. Lavoie), pp. 79-94. Springer, New York.

Wimmenauer, W. (1985) Petrographie der magmatischen und metamorphen Gesteine. Enke, Stuttgart, 382 pp.

Winter, A., Almogi-Labin, A., Erez, Y., Halicz, E., Luz, B. & Reiss, Z. (1983) Salinity tolerance or marine organisms deduced from Red Sea Quaternary record. Marine Geology, 53, M17-M22.

Woelk, S. & Quadfasel, D. (1996) Renewal of deep water in the Red Sea during 1982-1987. Journal of Geophysical Research, 101, 18155-18165.

Wyrtki, K. (1971) Oceanographic Atlas of the International Ocean Expedition, Washington DC, 531 pp.

PLATES OF MICROPHOTOGRAPHS

Plate 1: Foraminifers, molluscs, echinoderms and bryozoans

Plate 2: Scleractinians, coralline red algae, serpulids, spherolites and non biogenic components

Plate 3: Main lithofacies types

PLATE 1: FORAMINIFERS, MOLLUSCS, ECHINODERMS AND BRYOZOANS

Fig. 1: Planktic foraminifers (F) and fragments of pteropod shells (P). Holocene periplatform sediment.- Core S6, 60 cm, 100x.

Fig. 2: Oblique section through a small, thin walled (porcellaneous) foraminifer (F) of the quinqueloculine type (*Pyrgo*?). Calciturbidite within the lithified interval. - Core S3 (58-63 cm), 200x.

Fig. 3: Axial section through a rotaliid foraminifer (F). Note the two scleractinian fragments (S) in the lower right corner. Calciturbidite (skeletal grainstone) within the lithified interval. - Core S3 (83-88 cm), 100x.

Fig. 4: Axial-transversal section through a sessile foraminifer (F) of the genus *Planorbulinella*.. Calciturbidite (skeletal grainstone) of IS 3.- Core S3 (274-279 cm), 100x.

Fig. 5: Coiled pteropod shell (*Limacina?*) showing epitaxial growth of fibrous aragonite cement (AC) on the inner shell walls. Lithified interval. - Core S3 (72-77 cm), 200x.

Fig. 6: Fragment of a mollusc shell (M) showing cross lamelar structures in oblique section. Note the coralline algae (A) and scleractinian fragments (S). Calciturbidite (skeletal grainstone) of IS 3- Core S3 (274-279 cm), 200x.

Fig. 7: Transversal section through an echinoid spine (E). Calciturbidite (skeletal grainstone) within the lithified interval. - Core S3 (72-77 cm), 200x.

Fig. 8: Transverse section through a ramose bryozoan fragment (B). Note the growth of drusy cements (DC) on the inner walls of the skeleton. The uppermost chambers are filled with the characteristic clotted peloidal micrite (PM). - Core S3 (72-77 cm), 100x.

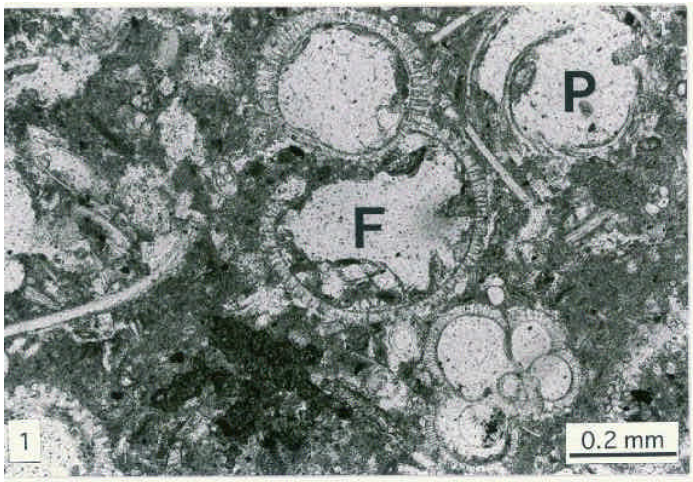
P
F
1
0.2 mm

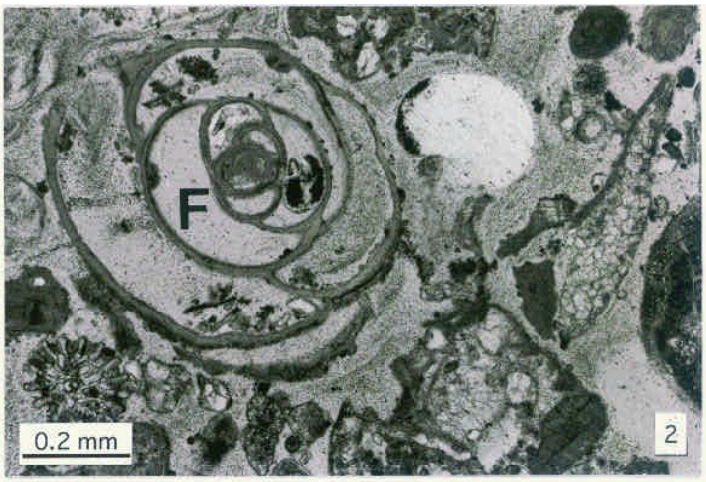
F
0.2 mm
2

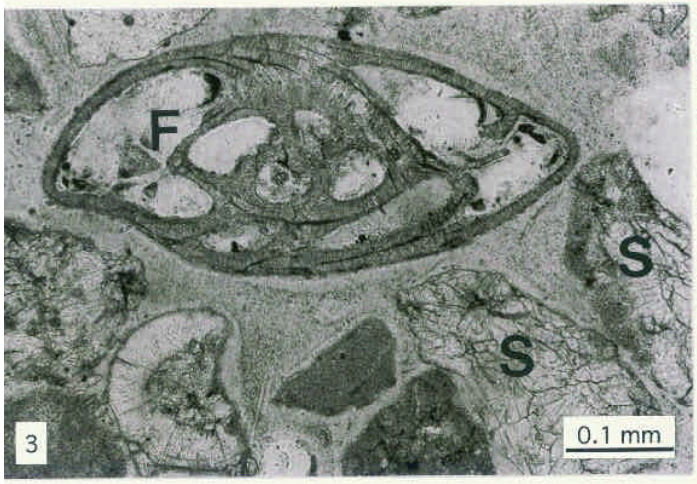
F
S
S
3
0.1 mm

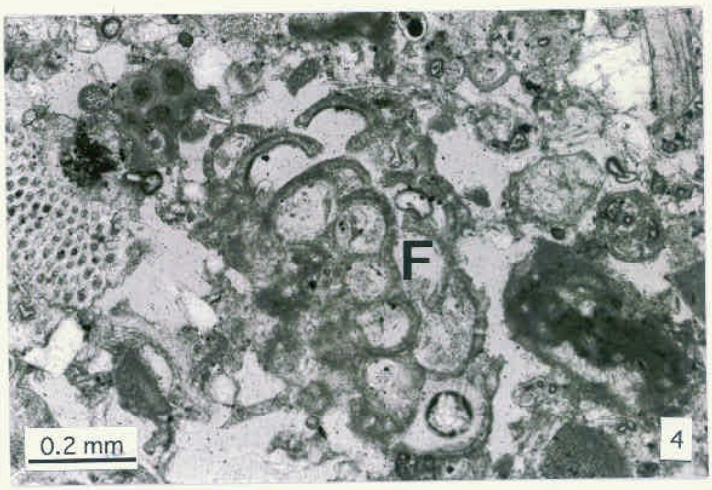
F
0.2 mm
4

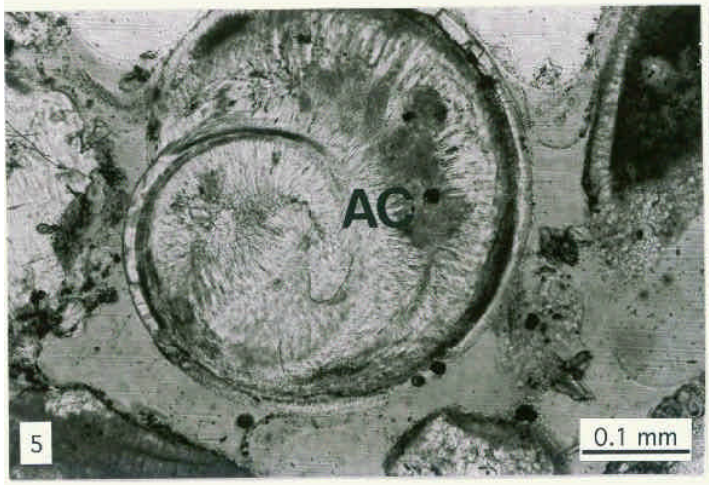
AC
5
0.1 mm

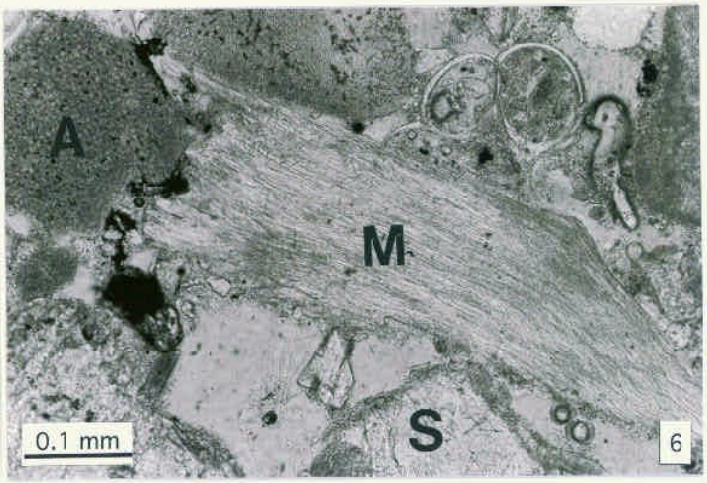
A
M
S
0.1 mm
6

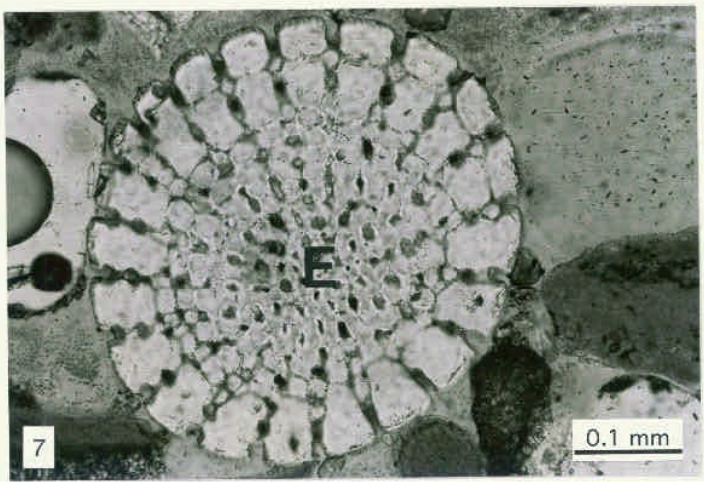
E
7
0.1 mm

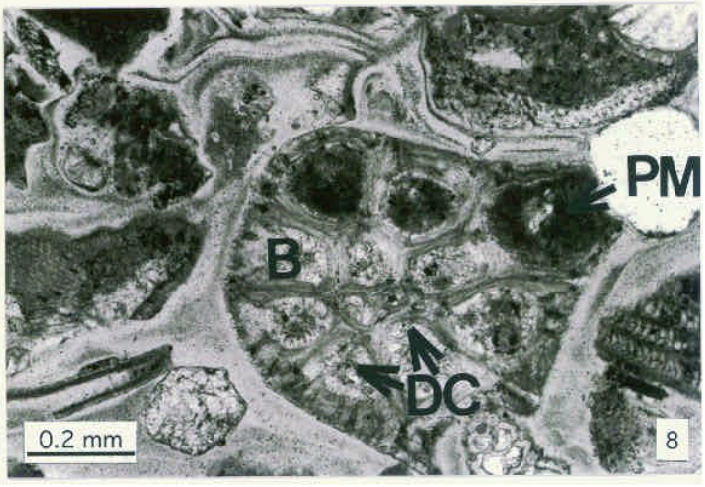
PM
B
DC
0.2 mm
8

PLATE 2: SCLERACTINIANS, CORALLINE RED ALGAE, SERPULIDS, SPHEROLITES AND NON BIOGENIC COMPONENTS

Fig. 1: Large scleractinian fragment (S) showing the beginning of micritisation along its rim (arrow).- Core S3 (274-279 cm), 200x.

Fig. 2: Coralgal fragment. Scleractinian (S) encrusted by a coralline red algae (RA).- Core S3 (58-63 cm), 100x.

Fig. 3: Oblique longitudinal section through a geniculate coralline algae (RA).- Core S6 (290 cm), 200x.

Fig. 4: Section through a small spherolite (SP) with radial-concentric structure. Note the micritic envelope at the left-hand rim of the component. Periplatform sediment (bioclastic, foraminifer- and pteropod-bearing mud- to wackestone).- Core S6 (cm), 200x.

Fig. 5: Transverse section of an encrusting annelid worm tube (W) with relicts of the biogenic substratum (S; scleractinian?) on the upper left rim.- Core S3 (198-203 cm), 100x.

Fig. 6: Large oval pellet (P), ellipsoidal type, composed of bioclasts, without internal structure.- Core S6 (cm), 100x.

Fig. 7: Compound grain (CG) composed of a large mollusc shell fragment (M) and a smaller bioclast (B; bryozoan or hydrozoan fragment) bound by detritic algal micrit. Calciturbidite (skeletal grainstone).- Core S3 (72-77 cm), 100x.

Fig. 8: Coated grain. Bioclast (*Homotrema* ?) with micritic envelope (ME).- Core S3 (83-88 cm), 200x.

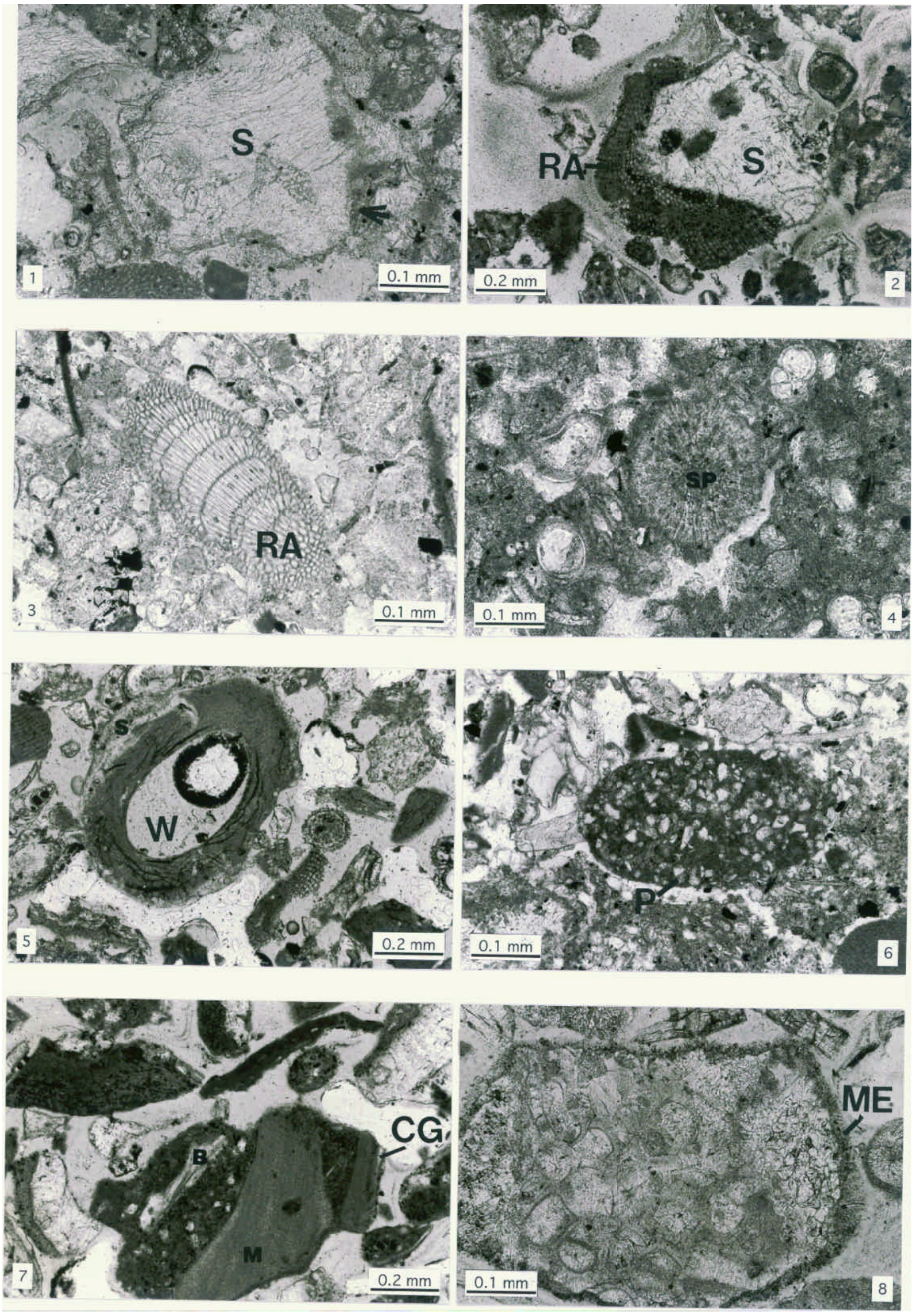
S
1
0.1 mm
RA
S
0.2 mm
2
RA
3
0.1 mm
SP
0.1 mm
4
S
W
5
0.2 mm
P
0.1 mm
6
CG
B
M
7
0.2 mm
ME
0.1 mm
8

PLATE 3: MAIN LITHOFACIES TYPES

Fig. 1: Holocene, biodetritic periplatform ooze (mud- to wackestone), rich in planktic foraminifers (F), pteropod shells (P) and fine-sandy bioclasts.- Core S6, 50 cm, 50x.

Fig. 2: Characterisitc periplatform sediment with planktic foraminifers (F), pteropods (P) and shallow-water derived components (large benthic foraminifer; BF). - Core S6, 350 cm, 100x.

Fig. 3: Siliciclastic-biodetritic periplatform ooze (wackestone), rich in quartz (Q) and feldspar (F).- Core S6, 100 cm, 25x.

Fig. 4: Sapropel on top of the lithified interval in core S3. Note the scarcity of planktic foraminifers when compared to normal periplatform ooze (Fig. 1) and the high abundance of fine-grained siliciclastic components.- Core S3, 3 cm, 50x.

Fig. 5: Lithified chip (LC) composed of cemented pteropods (P) and micritic bioclasts (B), which form the centres of accretion for the growth of syntaxial and drusy fibrous aragonite cements. Those fibres are interlocking in-between the components or grow into a micropelletoid carbonate (MP).- Core S3 (58-63 cm), 100x.

Fig. 6: Transition from a skeletal-peloidal grainstone (lower part) to a bioclastic pack- to wackestone (upper part) in a proximal calciturbidite, showing graded bedding with a fining upwards trend.- Core S3 (72-77 cm), 25x.

Fig. 7: Calciturbidite (skeletal grain- to packstone) composed of benthic foraminifers (F), scleractinians (S), algae (A) and unspecified bioclast. - Core S3 (58-63 cm), 50x

Fig. 8: Calciturbidite (skeletal grainstone) dominated by coralline red algae (RA) and scleractinians (S). - Core S3 (58-63 cm),100x

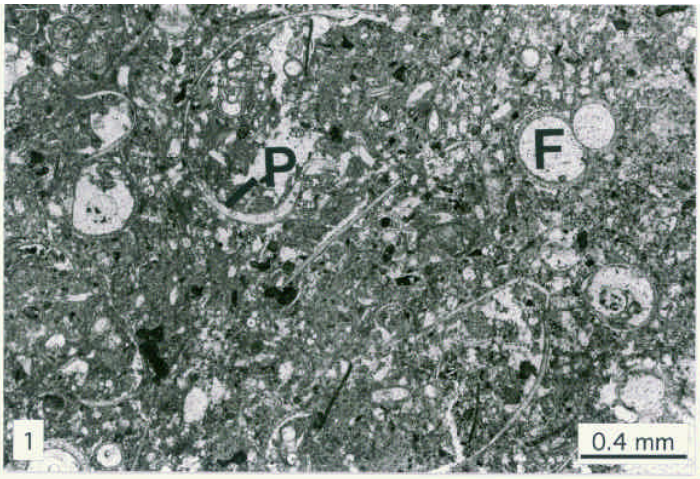
P
F
1
0.4 mm

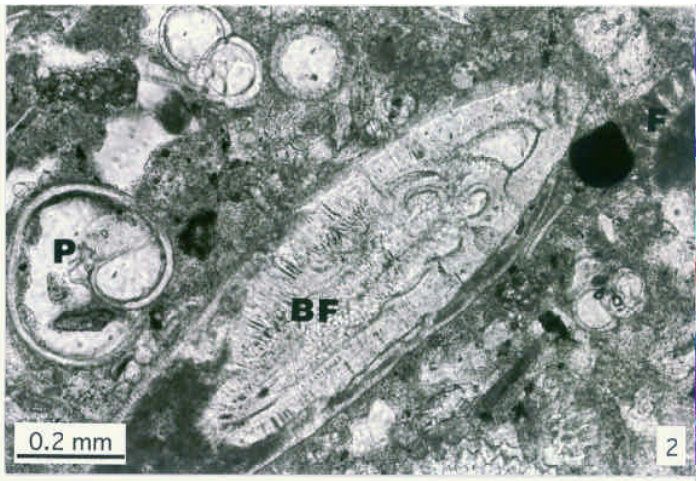
F
P
BF
0.2 mm
2

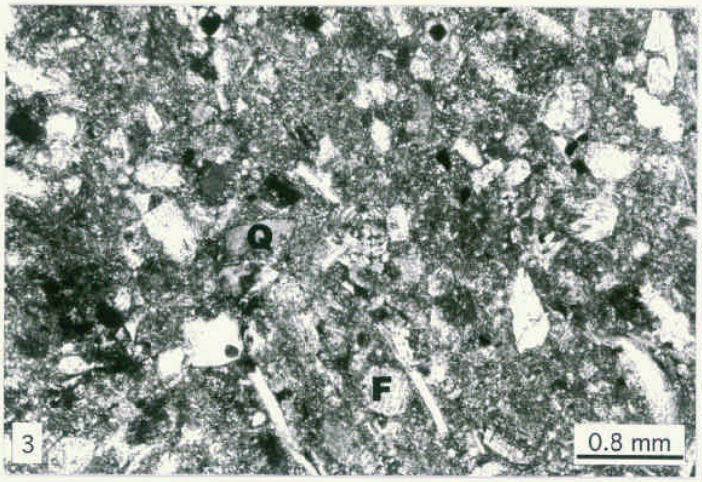
Q
F
3
0.8 mm

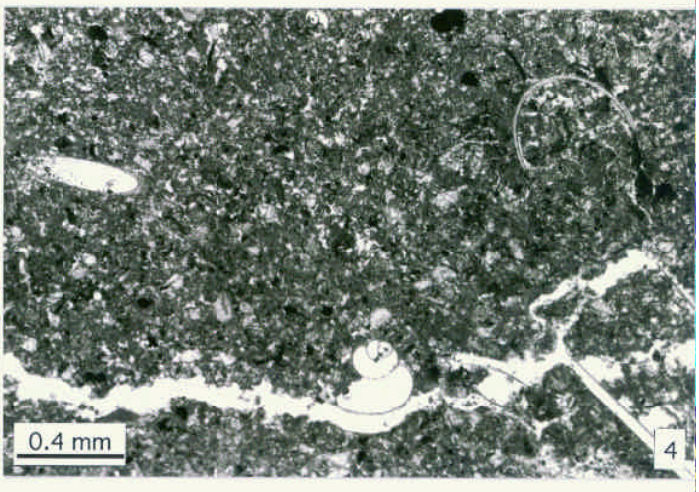
0.4 mm
4

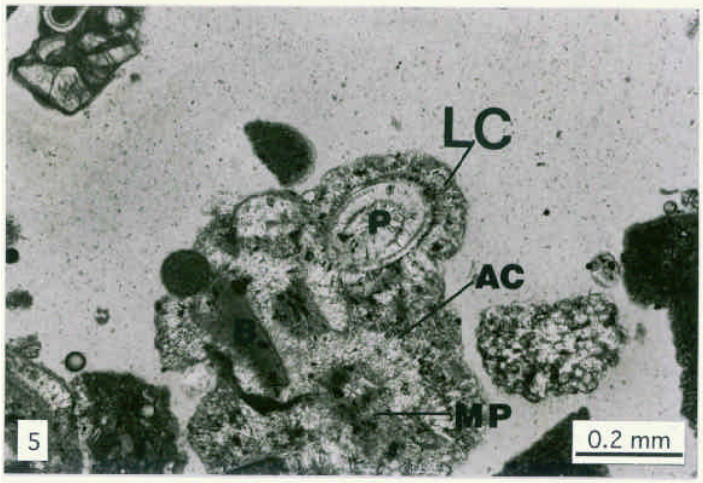
LC
P
AC
MP
5
0.2 mm

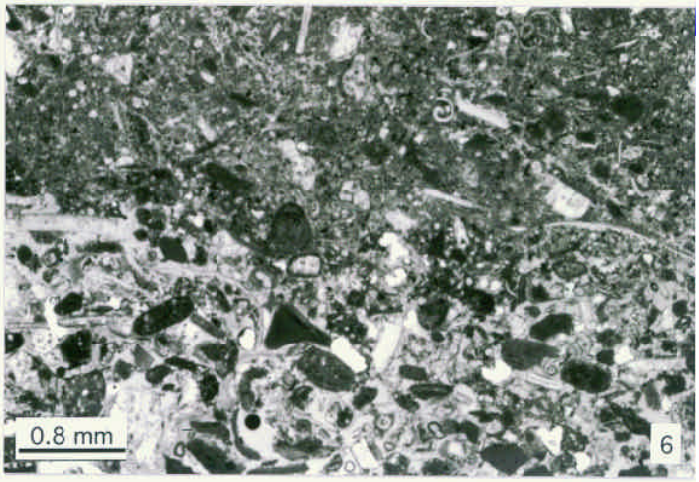
0.8 mm
6

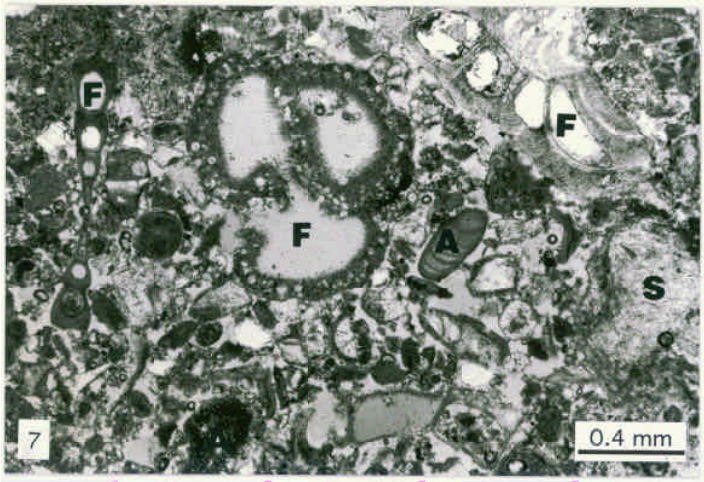
F
F
F
A
S
7
0.4 mm

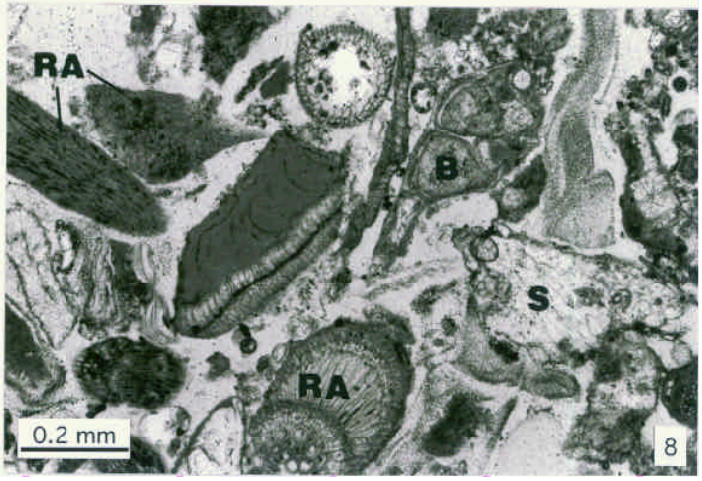
RA
B
S
RA
0.2 mm
8

DATA-APPENDICES

Appendix 1-A: Stable oxygen and carbon isotopes

Appendix 1-B: Oxygen isotope age model and stacks

Appendix 2: Grainsize distribution

Appendix 3: TOC- and carbonate-content (LECO analyser)

Appendix 4-A: Mineralogy of periplatform sediments (X-ray diffraction)

Appendix 4-B: Mineralogy, oxygen isotopes and salinities of the lithified interval

Appendix 4-C: $MgCO_3$ content

Appendix 4-D: Aragonite/calcite-stacks

Appendix 4-E: Average carbonate mineral abundances for isotope stages and sealevel sequences

Appendix 4-F: Stacked aragonite accumulation rates

Appendix 5-A: Element distribution (X-ray fluorescence)

Appendix 5-B: High- and low-strontium aragonite

Appendix 5-C: High- and low-strontium aragonite stacks

Appendix 5-D: Stacked high-strontium aragonite accumulation rates

Appendix 6: Component distribution (pointcounting)

Appendix 1-A: Stable oxygen and carbon isotopes

Depth (cm)	$\delta^{18}O$ (‰PDB)	stdev.	$\delta^{13}C$ (‰ PDB)	stdev.	Isotopic event
AL- *G. ruber*					
10	-1.50	0.01	1.49	0.01	
20	-1.22	0.03	1.54	0.01	
30	-1.24	0.03	1.43	0.01	
40	-1.15	0.04	1.65	0.01	
50	-1.44	0.02	1.36	0.02	1.1
60	-1.01	0.03	1.43	0.02	
70	-1.14	0.03	1.25	0.03	
80	-0.15	0.03	1.14	0.02	
170	2.68	0.04	1.49	0.02	
180	2.63	0.04	1.35	0.02	
190	1.72	0.04	0.95	0.03	
200	1.87	0.04	1.22	0.03	
210	1.39	0.02	1.05	0.02	
220	1.28	0.03	1.16	0.02	
230	1.25	0.03	1.12	0.02	
240	1.58	0.03	1.10	0.01	
250	1.50	0.03	1.34	0.02	
260	0.77	0.03	1.45	0.02	
270	1.27	0.04	1.21	0.02	
280	0.90	0.02	1.27	0.01	
280	0.92	0.03	1.27	0.02	
290	0.61	0.01	0.78	0.03	
300	0.54	0.02	0.86	0.01	3.3
310	1.05	0.03	0.82	0.01	
320	0.65	0.03	0.91	0.02	
330	0.79	0.03	0.74	0.01	4.0
340	2.40	0.03	0.90	0.02	4.2
350	2.08	0.04	0.74	0.01	
360	2.12	0.02	1.16	0.02	
370	1.84	0.03	0.97	0.03	
380	1.31	0.03	1.21	0.01	
390	0.88	0.02	1.19	0.01	5.0
400	0.02	0.05	1.05	0.03	
410	0.01	0.04	1.69	0.01	
420	-0.14	0.02	1.57	0.01	
430	-0.55	0.03	1.31	0.02	
440	-0.77	0.02	1.17	0.01	
450	-0.99	0.02	0.89	0.01	5.1
460	0.50	0.02	1.34	0.02	
470	0.73	0.04	1.49	0.03	5.2
480	0.18	0.02	1.29	0.02	
490	-0.15	0.03	1.01	0.01	
500	-0.18	0.04	1.30	0.02	
510	-0.37	0.04	1.23	0.04	
530	-0.55	0.04	1.26	0.03	
Standards (AL)					
Std./CO-1	-2.41	0.05	2.46	0.01	
Std./CO-1	-2.41	0.05	2.47	0.01	
Std./CO-1	-2.41	0.05	2.50	0.02	
Std./CO-1	-2.43	0.03	2.46	0.01	
Std./CO-1	-2.41	0.04	2.46	0.02	
Std./CO-1	-2.45	0.02	2.45	0.01	

Depth (cm)	$\delta^{18}O$ (‰PDB)	stdev.	$\delta^{13}C$ (‰ PDB)	stdev.	Isotopic event
MD- *G.ruber*					
2	-1.75	0.01	1.24	0.02	
10	-1.60	0.03	1.16	0.02	
40	-1.49	0.03	1.28	0.02	
84	0.12	0.02	0.46	0.02	
170	1.41	0.01	0.32	0.01	
180	0.96	0.03	0.61	0.02	
206	0.33	0.03	0.67	0.01	
229	0.23	0.03	0.24	0.02	
270	1.30	0.04	1.12	0.02	
304	0.07	0.02	0.75	0.01	
311	0.24	0.02	1.14	0.02	
319	-1.05	0.01	0.61	0.02	
332	-0.91	0.04	0.69	0.02	
343	0.21	0.03	0.96	0.02	
356	-0.82	0.02	0.61	0.03	
369	0.04	0.02	0.95	0.03	
375	0.24	0.02	1.07	0.02	
396	0.57	0.01	0.80	0.01	
454	0.44	0.02	1.22	0.03	
465	0.04	0.02	1.04	0.01	
472	0.51	0.03	1.04	0.01	
490	0.10	0.03	1.09	0.03	
510	0.31	0.02	1.07	0.01	
516	0.45	0.01	1.04	0.01	
521	0.01	0.04	0.99	0.01	
532	0.22	0.04	0.78	0.03	
615	0.27	0.03	1.19	0.02	
640	0.03	0.03	1.07	0.02	
667	0.70	0.03	0.94	0.01	
715	0.46	0.04	0.68	0.02	
760	-0.42	0.02	1.33	0.02	
790	-0.34	0.02	1.23	0.01	
820	0.31	0.02	1.24	0.03	
835	-0.56	0.03	0.91	0.02	
855	-0.59	0.03	0.83	0.02	
873	0.25	0.04	0.97	0.01	
880	0.16	0.02	1.26	0.02	
1052	0.58	0.03	0.83	0.01	
Standard (MD)					
Std/NBS19	-2.21	0.02	1.95	0.03	
Std/NBS19	-2.22	0.01	1.92	0.01	
Std/NBS19	-2.21	0.02	1.97	0.02	
Std/NBS19	-2.22	0.02	1.91	0.03	
Std/NBS19	-2.20	0.03	1.92	0.02	
Std/NBS19	-2.20	0.02	1.93	0.01	
Average	-2.21		1.93		
std.dev.	0.01		0.02		
standard	-2.19		1.95		
AL - lithified					
101	6.08		3.38		

Appendix 1-A: Stable oxygen and carbon isotopes

Depth (cm)	$\delta^{18}O$ (‰PDB)	stdev.	$\delta^{13}C$ (‰ PDB)	stdev.	Isotopic event
Std./CO-1	-2.48	0.04	2.47	0.02	
Std./CO-1	-2.44	0.03	2.44	0.02	
Average	-2.43		2.47		
st.dev.	0.02		0.02		
Standard	-2.44		2.48		
Standards (AL)					
Average A	-2.44		2.46		
Average B	-2.41		2.47		
S1- *G. ruber*					
0	-1.26				
10	-1.26	0.02	1.39	0.02	
20	-1.00	0.05	1.29	0.02	
30	-0.29	0.02	1.00	0.02	
50	-0.75	0.03	0.95	0.02	
70	-1.19	0.05	1.50	0.04	
80	-1.06	0.03	1.16	0.03	
90	-1.58	0.02	1.50	0.01	
120	1.91	0.04	1.11	0.02	
130	2.12	0.01	0.94	0.01	
140	1.61	0.04	0.90	0.02	
150	1.63	0.01	0.75	0.01	
160	1.71	0.02	0.71	0.03	
170	1.64	0.03	0.90	0.01	
180	1.40	0.04	0.99	0.02	
190	1.26	0.03	0.89	0.02	
200	1.17	0.03	0.89	0.02	
210	0.70	0.01	0.93	0.01	
220	0.75	0.03	0.91	0.01	
230	0.68	0.02	0.73	0.01	
240	0.62	0.02	0.61	0.02	3.3
250	1.01	0.03	0.47	0.01	4.0
260	2.31	0.03	0.54	0.01	4.2
270	1.87	0.02	0.45	0.02	
280	1.97	0.03	0.97	0.02	
290	1.57	0.02	0.91	0.02	
300	1.06	0.04	1.03	0.01	
310	0.81	0.03	1.29	0.02	5.0
320	-0.34	0.04	0.92	0.01	
330	-0.22	0.04	1.42	0.02	
340	-0.51	0.03	1.56	0.02	
350	-0.72	0.04	1.12	0.02	5.1
360	-0.17	0.01	1.05	0.02	
370	0.65	0.01	1.24	0.02	5.2
380	-0.05	0.02	1.10	0.01	
390	-0.11	0.03	0.83	0.01	
400	-0.20	0.03	0.98	0.01	
410	-0.40	0.03	1.08	0.02	
420	-0.47	0.03	1.10	0.01	
430	-0.58	0.03	1.02	0.02	
440	-0.62	0.01	1.06	0.01	
440	-0.57	0.02	1.23	0.02	
450	-0.50	0.01	1.31	0.02	

Depth (cm)	$\delta^{18}O$ (‰PDB)	stdev.	$\delta^{13}C$ (‰ PDB)	stdev.	Isotopic event
103	5.45		3.05		
105	5.42		3.14		
109	5.75	0.11	3.26	0.05	
111	5.32		3.07		
113	6.27		3.59		
115	5.99		3.57		
AL - lithified					
117	5.46		3.13		
119	6.39		3.94		
121	6.11	0.12	3.37	0.08	
125	5.93		3.28		
127	5.85	0.02	3.13	0.08	
131	5.79		3.28		
133	5.66		3.23		
135	5.64		3.21		
137	5.54		3.19		
139	5.57		3.33		
141	5.47		3.21		
143	5.53		3.26		
147	5.39		3.20		
149	5.02		2.89		
151	5.08		3.17		
155	5.41		3.30		
157	5.31	0.15	3.28	0.03	
159	4.96	0.48	3.35	0.03	
161	4.87		3.02		
163	5.18		3.31		
165	5.35		3.59		
169	4.98		3.02		
S1-lithified					
45	5.19		3.59		
47	5.29	0.14	3.62	0.02	
49	5.80	0.02	3.61	0.01	
51	6.10		3.64		
53	5.95		3.66		
55	6.01		3.64		
57	6.17		3.68		
60	6.29		3.68		
63	6.07		3.69		
65	6.56		3.97		
67	6.60		4.14		
69	6.54		4.05		
71	6.53		4.05		
73	6.63		4.02		
75	6.31		3.83		
77	6.48	0.06	3.99	0.03	
79	6.33		3.69		
81	6.27		3.82		
83	6.21	0.07	3.72	0.01	
85	6.07		3.65		
87	6.25	0.02	3.67	0.03	
89	6.03		3.65		
91	5.98		3.78		

Appendix 1-A: Stable oxygen and carbon isotopes

Depth (cm)	$\delta^{18}O$ (‰PDB)	stdev.	$\delta^{13}C$ (‰ PDB)	stdev.	Isotopic event
460	-0.34	0.02	1.15	0.02	
470	-0.83	0.04	0.94	0.01	
480	-0.40	0.02	0.96	0.02	
490	-0.44	0.04	1.05	0.01	
500	-0.35	0.02	0.82	0.01	
S2- *G. ruber*					
2	-1.52	0.04	1.14	0.01	
10	-1.45	0.02	1.43	0.03	
20	-1.50	0.04	1.26	0.04	
30	-1.43	0.02	1.57	0.01	
40	-1.35	0.02	1.38	0.01	
50	-1.19	0.04	1.48	0.01	
S2- *G. ruber*					
60	-1.17	0.03	1.58	0.03	
70	-1.11	0.01	1.12	0.03	
80	-1.39	0.02	1.60	0.02	1.1
90	-0.81	0.03	1.18	0.02	
100	-0.55	0.03	1.05	0.02	
110	1.11	0.03	0.80	0.02	
120	-1.20	0.04	2.03	0.03	
140	1.19	0.14	0.00	0.07	
160	0.61	0.02	0.91	0.02	
190	1.77	0.04	0.76	0.01	
220	2.30	0.04	1.07	0.02	
230	1.69	0.03	0.89	0.01	
240	1.45	0.03	0.94	0.03	
250	1.63	0.04	0.91	0.03	
260	1.71	0.03	1.07	0.03	
270	1.05	0.04	0.92	0.01	
280	1.52	0.04	1.06	0.02	
290	1.25	0.03	1.00	0.01	
300	1.18	0.03	1.06	0.02	
310	1.09	0.01	1.13	0.02	
320	0.76	0.02	1.20	0.03	
330	1.40	0.02	1.09	0.02	
340	0.77	0.06	0.72	0.03	
350	0.79	0.02	1.05	0.02	
360	0.47	0.03	0.89	0.01	
370	0.46	0.02	0.80	0.02	
380	1.02	0.04	0.73	0.01	
390	0.25	0.02	0.55	0.02	3.3
400	0.53	0.01	0.42	0.03	
410	2.02	0.02	0.91	0.02	4.0
420	2.15	0.03	0.81	0.01	4.2
430	1.39	0.02	0.64	0.02	
440	1.75	0.06	0.73	0.03	
450	2.01	0.03	0.71	0.02	
S3- *G. ruber*					
5	-1.05	0.02	1.26	0.02	
65	1.11	0.03	1.27	0.02	
89	1.83	0.02	0.96	0.02	
93	1.18	0.06	0.50	0.04	
100	1.98	0.02	1.14	0.01	

Depth (cm)	$\delta^{18}O$ (‰PDB)	stdev.	$\delta^{13}C$ (‰ PDB)	stdev.	Isotopic event
93	6.04		3.71		
95	6.01		3.72		
98	5.88		3.66		
101	5.70	0.04	3.16	0.02	
103	5.58		3.27		
105	5.97		3.63		
107	5.18	0.01	3.20	0.02	
109	5.63		3.71		
111	5.89		3.79		
113	5.94		3.80		
115	5.64		3.62		
117	5.56		3.73		
S1-lithified					
119	5.82		3.80		
121	5.54	0.10	3.54	0.05	
123	5.53	0.13	3.45	0.04	
125	5.71		3.60		
127	5.60		3.57		
S1 - unlithified fine fraction					
45	1.07		1.53		
47	2.73		2.72		
49	3.68		2.11		
51	3.71		2.08		
53	3.60		2.03		
55	3.69		2.03		
57	3.71		2.07		
60	3.43		1.99		
63	3.30		1.94		
65	3.60		2.12		
67	3.72		2.23		
69	3.60		2.32		
71	3.67		2.40		
73	3.84		2.48		
75	3.82		2.38		
77	3.55		2.26		
79	4.05		2.18		
81	3.95		2.22		
83	4.08		2.10		
85	4.34		2.16		
87	3.55		2.17		
89	3.55		2.17		
91	4.24		2.27		
93	4.30		2.44		
95	4.22		2.40		
98	4.36		2.44		
101	4.63		2.46		
103	4.57		2.42		
105	4.29		2.32		
109	4.38		2.40		
113	4.47		2.47		
115	4.53		2.48		
117	4.44		2.50		
119	4.18		2.49		

Appendix 1-A: Stable oxygen and carbon isotopes

Depth (cm)	$\delta^{18}O$ (‰PDB)	stdev.	$\delta^{13}C$ (‰ PDB)	stdev.	Isotopic event
110	2.06	0.03	1.09	0.02	
150	2.05	0.03	1.04	0.01	
160	2.54	0.04	1.13	0.02	
180	1.56	0.04	0.68	0.01	
190	1.39	0.03	1.05	0.01	
192	1.25	0.03	0.94	0.01	
195	1.44	0.03	1.01	0.03	
207	1.27	0.03	0.98	0.01	
210	1.28	0.03	0.94	0.02	
220	1.77	0.03	0.84	0.02	
230	0.97	0.03	0.73	0.03	
240	1.62	0.01	0.95	0.01	
250	1.48	0.04	0.90	0.02	
260	1.22	0.04	1.05	0.01	
270	1.04	0.02	1.22	0.02	
274	0.71	0.01	0.77	0.01	
276	1.20	0.03	0.95	0.02	
277	1.24	0.03	1.03	0.04	
S3- *G. ruber*					
280	1.07	0.02	0.96	0.03	
290	0.93	0.04	1.17	0.03	
300	0.50	0.04	1.02	0.02	
310	1.21	0.02	1.24	0.03	
314	1.15	0.02	1.02	0.02	
320	1.22	0.03	0.89	0.02	
330	0.94	0.03	0.98	0.02	
340	0.81	0.02	0.94	0.02	
350	0.61	0.02	0.93	0.02	
360	0.43	0.02	0.44	0.01	
370	0.76	0.03	0.64	0.03	
377	1.03	0.00	0.77	0.01	
380	0.92	0.02	0.78	0.01	
390	0.19	0.03	0.46	0.01	3.3
400	0.69	0.03	0.26	0.02	
410	1.92	0.02	0.64	0.01	4.0
420	2.20	0.02	0.50	0.01	4.2
430	2.11	0.04	0.59	0.01	
440	1.52	0.02	0.44	0.02	
450	1.72	0.02	0.77	0.02	
460	1.77	0.02	1.05	0.03	
Standards (S1-S3)					
Std./NBS 19	-2.20	0.05	1.95	0.02	
Std./NBS 19	-2.23	0.03	1.95	0.01	
Std./NBS 19	-2.20	0.02	1.93	0.02	
Std./NBS 19	-2.20	0.02	1.94	0.02	
Std./NBS 19	-2.20	0.03	1.97	0.02	
Std./NBS 19	-2.24	0.01	1.92	0.02	
Std./NBS 19	-2.20	0.03	1.95	0.03	
Std./NBS 19	-2.17	0.03	1.99	0.01	
Std./NBS 19	-2.17	0.03	1.95	0.02	
average	-2.20		1.95		
st.dev	0.02		0.02		

Depth (cm)	$\delta^{18}O$ (‰PDB)	stdev.	$\delta^{13}C$ (‰ PDB)	stdev.	Isotopic event
121	3.91		2.33		
123	3.15		1.97		
125	2.71		2.01		
127	2.97		1.99		
S6 - lithified					
115	4.78		3.64		
117	5.21		3.30		
119	5.32		3.57		
121	5.63	0.42	3.68	0.06	
123	5.44		3.46		
125	5.91	0.07	3.59	0.06	
127	5.83	0.27	3.36	0.06	
129	6.57		3.76		
131	5.73	0.31	3.83	0.21	
133	6.26		3.83		
135	6.29		4.02		
137	6.14		3.87		
139	6.40		4.12		
S6 - lithified					
141	5.98		3.97		
143	5.95		3.85		
145	6.39	0.04	3.98	0.01	
147	5.68		3.67		
149	5.53		3.54		
151	5.69		3.58		
153	5.35		3.56		
155	5.70		3.62		
157	6.15		3.63		
159	5.36		3.75		
161	5.62		3.67		
163	5.30		3.48		
165	5.86		3.38		
167	5.39		3.64		
169	5.28		3.54		
171	4.98		3.49		
173	5.02		3.60		
175	5.30	0.07	3.36	0.03	
177	5.53		3.17		
179	5.25		3.20		
181	6.26		3.83		
185	4.30		2.73		
187	5.39		3.14		
189	5.30	0.16	3.76	0.00	
191	5.62		3.55		
193	5.35	0.18	3.46	0.03	
195	5.59		3.68		
197	5.57		3.77		
199	5.05		3.53		
201	5.09		3.34		
203	4.54		3.77		
217	3.84		2.66		
219	5.05		3.29		
S6 - sapropel					

Appendix 1-A: Stable oxygen and carbon isotopes

Depth (cm)	$\delta^{18}O$ (‰PDB)	stdev.	$\delta^{13}C$ (‰ PDB)	stdev.	Isotopic event
standard	-2.20		1.95		
Std. /SOL 1	-5.63	0.02	0.13	0.02	
Std. /SOL 1	-5.63	0.02	0.14	0.02	
Std. /SOL 1	-5.59	0.03	0.14	0.01	
Std. /SOL 1	-5.65	0.04	0.15	0.01	
Std. /SOL 1	-5.62	0.02	0.14	0.01	
Std. /SOL 1	-5.62	0.03	0.12	0.01	
Std. /SOL 1	-5.65	0.05	0.13	0.01	
Std. /SOL 1	-5.65	0.03	0.14	0.01	
average	-5.63		0.14		
st.dev.	0.02		0.01		
standard	-5.62		0.15		
S6- *G. ruber*					
1	-1.54	0.01	1.38	0.01	
10	-1.37	0.03	1.60	0.02	
20	-1.70	0.05	1.17	0.01	
30	-1.49	0.03	1.22	0.03	
40	-1.58	0.06	1.33	0.02	
50	-1.56	0.02	1.58	0.03	
60	-1.59	0.03	1.36	0.02	1.1
70	-1.38	0.03	1.19	0.01	
S6- *G. ruber*					
80	-1.23	0.03	1.02	0.03	
86	-1.07	0.04	1.10	0.02	
90	-0.97	0.03	1.08	0.03	
240	1.95	0.02	0.92	0.02	
250	1.28	0.03	0.77	0.01	
260	1.73	0.02	0.73	0.02	
270	1.11	0.03	0.73	0.02	
274	1.96	0.03	0.97	0.02	
280	1.22	0.02	0.85	0.02	
285	0.89	0.05	0.81	0.01	
287	1.07	0.04	0.76	0.02	
290	0.66	0.05	0.83	0.02	
295	0.63	0.02	0.26	0.03	
300	1.53	0.04	0.90	0.01	
370	0.73	0.05	0.75	0.02	
380	0.62	0.02	0.91	0.01	
390	0.34	0.01	0.53	0.01	
310	1.12	0.03	1.06	0.02	
320	1.13	0.04	1.06	0.02	
330	0.94	0.05	0.93	0.02	
340	0.85	0.05	1.03	0.02	
350	0.56	0.02	0.90	0.01	
360	1.04	0.03	0.87	0.01	
400	0.52	0.03	0.63	0.01	
410	0.88	0.03	0.74	0.01	
420	0.47	0.04	0.44	0.02	
430	0.14	0.02	0.19	0.01	3.3
440	0.56	0.04	0.81	0.03	4.0

Depth (cm)	$\delta^{18}O$ (‰PDB)	stdev.	$\delta^{13}C$ (‰ PDB)	stdev.	Isotopic event
111	2.53	0.28	1.63	0.48	
113	2.32		2.70		
S6 - calciturbidites					
183	4.46	0.04	3.03	0.04	
121	5.63	0.42	3.68	0.06	
205	3.69		2.84		
207	3.51	0.03	2.92	0.06	
209	4.51	0.07	3.24	0.02	
211	3.73		2.96		
213	3.85	0.18	2.92	0.06	
215	3.54		2.88		
221	4.08	0.13	2.80	0.04	
223	3.85		2.69		
225	3.86	0.08	2.61	0.00	
227	3.75		2.42		
229	3.35	0.08	2.35	0.08	
Standards (lithified interval)					
MS-2 av	-1.31		2.21		
MS-2	-1.36		2.24		
MS-2	-1.34		2.20		
MS-2	-1.33		2.21		
MS-2	-1.27		2.22		
MS-2	-1.30		2.21		
MS-2	-1.33		2.20		
Standards (lithified interval)					
MS-2	-1.23		2.19		
Average	-1.31		2.21		
Stdev	0.04		0.02		
NBS-19	-2.20		1.96		
NBS-19	-2.20		1.94		
NBS-19	-2.20		1.95		
NBS-19 av	-2.20		1.95		
average	-2.20		1.95		
stdev	0.00		0.00		
standard	-2.20		1.95		

Appendix 1-A: Stable oxygen and carbon isotopes

Depth (cm)	$\delta^{18}O$ (‰PDB)	stdev.	$\delta^{13}C$ (‰ PDB)	stdev.	Isotopic event
450	1.98	0.03	0.62	0.01	4.2
460	1.93	0.02	0.60	0.03	
470	1.48	0.03	0.39	0.01	
Std/NBS 19	-2.21	0.03	1.91	0.01	
Std/NBS 19	-2.22	0.01	1.93	0.02	
Std/NBS 19	-2.17	0.03	1.96	0.02	
Std/NBS 19	-2.21	0.02	1.97	0.02	
average	-2.20		1.94		
Std.abw.	0.02		0.03		
standard	-2.20		1.95		

Depth (cm)	$\delta^{18}O$ (‰PDB)	stdev.	$\delta^{13}C$ (‰ PDB)	stdev.	Isotopic event

Appendix 1-B: Oxygen isotope age model and stacks

	Cores ($\delta^{18}O$, ‰ PDB)						Stacks (average $\delta^{18}O$, ‰ PDB)							
SPECMAP-age (ky)	**AL**	**AW**	**S1**	**S6**	**S3**	**S2**	**Sanganeb prox. cores**	stdev	**Sanganeb**	stdev	**Abington**	stdev	**Sudan**	stdev
1	-1.50					-1.47	-1.47	0.00	-1.47	0.00	-1.50	0.00	-1.49	0.01
2	-1.40					-1.49	-1.49	0.00	-1.49	0.00	-1.40	0.00	-1.44	0.05
3	-1.23					-1.38	-1.38	0.00	-1.38	0.00	-1.23	0.00	-1.30	0.08
4	-1.23					-1.19	-1.19	0.00	-1.19	0.00	-1.23	0.00	-1.21	0.02
5	-1.18					-1.14	-1.14	0.00	-1.14	0.00	-1.18	0.00	-1.16	0.02
6	-1.44			-1.59		-1.39	-1.49	0.10	-1.49	0.10	-1.44	0.00	-1.47	0.08
7	-1.12			-1.07		-1.04	-1.06	0.02	-1.06	0.02	-1.12	0.00	-1.08	0.03
8	0.04			-0.54		-0.76	-0.65	0.11	-0.65	0.11	0.04	0.00	-0.42	0.34
9	0.34		-0.65	-0.28	-1.05	-0.67	-0.66	0.31	-0.66	0.27	0.34	0.00	-0.46	0.47
10	0.37		-0.67	-0.26	-1.05	-0.64	-0.65	0.32	-0.65	0.28	0.37	0.00	-0.45	0.48
11	0.41		-0.70	-0.23	-0.93	-0.61	-0.59	0.28	-0.62	0.25	0.41	0.00	-0.41	0.47
12	0.44		-0.72	-0.21	-0.81	-0.58	-0.53	0.25	-0.58	0.23	0.44	0.00	-0.37	0.46
13	0.48		-0.74	-0.19	-0.69	-0.55	-0.48	0.21	-0.54	0.21	0.48	0.00	-0.34	0.45
14	0.70		-0.86	0.07	-0.31	1.11	0.29	0.60	0.00	0.72	0.70	0.00	0.14	0.70
15	0.92		-1.08	0.28	0.07	-1.20	-0.28	0.65	-0.48	0.66	0.92	0.00	-0.20	0.82
16	1.14		-1.13	0.43	0.44	-0.01	0.29	0.21	-0.07	0.64	1.14	0.00	0.17	0.75
17	1.36		-1.58	0.59	0.82	1.19	0.87	0.25	0.26	1.08	1.36	0.00	0.48	1.06
18	1.58		-1.19	0.88	1.19	0.90	0.99	0.14	0.44	0.95	1.58	0.00	0.67	0.97
19	1.80		-0.81	1.17	1.50	0.61	1.09	0.37	0.62	0.88	1.80	0.00	0.85	0.92
20	2.02		-0.42	1.28	1.68	1.00	1.32	0.28	0.88	0.79	2.02	0.00	1.11	0.84
21	2.24		1.13	1.39	1.86	1.38	1.54	0.23	1.44	0.26	2.24	0.00	1.60	0.40
22	2.46		1.95	1.49	2.06	1.77	1.77	0.23	1.82	0.22	2.46	0.00	1.94	0.32
23	2.68		2.03	1.60	2.06	1.95	1.87	0.20	1.91	0.19	2.68	0.00	2.06	0.35
24	2.45		2.11	1.71	2.05	2.09	1.95	0.17	1.99	0.16	2.45	0.00	2.08	0.24
25	1.78		1.95	1.82	2.35	2.23	2.13	0.22	2.09	0.21	1.78	0.00	2.03	0.22
26	1.58		1.76	1.92	1.46	2.06	1.81	0.26	1.80	0.22	1.58	0.00	1.76	0.22
27	1.30		1.61	1.45	1.29	1.64	1.46	0.15	1.50	0.14	1.30	0.00	1.46	0.15
28	1.25		1.62	1.49	0.97	1.45	1.30	0.24	1.38	0.25	1.25	0.00	1.36	0.23
29	1.37	1.70	1.63	1.63	1.39	1.56	1.53	0.10	1.55	0.10	1.54	0.16	1.55	0.12
30	1.49	1.63	1.65	1.20	1.58	1.65	1.47	0.20	1.52	0.19	1.56	0.07	1.53	0.16
31	1.57	1.57	1.68	1.76	1.49	1.69	1.65	0.12	1.66	0.10	1.57	0.00	1.63	0.09
32	1.54	1.50	1.71	1.05	1.34	1.45	1.28	0.17	1.38	0.24	1.52	0.02	1.43	0.20
33	1.52	1.43	1.69	0.68	1.18	1.05	0.97	0.21	1.15	0.36	1.47	0.04	1.26	0.33
34	1.39	1.37	1.66	0.93	1.07	1.34	1.11	0.17	1.25	0.28	1.38	0.01	1.29	0.24
35	1.12	1.30	1.61	1.38	0.96	1.47	1.27	0.22	1.35	0.24	1.21	0.09	1.31	0.21
36	0.86	1.29	1.51	1.12	1.05	1.31	1.16	0.11	1.25	0.18	1.07	0.22	1.19	0.21
37	0.89	1.28	1.42	1.13	0.96	1.23	1.11	0.11	1.19	0.17	1.09	0.19	1.15	0.18
38	1.07	1.27	1.36	1.05	0.76	1.18	0.99	0.18	1.09	0.22	1.17	0.10	1.11	0.19
39	1.25	1.26	1.31	0.93	0.53	1.13	0.86	0.25	0.97	0.29	1.25	0.00	1.07	0.27
40	1.15	1.24	1.26	0.86	0.98	1.03	0.96	0.07	1.03	0.14	1.20	0.04	1.09	0.14
41	1.03	1.23	1.23	0.69	1.18	0.83	0.90	0.21	0.98	0.23	1.13	0.10	1.03	0.21
42	0.90	1.21	1.19	0.70	1.22	1.02	0.98	0.21	1.03	0.21	1.06	0.16	1.04	0.19
43	0.79	1.20	1.08	1.03	1.05	1.40	1.16	0.17	1.14	0.15	0.99	0.20	1.09	0.18
44	0.68	1.18	0.91	0.83	0.91	1.03	0.92	0.08	0.92	0.07	0.93	0.25	0.92	0.15
45	0.60	1.16	0.72	0.69	0.83	0.77	0.76	0.06	0.75	0.05	0.88	0.28	0.80	0.18
46	0.58	1.15	0.72	0.60	0.71	0.79	0.70	0.08	0.70	0.07	0.86	0.28	0.76	0.19
47	0.55	1.13	0.74	0.40	0.58	0.66	0.55	0.11	0.60	0.13	0.84	0.29	0.68	0.23
48	0.64	1.05	0.74	0.43	0.47	0.47	0.45	0.02	0.53	0.13	0.85	0.20	0.63	0.22
49	0.83	0.96	0.72	0.59	0.58	0.47	0.54	0.05	0.59	0.09	0.90	0.07	0.69	0.17
50	1.01	0.88	0.69	0.84	0.79	0.57	0.73	0.12	0.72	0.10	0.95	0.07	0.80	0.14
51	0.94	0.80	0.67	0.64	0.94	0.91	0.83	0.13	0.79	0.14	0.87	0.07	0.81	0.12

Appendix 1-B: Oxygen isotope age model and stacks

	Cores ($\delta^{18}O$, ‰ PDB)						Stacks (average $\delta^{18}O$, ‰ PDB)							
SPECMAP-age (ky)	**AL**	**AW**	**S1**	**S6**	**S3**	**S2**	**Sanganeb prox. cores**	stdev	**Sanganeb**	stdev	**Abington**	stdev	**Sudan**	stdev
52	0.79	0.71	0.64	0.38	0.66	0.72	0.58	0.15	0.60	0.13	0.75	0.04	0.65	0.13
53	0.65	0.63	0.62	0.14	0.19	0.25	0.19	0.04	0.30	0.19	0.64	0.01	0.41	0.22
54	0.68	0.67	0.69	0.22	0.33	0.33	0.29	0.05	0.39	0.18	0.67	0.00	0.49	0.20
55	0.70	0.72	0.77	0.29	0.46	0.40	0.39	0.07	0.48	0.18	0.71	0.01	0.56	0.18
56	0.73	0.75	0.84	0.37	0.60	0.48	0.48	0.09	0.57	0.17	0.74	0.01	0.63	0.16
57	0.75	0.79	0.91	0.45	0.80	0.67	0.64	0.15	0.70	0.17	0.77	0.02	0.73	0.14
58	0.78	0.81	0.98	0.52	1.14	1.08	0.91	0.28	0.93	0.24	0.79	0.02	0.88	0.21
59	0.94	0.83	1.13	0.69	1.47	1.48	1.21	0.37	1.19	0.32	0.88	0.05	1.09	0.30
60	1.23	0.84	1.36	0.95	1.81	1.89	1.55	0.43	1.50	0.38	1.04	0.19	1.35	0.39
61	1.53	1.07	1.60	1.21	1.97	2.05	1.74	0.38	1.71	0.33	1.30	0.23	1.57	0.36
62	1.82	1.39	1.84	1.46	2.05	2.08	1.86	0.28	1.86	0.25	1.61	0.21	1.77	0.26
63	2.11	1.72	2.07	1.72	2.12	2.12	1.99	0.19	2.01	0.17	1.91	0.20	1.98	0.18
64	2.40	2.04	2.31	1.98	2.20	2.15	2.11	0.09	2.16	0.12	2.22	0.18	2.18	0.15
65	2.18	1.99	2.06						2.06	0.00	2.08	0.10	2.08	0.08
66	2.10	1.93	1.88						1.88	0.00	2.01	0.08	1.97	0.09
67	2.10	1.92	1.94						1.94	0.00	2.01	0.09	1.99	0.08
68	1.91	1.92	1.87						1.87	0.00	1.92	0.00	1.90	0.02
69	1.61	1.81	1.64						1.64	0.00	1.71	0.10	1.69	0.09
70	1.26	1.54	1.38						1.38	0.00	1.40	0.14	1.39	0.12
71	0.96	1.25	1.09						1.09	0.00	1.10	0.14	1.10	0.12
72	0.45	0.71	0.94						0.94	0.00	0.58	0.13	0.70	0.20
73	0.02	0.17	0.74						0.74	0.00	0.10	0.08	0.31	0.31
74	0.01	0.32	0.10						0.10	0.00	0.17	0.16	0.14	0.13
75	-0.08	0.59	-0.32						-0.32	0.00	0.25	0.33	0.06	0.38
76	-0.25	0.44	-0.25						-0.25	0.00	0.10	0.34	-0.02	0.32
77	-0.53	-0.03	-0.31						-0.31	0.00	-0.28	0.25	-0.29	0.20
78	-0.69	-0.45	-0.48						-0.48	0.00	-0.57	0.12	-0.54	0.11
79	-0.84	-0.72	-0.61						-0.61	0.00	-0.78	0.06	-0.72	0.09
80	-0.99	-0.99	-0.72						-0.72	0.00	-0.99	0.00	-0.90	0.13
81	-0.57	-0.62	-0.57						-0.57	0.00	-0.59	0.03	-0.58	0.02
82	-0.14	-0.25	-0.41						-0.41	0.00	-0.20	0.05	-0.27	0.11
83	0.29	0.12	-0.25						-0.25	0.00	0.21	0.08	0.05	0.22
84	0.53	0.34	-0.05						-0.05	0.00	0.44	0.10	0.27	0.24
85	0.60	0.39	0.18						0.18	0.00	0.50	0.11	0.39	0.17
86	0.67	0.44	0.42						0.42	0.00	0.55	0.11	0.51	0.11
87	0.73	0.49	0.65						0.65	0.00	0.61	0.12	0.62	0.10
88		0.37									0.37	0.00	0.37	0.00
89		0.24									0.24	0.00	0.24	0.00
90		0.12									0.12	0.00	0.12	0.00
91		-0.01									-0.01	0.00	-0.01	0.00
92		-0.08									-0.08	0.00	-0.08	0.00
93		-0.14									-0.14	0.00	-0.14	0.00
94		-0.21									-0.21	0.00	-0.21	0.00
95		-0.27									-0.27	0.00	-0.27	0.00
96		-0.35									-0.35	0.00	-0.35	0.00
97		-0.43									-0.43	0.00	-0.43	0.00
98		-0.51									-0.51	0.00	-0.51	0.00
99		-0.58									-0.58	0.00	-0.58	0.00
100		-0.49									-0.49	0.00	-0.49	0.00
101		-0.39									-0.39	0.00	-0.39	0.00
102		-0.32									-0.32	0.00	-0.32	0.00

Appendix 1-B: Oxygen isotope age model and stacks

	Cores ($\delta^{18}O$, ‰ PDB)						Stacks (average $\delta^{18}O$, ‰ PDB)							
SPECMAP-age (ky)	**AL**	**AW**	**S1**	**S6**	**S3**	**S2**	**Sanganeb prox. cores**	stdev	**Sanganeb**	stdev	**Abington**	stdev	**Sudan**	stdev
103		-0.34									-0.34	0.00	-0.34	0.00
104		-0.36									-0.36	0.00	-0.36	0.00
105		-0.38									-0.38	0.00	-0.38	0.00
106		-0.39									-0.39	0.00	-0.39	0.00
107		-0.41									-0.41	0.00	-0.41	0.00
108		-0.27									-0.27	0.00	-0.27	0.00
109		-0.09									-0.09	0.00	-0.09	0.00
110		0.09									0.09	0.00	0.09	0.00
111		-0.18									-0.18	0.00	-0.18	0.00
112		-0.44									-0.44	0.00	-0.44	0.00
113		-0.53									-0.53	0.00	-0.53	0.00
114		-0.50									-0.50	0.00	-0.50	0.00
115		-0.50									-0.50	0.00	-0.50	0.00
116		-0.59									-0.59	0.00	-0.59	0.00
117		-0.68									-0.68	0.00	-0.68	0.00
118		-0.79									-0.79	0.00	-0.79	0.00
119		-0.90									-0.90	0.00	-0.90	0.00
120		-1.17									-1.17	0.00	-1.17	0.00
121		-1.70									-1.70	0.00	-1.70	0.00
122		-2.22									-2.22	0.00	-2.22	0.00

Appendix 2: Grainsize distribution

	Dry weight (g)									Percentages						
Depth (cm)	total	< 63µm	63-125	125-250	250-500	500-1000	>1000	sum total	sum > 63µm	< 63µm	63-125	125-120	250-500	500-1000	> 1000	> 63µm
Core AL																
10	x	22.3	0.6	0.4	0.2	0.1	0.0	23.6	1.3	94.5	2.5	1.6	1.0	0.4	0.1	5.5
20	24.1	24.4	0.6	0.4	0.2	0.2	0.0	25.9	1.5	94.1	2.5	1.7	0.9	0.7	0.1	5.9
30	25.7	25.0	0.6	0.5	0.4	0.2	0.0	26.7	1.7	93.6	2.2	1.8	1.4	0.9	0.1	6.4
40	27.0	24.6	0.6	0.4	0.5	0.3	0.0	26.4	1.8	93.1	2.3	1.7	1.8	1.0	0.1	6.9
50	26.8	25.2	0.8	0.5	0.3	0.2	0.0	26.9	1.7	93.7	2.8	1.7	1.2	0.6	0.0	6.3
60	27.5	24.2	0.8	0.6	0.5	0.3	0.0	26.5	2.2	91.6	3.1	2.1	2.0	1.2	0.0	8.4
70	26.9	21.2	0.7	0.4	0.4	0.2	0.0	22.9	1.6	92.8	2.9	1.7	1.6	0.9	0.1	7.2
80	22.1	22.1	0.6	0.2	0.1	0.0	0.0	23.1	1.0	95.8	2.5	1.0	0.5	0.1	0.1	4.2
90	24.7	18.6	1.0	0.3	0.1	0.0	0.0	20.0	1.4	92.9	4.9	1.7	0.5	0.1	0.0	7.1
100	17.6	35.5	1.0	1.1	1.0	0.5	0.4	39.5	4.0	89.9	2.6	2.7	2.6	1.2	1.0	10.1
110	29.2	34.5	1.2	1.0	0.5	0.2	0.2	37.5	3.1	91.8	3.2	2.6	1.3	0.6	0.5	8.2
120	33.6	27.3	2.2	2.5	1.9	1.2	1.9	37.1	9.8	73.7	6.0	6.7	5.2	3.3	5.0	26.3
130	39.9	30.3	1.5	1.1	0.6	0.3	0.2	34.1	3.8	88.9	4.3	3.3	1.8	1.0	0.7	11.1
140	37.2	29.6	1.3	1.4	0.8	0.4	0.4	33.8	4.3	87.4	3.9	4.1	2.4	1.1	1.1	12.6
150	36.0	38.3	1.6	1.5	1.0	0.6	0.3	43.3	5.0	88.5	3.7	3.4	2.4	1.3	0.7	11.5
160	28.6	25.0	0.8	0.7	0.4	0.2	0.1	27.1	2.1	92.3	2.8	2.5	1.5	0.6	0.3	7.7
170	27.7	26.0	1.1	0.8	0.4	0.1	0.1	28.4	2.4	91.4	3.8	3.0	1.3	0.3	0.2	8.6
180	33.4	26.4	1.1	1.1	0.8	0.3	0.4	30.1	3.6	87.9	3.6	3.7	2.5	1.0	1.3	12.1
190	24.2	24.8	1.3	0.9	0.4	0.1	0.4	27.8	3.1	88.9	4.5	3.4	1.6	0.3	1.3	11.1
200	31.6	25.1	1.2	0.9	0.4	0.0	0.0	27.7	2.6	90.7	4.4	3.2	1.5	0.2	0.1	9.3
210	27.7	23.9	1.1	0.8	0.5	0.1	0.0	26.4	2.6	90.3	4.1	3.2	2.0	0.3	0.1	9.7
220	26.2	24.3	0.9	0.7	0.4	0.0	0.0	26.4	2.1	92.0	3.5	2.7	1.6	0.1	0.1	8.0
230	26.4	27.4	0.9	0.7	0.4	0.1	0.0	29.5	2.0	93.1	3.0	2.3	1.3	0.2	0.0	6.9
240	32.3	27.5	0.9	0.6	0.3	0.0	0.0	29.4	1.9	93.4	3.1	2.2	1.1	0.1	0.0	6.6
250	23.8	18.7	0.9	0.8	0.4	0.1	0.0	20.9	2.2	89.5	4.1	3.9	2.1	0.3	0.1	10.5
260	25.5	24.9	1.1	0.9	0.4	0.0	0.0	27.4	2.5	90.9	4.1	3.2	1.6	0.2	0.1	9.1
270	23.1	26.0	1.2	0.7	0.3	0.0	0.0	28.2	2.2	92.1	4.2	2.6	1.1	0.1	0.0	7.9
280	27.7	26.5	1.2	0.9	0.4	0.0	0.0	29.0	2.5	91.4	4.0	2.9	1.4	0.1	0.1	8.6
290	27.9	23.3	0.9	0.6	0.4	0.0	0.0	25.3	1.9	92.3	3.6	2.4	1.4	0.1	0.2	7.7
300	26.7	20.4	1.0	0.6	0.3	0.0	0.0	22.5	2.0	91.1	4.6	2.7	1.5	0.2	0.0	8.9
310	25.4	22.0	1.2	0.7	0.4	0.0	0.0	24.4	2.3	90.4	4.8	3.0	1.6	0.2	0.0	9.6
320	25.9	21.1	1.4	0.8	0.5	0.1	0.0	23.8	2.7	88.6	5.7	3.4	2.0	0.2	0.0	11.4
330	23.5	21.1	1.2	0.7	0.4	0.1	0.0	23.5	2.4	89.8	5.1	3.0	1.6	0.3	0.2	10.2
340	26.0	26.7	1.0	0.7	0.4	0.2	0.2	29.2	2.5	91.5	3.5	2.4	1.5	0.6	0.6	8.5
350	28.3	24.3	0.9	0.6	0.3	0.1	0.1	26.4	2.1	92.1	3.4	2.4	1.3	0.6	0.3	7.9
360	29.3	26.7	1.1	0.8	0.5	0.2	0.1	29.3	2.6	91.1	3.8	2.7	1.6	0.5	0.2	8.9
370	25.9	23.9	1.1	0.8	0.4	0.1	0.0	26.3	2.4	90.9	4.3	3.1	1.3	0.2	0.1	9.1
380	24.9	23.5	0.9	0.6	0.3	0.0	0.0	25.4	1.9	92.6	3.6	2.5	1.0	0.1	0.1	7.4
390	25.7	24.5	1.0	0.9	0.3	0.1	0.0	26.8	2.3	91.6	3.6	3.2	1.3	0.2	0.2	8.4
400	22.6	20.4	0.7	0.6	0.3	0.0	0.0	22.1	1.7	92.4	3.4	2.8	1.1	0.2	0.1	7.6
410	23.8	26.7	0.9	0.7	0.3	0.0	0.0	28.6	1.9	93.4	3.1	2.4	0.9	0.1	0.1	6.6
420	23.9	21.4	0.5	0.2	0.1	0.0	0.1	22.4	0.9	95.8	2.1	1.1	0.5	0.1	0.4	4.2
430	23.4	23.1	0.9	0.7	0.4	0.0	0.0	25.1	2.0	92.0	3.6	2.7	1.5	0.2	0.1	8.0
440	24.9	24.0	0.7	0.4	0.2	0.0	0.0	25.4	1.4	94.5	2.9	1.5	0.9	0.1	0.0	5.5
450	21.2	22.6	0.7	0.5	0.2	0.0	0.0	24.1	1.5	93.6	3.0	2.1	1.0	0.2	0.1	6.4
460	25.3	26.1	0.8	0.5	0.2	0.0	0.0	27.7	1.6	94.1	3.0	1.8	0.8	0.2	0.0	5.9
470	24.5	19.9	0.6	0.4	0.1	0.0	0.0	21.1	1.2	94.4	3.0	1.8	0.6	0.1	0.1	5.6
480	21.5	24.4	0.8	0.6	0.3	0.1	0.0	26.2	1.8	93.2	3.1	2.4	1.0	0.2	0.1	6.8
490	23.7	21.7	0.6	0.5	0.2	0.0	0.0	23.1	1.4	93.8	2.8	2.1	1.0	0.2	0.2	6.2
500	22.6	19.8	0.7	0.6	0.3	0.0	0.0	21.6	1.8	91.9	3.4	2.9	1.6	0.2	0.1	8.1
510	24.0	20.8	0.6	0.4	0.2	0.0	0.0	22.1	1.3	94.2	2.8	2.0	0.8	0.1	0.0	5.8
530	17.2	16.3	0.4	0.3	0.1	0.0	0.0	17.2	0.9	94.6	2.6	1.8	0.7	0.2	0.1	5.4

Appendix 2: Grainsize distribution

	Dry weight (g)									Percentages						
Depth (cm)	total	< 63µm	63-125	125-250	250-500	500-1000	>1000	sum total	sum > 63µm	< 63µm	63-125	125-120	250-500	500-1000	> 1000	> 63µm
Core AW																
10	28.3	12.7	0.9	0.7	0.7	0.9	12.6	28.4	15.7	44.7	3.1	2.6	2.3	3.1	44.3	55.3
20	32.9	18.9	1.5	1.4	1.6	1.7	7.7	32.8	13.9	57.5	4.6	4.3	4.9	5.1	23.5	42.5
30	38.4	22.2	2.5	2.3	1.8	1.5	7.9	38.2	15.9	58.2	6.6	6.0	4.7	3.8	20.7	41.8
40	27.4	17.7	1.5	1.3	1.1	0.9	4.8	27.3	9.5	65.0	5.6	4.6	3.9	3.3	17.5	35.0
50	29.0	11.9	0.9	1.0	1.0	0.7	13.4	28.9	17.0	41.3	3.0	3.3	3.3	2.5	46.5	58.7
60	10.3	7.0	0.6	0.6	0.4	0.2	1.5	10.3	3.3	68.1	5.7	5.7	3.7	1.9	14.9	31.9
70	22.6	17.3	1.6	1.5	1.1	0.5	0.4	22.5	5.2	77.1	7.1	6.8	5.0	2.1	1.8	22.9
80	16.9	13.4	1.4	1.0	0.6	0.1	0.2	16.7	3.3	80.3	8.3	6.0	3.4	0.7	1.3	19.7
90	20.7	15.4	2.3	1.8	0.9	0.1	0.1	20.5	5.1	75.0	11.1	8.7	4.5	0.3	0.5	25.0
100	19.7	16.2	1.5	1.1	0.6	0.1	0.1	19.6	3.4	82.8	7.8	5.6	3.1	0.4	0.3	17.2
110	21.1	16.7	1.8	1.5	0.8	0.1	0.0	21.0	4.2	79.8	8.7	7.3	3.7	0.4	0.1	20.2
120	21.7	17.9	1.8	1.1	0.6	0.1	0.1	21.5	3.6	83.2	8.2	5.2	2.6	0.3	0.5	16.8
130	21.5	17.9	1.6	1.0	0.6	0.1	0.1	21.3	3.4	83.9	7.7	4.9	2.7	0.4	0.4	16.1
140	20.6	17.0	1.7	0.9	0.4	0.1	0.2	20.4	3.3	83.6	8.6	4.6	2.1	0.4	0.8	16.4
150	20.5	17.7	1.4	0.8	0.4	0.1	0.1	20.3	2.6	87.2	6.7	3.8	1.7	0.2	0.3	12.8
160	23.2	19.8	1.4	0.7	0.4	0.2	0.5	23.0	3.2	86.1	5.9	3.1	1.7	1.0	2.1	13.9
170	18.0	15.5	0.8	0.5	0.4	0.3	0.5	18.0	2.4	86.4	4.2	2.9	2.0	1.6	2.9	13.6
180	23.2	19.3	1.2	1.0	0.6	0.4	0.7	23.1	3.9	83.3	5.0	4.2	2.7	1.9	2.9	16.7
190	20.6	16.8	1.4	1.2	0.7	0.2	0.1	20.5	3.7	82.1	6.8	6.1	3.4	0.9	0.7	17.9
200	17.5	14.6	1.3	1.0	0.4	0.1	0.0	17.4	2.8	83.8	7.3	5.8	2.5	0.4	0.2	16.2
210	24.0	19.7	1.7	1.6	0.8	0.1	0.1	23.9	4.3	82.2	7.0	6.6	3.3	0.6	0.4	17.8
220	19.8	17.0	1.1	1.0	0.5	0.1	0.1	19.8	2.8	86.0	5.6	4.8	2.5	0.5	0.5	14.0
230	20.4	17.0	1.2	1.1	0.8	0.1	0.0	20.3	3.3	83.6	6.1	5.4	4.1	0.6	0.2	16.4
240	14.1	11.7	0.9	0.8	0.5	0.1	0.0	14.1	2.3	83.5	6.7	5.4	3.8	0.6	0.1	16.5
250	19.5	16.6	1.2	1.0	0.5	0.1	0.0	19.4	2.7	85.9	6.1	4.9	2.5	0.5	0.1	14.1
260	22.6	18.8	1.5	1.4	0.7	0.1	0.1	22.5	3.8	83.3	6.7	6.3	2.9	0.6	0.2	16.7
270	11.6	9.0	0.9	1.0	0.5	0.7	0.0	12.1	3.1	74.6	7.4	7.9	4.3	5.5	0.2	25.4
280	23.7	17.6	2.4	2.3	1.1	0.2	0.1	23.7	6.1	74.3	10.2	9.5	4.6	1.0	0.4	25.7
290	16.9	14.1	1.1	0.9	0.5	0.1	0.0	16.9	2.7	83.9	6.7	5.6	3.1	0.5	0.2	16.1
300	27.4	21.6	2.1	1.9	1.1	0.3	0.2	27.3	5.7	79.3	7.7	7.1	4.2	0.9	0.8	20.7
310	25.1	21.3	1.4	1.2	0.8	0.2	0.1	25.0	3.8	85.0	5.7	4.9	3.3	0.6	0.4	15.0
320	24.2	20.4	1.4	1.2	0.8	0.2	0.1	24.1	3.7	84.7	5.6	4.9	3.2	0.9	0.5	15.3
330	24.9	19.7	1.8	1.8	1.1	0.3	0.1	24.8	5.1	79.3	7.3	7.3	4.6	1.2	0.4	20.7
340	21.2	16.5	1.2	1.3	0.9	0.5	0.6	21.1	4.6	78.2	5.9	6.0	4.5	2.5	3.0	21.8
350	25.5	21.2	1.6	1.4	0.9	0.3	0.2	25.5	4.2	83.4	6.1	5.4	3.4	1.1	0.6	16.6
360	24.9	21.6	1.3	1.1	0.6	0.2	0.1	24.9	3.3	86.9	5.2	4.4	2.3	0.7	0.5	13.1
370	15.0	12.9	0.8	0.7	0.3	0.1	0.1	14.9	2.0	86.4	5.6	4.5	2.3	0.8	0.4	13.6
380	23.7	19.8	1.7	1.0	0.8	0.2	0.2	23.6	3.8	83.9	7.2	4.2	3.4	0.7	0.7	16.1
390	25.4	21.5	1.2	0.9	1.0	0.4	0.2	25.3	3.8	85.1	4.7	3.7	3.8	1.7	0.9	14.9
400	22.1	18.9	0.9	0.7	0.6	0.3	0.5	22.0	3.1	86.1	4.2	3.2	2.6	1.6	2.3	13.9
410	20.7	18.6	1.0	0.5	0.3	0.1	0.1	20.6	2.0	90.5	4.7	2.4	1.4	0.7	0.4	9.5
420	30.2	25.4	2.4	1.0	0.5	0.3	0.5	30.0	4.6	84.7	7.9	3.3	1.6	0.9	1.6	15.3
430	21.9	18.3	1.6	0.8	0.4	0.3	0.3	21.8	3.5	84.1	7.5	3.7	2.0	1.4	1.3	15.9
440	19.6	15.9	1.7	0.7	0.4	0.2	0.6	19.5	3.6	81.6	8.6	3.7	2.0	1.0	3.2	18.4
450	19.2	17.0	1.2	0.5	0.2	0.1	0.0	19.1	2.1	88.8	6.5	2.8	1.3	0.4	0.2	11.2
460	19.5	16.3	1.7	0.7	0.5	0.1	0.0	19.4	3.1	83.8	8.7	3.9	2.8	0.7	0.1	16.2
470	18.6	15.2	1.5	0.8	0.6	0.2	0.1	18.5	3.3	82.1	8.4	4.3	3.4	1.3	0.6	17.9
480	27.6	22.3	2.2	1.6	1.0	0.4	0.1	27.5	5.2	81.0	7.8	5.7	3.6	1.5	0.5	19.0
490	17.8	15.3	1.3	0.7	0.4	0.1	0.0	17.7	2.4	86.4	7.2	3.8	2.1	0.3	0.2	13.6
500	21.2	18.6	1.2	0.6	0.6	0.1	0.0	21.1	2.5	88.2	5.5	2.9	2.7	0.4	0.2	11.8
510	24.1	21.4	1.1	0.6	0.6	0.2	0.0	23.9	2.6	89.2	4.6	2.5	2.6	1.0	0.2	10.8
520	20.8	17.7	1.5	0.6	0.8	0.1	0.0	20.7	3.0	85.4	7.0	3.1	3.8	0.6	0.1	14.6

Appendix 2: Grainsize distribution

	Dry weight (g)									Percentages						
Depth (cm)	total	< 63µm	63-125	125-250	250-500	500-1000	>1000	sum total	sum > 63µm	< 63µm	63-125	125-120	250-500	500-1000	> 1000	> 63µm
530	21.2	18.3	1.4	0.6	0.6	0.1	0.0	21.1	2.8	86.8	6.7	3.0	2.7	0.6	0.1	13.2
540	19.9	17.4	1.2	0.5	0.4	0.1	0.0	19.7	2.2	88.6	6.3	2.5	2.0	0.5	0.0	11.4
560	21.5	19.0	1.3	0.6	0.3	0.1	0.0	21.4	2.4	88.9	6.1	3.0	1.6	0.3	0.2	11.1
Core S1																
10	16.0	12.7	0.4	0.4	0.5	0.4	0.0	14.4	1.7	87.9	2.9	3.0	3.6	2.5	0.1	12.1
20	11.4	7.9	0.5	0.5	0.7	0.5	0.0	10.0	2.1	78.8	4.7	4.9	6.8	4.6	0.2	21.2
30	13.5	9.6	1.0	0.4	0.3	0.1	0.0	11.3	1.8	84.5	8.4	3.5	2.3	1.2	0.1	15.5
40	10.9	5.7	0.8	0.8	0.2	0.0	0.0	7.6	1.9	75.3	11.0	10.2	3.0	0.4	0.1	24.7
50	12.0	8.4	0.8	0.3	0.1	0.1	0.1	9.8	1.4	85.7	8.6	2.8	1.3	1.1	0.6	14.3
60	33.9	9.7	0.6	0.4	0.4	0.5	21.4	33.0	23.2	29.6	1.7	1.2	1.2	1.4	64.9	70.4
70	35.4	11.3	1.0	0.9	0.8	1.0	19.3	34.2	23.0	32.9	3.0	2.5	2.3	3.0	56.3	67.1
80	40.1	18.6	1.1	0.8	1.0	1.4	14.0	37.0	18.4	50.2	3.1	2.2	2.8	3.8	37.9	49.8
90	29.4	12.0	0.8	0.6	0.8	1.0	12.0	27.1	15.1	44.2	2.8	2.3	2.9	3.7	44.1	55.8
100	22.5	12.5	0.7	0.5	0.5	0.8	6.6	21.6	9.1	58.0	3.2	2.3	2.4	3.6	30.5	42.0
110	18.3	12.2	0.7	0.6	0.6	0.6	2.8	17.5	5.3	69.7	4.3	3.3	3.7	3.3	15.8	30.3
120	19.9	15.7	1.2	0.5	0.4	0.4	0.7	18.9	3.2	83.2	6.1	2.8	2.2	2.2	3.5	16.8
130	19.9	14.1	1.0	0.6	0.6	0.4	2.4	19.1	4.9	74.1	5.2	2.9	3.2	2.0	12.7	25.9
140	16.9	13.7	1.5	0.5	0.2	0.1	0.1	16.0	2.4	85.3	9.1	3.3	1.2	0.6	0.5	14.7
150	19.4	16.0	1.5	0.6	0.3	0.1	0.0	18.5	2.5	86.4	8.0	3.3	1.7	0.4	0.2	13.6
160	22.8	18.8	1.3	0.9	0.3	0.0	0.0	21.4	2.6	87.9	6.3	4.1	1.5	0.2	0.1	12.1
170	18.5	15.0	1.0	0.6	0.5	0.3	0.2	17.6	2.5	85.6	5.8	3.3	2.8	1.7	0.9	14.4
180	16.2	13.4	1.1	0.5	0.2	0.0	0.1	15.3	1.9	87.5	7.1	3.3	1.2	0.3	0.6	12.5
190	16.6	13.2	1.1	0.9	0.3	0.1	0.0	15.6	2.4	84.4	7.2	5.7	2.1	0.5	0.1	15.6
200	15.5	10.9	0.1	0.5	0.2	0.1	0.6	12.5	1.5	87.8	0.7	4.3	2.0	0.8	4.4	12.2
210	18.8	13.6	1.6	0.6	0.2	0.1	0.2	16.3	2.8	83.1	9.8	3.9	1.5	0.4	1.2	16.9
220	17.1	13.4	1.4	0.9	0.4	0.1	0.1	16.4	3.0	81.8	8.3	5.6	2.6	0.7	0.9	18.2
230	25.2	19.8	2.4	1.0	0.2	0.0	0.0	23.5	3.7	84.3	10.2	4.4	0.7	0.2	0.1	15.7
240	23.4	18.2	1.7	1.0	0.2	0.0	0.0	21.1	2.9	86.2	8.1	4.5	0.8	0.2	0.1	13.8
250	26.0	20.6	1.4	1.6	0.6	0.3	0.1	24.4	3.9	84.2	5.6	6.4	2.3	1.0	0.4	15.8
260	26.0	22.2	1.4	0.7	0.4	0.4	0.4	25.5	3.4	86.8	5.6	2.8	1.6	1.5	1.7	13.2
270	26.7	22.0	1.6	0.8	0.3	0.2	0.2	25.0	3.0	87.8	6.3	3.1	1.3	0.8	0.7	12.2
280	27.6	21.1	1.2	1.2	1.2	0.7	0.6	25.9	4.8	81.3	4.5	4.7	4.6	2.7	2.2	18.7
290	26.8	18.2	1.8	3.1	1.2	0.2	0.3	25.0	6.8	73.0	7.2	12.5	5.0	1.0	1.3	27.0
300	28.0	22.6	1.0	0.8	0.4	0.1	0.1	24.9	2.3	90.6	3.9	3.2	1.6	0.3	0.3	9.4
310	25.6	19.4	0.8	0.8	0.6	0.4	0.3	22.3	2.9	87.0	3.5	3.6	2.9	1.8	1.2	13.0
320	25.0	18.6	1.3	0.9	0.5	0.1	0.0	21.4	2.9	86.7	5.9	4.3	2.2	0.7	0.2	13.3
330	24.6	20.0	1.3	1.2	0.4	0.1	0.0	23.0	3.0	87.2	5.7	5.0	1.7	0.3	0.1	12.8
340	22.5	18.3	1.2	0.9	0.6	0.1	0.0	21.1	2.8	86.6	5.6	4.2	3.0	0.5	0.1	13.4
350	20.7	15.9	0.9	1.1	0.8	0.2	0.0	19.0	3.0	84.1	4.8	5.6	4.4	0.9	0.2	15.9
360	19.7	16.1	1.2	0.6	0.4	0.1	0.1	18.4	2.4	87.2	6.5	3.1	1.9	0.8	0.5	12.8
370	20.4	17.0	1.1	0.4	0.3	0.2	0.2	19.2	2.1	88.9	5.5	2.2	1.6	0.9	0.9	11.1
380	17.6	14.1	1.0	0.7	0.5	0.2	0.1	16.6	2.5	84.8	6.3	4.2	2.7	1.3	0.7	15.2
390	15.6	12.4	0.7	0.7	0.5	0.1	0.0	14.5	2.1	85.8	4.7	5.1	3.6	0.7	0.1	14.2
400	16.0	13.0	0.6	0.7	0.5	0.2	0.1	15.0	2.0	86.5	4.0	4.8	3.3	1.0	0.3	13.5
410	15.4	11.9	0.7	1.0	0.7	0.2	0.0	14.5	2.6	81.9	5.0	6.6	4.9	1.4	0.2	18.1
420	15.3	11.7	0.8	0.9	0.7	0.2	0.1	14.4	2.7	81.4	5.9	6.0	4.7	1.3	0.7	18.6
430	16.9	14.0	1.2	0.4	0.2	0.1	0.0	16.0	1.9	88.1	7.6	2.6	1.2	0.3	0.1	11.9
440	16.3	13.4	0.7	0.7	0.4	0.1	0.0	15.3	1.9	87.6	4.3	4.9	2.6	0.5	0.2	12.4
450	14.3	11.6	0.7	0.5	0.3	0.1	0.1	13.3	1.8	86.8	5.3	3.9	2.5	0.7	0.7	13.2
460	15.7	13.2	0.8	0.5	0.2	0.1	0.1	14.8	1.5	89.6	5.3	3.3	1.1	0.4	0.4	10.4
470	14.1	11.8	0.7	0.4	0.3	0.1	0.1	13.4	1.6	88.3	5.0	3.2	2.0	0.8	0.6	11.7
480	16.2	13.7	0.7	0.5	0.3	0.1	0.1	15.3	1.7	89.1	4.8	3.1	1.6	0.6	0.7	10.9
490	13.4	11.3	0.4	0.4	0.3	0.1	0.1	12.6	1.3	89.8	2.9	2.9	2.7	1.1	0.6	10.2

Appendix 2: Grainsize distribution

	Dry weight (g)									Percentages						
Depth (cm)	total	< 63µm	63-125	125-250	250-500	500-1000	>1000	sum total	sum > 63µm	< 63µm	63-125	125-120	250-500	500-1000	> 1000	> 63µm
500	16.5	13.7	0.6	0.4	0.3	0.2	0.1	15.2	1.5	90.2	4.0	2.6	1.9	1.0	0.3	9.8
Core S2																
2	20.6	13.1	2.0	0.7	0.4	0.2	0.0	16.5	3.4	79.6	12.1	4.5	2.7	0.9	0.2	20.4
10	14.4	10.4	0.9	0.4	0.3	0.2	0.0	12.2	1.7	85.7	7.2	3.0	2.5	1.2	0.3	14.3
20	17.1	13.4	0.9	0.4	0.3	0.2	0.0	15.2	1.9	87.7	5.7	2.9	2.2	1.2	0.3	12.3
30	14.7	11.3	0.7	0.5	0.4	0.3	0.0	13.2	1.9	85.4	5.4	3.6	2.8	2.6	0.2	14.6
40	16.6	12.7	0.8	0.5	0.5	0.3	0.0	14.9	2.1	85.7	5.6	3.7	3.0	1.9	0.1	14.3
50	15.2	11.8	0.6	0.4	0.4	0.2	0.0	13.4	1.7	87.6	4.3	3.2	3.0	1.8	0.1	12.4
60	15.4	21.8	0.6	0.4	0.4	0.3	0.1	23.6	1.8	92.3	2.7	1.9	1.7	1.1	0.2	7.7
70	14.5	14.0	0.3	0.2	0.2	0.1	0.0	14.9	0.8	94.4	2.1	1.2	1.4	0.9	0.1	5.6
80	16.0	14.1	0.1	0.1	0.1	0.1	0.0	14.5	0.3	97.8	0.6	0.6	0.6	0.4	0.1	2.2
90	18.8	17.6	0.1	0.0	0.0	0.0	0.0	17.7	0.1	99.2	0.5	0.2	0.1	0.1	0.0	0.8
100	19.0	11.6	4.6	0.8	0.2	0.1	0.0	17.2	5.6	67.3	26.7	4.7	0.9	0.4	0.0	32.7
110	27.6	11.8	0.9	0.5	0.4	0.5	11.9	26.0	14.2	45.2	3.4	2.1	1.5	1.9	45.8	54.8
120	40.5	14.2	1.7	1.1	1.0	1.1	19.3	38.5	24.3	36.8	4.5	2.9	2.7	2.9	50.2	63.2
130	26.7	31.5	1.8	0.8	0.7	1.1	8.3	44.1	12.6	71.3	4.1	1.9	1.5	2.4	18.8	28.7
140	32.6	14.3	2.5	1.0	0.4	0.3	12.1	30.5	16.3	46.7	8.3	3.2	1.2	1.1	39.6	53.3
150	30.8	35.3	1.9	1.0	1.0	1.3	6.9	47.2	12.0	74.7	4.0	2.0	2.0	2.8	14.5	25.3
160	30.6	18.7	1.2	0.5	0.3	0.6	7.7	28.9	10.3	64.5	4.0	1.6	1.2	1.9	26.7	35.5
170	21.7	12.8	5.0	0.4	0.1	0.1	0.3	18.6	5.9	68.5	26.8	2.0	0.5	0.4	1.8	31.5
180	24.7	9.1	0.7	0.4	0.4	0.4	12.7	23.8	14.7	38.2	3.1	1.7	1.7	1.8	53.4	61.8
190	26.2	14.8	1.7	0.9	0.6	0.6	6.5	25.0	10.2	59.2	6.8	3.4	2.5	2.3	25.8	40.8
200	24.7	20.3	0.3	0.1	0.1	0.1	3.3	24.2	3.9	84.1	1.2	0.5	0.3	0.3	13.7	15.9
210	18.8	15.2	1.5	0.5	0.2	0.1	0.3	17.8	2.6	85.3	8.6	2.6	1.2	0.8	1.4	14.7
220	16.6	12.6	1.5	0.5	0.4	0.2	0.4	15.7	3.1	80.4	9.7	3.2	2.4	1.6	2.7	19.6
230		16.2	2.8	0.7	0.2	0.1	0.1	19.9	3.7	81.3	13.8	3.3	0.8	0.3	0.5	18.7
240	21.6	12.6	2.6	0.7	0.2	0.1	0.1	16.3	3.7	77.3	16.0	4.3	1.4	0.4	0.5	22.7
250	17.6	16.7	2.8	0.8	0.3	0.1	0.0	20.7	4.0	80.6	13.6	4.0	1.5	0.2	0.1	19.4
260	21.7	15.5	2.2	0.6	0.2	0.0	0.0	18.6	3.0	83.6	11.7	3.3	1.2	0.2	0.1	16.4
270	20.5	14.7	2.1	1.1	0.3	0.1	0.0	18.2	3.6	80.5	11.3	5.9	1.9	0.3	0.2	19.5
280	19.2	15.5	1.7	0.4	0.1	0.0	0.0	17.8	2.3	87.1	9.6	2.3	0.7	0.2	0.2	12.9
290	20.0	13.4	1.6	0.5	0.1	0.0	0.0	15.7	2.3	85.5	10.2	3.4	0.9	0.1	0.0	14.5
300	16.8	15.6	1.6	0.5	0.1	0.0	0.0	17.9	2.3	87.2	8.9	2.9	0.7	0.1	0.1	12.8
310	19.1	17.2	2.1	0.7	0.2	0.1	0.0	20.3	3.1	84.7	10.2	3.6	1.1	0.3	0.1	15.3
320	21.0	13.8	1.3	0.2	0.1	0.0	0.0	15.5	1.7	89.1	8.7	1.5	0.5	0.0	0.0	10.9
330	18.4	14.2	2.3	0.5	0.1	0.0	0.0	17.2	3.0	82.5	13.5	3.1	0.7	0.1	0.1	17.5
340	17.0	13.0	2.0	0.6	0.2	0.0	0.1	16.0	3.0	81.4	12.6	3.9	1.3	0.3	0.5	18.6
350	17.5	10.8	1.5	0.5	0.1	0.0	0.0	12.9	2.2	83.2	11.3	4.1	1.1	0.2	0.0	16.8
360	14.9	12.2	2.7	0.6	0.1	0.0	0.0	15.6	3.4	78.2	17.2	3.6	0.8	0.2	0.0	21.8
370	16.1	16.1	2.4	0.6	0.2	0.0	0.0	19.3	3.2	83.2	12.5	3.2	0.9	0.1	0.0	16.8
380	21.2	14.7	2.1	0.7	0.2	0.1	0.0	17.8	3.1	82.7	11.7	3.9	1.1	0.4	0.2	17.3
390	19.3	10.9	1.6	0.4	0.1	0.0	0.0	13.0	2.1	83.7	12.1	3.2	0.7	0.3	0.1	16.3
400	16.1	15.1	1.3	0.4	0.2	0.1	0.2	17.2	2.1	87.7	7.3	2.0	0.9	0.6	1.4	12.3
410	18.6	16.6	1.4	0.4	0.2	0.1	0.1	18.7	2.1	88.8	7.3	2.2	0.9	0.6	0.3	11.2
420	19.8	15.8	2.9	0.8	0.3	0.1	0.2	20.1	4.3	78.4	14.4	3.9	1.4	0.6	1.2	21.6
430	19.0	27.1	2.7	0.8	0.3	0.1	0.1	31.1	4.0	87.2	8.6	2.6	1.0	0.4	0.2	12.8
440	33.6	26.0	2.2	0.7	0.3	0.1	0.1	29.4	3.4	88.5	7.5	2.3	0.9	0.5	0.4	11.5
450	32.2	23.6	2.6	0.7	0.3	0.2	0.2	27.6	4.0	85.5	9.3	2.7	1.1	0.7	0.7	14.5
Core S3																
5	18.9	11.8	1.3	1.6	0.4	0.2	1.4	16.6	4.8	71.2	7.6	9.5	2.1	1.0	8.6	28.8
10	10.5	5.3	1.0	0.5	0.1	0.1	2.3	9.1	3.9	57.7	10.7	5.0	0.9	0.9	24.8	42.3
13	13.2	10.3	0.9	0.4	0.2	0.2	0.5	12.5	2.2	82.4	6.8	3.5	1.8	1.7	3.8	17.6
20	21.9	10.3	0.9	0.6	0.4	0.3	8.5	21.0	10.7	49.0	4.4	2.9	1.9	1.6	40.3	51.0

Appendix 2: Grainsize distribution

	Dry weight (g)									Percentages						
Depth (cm)	total	< 63µm	63-125	125-250	250-500	500-1000	>1000	sum total	sum > 63µm	< 63µm	63-125	125-120	250-500	500-1000	> 1000	> 63µm
30	20.6	10.2	1.0	1.7	1.8	0.8	4.1	19.7	9.4	52.0	5.0	8.8	9.2	4.0	21.1	48.0
40	15.9	6.7	0.9	1.0	0.8	0.5	5.3	15.2	8.6	43.8	6.0	6.7	5.3	3.4	34.8	56.2
50	18.2	11.3	1.2	1.1	0.5	0.5	2.6	17.1	5.9	65.8	6.9	6.7	3.1	2.7	14.9	34.2
65	14.3	7.3	1.1	1.9	1.8	0.8	0.7	13.5	6.2	53.9	7.9	14.0	13.6	5.6	5.0	46.1
80	22.4	12.1	1.2	1.5	1.0	0.8	4.8	21.4	9.3	56.6	5.5	7.2	4.6	3.7	22.5	43.4
89	24.7	23.1	0.1	0.1	0.0	0.0	0.0	23.3	0.2	99.2	0.4	0.3	0.1	0.0	0.0	0.8
93	23.0	9.1	4.5	5.2	1.5	0.0	0.0	20.4	11.3	44.6	22.3	25.6	7.4	0.1	0.1	55.4
100	18.1	8.0	0.8	2.0	2.8	0.7	2.7	17.1	9.1	46.8	4.8	11.9	16.4	4.2	15.8	53.2
110	16.2	10.3	1.2	1.7	0.8	0.2	1.1	15.3	5.1	67.1	8.1	11.2	4.9	1.3	7.4	32.9
120	17.4	12.6	1.0	1.0	0.6	0.3	0.9	16.4	3.8	76.7	6.1	6.3	3.5	2.1	5.4	23.3
131	20.6	18.1	0.8	0.4	0.2	0.1	0.2	19.8	1.7	91.7	4.0	2.2	0.8	0.4	0.9	8.3
140	27.2	18.7	2.0	2.5	0.9	0.4	1.2	25.6	7.0	72.9	7.9	9.9	3.3	1.4	4.6	27.1
150	22.4	14.4	1.8	2.4	0.8	0.2	0.9	20.5	6.1	70.3	8.6	11.6	4.0	0.8	4.6	29.7
160	23.1	11.7	1.8	1.3	0.5	0.6	5.7	21.7	9.9	54.2	8.5	6.0	2.4	2.7	26.1	45.8
170	26.5	18.3	2.6	2.6	0.7	0.2	0.3	24.7	6.3	74.4	10.4	10.6	2.7	0.9	1.0	25.6
180	26.5	17.2	2.1	2.8	0.8	0.1	0.1	23.1	5.9	74.6	9.3	11.9	3.7	0.3	0.2	25.4
190	31.0	22.2	2.3	3.3	0.4	0.1	0.0	28.4	6.1	78.4	8.2	11.5	1.5	0.3	0.1	21.6
192	23.6	16.4	0.4	1.7	2.0	0.3	0.1	21.0	4.6	78.0	2.1	8.1	9.6	1.6	0.7	22.0
195	23.4	14.0	1.5	1.5	2.4	1.7	0.4	21.5	7.6	64.9	7.1	7.2	11.0	7.9	2.0	35.1
207	21.5	14.1	1.8	2.1	1.2	0.2	0.0	19.5	5.3	72.6	9.4	11.0	6.0	0.9	0.1	27.4
210	23.8	15.7	2.0	2.7	1.0	0.1	0.0	21.4	5.7	73.3	9.3	12.5	4.5	0.3	0.1	26.7
220	26.1	18.0	2.4	1.9	0.5	0.0	0.0	22.8	4.8	78.9	10.4	8.4	2.1	0.1	0.1	21.1
230	19.7	14.7	1.4	1.6	0.3	0.0	0.0	18.0	3.3	81.5	8.0	8.8	1.4	0.1	0.1	18.5
240	19.4	12.7	1.5	1.9	1.3	0.2	0.2	18.0	5.3	70.6	8.6	10.8	7.5	1.2	1.4	29.4
250	22.2	15.8	1.6	1.8	1.1	0.0	0.0	20.4	4.6	77.5	7.8	8.9	5.5	0.2	0.0	22.5
260	31.4	22.8	2.0	2.8	0.4	0.0	0.0	28.1	5.3	81.1	7.2	10.1	1.4	0.2	0.1	18.9
270	25.3	17.0	2.2	2.6	0.8	0.1	0.0	22.6	5.6	75.0	9.5	11.3	3.4	0.6	0.2	25.0
274	24.1	14.9	1.9	2.7	1.9	0.2	0.0	21.8	6.8	68.7	8.8	12.3	8.9	1.1	0.1	31.3
276	15.4	5.3	0.9	2.2	4.4	1.4	0.1	14.3	9.0	36.8	6.6	15.3	30.4	10.0	0.9	63.2
280	17.6	8.8	1.3	2.5	3.3	0.3	0.0	16.2	7.5	54.0	7.9	15.7	20.3	2.0	0.1	46.0
290	27.7	21.1	1.7	1.8	0.8	0.1	0.0	25.5	4.4	82.8	6.6	7.2	3.1	0.2	0.1	17.2
300	25.3	16.0	1.8	2.9	2.2	0.1	0.0	22.9	7.0	69.6	7.8	12.6	9.4	0.5	0.1	30.4
310	31.9	21.0	2.0	3.0	4.2	0.3	0.0	30.6	9.5	68.8	6.6	9.8	13.8	0.9	0.1	31.2
314	29.5	15.4	1.6	3.0	6.2	0.9	0.1	27.2	11.8	56.6	5.9	11.2	22.6	3.5	0.2	43.4
320	29.8	20.7	2.2	2.9	1.1	0.0	0.0	26.9	6.2	76.9	8.1	10.9	4.0	0.1	0.0	23.1
330	27.2	18.1	2.2	2.6	0.9	0.1	0.0	23.8	5.7	76.1	9.1	10.7	3.7	0.2	0.2	23.9
340	26.8	17.0	2.5	3.9	2.2	0.1	0.0	25.8	8.8	66.0	9.7	15.0	8.7	0.3	0.2	34.0
350	28.5	18.2	1.8	2.5	4.1	0.1	0.0	26.8	8.6	68.1	6.9	9.2	15.4	0.3	0.1	31.9
360	24.5	12.8	1.5	2.3	1.8	0.1	0.0	18.7	5.8	68.7	8.2	12.5	9.6	0.7	0.2	31.3
370	28.0	19.3	2.6	2.7	0.7	0.0	0.0	25.4	6.1	76.1	10.4	10.7	2.6	0.2	0.0	23.9
377	32.3	21.2	2.0	2.5	3.6	0.1	0.0	29.4	8.2	72.0	6.7	8.6	12.2	0.4	0.0	28.0
380	26.1	18.4	1.8	2.4	1.6	0.1	0.0	24.3	5.9	75.7	7.6	10.0	6.4	0.3	0.0	24.3
390	16.7	12.6	1.3	1.3	0.2	0.0	0.0	15.4	2.8	81.7	8.5	8.3	1.3	0.1	0.0	18.3
400	16.4	12.6	1.3	0.7	0.1	0.0	0.0	14.8	2.1	85.6	9.1	4.4	0.7	0.2	0.0	14.4
410	16.4	13.3	1.2	0.6	0.2	0.1	0.1	15.4	2.1	86.1	7.5	3.8	1.3	0.7	0.6	13.9
420	16.4	13.5	1.5	0.8	0.2	0.1	0.0	16.2	2.7	83.5	9.0	5.2	1.5	0.5	0.3	16.5
430	18.5	14.9	1.3	0.7	0.2	0.1	0.0	17.1	2.2	87.0	7.5	4.0	1.0	0.4	0.2	13.0
435	15.4	12.2	1.3	1.5	0.4	0.1	0.1	15.6	3.4	78.5	8.1	9.4	2.8	0.6	0.6	21.5
440	24.8	20.1	2.0	2.3	1.3	0.3	0.2	26.2	6.1	76.8	7.7	8.7	4.9	1.2	0.8	23.2
275-279	69.3	28.3	5.4	10.7	14.9	4.0	0.3	63.6	35.3	44.5	8.5	16.8	23.5	6.3	0.4	55.5

Appendix 2: Grainsize distribution

	Dry weight (g)									Percentages						
Depth (cm)	total	< 63µm	63-125	125-250	250-500	500-1000	>1000	sum total	sum > 63µm	< 63µm	63-125	125-120	250-500	500-1000	> 1000	> 63µm
Core S6																
1	18.0	14.0	1.0	1.6	0.8	0.4	0.1	17.8	3.9	78.3	5.8	8.8	4.7	2.1	0.3	21.7
10	18.0	9.4	0.7	1.3	2.5	2.2	0.4	16.7	7.2	56.6	4.4	8.0	15.0	13.3	2.7	43.4
20	21.6	14.5	1.1	2.0	1.1	0.5	0.1	19.2	4.8	75.3	5.8	10.3	5.8	2.4	0.3	24.7
30	18.6	12.6	0.7	1.7	1.0	0.6	0.0	16.7	4.1	75.5	4.3	10.4	6.2	3.3	0.3	24.5
40	19.1	13.5	0.9	1.4	0.7	0.4	0.0	16.9	3.4	80.1	5.4	8.2	3.9	2.4	0.1	19.9
50	18.7	13.2	0.9	1.3	0.8	0.4	0.0	16.7	3.4	79.5	5.3	8.0	4.7	2.2	0.2	20.5
60	18.7	12.8	0.8	1.1	0.9	0.4	0.0	16.1	3.3	79.4	4.8	7.1	5.6	2.7	0.3	20.6
70	18.7	12.2	0.9	1.7	1.2	0.7	0.0	16.7	4.5	72.8	5.1	10.4	7.4	4.1	0.1	27.2
80	18.1	10.7	0.8	1.7	1.8	1.2	0.0	16.1	5.4	66.2	5.0	10.4	11.0	7.2	0.2	33.8
86	15.1	5.0	0.8	2.5	3.8	1.8	0.4	14.2	9.2	34.9	5.5	17.6	26.5	12.9	2.6	65.1
90	20.8	13.0	1.7	2.1	2.0	0.9	0.1	19.8	6.8	65.8	8.4	10.4	10.1	4.6	0.6	34.2
100	21.5	14.6	2.4	1.1	0.5	0.2	0.0	18.7	4.1	78.0	12.7	5.6	2.6	0.9	0.1	22.0
110	23.3	16.6	2.4	1.9	1.0	0.1	0.0	21.9	5.4	75.5	10.7	8.5	4.5	0.7	0.1	24.5
120	19.9	11.1	2.8	1.4	0.4	0.1	0.0	15.9	4.7	70.1	17.5	9.0	2.6	0.6	0.2	29.9
126	10.6	3.6	0.7	2.3	2.2	0.1	0.0	8.9	5.3	40.8	7.3	25.8	24.4	1.7	0.0	59.2
130	21.3	14.1	2.3	1.1	0.2	0.1	0.1	17.9	3.8	78.7	13.0	6.2	1.0	0.6	0.5	21.3
132	14.0	8.1	1.1	1.0	0.1	0.1	2.2	12.6	4.5	64.1	8.8	7.9	1.0	1.1	17.0	35.9
140	28.0	11.4	0.9	1.6	1.7	0.5	11.0	27.0	15.6	42.3	3.2	5.9	6.2	1.8	40.6	57.7
150	33.7	11.1	0.8	2.1	5.5	3.9	9.1	32.5	21.3	34.3	2.5	6.4	16.8	12.0	28.0	65.7
160	28.4	5.6	1.4	2.6	2.4	1.1	7.8	20.8	15.2	27.0	6.5	12.5	11.4	5.1	37.4	73.0
170	36.4	14.6	1.0	1.9	4.0	2.7	11.1	35.2	20.6	41.4	2.8	5.3	11.4	7.7	31.5	58.6
180	32.6	15.5	0.8	1.5	1.9	1.4	10.3	31.4	15.9	49.5	2.5	4.9	5.9	4.3	32.9	50.5
185	31.3	5.4	0.7	2.7	10.4	7.7	3.6	30.4	25.0	17.8	2.4	8.8	34.1	25.3	11.7	82.2
190	33.6	13.5	0.9	2.0	5.7	2.9	7.4	32.5	19.0	41.6	2.8	6.1	17.6	9.0	22.8	58.4
200	51.7	17.6	0.8	2.3	11.2	11.6	6.4	49.8	32.2	35.4	1.6	4.6	22.4	23.2	12.8	64.6
210	37.5	21.5	1.2	2.8	3.8	0.8	6.3	36.4	14.9	59.1	3.4	7.6	10.4	2.2	17.3	40.9
220	40.0	25.3	1.9	3.8	4.3	0.6	1.2	37.1	11.8	68.1	5.2	10.2	11.6	1.7	3.2	31.9
230	35.6	1.0	1.4	2.9	3.6	0.2	0.6	9.6	8.6	10.5	14.9	29.8	36.9	1.8	6.2	89.5
240	37.4	25.4	2.6	3.3	3.6	0.5	0.3	35.6	10.3	71.2	7.4	9.2	10.1	1.3	0.9	28.8
250	21.4	14.4	1.8	2.4	1.2	0.1	0.1	20.0	5.6	72.1	9.2	12.0	6.0	0.3	0.4	27.9
260	22.6	15.4	1.4	2.0	1.9	0.1	0.0	20.8	5.4	74.1	6.8	9.5	9.3	0.3	0.1	25.9
270	22.0	15.9	2.4	1.5	0.7	0.1	0.0	20.6	4.6	77.4	11.6	7.2	3.3	0.4	0.1	22.6
274	22.9	12.1	2.4	2.5	3.0	1.2	0.4	21.5	9.5	56.1	11.1	11.5	13.9	5.6	1.8	43.9
280	19.5	11.3	2.1	2.4	2.2	0.5	0.1	18.5	7.2	61.1	11.3	13.0	11.6	2.6	0.4	38.9
285	17.6	6.5	2.1	3.8	3.4	0.7	0.1	16.5	10.0	39.4	12.7	22.8	20.6	4.0	0.5	60.6
287	9.8	9.3	1.3	1.3	0.9	0.2	0.0	13.1	3.8	71.2	9.7	10.3	7.1	1.5	0.2	28.8
290	21.0	13.8	2.8	2.1	0.9	0.1	0.0	19.7	5.8	70.3	14.2	10.7	4.4	0.4	0.1	29.7
295	17.2	5.5	2.2	0.9	0.3	0.1	0.1	9.1	3.6	60.7	24.3	9.7	3.7	0.9	0.6	39.3
300	21.7	12.4	2.5	3.5	2.0	0.2	0.1	20.8	8.4	59.7	12.0	17.0	9.5	1.2	0.5	40.3
310	18.2	12.8	4.1	1.4	0.7	0.1	0.0	19.1	6.3	66.8	21.4	7.4	3.8	0.5	0.1	33.2
320	18.5	12.5	2.3	2.0	0.7	0.1	0.1	17.6	5.1	70.8	12.8	11.1	4.2	0.4	0.7	29.2
330	22.3	14.5	2.5	2.5	1.2	0.2	0.0	21.0	6.4	69.4	11.7	12.0	6.0	0.8	0.1	30.6
340	20.1	13.1	2.9	2.1	0.7	0.1	0.0	18.9	5.8	69.5	15.2	11.2	3.7	0.4	0.0	30.5
350	19.3	11.9	2.3	1.2	0.5	0.1	0.1	16.1	4.2	73.7	14.4	7.5	3.3	0.8	0.3	26.3
360	23.5	15.7	2.9	2.2	1.1	0.1	0.1	22.2	6.5	70.8	13.1	10.1	5.1	0.6	0.4	29.2
370	21.5	13.3	3.5	2.3	0.9	0.1	0.0	20.2	6.9	65.9	17.3	11.4	4.6	0.7	0.2	34.1
380	28.1	16.4	4.2	3.6	1.9	0.3	0.0	26.3	9.9	62.3	15.8	13.6	7.1	1.0	0.1	37.7
390	26.5	13.9	4.1	3.9	2.5	0.2	0.0	24.6	10.7	56.6	16.6	15.7	10.0	1.0	0.1	43.4
400	25.4	16.3	4.3	3.0	2.1	0.3	0.0	26.0	9.7	62.8	16.5	11.4	8.0	1.2	0.1	37.2
410	28.2	16.4	3.5	3.1	1.2	0.1	0.0	24.4	8.0	67.3	14.5	12.5	5.1	0.6	0.1	32.7
420	23.9	14.4	2.3	2.1	1.5	0.5	0.1	20.9	6.6	68.6	10.9	10.3	7.4	2.3	0.6	31.4
430	21.1	14.4	2.9	1.4	0.4	0.1	0.0	19.2	4.7	75.3	14.9	7.3	1.9	0.3	0.2	24.7

Appendix 2: Grainsize distribution

	Dry weight (g)									**Percentages**						
Depth (cm)	total	< 63µm	63-125	125-250	250-500	500-1000	>1000	sum total	sum > 63µm	< 63µm	63-125	125-120	250-500	500-1000	> 1000	> 63µm
440	26.2	17.5	3.4	2.5	1.1	0.1	0.1	24.6	7.2	70.9	13.7	10.3	4.3	0.5	0.2	29.1
450	23.2	17.5	2.1	1.4	0.7	0.2	0.1	22.1	4.6	79.4	9.5	6.4	3.0	1.1	0.6	20.6
460	22.8	17.4	1.9	1.3	0.7	0.3	0.1	21.7	4.3	80.3	8.7	5.8	3.4	1.3	0.5	19.7
470	22.3	14.9	4.1	2.5	0.9	0.1	0.0	22.6	7.7	66.1	18.3	11.2	3.9	0.5	0.0	33.9

Appendix 3: TOC- and carbonate-content (LECO)

Core	Depth (cm)	TC I	TC II	ΔTC	stdev	TC (average)	CO2-total	TOC I	TOC II	ΔTOC	TOC (average)	CO2-org	stdev	CaCO3	error
		(all values in percent)													
S2	2	7.5	7.3	0.2	0.1	7.4	27.2	0.4	0.4	0.0	0.4	1.5	0.0	58.3	2.4
	10	7.0	7.1	-0.1	0.1	7.1	25.9	0.3	0.3	0.0	0.3	1.1	0.0	56.3	3.0
	20	7.6	7.5	0.1	0.0	7.5	27.6	0.3	0.3	0.0	0.3	1.0	0.0	60.4	1.7
	30	7.5	7.6	-0.1	0.1	7.5	27.5	0.3	0.3	0.0	0.3	1.0	0.0	60.2	4.4
	40	7.7	7.8	-0.1	0.1	7.7	28.3	0.3	0.2	0.0	0.3	0.9	0.0	62.2	3.4
	50	8.3	8.3	-0.1	0.0	8.3	30.5	0.2	0.2	0.0	0.2	0.7	0.0	67.6	1.3
	60	9.2	9.1	0.1	0.1	9.2	33.6	0.3	0.2	0.0	0.2	0.9	0.0	74.4	5.5
	70	7.7	7.7	0.0	0.0	7.7	28.2	0.4	0.3	-0.1	0.3	1.2	0.0	61.4	6.7
	80	7.0	6.9	0.0	0.0	6.9	25.5	0.3	0.3	0.0	0.3	1.1	0.0	55.3	0.5
	90	4.4	4.3	0.0	0.0	4.3	15.9	0.3	0.3	0.0	0.3	1.2	0.0	33.4	1.7
	100	4.5	4.5	0.0	0.0	4.5	16.6	0.2	0.1	0.0	0.1	0.5	0.0	36.4	4.8
	170	3.7	3.7	0.0	0.0	3.7	13.4	0.2	0.2	0.0	0.2	0.8	0.0	28.8	2.2
	210	6.1	6.0	0.1	0.1	6.0	22.1	0.3	0.3	0.0	0.3	1.0	0.0	47.8	0.1
	220	5.5	5.5	-0.1	0.0	5.5	20.1	0.2	0.2	0.0	0.2	0.9	0.0	43.8	2.6
	230	5.5	5.6	-0.2	0.1	5.6	20.4	0.1	0.2	0.1	0.1	0.5	0.0	45.1	8.2
	240	4.7	4.5	0.2	0.1	4.6	16.9	0.3	0.2	0.0	0.2	0.9	0.0	36.3	2.0
	250	4.6	4.6	0.0	0.0	4.6	16.9	0.2	0.2	0.0	0.2	0.6	0.0	37.0	1.2
	260	4.5	4.3	0.2	0.1	4.4	16.2	0.2	0.2	0.0	0.2	0.6	0.0	35.4	3.0
	270	4.8	4.5	0.2	0.1	4.7	17.1	0.3	0.2	0.0	0.3	1.0	0.0	36.5	2.0
	280	5.6	5.7	-0.1	0.0	5.7	20.7	0.2	0.2	0.0	0.2	0.6	0.0	45.7	1.9
	290	4.7	4.8	-0.1	0.0	4.7	17.4	0.2	0.2	0.0	0.2	0.7	0.0	38.0	0.7
	300	5.2	5.0	0.2	0.1	5.1	18.8	0.2	0.2	0.0	0.2	0.8	0.0	40.9	1.0
	310	5.4	5.4	0.0	0.0	5.4	19.8	0.2	0.2	0.0	0.2	0.7	0.0	43.4	0.1
	320	6.0	6.0	0.0	0.0	6.0	22.0	0.2	0.2	0.0	0.2	0.9	0.0	48.0	0.7
	330	5.0	5.1	-0.1	0.1	5.0	18.4	0.1	0.1	0.0	0.1	0.3	0.0	41.0	0.1
	340	4.7	4.8	-0.1	0.1	4.7	17.4	0.3	0.3	0.0	0.3	1.0	0.0	37.2	2.3
	350	6.0	6.1	-0.1	0.1	6.1	22.2	0.2	0.3	0.0	0.2	0.9	0.0	48.4	1.6
	360	7.0	7.0	0.0	0.0	7.0	25.6	0.6	0.6	0.0	0.6	2.1	0.0	53.5	0.6
	370	4.2	4.2	0.0	0.0	4.2	15.5	0.3	0.3	0.0	0.3	1.0	0.0	32.9	2.4
	380	4.1	4.2	-0.1	0.0	4.2	15.3	0.2	0.2	0.0	0.2	0.7	0.0	33.1	0.4
	390	5.5	5.7	-0.2	0.1	5.6	20.5	0.7	0.6	-0.1	0.6	2.4	0.0	41.2	1.0
	400	4.5	4.5	0.0	0.0	4.5	16.4	0.2	0.2	0.0	0.2	0.7	0.0	35.6	1.5
	410	5.4	5.4	-0.1	0.0	5.4	19.9	0.1	0.1	0.0	0.1	0.4	0.0	44.1	1.1
	420	6.0	5.8	0.2	0.1	5.9	21.7	0.1	0.1	0.0	0.1	0.4	0.0	48.4	0.6
	430	5.7	5.7	0.1	0.0	5.7	20.9	0.5	0.5	0.0	0.5	1.9	0.0	43.2	1.2
	440	5.3	5.3	0.0	0.0	5.3	19.4	0.1	0.1	0.0	0.1	0.4	0.0	43.1	1.5
	450	5.6	5.7	-0.2	0.1	5.7	20.7	0.1	0.1	0.0	0.1	0.4	0.0	46.1	1.1
S3	3	5.5	5.5	0.0	0.0	5.5	20.1	0.7	0.7	0.0	0.7	2.5	0.0	39.9	0.2
	35	5.4	5.4	0.0	0.0	5.4	19.8	0.1	0.1	0.0	0.1	0.5	0.0	44.0	2.5
	89	3.8	3.7	0.0	0.0	3.7	13.7	0.2	0.2	0.0	0.2	0.6	0.0	29.7	1.6
	93	3.7	3.5	0.2	0.1	3.6	13.1	0.2	0.2	0.0	0.2	0.6	0.0	28.3	0.7
	131	4.9	4.9	0.0	0.0	4.9	17.8	0.1	0.1	0.0	0.1	0.5	0.0	39.4	1.1
	140	7.4	7.3	0.1	0.0	7.3	26.8	0.1	0.1	0.0	0.1	0.5	0.0	59.9	1.3
	150	6.8	6.8	0.0	0.0	6.8	24.9	0.2	0.2	0.0	0.2	0.9	0.0	54.6	1.8
	160	6.7	6.8	0.0	0.0	6.8	24.8	0.2	0.2	0.0	0.2	0.6	0.0	54.9	0.1
	170	5.9	5.9	0.0	0.0	5.9	21.7	0.2	0.1	-0.1	0.1	0.5	0.0	48.2	9.9
	180	5.6	5.6	0.0	0.0	5.6	20.5	0.2	0.2	0.0	0.2	0.8	0.0	44.7	0.1
	190	4.7	4.7	0.0	0.0	4.7	17.1	0.2	0.2	0.0	0.2	0.7	0.0	37.3	0.1
	192	4.4	4.4	0.0	0.0	4.4	16.1	0.2	0.2	0.0	0.2	0.7	0.0	34.9	0.4
	195	6.8	6.9	-0.1	0.0	6.9	25.2	0.2	0.2	0.0	0.2	0.7	0.0	55.8	0.4
	207	5.1	5.0	0.0	0.0	5.0	18.5	0.2	0.1	0.0	0.2	0.6	0.0	40.7	2.3
	210	5.1	5.0	0.1	0.0	5.0	18.5	0.2	0.2	0.0	0.2	0.9	0.0	39.9	0.6

TC = total carbon
TOC = total organic carbon

Appendix 3: TOC- and carbonate-content (LECO)

Core	Depth (cm)	TC I	TC II	ΔTC	stdev	TC (average)	CO2-total	TOC I	TOC II	ΔTOC	TOC (average)	CO2-org	stdev	CaCO3	error
		(all values in percent)													
	220	4.4	4.4	0.0	0.0	4.4	16.2	0.2	0.2	0.0	0.2	0.6	0.0	35.4	2.4
	230	5.5	5.4	0.1	0.1	5.5	20.0	0.2	0.2	0.0	0.2	0.7	0.0	44.0	0.4
	240	6.0	6.0	0.1	0.0	6.0	22.0	0.2	0.3	0.0	0.2	0.9	0.0	48.0	3.8
	250	5.2	5.5	-0.3	0.1	5.3	19.6	0.2	0.2	0.0	0.2	0.8	0.0	42.6	0.1
	260	5.3	5.3	0.0	0.0	5.3	19.4	0.3	0.3	0.0	0.3	1.1	0.0	41.6	0.6
	270	5.8	5.9	-0.2	0.1	5.8	21.4	0.2	0.2	0.0	0.2	0.9	0.0	46.6	0.3
	274	6.6	6.4	0.2	0.1	6.5	23.9	0.2	0.2	0.0	0.2	0.9	0.0	52.3	0.2
	276	6.9	7.0	-0.1	0.1	6.9	25.4	0.3	0.3	0.0	0.3	1.1	0.0	55.3	1.3
	280	7.2	7.1	0.1	0.0	7.2	26.3	0.2	0.2	0.0	0.2	0.8	0.0	57.9	0.5
	290	6.4	6.2	0.2	0.1	6.3	23.2	0.2	0.2	0.0	0.2	0.9	0.0	50.6	0.9
	300	7.2	7.2	0.0	0.0	7.2	26.5	0.2	0.2	0.0	0.2	0.7	0.0	58.5	3.7
	310	6.8	6.8	0.0	0.0	6.8	24.8	0.2	0.2	0.0	0.2	0.8	0.0	54.6	0.6
	314	7.1	7.2	-0.1	0.0	7.2	26.2	0.2	0.2	0.0	0.2	0.7	0.0	58.0	0.3
	320	5.6	5.6	0.0	0.0	5.6	20.4	0.3	0.3	0.0	0.3	1.0	0.0	44.2	1.5
	330	5.9	6.0	-0.2	0.1	6.0	21.9	0.3	0.3	0.0	0.3	1.0	0.0	47.3	0.7
	340	6.8	6.7	0.1	0.1	6.7	24.6	0.2	0.2	0.0	0.2	0.7	0.0	54.3	1.0
	350	7.6	7.7	-0.1	0.0	7.7	28.1	0.2	0.2	0.0	0.2	0.9	0.0	61.8	0.1
	360	6.3	6.2	0.1	0.0	6.3	22.9	0.6	0.6	0.0	0.6	2.1	0.0	47.3	1.4
	370	4.9	4.8	0.0	0.0	4.8	17.7	0.2	0.3	0.0	0.2	0.9	0.0	38.2	3.4
	377	5.3	5.4	0.0	0.0	5.4	19.6	0.2	0.2	0.0	0.2	0.8	0.0	42.7	0.1
	380	4.7	4.8	-0.1	0.1	4.8	17.4	0.2	0.2	0.0	0.2	0.8	0.0	37.8	1.5
	390	6.0	6.1	0.0	0.0	6.0	22.1	*2.0*	*2.0*	0.1	2.0	7.3	0.0	33.7	0.6
	410	5.7	5.6	0.0	0.0	5.6	20.7	0.2	0.2	0.0	0.2	0.7	0.0	45.5	4.5
	420	5.9	6.0	-0.1	0.1	6.0	21.8	0.2	0.1	0.0	0.1	0.5	0.0	48.4	1.4
	430	5.6	5.7	-0.1	0.0	5.7	20.7	0.2	0.2	0.0	0.2	0.6	0.0	45.6	3.1
	440	6.8	6.7	0.1	0.1	6.8	24.9	0.2	0.2	0.0	0.2	0.7	0.0	54.9	0.9
S1	1	8.8	8.7	0.1	0.1	8.8	32.1	0.3	0.3	0.0	0.3	0.9	0.0	70.9	0.9
	10	9.0	8.9	0.1	0.1	9.0	32.9	0.3	0.3	0.0	0.3	0.9	0.0	72.6	0.1
	20	8.8	8.9	-0.1	0.0	8.8	32.4	0.3	0.3	0.0	0.3	1.1	0.0	71.1	0.4
	25	7.7	7.9	-0.2	0.1	7.8	28.6	0.3	0.3	0.0	0.3	1.2	0.0	62.3	0.1
	30	5.1	5.2	-0.1	0.0	5.1	18.8	0.5	0.4	0.0	0.5	1.7	0.0	39.0	1.5
	40	5.0	5.3	-0.3	0.1	5.2	19.0	1.0	1.0	0.0	1.0	3.6	0.0	35.0	0.9
	50	5.3	5.5	-0.2	0.1	5.4	19.8	0.8	0.8	0.0	0.8	2.9	0.0	38.4	0.1
	120	5.7	5.9	-0.1	0.1	5.8	21.2	0.2	0.1	0.0	0.2	0.6	0.0	46.8	3.9
	130	5.2	5.6	-0.4	0.2	5.4	19.8	0.1	0.1	0.0	0.1	0.5	0.0	43.9	1.2
	140	5.1	5.1	0.0	0.0	5.1	18.7	0.1	0.1	0.0	0.1	0.3	0.0	41.7	0.1
	150	4.9	4.8	0.1	0.0	4.9	17.9	0.2	0.1	0.0	0.1	0.5	0.0	39.5	3.6
	160	4.3	4.8	-0.6	0.3	4.6	16.7	0.1	0.2	0.0	0.1	0.5	0.0	36.8	1.2
	170	5.3	5.2	0.1	0.1	5.2	19.2	0.2	0.2	0.0	0.2	0.7	0.0	42.1	1.7
	180	5.1	5.1	0.0	0.0	5.1	18.6	0.2	0.2	0.0	0.2	0.6	0.0	40.8	1.8
	190	5.5	5.5	0.0	0.0	5.5	20.1	0.2	0.2	0.0	0.2	0.6	0.0	44.2	1.2
	200	6.0	6.1	-0.1	0.0	6.0	22.1	0.5	0.4	0.0	0.5	1.7	0.0	46.3	1.5
	210	5.1	5.1	0.0	0.0	5.1	18.8	0.2	0.2	0.0	0.2	0.8	0.0	40.9	2.4
	220	7.0	6.9	0.1	0.0	6.9	25.4	0.2	0.2	0.0	0.2	0.7	0.0	56.0	2.8
	230	4.0	4.0	-0.1	0.0	4.0	14.7	0.2	0.2	0.0	0.2	0.6	0.0	31.9	1.9
	240	5.7	5.6	0.1	0.0	5.7	20.7	0.3	0.3	0.0	0.3	1.3	0.0	44.2	0.1
	250	5.2	5.3	0.0	0.0	5.3	19.3	0.3	0.3	0.0	0.3	0.9	0.0	41.7	1.0
	260	6.6	6.7	-0.1	0.0	6.6	24.2	0.2	0.1	0.0	0.1	0.5	0.0	53.9	6.9
	270	6.5	6.4	0.1	0.0	6.5	23.7	0.1	0.1	0.0	0.1	0.4	0.0	52.7	1.3
	280	7.9	7.5	0.5	0.2	7.7	28.2	0.1	0.1	0.0	0.1	0.5	0.0	63.0	2.3
	290	8.4	8.5	-0.1	0.0	8.4	30.9	0.1	0.1	0.0	0.1	0.4	0.0	69.3	4.0
	300	7.2	7.1	0.1	0.0	7.1	26.1	0.2	0.2	0.0	0.2	0.6	0.0	57.8	1.4

TC = total carbon
TOC = total organic carbon

Appendix 3: TOC- and carbonate-content (LECO)

Core	Depth (cm)	TC I	TC II	Δ TC	stdev	TC (average)	CO2-total	TOC I	TOC II	Δ TOC	TOC (average)	CO2-org	stdev	CaCO3	error
		(all values in percent)													
	310	7.4	7.6	-0.1	0.1	7.5	27.6	0.2	0.2	0.0	0.2	0.6	0.0	61.2	2.3
	320	6.1	6.1	0.1	0.0	6.1	22.3	0.1	0.1	0.0	0.1	0.4	0.0	49.7	5.6
	340	7.6	7.7	-0.1	0.0	7.7	28.1	0.2	0.2	0.0	0.2	0.7	0.0	62.2	0.5
	350	9.0	8.9	0.1	0.1	8.9	32.8	0.2	0.2	0.0	0.2	0.8	0.0	72.6	0.4
	360	6.5	6.5	0.0	0.0	6.5	23.9	0.2	0.2	0.0	0.2	0.9	0.0	52.2	1.8
	370	6.0	6.0	0.0	0.0	6.0	22.0	0.2	0.1	0.0	0.2	0.6	0.0	48.7	5.6
	380	7.1	7.2	-0.1	0.0	7.1	26.1	0.1	0.1	-0.1	0.1	0.4	0.0	58.2	12.6
	390	8.1	8.0	0.1	0.0	8.1	29.6	0.2	0.2	0.0	0.2	0.7	0.0	65.6	2.8
	400	8.2	8.5	-0.3	0.1	8.4	30.6	0.2	0.2	0.0	0.2	0.7	0.0	67.9	0.1
	410	8.0	8.1	-0.1	0.1	8.1	29.5	0.2	0.2	0.0	0.2	0.6	0.0	65.7	0.5
	420	6.8	6.8	0.0	0.0	6.8	24.9	0.2	0.2	0.0	0.2	0.7	0.0	55.0	1.7
	430	5.3	5.3	0.0	0.0	5.3	19.6	0.2	0.2	0.0	0.2	0.7	0.0	42.9	0.7
	440	7.2	7.1	0.1	0.1	7.1	26.1	0.2	0.2	0.0	0.2	0.8	0.0	57.6	0.3
	450	8.2	8.2	0.0	0.0	8.2	30.2	0.2	0.2	0.0	0.2	0.9	0.0	66.6	0.2
	460	5.7	5.6	0.1	0.0	5.6	20.6	0.2	0.2	0.0	0.2	0.6	0.0	45.4	0.9
	470	8.1	8.0	0.1	0.0	8.1	29.5	0.1	0.2	0.0	0.2	0.6	0.0	65.8	9.7
	480	5.9	6.0	-0.1	0.0	6.0	21.9	0.1	0.1	0.0	0.1	0.5	0.0	48.7	1.8
	490	8.8	8.8	-0.1	0.0	8.8	32.3	0.1	0.1	0.0	0.1	0.4	0.0	72.5	0.1
	500	8.3	8.3	0.0	0.0	8.3	30.5	0.1	0.1	0.0	0.1	0.4	0.0	68.3	3.3
AL	10	9.7	9.9	-0.2	0.1	9.8	36.0	0.2	0.2	0.0	0.2	0.9	0.0	79.8	1.8
	20	9.7	9.6	0.1	0.0	9.6	35.3	0.2	0.2	0.0	0.2	0.8	0.0	78.4	0.1
	30	9.8	9.8	0.0	0.0	9.8	36.0	0.2	0.2	0.0	0.2	0.8	0.0	79.8	5.8
	40	9.8	10.0	-0.2	0.1	9.9	36.4	0.2	0.2	0.0	0.2	0.8	0.0	80.7	0.2
	50	10.9	10.6	0.3	0.2	10.8	39.4	0.2	0.2	0.0	0.2	0.6	0.0	88.2	5.2
	60	10.7	10.9	-0.2	0.1	10.8	39.6	0.2	0.2	0.0	0.2	0.8	0.0	88.2	0.6
	70	10.4	10.3	0.1	0.0	10.4	38.0	0.2	0.2	0.0	0.2	0.9	0.0	84.3	0.4
	80	7.8	7.7	0.1	0.0	7.7	28.4	0.3	0.3	0.0	0.3	1.1	0.0	62.0	1.9
	90	8.8	9.1	-0.2	0.1	8.9	32.8	0.9	0.9	0.0	0.9	3.3	0.0	66.9	0.1
	97	8.1	8.1	0.0	0.0	8.1	29.6	0.8	0.9	0.0	0.9	3.1	0.0	60.2	1.1
	170	8.6	8.7	-0.1	0.1	8.7	31.7	0.2	0.2	0.0	0.2	0.8	0.0	70.4	4.1
	180	9.4	9.5	-0.1	0.1	9.4	34.6	0.2	0.2	0.0	0.2	0.7	0.0	76.9	0.1
	190	8.3	8.6	-0.3	0.1	8.4	30.9	0.2	0.2	0.0	0.2	0.7	0.0	68.6	0.2
	200	8.1	8.0	0.1	0.1	8.0	29.4	0.2	0.2	0.0	0.2	0.9	0.0	64.7	0.8
	210	8.2	8.1	0.1	0.0	8.2	30.0	0.3	0.3	0.0	0.3	1.1	0.0	65.6	1.7
	220	8.5	8.7	-0.1	0.1	8.6	31.5	0.3	0.3	0.0	0.3	1.0	0.0	69.3	3.9
	230	8.6	8.6	0.0	0.0	8.6	31.4	0.3	0.3	0.0	0.3	0.9	0.0	69.3	0.7
	240	8.5	8.2	0.2	0.1	8.3	30.6	0.2	0.3	0.0	0.3	0.9	0.0	67.3	5.1
	250	9.1	9.1	0.0	0.0	9.1	33.3	0.3	0.3	0.0	0.3	1.0	0.0	73.3	2.4
	260	9.0	8.9	0.1	0.1	9.0	32.9	0.3	0.3	0.0	0.3	1.0	0.0	72.5	0.1
	270	8.6	8.6	-0.1	0.0	8.6	31.5	0.3	0.3	0.0	0.3	1.0	0.0	69.4	3.9
	280	8.5	8.4	0.1	0.0	8.5	31.0	0.3	0.3	0.0	0.3	1.1	0.0	68.1	4.3
	290	8.9	8.9	0.0	0.0	8.9	32.6	0.3	0.3	0.1	0.3	1.1	0.0	71.6	6.6
	300	8.8	8.9	-0.1	0.0	8.8	32.4	0.6	0.5	-0.1	0.5	2.0	0.0	69.1	5.3
	310	8.2	8.1	0.2	0.1	8.2	29.9	0.4	0.3	0.0	0.3	1.3	0.0	65.1	2.8
	320	8.1	7.9	0.2	0.1	8.0	29.4	0.3	0.3	0.0	0.3	1.1	0.0	64.3	0.3
	330	7.7	7.5	0.1	0.1	7.6	27.8	0.4	0.4	0.0	0.4	1.4	0.0	60.1	1.0
	340	8.6	8.4	0.2	0.1	8.5	31.1	0.2	0.2	0.0	0.2	0.7	0.0	69.1	0.8
	350	8.4	8.5	-0.1	0.0	8.4	30.9	0.2	0.2	0.1	0.2	0.7	0.0	68.6	9.3
	360	8.7	8.7	0.0	0.0	8.7	31.8	0.2	0.2	0.0	0.2	0.8	0.0	70.5	0.7
	370	9.2	9.1	0.1	0.1	9.1	33.5	0.2	0.2	0.0	0.2	0.6	0.0	74.8	2.0
	380	9.3		9.3	0.0	9.3	34.2	0.2	0.2	0.0	0.2	0.7	0.0	76.1	3.1
	390	9.4	8.7	0.7	0.3	9.0	33.1	0.2	0.2	0.0	0.2	0.8	0.0	73.4	2.5

TC = total carbon
TOC = total organic carbon

Appendix 3: TOC- and carbonate-content (LECO)

Core	Depth (cm)	TC I	TC II	Δ TC	stdev	TC (average)	CO2-total	TOC I	TOC II	Δ TOC	TOC (average)	CO2-org	stdev	CaCO3	error
		(all values in percent)													
	400	8.9	8.9	0.0	0.0	8.9	32.5	0.3	0.3	0.0	0.3	1.0	0.0	71.6	3.4
	410	8.2	8.1	0.2	0.1	8.1	29.8	0.3	0.2	0.0	0.2	0.9	0.0	65.8	0.9
	420	8.4	8.4	0.0	0.0	8.4	30.7	0.3	0.3	0.0	0.3	1.2	0.0	66.9	2.4
	430	10.0	10.0	0.0	0.0	10.0	36.6	0.3	0.3	0.0	0.3	1.0	0.0	81.0	3.0
	440	10.9	10.7	0.2	0.1	10.8	39.6	0.3	0.4	0.1	0.4	1.3	0.1	86.9	12.5
	450	10.8	10.6	0.2	0.1	10.7	39.2	0.4	0.4	0.0	0.4	1.4	0.0	86.0	0.3
	460	8.5	8.5	0.0	0.0	8.5	31.0	0.2	0.2	-0.1	0.2	0.8	0.0	68.7	8.6
	480	9.0	9.1	-0.1	0.0	9.1	33.3	0.1	0.1	0.0	0.1	0.5	0.0	74.4	3.4
	490	9.8	10.4	-0.6	0.3	10.1	37.0	0.3	0.3	0.0	0.3	1.0	0.0	81.8	0.6
	500	10.3	10.1	0.2	0.1	10.2	37.4	0.2	0.2	0.0	0.2	0.6	0.0	83.5	0.3
	510	10.0	10.2	-0.2	0.1	10.1	37.0	0.2	0.2	0.0	0.2	0.8	0.0	82.3	4.9
	530	9.8	9.9	-0.1	0.1	9.9	36.2	0.2	0.2	0.0	0.2	0.7	0.0	80.6	3.3
S6	1	6.7	6.7	0.0	0.0	6.7	24.5	0.3	0.3	0.0	0.3	1.2	0.0	52.8	0.3
	10	8.5	8.5	0.0	0.0	8.5	31.2	0.2	0.2	0.0	0.2	0.9	0.0	68.9	0.1
	20	7.7	7.5	0.2	0.1	7.6	27.8	0.2	0.2	0.0	0.2	0.9	0.0	61.1	0.5
	30	7.5	7.5	0.0	0.0	7.5	27.4	0.2	0.2	0.0	0.2	0.7	0.0	60.7	0.9
	40	7.6	7.8	-0.2	0.1	7.7	28.3	0.3	0.3	0.0	0.3	1.0	0.0	62.2	1.0
	50	7.9	7.9	0.0	0.0	7.9	28.9	0.3	0.3	0.0	0.3	1.0	0.0	63.5	0.9
	60	9.1	9.1	-0.1	0.0	9.1	33.4	0.3	0.3	0.0	0.3	1.0	0.0	73.6	0.7
	70	10.1	10.1	0.0	0.0	10.1	37.0	0.2	0.2	0.0	0.2	0.7	0.0	82.6	2.5
	80	9.7	9.8	-0.1	0.1	9.7	35.7	0.2	0.3	0.0	0.3	1.0	0.0	78.8	6.6
	86	10.6	10.6	0.0	0.0	10.6	38.9	0.2	0.2	0.0	0.2	0.9	0.0	86.3	1.8
	90	9.2	8.9	0.3	0.1	9.0	33.2	0.3	0.3	0.0	0.3	1.2	0.0	72.7	0.9
	100	5.9	6.0	-0.1	0.1	6.0	21.8	0.9	0.9	0.0	0.9	3.2	0.0	42.3	0.2
	110	4.5	4.5	0.0	0.0	4.5	16.5	0.2	0.1	0.0	0.2	0.6	0.0	36.2	3.6
	120	6.5	6.3	0.2	0.1	6.4	23.4	1.7	1.4	-0.3	1.6	5.8	0.2	40.0	3.8
	130	5.2	5.3	-0.1	0.1	5.3	19.3	0.8	0.7	0.0	0.7	2.7	0.0	37.6	0.0
	200	4.8	5.0	-0.2	0.1	4.9	17.9	0.1	0.1	0.0	0.1	0.5	0.0	39.5	0.5
	250	5.4	5.6	-0.1	0.1	5.5	20.1	0.1	0.1	0.0	0.1	0.4	0.0	44.9	8.8
	270	4.7	4.6	0.0	0.0	4.6	17.0	0.2	0.2	0.0	0.2	0.7	0.0	37.1	0.1
	280	6.0	6.1	-0.1	0.1	6.1	22.2	0.2	0.2	0.0	0.2	0.7	0.0	48.9	1.1
	290	5.7	5.7	-0.1	0.0	5.7	20.9	0.2	0.2	0.0	0.2	0.7	0.0	45.9	1.8
	295	5.2	5.3	-0.2	0.1	5.2	19.2	1.0	1.0	0.0	1.0	3.6	0.0	35.6	0.5
	300	6.7	6.8	-0.1	0.1	6.8	24.8	0.1	0.1	0.0	0.1	0.5	0.0	55.3	3.0
	310	5.4	5.5	-0.1	0.0	5.4	19.8	0.1	0.1	0.0	0.1	0.5	0.0	43.9	1.5
	320	5.4	5.5	-0.1	0.0	5.4	19.8	0.2	0.2	0.0	0.2	0.6	0.0	43.6	2.0
	330	6.3	6.2	0.1	0.0	6.3	23.0	0.1	0.1	0.0	0.1	0.4	0.0	51.3	9.8
	340	6.9	6.9	-0.1	0.0	6.9	25.3	0.2	0.2	0.0	0.2	0.6	0.0	56.0	1.2
	350	5.9	6.1	-0.2	0.1	6.0	21.9	0.9	0.9	0.0	0.9	3.3	0.0	42.1	0.1
	360	5.5	5.8	-0.3	0.1	5.7	20.7	1.4	1.4	0.0	1.4	5.1	0.0	35.4	0.3
	370	5.7	5.8	-0.1	0.0	5.7	21.0	0.2	0.2	0.0	0.2	0.8	0.0	45.9	4.6
	380	7.5	7.7	-0.2	0.1	7.6	27.8	0.2	0.2	0.0	0.2	0.7	0.0	61.6	0.7
	390	7.5	7.1	0.4	0.2	7.3	26.8	0.3	0.3	0.0	0.3	1.3	0.0	58.1	1.4
	400	4.9	5.0	-0.1	0.0	5.0	18.2	0.2	0.2	0.0	0.2	0.6	0.0	40.1	0.1
	410	5.6	5.7	-0.1	0.0	5.7	20.8	0.2	0.3	0.0	0.3	0.9	0.0	45.0	1.6
	420	6.8	6.9	-0.1	0.1	6.9	25.2	0.3	0.3	0.0	0.3	1.0	0.0	54.9	3.1
	430	5.7	6.0	-0.3	0.1	5.8	21.4	0.5	0.5	0.0	0.5	1.7	0.0	44.8	0.6
	440	5.4	5.4	0.0	0.0	5.4	19.8	0.2	0.2	0.0	0.2	0.9	0.0	43.0	1.3
	450	6.1	6.2	-0.1	0.1	6.1	22.5	0.2	0.2	0.0	0.2	0.6	0.0	49.6	2.1
	460	6.3	6.3	-0.1	0.0	6.3	23.0	0.2	0.1	0.0	0.2	0.6	0.0	51.0	3.8
	470	7.1	6.9	0.2	0.1	7.0	25.7	0.1	0.1	0.0	0.1	0.4	0.0	57.4	5.5

TC = total carbon
TOC = total organic carbon

Appendix 4-A: Mineralogy of periplatform sediments (XRD)

	peak areas			ratio	percentages					peak height	
Depth (cm)	**Aragonite**	**LMC**	**HMC**	**Ar/Ar+Cc**	**Aragonite**	**Calcite**	**LMC**	**HMC**	**Aragonite + HMC**	**Quartz**	**Dolomite**
AL-bulk											
5	4126	10546	16830	0.131	62.4	37.6	14.5	23.1	85.5	191	27
15	4322	8084	16302	0.151	65.2	34.8	11.5	23.3	88.5	172	23
25	4140	9134	16528	0.139	63.6	36.4	13.0	23.4	87.0	152	12
35	4442	10522	16216	0.142	64.1	35.9	14.1	21.8	85.9	173	25
45	3986	8864	16966	0.134	62.8	37.2	12.7	24.4	87.3	127	14
55	4816	11216	16200	0.149	65.0	35.0	14.3	20.7	85.7	78	20
65	4828	9176	14978	0.167	67.2	32.8	12.5	20.4	87.5	93	16
75	4222	8308	12142	0.171	67.7	32.3	13.1	19.2	86.9	200	37
85	3894	7696	11076	0.172	67.8	32.2	13.2	19.0	86.8	381	54
95	4344	6556	11748	0.192	69.9	30.1	10.8	19.3	89.2	374	34
155	2266	5206	25672	0.068	49.7	50.3	8.5	41.8	91.5	277	84
165	3070	6988	19350	0.104	58.0	42.0	11.1	30.9	88.9	420	66
175	3334	6278	16978	0.125	61.6	38.4	10.4	28.0	89.6	350	70
185	3036	8990	19352	0.097	56.5	43.5	13.8	29.7	86.2	303	49
195	3514	7846	10770	0.159	66.2	33.8	14.2	19.5	85.8	409	43
205	2812	8790	13166	0.114	59.6	40.4	16.2	24.2	83.8	442	62
215	2940	9100	14528	0.111	59.1	40.9	15.7	25.1	84.3	304	44
225	3154	8662	16096	0.113	59.5	40.5	14.2	26.3	85.8	284	61
235	3004	9640	13150	0.116	60.1	39.9	16.9	23.0	83.1	300	60
245	4184	8234	13060	0.164	66.9	33.1	12.8	20.3	87.2	296	84
255	3804	8638	11374	0.160	66.3	33.7	14.5	19.1	85.5	270	50
265	3980	9842	12730	0.150	65.1	34.9	15.2	19.7	84.8	305	52
275	3332	10370	12516	0.127	61.9	38.1	17.3	20.9	82.7	466	39
285	4276	9766	13752	0.154	65.6	34.4	14.3	20.1	85.7	290	36
295	3868	10108	11890	0.150	65.1	34.9	16.1	18.9	83.9	316	38
305	4162	8534	12000	0.169	67.4	32.6	13.5	19.1	86.5	299	41
315	4014	9806	12182	0.154	65.7	34.3	15.3	19.0	84.7	343	27
325	3866	11622	10686	0.148	64.8	35.2	18.3	16.9	81.7	430	37
335	2728	9008	17764	0.092	55.6	44.4	14.9	29.5	85.1	388	46
345	1968	7020	21470	0.065	48.6	51.4	12.7	38.8	87.3	275	28
355	2486	9512	16694	0.087	54.3	45.7	16.6	29.1	83.4	312	51
365	2520	8958	19570	0.081	53.0	47.0	14.7	32.2	85.3	251	38
375	3064	11364	17262	0.097	56.5	43.5	17.3	26.2	82.7	434	35
385	2954	10508	13824	0.108	58.7	41.3	17.8	23.5	82.2	323	63
395	2970	12898	14012	0.099	57.0	43.0	20.6	22.4	79.4	225	19
405	2404	10586	15272	0.085	54.0	46.0	18.8	27.2	81.2	348	21
415	2840	11106	14274	0.101	57.3	42.7	18.7	24.0	81.3	396	14
425	3552	11774	12466	0.128	62.0	38.0	18.5	19.6	81.5	258	9
435	4380	10740	11942	0.162	66.6	33.4	15.8	17.6	84.2	154	44
445	4298	8878	12580	0.167	67.2	32.8	13.6	19.2	86.4	202	9
455	3342	10516	12932	0.125	61.5	38.5	17.3	21.2	82.7	130	24
465	2356	9526	17862	0.079	52.6	47.4	16.5	30.9	83.5	253	19
475	2092	9494	14528	0.080	52.8	47.2	18.7	28.6	81.3	188	26
485	2554	10904	14990	0.090	55.0	45.0	18.9	26.0	81.1	207	14
495	2692	13290	14134	0.089	54.9	45.1	21.8	23.2	78.2	130	17
505	2934	12566	14472	0.098	56.7	43.3	20.1	23.2	79.9	179	29
515	3038	11264	15908	0.101	57.3	42.7	17.7	25.0	82.3	161	
525	2700	8206	11750	0.119	60.6	39.4	16.2	23.2	83.8	291	15
AW-bulk											
60	3250	6710	19712	0.110	58.9	41.1	10.4	30.6	89.6	634	49
70	1904	7730	20488	0.063	48.1	51.9	14.2	37.7	85.8	268	64
80	2882	10824	12102	0.112	59.3	40.7	19.2	21.5	80.8	507	82
90	3366	10700	13192	0.123	61.3	38.7	17.3	21.4	82.7	533	72

Appendix 4-A: Mineralogy of periplatform sediments (XRD)

Depth (cm)	Aragonite	LMC	HMC	Ar/Ar+Cc	Aragonite	Calcite	LMC	HMC	Aragonite + HMC	Quartz	Dolomite
100	2900	10500	12994	0.110	59.0	41.0	18.3	22.7	81.7	425	70
110	2808	10002	11544	0.115	59.9	40.1	18.6	21.5	81.4	394	54
120	3514	12030	10922	0.133	62.7	37.3	19.5	17.7	80.5	472	37
130	2802	9844	12574	0.111	59.2	40.8	17.9	22.9	82.1	353	28
140	2972	10900	8694	0.132	62.6	37.4	20.8	16.6	79.2	403	35
150	2734	12104	8540	0.117	60.2	39.8	23.3	16.5	76.7	509	38
160	1770	11152	10486	0.076	51.7	48.3	24.9	23.4	75.1	565	36
170	1316	7604	21436	0.043	40.7	59.3	15.5	43.7	84.5	659	34
180	1658	11098	17116	0.056	45.6	54.4	21.4	33.0	78.6	361	59
190	1668	10022	19576	0.053	44.8	55.2	18.7	36.5	81.3	299	44
200	2418	12110	16640	0.078	52.2	47.8	20.2	27.7	79.8	302	33
210	2364	11286	15066	0.082	53.3	46.7	20.0	26.7	80.0	292	63
220	2084	11108	13186	0.079	52.5	47.5	21.7	25.8	78.3	365	15
230	2750	12828	12682	0.097	56.6	43.4	21.8	21.6	78.2	296	20
240	3722	13406	13350	0.122	61.1	38.9	19.5	19.4	80.5	261	31
250	2812	12466	15410	0.092	55.4	44.6	19.9	24.6	80.1	358	
260	1710	12280	18386	0.053	44.6	55.4	22.2	33.2	77.8	408	33
270	2790	13806	15834	0.086	54.2	45.8	21.3	24.5	78.7	246	14
280	3204	12718	14642	0.105	58.1	41.9	19.5	22.4	80.5	309	18
290	2308	13024	13260	0.081	52.9	47.1	23.3	23.7	76.7	281	9
300	2786	13076	13912	0.094	55.8	44.2	21.4	22.8	78.6	236	8
310	1772	13366	13804	0.061	47.5	52.5	25.8	26.7	74.2	280	20
320	2154	11462	17342	0.070	50.0	50.0	19.9	30.1	80.1	253	15
330	2264	14606	19440	0.062	47.9	52.1	22.4	29.8	77.6	179	11
340	2448	12696	17350	0.075	51.6	48.4	20.5	28.0	79.5	231	13
350	3036	12764	15108	0.098	56.8	43.2	19.8	23.4	80.2	156	14
360	2420	12640	13594	0.084	53.8	46.2	22.2	23.9	77.8	210	19
370	3088	14476	11064	0.108	58.6	41.4	23.4	17.9	76.6	183	
380	3490	18238	9134	0.113	59.6	40.4	26.9	13.5	73.1	187	
390	3980	14014	12992	0.128	62.1	37.9	19.7	18.3	80.3	248	15
400	2224	12462	15370	0.074	51.2	48.8	21.8	26.9	78.2	368	70
410	2298	11420	13420	0.085	53.9	46.1	21.2	24.9	78.8	403	56
420	2728	10852	12684	0.104	57.9	42.1	19.4	22.7	80.6	371	84
430	2314	12100	14218	0.081	53.0	47.0	21.6	25.4	78.4	371	71
440	2310	13384	13114	0.080	52.8	47.2	23.8	23.4	76.2	419	82
450	1748	12302	14288	0.062	47.7	52.3	24.2	28.1	75.8	920	46
460	1840	11624	10946	0.075	51.6	48.4	24.9	23.5	75.1	1429	44
470	1782	11682	14024	0.065	48.6	51.4	23.3	28.0	76.7	573	72
480	1298	11442	16224	0.045	41.4	58.6	24.2	34.4	75.8	351	69
490	1942	17186	9444	0.068	49.6	50.4	32.5	17.9	67.5	418	55
500	1562	18850	6480	0.058	46.5	53.5	39.8	13.7	60.2	381	64
510	1496	16348	11616	0.051	43.8	56.2	32.8	23.3	67.2	443	40
520	2256	16970	5866	0.090	55.1	44.9	33.4	11.5	66.6	922	39
530	2114	16708	5910	0.085	54.1	45.9	33.9	12.0	66.1	454	28
540	2102	15470	6270	0.088	54.7	45.3	32.3	13.1	67.7	418	39
550	1518	14372	6934	0.067	49.1	50.9	34.3	16.6	65.7	524	38
S1-bulk											
1	4196	16696	16308	0.113	59.5	40.5	20.5	20.0	79.5	164	19
10	4330	19762	17290	0.105	58.0	42.0	22.4	19.6	77.6	220	14
20	3550	18342	13556	0.100	57.2	42.8	24.6	18.2	75.4	258	24
25	3256	18812	13914	0.090	55.2	44.8	25.8	19.1	74.2	436	33
30	2194	12466	8546	0.095	56.0	44.0	26.1	17.9	73.9	797	34
40	3880	12598	5620	0.176	68.2	31.8	22.0	9.8	78.0	1138	38
50	4182	9128	6424	0.212	71.9	28.1	16.5	11.6	83.5	607	76
120	1980	10764	35284	0.041	39.7	60.3	14.1	46.2	85.9	659	54

Appendix 4-A: Mineralogy of periplatform sediments (XRD)

Depth (cm)	Aragonite	LMC	HMC	Ar/Ar+Cc	Aragonite	Calcite	LMC	HMC	Aragonite + HMC	Quartz	Dolomite
130	1966	11632	12300	0.076	51.7	48.3	23.5	24.8	76.5	893	75
140	1614	12210	15716	0.055	45.3	54.7	23.9	30.8	76.1	717	54
150	1110	10348	19986	0.035	36.7	63.3	21.6	41.7	78.4	841	50
160	1628	9238	13284	0.067	49.4	50.6	20.8	29.8	79.2	1008	54
170	1402	21996	16922	0.035	36.4	63.6	35.9	27.7	64.1	587	36
180	1580	12926	14248	0.055	45.4	54.6	26.0	28.6	74.0	830	72
190	2006	10536	14592	0.074	51.2	48.8	20.5	28.3	79.5	614	66
200	3396	11894	15750	0.109	58.9	41.1	17.7	23.4	82.3	972	44
210	1594	13482	11682	0.060	47.0	53.0	28.4	24.6	71.6	604	58
220	2354	16612	16898	0.066	48.9	51.1	25.3	25.8	74.7	516	51
230	1836	10090	8468	0.090	55.1	44.9	24.4	20.5	75.6	804	36
240	2078	15388	10324	0.075	51.4	48.6	29.1	19.5	70.9	694	68
250	920	11122	14742	0.034	36.2	63.8	27.5	36.4	72.5	961	72
260	920	7394	30296	0.024	29.0	71.0	13.9	57.1	86.1	609	58
270	860	18460	27126	0.019	24.0	76.0	30.8	45.2	69.2	536	39
280	1162	10790	30642	0.027	31.6	68.4	17.8	50.6	82.2	408	29
290	2264	12468	31292	0.049	43.2	56.8	16.2	40.6	83.8	301	21
300	1506	16928	19698	0.039	38.9	61.1	28.2	32.9	71.8	382	46
310	884	11468	24222	0.024	29.3	70.7	22.7	48.0	77.3	333	24
320	1382	16268	17354	0.039	38.9	61.1	29.6	31.5	70.4	641	29
330	1170	13422	14494	0.040	39.3	60.7	29.2	31.5	70.8	540	31
340	2184	18436	15442	0.061	47.3	52.7	28.7	24.0	71.3	316	4
350	3486	19954	16492	0.087	54.5	45.5	24.9	20.6	75.1	168	11
360	1526	12458	20120	0.045	41.4	58.6	22.4	36.2	77.6	592	14
370	1124	12546	21354	0.032	34.8	65.2	24.1	41.1	75.9	764	27
380	1466	19588	19034	0.037	37.4	62.6	31.8	30.9	68.2	586	44
390	1258	18886	20530	0.031	34.1	65.9	31.6	34.3	68.4	316	12
400	1292	15486	22594	0.033	35.3	64.7	26.3	38.4	73.7	296	7
410	3110	13746	20816	0.083	53.4	46.6	18.5	28.1	81.5	350	21
420	1134	14190	20354	0.032	34.6	65.4	26.9	38.5	73.1	460	24
430	2068	15042	14408	0.066	48.9	51.1	26.1	25.0	73.9	615	23
440	2052	17980	20612	0.050	43.7	56.3	26.2	30.1	73.8	345	13
450	2254	17130	17430	0.061	47.5	52.5	26.0	26.5	74.0	217	13
460	1652	13170	15078	0.055	45.5	54.5	25.4	29.1	74.6	618	12
470	1888	20738	16252	0.049	43.0	57.0	32.0	25.1	68.0	341	19
480	1396	13448	18474	0.042	40.1	59.9	25.3	34.7	74.7	651	15
500	1244	12950	24690	0.032	34.8	65.2	22.4	42.8	77.6	190	16
S1 < 63µm											
10	4945	17770	22244	0.110	59.0	41.0	18.2	22.8	81.8	368	0
20	5141	24956	19022	0.105	58.0	42.0	23.8	18.1	76.2	841	0
30	2615	17572	7826	0.093	55.8	44.2	30.6	13.6	69.4	1410	70
40	2798	15338	5718	0.117	60.3	39.7	28.9	10.8	71.1	997	81
50	6050	11928	6432	0.248	75.0	25.0	16.3	8.8	83.7	948	117
60	3490	11914	14940	0.115	59.9	40.1	17.8	22.3	82.2	1599	117
70	4910	11198	11626	0.177	68.4	31.6	15.5	16.1	84.5	1493	85
80	3151	16024	25760	0.070	50.2	49.8	19.1	30.7	80.9	760	134
90	3360	9982	25310	0.087	54.4	45.6	12.9	32.7	87.1	913	69
100	2859	15734	38764	0.050	43.5	56.5	16.3	40.2	83.7	1226	77
110	2139	11818	48144	0.034	36.2	63.8	12.6	51.2	87.4	559	56
120	2408	12712	15946	0.078	52.1	47.9	21.2	26.6	78.8	1371	0
130	2011	14316	13364	0.068	49.5	50.5	26.1	24.4	73.9	1490	141
140	2382	11708	14002	0.085	53.9	46.1	21.0	25.1	79.0	1444	83
150	1654	13432	20724	0.046	42.0	58.0	22.8	35.2	77.2	1504	0
160	1806	14864	12816	0.061	47.5	52.5	28.2	24.3	71.8	1391	0
170	1471	14084	20614	0.041	39.5	60.5	24.6	36.0	75.4	1375	0

Appendix 4-A: Mineralogy of periplatform sediments (XRD)

Depth (cm)	Aragonite	LMC	HMC	Ar/Ar+Cc	Aragonite	Calcite	LMC	HMC	Aragonite + HMC	Quartz	Dolomite
180	2028	14046	16526	0.062	47.8	52.2	24.0	28.2	76.0	1267	0
190	2265	13528	16622	0.070	50.1	49.9	22.4	27.5	77.6	1335	124
200	2001	19214	22816	0.045	41.7	58.3	26.7	31.7	73.3	1132	68
210	2492	16216	12050	0.081	53.0	47.0	27.0	20.0	73.0	1090	91
220	2796	15734	20776	0.071	50.5	49.5	21.4	28.2	78.6	856	37
230	2160	14892	9334	0.082	53.2	46.8	28.8	18.0	71.2	1433	126
240	2704	18152	13546	0.079	52.4	47.6	27.2	20.3	72.8	1437	77
250	1391	11816	20300	0.042	39.9	60.1	22.1	38.0	77.9	1783	0
260	0	10550	38916	0.000	0.0	100.0	21.3	78.7	78.7	1124	0
270	731	12002	31994	0.016	21.6	78.4	21.4	57.0	78.6	1044	0
280	887	15560	33802	0.018	23.1	76.9	24.2	52.7	75.8	907	0
290	2078	18722	32680	0.039	38.6	61.4	22.4	39.0	77.6	664	0
300	816	17048	21172	0.021	26.4	73.6	32.8	40.8	67.2	963	0
310	1550	17168	29604	0.032	34.8	65.2	23.9	41.3	76.1	954	0
320	1140	18758	22014	0.027	31.6	68.4	31.5	36.9	68.5	1272	0
330	2237	17490	14646	0.065	48.7	51.3	27.9	23.4	72.1	782	0
340	3045	30960	17878	0.059	46.7	53.3	33.8	19.5	66.2	820	0
350	3561	22790	20734	0.076	51.7	48.3	25.3	23.0	74.7	406	0
360	1710	17456	23756	0.040	39.1	60.9	25.8	35.1	74.2	1062	0
370	0	14334	19456	0.000	0.0	100.0	42.4	57.6	57.6	1986	0
380	1493	14282	23858	0.038	38.0	62.0	23.2	38.8	76.8	773	0
390	2112	21906	22264	0.046	41.7	58.3	28.9	29.4	71.1	625	0
400	1277	23102	26194	0.025	30.1	69.9	32.8	37.1	67.2	364	0
410	0	18810	24868	0.000	0.0	100.0	43.1	56.9	56.9	811	0
420	2248	17128	25756	0.050	43.5	56.5	22.6	34.0	77.4	844	0
430	1782	16010	13904	0.056	45.8	54.2	29.0	25.2	71.0	1265	521
440	2582	23142	23292	0.053	44.6	55.4	27.6	27.8	72.4	706	4
450	2381	24406	23204	0.048	42.6	57.4	29.4	28.0	70.6	471	53
460	1783	14928	23140	0.045	41.4	58.6	23.0	35.7	77.0	912	66
470	2123	26846	23638	0.040	39.3	60.7	32.3	28.4	67.7	522	14
480	2020	15494	22700	0.050	43.6	56.4	22.9	33.5	77.1	669	33
490	1649	27462	33332	0.026	31.0	69.0	31.2	37.8	68.8	367	11
500	1420	26820	27180	0.026	30.4	69.6	34.6	35.0	65.4	403	9
S2-bulk											
2	4666	13086	14048	0.147	64.7	35.3	17.0	18.3	83.0	603	15
10	3658	13498	15432	0.112	59.4	40.6	18.9	21.6	81.1	431	19
20	3494	13330	17844	0.101	57.3	42.7	18.3	24.4	81.7	359	12
30	3560	12376	17088	0.108	58.6	41.4	17.4	24.0	82.6	374	21
40	3774	13840	15330	0.115	59.8	40.2	19.1	21.1	80.9	319	21
50	3722	16192	15430	0.105	58.2	41.8	21.4	20.4	78.6	214	18
60	3928	16298	18276	0.102	57.5	42.5	20.0	22.4	80.0	148	16
70	4052	15922	16888	0.110	59.0	41.0	19.9	21.1	80.1	178	16
80	3662	13562	14060	0.117	60.2	39.8	19.5	20.2	80.5	251	14
90	4678	7278	5200	0.273	76.8	23.2	13.5	9.6	86.5	459	21
100	6332	4474	5466	0.389	83.8	16.2	7.3	8.9	92.7	1072	102
170	4714	6398	4524	0.301	78.8	21.2	12.4	8.8	87.6	667	38
210	2454	9660	19586	0.077	52.1	47.9	15.8	32.1	84.2	916	61
220	2238	8620	15074	0.086	54.3	45.7	16.6	29.1	83.4	696	49
230	1932	8452	16706	0.071	50.5	49.5	16.6	32.9	83.4	891	49
240	2498	8068	12642	0.108	58.6	41.4	16.1	25.3	83.9	1740	56
250	1716	8380	16770	0.064	48.3	51.7	17.2	34.4	82.8	676	39
260	1518	7918	14136	0.064	48.5	51.5	18.5	33.0	81.5	1365	49
270	2592	10130	10004	0.114	59.7	40.3	20.3	20.0	79.7	834	23
280	1800	7736	19284	0.062	47.9	52.1	14.9	37.2	85.1	707	50
290	1690	12670	12462	0.063	48.1	51.9	26.2	25.7	73.8	856	41

Appendix 4-A: Mineralogy of periplatform sediments (XRD)

Depth (cm)	Aragonite	LMC	HMC	Ar/Ar+Cc	Aragonite	Calcite	LMC	HMC	Aragonite + HMC	Quartz	Dolomite
300	1954	10054	11920	0.082	53.2	46.8	21.4	25.4	78.6	660	35
310	2294	11844	11884	0.088	54.7	45.3	22.6	22.7	77.4	608	39
320	2848	11052	14680	0.100	57.1	42.9	18.4	24.5	81.6	446	41
330	2162	11754	13148	0.080	52.7	47.3	22.3	25.0	77.7	683	37
340	2176	10986	9396	0.096	56.4	43.6	23.5	20.1	76.5	656	46
350	2768	10712	13458	0.103	57.7	42.3	18.8	23.6	81.2	512	41
360	3408	12628	12420	0.120	60.7	39.3	19.8	19.5	80.2	552	29
370	1948	9360	10188	0.091	55.2	44.8	21.4	23.3	78.6	995	30
380	2180	10512	8360	0.104	57.8	42.2	23.5	18.7	76.5	809	36
390	3260	13872	8990	0.125	61.5	38.5	23.4	15.1	76.6	611	31
400	1820	12670	10320	0.073	51.1	48.9	27.0	22.0	73.0	793	40
410	1474	8000	22538	0.046	41.9	58.1	15.2	42.9	84.8	674	29
420	1040	8472	25060	0.030	33.6	66.4	16.8	49.7	83.2	567	29
S2 < 63µm											
2	6261	10720	19254	0.173	67.9	32.1	11.5	20.6	88.5	1018	14
10	5230	15530	20486	0.127	61.8	38.2	16.5	21.7	83.5	534	15
20	5466	13970	19858	0.139	63.6	36.4	15.0	21.4	85.0	983	23
30	5212	16286	18204	0.131	62.5	37.5	17.7	19.8	82.3	541	29
40	5850	16690	21364	0.133	62.8	37.2	16.3	20.9	83.7	446	39
50	5014	21432	24396	0.099	56.9	43.1	20.2	23.0	79.8	390	14
60	5938	18320	24110	0.123	61.2	38.8	16.8	22.1	83.2	188	49
70	7894	7970	6360	0.355	82.0	18.0	10.0	8.0	90.0	838	129
80	5708	13810	11332	0.185	69.2	30.8	16.9	13.9	83.1	527	35
90	6760	10768	9378	0.251	75.2	24.8	13.2	11.5	86.8	780	48
100	9106	6480	6096	0.420	85.3	14.7	7.6	7.1	92.4	974	43
110	5438	10446	14812	0.177	68.4	31.6	13.1	18.5	86.9	1051	100
120	4468	10480	15218	0.148	64.9	35.1	14.3	20.8	85.7	1115	96
130	5064	10288	16498	0.159	66.3	33.7	13.0	20.8	87.0	720	61
140	6830	8326	16214	0.218	72.4	27.6	9.4	18.2	90.6	1269	89
150	6262	12534	30628	0.127	61.8	38.2	11.1	27.1	88.9	626	48
160	6284	10804	28978	0.136	63.2	36.8	10.0	26.8	90.0	541	53
170	5518	14404	17024	0.149	65.0	35.0	16.0	18.9	84.0	388	21
180	3014	11714	30486	0.067	49.2	50.8	14.1	36.7	85.9	793	92
190	2922	11206	32448	0.063	48.0	52.0	13.4	38.7	86.6	838	53
200	4216	9834	10446	0.172	67.8	32.2	15.6	16.6	84.4	1273	55
210	3346	15612	18086	0.090	55.1	44.9	20.8	24.1	79.2	1211	68
220	3448	12856	15012	0.110	59.0	41.0	18.9	22.1	81.1	1301	96
230	3132	11670	21024	0.087	54.5	45.5	16.2	29.3	83.8	1190	121
240	3028	11348	15230	0.102	57.6	42.4	18.1	24.3	81.9	1333	91
250	2216	11918	18524	0.068	49.5	50.5	19.8	30.7	80.2	1706	84
260	2798	12396	14292	0.095	56.1	43.9	20.4	23.5	79.6	1474	76
270	2760	12806	14518	0.092	55.5	44.5	20.9	23.7	79.1	1127	196
280	2158	12462	20736	0.061	47.5	52.5	19.7	32.8	80.3	1183	95
290	2472	16164	15076	0.073	51.1	48.9	25.3	23.6	74.7	1245	122
300	3212	13292	16364	0.098	56.7	43.3	19.4	23.9	80.6	1067	72
310	3426	13250	15068	0.108	58.6	41.4	19.3	22.0	80.7	852	62
320	5090	12262	15706	0.154	65.6	34.4	15.1	19.3	84.9	960	91
330	2400	15064	15718	0.072	50.8	49.2	24.1	25.1	75.9	1158	83
340	3252	14532	12402	0.108	58.6	41.4	22.3	19.1	77.7	1486	56
350	4266	12264	19714	0.118	60.3	39.7	15.2	24.4	84.8	845	60
360	5646	19436	18520	0.129	62.2	37.8	19.3	18.4	80.7	783	49
370	3160	13316	12316	0.110	59.0	41.0	21.3	19.7	78.7	1117	37
380	3036	15166	11406	0.103	57.6	42.4	24.2	18.2	75.8	1577	47
390	4322	16532	11700	0.133	62.7	37.3	21.8	15.5	78.2	837	58
400	2640	16446	15188	0.077	52.0	48.0	24.9	23.0	75.1	1225	51

Appendix 4-A: Mineralogy of periplatform sediments (XRD)

Depth (cm)	Aragonite	LMC	HMC	Ar/Ar+Cc	Aragonite	Calcite	LMC	HMC	Aragonite + HMC	Quartz	Dolomite
410	1562	10420	25506	0.042	40.0	60.0	17.4	42.6	82.6	1149	46
420	1148	10754	31348	0.027	31.1	68.9	17.6	51.3	82.4	759	51
430	2006	14528	22372	0.052	44.1	55.9	22.0	33.9	78.0	1232	89
440	1654	13106	21490	0.046	41.7	58.3	22.1	36.2	77.9	1084	64
450	1902	9108	28396	0.048	42.8	57.2	13.9	43.3	86.1	1597	51
S3-bulk											
3	3530	7540	6812	0.197	70.5	29.5	15.5	14.0	84.5	616	71
35	1590	10538	20294	0.049	43.2	56.8	19.4	37.4	80.6	672	33
89	4210	7428	3824	0.272	76.8	23.2	15.3	7.9	84.7	589	37
93	4646	4726	5268	0.317	79.8	20.2	9.5	10.6	90.5	1227	49
131	2480	8292	13860	0.101	57.3	42.7	16.0	26.7	84.0	665	50
140	2102	7620	24932	0.061	47.3	52.7	12.3	40.3	87.7	550	29
150	2880	10076	15138	0.103	57.6	42.4	16.9	25.4	83.1	815	102
160	3404	7428	17598	0.120	60.7	39.3	11.7	27.6	88.3	600	40
170	1942	11016	17046	0.065	48.6	51.4	20.2	31.2	79.8	1399	46
180	2222	9350	14270	0.086	54.2	45.8	18.1	27.7	81.9	715	47
190	2096	10122	12416	0.085	54.0	46.0	20.7	25.4	79.3	712	53
192	2086	8368	10502	0.100	57.1	42.9	19.0	23.9	81.0	1046	61
195	2324	8770	16174	0.085	54.0	46.0	16.2	29.8	83.8	640	35
207	2566	10870	11222	0.104	57.9	42.1	20.7	21.4	79.3	777	40
210	1894	13272	9960	0.075	51.6	48.4	27.7	20.8	72.3	876	49
220	1776	8502	11464	0.082	53.2	46.8	19.9	26.9	80.1	852	30
230	2944	10516	11510	0.118	60.4	39.6	18.9	20.7	81.1	599	36
240	1970	6194	17648	0.076	51.8	48.2	12.5	35.6	87.5	1002	52
250	2058	8214	12716	0.090	55.0	45.0	17.7	27.4	82.3	588	35
260	2300	11390	11938	0.090	55.0	45.0	22.0	23.0	78.0	1150	32
270	2562	9652	11978	0.106	58.3	41.7	18.6	23.1	81.4	963	33
274	3366	11246	14112	0.117	60.3	39.7	17.6	22.1	82.4	506	32
276	3398	9284	13326	0.131	62.4	37.6	15.4	22.2	84.6	695	41
280	3096	8764	13044	0.124	61.4	38.6	15.5	23.1	84.5	951	21
290	2884	10856	12818	0.109	58.8	41.2	18.9	22.3	81.1	488	30
300	4190	9324	13924	0.153	65.5	34.5	13.9	20.7	86.1	431	37
310	2716	11066	16058	0.091	55.3	44.7	18.2	26.5	81.8	744	23
314	2408	10136	15250	0.087	54.3	45.7	18.2	27.4	81.8	689	39
320	2434	9778	10928	0.105	58.1	41.9	19.8	22.1	80.2	861	28
330	3186	11886	12404	0.116	60.1	39.9	19.5	20.4	80.5	736	55
340	3340	9294	13212	0.129	62.2	37.8	15.6	22.2	84.4	799	18
350	4212	12406	15428	0.131	62.5	37.5	16.7	20.8	83.3	340	20
360	3038	12758	10664	0.115	59.9	40.1	21.9	18.3	78.1	587	108
370	3002	11436	8910	0.129	62.1	37.9	21.3	16.6	78.7	1248	28
377	1926	9632	10708	0.086	54.3	45.7	21.6	24.1	78.4	1036	27
380	4236	11338	9828	0.167	67.2	32.8	17.6	15.2	82.4	1457	33
390	3122	13948	11998	0.107	58.5	41.5	22.3	19.2	77.7	620	26
400	1882	11304	6964	0.093	55.8	44.2	27.3	16.8	72.7	867	25
410	1644	12302	20950	0.047	42.4	57.6	21.3	36.3	78.7	689	62
420	1138	8056	22734	0.036	36.9	63.1	16.5	46.6	83.5	597	28
430	1364	8104	42616	0.026	30.8	69.2	11.1	58.1	88.9	820	61
440	1766	12416	16064	0.058	46.6	53.4	23.3	30.1	76.7	693	43
450	1400	10398	47708	0.024	28.7	71.3	12.8	58.5	87.2	777	43
S3 < 63µm											
5	6261	6784	10232	0.269	76.6	23.4	9.3	14.1	90.7	1042	57
10	15798	4288	5022	0.629	93.3	6.7	3.1	3.6	96.9	1071	40
13	2580	7968	27248	0.068	49.6	50.4	11.4	39.0	88.6	1048	145
20	2678	10286	17706	0.087	54.5	45.5	16.7	28.8	83.3	611	55
30	3968	12342	16316	0.122	61.0	39.0	16.8	22.2	83.2	823	93

Appendix 4-A: Mineralogy of periplatform sediments (XRD)

Depth (cm)	Aragonite	LMC	HMC	Ar/Ar+Cc	Aragonite	Calcite	LMC	HMC	Aragonite + HMC	Quartz	Dolomite
40	3504	13754	19164	0.096	56.4	43.6	18.2	25.4	81.8	975	72
50	4140	10048	20298	0.120	60.7	39.3	13.0	26.3	87.0	1111	76
65	4426	12354	16102	0.135	63.0	37.0	16.1	20.9	83.9	899	60
80	3370	10660	27648	0.081	53.0	47.0	13.1	33.9	86.9	567	75
89	6650	10468	3726	0.319	79.9	20.1	14.8	5.3	85.2	759	55
93	6164	6856	7684	0.298	78.6	21.4	10.1	11.3	89.9	1131	56
100	4228	12632	25082	0.101	57.3	42.7	14.3	28.4	85.7	839	72
110	3530	11182	32388	0.075	51.5	48.5	12.5	36.1	87.5	489	67
120	3206	11462	28304	0.075	51.4	48.6	14.0	34.6	86.0	525	68
131	3602	10792	14968	0.123	61.2	38.8	16.3	22.6	83.7	941	65
140	3346	9666	23320	0.092	55.5	44.5	13.0	31.4	87.0	899	60
150	3838	13118	18198	0.109	58.9	41.1	17.2	23.9	82.8	862	90
160	2566	13102	16414	0.080	52.8	47.2	21.0	26.3	79.0	1140	95
170	2880	10864	17286	0.093	55.7	44.3	17.1	27.2	82.9	1236	69
180	3546	12248	13236	0.122	61.1	38.9	18.7	20.2	81.3	1435	68
190	2406	9158	10698	0.108	58.7	41.3	19.1	22.3	80.9	1734	98
192	2532	12902	10264	0.099	56.9	43.1	24.0	19.1	76.0	1947	87
195	2650	11556	11350	0.104	57.9	42.1	21.3	20.9	78.7	1624	87
207	2518	11350	9918	0.106	58.3	41.7	22.3	19.5	77.7	1958	82
210	3138	12418	9032	0.128	61.9	38.1	22.0	16.0	78.0	1617	44
220	2446	11176	11650	0.097	56.5	43.5	21.3	22.2	78.7	1255	119
230	3922	12402	13240	0.133	62.7	37.3	18.0	19.3	82.0	774	87
240	2006	9918	17784	0.068	49.4	50.6	18.1	32.5	81.9	1200	52
250	2496	12646	13786	0.086	54.2	45.8	21.9	23.9	78.1	1351	94
260	2956	11678	13224	0.106	58.3	41.7	19.5	22.1	80.5	1857	170
270	3786	11724	13326	0.131	62.5	37.5	17.6	20.0	82.4	1353	187
274	3356	12568	11632	0.122	61.0	39.0	20.2	18.7	79.8	972	56
276	3212	11700	14134	0.111	59.1	40.9	18.5	22.4	81.5	807	35
278	3748	10546	11464	0.146	64.5	35.5	17.0	18.5	83.0	1001	55
280	3082	12968	18360	0.090	55.0	45.0	18.6	26.4	81.4	1335	75
290	4272	10984	12176	0.156	65.8	34.2	16.2	18.0	83.8	879	54
300	5864	10928	14002	0.190	69.8	30.2	13.2	17.0	86.8	1237	48
310	3094	12838	14092	0.103	57.7	42.3	20.1	22.1	79.9	1339	75
314	3722	12868	13200	0.125	61.5	38.5	19.0	19.5	81.0	1048	70
320	3058	12206	9538	0.123	61.3	38.7	21.7	17.0	78.3	1554	70
330	3374	10290	10660	0.139	63.6	36.4	17.9	18.5	82.1	1493	43
340	4870	13494	16794	0.139	63.5	36.5	16.2	20.2	83.8	1178	43
350	5488	12106	17988	0.154	65.7	34.3	13.8	20.5	86.2	557	39
360	3904	10138	11456	0.153	65.5	34.5	16.2	18.3	83.8	1414	90
370	4242	9052	8460	0.195	70.3	29.7	15.4	14.4	84.6	1317	79
377	3478	9564	9308	0.156	65.8	34.2	17.3	16.9	82.7	1354	93
380	3232	10714	9266	0.139	63.6	36.4	19.5	16.9	80.5	1529	66
390	4170	19184	11762	0.119	60.5	39.5	24.5	15.0	75.5	962	55
400	2488	11728	8776	0.108	58.7	41.3	23.6	17.7	76.4	1194	125
410	1744	14540	22178	0.045	41.6	58.4	23.1	35.3	76.9	1395	75
420	1714	19450	21344	0.040	39.3	60.7	28.9	31.8	71.1	1377	87
430	1820	9728	22300	0.054	45.0	55.0	16.7	38.3	83.3	1113	44
435	1432	9062	16328	0.053	44.8	55.2	19.7	35.5	80.3	1189	77
440	2792	14168	16300	0.084	53.7	46.3	21.5	24.8	78.5	1350	53
445	2216	12694	26126	0.054	45.0	55.0	18.0	37.0	82.0	825	49
S6-bulk I											
1	4084	17462	16136	0.108	58.7	41.3	21.5	19.8	78.5	666	27
10	4412	12602	16842	0.130	62.3	37.7	16.1	21.5	83.9	1004	8
20	3922	20646	17242	0.094	55.9	44.1	24.0	20.1	76.0	559	29
30	3910	17136	18598	0.099	56.9	43.1	20.7	22.4	79.3	499	

Appendix 4-A: Mineralogy of periplatform sediments (XRD)

Depth (cm)	Aragonite	LMC	HMC	Ar/Ar+Cc	Aragonite	Calcite	LMC	HMC	Aragonite + HMC	Quartz	Dolomite
40	3962	17776	19202	0.097	56.5	43.5	20.9	22.6	79.1	433	55
50	4720	21400	18910	0.105	58.1	41.9	22.3	19.7	77.7	273	54
60	4548	23780	20626	0.093	55.7	44.3	23.7	20.6	76.3	388	49
70	5590	21340	22224	0.114	59.7	40.3	19.8	20.6	80.2	131	51
80	4664	19584	18534	0.109	58.8	41.2	21.1	20.0	78.9	254	55
100	2824	15770	9800	0.099	57.0	43.0	26.5	16.5	73.5	635	44
110	2740	13898	9220	0.106	58.3	41.7	25.1	16.6	74.9	907	62
120	3284	13064	12094	0.115	60.0	40.0	20.8	19.2	79.2	782	49
130	5280	12514	7380	0.210	71.7	28.3	17.8	10.5	82.2	1125	62
140	2012	14900	15074	0.063	48.0	52.0	25.8	26.1	74.2	851	62
150	2704	11496	17226	0.086	54.2	45.8	18.3	27.5	81.7	1133	82
160	2514	12872	9988	0.099	57.0	43.0	24.2	18.8	75.8	1352	101
170	3410	12662	13342	0.116	60.1	39.9	19.5	20.5	80.5	1029	34
200	3364	14588	15064	0.102	57.5	42.5	20.9	21.6	79.1	1099	36
220	2806	16442	8292	0.102	57.5	42.5	28.2	14.2	71.8	1094	54
230	3432	11042	18914	0.103	57.7	42.3	15.6	26.7	84.4	801	51
250	2144	15820	12462	0.070	50.3	49.7	27.8	21.9	72.2	960	124
270	2514	12872	9988	0.099	57.0	43.0	24.2	18.8	75.8	1352	101
280	3410	12662	13342	0.116	60.1	39.9	19.5	20.5	80.5	1029	34
290	3364	14588	15064	0.102	57.5	42.5	20.9	21.6	79.1	1099	36
295	2806	16442	8292	0.102	57.5	42.5	28.2	14.2	71.8	1094	54
300	3432	11042	18914	0.103	57.7	42.3	15.6	26.7	84.4	801	51
310	2144	15820	12462	0.070	50.3	49.7	27.8	21.9	72.2	960	124
320	2388	15712	12720	0.077	52.1	47.9	26.5	21.4	73.5	919	103
330	3596	12752	17516	0.106	58.3	41.7	17.6	24.1	82.4	614	45
340	3860	14584	16398	0.111	59.2	40.8	19.2	21.6	80.8	542	91
350	2696	15980	9894	0.094	56.0	44.0	27.2	16.8	72.8	753	67
360	3158	13994	12732	0.106	58.2	41.8	21.9	19.9	78.1	801	72
370	3290	14274	13112	0.107	58.5	41.5	21.6	19.9	78.4	904	24
380	4472	15126	18914	0.116	60.1	39.9	17.7	22.2	82.3	1126	59
390	4720	15618	13034	0.141	64.0	36.0	19.6	16.4	80.4	677	28
400	3358	10234	10376	0.140	63.8	36.2	18.0	18.2	82.0	982	36
410	4210	12818	13186	0.139	63.7	36.3	17.9	18.4	82.1	872	41
420	3830	15898	13968	0.114	59.7	40.3	21.5	18.9	78.5	1136	31
430	2984	15402	10404	0.104	57.9	42.1	25.2	17.0	74.8	1036	35
440	2232	14238	15222	0.070	50.3	49.7	24.0	25.7	76.0	827	157
450	1340	10666	29212	0.033	35.1	64.9	17.4	47.6	82.6	710	64
460	1632	9238	27504	0.043	40.4	59.6	15.0	44.6	85.0	737	60
470	2038	14986	19190	0.056	45.9	54.1	23.7	30.4	76.3	912	45
S6-bulk II											
1	2828	14566	12552	0.094	56.0	44.0	23.6	20.4	76.4	435	27
10	3502	14698	14624	0.107	58.4	41.6	20.8	20.7	79.2	376	31
20	8044	26742	28972	0.126	61.7	38.3	18.4	19.9	81.6	464	
30	3552	14576	11944	0.118	60.4	39.6	21.8	17.8	78.2	466	27
40	3222	15556	14296	0.097	56.6	43.4	22.6	20.8	77.4	403	29
50	3462	17566	14018	0.099	56.9	43.1	24.0	19.1	76.0	214	34
60	3970	18622	16868	0.101	57.3	42.7	22.4	20.3	77.6	188	32
70	5078	17860	18216	0.123	61.3	38.7	19.2	19.6	80.8	115	13
80	4140	17060	15914	0.112	59.3	40.7	21.1	19.6	78.9	138	13
86	5764	12310	17366	0.163	66.7	33.3	13.8	19.5	86.2	173	26
90	4056	17046	12558	0.120	60.8	39.2	22.6	16.6	77.4	308	33
100	3464	12052	6716	0.156	65.9	34.1	21.9	12.2	78.1	668	53
110	1922	8934	7294	0.106	58.3	41.7	23.0	18.8	77.0	808	55
120	3182	10262	9408	0.139	63.6	36.4	19.0	17.4	81.0	651	46
130	3752	8864	6094	0.201	70.8	29.2	17.3	11.9	82.7	787	37

Appendix 4-A: Mineralogy of periplatform sediments (XRD)

Depth (cm)	Aragonite	LMC	HMC	Ar/Ar+Cc	Aragonite	Calcite	LMC	HMC	Aragonite + HMC	Quartz	Dolomite
200	1884	10626	11956	0.077	52.0	48.0	22.6	25.4	77.4	750	72
250	2176	10998	15170	0.077	52.0	48.0	20.2	27.9	79.8	1076	41
270	2554	10720	8354	0.118	60.4	39.6	22.2	17.3	77.8	1339	25
280	2688	10184	9528	0.120	60.7	39.3	20.3	19.0	79.7	611	38
290	2490	11614	11618	0.097	56.5	43.5	21.7	21.7	78.3	620	74
295	1846	11778	7082	0.089	54.9	45.1	28.2	16.9	71.8	969	48
300	1964	9462	14346	0.076	51.8	48.2	19.2	29.0	80.8	529	70
310	1964	11124	11462	0.080	52.8	47.2	23.3	24.0	76.7	906	42
320	2290	9432	10130	0.105	58.1	41.9	20.2	21.7	79.8	869	55
330	3080	9600	15066	0.111	59.2	40.8	15.9	24.9	84.1	845	30
340	2920	13246	14050	0.097	56.5	43.5	21.1	22.4	78.9	559	49
350	2170	12964	10146	0.086	54.1	45.9	25.7	20.1	74.3	614	33
360	1920	13390	11244	0.072	50.8	49.2	26.8	22.5	73.2	801	38
370	3174	13120	12138	0.112	59.3	40.7	21.1	19.6	78.9	913	37
380	3014	14420	16380	0.089	54.9	45.1	21.1	24.0	78.9	777	34
390	3810	14184	10162	0.135	63.1	36.9	21.5	15.4	78.5	530	44
400	2814	7512	9704	0.140	63.8	36.2	15.8	20.4	84.2	1515	45
410	2888	10122	9558	0.128	62.0	38.0	19.5	18.5	80.5	704	42
420	3006	14082	11036	0.107	58.5	41.5	23.3	18.3	76.7	621	40
430	2684	16672	8956	0.095	56.1	43.9	28.6	15.3	71.4	537	29
440	1826	14272	11590	0.066	49.0	51.0	28.2	22.9	71.8	700	53
450	1098	7916	19836	0.038	38.2	61.8	17.6	44.2	82.4	596	34
460	1106	7916	19836	0.038	38.3	61.7	17.6	44.1	82.4	596	34
470	1620	12208	16686	0.053	44.7	55.3	23.4	31.9	76.6	715	52
S6<63											
1	3326	17470	14938	0.093	55.7	44.3	23.9	20.4	76.1	812	16
10	3628	21612	20678	0.079	52.5	47.5	24.3	23.2	75.7	488	30
20	4314	19226	20164	0.099	56.9	43.1	21.0	22.1	79.0	484	15
30	3758	18110	20602	0.088	54.7	45.3	21.2	24.1	78.8	537	20
40	4192	18978	21708	0.093	55.8	44.2	20.6	23.6	79.4	673	21
50	3944	24202	21290	0.080	52.7	47.3	25.2	22.1	74.8	628	17
60	3768	24308	24506	0.072	50.6	49.4	24.6	24.8	75.4	276	9
70	5052	24210	25442	0.092	55.6	44.4	21.7	22.8	78.3	158	17
80	6372	23720	21444	0.124	61.3	38.7	20.3	18.4	79.7	377	20
86	6214	18902	23530	0.128	62.0	38.0	16.9	21.1	83.1	448	23
90	5384	20844	20910	0.114	59.8	40.2	20.1	20.2	79.9	421	40
100	2766	14792	7424	0.111	59.1	40.9	27.2	13.7	72.8	2515	82
110	2764	10094	6836	0.140	63.8	36.2	21.6	14.6	78.4	1547	85
120	3372	11580	7932	0.147	64.8	35.2	20.9	14.3	79.1	1097	62
126	2988	10064	6858	0.150	65.1	34.9	20.7	14.1	79.3	1034	89
130	5708	13414	9164	0.202	70.9	29.1	17.3	11.8	82.7	898	95
132	15534	4736	10140	0.511	89.2	10.8	3.4	7.4	96.6	691	44
140	4222	12536	12954	0.142	64.0	36.0	17.7	18.3	82.3	859	89
150	3790	12516	15196	0.120	60.8	39.2	17.7	21.5	82.3	968	120
160	2694	13464	3032	0.140	63.8	36.2	29.5	6.7	70.5	822	89
170	3894	12850	16640	0.117	60.2	39.8	17.4	22.5	82.6	739	97
180	2722	13494	10048	0.104	57.8	42.2	24.2	18.0	75.8	1098	84
185	6700	15886	18348	0.164	66.8	33.2	15.4	17.8	84.6	755	58
190	4484	15006	20698	0.112	59.3	40.7	17.1	23.6	82.9	586	111
200	2536	11186	27976	0.061	47.4	52.6	15.0	37.6	85.0	804	91
210	2620	12216	36160	0.051	44.1	55.9	14.1	41.8	85.9	791	57
220	3096	10786	24960	0.080	52.7	47.3	14.3	33.0	85.7	918	112
230	4016	12630	16074	0.123	61.2	38.8	17.1	21.7	82.9	737	48
240	2830	8524	15180	0.107	58.4	41.6	15.0	26.6	85.0	1338	69
250	2320	12882	12906	0.083	53.4	46.6	23.3	23.3	76.7	1006	71

Appendix 4-A: Mineralogy of periplatform sediments (XRD)

Depth (cm)	Aragonite	LMC	HMC	Ar/Ar+Cc	Aragonite	Calcite	LMC	HMC	Aragonite + HMC	Quartz	Dolomite
260	2868	11150	10534	0.117	60.2	39.8	20.5	19.3	79.5	1455	58
270	2192	12338	11596	0.084	53.7	46.3	23.9	22.4	76.1	1197	154
274	1898	8266	17280	0.069	49.9	50.1	16.2	33.9	83.8	1198	79
280	2162	12810	8566	0.092	55.5	44.5	26.7	17.8	73.3	2212	90
285	2798	12434	11922	0.103	57.7	42.3	21.6	20.7	78.4	1037	65
287	286	5310	2332	0.036	37.1	62.9	43.7	19.2	56.3	4436	115
290	3452	10940	9372	0.145	64.5	35.5	19.1	16.4	80.9	1795	36
295	2116	12554	7368	0.096	56.3	43.7	27.5	16.1	72.5	1812	91
300	1870	15330	11710	0.065	48.6	51.4	29.1	22.3	70.9	1546	67
310	1920	9980	7632	0.098	56.8	43.2	24.5	18.7	75.5	2016	45
320	3376	11278	9170	0.142	64.0	36.0	19.9	16.1	80.1	1038	69
330	3016	13402	8966	0.119	60.5	39.5	23.6	15.8	76.4	1378	52
340	3232	13970	14048	0.103	57.8	42.2	21.0	21.2	79.0	991	35
350	2220	14526	9352	0.085	54.0	46.0	28.0	18.0	72.0	2083	60
360	2594	14896	8638	0.099	57.0	43.0	27.2	15.8	72.8	1260	89
370	3400	13070	10542	0.126	61.7	38.3	21.2	17.1	78.8	1496	62
380	4894	19016	15490	0.124	61.4	38.6	21.3	17.3	78.7	1009	50
390	4914	15432	10630	0.159	66.2	33.8	20.0	13.8	80.0	783	125
400	2436	10902	7548	0.117	60.2	39.8	23.5	16.3	76.5	1733	74
410	2688	11824	6918	0.125	61.6	38.4	24.2	14.2	75.8	1511	86
420	4026	16408	7992	0.142	64.0	36.0	24.2	11.8	75.8	1111	67
430	3042	17714	8386	0.104	58.0	42.0	28.5	13.5	71.5	929	93
440	1782	12520	8640	0.078	52.2	47.8	28.3	19.5	71.7	1076	44
450	1160	13714	22930	0.031	33.9	66.1	24.7	41.3	75.3	2204	73
460	1324	8532	20688	0.043	40.7	59.3	17.3	42.0	82.7	826	81
470	1802	12936	14668	0.061	47.5	52.5	24.6	27.9	75.4	1580	56
MD > 63µm											
70	9546	66656	10614	0.110	59.0	41.0	35.4	5.6	64.6	98	
84	13988	9156	29002	0.268	76.5	23.5	5.6	17.8	94.4	1255	
89	23434	2070	10858	0.644	100.0	0.0	0.0	0.0	100.0	197	
89	14758	7532	31144	0.276	77.1	22.9	4.5	18.4	95.5	409	
101	28038	2280	6926	0.753	100.0	0.0	0.0	0.0	100.0	259	
101	21656	4846	21112	0.455	86.9	13.1	2.4	10.7	97.6	96	
114	18128	3876	17164	0.463	87.2	12.8	2.4	10.4	97.6	291	
114	12442	7088	43066	0.199	70.6	29.4	4.1	25.2	95.9	292	
121	5658	8384	59868	0.077	51.9	48.1	5.9	42.2	94.1	315	
121	7426	8778	55628	0.103	57.8	42.2	5.8	36.4	94.2	217	
131	19816	3528	22642	0.431	85.8	14.2	1.9	12.3	98.1	235	
131	11602	5620	39134	0.206	71.3	28.7	3.6	25.1	96.4	234	
140	10184	10980	57116	0.130	62.3	37.7	6.1	31.6	93.9	1205	
160	6610	18522	43748	0.096	56.3	43.7	13.0	30.7	87.0	1530	
170	9806	20824	40618	0.138	63.4	36.6	12.4	24.2	87.6	974	
180	8310	16758	43900	0.120	60.8	39.2	10.8	28.4	89.2	1063	
229	10630	22496	18168	0.207	71.5	28.5	15.8	12.8	84.2	1230	
247	7516	22878	48422	0.095	56.2	43.8	14.0	29.7	86.0	653	
270	9222	19460	56260	0.109	58.8	41.2	10.6	30.6	89.4	608	
304	11022	24238	56464	0.120	60.8	39.2	11.8	27.5	88.2	368	
319	7618	44376	45856	0.078	52.2	47.8	23.5	24.3	76.5	46	
332	5994	46974	47296	0.060	47.0	53.0	26.4	26.6	73.6	49	
356	6052	44234	51044	0.060	47.0	53.0	24.6	28.4	75.4	118	
369	10742	25366	54744	0.118	60.4	39.6	12.5	27.0	87.5	317	
396	14062	5634	55950	0.186	69.3	30.7	2.8	27.9	97.2		
465	16568	9572	50780	0.215	72.2	27.8	4.4	23.4	95.6		
472	15710	1914	52816	0.223	72.9	27.1	0.9	26.2	99.1		
490	14758	9998	54296	0.187	69.4	30.6	4.8	25.8	95.2		

Appendix 4-A: Mineralogy of periplatform sediments (XRD)

Depth (cm)	Aragonite	LMC	HMC	Ar/Ar+Cc	Aragonite	Calcite	LMC	HMC	Aragonite + HMC	Quartz	Dolomite
510	16392	8542	63286	0.186	69.3	30.7	3.6	27.0	96.4	48	
532	18632	6754	52588	0.239	74.3	25.7	2.9	22.8	97.1	36	
615	14522	6900	58802	0.181	68.8	31.2	3.3	27.9	96.7		
640	14848	0	57260	0.206	71.3	28.7	0.0	28.7	100.0		
715	17142	10058	52074	0.216	72.3	27.7	4.5	23.2	95.5	40	
760	13006	28986	32756	0.174	68.0	32.0	15.0	17.0	85.0	554	
790	13108	26118	46116	0.154	65.6	34.4	12.4	22.0	87.6	484	
820	11020	35268	30408	0.144	64.3	35.7	19.2	16.5	80.8	1382	
835	8870	30722	51000	0.098	56.7	43.3	16.3	27.0	83.7	245	
855	9290	25428	45506	0.116	60.0	40.0	14.3	25.6	85.7	3140	
1052	17262	12434	46498	0.227	73.2	26.8	5.7	21.1	94.3	32	
MD 63-2µm											
2	9426	14014	14336	0.250	75.1	24.9	12.3	12.6	87.7	2284	70
10	12892	14646	17774	0.285	77.7	22.3	10.1	12.2	89.9	2150	59
40	12482	16096	19989	0.257	75.7	24.3	10.8	13.5	89.2	1701	81
70	12496	22842	17837	0.235	73.9	26.1	14.6	11.4	85.4	861	29
84	8158	11616	13677	0.244	74.7	25.3	11.6	13.7	88.4	2043	46
140	10300	13010	17079	0.255	75.5	24.5	10.6	13.9	89.4	2164	102
160	5532	12766	9410	0.200	70.7	29.3	16.9	12.4	83.1	3152	223
170	7644	13954	13097	0.220	72.7	27.3	14.1	13.2	85.9	3500	81
180	6836	15762	15344	0.180	68.7	31.3	15.9	15.4	84.1	2667	99
206	8640	14496	16647	0.217	72.4	27.6	12.9	14.8	87.1	2872	109
229	9740	13322	10854	0.287	77.9	22.1	12.2	9.9	87.8	2911	113
247	6042	14592	15939	0.165	67.0	33.0	15.8	17.2	84.2	2874	200
270	8410	16050	24493	0.172	67.8	32.2	12.8	19.5	87.2	2411	143
304	9332	15740	17057	0.222	72.8	27.2	13.1	14.2	86.9	2193	89
311	11840	10590	25622	0.246	74.9	25.1	7.4	17.8	92.6	1715	109
319	13930	24850	27691	0.210	71.7	28.3	13.4	14.9	86.6	680	44
332	12548	23884	26885	0.198	70.6	29.4	13.8	15.6	86.2	858	78
343	9746	12358	25715	0.204	71.1	28.9	9.4	19.5	90.6	1789	97
356	12868	20748	27026	0.212	71.9	28.1	12.2	15.9	87.8	1115	
369	7106	12546	16688	0.196	70.3	29.7	12.7	16.9	87.3	2427	121
375	15462	12920	30103	0.264	76.2	23.8	7.1	16.6	92.9	1138	243
396	9600	11710	29727	0.188	69.6	30.4	8.6	21.8	91.4	1159	148
465	12184	17650	31209	0.200	70.7	29.3	10.6	18.7	89.4	1535	76
472	11180	10428	34857	0.198	70.6	29.4	6.8	22.7	93.2	1343	118
490	11454	13956	31360	0.202	70.9	29.1	9.0	20.1	91.0	773	52
510	11698	20020	23775	0.211	71.8	28.2	12.9	15.3	87.1	1046	106
516	10986	16784	29416	0.192	70.0	30.0	10.9	19.1	89.1	1320	51
532	12382	17482	29232	0.210	71.7	28.3	10.6	17.7	89.4	844	89
615	12036	17768	29387	0.203	71.1	28.9	10.9	18.0	89.1	1207	74
715	11182	16830	20341	0.231	73.6	26.4	11.9	14.4	88.1	1913	97
760	9660	19550	14540	0.221	72.7	27.3	15.7	11.6	84.3	1688	100
790	8684	13812	15708	0.227	73.3	26.7	12.5	14.2	87.5	1522	83
820	6916	12020	15242	0.202	71.0	29.0	12.8	16.2	87.2	2322	112
835	8898	16074	18886	0.203	71.0	29.0	13.3	15.6	86.7	1594	76
855	9010	14578	19625	0.209	71.6	28.4	12.1	16.3	87.9	2103	73
1052	11726	17686	22144	0.227	73.3	26.7	11.9	14.9	88.1	1395	228
MD < 2µm											
10	5498	26954	38940	0.077	52.0	48.0	19.6	28.4	80.4	857	
70	6330	31918	34442	0.087	54.4	45.6	21.9	23.7	78.1	624	
84	3146	30260	34430	0.046	42.1	57.9	27.1	30.8	72.9	1032	
140	3834	27628	18078	0.077	52.1	47.9	28.9	18.9	71.1	1093	
170	3182	29236	38320	0.045	41.5	58.5	25.3	33.2	74.7	660	
180	4428	18866	23934	0.094	55.9	44.1	19.4	24.7	80.6	1714	

Appendix 4-A: Mineralogy of periplatform sediments (XRD)

Depth (cm)	Aragonite	LMC	HMC	Ar/Ar+Cc	Aragonite	Calcite	LMC	HMC	Aragonite + HMC	Quartz	Dolomite
229	6076	24388	23032	0.114	59.6	40.4	20.8	19.6	79.2	1644	
247	2350	25802	31546	0.039	38.8	61.2	27.5	33.6	72.5	1425	
270	2544	20442	41378	0.040	38.9	61.1	20.2	40.9	79.8	1209	
304	3202	31342	31402	0.049	43.0	57.0	28.5	28.5	71.5	1298	
319	4454	45080	38536	0.051	43.8	56.2	30.3	25.9	69.7	446	
332	6598	38032	37132	0.081	52.9	47.1	23.8	23.3	76.2	1139	
356	4554	38456	36790	0.057	46.1	53.9	27.5	26.3	72.5	711	
369	3358	18750	21570	0.077	52.0	48.0	22.3	25.7	77.7	1699	
760	5228	23224	23722	0.100	57.2	42.8	21.2	21.6	78.8	1669	
790	4344	42118	32280	0.055	45.5	54.5	30.9	23.7	69.1	943	
820	2242	27978	34226	0.035	36.4	63.6	28.6	35.0	71.4	963	
835	3020	40178	34078	0.039	38.7	61.3	33.2	28.1	66.8	837	
855	5160	26256	34122	0.079	52.5	47.5	20.7	26.9	79.3	1485	

Appendix 4-B: Mineralogy, stable oxygen isotopes and salinities of the lithified interval

	Peak areas							Percentages			Salinities					
Depth (cm)	**Aragonite**	**LMC**	**HMC**	**HMC-Peak(Å)**	**$MgCO_3$**	**Ar/Ar+Cc**	**Quartz (int.)**	**Aragonite**	**LMC**	**HMC**	**$\delta^{18}O$**	**$\delta^{18}O$ (calcite)**	**$\delta^{18}O$ Cc (SMOW)**	**$\delta^{18}O$ ocean water**	**Salinity (21°)**	**^{14}C-Age (ky BP)**
Lithified bulk sediment																
45	5646	172	0	2.99	14.3	0.970	18	89.4	10.6	0.0	5.19	3.62	34.65	5.42	52.8	
47	6335	211	399	2.96	25.3	0.912	17	88.2	4.1	7.7	5.29	3.61	34.63	5.40	52.7	12930
49	4374	575	2720			0.570	81	79.5	3.6	16.9	5.80	4.10	35.13	5.90	54.5	13310
51	1360	232	770	3.00	13.6	0.576	51	79.7	4.7	15.6	6.10	4.42	35.47	6.24	55.6	
53	4459	681	2429	2.99	14.3	0.589	92	80.1	4.3	15.5	5.95	4.26	35.30	6.07	55.0	*12900*
55	4757	621	2519	2.99	14.7	0.602	89	80.5	3.8	15.6	6.01	4.31	35.36	6.13	55.2	
57	4834	866	1664	3.00	13.3	0.656	86	82.1	6.1	11.7	6.17	4.52	35.57	6.34	56.0	14080
60	5156	623	1415	3.00	12.9	0.717	115	83.8	5.0	11.3	6.29	4.62	35.67	6.44	56.3	
63	5079	726	2013	2.99	14.0	0.650	78	82.0	4.8	13.3	6.07	4.39	35.43	6.20	55.5	
65	4631	588	1355	3.00	13.6	0.704	107	83.5	5.0	11.5	6.56	4.88	35.94	6.72	57.3	
67	5012	769	1203	3.00	13.6	0.718	61	83.8	6.3	9.9	6.60	4.95	36.01	6.78	57.5	14840
69	5020	685	1250	2.98	20.2	0.722	37	83.9	5.7	10.4	6.54	4.87	35.94	6.71	57.3	
71	5003	676	1381	2.99	14.0	0.709	90	83.6	5.4	11.0	6.53	4.87	35.93	6.70	57.2	
73	5143	597	1457	2.99	14.0	0.715	96	83.7	4.7	11.6	6.63	4.96	36.02	6.79	57.5	14890
75	5012	802	1948	3.00	13.6	0.646	73	81.8	5.3	12.9	6.31	4.64	35.69	6.47	56.4	
77	5006	1246	2165	3.00	13.6	0.595	60	80.3	7.2	12.5	6.48	4.84	35.90	6.67	57.1	
79	4653	977	2003	2.99	14.3	0.610	54	80.8	6.3	12.9	6.33	4.67	35.73	6.50	56.5	16160
81	4787	930	1881	2.99	14.0	0.630	95	81.4	6.2	12.5	6.27	4.62	35.67	6.44	56.3	
83	2407	733	1578	3.00	12.9	0.510	82	77.5	7.1	15.4	6.21	4.57	35.62	6.40	56.2	
85	4298	1061	3278	2.99	14.3	0.498	56	77.0	5.6	17.4	6.07	4.40	35.45	6.22	55.6	
87	4605	1037	3180	2.99	14.0	0.522	50	77.9	5.4	16.7	6.25	4.58	35.63	6.40	56.2	17010
89	4822	736	3071	3.00	13.6	0.559	55	79.2	4.0	16.8	6.03	4.33	35.38	6.15	55.3	*14010*
91	5062	746	2634	2.97	21.2	0.600	52	80.5	4.3	15.2	5.98	4.29	35.34	6.11	55.2	
93	4568	777	2547	2.99	14.0	0.579		79.8	4.7	15.5	6.04	4.35	35.40	6.17	55.4	
95	4191	975	3370	2.99	14.7	0.491	47	76.8	5.2	18.0	6.01	4.33	35.37	6.14	55.3	
98	3897	994	3990	2.99	14.0	0.439	57	74.7	5.1	20.3	5.88	4.20	35.24	6.01	54.8	
101	2045	1034	8832	2.99	14.7	0.172	70	57.3	4.5	38.2	5.70	3.99	35.02	5.79	54.1	19540
103	2617	903	7296	2.99	14.7	0.242	77	63.6	4.0	32.4	5.58	3.87	34.90	5.67	53.6	
105	3605	895	4406	2.99	14.7	0.405	61	73.2	4.5	22.3	5.97	4.28	35.32	6.09	55.1	*19060*
107	2380	1266	6941	2.99	14.3	0.225	82	62.3	5.8	31.9	5.18	3.50	34.52	5.29	52.3	
109	4215	913	4796	2.99	14.7	0.425	74	74.1	4.1	21.8	5.63	3.93	34.96	5.73	53.9	19640
111	4243	773	3874	2.99	15.0	0.477	71	76.2	4.0	19.8	5.89	4.19	35.23	6.00	54.8	
113	1162	258	1264	3.00	13.6	0.433	31	74.4	4.3	21.2	5.94	4.25	35.29	6.06	55.0	
115	3399	814	7359	2.99	14.7	0.294	110	67.2	3.3	29.5	5.64	3.92	34.95	5.72	53.8	
117	3683	1038	4744	2.99	14.0	0.389	143	72.4	4.9	22.6	5.56	3.87	34.90	5.67	53.7	21040
119	3975	822	4188	2.99	14.0	0.442	82	74.8	4.1	21.0	5.82	4.12	35.16	5.93	54.5	
121	2891	1001	6851	2.99	14.3	0.269	128	65.6	4.4	30.0	5.54	3.84	34.87	5.64	53.5	22200
123	2268	1181	6044	3.00	13.6	0.239	190	63.4	6.0	30.6	5.53	3.86	34.89	5.66	53.6	
125	3146	1139	5993	2.99	14.0	0.306	95	68.0	5.1	26.9	5.71	4.02	35.06	5.83	54.2	
127	2705	1029	6371	2.99	14.0	0.268	134	65.5	4.8	29.7	5.60	3.91	34.94	5.71	53.8	
Max	6335	1266	8832	3.00	25.3	1	190	89	11	38	7	5	36	7	57.5	
Min	1162	172	0	2.96	12.9	0	17	57	3	0	5	4	35	5	52.3	
Average	4061	803	3279	2.99	14.7	1	78	77	5	18	6	4	35	6	55.2	
Stdev	1197	267	2207	0.01	2.4	0	34	8	1	8	0	0	0	0	1.4	
Unlithified fine fraction																
45	2088	13713	10498	3.03	0.9	0.079	2414	52.6	26.8	20.5	1.07	-0.23	30.67	1.44	38.9	
47	5958	10011	10862	3.03	0.2	0.222	1290	72.8	13.0	14.1	2.73	1.19	32.14	2.91	44.0	12840
49	246	9138	19265	3.03	0.5	0.009	1682	8.9	29.3	61.8	3.68	2.38	33.36	4.14	48.3	*14070*

Appendix 4-B: Mineralogy, stable oxygen isotopes and salinities of the lithified interval

	Peak areas							Percentages			Salinities					
Depth (cm)	**Aragonite**	**LMC**	**HMC**	**HMC-Peak(Å)**	**$MgCO_3$**	**Ar/Ar+Cc**	**Quartz (int.)**	**Aragonite**	**LMC**	**HMC**	**$\delta^{18}O$**	**$\delta^{18}O$ (calcite)**	**$\delta^{18}O$ Cc (SMOW)**	**$\delta^{18}O$ ocean water**	**Salinity (21°)**	**^{14}C-Age (ky BP)**
51	2781	9172	16470	3.03	0.2	0.098	1585	56.7	15.5	27.8	3.71	2.20	33.18	3.95	47.6	
53	2865	8554	18427	3.03	1.2	0.096	1223	56.3	13.8	29.8	3.60	2.06	33.04	3.81	47.1	13810
55	2803	9449	19986	3.03	0.9	0.087	1610	54.4	14.6	31.0	3.69	2.16	33.14	3.91	47.5	
57	3040	9537	15881	3.03	0.9	0.107	1238	58.4	15.6	26.0	3.71	2.20	33.18	3.95	47.7	14630
60	2388	10369	11938	3.03	1.2	0.097	893	56.5	20.2	23.3	3.43	2.01	32.98	3.75	46.9	
63	2907	10092	12889	3.03	0.5	0.112	1688	59.4	17.8	22.8	3.30	1.84	32.80	3.58	46.3	
65	3652	12706	12237	3.03	1.2	0.128	1171	62.0	19.4	18.7	3.60	2.17	33.15	3.92	47.5	
67	4595	11244	12186	3.03	0.9	0.164	1414	66.9	15.9	17.2	3.72	2.23	33.21	3.98	47.7	*16150*
69	3722	10962	12141	3.04	-0.5	0.139	2101	63.6	17.3	19.1	3.60	2.13	33.11	3.88	47.4	
71	4352	12197	11928	3.04	-0.2	0.153	1646	65.5	17.5	17.1	3.67	2.21	33.19	3.96	47.7	
73	4603	8730	12030	3.03	0.2	0.181	1070	68.9	13.1	18.0	3.84	2.30	33.29	4.06	48.0	15810
75	4244	9038	14353	3.03	0.2	0.154	1888	65.6	13.3	21.1	3.82	2.28	33.26	4.03	47.9	
77	3713	11479	18935	3.03	0.9	0.109	1179	58.8	15.5	25.6	3.55	2.05	33.02	3.79	47.1	
79	2938	13952	21177	3.03	0.9	0.077	1031	52.1	19.0	28.9	4.05	2.61	33.60	4.37	49.1	16930
81	2821	11820	21652	3.03	0.5	0.078	1302	52.2	16.9	30.9	3.95	2.46	33.45	4.22	48.6	
83	2518	12588	23447	3.03	0.2	0.065	3866	48.8	17.9	33.3	4.08	2.61	33.60	4.37	49.1	
85	2687	12031	26703	3.03	0.5	0.065	1080	48.6	16.0	35.4	4.34	2.83	33.83	4.60	49.9	
87	2712	14176	23075	3.03	0.9	0.068	1237	49.5	19.2	31.3	3.55	2.11	33.09	3.86	47.3	*15330*
89	2996	13343	20559	3.04	-0.2	0.081	939	53.1	18.5	28.5	3.55	2.10	33.07	3.84	47.3	*15290*
91	2339	11032	26413	3.03	0.5	0.059	1110	46.7	15.7	37.6	4.24	2.73	33.72	4.49	49.5	
93	2775	12737	24778	3.03	0.2	0.069	752	49.8	17.0	33.1	4.30	2.82	33.81	4.58	49.9	
95	3097	13846	26686	3.03	0.5	0.071	1892	50.4	16.9	32.6	4.22	2.73	33.73	4.50	49.6	
98	1431	5085	14977	3.00	12.6	0.067	1014	49.2	12.9	38.0	4.36	2.80	33.80	4.57	49.8	
101	1370	6350	17511	3.00	12.9	0.054	814	45.2	14.6	40.3	4.63	3.09	34.10	4.87	50.9	19280
103	1433	6199	15212	3.00	12.6	0.063	803	48.0	15.1	37.0	4.57	3.05	34.05	4.82	50.7	
105	1447	6224	15674	3.00	12.9	0.062	879	47.8	14.8	37.4	4.29	2.76	33.76	4.53	49.7	19380
109	1206	6438	15418	3.00	13.6	0.052	689	44.4	16.4	39.2	4.38	2.88	33.88	4.65	50.1	19880
111	1342	8127	15540	3.00	12.9	0.054	692					0.00	30.91	1.68	39.7	
113	1293	5660	16318	3.00	12.9	0.056	1308	44.9	18.9	36.2	4.47	3.01	34.02	4.79	50.6	
115	1244	6163	16394	3.00	13.6	0.052	569	45.6	14.0	40.4	4.53	2.98	33.98	4.76	50.5	
117	1083	5460	14377	3.00	12.9	0.052	704	44.4	15.2	40.4	4.44	2.92	33.92	4.69	50.2	20420
119	1492	6878	14090	3.00	13.6	0.066	1023	44.2	15.4	40.4	4.18	2.66	33.65	4.42	49.3	
121	1431	6791	9079	3.00	12.6	0.083	1029	49.1	16.7	34.2	3.91	2.42	33.40	4.17	48.4	20730
123	1395	7130	7785	3.00	11.9	0.086	2052	53.4	19.9	26.6	3.15	1.72	32.68	3.46	45.9	
125						54.1	22	24.0	2.71	1.32	32.27	3.04	44.48			
127	1427	6986	9652	3.00	11.9	52.5	20	27.5	2.97	1.54	32.50	3.27	45.28			
Max	5958	14176	26703	3.04	13.6	54.08	3866	72.82	29.30	61.77	32.50	3.27	45.28	4.87	50.9	
Min	246	5085	7785	3.00	-0.5	0.01	20	8.93	2.71	1.32	1.07	-0.23	30.67	1.44	38.9	
Average	2538	9616	16488	3.02	4.7	2.82	1254	51.22	16.19	28.91	5.33	2.33	33.86	4.03	47.9	
Stdev	1228	2787	5093	0.02	6.0	11.89	667	12.07	4.60	11.32	6.49	0.72	2.69	0.74	2.6	

Appendix 4-C: $MgCO_3$ content

	Bulk sediment		Fine fraction	
Depth (cm)	Peak (Å)	$MgCO_3$	Peak (Å)	$MgCO_3$
Core AL				
10	2.997	13.10		
20	2.998	12.76		
30	2.999	12.24		
40	2.998	12.59		
50	2.996	13.45		
60	2.994	13.97		
70	2.995	13.62		
80	2.999	12.41		
90	3.000	12.07		
100	2.999	12.27		
110	2.999	12.33		
120	2.999	12.39		
130	2.998	12.44		
140	2.998	12.50		
150	2.998	12.56		
160	2.999	12.41		
170	2.999	12.41		
180	2.998	12.59		
190	3.000	11.90		
200	3.001	11.72		
210	3.000	12.07		
220	3.000	11.90		
230	3.001	11.72		
240	3.000	11.90		
250	2.995	13.62		
260	2.995	13.79		
270	2.998	12.59		
280	2.999	12.24		
290	2.999	12.24		
300	2.999	12.41		
310	2.999	12.41		
320	2.999	12.41		
330	2.999	12.41		
340	2.998	12.59		
350	2.998	12.59		
360	2.998	12.76		
370	2.999	12.41		
380	2.999	12.24		
390	2.998	12.76		
400	2.998	12.76		
410	2.999	12.41		
420	2.998	12.59		
430	2.997	13.10		
440	2.996	13.45		
450	2.997	13.10		
460	2.998	12.59		
470	2.998	12.59		
480	2.998	12.59		
490	2.998	12.59		
500	2.998	12.59		
510	2.998	12.59		
520	2.996	13.45		
Core AW				
60	2.996	13.28		
70	2.998	12.59		
80	3.001	11.55		

	Bulk sediment		Fine fraction	
Depth (cm)	Peak (Å)	$MgCO_3$	Peak (Å)	$MgCO_3$
Core S2				
2	2.997	12.93	2.997	12.93
10	2.997	12.93	2.995	13.62
20	2.998	12.59	2.99	15.34
30	2.997	12.93	2.994	13.97
40	2.995	13.62	2.997	12.93
50	2.991	15.00	2.996	13.28
60	2.998	12.59	2.997	12.93
70	2.999	12.24	2.998	12.59
80	2.998	12.59	2.998	12.59
90	2.997	12.93	2.998	12.59
100	2.998	12.59	2.997	12.93
110			2.998	12.59
120			2.999	12.24
130			2.998	12.59
140			2.998	12.59
150			2.995	13.62
160			2.994	13.97
170	2.998	12.59	2.995	13.62
180			2.996	13.28
190			2.995	13.62
200			2.997	12.93
210	2.999	12.24	2.999	12.24
220	2.997	12.93	2.998	12.59
230	2.996	13.28	2.998	12.59
240	2.999	12.24	2.999	12.24
250	2.998	12.59	2.998	12.59
260	3.001	11.55	2.998	12.59
270	2.999	12.24	3	11.90
280	2.998	12.59	2.998	12.59
290	2.999	12.24	2.998	12.59
300	2.998	12.59	2.997	12.93
310	2.999	12.24	2.999	12.24
320	2.998	12.59	2.997	12.93
330	2.998	12.59	2.998	12.59
340	2.998	12.59	3.002	11.21
350	3.002	11.21	3	11.90
360	3.001	11.55	3	11.90
370	2.998	12.59	3.001	11.55
380	2.998	12.59	3.001	11.55
390	3.003	10.86	3	11.90
400	2.998	12.59	2.995	13.62
410	2.996	13.28	2.997	12.93
420	2.996	13.28	2.996	13.28
430			2.998	12.59
440			2.998	12.59
450			2.997	12.93
Core S3				
5			2.998	12.59
10			3	11.90
13			2.994	13.97
20			2.996	13.28
30			2.997	12.93
35	2.999	12.24		
40			2.999	12.24
50			2.996	13.28
65			2.998	12.59

Appendix 4-C: $MgCO_3$ content

	Bulk sediment		Fine fraction	
Depth (cm)	Peak (Å)	$MgCO_3$	Peak (Å)	$MgCO_3$
90	2.998	12.59		
100	2.999	12.24		
110	3.001	11.55		
120	2.999	12.24		
130	3	11.90		
140	2.998	12.59		
150	2.998	12.59		
160	2.996	13.28		
170	2.997	12.93		
180	2.998	12.59		
190	2.996	13.28		
200	2.998	12.59		
210	2.997	12.93		
220	2.997	12.93		
230	2.999	12.24		
240	2.998	12.59		
250	2.998	12.59		
260	2.999	12.24		
280	2.995	13.62		
290	2.996	13.28		
300	2.996	13.28		
310	2.996	13.28		
320	2.996	13.28		
330	2.994	13.97		
340	2.996	13.28		
400	2.997	12.93		
410	3	11.90		
420	2.999	12.24		
430	3	11.90		
440	3.001	11.55		
450	2.997	12.93		
460	2.999	12.24		
470	3	11.90		
480	2.999	12.24		
500	3.02	5.00		
520	3.02	5.00		
530	3.02	5.00		
540	3.02	5.00		
550	3.02	5.00		
Core S1				
1	2.998	12.59		
10	3	11.90	2.997	12.93
20	3.001	11.55	3	11.90
25	3.005	10.17		
30	3.002	11.21	3.001	11.55
40	3.02	5.00		
50	3.003	10.86		
60			2.998	
70			2.998	
80			2.997	
90			2.997	
100			2.997	
110			2.995	
120	2.998	12.59	3	11.90
130	2.998	12.59	2.999	12.24
140	2.999	12.24	2.998	12.59
150	2.999	12.24	2.997	12.93

	Bulk sediment		Fine fraction	
Depth (cm)	Peak (Å)	$MgCO_3$	Peak (Å)	$MgCO_3$
80			2.998	12.59
93	2.999	12.24	2.992	14.66
100			2.997	12.93
110			2.997	12.93
120			2.996	13.28
131	2.996	13.28	2.996	13.28
140	2.998	12.59	2.997	12.93
150	3.001	11.55	2.998	12.59
160	2.995	13.62	2.997	12.93
170	2.999	12.24	2.998	12.59
180	3.001	11.55	2.998	12.59
190	2.998	12.59	3	11.90
192	2.997	12.93	2.997	12.93
195	2.999	12.24	2.998	12.59
207	2.999	12.24	2.996	13.28
210	2.999	12.24	2.997	12.93
220	2.998	12.59	2.999	12.24
230	2.999	12.24	2.998	12.59
240	2.998	12.59	2.998	12.59
250	2.999	12.24	2.998	12.59
260	2.999	12.24	2.998	12.59
270	3	11.90	3	11.90
274	2.999	12.24	2.998	12.59
276	2.997	12.93	2.996	13.28
277			2.998	12.59
280	2.999	12.24	2.99	15.34
290	2.998	12.59	2.996	13.28
300	2.998	12.59	2.996	13.28
310	3.001	11.55	2.998	12.59
314	2.998	12.59	2.999	12.24
320	3	11.90	2.997	12.93
330	3	11.90	2.998	12.59
340	2.999	12.24	3.001	11.55
350	2.998	12.59	2.998	12.59
360	2.999	12.24	2.998	12.59
370	2.998	12.59	2.998	12.59
377	3	11.90	2.998	12.59
380	3.008	9.14	3.003	10.86
390	3	11.90	3.003	10.86
400			3	11.90
410	2.998	12.59	2.998	12.59
420	2.996	13.28	2.995	13.62
430	2.998	12.59	2.998	12.59
435			2.998	12.59
440	2.998	12.59	2.998	12.59
445			2.998	12.59
450	2.996	13.28		
Core S6				
1	2.998	12.59	2.997	12.93
10			2.998	12.59
20	2.996	13.28	2.997	12.93
30	2.998	12.59	2.998	12.59
40	2.998	12.59	2.999	12.24
50	2.998	12.59	2.999	12.24
60	2.999	12.24	2.999	12.24
70	2.998	12.59	2.998	12.59
80	2.998	12.59	3.001	11.55

Appendix 4-C: $MgCO_3$ content

	Bulk sediment		Fine fraction	
Depth (cm)	Peak (Å)	$MgCO_3$	Peak (Å)	$MgCO_3$
160	2.998	12.59	2.998	12.59
170	2.997	12.93	2.995	13.62
180	2.999	12.24	2.999	12.24
190	2.997	12.93	2.999	12.24
200	2.998	12.59	3	11.90
210	2.998	12.59	3	11.90
220	2.998	12.59	2.998	12.59
230	3	11.90	3.001	11.55
240	3.002	11.21	3	11.90
250	2.997	12.93	2.997	12.93
260	2.995	13.62	2.997	12.93
270	2.995	13.62	2.995	13.62
280	2.997	12.93	2.997	12.93
290	2.998	12.59	2.998	12.59
300	2.998	12.59	2.998	12.59
310	2.996	13.28	2.998	12.59
320	2.998	12.59	2.998	12.59
330	2.997	12.93		
360	2.998	12.59	2.998	12.59
370	2.998	12.59	2.999	12.24
380	2.998	12.59	2.998	12.59
390	2.998	12.59	2.997	12.93
400	2.996	13.28	2.997	12.93
410	2.996	13.28	2.996	13.28
420	2.997	12.93	2.996	13.28
430	2.995	13.62	2.998	12.59
440	2.999	12.24	2.999	12.24
450	2.997	12.93	2.998	12.59
460	2.995	13.62	2.997	12.93
470	2.997	12.93		
480	2.997	12.93	2.997	12.93
490	2.996	13.28	2.996	13.28
500			2.996	13.28

	Bulk sediment		Fine fraction	
Depth (cm)	Peak (Å)	$MgCO_3$	Peak (Å)	$MgCO_3$
86	2.998	12.59	3	11.90
90	2.998	12.59	3	11.90
100	3.002	11.21	2.998	12.59
110	2.997	12.93		
120	3.002	11.21	2.998	12.59
126			2.997	12.93
130			3.001	11.55
132			2.998	12.59
140			2.995	13.62
150			2.999	12.24
160	2.999	12.24		
170	2.997	12.93	2.998	12.59
180			2.998	12.59
185			2.998	12.59
190			2.998	12.59
200	2.999	12.24	2.998	12.59
210			2.997	12.93
220			2.997	12.93
230	2.998	12.59	2.998	12.59
240			2.998	12.59
250	2.999	12.24	2.998	12.59
260			2.998	12.59
270			3	11.90
274			2.996	13.28
280			2.999	12.24
285			2.999	12.24
287				
290			2.996	13.28
295			2.998	12.59
300			3	11.90
310			2.998	12.59
320	2.998	12.59	2.998	12.59
330	2.999	12.24	2.997	12.93
340	2.998	12.59	3.001	11.55
350	2.999	12.24	3	11.90
360	2.998	12.59	2.998	12.59
370	2.998	12.59	2.999	12.24
380	3	11.90	3.001	11.55
390	3.001	11.55	2.998	12.59
400	2.996	13.28	2.999	12.24
410	3	11.90	3	11.90
420	2.999	12.24		
430	3.007	9.48		
440	2.998	12.59	3.002	11.21
450	2.998	12.59	2.996	13.28
460	2.996	13.28	2.997	12.93
470	2.998	12.59	2.999	12.24

Appendix 4-D: Aragonite/calcite-stacks

	Cores (mineral %)						Stacks (average mineral %)					
Age (ky)	**AL**	**AW**	**S1**	**S2**	**S3**	**S6**	**Abington**	**stdev**	**Sanganeb**	**stdev**	**Sudan**	**stdev**
Aragonite												
1				60.9					60.9	0.0	60.9	0.0
2	64.0			57.5			64.0	0.0	57.5	0.0	60.8	3.2
3	64.3			59.4			64.3	0.0	59.4	0.0	61.8	2.4
4	63.8			58.1			63.8	0.0	58.1	0.0	61.0	2.8
5	63.5			58.3			63.5	0.0	58.3	0.0	60.9	2.6
6	63.9			60.2		55.7	63.9	0.0	58.0	2.3	59.9	3.4
7	67.1			70.1		58.3	67.1	0.0	64.2	5.9	65.2	5.0
8	68.4			77.2		58.6	68.4	0.0	67.9	9.3	68.1	7.6
9	68.0			78.5		61.7	68.0	0.0	70.1	8.4	69.4	6.9
10	66.9			79.9	70.5	64.2	66.9	0.0	71.5	6.4	70.4	5.9
11	65.8			81.2	64.9	66.7	65.8	0.0	70.9	7.3	69.6	6.7
12	64.6			82.5	59.4	69.2	64.6	0.0	70.3	9.5	68.9	8.6
13	63.5			83.8	53.8	71.7	63.5	0.0	69.8	12.3	68.2	11.0
14	62.4		69.9	83.1	48.2	50.1	62.4	0.0	62.8	14.5	62.7	12.9
15	61.2		65.9	82.4	43.8	55.3	61.2	0.0	61.8	14.2	61.7	12.7
16	60.1		61.8	81.7	50.3	57.6	60.1	0.0	62.8	11.6	62.3	10.5
17	59.0		57.8	80.9	56.7	60.1	59.0	0.0	63.9	9.9	62.9	9.1
18	57.8		53.8	80.2	63.1	58.8	57.8	0.0	64.0	9.9	62.7	9.2
19	56.7		49.8	79.5	69.5	57.5	56.7	0.0	64.1	11.4	62.6	10.6
20	55.6		45.7	78.8	75.9	57.5	55.6	0.0	64.5	13.6	62.7	12.6
21	54.4		41.7	72.5	71.7	57.5	54.4	0.0	60.9	12.6	59.6	11.5
22	55.6		42.0	66.2	65.8	57.6	55.6	0.0	57.9	9.8	57.5	8.8
23	59.8		46.5	60.0	60.0	57.2	59.8	0.0	55.9	5.5	56.7	5.2
24	59.5		51.1	53.7	49.4	55.6	59.5	0.0	52.4	2.4	53.8	3.5
25	62.0		49.6	53.4	55.9	54.0	62.0	0.0	53.2	2.3	55.0	4.1
26	60.8		47.1	52.8	54.1	52.4	60.8	0.0	51.6	2.7	53.4	4.4
27	59.3		44.5	52.1	51.9	50.9	59.3	0.0	49.8	3.1	51.7	4.7
28	59.8		41.2	58.6	60.4	51.8	59.8	0.0	53.0	7.5	54.4	7.3
29	61.1	59.0	37.9	52.4	54.9	54.2	60.1	1.1	49.9	6.9	53.3	7.5
30	62.5	59.2	39.7	48.3	52.7	56.5	60.8	1.7	49.3	6.3	53.1	7.5
31	63.7	59.3	44.6	48.5	54.7	58.7	61.5	2.2	51.6	5.5	54.9	6.6
32	64.9	59.5	49.4	53.0	55.0	59.4	62.2	2.7	54.2	3.6	56.9	5.0
33	66.0	59.6	44.5	59.7	55.7	57.6	62.8	3.2	54.4	5.9	57.2	6.5
34	66.5	59.8	39.5	52.6	57.8	57.6	63.1	3.4	51.9	7.4	55.6	8.3
35	66.1	59.9	37.7	47.9	60.2	55.0	63.0	3.1	50.2	8.4	54.5	9.3
36	65.8	60.4	41.1	48.1	61.1	50.4	63.1	2.7	50.2	7.2	54.5	8.6
37	65.2	60.8	44.5	50.1	59.4	51.7	63.0	2.2	51.5	5.3	55.3	7.1
38	64.4	61.3	47.1	53.2	61.5	55.0	62.8	1.5	54.2	5.1	57.1	5.9
39	63.6	61.8	49.3	54.1	65.1	58.5	62.7	0.9	56.7	5.8	58.7	5.5
40	63.6	62.2	51.6	55.2	58.6	59.1	62.9	0.7	56.1	3.0	58.4	4.1
41	63.6	62.7	54.5	56.6	54.7	57.4	63.2	0.5	55.8	1.2	58.2	3.6
42	63.8	62.1	57.4	55.3	57.8	56.6	62.9	0.8	56.8	0.9	58.8	3.0
43	64.3	61.5	56.6	52.7	59.3	58.2	62.9	1.4	56.7	2.5	58.8	3.7
44	64.9	61.0	52.1	54.9	60.6	58.4	62.9	2.0	56.5	3.2	58.6	4.2
45	65.4	60.4	47.6	56.7	61.9	59.1	62.9	2.5	56.3	5.4	58.5	5.6
46	65.7	59.8	47.6	57.4	62.4	60.4	62.8	3.0	57.0	5.7	58.9	5.6
47	66.1	59.2	48.4	58.9	62.1	63.2	62.6	3.4	58.1	5.9	59.6	5.6
48	66.3	59.8	49.5	60.7	60.4	63.9	63.0	3.2	58.6	5.5	60.1	5.3
49	66.4	60.3	51.8	57.4	60.9	63.8	63.4	3.0	58.5	4.4	60.1	4.6
50	66.5	60.9	54.2	55.7	62.5	63.7	63.7	2.8	59.0	4.1	60.6	4.3
51	66.1	61.5	54.2	57.3	65.8	61.3	63.8	2.3	59.6	4.3	61.0	4.3
52	65.7	62.0	52.8	59.3	64.1	59.2	63.9	1.8	58.8	4.0	60.5	4.2
53	65.2	62.6	51.4	61.5	58.5	57.9	63.9	1.3	57.3	3.7	59.5	4.4

Appendix 4-D: Aragonite/calcite-stacks

	Cores (mineral %)						Stacks (average mineral %)					
Age (ky)	**AL**	**AW**	**S1**	**S2**	**S3**	**S6**	**Abington**	**stdev**	**Sanganeb**	**stdev**	**Sudan**	**stdev**
54	64.3	61.9	48.6	58.7	57.8	56.5	63.1	1.2	55.4	4.0	58.0	4.9
55	63.4	61.3	45.9	55.8	57.0	55.1	62.3	1.0	53.5	4.4	56.4	5.6
56	62.5	60.6	43.1	53.0	56.3	53.8	61.6	0.9	51.5	5.0	54.9	6.3
57	61.6	59.4	40.3	50.3	54.6	52.4	60.5	1.1	49.4	5.4	53.1	6.9
58	60.7	57.1	37.6	47.8	50.9	51.0	58.9	1.8	46.8	5.5	50.8	7.3
59	59.5	54.8	35.5	45.2	47.3	48.9	57.1	2.3	44.2	5.2	48.5	7.5
60	58.0	52.5	34.2	42.7	43.6	46.2	55.2	2.8	41.7	4.5	46.2	7.5
61	56.5	49.7	32.9	40.4	41.4	43.4	53.1	3.4	39.5	4.0	44.1	7.4
62	55.0	46.7	31.6	38.1	39.9	40.6	50.9	4.2	37.6	3.6	42.0	7.3
63	53.6	43.7	30.3	35.9	38.4	37.9	48.6	4.9	35.6	3.2	40.0	7.3
64	52.1	40.7	29.0	33.6	36.9	35.1	46.4	5.7	33.7	2.9	37.9	7.3
65	51.7	42.8	26.2				47.3	4.4	26.2	0.0	40.2	10.6
66	52.3	45.0	24.9				48.7	3.7	24.9	0.0	40.7	11.6
67	53.8	45.4	29.2				49.6	4.2	29.2	0.0	42.8	10.2
68	54.5	45.0	34.5				49.8	4.8	34.5	0.0	44.7	8.2
69	56.0	46.2	41.0				51.1	4.9	41.0	0.0	47.8	6.2
70	57.6	49.4	41.6				53.5	4.1	41.6	0.0	49.5	6.6
71	57.8	52.3	39.2				55.1	2.8	39.2	0.0	49.8	7.8
72	56.7	52.8	34.1				54.7	2.0	34.1	0.0	47.9	9.9
73	55.5	53.2	29.9				54.4	1.1	29.9	0.0	46.2	11.6
74	55.6	53.0	35.3				54.3	1.3	35.3	0.0	48.0	9.0
75	57.8	52.7	39.0				55.2	2.6	39.0	0.0	49.8	8.0
76	60.8	53.5	39.2				57.1	3.6	39.2	0.0	51.2	9.0
77	64.0	55.3	41.8				59.7	4.3	41.8	0.0	53.7	9.1
78	65.9	57.2	46.3				61.5	4.4	46.3	0.0	56.5	8.0
79	66.1	59.1	50.5				62.6	3.5	50.5	0.0	58.6	6.4
80	64.3	61.1	54.5				62.7	1.6	54.5	0.0	60.0	4.1
81	62.2	59.5	50.8				60.8	1.4	50.8	0.0	57.5	4.9
82	60.1	57.8	47.0				59.0	1.1	47.0	0.0	55.0	5.7
83	58.0	56.2	43.3				57.1	0.9	43.3	0.0	52.5	6.6
84	56.4	53.9	40.5				55.1	1.3	40.5	0.0	50.2	7.0
85	55.2	50.8	38.6				53.0	2.2	38.6	0.0	48.2	7.0
86	53.9	47.7	36.7				50.8	3.1	36.7	0.0	46.1	7.1
87	52.7	44.6	34.8				48.7	4.0	34.8	0.0	44.0	7.3
88		47.0					47.0	0.0			47.0	0.0
89		49.4					49.4	0.0			49.4	0.0
90		51.8					51.8	0.0			51.8	0.0
91		54.2					54.2	0.0			54.2	0.0
92		55.2					55.2	0.0			55.2	0.0
93		56.2					56.2	0.0			56.2	0.0
94		57.1					57.1	0.0			57.1	0.0
95		58.1					58.1	0.0			58.1	0.0
96		56.8					56.8	0.0			56.8	0.0
97		55.5					55.5	0.0			55.5	0.0
98		54.2					54.2	0.0			54.2	0.0
99		52.9					52.9	0.0			52.9	0.0
100		54.0					54.0	0.0			54.0	0.0
101		55.0					55.0	0.0			55.0	0.0
102		55.0					55.0	0.0			55.0	0.0
103		52.0					52.0	0.0			52.0	0.0
104		49.0					49.0	0.0			49.0	0.0
105		48.0					48.0	0.0			48.0	0.0
106		48.9					48.9	0.0			48.9	0.0
107		49.8					49.8	0.0			49.8	0.0

Appendix 4-D: Aragonite/calcite-stacks

	Cores (mineral %)						Stacks (average mineral %)					
Age (ky)	**AL**	**AW**	**S1**	**S2**	**S3**	**S6**	**Abington**	**stdev**	**Sanganeb**	**stdev**	**Sudan**	**stdev**
108		49.4					49.4	0.0			49.4	0.0
109		48.7					48.7	0.0			48.7	0.0
110		47.9					47.9	0.0			47.9	0.0
111		49.4					49.4	0.0			49.4	0.0
112		51.0					51.0	0.0			51.0	0.0
113		52.9					52.9	0.0			52.9	0.0
114		55.1					55.1	0.0			55.1	0.0
115		56.6					56.6	0.0			56.6	0.0
116		55.3					55.3	0.0			55.3	0.0
117		54.1					54.1	0.0			54.1	0.0
118		55.4					55.4	0.0			55.4	0.0
119		57.4					57.4	0.0			57.4	0.0
120		58.8					58.8	0.0			58.8	0.0
121		59.2					59.2	0.0			59.2	0.0
122		59.6					59.6	0.0			59.6	0.0
Mg-calcite												
1	23.1			20.7			23.1	0.0	20.7	0.0	21.9	1.2
2	23.3			24.3			23.3	0.0	24.3	0.0	23.8	0.5
3	23.2			22.2			23.2	0.0	22.2	0.0	22.7	0.5
4	22.7			20.6			22.7	0.0	20.6	0.0	21.6	1.1
5	23.0			21.7			23.0	0.0	21.7	0.0	22.4	0.7
6	22.5			20.2		55.7	22.5	0.0	38.0	17.8	32.8	16.2
7	19.9			13.9		58.3	19.9	0.0	36.1	22.2	30.7	19.7
8	19.2			9.6		58.6	19.2	0.0	34.1	24.5	29.1	21.2
9	20.2			9.4		61.7	20.2	0.0	35.6	26.1	30.4	22.5
10	21.5			9.3	14.0	64.2	21.5	0.0	29.2	24.9	27.2	21.8
11	22.8			9.2	18.8	66.7	22.8	0.0	31.5	25.2	29.4	22.1
12	24.0			9.0	23.6	69.2	24.0	0.0	33.9	25.6	31.5	22.6
13	25.3			8.9	28.3	71.7	25.3	0.0	36.3	26.3	33.6	23.2
14	26.6		13.8	8.9	33.1	50.1	26.6	0.0	26.5	16.4	26.5	14.6
15	27.9		18.1	8.9	36.8	55.3	27.9	0.0	29.8	17.9	29.4	16.0
16	29.2		22.4	8.9	31.2	57.6	29.2	0.0	30.0	17.8	29.9	15.9
17	30.4		26.7	8.8	25.6	60.1	30.4	0.0	30.3	18.6	30.3	16.6
18	31.7		31.1	8.8	19.9	58.8	31.7	0.0	29.7	18.6	30.1	16.6
19	33.0		35.4	8.8	14.3	57.5	33.0	0.0	29.0	19.2	29.8	17.3
20	34.3		39.7	8.8	8.7	57.5	34.3	0.0	28.7	20.9	29.8	18.8
21	35.6		44.0	14.3	12.8	57.5	35.6	0.0	32.2	19.2	32.8	17.3
22	34.3		42.1	19.8	18.5	57.6	34.3	0.0	34.5	16.3	34.4	14.6
23	29.5		34.0	25.2	24.1	57.2	29.5	0.0	35.1	13.3	34.0	12.1
24	28.0		25.9	30.7	37.3	55.6	28.0	0.0	37.4	11.3	35.5	10.8
25	23.5		26.8	30.3	29.0	54.0	23.5	0.0	35.0	11.0	32.7	10.9
26	23.6		29.1	30.6	26.3	52.4	23.6	0.0	34.6	10.4	32.4	10.3
27	25.5		31.8	31.4	22.0	50.9	25.5	0.0	34.0	10.5	32.3	10.0
28	24.6		36.0	25.3	20.7	51.8	24.6	0.0	33.5	12.0	31.7	11.3
29	23.6	22.7	40.1	30.7	30.3	54.2	23.1	0.4	38.8	9.7	33.6	10.8
30	22.5	22.5	38.9	34.1	33.3	56.5	22.5	0.0	40.7	9.4	34.6	11.5
31	21.5	22.3	34.3	33.3	28.1	58.7	21.9	0.4	38.6	11.9	33.0	12.5
32	20.8	22.1	29.8	27.8	24.9	59.4	21.5	0.6	35.5	13.9	30.8	13.2
33	20.1	21.9	29.0	20.0	23.0	57.6	21.0	0.9	32.4	14.9	28.6	13.3
34	19.7	21.7	28.2	30.3	23.1	57.6	20.7	1.0	34.8	13.4	30.1	12.8
35	19.5	21.5	27.8	34.9	22.1	55.0	20.5	1.0	35.0	12.4	30.2	12.2
36	19.4	20.9	28.2	28.0	23.0	50.4	20.2	0.7	32.4	10.6	28.3	10.4
37	19.6	20.2	28.5	25.6	22.5	51.7	19.9	0.3	32.1	11.5	28.0	11.0

Appendix 4-D: Aragonite/calcite-stacks

	Cores (mineral %)						Stacks (average mineral %)					
Age (ky)	**AL**	**AW**	**S1**	**S2**	**S3**	**S6**	**Abington**	**stdev**	**Sanganeb**	**stdev**	**Sudan**	**stdev**
38	19.9	19.6	28.5	25.4	21.7	55.0	19.8	0.2	32.7	13.1	28.4	12.3
39	20.3	19.0	28.4	23.8	20.9	58.5	19.6	0.6	32.9	15.0	28.5	13.8
40	20.4	18.3	28.1	23.1	24.6	59.1	19.3	1.0	33.7	14.8	28.9	13.8
41	20.4	17.7	26.2	24.1	27.1	57.4	19.1	1.4	33.7	13.7	28.8	13.2
42	20.5	18.6	24.3	24.7	22.5	56.6	19.5	0.9	32.0	14.2	27.9	13.0
43	20.1	19.4	23.6	25.0	21.1	58.2	19.8	0.3	32.0	15.2	27.9	13.7
44	19.7	20.3	24.1	22.1	20.8	58.4	20.0	0.3	31.3	15.7	27.6	13.9
45	19.4	21.2	24.5	20.8	22.0	59.1	20.3	0.9	31.6	15.9	27.8	14.1
46	19.3	22.0	25.0	22.9	21.5	60.4	20.6	1.4	32.5	16.2	28.5	14.4
47	19.1	22.9	25.5	22.0	20.4	63.2	21.0	1.9	32.7	17.7	28.8	15.5
48	19.0	21.9	25.3	19.5	18.8	63.9	20.4	1.4	31.9	18.7	28.1	16.2
49	19.0	20.8	23.3	21.8	17.6	63.8	19.9	0.9	31.6	18.7	27.7	16.2
50	19.0	19.8	21.3	22.4	16.5	63.7	19.4	0.4	31.0	19.0	27.1	16.5
51	18.7	18.7	20.3	19.6	15.6	61.3	18.7	0.0	29.2	18.6	25.7	16.0
52	18.3	17.7	19.9	17.3	16.6	59.2	18.0	0.3	28.2	17.9	24.8	15.4
53	17.9	16.6	19.5	15.1	19.2	57.9	17.3	0.7	27.9	17.4	24.4	15.1
54	18.9	16.6	22.6	17.0	18.5	56.5	17.7	1.1	28.7	16.2	25.0	14.2
55	19.8	16.5	25.6	18.9	17.9	55.1	18.2	1.6	29.4	15.2	25.7	13.5
56	20.8	16.5	28.7	20.7	17.2	53.8	18.7	2.1	30.1	14.3	26.3	12.9
57	21.8	17.1	31.8	23.9	18.6	52.4	19.4	2.3	31.7	12.9	27.6	12.0
58	22.7	19.0	34.9	29.6	23.9	51.0	20.9	1.9	34.8	10.1	30.2	10.6
59	24.2	20.9	38.3	35.3	29.2	48.9	22.5	1.6	37.9	7.1	32.8	9.4
60	26.2	22.8	42.0	41.0	34.5	46.2	24.5	1.7	40.9	4.2	35.5	8.5
61	28.2	27.1	45.8	44.1	38.2	43.4	27.6	0.5	42.9	2.9	37.8	7.6
62	30.1	32.6	49.6	46.0	41.0	40.6	31.4	1.3	44.3	3.7	40.0	6.8
63	32.1	38.2	53.3	47.8	43.8	37.9	35.1	3.0	45.7	5.7	42.2	7.0
64	34.1	43.7	57.1	49.7	46.6	35.1	38.9	4.8	47.1	7.9	44.4	8.0
65	34.0	39.0	50.4				36.5	2.5	50.4	0.0	41.1	6.9
66	32.7	34.4	45.9				33.5	0.8	45.9	0.0	37.6	5.9
67	30.6	34.1	48.9				32.3	1.7	48.9	0.0	37.9	7.9
68	29.6	35.6	48.1				32.6	3.0	48.1	0.0	37.8	7.7
69	27.3	34.8	42.5				31.1	3.8	42.5	0.0	34.9	6.2
70	24.7	31.0	37.7				27.8	3.2	37.7	0.0	31.1	5.3
71	23.3	27.6	33.4				25.5	2.2	33.4	0.0	28.1	4.1
72	23.9	27.2	40.5				25.5	1.7	40.5	0.0	30.5	7.2
73	24.9	26.8	47.0				25.9	0.9	47.0	0.0	32.9	10.0
74	25.5	26.4	37.7				25.9	0.4	37.7	0.0	29.9	5.6
75	23.5	26.0	31.5				24.7	1.3	31.5	0.0	27.0	3.4
76	21.0	24.8	31.5				22.9	1.9	31.5	0.0	25.8	4.3
77	18.8	22.9	29.1				20.9	2.1	29.1	0.0	23.6	4.3
78	18.5	21.3	24.9				19.9	1.4	24.9	0.0	21.6	2.6
79	19.0	20.4	22.5				19.7	0.7	22.5	0.0	20.6	1.5
80	20.2	19.4	20.6				19.8	0.4	20.6	0.0	20.1	0.5
81	21.9	20.9	25.1				21.4	0.5	25.1	0.0	22.6	1.8
82	23.6	22.4	29.5				23.0	0.6	29.5	0.0	25.2	3.1
83	25.3	23.9	34.0				24.6	0.7	34.0	0.0	27.7	4.5
84	26.6	25.8	36.9				26.2	0.4	36.9	0.0	29.8	5.0
85	27.6	28.3	38.3				28.0	0.3	38.3	0.0	31.4	4.9
86	28.7	30.7	39.7				29.7	1.0	39.7	0.0	33.0	4.8
87	29.7	33.2	41.1				31.5	1.7	41.1	0.0	34.7	4.8
88		31.0					31.0	0.0			31.0	0.0
89		28.9					28.9	0.0			28.9	0.0
90		26.7					26.7	0.0			26.7	0.0
91		24.5					24.5	0.0			24.5	0.0

Appendix 4-D: Aragonite/calcite-stacks

	Cores (mineral %)						Stacks (average mineral %)					
Age (ky)	**AL**	**AW**	**S1**	**S2**	**S3**	**S6**	**Abington**	**stdev**	**Sanganeb**	**stdev**	**Sudan**	**stdev**
92		24.0					24.0	0.0			24.0	0.0
93		23.5					23.5	0.0			23.5	0.0
94		22.9					22.9	0.0			22.9	0.0
95		22.4					22.4	0.0			22.4	0.0
96		22.7					22.7	0.0			22.7	0.0
97		23.1					23.1	0.0			23.1	0.0
98		23.4					23.4	0.0			23.4	0.0
99		23.7					23.7	0.0			23.7	0.0
100		23.4					23.4	0.0			23.4	0.0
101		23.0					23.0	0.0			23.0	0.0
102		23.2					23.2	0.0			23.2	0.0
103		24.6					24.6	0.0			24.6	0.0
104		26.0					26.0	0.0			26.0	0.0
105		27.3					27.3	0.0			27.3	0.0
106		28.6					28.6	0.0			28.6	0.0
107		29.8					29.8	0.0			29.8	0.0
108		30.0					30.0	0.0			30.0	0.0
109		29.9					29.9	0.0			29.9	0.0
110		29.8					29.8	0.0			29.8	0.0
111		29.1					29.1	0.0			29.1	0.0
112		28.3					28.3	0.0			28.3	0.0
113		26.9					26.9	0.0			26.9	0.0
114		24.9					24.9	0.0			24.9	0.0
115		23.4					23.4	0.0			23.4	0.0
116		23.7					23.7	0.0			23.7	0.0
117		23.9					23.9	0.0			23.9	0.0
118		21.9					21.9	0.0			21.9	0.0
119		19.4					19.4	0.0			19.4	0.0
120		17.2					17.2	0.0			17.2	0.0
121		15.3					15.3	0.0			15.3	0.0
122		13.5					13.5	0.0			13.5	0.0
HMC + Aragonite												
1				81.6					81.6	0.0	81.6	0.0
2	87.3			81.9			87.3	0.0	81.9	0.0	84.6	2.7
3	87.4			81.5			87.4	0.0	81.5	0.0	84.5	3.0
4	86.5			78.7			86.5	0.0	78.7	0.0	82.6	3.9
5	86.6			80.0			86.6	0.0	80.0	0.0	83.3	3.3
6	86.4			80.4		76.3	86.4	0.0	78.4	2.1	81.0	4.1
7	87.1			84.0		77.2	87.1	0.0	80.6	3.4	82.8	4.1
8	87.6			86.8		75.8	87.6	0.0	81.3	5.5	83.4	5.4
9	88.2			88.0		79.6	88.2	0.0	83.8	4.2	85.3	4.0
10	88.4			89.2	84.5	80.3	88.4	0.0	84.6	3.6	85.6	3.5
11	88.5			90.3	83.7	80.9	88.5	0.0	85.0	3.9	85.9	3.7
12	88.7			91.5	82.9	81.6	88.7	0.0	85.3	4.4	86.2	4.1
13	88.8			92.7	82.1	82.2	88.8	0.0	85.7	5.0	86.5	4.5
14	89.0		83.7	92.0	81.3	76.6	89.0	0.0	83.4	5.6	84.5	5.4
15	89.1		84.0	91.2	80.7	79.3	89.1	0.0	83.8	4.6	84.9	4.6
16	89.3		84.3	90.5	81.5	76.8	89.3	0.0	83.2	5.0	84.5	5.1
17	89.4		84.6	89.8	82.2	80.6	89.4	0.0	84.3	3.5	85.3	3.7
18	89.6		84.9	89.1	83.0	79.9	89.6	0.0	84.2	3.3	85.3	3.7
19	89.7		85.2	88.3	83.8	79.1	89.7	0.0	84.1	3.3	85.2	3.7
20	89.9		85.5	87.6	84.6	75.1	89.9	0.0	83.2	4.8	84.5	5.1
21	90.0		85.8	86.8	84.5	72.9	90.0	0.0	82.5	5.6	84.0	5.9

Appendix 4-D: Aragonite/calcite-stacks

	Cores (mineral %)						Stacks (average mineral %)					
Age (ky)	AL	AW	S1	S2	S3	S6	Abington	stdev	Sanganeb	stdev	Sudan	stdev
22	89.9		84.1	86.0	84.3	79.8	89.9	0.0	83.5	2.3	84.8	3.3
23	89.3		80.5	85.2	84.1	83.5	89.3	0.0	83.3	1.7	84.5	2.8
24	87.5		77.0	84.4	86.7	80.9	87.5	0.0	82.2	3.7	83.3	3.9
25	85.5		76.4	83.7	84.9	78.3	85.5	0.0	80.8	3.6	81.8	3.7
26	84.4		76.2	83.4	80.4	75.7	84.4	0.0	78.9	3.2	80.0	3.6
27	84.8		76.3	83.5	73.9	73.1	84.8	0.0	76.7	4.1	78.3	4.9
28	84.4		77.2	83.9	81.1	73.0	84.4	0.0	78.8	4.1	79.9	4.3
29	84.7	81.7	78.1	83.2	85.1	74.3	83.2	1.5	80.2	4.3	81.2	3.9
30	85.0	81.7	78.6	82.5	86.0	75.5	83.3	1.7	80.6	3.9	81.5	3.6
31	85.3	81.6	78.9	81.7	82.8	78.5	83.4	1.8	80.5	1.8	81.5	2.3
32	85.7	81.6	79.2	80.8	79.9	80.2	83.6	2.1	80.0	0.6	81.2	2.1
33	86.1	81.5	73.5	79.7	78.7	79.2	83.8	2.3	77.7	2.5	79.8	3.7
34	86.1	81.5	67.7	82.9	80.9	75.9	83.8	2.3	76.9	5.9	79.2	5.9
35	85.7	81.4	65.5	82.9	82.4	79.9	83.5	2.1	77.7	7.1	79.6	6.5
36	85.2	81.2	69.3	76.0	84.1	72.3	83.2	2.0	75.4	5.5	78.0	6.0
37	84.8	81.1	73.1	75.7	81.9	73.2	82.9	1.9	76.0	3.6	78.3	4.5
38	84.3	80.9	75.6	78.6	83.1	77.7	82.6	1.7	78.7	2.8	80.0	3.1
39	83.9	80.7	77.7	77.9	86.0	82.1	82.3	1.6	80.9	3.4	81.4	3.0
40	83.9	80.6	79.6	78.2	83.2	81.0	82.2	1.7	80.5	1.8	81.1	2.0
41	84.1	80.4	80.7	80.8	81.7	76.2	82.2	1.8	79.8	2.2	80.6	2.3
42	84.2	80.7	81.8	80.0	80.3	74.3	82.5	1.8	79.1	2.9	80.2	3.0
43	84.4	81.0	80.3	77.7	80.4	78.0	82.7	1.7	79.1	1.2	80.3	2.2
44	84.7	81.3	76.2	77.0	81.4	78.3	83.0	1.7	78.2	2.0	79.8	2.9
45	84.8	81.5	72.1	77.5	83.9	79.9	83.2	1.7	78.4	4.3	80.0	4.3
46	85.0	81.8	72.6	80.3	83.8	82.1	83.4	1.6	79.7	4.3	81.0	4.0
47	85.1	82.1	73.8	80.9	82.5	80.8	83.6	1.5	79.5	3.3	80.9	3.5
48	85.3	81.6	74.8	80.2	79.2	81.2	83.4	1.8	78.8	2.4	80.4	3.1
49	85.4	81.1	75.1	79.2	78.4	82.0	83.3	2.1	78.7	2.5	80.2	3.2
50	85.5	80.7	75.5	78.1	79.0	82.1	83.1	2.4	78.7	2.4	80.1	3.2
51	84.8	80.2	74.5	76.9	81.4	80.0	82.5	2.3	78.2	2.7	79.6	3.3
52	84.0	79.7	72.7	76.5	80.7	77.5	81.8	2.1	76.9	2.9	78.5	3.5
53	83.1	79.2	70.9	76.6	77.7	74.9	81.2	1.9	75.0	2.6	77.1	3.7
54	83.2	78.5	71.2	75.6	76.3	75.1	80.8	2.3	74.6	2.0	76.7	3.6
55	83.2	77.8	71.5	74.7	74.9	75.3	80.5	2.7	74.1	1.5	76.2	3.6
56	83.3	77.2	71.8	73.7	73.5	75.5	80.2	3.1	73.6	1.3	75.8	3.7
57	83.3	76.6	72.1	74.2	73.2	75.7	79.9	3.4	73.8	1.3	75.8	3.7
58	83.4	76.1	72.4	77.4	74.8	75.9	79.7	3.6	75.1	1.8	76.7	3.4
59	83.7	75.7	73.8	80.5	76.5	76.6	79.7	4.0	76.9	2.4	77.8	3.3
60	84.2	75.2	76.3	83.7	78.2	77.8	79.7	4.5	79.0	2.8	79.2	3.5
61	84.7	76.8	78.7	84.5	79.6	79.0	80.7	3.9	80.5	2.4	80.6	3.0
62	85.2	79.3	81.2	84.1	80.9	80.3	82.3	2.9	81.6	1.5	81.8	2.1
63	85.7	81.9	83.6	83.7	82.2	81.5	83.8	1.9	82.8	1.0	83.1	1.4
64	86.2	84.4	86.1	83.3	83.5	82.7	85.3	0.9	83.9	1.3	84.4	1.4
65	85.6	81.9	76.6				83.8	1.9	76.6	0.0	81.4	3.7
66	85.0	79.3	70.8				82.2	2.8	70.8	0.0	78.4	5.8
67	84.4	79.4	78.1				81.9	2.5	78.1	0.0	80.6	2.7
68	84.1	80.6	82.6				82.4	1.7	82.6	0.0	82.4	1.4
69	83.3	81.0	83.5				82.2	1.2	83.5	0.0	82.6	1.1
70	82.3	80.4	79.3				81.4	0.9	79.3	0.0	80.7	1.2
71	81.1	79.9	72.5				80.5	0.6	72.5	0.0	77.9	3.8
72	80.6	80.0	74.6				80.3	0.3	74.6	0.0	78.4	2.7
73	80.5	80.0	76.9				80.2	0.2	76.9	0.0	79.1	1.6
74	81.1	79.4	73.0				80.2	0.9	73.0	0.0	77.8	3.5
75	81.3	78.6	70.5				80.0	1.3	70.5	0.0	76.8	4.6

Appendix 4-D: Aragonite/calcite-stacks

	Cores (mineral %)						Stacks (average mineral %)					
Age (ky)	**AL**	**AW**	**S1**	**S2**	**S3**	**S6**	**Abington**	**stdev**	**Sanganeb**	**stdev**	**Sudan**	**stdev**
76	81.8	78.3	70.7				80.0	1.7	70.7	0.0	76.9	4.6
77	82.8	78.2	71.0				80.5	2.3	71.0	0.0	77.3	4.9
78	84.4	78.5	71.2				81.4	3.0	71.2	0.0	78.0	5.4
79	85.1	79.5	73.0				82.3	2.8	73.0	0.0	79.2	4.9
80	84.5	80.5	75.1				82.5	2.0	75.1	0.0	80.0	3.9
81	84.1	80.4	75.8				82.2	1.9	75.8	0.0	80.1	3.4
82	83.7	80.2	76.5				82.0	1.7	76.5	0.0	80.1	2.9
83	83.3	80.1	77.2				81.7	1.6	77.2	0.0	80.2	2.5
84	83.0	79.7	77.4				81.3	1.7	77.4	0.0	80.0	2.3
85	82.8	79.1	76.9				80.9	1.9	76.9	0.0	79.6	2.4
86	82.6	78.4	76.4				80.5	2.1	76.4	0.0	79.1	2.6
87	82.4	77.8	75.9				80.1	2.3	75.9	0.0	78.7	2.7
88		78.0					78.0	0.0			78.0	0.0
89		78.3					78.3	0.0			78.3	0.0
90		78.5					78.5	0.0			78.5	0.0
91		78.7					78.7	0.0			78.7	0.0
92		79.2					79.2	0.0			79.2	0.0
93		79.6					79.6	0.0			79.6	0.0
94		80.1					80.1	0.0			80.1	0.0
95		80.5					80.5	0.0			80.5	0.0
96		79.5					79.5	0.0			79.5	0.0
97		78.6					78.6	0.0			78.6	0.0
98		77.6					77.6	0.0			77.6	0.0
99		76.6					76.6	0.0			76.6	0.0
100		77.3					77.3	0.0			77.3	0.0
101		78.1					78.1	0.0			78.1	0.0
102		78.2					78.2	0.0			78.2	0.0
103		76.6					76.6	0.0			76.6	0.0
104		75.0					75.0	0.0			75.0	0.0
105		75.3					75.3	0.0			75.3	0.0
106		77.4					77.4	0.0			77.4	0.0
107		79.6					79.6	0.0			79.6	0.0
108		79.4					79.4	0.0			79.4	0.0
109		78.6					78.6	0.0			78.6	0.0
110		77.7					77.7	0.0			77.7	0.0
111		78.5					78.5	0.0			78.5	0.0
112		79.3					79.3	0.0			79.3	0.0
113		79.8					79.8	0.0			79.8	0.0
114		80.0					80.0	0.0			80.0	0.0
115		80.0					80.0	0.0			80.0	0.0
116		79.0					79.0	0.0			79.0	0.0
117		77.9					77.9	0.0			77.9	0.0
118		77.3					77.3	0.0			77.3	0.0
119		76.8					76.8	0.0			76.8	0.0
120		75.9					75.9	0.0			75.9	0.0
121		74.5					74.5	0.0			74.5	0.0
122		73.1					73.1	0.0			73.1	0.0
Calcite												
1				18.4					18.4	0.0	18.4	0.0
2	12.7			18.1			12.7	0.0	18.1	0.0	15.4	2.7
3	12.6			18.5			12.6	0.0	18.5	0.0	15.5	3.0
4	13.5			21.3			13.5	0.0	21.3	0.0	17.4	3.9
5	13.4			20.0			13.4	0.0	20.0	0.0	16.7	3.3

Appendix 4-D: Aragonite/calcite-stacks

	Cores (mineral %)						Stacks (average mineral %)					
Age (ky)	**AL**	**AW**	**S1**	**S2**	**S3**	**S6**	**Abington**	**stdev**	**Sanganeb**	**stdev**	**Sudan**	**stdev**
6	13.6			19.6		23.7	13.6	0.0	21.7	2.1	19.0	4.1
7	12.9			16.0		22.8	12.9	0.0	19.4	3.4	17.2	4.1
8	12.4			13.2		24.2	12.4	0.0	18.7	5.5	16.6	5.4
9	11.8			12.0		20.4	11.8	0.0	16.2	4.2	14.7	4.0
10	11.6			10.8	15.5	19.7	11.6	0.0	15.4	3.6	14.4	3.5
11	11.5			9.7	16.3	19.1	11.5	0.0	15.0	3.9	14.1	3.7
12	11.3			8.5	17.1	18.4	11.3	0.0	14.7	4.4	13.8	4.1
13	11.2			7.3	17.9	17.8	11.2	0.0	14.3	5.0	13.5	4.5
14	11.0		16.4	8.0	18.7	23.4	11.0	0.0	16.6	5.6	15.5	5.4
15	10.9		16.1	8.8	19.3	20.7	10.9	0.0	16.2	4.6	15.1	4.6
16	10.7		15.8	9.5	18.5	23.2	10.7	0.0	16.8	5.0	15.5	5.1
17	10.6		15.5	10.2	17.8	19.4	10.6	0.0	15.7	3.5	14.7	3.7
18	10.4		15.2	10.9	17.0	20.2	10.4	0.0	15.8	3.3	14.7	3.7
19	10.3		14.9	11.7	16.2	20.9	10.3	0.0	15.9	3.3	14.8	3.7
20	10.1		14.6	12.4	15.4	24.9	10.1	0.0	16.8	4.8	15.5	5.1
21	10.0		14.3	13.2	15.5	27.1	10.0	0.0	17.5	5.6	16.0	5.9
22	10.1		15.9	14.0	15.7	20.2	10.1	0.0	16.5	2.3	15.2	3.3
23	10.7		19.5	14.8	15.9	16.5	10.7	0.0	16.7	1.7	15.5	2.8
24	12.5		23.0	15.6	13.3	19.1	12.5	0.0	17.8	3.7	16.7	3.9
25	14.5		23.6	16.3	15.1	21.7	14.5	0.0	19.2	3.6	18.2	3.7
26	15.6		23.8	16.6	19.6	24.3	15.6	0.0	21.1	3.2	20.0	3.6
27	15.2		23.7	16.5	26.1	26.9	15.2	0.0	23.3	4.1	21.7	4.9
28	15.6		22.8	16.1	18.9	27.0	15.6	0.0	21.2	4.1	20.1	4.3
29	15.3	18.3	21.9	16.8	14.9	25.7	16.8	1.5	19.8	4.3	18.8	3.9
30	15.0	18.4	21.4	17.5	14.0	24.5	16.7	1.7	19.4	3.9	18.5	3.6
31	14.7	18.4	21.1	18.3	17.2	21.5	16.6	1.8	19.5	1.8	18.5	2.3
32	14.3	18.5	20.8	19.2	20.1	19.8	16.4	2.1	20.0	0.6	18.8	2.1
33	13.9	18.5	26.5	20.3	21.3	20.8	16.2	2.3	22.3	2.5	20.2	3.7
34	13.9	18.6	32.3	17.1	19.1	24.1	16.2	2.3	23.1	5.9	20.8	5.9
35	14.3	18.6	34.5	17.1	17.6	20.1	16.5	2.1	22.3	7.1	20.4	6.5
36	14.8	18.8	30.7	24.0	15.9	27.7	16.8	2.0	24.6	5.5	22.0	6.0
37	15.2	18.9	26.9	24.3	18.1	26.8	17.1	1.9	24.0	3.6	21.7	4.5
38	15.7	19.1	24.4	21.4	16.9	22.3	17.4	1.7	21.3	2.8	20.0	3.1
39	16.1	19.3	22.3	22.1	14.0	17.9	17.7	1.6	19.1	3.4	18.6	3.0
40	16.1	19.4	20.4	21.8	16.8	19.0	17.8	1.7	19.5	1.8	18.9	2.0
41	15.9	19.6	19.3	19.2	18.3	23.8	17.8	1.8	20.2	2.2	19.4	2.3
42	15.8	19.3	18.2	20.0	19.7	25.7	17.5	1.8	20.9	2.9	19.8	3.0
43	15.6	19.0	19.7	22.3	19.6	22.0	17.3	1.7	20.9	1.2	19.7	2.2
44	15.3	18.8	23.8	23.0	18.6	21.7	17.0	1.7	21.8	2.0	20.2	2.9
45	15.2	18.5	27.9	22.5	16.1	20.1	16.8	1.7	21.6	4.3	20.0	4.3
46	15.0	18.2	27.4	19.7	16.2	17.9	16.6	1.6	20.3	4.3	19.0	4.0
47	14.9	17.9	26.2	19.1	17.5	19.2	16.4	1.5	20.5	3.3	19.1	3.5
48	14.7	18.4	25.2	19.8	20.8	18.8	16.6	1.8	21.2	2.4	19.6	3.1
49	14.6	18.9	24.9	20.8	21.6	18.0	16.7	2.1	21.3	2.5	19.8	3.2
50	14.5	19.4	24.5	21.9	21.0	17.9	16.9	2.4	21.3	2.4	19.9	3.2
51	15.2	19.8	25.5	23.1	18.6	20.0	17.5	2.3	21.8	2.7	20.4	3.3
52	16.0	20.3	27.3	23.5	19.3	22.5	18.2	2.1	23.1	2.9	21.5	3.5
53	16.9	20.8	29.1	23.4	22.3	25.1	18.9	1.9	25.0	2.6	22.9	3.7
54	16.8	21.5	28.8	24.4	23.7	24.9	19.2	2.3	25.4	2.0	23.3	3.6
55	16.8	22.2	28.5	25.3	25.1	24.7	19.5	2.7	25.9	1.5	23.8	3.6
56	16.7	22.8	28.2	26.3	26.5	24.5	19.8	3.1	26.4	1.3	24.2	3.7
57	16.7	23.4	27.9	25.8	26.9	24.3	20.1	3.4	26.2	1.3	24.2	3.7
58	16.6	23.9	27.6	22.6	25.2	24.1	20.3	3.6	24.9	1.8	23.3	3.4
59	16.3	24.3	26.2	19.5	23.5	23.4	20.3	4.0	23.1	2.4	22.2	3.3

Appendix 4-D: Aragonite/calcite-stacks

	Cores (mineral %)						Stacks (average mineral %)					
Age (ky)	AL	AW	S1	S2	S3	S6	Abington	stdev	Sanganeb	stdev	Sudan	stdev
60	15.8	24.8	23.7	16.3	21.9	22.2	20.3	4.5	21.0	2.8	20.8	3.5
61	15.3	23.2	21.3	15.5	20.4	21.0	19.3	3.9	19.5	2.4	19.4	3.0
62	14.8	20.7	18.8	15.9	19.1	19.7	17.7	2.9	18.4	1.5	18.2	2.1
63	14.3	18.1	16.4	16.3	17.8	18.5	16.2	1.9	17.2	1.0	16.9	1.4
64	13.8	15.6	13.9	16.7	16.5	17.3	14.7	0.9	16.1	1.3	15.6	1.4
65	14.4	18.1	23.4				16.2	1.9	23.4	0.0	18.6	3.7
66	15.0	20.7	29.2				17.8	2.8	29.2	0.0	21.6	5.8
67	15.6	20.6	21.9				18.1	2.5	21.9	0.0	19.4	2.7
68	15.9	19.4	17.4				17.6	1.7	17.4	0.0	17.6	1.4
69	16.7	19.0	16.5				17.8	1.2	16.5	0.0	17.4	1.1
70	17.7	19.6	20.7				18.6	0.9	20.7	0.0	19.3	1.2
71	18.9	20.1	27.5				19.5	0.6	27.5	0.0	22.1	3.8
72	19.5	20.1	25.5				19.8	0.3	25.5	0.0	21.7	2.7
73	19.5	20.0	23.1				19.8	0.2	23.1	0.0	20.9	1.6
74	18.9	20.6	27.0				19.8	0.9	27.0	0.0	22.2	3.5
75	18.7	21.4	29.5				20.0	1.3	29.5	0.0	23.2	4.6
76	18.2	21.7	29.3				20.0	1.7	29.3	0.0	23.1	4.6
77	17.2	21.8	29.0				19.5	2.3	29.0	0.0	22.7	4.9
78	15.6	21.5	28.8				18.6	3.0	28.8	0.0	22.0	5.4
79	14.9	20.5	27.0				17.7	2.8	27.0	0.0	20.8	4.9
80	15.5	19.5	24.9				17.5	2.0	24.9	0.0	20.0	3.9
81	15.9	19.6	24.2				17.8	1.9	24.2	0.0	19.9	3.4
82	16.3	19.8	23.5				18.0	1.7	23.5	0.0	19.9	2.9
83	16.7	19.9	22.8				18.3	1.6	22.8	0.0	19.8	2.5
84	17.0	20.3	22.6				18.7	1.7	22.6	0.0	20.0	2.3
85	17.2	20.9	23.1				19.1	1.9	23.1	0.0	20.4	2.4
86	17.4	21.6	23.6				19.5	2.1	23.6	0.0	20.9	2.6
87	17.6	22.2	24.1				19.9	2.3	24.1	0.0	21.3	2.7
88		22.0					22.0	0.0			22.0	0.0
89		21.8					21.8	0.0			21.8	0.0
90		21.5					21.5	0.0			21.5	0.0
91		21.3					21.3	0.0			21.3	0.0
92		20.9					20.9	0.0			20.9	0.0
93		20.4					20.4	0.0			20.4	0.0
94		20.0					20.0	0.0			20.0	0.0
95		19.5					19.5	0.0			19.5	0.0
96		20.5					20.5	0.0			20.5	0.0
97		21.5					21.5	0.0			21.5	0.0
98		22.4					22.4	0.0			22.4	0.0
99		23.4					23.4	0.0			23.4	0.0
100		22.7					22.7	0.0			22.7	0.0
101		21.9					21.9	0.0			21.9	0.0
102		21.8					21.8	0.0			21.8	0.0
103		23.4					23.4	0.0			23.4	0.0
104		25.0					25.0	0.0			25.0	0.0
105		24.7					24.7	0.0			24.7	0.0
106		22.6					22.6	0.0			22.6	0.0
107		20.4					20.4	0.0			20.4	0.0
108		20.6					20.6	0.0			20.6	0.0
109		21.4					21.4	0.0			21.4	0.0
110		22.3					22.3	0.0			22.3	0.0
111		21.5					21.5	0.0			21.5	0.0
112		20.7					20.7	0.0			20.7	0.0
113		20.3					20.3	0.0			20.3	0.0

Appendix 4-D: Aragonite/calcite-stacks

	Cores (mineral %)						Stacks (average mineral %)					
Age (ky)	**AL**	**AW**	**S1**	**S2**	**S3**	**S6**	**Abington**	**stdev**	**Sanganeb**	**stdev**	**Sudan**	**stdev**
114		20.0					20.0	0.0			20.0	0.0
115		20.0					20.0	0.0			20.0	0.0
116		21.1					21.1	0.0			21.1	0.0
117		22.1					22.1	0.0			22.1	0.0
118		22.7					22.7	0.0			22.7	0.0
119		23.2					23.2	0.0			23.2	0.0
120		24.1					24.1	0.0			24.1	0.0
121		25.5					25.5	0.0			25.5	0.0
122		26.9					26.9	0.0			26.9	0.0

Appendix 4-E: Average mineral abundances for isotope stages and sealevel sequences

	Percentages of bulk sediment												Percentages of fine fracrion							
Isotope stage/ sealevel cycle	**Ar/Ar+Cc**	**Aragonite**	**Ar (total)**	**Calcite**	**LMC**	**LMC(total)**	**HMC**	**HMC (total)**	**Quartz**	**Dolomite**	**Ar+HMC**	**Ar+HMC (total)**	**Ar/Ar+Cc**	**Aragonite**	**Calcite**	**LMC**	**HMC**	**Quartz**	**Dolomite**	**Ar+HMC**
Core AL																				
Holocene	0.15	65	52	35	13	11	22	17	160	23	87	70								
Sapropel	0.18	69	44	31	12	8	19	12	378	44	88	56								
LI	0.10	57	37	43	10	7	33	21	367	72	90	59								
IS 3	0.14	63	43	37	15	10	22	15	342	50	85	58								
IS 4	0.09	55	39	45	16	11	28	20	330	41	84	59								
IS 5a	0.12	60	45	40	18	13	22	17	250	23	82	62								
IS 5b	0.09	56	44	44	19	15	26	20	190	18	81	64								
Top-1.1	0.14	64	52	36	13	11	23	19	152	20	87	71								
1.1-SA	0.16	66	53	34	13	11	20	17	156	27	87	70								
LI-3.3	0.14	63	44	37	15	10	22	15	338	50	85	59								
3.3-4.2	0.12	59	38	41	16	10	25	16	376	37	84	54								
4.2-5.1	0.11	58	43	42	17	12	25	19	286	31	83	62								
5.1-5.2	0.11	58	45	42	17	13	25	20	193	20	83	64								
Max	**0.18**	**69**	**61**	**49**	**21**	**18**	**36**	**32**	**426**	**75**	105	93								
Min	**0.08**	**51**	**31**	**31**	**10**	**6**	**18**	**11**	**86**	**8**	69	42								
Average	**0.12**	**61**	**45**	**39**	**15**	**11**	**24**	**17**	**274**	**36**	85	62								
Stdev.	**0.03**	**5**	**0**	**5**	**2**	**0**	**4**	**0**	**90**	**17**	9	1								
Core AW																				
IS 3	0.11	59		41	17		24		443	55	83	0								
IS 4	0.06	48		52	20		32		413	45	80	0								
IS 5	0.09	54		46	22		24		282	30	78	0								
IS 5a	0.09	56		44	21		24		314	32	79	0								
IS 5b	0.08	51		49	21		27		337	24	79	0								
IS 5c	0.09	55		45	21		23		268	12	79	0								
IS 5d	0.08	52		48	22		27		223	14	78	0								
IS 5e	0.09	54		46	21		25		322	23	79	0								
IS 6	0.07	50		50	29		21		586	53	71	0								
LI-3.3	0.11	59		41	17		24		443	55	83	0								

LI = lithified interval (IS 2), SA = sapropel

Appendix 4-E: Average mineral abundances for isotope stages and sealevel sequences

	Percentages of bulk sediment												Percentages of fine fracrion							
Isotope stage/ sealevel cycle	**Ar/Ar+Cc**	**Aragonite**	**Ar (total)**	**Calcite**	**LMC**	**LMC(total)**	**HMC**	**HMC (total)**	**Quartz**	**Dolomite**	**Ar+HMC**	**Ar+HMC (total)**	**Ar/Ar+Cc**	**Aragonite**	**Calcite**	**LMC**	**HMC**	**Quartz**	**Dolomite**	**Ar+HMC**
3.3-4.2	0.09	54		46	21		25		534	36	79	0								
4.2-5.1	0.08	51		49	20		29		354	37	80	0								
5.1-5.2	0.08	52		48	22		27		223	14	78	0								
5.2-5.3	0.08	52		48	21		27		321	22	79	0								
5.3-5.4	0.08	52		48	22		26		256	14	78	0								
5.4-5.5	0.10	56		44	22		22		199	14	78	0								
5.5-6.2	0.08	51		49	25		24		515	59	75	0								
Max	**0.13**	**63**		**59**	**40**		**44**		**1429**	**84**	106	0								
Min	**0.04**	**41**		**37**	**10**		**12**		**156**	**8**	52	0								
Average	**0.09**	**53**		**47**	**23**		**24**		**409**	**41**	77	0								
Stdev.	**0.02**	**6**		**6**	**6**		**7**		**218**	**22**	12	0								
Core S1																				
Holocene	0.11	59	34	41	24	14	17	10	502	27	76	44	0.11	58	42	25	16	904	38	75
Sapropel	0.21	72	28	28	16	6	12	4	607	76	84	32	0.25	75	25	16	9	948	117	84
LI	0.13	56	23	44	15	7	29	12	633	65	85	35	0.11	55	45	16	29	1109	82	84
IS 3	0.06	47	20	53	24	10	29	12	764	56	76	32	0.06	48	52	25	27	1351	53	75
IS 4	0.03	33	19	67	22	13	44	25	504	41	78	44	0.02	26	74	24	50	1063	0	76
IS 5a	0.05	42	21	58	26	16	32	19	432	19	74	40	0.05	42	58	28	30	883	0	72
IS 5b	0.05	41	24	59	26	15	33	19	453	19	74	43	0.04	34	66	30	36	785	47	70
LI-3.3	0.06	47	20	53	24	10	29	12	749	55	76	32	0.07	49	51	25	27	1317	57	75
3.3-4.2	0.04	39	18	61	23	11	38	18	755	66	77	35	0.04	31	69	24	46	1448	26	76
4.2-5.1	0.04	38	21	62	24	15	38	23	423	29	76	44	0.04	32	68	26	41	894	0	74
5.1-5.2	0.05	44	26	56	24	14	33	19	508	17	76	45	0.04	30	70	31	39	1151	0	69
Max	**0.21**	**72**	**42**	**76**	**36**	**26**	**57**	**41**	**1138**	**76**		84	**0.25**	**75**	**100**	**43**	**79**	**1986**	**521**	154
Min	**0.02**	**24**	**0**	**28**	**14**	**4**	**10**	**3**	**164**	**4**		3	**0.00**	**0**	**25**	**13**	**9**	**364**	**0**	9
Average	**0.06**	**45**	**23**	**55**	**25**	**13**	**30**	**16**	**553**	**35**	75	40	**0.06**	**43**	**57**	**25**	**32**	**1015**	**45**	75
Stdev.	**0.04**	**10**	**8**	**10**	**5**	**1**	**10**	**1**	**246**	**21**	21	9	**0.04**	**15**	**15**	**6**	**13**	**395**	**83**	28
Core S2											0									0

LI = lithified interval (IS 2), SA = sapropel

Appendix 4-E: Average mineral abundances for isotope stages and sealevel sequences

	Percentages of bulk sediment												Percentages of fine fracrion							
Isotope stage/ sealevel cycle	**Ar/Ar+Cc**	**Aragonite**	**Ar (total)**	**Calcite**	**LMC**	**LMC(total)**	**HMC**	**HMC (total)**	**Quartz**	**Dolomite**	**Ar+HMC**	**Ar+HMC (total)**	**Ar/Ar+Cc**	**Aragonite**	**Calcite**	**LMC**	**HMC**	**Quartz**	**Dolomite**	**Ar+HMC**
Holocene	0.13	61	36	39	19	11	20	12	334	17	81	48	0.17	66	34	15	18	625	40	85
Sapropel	0.39	84	30	16	7	3	9	3	1072	102	93	34	0.42	85	15	8	7	974	43	92
LI	0.35	81	26	19	10	3	9	3	870	70	90	29	0.17	65	35	13	23	872	65	88
IS 3	0.09	54	22	46	20	8	26	11	794	41	80	33	0.10	56	44	20	24	1186	78	80
IS 4	0.04	38	17	62	16	7	46	21	621	29	84	38	0.04	40	60	19	41	1164	60	81
Top-1.1	0.11	59	37	41	19	12	22	13	320	17	81	50	0.16	65	35	16	19	607	39	84
1.1-SA	0.20	69	30	32	17	7	15	7	355	18	83	37	0.22	72	28	15	13	654	42	85
LI-3.3	0.09	54	23	46	20	8	26	11	801	41	80	33	0.10	57	43	20	23	1186	81	80
3.3-4.2	0.07	47	20	53	21	9	32	14	661	32	79	34	0.07	46	54	20	33	993	52	80
Max	**0.39**	**84**	**62**	**66**	**27**	**20**	**50**	**37**	**1740**	**102**	134	99	**0.42**	**85**	**69**	**25**	**51**	**1706**	**196**	137
Min	**0.03**	**34**	**10**	**16**	**7**	**2**	**9**	**3**	**148**	**12**	42	12	**0.03**	**31**	**15**	**8**	**7**	**188**	**14**	38
Average	**0.11**	**57**	**26**	**43**	**19**	**9**	**24**	**11**	**657**	**35**	81	37	**0.13**	**59**	**41**	**17**	**24**	**985**	**66**	83
Stdev.	**0.07**	**9**	**1**	**9**	**4**	**0**	**9**	**1**	**326**	**18**	18	2	**0.07**	**10**	**10**	**4**	**9**	**349**	**35**	19
Core S3											0									0
Sapropel	0.20	71	28	29	15	6	14	6	616	71	85	34	0.27	77	23	9	14	1042	57	91
LI	0.27	77	23	23	15	5	8	2	589	37	85	25	0.14	61	39	15	25	769	65	85
IS 3	0.10	57	25	43	19	8	24	11	820	42	81	36	0.11	59	41	19	22	1272	81	81
IS 4	0.04	37	19	63	17	9	46	21	715	47	83	40	0.06	45	55	21	34	1208	64	79
LI-3.3	0.10	57	27	43	18	9	24	11	792	40	82	39	0.12	60	40	19	21	1248	76	81
3.3-4.2	0.04	37	17	63	16	8	47	22	702	50	84	39	0.05	43	57	22	35	1269	71	78
Max	**0.32**	**80**	**39**	**71**	**28**	**17**	**59**	**36**	**1457**	**108**	138	75	**0.63**	**93**	**61**	**29**	**39**	**1958**	**187**	132
Min	**0.02**	**29**	**0**	**20**	**10**	**3**	**8**	**2**	**340**	**18**	37	2	**0.04**	**39**	**7**	**3**	**4**	**489**	**35**	43
Average	**0.11**	**56**	**25**	**44**	**18**	**8**	**26**	**12**	**783**	**42**	82	37	**0.13**	**59**	**41**	**18**	**23**	**1154**	**75**	82
Stdev.	**0.05**	**10**	**7**	**10**	**4**	**0**	**10**	**1**	**247**	**19**	20	8	**0.09**	**9**	**9**	**4**	**8**	**349**	**30**	17
											0									0
Core S6																				
Holocene	0.10	58	34	42	22	13	20	12	502	48	78	46	0.10	57	43	23	20	828	33	77
Sapropel	0.21	72	27	28	18	7	11	4	1125	62	82	31	0.18	68	32	19	13	966	92	81
LI	0.12	59	27	41	22	7	19	4	968	57	78	31	0.16	62	38	16	22	880	79	84

LI = lithified interval (IS 2), SA = sapropel

Appendix 4-E: Average mineral abundances for isotope stages and sealevel sequences

	Percentages of bulk sediment												Percentages of fine fracrion							
Isotope stage/ sealevel cycle	**Ar/Ar+Cc**	**Aragonite**	**Ar (total)**	**Calcite**	**LMC**	**LMC(total)**	**HMC**	**HMC (total)**	**Quartz**	**Dolomite**	**Ar+HMC**	**Ar+HMC (total)**	**Ar/Ar+Cc**	**Aragonite**	**Calcite**	**LMC**	**HMC**	**Quartz**	**Dolomite**	**Ar+HMC**
IS 3	0.10	57	26	43	23	10	21	9	893	71	77	35	0.10	57	43	25	18	1584	68	75
IS 4	0.05	43	21	57	20	10	37	19	797	82	80	40	0.05	44	56	24	33	1422	64	76
Top-1.1	0.10	58	37	42	21	13	21	13	546	37	79	50	0.09	54	46	23	23	557	18	77
1.1-SA	0.11	58	34	42	23	15	19	12	516	52	77	46	0.12	60	40	22	18	875	47	78
LI-3.3	0.11	58	27	42	22	10	20	9	929	61	78	37	0.11	57	43	24	19	1515	75	76
3.3-4.2	0.07	48	22	52	22	10	30	14	858	85	78	35	0.07	48	52	27	25	1403	70	73
Max	**0.21**	**72**	**49**	**65**	**28**	**24**	**48**	**41**	**1352**	**157**	119	90	**0.51**	**89**	**66**	**44**	**42**	**4436**	**154**	131
Min	**0.03**	**35**	**17**	**28**	**15**	**5**	**11**	**4**	**131**	**8**	46	21	**0.03**	**34**	**11**	**3**	**7**	**158**	**9**	41
Average	**0.10**	**57**	**29**	**43**	**22**	**11**	**22**	**11**	**834**	**58**	78	40	**0.11**	**58**	**42**	**22**	**21**	**1147**	**66**	78
Stdev.	**0.03**	**6**	**8**	**6**	**4**	**1**	**7**	**1**	**282**	**30**	13	9	**0.06**	**8**	**8**	**6**	**8**	**687**	**32**	16

LI = lithified interval (IS 2), SA = sapropel

Appendix 4-F: Stacked aragonite accumulation rates

	Core AL			Core S1			Core S2			Core S3			Core S6			Aragonite AR stack			
Age (kyr)	Aragonite	Carbonate SR	Aragonite AR	Aragonite	Carbonate SR	Aragonite AR	Aragonite	Carbonate SR	Aragonite AR	Aragonite	Carbonate SR	Aragonite AR	Aragonite	Carbonate SR	Aragonite AR	Sanganeb AR stack	stdev.	Sudan AR stack	st.dev.
1							60.9	8.2	39.1					6.3		39.1	0.0	39.1	0.0
2	64.0	6.8	33.9				57.5	8.2	37.0					6.3		37.0	0.0	35.4	1.6
3	64.3	6.8	34.0				59.4	8.2	38.2					6.3		38.2	0.0	36.1	2.1
4	63.8	6.8	33.8				58.1	8.2	37.4					6.3		37.4	0.0	35.6	1.8
5	63.5	6.8	33.6				58.3	8.2	37.5					6.3		37.5	0.0	35.5	1.9
6	63.9	14.5	72.4				60.2	2.7	12.5				55.7	12.8	55.7	34.1	21.6	46.8	25.2
7	67.1	14.5	76.0				70.1	2.7	14.6				58.3	12.8	58.2	36.4	21.8	49.6	25.8
8	68.4	14.5	77.5				77.2	2.7	16.0				58.6	12.8	58.6	37.3	21.3	50.7	25.7
9	68.0	0.7	3.8				78.5	0.4	2.5				61.7	0.4	2.0	2.2	0.2	2.7	0.7
10	66.9	0.7	3.7				79.9	0.4	2.5	70.5	0.6	3.4	64.2	0.4	2.1	2.7	0.5	2.9	0.7
11	65.8	0.7	3.6				81.2	0.4	2.5	64.9	0.6	3.1	66.7	0.4	2.2	2.6	0.4	2.9	0.6
12	64.6	0.7	3.6				82.5	0.4	2.6	59.4	0.6	2.9	69.2	0.4	2.3	2.6	0.2	2.8	0.5
13	63.5	4.6	22.6				83.8	3.3	21.3	53.8	3.4	14.3	71.7	3.9	21.6	19.1	3.4	19.9	3.3
14	62.4	4.6	22.2	69.9	3.0	16.2	83.1	3.3	21.1	48.2	3.4	12.8	50.1	3.9	15.1	16.3	3.0	17.5	3.6
15	61.2	4.6	21.8	65.9	3.0	15.3	82.4	3.3	20.9	43.8	3.4	11.6	55.3	3.9	16.7	16.1	3.3	17.3	3.8
16	60.1	4.6	21.4	61.8	3.0	14.4	81.7	3.3	20.8	50.3	3.4	13.3	57.6	3.9	17.3	16.5	2.9	17.4	3.3
17	59.0	4.6	21.0	57.8	3.0	13.4	80.9	3.3	20.6	56.7	3.4	15.0	60.1	3.9	18.1	16.8	2.8	17.6	3.0
18	57.8	4.6	20.6	53.8	3.0	12.5	80.2	3.3	20.4	63.1	3.4	16.7	58.8	3.9	17.7	16.8	2.8	17.6	3.0
19	56.7	4.6	20.2	49.8	3.0	11.6	79.5	3.3	20.2	69.5	3.4	18.4	57.5	3.9	17.3	16.9	3.2	17.5	3.2
20	55.6	4.6	19.8	45.7	3.0	10.6	78.8	3.3	20.0	75.9	3.4	20.1	57.5	3.9	17.3	17.0	3.9	17.6	3.6
21	54.4	4.6	19.4	41.7	3.0	9.7	72.5	3.3	18.4	71.7	3.4	19.0	57.5	3.9	17.3	16.1	3.8	16.8	3.6
22	55.6	4.6	19.8	42.0	3.0	9.8	66.2	3.3	16.8	65.8	3.4	17.5	57.6	3.9	17.4	15.4	3.2	16.2	3.4
23	59.8	3.1	14.2	46.5	1.5	5.6	60.0	2.4	11.2	60.0	3.7	17.2	57.2	2.4	10.7	11.2	4.1	11.8	3.9
24	59.5	3.1	14.2	51.1	1.5	6.1	53.7	2.4	10.0	49.4	3.7	14.2	55.6	2.4	10.4	10.2	2.8	11.0	3.0
25	62.0	3.1	14.7	49.6	1.5	6.0	53.4	2.4	10.0	55.9	3.7	16.0	54.0	2.4	10.1	10.5	3.6	11.4	3.6
26	60.8	3.1	14.5	47.1	1.5	5.7	52.8	2.4	9.9	54.1	3.7	15.5	52.4	2.4	9.8	10.2	3.5	11.1	3.6
27	59.3	3.1	14.1	44.5	1.5	5.3	52.1	2.4	9.8	51.9	3.7	14.9	50.9	2.4	9.5	9.9	3.4	10.7	3.5
28	59.8	3.1	14.2	41.2	1.5	5.0	58.6	2.4	11.0	60.4	3.7	17.3	51.8	2.4	9.7	10.7	4.4	11.4	4.2
29	61.1	3.1	14.5	37.9	1.5	4.6	52.4	2.4	9.8	54.9	3.7	15.8	54.2	2.4	10.1	10.1	4.0	11.0	4.0
30	62.5	3.1	14.9	39.7	1.5	4.8	48.3	2.4	9.0	52.7	3.7	15.1	56.5	2.4	10.6	9.9	3.7	10.9	3.9
31	63.7	3.1	15.2	44.6	1.5	5.4	48.5	2.4	9.1	54.7	3.7	15.7	58.7	2.4	11.0	10.3	3.7	11.3	3.9
32	64.9	3.1	15.4	49.4	1.5	5.9	53.0	2.4	9.9	55.0	3.7	15.8	59.4	2.4	11.1	10.7	3.5	11.6	3.7
33	66.0	3.1	15.7	44.5	1.5	5.3	59.7	2.4	11.2	55.7	3.7	16.0	57.6	2.4	10.8	10.8	3.8	11.8	3.9
34	66.5	3.1	15.8	39.5	1.5	4.7	52.6	2.4	9.9	57.8	3.7	16.6	57.6	2.4	10.8	10.5	4.2	11.6	4.3
35	66.1	3.1	15.7	37.7	1.5	4.5	47.9	2.4	9.0	60.2	3.7	17.3	55.0	2.4	10.3	10.3	4.6	11.4	4.6
36	65.8	3.1	15.7	41.1	1.5	4.9	48.1	2.4	9.0	61.1	3.7	17.5	50.4	2.4	9.4	10.2	4.6	11.3	4.6
37	65.2	3.1	15.5	44.5	1.5	5.4	50.1	2.4	9.4	59.4	3.7	17.1	51.7	2.4	9.7	10.4	4.2	11.4	4.3
38	64.4	3.1	15.3	47.1	1.5	5.7	53.2	2.4	10.0	61.5	3.7	17.6	55.0	2.4	10.3	10.9	4.3	11.8	4.2
39	63.6	3.1	15.1	49.3	1.5	5.9	54.1	2.4	10.1	65.1	3.7	18.7	58.5	2.4	10.9	11.4	4.6	12.2	4.4
40	63.6	3.1	15.1	51.6	1.5	6.2	55.2	2.4	10.3	58.6	3.7	16.8	59.1	2.4	11.1	11.1	3.8	11.9	3.7
41	63.6	3.1	15.1	54.5	1.5	6.5	56.6	2.4	10.6	54.7	3.7	15.7	57.4	2.4	10.7	10.9	3.2	11.7	3.4
42	63.8	3.1	15.2	57.4	1.5	6.9	55.3	2.4	10.4	57.8	3.7	16.6	56.6	2.4	10.6	11.1	3.5	11.9	3.5
43	64.3	3.1	15.3	56.6	1.5	6.8	52.7	2.4	9.9	59.3	3.7	17.0	58.2	2.4	10.9	11.1	3.7	12.0	3.7
44	64.9	3.1	15.4	52.1	1.5	6.3	54.9	2.4	10.3	60.6	3.7	17.4	58.4	2.4	10.9	11.2	4.0	12.1	3.9
45	65.4	3.1	15.6	47.6	1.5	5.7	56.7	2.4	10.6	61.9	3.7	17.8	59.1	2.4	11.1	11.3	4.3	12.1	4.2
46	65.7	3.1	15.6	47.6	1.5	5.7	57.4	2.4	10.8	62.4	3.7	17.9	60.4	2.4	11.3	11.4	4.3	12.3	4.2
47	66.1	3.1	15.7	48.4	1.5	5.8	58.9	2.4	11.0	62.1	3.7	17.8	63.2	2.4	11.8	11.6	4.3	12.4	4.1
48	66.3	3.1	15.8	49.5	1.5	5.9	60.7	2.4	11.4	60.4	3.7	17.3	63.9	2.4	12.0	11.7	4.0	12.5	4.0
49	66.4	3.1	15.8	51.8	1.5	6.2	57.4	2.4	10.7	60.9	3.7	17.5	63.8	2.4	11.9	11.6	4.0	12.4	4.0
50	66.5	3.1	15.8	54.2	1.5	6.5	55.7	2.4	10.4	62.5	3.7	17.9	63.7	2.4	11.9	11.7	4.1	12.5	4.0
51	66.1	3.1	15.7	54.2	1.5	6.5	57.3	2.4	10.7	65.8	3.7	18.9	61.3	2.4	11.5	11.9	4.5	12.7	4.3

all values in percent

Appendix 4-F: Stacked aragonite accumulation rates

	Core AL			Core S1			Core S2			Core S3			Core S6			Aragonite AR stack			
Age (kyr)	Aragonite	Carbonate SR	Aragonite AR	Aragonite	Carbonate SR	Aragonite AR	Aragonite	Carbonate SR	Aragonite AR	Aragonite	Carbonate SR	Aragonite AR	Aragonite	Carbonate SR	Aragonite AR	Sanganeb AR stack	stdev.	Sudan AR stack	st.dev.
52	65.7	3.1	15.6	52.8	1.5	6.3	59.3	2.4	11.1	64.1	3.7	18.4	59.2	2.4	11.1	11.7	4.3	12.5	4.2
53	65.2	3.1	15.5	51.4	1.5	6.2	61.5	2.4	11.5	58.5	3.7	16.8	57.9	2.4	10.8	11.3	3.8	12.2	3.8
54	64.3	3.1	15.3	48.6	1.5	5.8	58.7	2.4	11.0	57.8	3.7	16.6	56.5	2.4	10.6	11.0	3.8	11.9	3.8
55	63.4	3.1	15.1	45.9	1.5	5.5	55.8	2.4	10.5	57.0	3.7	16.4	55.1	2.4	10.3	10.7	3.8	11.5	3.9
56	62.5	3.1	14.9	43.1	1.5	5.2	53.0	2.4	9.9	56.3	3.7	16.2	53.8	2.4	10.1	10.3	3.9	11.2	3.9
57	61.6	3.1	14.6	40.3	1.5	4.8	50.3	2.4	9.4	54.6	3.7	15.7	52.4	2.4	9.8	9.9	3.8	10.9	3.9
58	60.7	3.1	14.4	37.6	1.5	4.5	47.8	2.4	8.9	50.9	3.7	14.6	51.0	2.4	9.5	9.4	3.6	10.4	3.8
59	59.5	3.1	14.1	35.5	1.5	4.3	45.2	2.4	8.5	47.3	3.7	13.6	48.9	2.4	9.2	8.9	3.3	9.9	3.6
60	58.0	3.5	15.9	34.2	2.9	7.6	42.7			43.6			46.2			7.6	0.0	11.8	4.2
61	56.5	3.5	15.5	32.9	2.9	7.3	40.4			41.4			43.4			7.3	0.0	11.4	4.1
62	55.0	3.5	15.1	31.6	2.9	7.0	38.1			39.9			40.6			7.0	0.0	11.1	4.0
63	53.6	3.5	14.7	30.3	2.9	6.7	35.9			38.4			37.9			6.7	0.0	10.7	4.0
64	52.1	3.5	14.3	29.0	2.9	6.4	33.6			36.9			35.1			6.4	0.0	10.4	3.9
65	51.7	3.5	14.2	26.2	2.9	5.8										5.8	0.0	10.0	4.2
66	52.3	3.5	14.4	24.9	2.9	5.5										5.5	0.0	10.0	4.4
67	53.8	3.5	14.8	29.2	2.9	6.5										6.5	0.0	10.6	4.1
68	54.5	3.5	15.0	34.5	2.9	7.7										7.7	0.0	11.3	3.7
69	56.0	3.5	15.4	41.0	2.9	9.1										9.1	0.0	12.3	3.1
70	57.6	3.5	15.8	41.6	2.9	9.2										9.2	0.0	12.5	3.3
71	57.8	4.0	18.2	39.2	2.3	7.0										7.0	0.0	12.6	5.6
72	56.7	4.0	17.9	34.1	2.3	6.1										6.1	0.0	12.0	5.9
73	55.5	4.0	17.5	29.9	2.3	5.3										5.3	0.0	11.4	6.1
74	55.6	4.0	17.5	35.3	2.3	6.3										6.3	0.0	11.9	5.6
75	57.8	4.0	18.2	39.0	2.3	7.0										7.0	0.0	12.6	5.6
76	60.8	4.0	19.1	39.2	2.3	7.0										7.0	0.0	13.1	6.1
77	64.0	4.0	20.2	41.8	2.3	7.5										7.5	0.0	13.8	6.4
78	65.9	4.0	20.8	46.3	2.3	8.3										8.3	0.0	14.5	6.3
79	66.1	4.0	20.8	50.5	2.3	9.0										9.0	0.0	14.9	5.9
80	64.3	4.0	20.3	54.5	2.3	9.7										9.7	0.0	15.0	5.3
81	62.2	4.0	19.6	50.8	2.3	9.1										9.1	0.0	14.3	5.3
82	60.1	4.0	18.9	47.0	2.3	8.4										8.4	0.0	13.7	5.3
83	58.0	4.0	18.3	43.3	2.3	7.7										7.7	0.0	13.0	5.3
84	56.4	4.0	17.8	40.5	2.3	7.2										7.2	0.0	12.5	5.3
85	55.2			38.6															
86	53.9			36.7															
87	52.7			34.8															

all values in percent

Appendix 5-A: Element distribution (XRF)

	Main elements (in percent)										Trace elements (in ppm)																
Depth (cm)	**SiO_2**	**Al_2O_3**	**MnO**	**MgO**	**Na_2O**	**CaO**	**TiO_2**	**P_2O_5**	**K_2O**	**Fe_2O_3**	**Ba**	**Co**	**Cr**	**Cu**	**La**	**Nb**	**Ni**	**Ga**	**Pb**	**Pr**	**Rb**	**Sr**	**Th**	**V**	**Y**	**Zr**	**Zn**
Core S1																											
Standards																											
AN	<0,80	<0,10	<0,00	0.5	<0,04	39.2	<0,02	<0,006	<0,02	0.1	12	<4	<18	<4	<14	<2	<2	<8	15	<8	<4	1422	7	<12	<2	<4	<15
AN	<0,80	<0,10	<0,00	0.5	<0,04	39.2	<0,02	<0,006	<0,02	0.1	<8	<4	<18	<4	<14	<2	<2	<8	11	<8	<4	1424	6	<12	<2	<4	<15
NBS-97a	43.9	39.9	0.0	0.2	<0,04	0.1	2.0	0.4	0.6	0.5	514	<4	217	9	91	41	46	46	42	22	15	1491	38	206	89	441	33
NBS-97a	43.9	39.9	0.0	0.2	<0,04	0.1	2.0	0.4	0.6	0.5	514	<4	217	9	91	41	46	46	42	22	15	1491	38	206	89	441	33
1	15.1	5.2	0.1	3.4	2.3	38.7	0.3	0.2	0.8	2.9	83	11	35	4	<14	12	25	9	4	<8	25	2009	<4	57	<2	47	68
10	13.4	4.5	0.1	3.2	2.2	41.1	0.3	0.2	0.7	2.5	68	9	31	12	<14	3	23	<8	<4	<8	23	2133	<4	59	<2	41	62
20	15.9	5.0	0.1	3.2	1.8	39.8	0.4	0.2	0.7	2.7	74	9	42	8	<14	11	21	10	<4	<8	26	2062	<4	56	<2	54	71
25	19.4	5.8	0.1	3.4	2.6	35.5	0.5	0.2	0.8	3.1	79	10	51	<4	14	10	25	<8	6	<8	26	1882	<4	80	<2	74	67
30	34.0	9.3	0.1	4.1	3.1	22.4	0.9	0.2	1.1	5.4	160	20	95	20	<14	17	52	12	4	9	34	1352	<4	137	13	159	90
40	35.7	9.9	0.1	4.2	3.1	20.1	0.9	0.2	1.2	5.6	155	18	103	34	19	13	63	15	8	<8	37	1209	<4	132	13	168	85
50	33.7	8.9	0.1	3.7	3.0	22.6	0.9	0.2	1.1	5.2	142	18	98	25	<14	14	50	11	10	<8	34	1965	<4	165	7	164	105
120	31.2	8.4	0.1	4.3	2.2	26.2	0.7	0.2	1.2	4.5	159	12	74	17	<14	14	34	10	<4	<8	32	1210	<4	91	9	147	81
120	31.2	8.4	0.1	4.3	2.2	26.2	0.7	0.2	1.2	4.5	159	12	74	17	<14	14	34	10	<4	<8	32	1210	<4	91	9	147	81
130	32.2	8.5	0.1	4.0	2.1	25.8	0.7	0.2	1.2	4.7	157	14	68	18	<14	13	36	15	<4	<8	37	1517	<4	91	5	136	77
140	34.8	9.1	0.1	4.1	2.4	23.6	0.7	0.2	1.2	4.7	162	16	81	20	<14	15	36	15	8	<8	35	1071	4	92	13	153	83
150	35.9	9.4	0.1	4.3	2.4	22.4	0.8	0.2	1.2	5.2	182	16	83	22	23	10	37	13	5	<8	36	844	5	109	14	156	94
160	38.2	10.4	0.1	4.2	2.3	20.3	0.9	0.2	1.3	5.7	191	26	92	29	<14	14	47	16	10	<8	37	897	8	118	19	171	90
170	33.2	9.1	0.1	4.6	2.5	23.3	0.8	0.2	1.2	5.1	146	16	78	23	22	17	55	16	14	<8	38	897	8	124	17	155	89
180	35.4	9.3	0.1	4.1	2.5	23.1	0.8	0.2	1.2	5.0	409	18	86	19	<14	16	38	11	8	<8	36	992	4	98	19	158	88
190	32.2	8.9	0.1	4.0	2.4	25.1	0.8	0.2	1.2	4.9	150	16	76	23	16	16	31	11	5	<8	35	1027	<4	98	15	141	81
200	31.4	8.6	0.1	4.0	2.2	25.6	0.7	0.2	1.1	4.9	149	20	64	21	<14	11	43	11	7	<8	33	1096	4	111	10	137	101
210	35.0	9.4	0.1	3.9	2.7	23.4	0.7	0.2	1.2	4.7	155	15	71	26	<14	10	32	13	<4	<8	35	1081	<4	94	15	138	82
220	26.7	7.4	0.1	3.8	2.1	30.7	0.5	0.3	1.0	3.8	100	13	52	13	<14	11	32	15	<4	<8	30	1398	<4	73	6	100	69
230	40.7	10.9	0.1	3.9	2.5	19.0	0.8	0.2	1.3	5.5	198	17	86	27	19	11	51	14	<4	<8	41	943	<4	116	14	169	92
240	32.4	9.0	0.1	3.7	2.6	25.0	0.7	0.2	1.2	4.8	160	18	73	18	27	9	48	13	12	<8	37	1311	7	96	14	129	73
250	34.6	9.5	0.1	4.2	2.5	23.1	0.9	0.2	1.2	5.0	193	17	85	35	26	16	43	13	<4	<8	38	904	<4	112	16	176	79
260	27.9	7.7	0.1	4.6	2.2	28.4	0.7	0.2	1.1	4.1	148	15	70	13	17	18	34	9	5	<8	32	892	<4	82	12	126	66
270	28.7	7.9	0.1	4.5	2.3	27.7	0.7	0.2	1.1	4.3	136	16	83	29	28	12	48	12	5	<8	30	893	<4	87	12	125	65
280	23.0	6.6	0.1	4.5	1.8	32.7	0.5	0.2	0.9	3.5	121	10	51	26	<14	8	27	9	11	<8	30	1055	6	67	6	97	65
290	18.3	5.3	0.1	4.3	1.9	37.2	0.4	0.2	0.8	2.9	93	8	30	24	<14	8	17	<8	<4	<8	25	1642	<4	54	<2	72	63
300	24.4	7.4	0.1	4.0	1.8	31.4	0.6	0.2	1.0	4.1	141	13	56	25	18	14	39	<8	13	<8	32	1112	7	72	9	90	66
310	23.1	7.0	0.1	4.3	1.8	32.4	0.6	0.2	1.0	3.7	112	15	60	28	<14	11	30	14	5	<8	33	1067	<4	83	7	91	66

Appendix 5-A: Element distribution (XRF)

	Main elements (in percent)										Trace elements (in ppm)																
Depth (cm)	**SiO_2**	**Al_2O_3**	**MnO**	**MgO**	**Na_2O**	**CaO**	**TiO_2**	**P_2O_5**	**K_2O**	**Fe_2O_3**	**Ba**	**Co**	**Cr**	**Cu**	**La**	**Nb**	**Ni**	**Ga**	**Pb**	**Pr**	**Rb**	**Sr**	**Th**	**V**	**Y**	**Zr**	**Zn**
320	30.2	8.6	0.1	3.7	2.2	27.6	0.7	0.2	1.1	4.3	144	20	58	22	20	11	31	8	10	<8	31	983	6	75	15	120	72
330	32.0	9.4	0.1	3.7	2.5	25.5	0.7	0.2	1.2	4.6	154	16	65	24	17	12	29	8	9	<8	35	1014	6	93	13	135	87
340	21.9	6.8	0.1	3.5	2.2	34.0	0.5	0.2	0.9	3.6	126	14	51	31	<14	10	32	9	5	<8	29	1514	<4	62	<2	82	75
350	15.8	5.0	0.1	3.3	2.1	39.5	0.3	0.2	0.7	2.7	90	10	39	15	<14	10	23	<8	4	<8	25	1774	<4	53	<2	59	50
360	28.3	8.1	0.1	4.0	2.3	28.2	0.6	0.2	1.0	4.3	136	11	65	30	<14	9	37	10	5	<8	32	1093	5	92	11	124	62
370	30.1	8.7	0.1	4.2	2.4	26.7	0.7	0.2	1.1	4.7	152	15	68	30	<14	11	40	13	10	9	31	926	<4	89	14	132	63
380	24.6	7.2	0.1	3.8	2.6	31.5	0.6	0.2	0.9	3.8	118	10	45	21	<14	11	26	<8	6	<8	28	1154	7	65	7	97	57
390	19.2	5.9	0.1	3.7	2.4	35.5	0.5	0.2	0.8	3.3	93	9	40	22	<14	8	27	<8	<4	<8	27	1328	<4	73	3	74	51
400	18.3	5.7	0.1	3.7	2.3	36.5	0.4	0.2	0.7	3.1	90	11	40	24	<14	7	21	<8	<4	<8	25	1359	<4	64	<2	69	52
410	20.9	6.3	0.1	3.9	2.0	35.1	0.5	0.2	0.8	3.3	87	11	48	22	<14	12	25	<8	<4	<8	25	1408	<4	56	<2	81	58
420	26.7	7.9	0.1	3.9	2.0	30.1	0.6	0.2	1.0	3.9	133	15	53	24	<14	14	33	<8	6	<8	31	1189	<4	70	10	102	68
430	33.2	9.7	0.1	3.8	2.3	24.6	0.7	0.2	1.1	4.7	189	12	67	38	14	12	35	11	9	<8	37	1009	<4	93	12	123	77
440	24.0	7.3	0.1	3.7	2.4	32.0	0.5	0.2	0.9	3.6	117	11	50	21	<14	6	30	<8	7	<8	30	1332	<4	67	3	82	71
450	22.3	6.9	0.1	4.3	2.7	42.1	0.4	0.2	1.0	3.7	117	13	53	24	<14	9	31	8	7	<8	30	1758	<4	72	<2	65	72
460	31.3	9.2	0.1	4.0	2.1	26.0	0.6	0.2	1.1	4.6	123	18	68	34	16	10	43	9	10	<8	36	1092	<4	90	14	140	78
470	19.4	6.1	0.1	3.5	1.9	36.6	0.4	0.2	0.8	3.2	87	10	45	19	14	15	22	10	<4	<8	25	1437	6	54	5	76	63
480	29.0	8.5	0.1	4.0	2.4	27.2	0.7	0.2	1.1	4.8	168	15	70	37	<14	10	43	11	5	<8	30	996	<4	95	10	126	80
490	15.6	5.0	0.1	3.9	2.2	38.9	0.4	0.3	0.7	2.6	94	9	36	8	<14	11	20	<8	4	<8	24	1171	7	51	5	69	48
500	21.4	6.6	0.1	4.7	2.5	42.7	0.5	0.3	0.9	3.4	115	13	46	24	<14	8	26	<8	8	<8	24	1355	5	64	<2	84	67
Core S2																											
Standards																											
AN	<0,80	<0,10	<0,00	0.5	0.1	39.1	<0,02	<0,006	<0,02	0.1	<8	<4	<18	<4	<14	<2	<2	<8	13	<8	<4	1412	5	<12	<2	<4	<15
AN	<0,80	<0,10	<0,00	0.5	0.1	39.1	<0,02	<0,006	<0,02	0.1	<8	<4	<18	<4	<14	<2	<2	<8	9	<8	<4	1419	<12	<2	<4	<15	40
NBS-97a	43.7	39.5	<0,00	0.2	<0,04	0.1	1.9	0.4	0.6	0.5	487	<4	219	8	98	40	45	50	41	19	11	1482	37	195	86	441	32
NBS-97a	43.7	39.2	<0,00	0.2	<0,04	0.1	2.0	0.4	0.5	0.5	490	5	215	11	114	46	45	53	46	23	15	1485	34	197	87	443	31
2	23.3	6.8	0.1	3.3	2.1	32.5	0.5	0.2	0.8	3.8	119	12	46	21	<14	9	25	11	5	<8	28	1966	<4	73	<2	83	62
10	23.4	6.7	0.1	3.2	2.2	32.8	0.5	0.3	0.8	3.7	132	12	51	26	<14	8	23	<8	<4	<8	26	1907	<4	75	<2	77	60
20	21.0	6.3	0.1	3.3	2.7	33.8	0.5	0.3	0.8	3.3	99	12	44	9	<14	8	23	<8	5	<8	28	1927	<4	68	<2	73	66
30	25.2	7.6	0.1	3.9	2.9	39.3	0.5	0.3	1.0	3.9	121	13	55	23	<14	8	29	8	6	<8	32	2116	<4	78	<2	81	72
40	20.9	6.5	0.1	3.2	1.9	34.8	0.5	0.2	0.8	3.3	114	12	41	18	<14	11	26	12	<4	<8	29	1905	<4	61	<2	72	66
50	17.9	5.7	0.1	3.2	1.7	37.4	0.4	0.2	0.8	3.1	61	6	41	16	<14	13	24	<8	<4	<8	27	2070	<4	55	<2	58	63
60	12.6	4.2	0.1	3.1	2.2	41.6	0.3	0.2	0.6	2.3	63	5	24	9	<14	4	19	<8	<4	<8	21	2330	<4	34	<2	32	51
70	19.0	6.6	0.1	3.7	2.4	33.7	0.4	0.2	1.0	3.7	72	11	47	14	<14	13	30	10	4	<8	34	2207	<4	70	<2	57	73
80	22.0	7.3	0.1	3.7	2.6	31.1	0.5	0.2	1.1	4.2	96	13	50	19	<14	9	33	10	<4	<8	32	1997	4	72	<2	67	68

Appendix 5-A: Element distribution (XRF)

	Main elements (in percent)										Trace elements (in ppm)																
Depth (cm)	**SiO_2**	**Al_2O_3**	**MnO**	**MgO**	**Na_2O**	**CaO**	**TiO_2**	**P_2O_5**	**K_2O**	**Fe_2O_3**	**Ba**	**Co**	**Cr**	**Cu**	**La**	**Nb**	**Ni**	**Ga**	**Pb**	**Pr**	**Rb**	**Sr**	**Th**	**V**	**Y**	**Zr**	**Zn**
90	33.6	11.0	0.1	4.4	3.1	19.4	0.8	0.2	1.5	6.5	171	23	79	31	<14	13	50	16	<4	<8	46	1933	<4	114	<2	118	76
100	39.1	9.6	0.1	2.9	2.9	21.8	0.7	0.1	1.0	4.6	171	10	67	14	<14	11	26	14	6	<8	29	2352	<4	96	<2	112	53
170	39.9	11.3	0.1	3.7	2.8	17.5	0.9	0.2	1.3	6.2	187	22	80	33	15	16	49	12	6	<8	39	1832	<4	131	6	150	73
210	29.2	8.2	0.1	4.2	2.7	26.0	0.6	0.2	1.1	4.5	142	13	63	23	<14	12	33	13	8	<8	35	1437	<4	82	7	119	76
220	32.4	8.5	0.1	3.9	2.5	25.2	0.7	0.2	1.1	4.3	145	17	71	19	<14	15	30	10	7	<8	32	1525	<4	90	5	135	80
230	32.8	8.4	0.1	3.9	2.6	25.2	0.7	0.2	1.1	4.2	175	14	57	15	<14	8	29	11	<4	<8	32	1287	<4	82	10	141	71
240	38.0	9.4	0.1	3.7	2.8	21.2	0.8	0.2	1.2	4.9	151	14	71	27	<14	10	33	10	5	9	34	1323	<4	106	7	167	78
250	37.3	9.5	0.1	4.1	2.8	21.3	0.8	0.2	1.2	5.1	168	14	72	24	<14	16	38	9	8	<8	35	1050	4	98	12	161	95
260	36.6	9.5	0.1	4.0	2.9	21.1	0.9	0.2	1.2	5.2	190	21	84	17	<14	12	39	12	6	<8	36	1174	<4	111	10	165	80
270	36.4	9.5	0.1	3.7	2.8	21.9	0.8	0.2	1.1	5.1	182	19	82	21	<14	10	39	12	4	<8	34	1328	<4	106	11	147	83
280	31.0	8.5	0.1	4.1	2.5	25.5	0.8	0.2	1.1	4.6	134	16	64	18	23	16	29	15	8	<8	34	1366	6	97	5	136	82
290	34.8	9.1	0.1	3.9	2.9	22.2	0.8	0.2	1.2	5.0	162	12	69	21	<14	12	40	18	9	<8	37	1213	104	11	156	82	80
300	33.3	9.0	0.1	3.7	2.8	23.5	0.8	0.2	1.1	4.9	141	17	71	34	21	14	39	16	9	<8	36	1305	<4	110	10	141	84
310	31.3	8.7	0.1	3.7	2.8	24.6	0.8	0.2	1.1	4.8	144	13	73	30	18	11	39	16	<4	<8	35	1399	5	101	11	134	82
320	28.7	7.9	0.1	3.6	3.0	26.7	0.6	0.2	1.0	4.2	147	11	62	29	<14	13	30	14	7	<8	31	1628	<4	90	<2	113	77
330	33.3	9.1	0.1	3.8	2.9	23.2	0.7	0.2	1.2	4.6	173	10	65	27	17	14	32	9	<4	<8	38	1283	<4	88	11	138	84
340	35.1	9.4	0.1	3.6	3.4	21.7	0.7	0.2	1.2	4.6	171	13	63	23	<14	10	34	14	11	<8	33	1320	4	93	11	136	77
350	29.5	8.0	0.1	3.6	2.9	27.3	0.6	0.2	1.0	3.8	141	8	60	14	<14	13	22	11	7	<8	31	1615	<4	83	6	116	66
360	23.8	6.6	0.1	3.4	3.0	30.3	0.5	0.2	0.9	3.4	100	8	57	18	14	6	30	<8	5	<8	29	1993	5	78	<2	90	66
370	37.7	10.0	0.1	3.6	3.3	20.0	0.8	0.2	1.2	5.0	173	15	73	18	<14	13	36	9	12	<8	35	1303	106	12	150	75	82
380	38.3	10.2	0.1	3.6	3.1	19.4	0.8	0.2	1.2	5.3	183	19	82	30	<14	14	41	12	<4	<8	37	1195	<4	103	13	153	77
390	31.5	8.5	0.1	3.4	3.7	23.7	0.6	0.2	1.1	4.5	147	12	70	16	<14	13	42	13	6	<8	32	1502	93	4	139	75	78
400	35.5	9.7	0.1	3.9	3.1	20.9	0.8	0.2	1.2	5.3	163	17	83	25	<14	15	46	10	8	<8	34	1124	101	13	162	74	81
410	31.8	8.6	0.1	4.1	2.8	24.4	0.8	0.2	1.1	4.5	138	15	73	8	19	11	30	11	6	<8	35	1032	101	12	146	67	79
420	29.1	7.9	0.1	4.1	2.8	26.7	0.7	0.2	1.1	4.2	160	12	63	11	15	13	29	8	8	<8	32	1046	6	80	11	132	63
430	29.5	8.2	0.1	3.9	3.0	26.2	0.7	0.2	1.1	4.3	149	13	61	19	<14	15	33	<8	<4	<8	32	1122	<4	84	7	123	73
440	31.6	8.7	0.1	3.9	2.9	24.5	0.8	0.2	1.1	4.7	146	17	61	21	<14	8	38	12	<4	<8	34	1072	<4	91	11	146	110
450	30.2	8.2	0.1	4.1	2.8	25.7	0.8	0.2	1.1	4.4	136	13	69	20	<14	16	33	17	6	<8	33	1072	<4	92	13	136	72
Core S3																											
Standards																											
AN	<0,80	<0,10	<0,00	0.5	0.1	39.1	<0,02	<0,006	<0,02	0.1	<8	<4	<18	<4	<14	<2	<2	<8	14	<8	<4	1415	6	<12	<2	<4	<15
AN	<0,80	<0,10	<0,00	0.5	<0,04	39.2	<0,02	<0,006	<0,02	0.1	<8	<4	<18	<4	<14	<2	<2	<8	15	<8	<4	1424	6	<12	<2	<4	<15
NBS-97a	43.7	39.3	0.0	0.2	<0,04	0.1	1.9	0.4	0.6	0.5	505	7	209	8	90	39	46	47	40	23	15	1485	32	198	87	442	34
NBS-97a	43.8	39.8	0.0	0.2	<0,04	0.1	1.9	0.4	0.6	0.5	507	6	217	12	91	38	44	55	46	23	14	1490	37	216	87	445	34

Appendix 5-A: Element distribution (XRF)

	Main elements (in percent)										Trace elements (in ppm)																
Depth (cm)	**SiO_2**	**Al_2O_3**	**MnO**	**MgO**	**Na_2O**	**CaO**	**TiO_2**	**P_2O_5**	**K_2O**	**Fe_2O_3**	**Ba**	**Co**	**Cr**	**Cu**	**La**	**Nb**	**Ni**	**Ga**	**Pb**	**Pr**	**Rb**	**Sr**	**Th**	**V**	**Y**	**Zr**	**Zn**
3	33.3	8.7	0.1	3.8	3.0	22.2	0.8	0.2	1.1	5.4	168	18	90	30	<14	14	49	12	7	<8	33	1921	5	147	8	150	84
35	33.5	9.1	0.1	4.1	2.1	24.7	0.8	0.2	1.2	4.8	171	14	76	23	18	11	38	12	12	<8	35	1119	<4	96	15	154	73
89	37.3	12.1	0.1	4.6	2.3	17.1	0.9	0.2	1.7	7.3	188	20	80	36	<14	14	55	18	9	<8	50	1721	<4	118	12	118	86
93	43.7	10.7	0.1	3.2	3.5	17.9	0.8	0.2	1.1	4.8	203	13	61	30	<14	11	26	12	<4	<8	29	1741	<4	98	4	138	59
131	34.6	9.8	0.1	4.5	2.3	22.3	0.8	0.2	1.3	5.5	148	17	75	27	16	7	43	12	9	<8	39	1438	5	100	10	119	77
140	25.5	6.8	0.1	4.4	1.8	31.8	0.5	0.2	0.9	3.5	130	8	49	14	<14	14	25	14	<4	<8	29	1656	<4	74	<2	98	67
150	27.6	7.2	0.1	3.8	2.1	29.9	0.6	0.2	1.0	3.8	132	13	58	19	<14	9	25	10	<4	<8	31	2001	<4	84	<2	113	66
160	28.3	7.3	0.1	4.0	2.0	29.7	0.6	0.2	0.9	3.9	140	16	59	17	<14	11	28	14	5	<8	29	2012	<4	79	<2	115	74
170	32.2	8.3	0.1	4.0	2.1	26.5	0.7	0.2	1.1	4.2	151	16	69	19	<14	13	31	11	10	10	30	1384	5	90	10	139	72
180	33.4	8.8	0.1	4.0	2.4	24.7	0.7	0.2	1.1	4.5	170	14	69	21	<14	5	33	9	10	<8	34	1522	6	93	5	137	76
190	37.4	9.6	0.1	4.1	2.4	21.7	0.8	0.2	1.2	5.1	175	13	86	28	38	15	38	9	4	<8	36	1198	<4	110	12	167	91
192	38.1	9.6	0.1	4.0	2.4	21.2	0.8	0.2	1.2	5.0	184	14	80	26	14	10	35	16	10	<8	33	1210	5	99	14	164	82
195	26.6	7.0	0.1	4.0	2.0	30.6	0.6	0.2	0.9	3.7	147	10	54	23	<14	14	26	<8	9	<8	29	2050	<4	76	<2	104	65
207	35.1	9.1	0.1	4.0	2.5	23.6	0.8	0.2	1.1	4.8	160	13	69	26	14	14	33	15	<4	<8	32	1453	<4	90	11	152	77
210	35.2	9.3	0.1	3.9	2.7	22.9	0.8	0.2	1.2	4.9	146	13	79	30	<14	5	34	9	<4	<8	34	1382	<4	104	11	146	79
220	37.6	9.8	0.1	4.2	2.5	20.8	0.9	0.2	1.2	5.4	174	14	88	33	25	16	40	15	9	<8	36	1216	<4	109	15	165	81
230	32.2	8.6	0.1	3.8	2.6	25.5	0.8	0.2	1.1	4.6	119	16	72	21	<14	16	29	14	4	<8	31	1622	<4	95	7	134	78
240	29.9	7.8	0.1	4.1	2.3	27.6	0.7	0.2	1.0	4.2	138	12	67	23	<14	11	26	12	6	<8	28	1543	<4	91	8	139	69
250	33.7	8.9	0.1	4.1	2.4	24.2	0.8	0.2	1.1	4.7	151	13	72	19	<14	13	33	14	9	<8	33	1421	6	102	8	147	74
260	34.3	9.1	0.1	4.0	2.4	23.9	0.8	0.2	1.1	4.8	174	15	77	30	19	14	33	9	13	<8	35	1401	<4	104	11	152	79
270	30.6	8.3	0.1	3.8	2.2	26.4	0.7	0.2	1.1	4.5	145	11	66	18	<14	13	33	12	10	<8	33	1482	9	89	6	121	71
280	25.1	6.7	0.1	3.5	2.1	31.3	0.6	0.2	0.9	3.7	113	12	49	10	<14	11	26	11	<4	<8	28	2032	<4	77	<2	95	54
290	28.7	8.0	0.1	3.7	2.3	27.8	0.6	0.2	1.1	4.3	141	11	59	27	<14	14	31	10	<4	<8	31	1709	<4	87	3	112	70
300	24.5	6.5	0.1	3.3	2.1	32.1	0.5	0.2	0.8	3.5	109	11	49	17	<14	4	25	9	8	<8	25	2125	<4	73	<2	90	63
310	26.6	7.5	0.1	3.8	2.0	29.8	0.6	0.2	1.0	3.9	122	11	54	16	<14	10	28	<8	5	<8	33	1897	<4	73	<2	108	79
314	24.4	6.7	0.1	3.5	1.8	32.0	0.5	0.2	0.9	3.5	115	7	48	24	<14	13	27	9	<4	<8	31	2268	<4	66	<2	92	60
320	32.3	8.6	0.1	3.6	2.3	25.4	0.7	0.2	1.1	4.3	150	12	62	23	<14	13	30	11	7	<8	33	1618	<4	86	4	125	73
330	31.7	8.6	0.1	3.6	2.1	26.1	0.6	0.2	1.1	4.3	142	13	61	23	<14	10	31	10	8	<8	33	1607	5	85	6	119	69
340	27.9	7.4	0.1	3.4	2.1	29.9	0.5	0.2	0.9	3.5	131	8	56	24	<14	12	23	12	4	9	28	1916	<4	66	<2	105	59
350	22.9	6.1	0.1	3.3	2.2	33.6	0.4	0.2	0.8	3.0	95	8	48	11	<14	8	17	<8	<4	<8	27	2291	<4	60	<2	83	56
360	30.6	8.1	0.1	3.4	2.1	26.7	0.6	0.2	1.0	4.5	141	12	67	24	<14	12	42	13	8	<8	33	1758	<4	108	4	126	69
370	36.6	9.6	0.1	3.7	2.4	22.2	0.7	0.2	1.2	4.9	173	13	83	34	<14	14	35	9	<4	<8	37	1471	<4	107	9	150	73
380	36.5	9.7	0.1	3.6	2.4	21.7	0.8	0.2	1.2	4.9	180	13	80	28	<14	14	41	18	<4	8	39	1431	<4	98	6	153	67
390	29.9	8.3	0.1	3.5	2.5	26.7	0.6	0.2	1.1	4.3	150	14	69	26	<14	11	36	12	8	<8	32	1695	<4	82	2	108	75

Appendix 5-A: Element distribution (XRF)

	Main elements (in percent)										Trace elements (in ppm)																
Depth (cm)	**SiO_2**	**Al_2O_3**	**MnO**	**MgO**	**Na_2O**	**CaO**	**TiO_2**	**P_2O_5**	**K_2O**	**Fe_2O_3**	**Ba**	**Co**	**Cr**	**Cu**	**La**	**Nb**	**Ni**	**Ga**	**Pb**	**Pr**	**Rb**	**Sr**	**Th**	**V**	**Y**	**Zr**	**Zn**
400	39.3	10.3	0.1	3.5	2.7	19.0	0.9	0.2	1.2	5.5	184	20	82	28	14	13	43	16	10	<8	36	1106	8	120	12	167	73
410	31.8	8.5	0.1	4.0	2.1	25.2	0.8	0.2	1.1	4.4	174	16	74	20	24	15	30	15	9	<8	34	1134	<4	96	12	136	71
420	31.1	8.3	0.1	4.2	2.1	25.9	0.8	0.2	1.1	4.5	161	9	71	20	21	12	34	13	15	<8	35	1054	6	86	13	140	65
430	31.4	8.4	0.1	4.1	2.2	25.8	0.8	0.2	1.1	4.4	142	11	59	23	15	13	36	11	<4	<8	32	1122	<4	92	11	139	64
440	31.9	8.7	0.1	3.8	2.0	25.7	0.7	0.2	1.1	4.5	143	15	72	12	<14	12	31	11	4	8	34	1153	<4	96	9	134	67
450	27.0	7.5	0.1	4.1	1.8	29.6	0.6	0.2	1.0	3.9	120	10	64	25	<14	10	37	14	11	<8	31	1181	<4	73	8	114	72
Core S6																											
Standards																											
AN	<0,80	<0,10	<0,00	0.5	<0,04	39.1	<0,02	<0,006	<0,02	0.1	<8	<4	<18	<4	<14	<2	0	<8	12	<8	<4	1416	<4	<12	<2	<4	<15
AN	<0,80	<0,10	<0,00	0.5	<0,04	39.1	<0,02	<0,006	<0,02	0.1	<8	<4	<18	<4	<14	<2	-1	<8	14	<8	<4	1419	5	<12	<2	<4	<15
AN	<0,80	<0,10	<0,00	0.5	<0,04	39.1	<0,02	<0,006	<0,02	0.1	<8	<4	<18	<4	<14	<2	<2	<8	12	<8	<4	1418	<4	<12	<2	<4	<15
NBS-97a	43.8	40.0	0.0	0.2	<0,04	0.1	2.0	0.4	0.6	0.5	508	4	220	12	92	42	47	53	40	19	14	1488	37	195	86	442	31
NBS-97a	43.9	40.0	<0,00	0.2	<0,04	0.1	1.9	0.4	0.6	0.5	488	<4	217	7	79	42	44	45	41	21	13	1490	33	197	85	444	35
NBS-97a	43.7	39.8	0.0	0.2	0.1	0.1	1.9	0.4	0.6	0.5	513	<4	216	9	78	45	46	56	41	18	15	1487	31	202	91	444	31
1	27.0	7.7	0.2	3.2	2.1	30.0	0.6	0.2	0.8	4.0	131	16	53	33	19	11	30	9	9	<8	30	1580	<4	80	<2	99	69
10	15.8	4.9	0.1	3.2	2.3	39.2	0.3	0.2	0.6	2.5	73	10	30	17	<14	7	10	<8	<4	<8	24	2349	<4	51	<2	52	50
30	22.3	6.6	0.1	3.2	1.8	34.5	0.5	0.2	0.8	3.5	126	10	44	15	<14	10	27	<8	5	<8	28	1849	<4	62	<2	84	64
40	22.0	6.7	0.1	3.2	1.6	34.5	0.5	0.3	0.9	3.4	105	9	50	16	<14	12	25	8	4	<8	30	1845	<4	61	<2	78	67
50	22.3	7.0	0.1	3.7	2.7	42.0	0.5	0.3	1.0	3.5	117	13	49	39	17	11	42	8	9	<8	30	2090	<4	66	<2	73	77
60	13.2	4.4	0.1	3.2	2.5	40.4	0.3	0.2	0.7	2.3	75	12	31	16	25	7	21	<8	<4	<8	23	2048	<4	42	<2	39	64
70	9.0	3.0	0.1	2.9	1.8	45.7	0.2	0.2	0.5	1.6	53	5	<18	<4	<14	5	11	<8	<4	<8	19	2624	<4	33	<2	18	45
80	11.3	3.6	0.1	3.0	2.1	43.5	0.2	0.2	0.6	1.9	57	9	26	14	<14	6	15	<8	<4	9	21	2566	<4	28	<2	33	63
86	10.0	3.1	0.1	3.6	1.6	55.0	0.2	0.1	0.4	1.7	45	7	30	7	<14	4	14	<8	<4	<8	22	4554	<4	35	<2	17	45
90	14.5	4.4	0.1	3.1	2.2	40.6	0.3	0.2	0.6	2.2	75	8	29	<4	<14	6	13	<8	8	<8	23	2463	<4	42	<2	63	56
100	38.4	10.3	0.1	4.5	2.7	27.6	1.0	0.2	1.2	6.2	180	26	123	41	<14	13	69	10	10	<8	35	1907	<4	202	5	185	105
110	36.6	9.9	0.1	4.2	2.2	21.6	1.0	0.2	1.2	5.6	172	16	100	31	19	15	47	14	<4	<8	36	1410	<4	120	11	164	83
120	30.8	8.5	0.1	4.1	3.2	23.4	0.8	0.3	1.1	5.3	134	17	84	29	<14	12	54	13	<4	<8	33	1715	<4	138	5	142	64
130	33.8	8.8	0.1	3.8	3.3	21.6	0.9	0.2	1.1	5.4	159	17	97	22	<14	17	48	14	5	<8	32	1927	<4	163	<2	159	81
200	36.3	9.3	0.1	4.2	2.5	22.6	0.8	0.2	1.2	4.9	182	15	78	23	<14	11	36	12	<4	<8	35	1202	<4	99	18	161	81
250	33.8	8.7	0.1	3.9	2.1	24.9	0.7	0.2	1.1	4.6	160	13	70	29	<14	12	31	13	8	<8	29	1373	<4	96	11	140	76
270	37.6	9.6	0.1	3.8	2.7	21.8	0.8	0.2	1.2	4.9	179	13	81	39	<14	14	34	9	5	<8	34	1229	<4	104	12	161	88
280	29.5	7.9	0.1	3.9	2.2	27.9	0.7	0.2	1.0	4.3	143	15	70	39	<14	10	30	13	<4	<8	31	1873	<4	89	2	123	69
290	32.1	8.5	0.1	3.8	2.5	26.2	0.7	0.2	1.0	4.5	152	12	72	20	24	11	32	12	5	<8	31	1577	<4	87	10	142	71
295	42.1	11.0	0.1	4.6	3.8	23.6	1.0	0.3	1.4	6.3	182	24	104	36	<14	11	56	16	4	<8	38	1368	<4	156	15	193	92

Appendix 5-A: Element distribution (XRF)

	Main elements (in percent)										Trace elements (in ppm)																
Depth (cm)	**SiO_2**	**Al_2O_3**	**MnO**	**MgO**	**Na_2O**	**CaO**	**TiO_2**	**P_2O_5**	**K_2O**	**Fe_2O_3**	**Ba**	**Co**	**Cr**	**Cu**	**La**	**Nb**	**Ni**	**Ga**	**Pb**	**Pr**	**Rb**	**Sr**	**Th**	**V**	**Y**	**Zr**	**Zn**
310	33.0	8.7	0.1	3.9	2.2	25.3	0.8	0.2	1.1	4.6	176	15	72	20	<14	12	38	14	<4	<8	32	1419	<4	91	8	148	74
320	32.9	8.7	0.1	3.8	2.1	25.6	0.8	0.2	1.1	4.7	156	14	77	26	21	11	34	11	<4	<8	30	1449	6	106	7	143	75
330	27.5	7.5	0.1	3.8	2.1	29.5	0.7	0.2	1.0	4.0	131	9	60	20	<14	8	26	<8	5	10	31	1699	<4	95	<2	118	66
340	26.2	7.0	0.1	3.6	1.8	32.0	0.6	0.2	0.9	3.7	127	10	53	<4	<14	7	22	8	7	<8	28	1848	<4	78	<2	113	59
350	31.2	8.4	0.1	3.7	3.1	24.2	0.7	0.3	1.1	4.8	163	15	73	26	<14	9	44	13	9	<8	35	1451	<4	120	6	139	89
360	32.0	8.7	0.1	3.8	2.1	26.0	0.7	0.2	1.1	4.4	145	13	70	18	17	10	30	9	7	<8	36	1584	<4	94	5	142	75
370	37.1	9.9	0.1	4.2	2.5	31.2	0.7	0.3	1.2	4.7	181	13	73	21	14	12	39	10	5	<8	36	1815	<4	96	5	150	78
380	22.6	6.1	0.1	3.5	2.0	34.8	0.5	0.2	0.8	2.9	111	8	41	8	<14	8	14	<8	8	<8	25	2244	<4	68	<2	83	50
390	24.5	6.6	0.1	3.3	1.9	33.0	0.5	0.2	0.8	3.3	102	7	53	37	<14	5	29	10	4	<8	27	2261	<4	73	<2	97	58
400	35.7	9.1	0.1	3.7	2.7	23.6	0.7	0.2	1.1	4.4	168	15	69	16	<14	13	31	15	4	<8	32	1506	<4	102	10	143	66
420	26.2	7.2	0.1	3.4	2.0	31.0	0.5	0.2	0.9	3.7	107	11	56	15	<14	7	31	<8	4	<8	33	2033	<4	67	<2	103	59
430	31.8	8.7	0.1	3.6	2.8	25.3	0.7	0.2	1.1	4.5	168	14	70	24	<14	13	42	9	8	<8	35	1475	5	97	8	145	81
440	33.9	9.1	0.1	3.7	2.0	24.5	0.8	0.2	1.1	4.7	177	15	72	30	20	14	37	15	5	<8	32	1269	<4	111	16	162	69
450	30.4	8.1	0.1	4.2	1.8	27.5	0.8	0.2	1.0	4.2	173	13	74	28	22	15	34	13	<4	<8	30	1146	<4	88	7	142	64
460	34.1	9.2	0.1	5.1	2.6	32.1	0.8	0.2	1.2	4.8	183	12	81	26	18	9	31	12	14	11	34	1268	6	91	11	140	77
470	26.5	7.3	0.1	4.0	1.7	30.9	0.6	0.2	0.9	3.8	121	12	62	18	<14	11	32	9	10	<8	30	1550	<4	86	<2	114	60

Appendix 5-B: High- and low- strontium aragonite

Depth (cm)	Aragonite	Sr ($CaCO_3$)	High-Sr-aragonite	Low-Sr-aragonite
S1 - bulk				
1	59.51	2834	28.7	30.8
10	58.04	2940	29.6	28.5
20	57.18	2902	29.0	28.2
25	55.18	3020	29.8	25.4
30	56.05	3471	34.5	21.6
40	68.20	3459	36.7	31.5
50	71.90	5115	55.1	16.8
120	39.74	2585	22.4	17.3
130	51.73	3459	33.4	18.4
140	45.28	2566	23.5	21.8
150	36.70	2138	17.9	18.8
160	49.40	2438	23.1	26.3
170	36.40	2132	17.8	18.6
180	45.39	2432	22.3	23.1
190	51.21	2323	22.3	28.9
200	58.91	2367	23.9	35.0
210	46.97	2641	24.5	22.4
220	48.88	2495	23.6	25.3
230	55.08	2953	29.2	25.9
240	51.44	2965	28.5	22.9
250	36.16	2169	18.0	18.1
260	28.98	1655	12.3	16.6
270	24.02	1694	11.4	12.6
280	31.64	1674	13.1	18.6
290	43.21	2369	21.3	21.9
300	38.90	1922	16.5	22.4
310	29.26	1743	13.1	16.2
320	38.89	1977	17.0	21.9
340	47.30	2434	22.7	24.6
350	54.48	2445	24.0	30.4
360	41.35	2094	18.5	22.9
370	34.83	1901	15.5	19.3
380	37.39	1982	16.7	20.7
390	34.10	2024	16.4	17.7
400	35.26	2002	16.4	18.8
410	53.38	2143	20.9	32.5
420	34.64	2163	17.6	17.0
430	48.87	2353	22.2	26.7
440	43.72	2312	20.9	22.8
450	47.51	2640	24.7	22.9
460	45.50	2408	22.1	23.4
470	42.96	2184	19.6	23.4
480	40.06	2047	17.8	22.2
500	34.76	1983	16.2	18.6
S2 - bulk				
2	64.7	3375	35.2	29.5
10	59.4	3388	34.3	25.1
20	57.3	3188	31.9	25.4
30	58.6	3513	35.4	23.2
40	59.8	3063	31.1	28.7

Depth (cm)	Aragonite	Sr ($CaCO_3$)	High-Sr-aragonite	Low-Sr-aragonite
S3 - bulk				
5	70.5	4811	51.5	19.0
35	43.2	2545	22.9	20.3
89	76.8	5791	63.6	13.2
93	79.8	6162	68.4	11.4
131	57.3	3646	36.5	20.8
140	47.3	2767	25.8	21.5
150	57.6	3663	36.7	20.9
160	60.7	3662	37.4	23.3
170	48.6	2872	27.1	21.5
180	54.2	3402	33.4	20.8
190	54	3216	31.5	22.5
192	57.1	3470	34.7	22.4
195	54	3674	36.0	18.0
207	57.9	3569	35.9	22.0
210	51.6	3461	33.4	18.2
220	53.2	3438	33.5	19.7
230	60.4	3685	37.6	22.8
240	51.8	3215	31.0	20.8
250	55	3337	32.9	22.1
260	55	3364	33.2	21.8
270	58.3	3181	32.0	26.3
280	61.4	3510	36.0	25.4
290	58.8	3378	34.1	24.7
300	65.5	3633	38.0	27.5
310	55.3	3475	34.3	21.0
314	54.3	3912	38.4	15.9
320	58.1	3658	36.8	21.3
330	60.1	3395	34.5	25.6
340	62.2	3527	36.3	25.9
350	62.5	3708	38.2	24.3
360	59.9	3719	37.8	22.1
370	62.1	3851	39.6	22.5
380	67.2	3789	40.0	27.2
390	58.5	5024	50.7	7.8
410	42.4	2492	22.2	20.2
420	36.9	2179	18.3	18.6
430	30.8	2458	18.9	11.9
440	46.6	2101	19.5	27.1
S6 - bulk				
1	58.7	2995	30.2	28.5
10	62.3	3409	35.1	27.2
30	56.9	3048	30.4	26.5
40	56.5	2968	29.6	26.9
50	58.1	3293	33.1	25.0
60	55.7	2784	27.6	28.1
70	59.7	3176	32.2	27.5
80	58.8	3255	32.9	25.9
100	57	4511	45.1	11.9
110	58.3	3898	39.3	19.0
120	60	4290	43.6	16.4

Aragonite values in %, Sr in ppm

Appendix 5-B: High- and low- strontium aragonite

Depth (cm)	Aragonite	Sr ($CaCO_3$)	High-Sr-aragonite	Low-Sr-aragonite
50	58.2	3061	30.8	27.4
60	57.5	3133	31.4	26.1
70	59	3596	36.4	22.6
80	60.2	3613	36.8	23.4
90	76.8	5794	63.6	13.2
100	83.8	6467	72.8	11.0
170	78.8	6366	70.4	8.4
210	52.1	3008	29.1	23.0
220	54.3	3479	34.2	20.1
230	50.5	2852	27.3	23.2
240	58.6	3641	36.7	21.9
250	48.3	2841	26.7	21.6
260	48.5	3312	31.2	17.3
270	59.7	3639	36.9	22.8
280	47.9	2986	28.0	19.9
290	48.1	3194	30.0	18.1
300	53.2	3188	31.1	22.1
310	54.7	3224	31.7	23.0
320	57.1	3393	33.9	23.2
330	52.7	3126	30.4	22.3
340	56.4	3551	35.3	21.1
350	57.7	3340	33.5	24.2
360	60.7	3725	38.0	22.7
370	55.2	3965	39.2	16.0
380	57.8	3610	36.2	21.6
390	61.5	3647	37.4	24.1
400	51.1	3156	30.3	20.8
410	41.9	2338	20.7	21.2
420	33.6	2161	17.4	16.2

Depth (cm)	Aragonite	Sr ($CaCO_3$)	High-Sr-aragonite	Low-Sr-aragonite
130	71.7	5122	55.1	16.6
200	57.5	3040	30.5	27.0
250	50.3	3059	29.2	21.1
270	57	3315	33.1	23.9
280	60.1	3829	39.0	21.1
290	57.5	3433	34.4	23.1
295	57.5	3844	38.5	19.0
310	50.3	3229	30.8	19.5
320	52.1	3327	32.2	19.9
330	58.3	3314	33.4	24.9
340	59.2	3298	33.4	25.8
350	56	3442	34.2	21.8
360	58.2	4470	45.0	13.2
370	58.5	3957	39.9	18.6
380	60.1	3643	37.1	23.0
390	64	3895	40.5	23.5
400	63.8	3759	39.0	24.8
420	59.7	3704	37.6	22.1
430	57.9	3292	33.1	24.8
440	50.3	2952	28.2	22.1
450	35.1	2309	18.9	16.2
460	40.4	2486	21.7	18.7
470	45.9	2701	24.9	21.0

Aragonite values in %, Sr in ppm

Appendix 5-C: High- and low-strontium aragonite stacks

	High-Sr aragonite (%)						Low-Sr aragonite (%)					
Age (ky)	**S1**	**S2**	**S3**	**S6**	**stack**	**stdev.**	**S1**	**S2**	**S3**	**S6**	**stack**	**stdev.**
1		34.6			34.6	0.0		26.3			26.3	0.0
2		32.5			32.5	0.0		25.0			25.0	0.0
3		32.7			32.7	0.0		26.7			26.7	0.0
4		30.9			30.9	0.0		27.3			27.3	0.0
5		34.1			34.1	0.0		24.2			24.2	0.0
6		36.8		27.6	32.2	4.6		23.4		28.1	25.8	2.3
7		52.9		36.5	44.7	8.2		17.3		21.7	19.5	2.2
8		64.2		40.1	52.2	12.0		13.0		18.5	15.8	2.7
9		65.9		45.3	55.6	10.3		12.6		16.4	14.5	1.9
10		67.6	51.5	47.8	55.6	8.6		12.2	19.0	16.4	15.9	2.8
11		69.3	45.7	50.2	55.1	10.3		11.8	19.2	16.5	15.9	3.1
12		71.1	39.8	52.7	54.5	12.8		11.4	19.5	16.5	15.8	3.3
13	57.2	72.8	34.0	55.1	54.8	13.8	16.8	11.0	19.8	16.6	16.0	3.2
14	53.1	72.4	28.1	51.0	51.2	15.7	16.8	10.6	20.1	18.3	16.5	3.6
15	49.0	72.1	23.6	46.9	47.9	17.1	16.9	10.3	20.2	20.1	16.9	4.0
16	44.9	71.8	31.4	42.8	47.7	14.8	17.0	9.9	18.8	21.8	16.9	4.4
17	40.8	71.4	39.2	38.7	47.5	13.8	17.0	9.5	17.5	23.5	16.9	5.0
18	36.7	71.1	47.0	34.6	47.3	14.5	17.1	9.1	16.1	25.3	16.9	5.7
19	32.6	70.8	54.7	30.5	47.2	16.6	17.2	8.7	14.7	27.0	16.9	6.6
20	28.5	70.4	62.5	30.3	48.0	18.7	17.2	8.4	13.4	26.3	16.3	6.6
21	24.5	60.7	56.6	30.2	43.0	15.9	17.3	11.8	15.2	25.6	17.5	5.1
22	24.5	51.0	48.4	30.0	38.5	11.4	17.5	15.3	17.5	24.9	18.8	3.6
23	28.7	41.3	40.2	29.9	35.0	5.8	17.9	18.7	19.8	24.2	20.1	2.4
24	32.8	31.5	28.0	29.7	30.5	1.8	18.3	22.1	21.4	23.5	21.3	1.9
25	30.1	32.1	33.3	29.6	31.3	1.5	19.5	21.3	22.6	22.8	21.5	1.3
26	26.3	31.4	32.3	29.4	29.8	2.3	20.8	21.4	21.8	22.1	21.5	0.5
27	23.0	29.2	33.7	29.3	28.8	3.8	21.5	23.0	18.2	21.3	21.0	1.7
28	20.8	36.7	37.6	30.1	31.3	6.7	20.4	21.9	22.8	21.7	21.7	0.9
29	18.7	30.7	33.4	31.5	28.6	5.8	19.2	21.7	21.5	22.7	21.3	1.3
30	19.1	27.6	31.6	32.8	27.8	5.4	20.6	20.7	21.1	23.7	21.5	1.3
31	21.1	30.3	32.8	36.4	30.1	5.6	23.4	18.2	22.0	22.3	21.5	2.0
32	23.1	33.5	33.1	37.8	31.9	5.4	26.3	19.5	21.9	21.7	22.3	2.5
33	21.1	36.9	33.0	34.6	31.4	6.1	23.4	22.8	22.7	23.0	23.0	0.3
34	19.1	31.6	32.2	37.7	30.1	6.8	20.5	21.1	25.6	19.0	21.5	2.4
35	18.4	28.4	33.9	34.1	28.7	6.4	19.3	19.6	25.9	19.3	21.0	2.8
36	20.1	29.6	35.7	30.9	29.1	5.7	21.0	18.5	25.3	19.5	21.1	2.6
37	21.9	30.4	34.6	31.9	29.7	4.7	22.7	19.7	24.9	19.8	21.8	2.1
38	22.3	31.1	35.7	32.7	30.4	5.0	24.7	22.1	25.8	22.3	23.7	1.6
39	22.3	31.5	37.9	33.4	31.3	5.7	26.9	22.6	27.2	25.1	25.5	1.8
40	22.4	32.2	35.5	33.4	30.9	5.0	29.2	23.0	23.0	25.7	25.2	2.5
41	23.0	33.5	37.0	33.8	31.8	5.3	31.5	23.1	17.7	23.5	24.0	4.9
42	23.6	32.5	36.9	37.2	32.6	5.5	33.8	22.8	20.9	19.4	24.2	5.7
43	24.0	30.4	35.4	44.8	33.7	7.6	32.6	22.3	23.9	13.4	23.0	6.8
44	24.3	33.3	35.0	41.5	33.5	6.1	27.8	21.6	25.6	16.9	23.0	4.2
45	24.5	35.0	36.1	38.8	33.6	5.4	23.1	21.7	25.9	20.3	22.7	2.1
46	24.2	33.9	37.3	37.4	33.2	5.4	23.4	23.6	25.1	23.1	23.8	0.8
47	23.8	35.3	38.2	39.8	34.3	6.2	24.5	23.6	23.9	23.4	23.9	0.4
48	24.1	38.0	37.9	39.8	34.9	6.3	25.4	22.7	22.5	24.1	23.7	1.2
49	26.2	38.7	38.6	38.9	35.6	5.4	25.6	18.7	22.3	24.5	22.8	2.6
50	28.3	38.6	39.6	38.4	36.2	4.6	25.8	17.1	22.8	23.6	22.4	3.2
51	29.0	36.8	39.9	37.9	35.9	4.1	25.2	20.5	25.9	22.6	23.6	2.2
52	28.8	36.7	43.8	36.3	36.4	5.3	24.1	22.6	20.3	22.9	22.5	1.4
53	28.5	37.4	50.7	33.1	37.4	8.3	22.9	24.1	7.9	24.8	19.9	7.0
54	26.6	35.5	46.8	32.2	35.3	7.4	22.0	23.2	9.5	24.3	19.8	6.0
55	24.7	33.5	42.9	31.3	33.1	6.5	21.2	22.3	11.2	23.8	19.6	5.0
56	22.8	31.6	39.0	30.4	31.0	5.7	20.3	21.4	12.9	23.4	19.5	4.0
57	20.9	29.4	35.1	29.5	28.7	5.1	19.4	20.8	14.6	22.9	19.4	3.1

Appendix 5-C: High- and low-strontium aragonite stacks

	High-Sr aragonite (%)						Low-Sr aragonite (%)					
Age (ky)	**S1**	**S2**	**S3**	**S6**	**stack**	**stdev.**	**S1**	**S2**	**S3**	**S6**	**stack**	**stdev.**
58	19.0	26.8	31.3	28.6	26.4	4.6	18.6	20.9	16.3	22.4	19.5	2.3
59	17.5	24.2	27.4	27.3	24.1	4.0	18.0	21.0	17.9	21.6	19.6	1.7
60	16.5	21.6	23.5	25.7	21.8	3.4	17.7	21.1	19.6	20.5	19.7	1.3
61	15.4	20.1	21.5	24.0	20.3	3.1	17.4	20.3	19.9	19.4	19.3	1.1
62	14.4	19.2	20.4	22.3	19.1	2.9	17.2	18.9	19.5	18.3	18.5	0.9
63	13.4	18.3	19.4	20.6	17.9	2.7	16.9	17.6	19.0	17.3	17.7	0.8
64	12.4	17.4	18.3	18.9	16.7	2.6	16.6	16.3	18.6	16.2	16.9	1.0
65	11.8		39.6		25.7	13.9	14.4		22.5		18.4	4.1
66	11.6				11.6	0.0	13.3				13.3	0.0
67	12.5		40.0		26.3	13.7	16.7		27.2		22.0	5.3
68	15.1		50.7		32.9	17.8	19.4		7.8		13.6	5.8
69	19.7				19.7	0.0	21.3				21.3	0.0
70	19.5		22.2		20.9	1.4	22.1		20.2		21.1	1.0
71	16.8		18.3		17.5	0.7	22.4		18.6		20.5	1.9
72	14.8				14.8	0.0	19.3				19.3	0.0
73	13.3				13.3	0.0	16.5				16.5	0.0
74	15.5				15.5	0.0	19.8				19.8	0.0
75	17.5				17.5	0.0	22.2				22.2	0.0
76	19.1				19.1	0.0	22.9				22.9	0.0
77	20.7				20.7	0.0	23.7				23.7	0.0
78	22.3				22.3	0.0	24.4				24.4	0.0
79	23.3				23.3	0.0	27.2				27.2	0.0
80	24.0				24.0	0.0	30.4				30.4	0.0
81	22.4				22.4	0.0	28.3				28.3	0.0
82	20.9				20.9	0.0	26.1				26.1	0.0
83	19.3				19.3	0.0	24.0				24.0	0.0
84	18.0				18.0	0.0	22.4				22.4	0.0
85	17.2				17.2	0.0	21.3				21.3	0.0
86	16.4				16.4	0.0	20.3				20.3	0.0
87	15.5				15.5	0.0	19.3				19.3	0.0

Appendix 5-D: Stacked high-strontium aragonite accumulation rates

	S1			S2			S3			S6			HSA AR stack	
Age (ky)	HSA	carbonate SR	HSA AR	HSA	carbonate SR	HSA AR	HSA	carbonate SR	HSA AR	HSA	carbonate SR	HSA AR	Sanganeb	st.dev.
1				34.6	8.2	22.2					6.3		22.2	0.0
2				32.5	8.2	20.9					6.3		20.9	0.0
3				32.7	8.2	21.0					6.3		21.0	0.0
4				30.9	8.2	19.8					6.3		19.8	0.0
5				34.1	8.2	21.9					6.3		21.9	0.0
6				36.8	2.7	7.6				27.6	12.8	27.6	17.6	10.0
7				52.9	2.7	11.0				36.5	12.8	36.5	23.7	12.8
8				64.2	2.7	13.3				40.1	12.8	40.1	26.7	13.4
9				65.9	0.4	2.1				45.3	0.4	1.5	1.8	0.3
10				67.6	0.4	2.1	51.5	0.6	2.5	47.8	0.4	1.6	2.1	0.4
11				69.3	0.4	2.2	45.7	0.6	2.2	50.2	0.4	1.6	2.0	0.3
12				71.1	0.4	2.2	39.8	0.6	1.9	52.7	0.4	1.7	2.0	0.2
13				72.8	3.3	18.5	34.0	3.4	9.0	55.1	3.9	16.6	14.7	4.1
14	53.1	3.0	12.3	72.4	3.3	18.4	28.1	3.4	7.5	51.0	3.9	15.4	13.4	4.0
15	49.0	3.0	11.4	72.1	3.3	18.3	23.6	3.4	6.3	46.9	3.9	14.1	12.5	4.4
16	44.9	3.0	10.4	71.8	3.3	18.3	31.4	3.4	8.3	42.8	3.9	12.9	12.5	3.7
17	40.8	3.0	9.5	71.4	3.3	18.2	39.2	3.4	10.4	38.7	3.9	11.6	12.4	3.4
18	36.7	3.0	8.5	71.1	3.3	18.1	47.0	3.4	12.5	34.6	3.9	10.4	12.4	3.6
19	32.6	3.0	7.6	70.8	3.3	18.0	54.7	3.4	14.5	30.5	3.9	9.2	12.3	4.2
20	28.5	3.0	6.6	70.4	3.3	17.9	62.5	3.4	16.6	30.3	3.9	9.1	12.6	4.8
21	24.5	3.0	5.7	60.7	3.3	15.4	56.6	3.4	15.0	30.2	3.9	9.1	11.3	4.1
22	24.5	3.0	5.7	51.0	3.3	13.0	48.4	3.4	12.8	30.0	3.9	9.0	10.1	3.0
23	28.7	1.5	3.4	41.3	2.4	7.7	40.2	3.7	11.5	29.9	2.4	5.6	7.1	3.0
24	32.8	1.5	3.9	31.5	2.4	5.9	28.0	3.7	8.0	29.7	2.4	5.6	5.9	1.5
25	30.1	1.5	3.6	32.1	2.4	6.0	33.3	3.7	9.5	29.6	2.4	5.5	6.2	2.1
26	26.3	1.5	3.2	31.4	2.4	5.9	32.3	3.7	9.3	29.4	2.4	5.5	6.0	2.2
27	23.0	1.5	2.8	29.2	2.4	5.5	33.7	3.7	9.7	29.3	2.4	5.5	5.8	2.5
28	20.8	1.5	2.5	36.7	2.4	6.9	37.6	3.7	10.8	30.1	2.4	5.6	6.4	3.0
29	18.7	1.5	2.2	30.7	2.4	5.8	33.4	3.7	9.6	31.5	2.4	5.9	5.9	2.6
30	19.1	1.5	2.3	27.6	2.4	5.2	31.6	3.7	9.1	32.8	2.4	6.1	5.7	2.4
31	21.1	1.5	2.5	30.3	2.4	5.7	32.8	3.7	9.4	36.4	2.4	6.8	6.1	2.5
32	23.1	1.5	2.8	33.5	2.4	6.3	33.1	3.7	9.5	37.8	2.4	7.1	6.4	2.4
33	21.1	1.5	2.5	36.9	2.4	6.9	33.0	3.7	9.5	34.6	2.4	6.5	6.3	2.5
34	19.1	1.5	2.3	31.6	2.4	5.9	32.2	3.7	9.2	37.7	2.4	7.0	6.1	2.5
35	18.4	1.5	2.2	28.4	2.4	5.3	33.9	3.7	9.7	34.1	2.4	6.4	5.9	2.7
36	20.1	1.5	2.4	29.6	2.4	5.5	35.7	3.7	10.3	30.9	2.4	5.8	6.0	2.8
37	21.9	1.5	2.6	30.4	2.4	5.7	34.6	3.7	9.9	31.9	2.4	6.0	6.1	2.6
38	22.3	1.5	2.7	31.1	2.4	5.8	35.7	3.7	10.2	32.7	2.4	6.1	6.2	2.7
39	22.3	1.5	2.7	31.5	2.4	5.9	37.9	3.7	10.9	33.4	2.4	6.2	6.4	2.9
40	22.4	1.5	2.7	32.2	2.4	6.0	35.5	3.7	10.2	33.4	2.4	6.3	6.3	2.7
41	23.0	1.5	2.8	33.5	2.4	6.3	37.0	3.7	10.6	33.8	2.4	6.3	6.5	2.8
42	23.6	1.5	2.8	32.5	2.4	6.1	36.9	3.7	10.6	37.2	2.4	7.0	6.6	2.8
43	24.0	1.5	2.9	30.4	2.4	5.7	35.4	3.7	10.2	44.8	2.4	8.4	6.8	2.8
44	24.3	1.5	2.9	33.3	2.4	6.2	35.0	3.7	10.0	41.5	2.4	7.8	6.7	2.6
45	24.5	1.5	2.9	35.0	2.4	6.5	36.1	3.7	10.4	38.8	2.4	7.3	6.8	2.6
46	24.2	1.5	2.9	33.9	2.4	6.3	37.3	3.7	10.7	37.4	2.4	7.0	6.7	2.8
47	23.8	1.5	2.9	35.3	2.4	6.6	38.2	3.7	11.0	39.8	2.4	7.4	7.0	2.9
48	24.1	1.5	2.9	38.0	2.4	7.1	37.9	3.7	10.9	39.8	2.4	7.4	7.1	2.8
49	26.2	1.5	3.1	38.7	2.4	7.2	38.6	3.7	11.1	38.9	2.4	7.3	7.2	2.8
50	28.3	1.5	3.4	38.6	2.4	7.2	39.6	3.7	11.4	38.4	2.4	7.2	7.3	2.8
51	29.0	1.5	3.5	36.8	2.4	6.9	39.9	3.7	11.4	37.9	2.4	7.1	7.2	2.8
52	28.8	1.5	3.5	36.7	2.4	6.9	43.8	3.7	12.6	36.3	2.4	6.8	7.4	3.3
53	28.5	1.5	3.4	37.4	2.4	7.0	50.7	3.7	14.5	33.1	2.4	6.2	7.8	4.1

HSA = high-strontium aragonite; SR = sedimentation rate; AR= accumulation rate

Appendix 5-D: Stacked high-strontium aragonite accumulation rates

	S1			S2			S3			S6			HSA AR stack	
Age (ky)	HSA	carbonate SR	HSA AR	HSA	carbonate SR	HSA AR	HSA	carbonate SR	HSA AR	HSA	carbonate SR	HSA AR	Sanganeb	st.dev.
54	26.6	1.5	3.2	35.5	2.4	6.6	46.8	3.7	13.4	32.2	2.4	6.0	7.3	3.8
55	24.7	1.5	3.0	33.5	2.4	6.3	42.9	3.7	12.3	31.3	2.4	5.9	6.9	3.4
56	22.8	1.5	2.7	31.6	2.4	5.9	39.0	3.7	11.2	30.4	2.4	5.7	6.4	3.0
57	20.9	1.5	2.5	29.4	2.4	5.5	35.1	3.7	10.1	29.5	2.4	5.5	5.9	2.7
58	19.0	1.5	2.3	26.8	2.4	5.0	31.3	3.7	9.0	28.6	2.4	5.4	5.4	2.4
59	17.5	1.5	2.1	24.2	2.4	4.5	27.4	3.7	7.9	27.3	2.4	5.1	4.9	2.0
60	16.5	2.9	3.7	21.6			23.5			25.7			3.7	0.0
61	15.4	2.9	3.4	20.1			21.5			24.0			3.4	0.0
62	14.4	2.9	3.2	19.2			20.4			22.3			3.2	0.0
63	13.4	2.9	3.0	18.3			19.4			20.6			3.0	0.0
64	12.4	2.9	2.7	17.4			18.3			18.9			2.7	0.0
65	11.8	2.9	2.6										2.6	0.0
66	11.6	2.9	2.6										2.6	0.0
67	12.5	2.9	2.8										2.8	0.0
68	15.1	2.9	3.4										3.4	0.0
69	19.7	2.9	4.4										4.4	0.0
70	19.5	2.9	4.3										4.3	0.0
71	16.8	2.3	3.0										3.0	0.0
72	14.8	2.3	2.6										2.6	0.0
73	13.3	2.3	2.4										2.4	0.0
74	15.5	2.3	2.8										2.8	0.0
75	17.5	2.3	3.1										3.1	0.0
76	19.1	2.3	3.4										3.4	0.0
77	20.7	2.3	3.7										3.7	0.0
78	22.3	2.3	4.0										4.0	0.0
79	23.3	2.3	4.2										4.2	0.0
80	24.0	2.3	4.3										4.3	0.0
81	22.4	2.3	4.0										4.0	0.0
82	20.9	2.3	3.7										3.7	0.0
83	19.3	2.3	3.4										3.4	0.0
84	18.0	2.3	3.2										3.2	0.0
85	17.2													
86	16.4													
87	15.5													

HSA = high-strontium aragonite; SR = sedimentation rate; AR= accumulation rate

Appendix 6: Component distribution (pointcounting)

Isotope stage / position of calciturbidites (cm)	Depth (cm)	pteropods	plankt.foram	**1. Plankton**	corallinacean	scleractinian	encrusters	**2. Reef builders**	peloids	compound grains	coated grains	algae	echinoderms	large benthics	molluscs	**3. Shallow-water grains**	**4. Bioclasts**	carbonate-clasts	intra-clasts	**5. Lithoclasts**	**6. Terrigenous input**	**7. Matrix**	intra-porosity	inter-porosity	plant remains	bryozoan	small benthics	pyrite+ore	glauconite	undetermined	**8. Others**
Core S2																															
IS1	2	3.5	6.0	**9.5**	2.0	0.0	0.0	**2.0**	3.0	0.0	0.0	0.0	1.0	0.0	1.0	**5.0**	**17.0**	0.0	0.0	**0.0**	**13.5**	**41.5**	3.5	1.0	1.0	0.0	0.0	1.0	0.5	2.0	**9.0**
	10	7.5	6.5	**14.0**	0.0	0.5	0.0	**0.5**	1.5	0.0	0.0	0.0	0.0	0.0	0.0	**1.5**	**10.5**	3.5	0.0	**3.5**	**7.0**	**47.5**	3.0	1.0	3.5	0.0	0.0	1.5	1.0	5.5	**15.5**
	20	7.0	10.5	**17.5**	0.5	0.0	0.0	**0.5**	0.0	0.0	0.0	0.0	1.0	0.0	0.0	**1.0**	**17.5**	2.0	0.0	**2.0**	**9.5**	**43.0**	3.5	0.5	2.0	0.0	0.5	1.0	0.5	1.0	**9.0**
	30	6.5	7.5	**14.0**	0.0	0.0	0.0	**0.0**	1.0	0.0	0.0	0.0	0.0	0.5	1.0	**2.5**	**10.0**	2.0	0.5	**2.5**	**11.0**	**45.0**	3.5	3.0	0.5	0.0	1.0	2.0	0.0	5.0	**15.0**
	40	5.0	5.0	**10.0**	0.5	0.0	0.0	**0.5**	1.0	0.5	0.0	0.0	0.5	0.0	0.5	**2.5**	**14.5**	2.0	0.0	**2.0**	**8.0**	**48.0**	4.0	2.0	1.5	0.0	2.0	0.5	2.5	1.5	**14.0**
	50	8.0	7.0	**15.0**	0.0	0.0	0.0	**0.0**	2.0	0.0	0.0	0.5	0.0	0.0	0.0	**2.5**	**9.0**	2.5	0.0	**2.5**	**5.5**	**53.0**	3.5	0.5	1.5	0.5	0.0	1.0	1.0	3.5	**11.5**
	60	4.0	9.0	**13.0**	0.5	0.0	0.0	**0.5**	2.5	0.0	0.0	0.0	2.0	0.0	1.0	**5.5**	**18.5**	1.0	0.0	**1.0**	**3.0**	**47.0**	3.0	3.5	0.0	0.0	1.0	0.5	0.5	3.0	**11.5**
	70	3.0	4.0	**7.0**	0.5	0.0	0.0	**0.5**	0.0	0.0	0.0	0.0	0.0	0.0	0.0	**0.0**	**11.5**	2.5	0.0	**2.5**	**2.0**	**66.0**	6.0	0.0	0.0	0.0	0.5	0.0	0.5	1.5	**8.5**
	80	3.0	5.0	**8.0**	0.5	0.0	0.0	**0.5**	0.0	0.0	0.0	0.0	1.0	0.0	0.0	**1.0**	**7.0**	3.5	0.0	**3.5**	**3.0**	**72.5**	2.5	0.0	0.0	0.0	0.0	0.5	0.0	1.5	**4.5**
	90	0.0	0.0	**0.0**	8.0	0.0	0.0	**8.0**	2.0	0.0	0.0	0.0	0.0	0.0	0.0	**2.0**	**15.0**	3.0	1.0	**4.0**	**4.0**	**61.5**	0.0	0.0	0.0	0.0	0.0	2.5	0.5	2.5	**5.5**
Sapropel	100	4.5	3.0	**7.5**	1.5	0.0	0.0	**1.5**	1.5	0.5	0.0	0.0	0.0	0.0	0.5	**2.5**	**7.5**	15.0	0.0	**15.0**	**27.5**	**1.0**	6.0	12.0	2.0	1.5	0.0	2.0	0.5	4.5	**28.5**
IS2	170	1.0	0.5	**1.5**	1.0	0.0	0.0	**1.0**	2.5	0.0	0.0	0.0	0.0	0.0	0.5	**3.0**	**6.5**	11.0	0.0	**11.0**	**28.5**	**29.0**	0.0	10.0	2.0	0.0	0.0	2.0	1.5	2.0	**17.5**
	210	6.0	0.0	**6.0**	1.5	0.5	0.0	**2.0**	3.5	0.0	0.5	0.0	0.0	0.0	0.5	**4.5**	**6.0**	1.0	0.0	**1.0**	**14.5**	**55.0**	1.0	1.0	1.5	0.0	0.5	2.5	1.0	3.5	**11.0**
	220	6.0	0.5	**6.5**	1.5	0.0	0.0	**1.5**	5.5	0.0	0.5	0.5	1.0	0.0	0.5	**8.0**	**15.5**	2.5	0.5	**3.0**	**20.0**	**36.5**	1.0	2.5	2.0	0.5	0.0	0.5	0.0	3.0	**9.5**
	230	2.0	3.5	**5.5**	2.0	0.0	0.0	**2.0**	3.5	0.0	0.0	0.0	0.5	0.0	0.0	**4.0**	**8.5**	1.0	1.5	**2.5**	**29.0**	**35.0**	1.5	1.5	1.5	0.0	1.0	1.5	1.5	4.0	**12.5**
	240	5.0	3.5	**8.5**	2.5	1.0	0.0	**3.5**	4.0	0.0	0.0	0.5	0.0	0.5	0.0	**5.0**	**8.5**	4.5	0.0	**4.5**	**36.0**	**17.0**	3.5	6.5	1.0	1.0	0.5	1.0	1.0	1.5	**16.0**
IS3	250	0.5	1.5	**2.0**	0.0	0.0	0.0	**0.0**	6.0	0.0	0.0	0.0	0.5	0.0	0.0	**6.5**	**8.0**	5.0	1.0	**6.0**	**25.5**	**38.5**	1.5	4.0	1.5	0.0	0.0	3.0	0.5	3.0	**13.5**
	260	4.5	2.0	**6.5**	2.5	0.0	0.0	**2.5**	4.0	0.0	0.0	0.0	0.0	0.0	0.0	**4.0**	**16.0**	4.5	0.0	**4.5**	**18.5**	**32.5**	2.0	2.5	1.5	1.0	1.5	3.0	1.5	2.0	**15.0**
	270	3.5	4.5	**8.0**	1.5	0.5	0.0	**2.0**	3.5	0.0	0.0	0.0	0.5	0.0	0.5	**4.5**	**11.0**	4.5	0.0	**4.5**	**24.0**	**32.0**	0.0	5.5	0.5	0.0	0.0	4.0	0.0	4.0	**14.0**
	280	3.0	2.0	**5.0**	0.5	0.0	0.0	**0.5**	3.5	0.0	0.0	0.5	1.0	0.0	0.0	**5.0**	**12.0**	2.0	0.0	**2.0**	**16.0**	**48.0**	0.0	2.0	0.0	0.5	1.0	3.5	1.0	3.5	**11.5**
	290	0.0	4.5	**4.5**	1.5	0.0	0.0	**1.5**	1.5	0.0	0.0	0.0	0.5	0.0	0.0	**2.0**	**11.0**	1.5	0.0	**1.5**	**17.5**	**50.5**	1.5	4.0	1.0	0.0	0.0	2.0	2.0	0.5	**11.0**
	300	6.5	3.5	**10.0**	0.5	0.0	0.0	**0.5**	3.5	0.0	0.0	0.5	0.5	0.0	0.0	**4.5**	**12.5**	3.5	0.0	**3.5**	**13.5**	**41.5**	1.5	5.0	0.5	0.0	0.0	1.5	2.5	3.0	**14.0**
	310	2.0	2.5	**4.5**	4.0	0.0	0.0	**4.0**	2.0	0.0	0.0	0.0	1.0	0.5	0.0	**3.5**	**16.5**	1.0	0.0	**1.0**	**17.5**	**41.0**	1.5	1.0	1.5	0.5	0.5	2.0	1.0	4.0	**12.0**
	320	4.0	4.0	**8.0**	1.0	1.5	0.5	**3.0**	4.0	0.0	0.0	0.0	1.0	1.0	0.5	**6.5**	**17.0**	4.0	0.0	**4.0**	**18.5**	**27.0**	4.0	2.0	1.0	0.5	0.5	3.0	0.5	4.0	**15.5**
	330	1.0	3.0	**4.0**	1.5	0.0	0.0	**1.5**	1.5	0.0	1.0	0.5	0.5	0.5	0.0	**4.0**	**11.0**	5.0	0.0	**5.0**	**16.0**	**45.0**	1.0	2.5	1.0	0.5	0.5	3.5	0.5	3.5	**13.0**
	340	3.0	3.0	**6.0**	1.5	0.0	0.0	**1.5**	3.5	0.0	0.0	1.5	1.0	0.0	0.0	**6.0**	**11.5**	4.5	0.0	**4.5**	**25.5**	**30.5**	1.5	2.0	2.0	0.0	2.0	3.0	0.0	3.5	**14.0**
	350	3.5	5.5	**9.0**	1.0	0.0	0.0	**1.0**	0.5	0.0	0.0	0.0	0.0	0.0	0.0	**0.5**	**13.0**	3.5	0.0	**3.5**	**25.5**	**39.5**	1.0	2.0	0.0	0.0	1.0	0.5	1.0	2.5	**8.0**
	360	3.5	4.5	**8.0**	1.5	0.0	0.0	**1.5**	7.5	0.0	0.0	0.0	0.5	0.0	0.5	**8.5**	**17.0**	2.5	0.0	**2.5**	**18.0**	**34.0**	0.5	2.5	0.0	0.0	0.0	0.5	2.0	4.5	**10.0**
	370	3.0	4.0	**7.0**	2.0	0.0	0.0	**2.0**	1.5	0.0	0.5	0.5	0.5	0.0	1.0	**4.0**	**13.0**	7.5	0.5	**8.0**	**27.5**	**29.5**	0.5	0.0	0.5	0.5	0.5	1.5	1.5	2.5	**7.5**
	380	2.0	4.0	**6.0**	2.0	0.5	0.0	**2.5**	2.5	0.0	0.0	0.0	1.0	0.0	0.0	**3.5**	**9.0**	2.0	0.0	**2.0**	**24.5**	**36.0**	1.5	3.5	0.0	0.5	0.5	2.5	0.5	6.5	**15.5**
	390	3.0	3.5	**6.5**	0.5	0.0	0.0	**0.5**	12.0	0.0	0.0	0.0	0.5	0.5	0.0	**13.0**	**8.5**	3.5	0.0	**3.5**	**17.5**	**30.0**	2.0	6.0	0.5	1.0	1.5	1.0	1.5	7.0	**20.5**
	400	2.0	2.0	**4.0**	1.5	0.0	0.0	**1.5**	1.0	0.0	0.0	0.0	0.0	0.0	0.5	**1.5**	**6.5**	1.0	0.0	**1.0**	**16.5**	**58.5**	0.0	0.0	1.5	0.0	1.5	3.5	0.5	3.5	**10.5**

all values in percent, max. abs. error of pointcounting = ± 3.5%; T = turbidite

Appendix 6: Component distribution (pointcounting)

Isotope stage / position of calciturbidites (cm)	Depth (cm)	pteropods	plankt.foram	**1. Plankton**	corallinacean	scleractinian	encrusters	**2. Reef builders**	peloids	compound grains	coated grains	algae	echinoderms	large benthics	molluscs	**3. Shallow-water grains**	**4. Bioclasts**	carbonate-clasts	intra-clasts	**5. Lithoclasts**	**6. Terrigenous input**	**7. Matrix**	intra-porosity	inter-porosity	plant remains	bryozoan	small benthics	pyrite+ore	glauconite	undetermined	**8. Others**
IS4	410	1.5	1.5	**3.0**	1.5	0.0	0.0	**1.5**	1.0	0.0	0.0	0.0	0.0	0.0	0.0	**1.0**	**7.0**	3.5	0.5	**4.0**	**17.5**	**54.5**	0.0	3.0	1.0	0.0	0.5	3.0	2.5	1.5	**11.5**
	420	3.0	2.0	**5.0**	3.0	0.0	0.0	**3.0**	0.0	0.0	0.0	0.0	0.0	0.0	0.0	**0.0**	**6.0**	2.0	0.0	**2.0**	**15.5**	**60.5**	0.0	2.5	0.5	0.5	1.0	3.0	1.0	0.5	**9.0**
	430	1.0	1.0	**2.0**	2.0	0.0	0.0	**2.0**	4.0	0.0	0.0	0.0	0.0	0.0	0.0	**4.0**	**10.0**	2.0	0.5	**2.5**	**20.0**	**48.0**	0.0	1.5	3.0	0.0	0.5	0.5	1.5	3.0	**10.0**
	440	1.5	2.0	**3.5**	1.0	0.0	0.0	**1.0**	3.0	0.0	0.0	0.0	0.0	0.0	0.0	**3.0**	**6.0**	4.5	0.0	**4.5**	**16.5**	**52.0**	3.5	0.5	0.5	0.5	1.0	1.0	0.5	6.0	**13.5**
	450	2.0	1.5	**3.5**	3.5	0.0	0.0	**3.5**	5.0	0.0	0.0	0.0	1.0	0.0	0.0	**6.0**	**6.0**	1.0	0.0	**1.0**	**15.0**	**54.5**	1.0	1.0	0.5	0.0	0.5	2.5	2.5	2.5	**10.5**
Core S3 Sapropel	3	3.0	0.0	**3.0**	1.0	0.0	0.0	**1.0**	6.5	0.0	0.0	0.0	0.0	0.0	0.0	**6.5**	**7.5**	10.5	0.5	**11.0**	**12.5**	**34.0**	5.0	6.0	1.5	0.5	0.5	3.5	3.5	4.0	**24.5**
IS2	35	1.5	4.0	**5.5**	1.5	0.0	1.0	**2.5**	2.0	0.0	0.5	0.0	0.0	0.0	1.0	**3.5**	**8.5**	3.5	0.0	**3.5**	**14.5**	**41.0**	0.5	2.0	2.5	0.5	2.5	1.5	5.0	6.0	**20.5**
T1 (37-85)	37	0.0	0.0	**0.0**	10.5	5.5	0.5	**16.5**	1.0	8.5	1.5	0.5	0.0	0.5	1.0	**13.0**	**11.0**	6.5	0.0	**6.5**	**1.0**	**1.0**	1.5	34.5	0.0	7.0	2.5	0.0	0.5	4.0	**50.0**
A:32-40	60	1.5	0.0	**1.5**	13.5	11.5	3.5	**28.5**	0.5	3.0	2.0	1.5	0.5	0.5	3.0	**11.0**	**7.5**	5.5	0.0	**5.5**	**0.0**	**3.5**	1.5	29.5	0.0	1.5	3.5	0.0	0.5	4.0	**40.5**
B:58-78	66	2.5	0.0	**2.5**	3.0	4.5	0.0	**7.5**	1.0	1.5	0.5	0.5	0.0	1.0	0.0	**4.5**	**10.0**	6.5	2.0	**8.5**	**9.0**	**37.5**	0.5	7.0	0.5	1.0	2.5	0.0	0.5	2.0	**14.0**
	70	2.0	1.5	**3.5**	7.5	7.0	1.5	**16.0**	1.0	5.0	1.0	4.0	2.0	0.0	5.5	**18.5**	**8.5**	5.0	0.0	**5.0**	**4.5**	**6.0**	3.5	20.5	0.5	3.5	4.5	0.0	0.0	3.0	**35.5**
	73	3.0	0.0	**3.0**	6.5	13.5	1.0	**21.0**	2.0	9.5	3.0	4.0	1.0	1.0	0.5	**21.0**	**10.5**	6.0	0.0	**6.0**	**0.5**	**0.0**	0.0	28.5	0.0	3.0	2.5	0.0	0.0	2.0	**36.0**
	75	4.5	1.0	**5.5**	1.0	2.0	1.5	**4.5**	12.5	0.0	0.5	0.5	0.0	0.5	1.0	**15.0**	**7.0**	2.5	0.0	**2.5**	**11.0**	**23.0**	4.0	8.0	2.5	1.5	2.5	2.0	5.0	5.0	**30.5**
	85	2.0	0.0	**2.0**	7.0	13.0	1.5	**21.5**	0.0	5.0	1.5	2.0	0.5	1.5	1.0	**11.5**	**15.5**	12.0	0.0	**12.0**	**1.5**	**0.0**	0.5	27.0	0.0	3.0	1.5	0.0	0.5	2.0	**34.5**
	89	0.0	0.0	**0.0**	0.0	0.0	0.0	**0.0**	1.5	0.0	0.0	0.0	0.0	0.0	0.0	**1.5**	**1.0**	4.0	0.0	**4.0**	**0.0**	**90.5**	0.0	0.0	1.5	0.0	0.0	0.5	0.0	1.0	**3.0**
	93	4.5	1.0	**5.5**	0.5	0.5	0.0	**1.0**	2.5	0.0	0.5	1.0	1.0	0.0	0.5	**5.5**	**5.5**	0.0	11.0	**11.0**	**23.0**	**11.0**	3.0	17.0	3.5	0.0	0.5	0.5	8.5	3.5	**36.5**
T2 (96)	96	11.5	0.0	**11.5**	1.0	1.0	0.0	**2.0**	1.5	0.0	0.0	3.5	1.5	0.0	0.0	**6.5**	**7.0**	15.5	0.0	**15.5**	**28.5**	**1.5**	2.0	16.0	2.0	0.0	1.0	0.5	1.0	4.0	**26.5**
115-120	131	0.0	0.0	**0.0**	0.0	0.0	0.5	**0.5**	0.0	0.0	0.0	0.0	0.0	0.5	1.0	**1.5**	**11.5**	0.5	1.0	**1.5**	**3.0**	**74.0**	0.5	1.5	0.5	0.0	0.0	1.5	0.5	3.0	**7.5**
	140	1.0	0.0	**1.0**	2.5	0.5	0.5	**3.5**	6.5	1.0	2.0	1.0	0.0	0.0	0.0	**10.5**	**9.5**	2.5	2.0	**4.5**	**10.5**	**39.5**	1.0	3.0	3.5	2.0	1.5	2.5	3.0	4.5	**21.0**
	150	4.0	0.0	**4.0**	2.0	0.5	0.5	**3.0**	2.0	0.0	0.5	1.5	0.5	0.0	1.0	**5.5**	**11.5**	4.0	0.5	**4.5**	**10.5**	**36.5**	0.5	8.0	1.0	2.0	2.0	2.5	2.5	0.5	**19.0**
	160	9.0	1.0	**10.0**	1.0	0.0	0.0	**1.0**	3.0	0.0	0.0	0.5	0.0	0.0	1.0	**4.5**	**4.5**	1.5	4.0	**5.5**	**11.0**	**50.5**	1.0	1.5	1.5	0.0	0.0	2.5	2.0	3.5	**12.0**
	170	1.5	2.5	**4.0**	1.5	0.5	0.0	**2.0**	2.5	0.0	0.0	0.5	0.0	0.0	0.0	**3.0**	**9.0**	3.5	0.0	**3.5**	**8.5**	**46.5**	2.0	6.5	4.0	0.0	2.0	2.5	2.5	3.0	**22.5**
IS3	180	2.0	3.0	**5.0**	1.5	1.5	0.0	**3.0**	0.5	0.0	0.0	1.0	0.5	0.0	1.0	**3.0**	**8.5**	0.0	2.5	**2.5**	**6.5**	**32.0**	0.0	8.0	8.0	1.0	1.5	3.0	5.0	4.5	**31.0**
	190	2.0	2.0	**4.0**	1.0	0.5	0.5	**2.0**	4.0	0.0	0.0	1.5	0.5	0.0	2.0	**8.0**	**8.5**	2.5	0.0	**2.5**	**21.0**	**34.5**	0.0	2.5	4.0	0.0	2.5	2.0	3.5	5.0	**19.5**
	192	5.0	1.5	**6.5**	1.0	0.0	1.0	**2.0**	1.5	0.0	0.5	0.0	0.5	0.0	1.0	**3.5**	**5.0**	5.5	1.0	**6.5**	**27.5**	**27.5**	0.0	4.0	2.0	0.0	1.0	3.5	4.0	6.5	**21.0**
	195	1.0	2.0	**3.0**	3.0	16.5	0.5	**20.0**	1.0	0.0	0.0	2.0	2.5	1.0	2.5	**9.0**	**2.5**	0.0	1.5	**1.5**	**4.5**	**40.0**	0.5	4.5	4.0	3.5	2.5	2.0	1.0	1.5	**19.5**
T3	198	2.0	0.0	**2.0**	6.0	12.5	2.0	**20.5**	3.5	2.5	0.0	6.5	1.5	2.0	3.0	**19.0**	**14.0**	1.0	0.0	**1.0**	**4.5**	**14.5**	2.0	8.0	0.0	0.0	2.5	2.5	0.0	7.5	**22.5**
195-205	200	2.5	1.5	**4.0**	5.5	9.0	2.0	**16.5**	0.5	2.0	2.5	2.5	1.5	3.0	1.5	**13.5**	**15.5**	6.5	0.0	**6.5**	**3.0**	**5.5**	2.0	22.0	1.5	0.5	2.5	0.5	2.5	2.5	**34.0**
	204	1.0	1.0	**2.0**	5.0	6.0	4.5	**15.5**	1.5	0.0	1.5	4.0	3.5	4.0	2.5	**17.0**	**19.5**	2.0	0.5	**2.5**	**1.0**	**1.0**	2.0	31.0	0.0	0.5	2.5	1.0	0.0	2.5	**39.5**
	207	2.0	5.5	**7.5**	0.0	1.0	0.0	**1.0**	0.5	0.0	0.0	0.0	0.0	0.5	1.0	**2.0**	**20.0**	0.0	2.0	**2.0**	**17.5**	**32.5**	2.0	4.0	2.5	2.0	2.5	0.0	0.0	4.5	**17.5**
	210	2.0	2.5	**4.5**	5.0	1.0	0.5	**6.5**	3.0	0.0	0.5	0.0	1.0	0.0	0.5	**5.0**	**8.5**	4.0	0.0	**4.0**	**14.5**	**36.0**	1.0	7.0	2.5	0.5	0.5	2.5	2.5	4.5	**21.0**

all values in percent, max. abs. error of pointcounting = ± 3.5%; T = turbidite

Appendix 6: Component distribution (pointcounting)

Isotope stage / position of calciturbidites (cm)	Depth (cm)	pteropods	plankt.foram	**1. Plankton**	corallinacean	scleractinian	encrusters	**2. Reef builders**	peloids	compound grains	coated grains	algae	echinoderms	large benthics	molluscs	**3. Shallow-water grains**	**4. Bioclasts**	carbonate-clasts	intra-clasts	**5. Lithoclasts**	**6. Terrigenous input**	**7. Matrix**	intra-porosity	inter-porosity	plant remains	bryozoan	small benthics	pyrite+ore	glauconite	undetermined	**8. Others**
	220	1.5	2.5	**4.0**	2.0	0.5	0.0	**2.5**	1.0	0.0	0.0	0.5	2.0	0.0	0.5	**4.0**	**9.0**	3.5	0.0	**3.5**	**22.0**	**35.0**	1.0	4.0	4.5	0.0	1.0	3.5	2.5	3.5	**20.0**
	230	2.0	2.5	**4.5**	0.0	0.0	0.0	**0.0**	1.0	0.0	0.0	0.0	1.5	0.0	0.5	**3.0**	**17.5**	0.0	2.5	**2.5**	**14.0**	**41.0**	1.0	2.0	1.5	2.0	3.5	1.5	0.0	6.0	**17.5**
	250	3.5	3.5	**7.0**	4.5	0.5	0.0	**5.0**	4.0	0.0	0.0	4.0	0.0	0.0	0.5	**8.5**	**12.0**	2.5	0.0	**2.5**	**21.0**	**27.5**	0.5	1.0	2.5	0.0	2.5	2.5	3.5	4.0	**16.5**
	270	5.0	4.0	**9.0**	0.0	1.0	0.0	**1.0**	1.5	0.0	0.0	0.0	1.0	0.5	1.5	**4.5**	**19.0**	0.0	4.0	**4.0**	**19.0**	**31.0**	1.5	2.0	2.0	1.0	0.5	0.0	0.5	5.0	**12.5**
T4 (276)	276	2.5	3.0	**5.5**	4.5	7.5	1.0	**13.0**	1.0	1.0	0.0	1.0	3.0	0.0	3.5	**9.5**	**12.0**	0.0	3.5	**3.5**	**2.0**	**10.5**	3.5	23.5	0.0	4.5	4.0	0.5	1.0	5.0	**42.0**
275-280	276	2.5	1.5	**4.0**	2.5	4.5	0.5	**7.5**	1.5	0.0	0.0	0.5	1.5	0.5	3.0	**7.0**	**17.0**	0.0	4.5	**4.5**	**4.0**	**23.0**	3.5	13.5	4.5	0.0	0.5	3.5	4.0	3.5	**33.0**
	280	5.5	1.5	**7.0**	3.0	8.5	1.5	**13.0**	3.5	0.0	0.0	3.5	2.5	0.5	5.0	**15.0**	**10.0**	0.0	1.0	**1.0**	**8.0**	**19.5**	2.0	13.5	2.5	1.0	2.0	1.0	1.0	2.0	**25.0**
	300	4.0	4.5	**8.5**	4.0	3.5	0.0	**7.5**	2.5	0.0	0.0	0.5	0.0	0.0	2.0	**5.0**	**22.5**	2.5	0.0	**2.5**	**12.5**	**22.0**	1.0	7.0	2.5	0.5	2.0	2.5	3.5	3.5	**22.5**
T5 (313)	313	2.0	4.5	**6.5**	4.5	5.5	1.0	**11.0**	2.5	1.5	0.5	3.0	0.5	1.0	1.0	**10.0**	**13.5**	2.0	0.0	**2.0**	**4.5**	**31.0**	0.0	2.0	3.5	4.0	2.0	1.5	2.5	5.5	**21.0**
303-313	320	0.5	1.5	**2.0**	2.0	3.0	0.5	**5.5**	3.5	0.0	0.0	0.0	1.0	0.0	1.5	**6.0**	**14.0**	0.0	0.5	**0.5**	**8.5**	**44.5**	0.5	5.5	2.5	1.0	2.5	2.0	1.0	3.5	**18.5**
	340	2.0	4.0	**6.0**	0.5	2.0	1.0	**3.5**	4.0	0.0	0.0	0.5	0.5	0.0	0.5	**5.5**	**12.5**	0.0	4.0	**4.0**	**9.0**	**33.0**	3.0	9.5	2.0	0.0	1.0	1.0	5.0	4.5	**26.0**
T6 (377)	377	1.0	2.5	**3.5**	1.0	0.5	0.5	**2.0**	2.5	0.0	0.5	1.5	1.0	0.0	0.0	**5.5**	**21.0**	0.0	0.0	**0.0**	**11.0**	**39.5**	0.0	2.0	4.0	0.0	1.5	2.0	0.5	8.0	**18.0**
375-377	380	4.0	1.0	**5.0**	1.5	0.5	1.0	**3.0**	0.5	0.0	1.0	0.5	0.0	0.0	1.0	**3.0**	**14.0**	5.0	0.0	**5.0**	**17.0**	**30.0**	2.0	0.5	3.0	2.0	3.0	0.5	2.0	9.5	**22.5**
IS4	410	1.5	2.0	**3.5**	0.5	0.0	0.5	**1.0**	0.5	0.0	0.0	0.0	0.5	0.0	0.0	**1.0**	**8.0**	0.0	2.0	**2.0**	**6.0**	**58.0**	1.0	6.5	3.5	0.5	0.0	2.5	2.0	1.5	**17.5**
	450	3.0	4.0	**7.0**	1.0	0.0	0.0	**1.0**	2.5	0.0	0.5	1.0	0.0	0.0	0.0	**4.0**	**4.0**	3.5	0.0	**3.5**	**16.5**	**47.5**	0.0	1.5	1.5	0.5	2.5	2.0	1.0	7.0	**16.0**
Core S6																															
IS1	1	13.0	12.0	**25.0**	0.0	0.0	0.0	**0.0**	0.0	0.0	0.0	0.0	0.0	0.0	1.5	**1.5**	**15.0**	0.0	1.0	**1.0**	**2.0**	**47.0**	4.5	0.0	0.0	0.0	0.5	0.0		3.5	**8.5**
T1 (10)	10	2.5	13.0	**15.5**	1.0	0.0	0.0	**1.0**	0.5	0.0	0.0	2.5	0.0	0.0	1.5	**4.5**	**6.5**	0.0	2.0	**2.0**	**2.0**	**48.5**	10.0	0.0	0.0	0.0	3.0	0.0		5.5	**18.5**
	20	5.5	15.0	**20.5**	0.0	0.0	0.0	**0.0**	0.5	0.0	0.0	0.0	0.0	0.0	3.0	**3.5**	**5.5**	0.0	0.5	**0.5**	**8.0**	**47.0**	8.0	0.0	0.0	0.0	0.5	0.0		6.5	**15.0**
	30	3.5	10.5	**14.0**	0.0	0.0	0.0	**0.0**	1.0	0.0	0.5	1.5	1.5	0.0	2.0	**6.5**	**7.5**	0.0	0.5	**0.5**	**10.5**	**50.5**	6.5	0.0	0.0	0.0	0.0	0.0		3.5	**10.0**
	40	2.5	9.0	**11.5**	0.0	1.5	0.0	**1.5**	0.0	0.0	0.5	0.0	0.5	0.0	2.0	**3.0**	**12.0**	0.0	1.0	**1.0**	**7.0**	**50.0**	8.5	0.0	0.0	0.0	0.5	0.0		3.0	**12.0**
	50	4.0	5.0	**9.0**	0.0	1.0	0.0	**1.0**	0.0	0.0	0.0	0.0	0.5	0.0	1.5	**2.0**	**14.5**	0.0	2.0	**2.0**	**11.0**	**47.0**	6.0	0.0	0.0	0.0	1.5	0.0		5.5	**13.0**
	60	3.5	5.5	**9.0**	0.0	0.0	0.0	**0.0**	0.5	0.0	0.0	0.5	0.0	0.0	1.0	**2.0**	**13.5**	0.0	0.0	**0.0**	**2.0**	**62.0**	6.0	1.5	0.5	0.0	0.0	0.5		2.0	**10.5**
	70	6.5	9.5	**16.0**	0.0	0.5	0.0	**0.5**	1.5	0.0	0.0	0.0	2.0	0.0	3.5	**7.0**	**19.0**	0.0	0.0	**0.0**	**3.0**	**44.0**	7.0	1.5	0.5	0.5	0.0	0.5		0.5	**10.5**
	80	3.5	13.0	**16.5**	0.0	1.0	0.0	**1.0**	1.5	0.0	0.5	1.0	0.0	0.5	2.0	**5.5**	**17.5**	0.0	0.0	**0.0**	**1.0**	**39.5**	8.0	2.0	5.0	0.5	0.5	5.0		7.5	**28.5**
T2 (86)	86	2.5	3.5	**6.0**	3.0	4.5	0.5	**8.0**	3.5	0.5	3.0	3.5	0.0	2.5	4.0	**17.0**	**7.5**	0.0	6.0	**6.0**	**3.0**	**27.5**	3.0	13.0	5.0	1.5	0.5	5.0		4.5	**32.5**
	90	4.0	12.0	**16.0**	0.0	0.0	0.0	**0.0**	0.0	0.0	0.0	1.0	0.0	1.0	3.5	**5.5**	**12.5**	0.0	3.5	**3.5**	**3.5**	**38.5**	11.5	2.0	0.6	0.5	0.0	0.5		5.0	**20.1**
	100	1.5	2.0	**3.5**	0.0	0.0	0.5	**0.5**	0.0	0.5	0.0	0.0	0.0	1.0	1.5	**3.0**	**14.5**	0.0	3.0	**3.0**	**36.0**	**24.0**	2.5	1.5	2.0	0.0	1.5	2.0		6.0	**15.5**
	110	1.5	1.0	**2.5**	0.0	3.0	1.0	**4.0**	0.5	0.0	0.0	0.0	0.5	0.0	3.5	**4.5**	**9.5**	0.0	6.5	**6.5**	**26.5**	**23.0**	2.5	11.0	1.5	2.0	1.0	1.5		3.0	**22.5**
	120	2.5	0.0	**2.5**	0.0	2.0	0.0	**2.0**	0.5	0.0	0.0	0.0	0.0	0.0	1.5	**2.0**	**18.0**	0.0	6.5	**6.5**	**19.5**	**31.5**	3.0	4.5	15.0	1.0	0.5	15.0		4.5	**43.5**
	130	0.5	0.5	**1.0**	0.0	0.5	0.0	**0.5**	1.5	0.0	0.0	0.0	0.0	0.0	0.0	**1.5**	**15.0**	0.0	10.0	**10.0**	**35.0**	**25.0**	0.0	2.0	2.3	0.0	0.0	2.3		4.0	**10.5**
T3 (200)	200	0.5	5.0	**5.5**	0.5	2.0	0.0	**2.5**	1.0	0.0	0.0	1.5	0.5	2.0	0.5	**5.5**	**7.0**	0.0	7.0	**7.0**	**31.5**	**28.5**	2.0	2.0	0.5	2.5	1.0	0.5		2.5	**11.0**

all values in percent, max. abs. error of pointcounting = ± 3.5%; T = turbidite

Appendix 6: Component distribution (pointcounting)

Isotope stage / position of calciturbidites (cm)	Depth (cm)	pteropods	plankt.foram	**1. Plankton**	corallinacean	scleractinian	encrusters	**2. Reef builders**	peloids	compound grains	coated grains	algae	echinoderms	large benthics	molluscs	**3. Shallow-water grains**	**4. Bioclasts**	carbonate-clasts	intra-clasts	**5. Lithoclasts**	**6. Terrigenous input**	**7. Matrix**	intra-porosity	inter-porosity	plant remains	bryozoan	small benthics	pyrite+ore	glauconite	undetermined	**8. Others**
IS2	250	2.0	1.0	**3.0**	0.5	2.5	0.0	**3.0**	2.0	0.0	0.0	0.5	1.5	1.0	4.0	**9.0**	**12.5**	1.5	3.5	**5.0**	**24.5**	**24.5**	2.5	2.5	2.5	0.5	0.0	2.5		3.0	**13.5**
IS3	270	2.5	2.0	**4.5**	0.0	2.5	0.0	**2.5**	2.5	0.0	0.5	0.5	0.5	0.0	1.5	**5.5**	**9.0**	2.5	1.5	**4.0**	**19.5**	**37.5**	0.5	0.5	3.3	1.0	0.0	3.3		5.5	**14.0**
T4	280	3.0	6.0	**9.0**	3.0	16.5	0.0	**19.5**	3.0	0.5	3.0	0.5	1.5	0.5	5.5	**14.5**	**11.5**	1.0	2.0	**3.0**	**14.0**	**12.0**	2.5	8.0	5.0	2.5	0.5	5.0		2.0	**25.5**
(280-290)	290	1.5	2.0	**3.5**	0.0	1.0	0.0	**1.0**	0.0	0.0	0.0	0.0	3.0	1.0	3.5	**7.5**	**13.5**	0.0	1.5	**1.5**	**27.0**	**29.0**	2.0	5.0	5.0	4.0	0.0	5.0		3.0	**24.0**
	295	4.5	2.5	**7.0**	0.5	1.5	0.0	**2.0**	0.5	0.0	0.5	0.0	1.0	0.5	2.0	**4.5**	**14.0**	1.5	4.0	**5.5**	**18.0**	**32.0**	3.0	2.5	2.5	0.5	0.0	2.5		4.0	**15.0**
	300	2.0	0.5	**2.5**	4.5	8.0	0.0	**12.5**	1.5	0.0	1.0	3.0	0.5	1.0	3.0	**10.0**	**11.5**	4.5	3.5	**8.0**	**10.5**	**33.0**	0.0	4.0	2.0	1.0	1.0	2.0		2.0	**12.0**
	310	2.5	3.5	**6.0**	1.0	6.0	1.0	**8.0**	3.0	0.5	1.0	1.0	3.0	1.0	5.0	**14.5**	**8.0**	3.5	3.5	**7.0**	**15.5**	**28.5**	0.0	2.5	2.0	0.5	0.5	2.0		2.0	**9.5**
	320	2.5	2.0	**4.5**	1.0	3.0	1.5	**5.5**	2.0	0.5	0.5	2.0	1.0	0.5	2.5	**9.0**	**12.5**	3.0	3.5	**6.5**	**16.0**	**34.0**	0.0	2.0	1.8	0.5	0.5	1.8		3.5	**10.0**
	330	4.5	2.5	**7.0**	1.5	3.5	0.0	**5.0**	2.5	0.5	1.0	0.0	1.0	1.0	4.5	**10.5**	**12.5**	0.0	3.5	**3.5**	**10.5**	**40.0**	2.0	1.0	0.5	1.0	0.5	0.5		3.0	**8.5**
	340	4.5	3.0	**7.5**	1.0	4.5	0.0	**5.5**	1.5	0.0	0.0	1.5	0.0	0.0	5.0	**8.0**	**23.5**	1.5	1.5	**3.0**	**10.5**	**32.0**	3.5	1.0	0.0	0.5	0.0	0.0		2.5	**7.5**
	350	4.0	1.0	**5.0**	0.0	0.0	0.5	**0.5**	2.0	0.0	0.0	0.0	0.0	0.5	1.0	**3.5**	**18.0**	1.5	3.0	**4.5**	**17.5**	**34.0**	5.5	2.5	1.0	2.0	1.0	1.0		3.0	**16.0**
T5	360	1.5	1.5	**3.0**	1.5	4.0	0.5	**6.0**	5.0	0.0	0.5	1.0	0.5	0.5	3.0	**10.5**	**16.0**	0.0	2.5	**2.5**	**13.0**	**35.0**	0.5	2.0	0.6	1.0	2.0	0.5		3.5	**10.1**
(360-390)	370	3.5	4.0	**7.5**	0.0	8.0	1.5	**9.5**	1.5	0.5	1.0	1.5	3.0	1.0	2.5	**11.0**	**17.0**	0.5	1.0	**1.5**	**21.0**	**21.0**	0.5	3.5	2.0	2.0	0.0	15.0		1.5	**24.5**
	380	3.5	1.5	**5.0**	1.5	3.5	0.5	**5.5**	3.0	0.5	0.5	9.5	4.0	0.0	2.5	**20.0**	**11.5**	0.5	3.5	**4.0**	**12.0**	**30.5**	1.0	2.5	0.5	2.0	0.5	5.0		3.5	**15.0**
	390	2.5	4.0	**6.5**	1.0	7.5	0.0	**8.5**	5.0	0.0	0.5	0.5	2.5	1.0	4.0	**13.5**	**18.5**	1.0	0.0	**1.0**	**14.0**	**24.5**	2.5	4.5	2.0	0.5	1.0	0.6		2.5	**13.6**
	400	3.5	3.5	**7.0**	1.0	3.0	1.0	**5.0**	4.0	1.0	1.0	0.5	1.5	2.0	4.5	**14.5**	**15.5**	0.5	1.0	**1.5**	**14.5**	**29.0**	0.5	2.0	1.5	2.0	1.5	1.5		3.5	**12.5**
	410	1.5	1.5	**3.0**	2.5	6.0	0.5	**9.0**	3.5	0.0	0.5	0.5	1.0	1.5	4.5	**11.5**	**13.5**	0.0	5.0	**5.0**	**17.0**	**29.5**	0.5	5.5	0.6	1.5	1.0	0.6		1.5	**11.1**
	420	4.5	4.0	**8.5**	3.0	6.0	1.0	**10.0**	3.5	1.0	1.5	2.0	0.5	1.5	4.0	**14.0**	**14.0**	0.0	1.0	**1.0**	**12.0**	**28.0**	1.0	5.0	0.5	1.5	3.5	0.0		1.0	**12.5**
	430	3.5	3.0	**6.5**	0.5	2.5	0.0	**3.0**	2.0	0.0	0.0	0.0	1.5	1.0	2.5	**7.0**	**16.5**	0.0	2.5	**2.5**	**19.0**	**28.5**	4.0	1.5	3.3	2.0	1.0	3.3		2.0	**17.0**
	440	3.0	3.0	**6.0**	1.5	1.5	0.0	**3.0**	4.0	0.0	1.5	2.5	0.0	1.0	2.0	**11.0**	**11.0**	0.0	3.5	**3.5**	**21.5**	**30.5**	0.5	3.5	2.5	0.5	1.5	1.5		2.5	**12.5**
IS4	450	1.5	2.5	**4.0**	0.0	2.0	0.0	**2.0**	1.0	0.0	0.0	1.5	1.0	0.5	0.5	**4.5**	**14.5**	0.0	2.5	**2.5**	**17.0**	**42.0**	3.0	1.5	2.5	2.0	1.0	1.0		2.5	**13.5**
	460	0.5	2.0	**2.5**	0.0	0.5	0.0	**0.5**	2.0	0.0	0.0	0.5	0.0	1.0	2.0	**5.5**	**11.5**	0.0	0.5	**0.5**	**8.5**	**60.0**	0.5	0.0	4.3	1.0	0.0	0.6		4.0	**10.3**
	470	1.0	2.5	**3.5**	2.0	2.5	0.0	**4.5**	3.0	0.0	0.5	3.5	0.0	2.5	2.0	**11.5**	**14.0**	0.0	3.0	**3.0**	**7.0**	**40.5**	0.5	3.0	2.8	1.5	1.0	5.0		5.0	**18.8**

all values in percent, max. abs. error of pointcounting = ± 3.5%; T = turbidite